

Complex processes in simple ices

Laboratory and observational studies of
gas-grain interactions during star formation

PROEFSCHRIFT

ter verkrijging van
de graad van Doctor aan de Universiteit Leiden,
op gezag van de Rector Magnificus prof. mr. P. F. van der Heijden,
volgens besluit van het College voor Promoties
te verdedigen op woensdag 16 september 2009
klokke 15.00 uur

door

Karin Ingegerd Öberg
geboren te Nyköping, Zweden
in 1982

PROMOTIECOMMISSIE

Promotores: Prof. dr. E. F. van Dishoeck
Prof. dr. H. V. J. Linnartz

Overige leden: Prof. dr. A. G. G. M. Tielens
Prof. dr. E. Bergin (University of Michigan)
Prof. dr. Th. Henning (Max-Planck-Institut für Astronomie)
Prof. dr. E. Herbst (Ohio State University)
Prof. dr. K. Kuijken

Till Pappa och Mamma

ma li elementi che tu hai nomati
e quelle cose che di lor si fanno
da creata vertu' sono informati.

Creata fu la materia ch'elli hanno;
creata fu la vertu' informante
in queste stelle che 'ntorno a lor vanno

ma vostra vita senza mezzo spira
la somma beninanza, e la innamora
di se' si' che poi sempre la disira.

La Divina Commedia di Dante: Paradiso, Canto VII
lines 85–90, 94–96

TABLE OF CONTENTS

1	INTRODUCTION	1
1.1	The first molecule	2
1.2	Stellar birth, life and death	3
1.3	Ices in star forming regions	6
1.3.1	Ice observations and infrared spectroscopy	6
1.3.2	The first ices	9
1.3.3	A complex ice chemistry?	11
1.3.4	Observations of evaporated ices in the gas phase	12
1.4	Ices in the laboratory	13
1.4.1	The need for laboratory experiments	13
1.4.2	Spectroscopy of astrophysical ice equivalents	14
1.4.3	Ice dynamics – mixing, segregation and desorption	16
1.4.4	Ice chemistry	18
1.4.5	CRYOPAD	19
1.5	This thesis	20
1.6	Summary of main discoveries	24
2	THE <i>c2d</i> SPITZER LEGACY: ICE FORMATION IN STAR-FORMING REGIONS	25
2.1	Introduction	26
2.2	Observations and spectral analysis	29
2.3	Results	32
2.3.1	Abundance variations of different ices	32
2.3.2	Protostars versus background stars	37
2.3.3	Heating (in)dependencies	37
2.3.4	Ice maps of the Oph-F core	38
2.3.5	XCN ice abundance correlations	40
2.3.6	Principal component analysis and ice abundance correlations	41
2.4	Discussion	43
2.4.1	The XCN feature and other unidentified ice bands	44
2.4.2	Early versus late ice formation during low-mass star formation	46
2.4.3	Ice formation in low-mass versus high-mass protostars	48
2.5	Conclusions	49
3	THE <i>c2d</i> SPITZER SPECTROSCOPIC SURVEY OF CH₄ ICE AROUND LOW-MASS YOUNG STELLAR OBJECTS	51
3.1	Introduction	52
3.2	Source sample selection, observations and data reduction	53
3.3	Results	56

3.3.1	CH ₄ column densities	56
3.3.2	Upper limits of solid CH ₄	60
3.3.3	Molecular correlations	61
3.3.4	Spatial trends	63
3.4	Discussion	64
3.4.1	Low vs. high mass YSOs	64
3.4.2	Formation scenarios	65
3.4.3	Differences between clouds	66
3.4.4	Comparison with models	66
3.5	Conclusions	66
4	EFFECTS OF CO₂ ON H₂O BAND PROFILES AND BAND STRENGTHS IN MIXED H₂O:CO₂ ICES	69
4.1	Introduction	70
4.1.1	Previous laboratory data	71
4.2	Experiment and data analysis	72
4.2.1	Experiment	72
4.2.2	Data analysis	73
4.3	Results	76
4.3.1	Changes in H ₂ O band strengths and profiles with mixture composition	76
4.3.2	Temperature dependence	79
4.3.3	Dependence on additional parameters: deposition temperature and ice thickness	82
4.4	Discussion	83
4.4.1	Ice structure	83
4.4.2	Astrophysical implications	87
4.5	Conclusions	90
5	QUANTIFICATION OF SEGREGATION DYNAMICS IN ICE MIXTURES	93
5.1	Introduction	94
5.2	Experiments	96
5.3	Monte Carlo simulations	97
5.4	Results and analysis	101
5.4.1	UHV CO ₂ ice mixture experiments	101
5.4.2	HV CO ₂ ice mixture experiments	107
5.4.3	UHV CO ice mixture experiments	108
5.4.4	Monte Carlo simulations	110
5.5	Discussion	111
5.5.1	Comparison with previous experiments	112
5.5.2	Segregation mechanisms	113
5.5.3	Astrophysical implications	114
5.6	Conclusions	116

6	ENTRAPMENT AND DESORPTION OF VOLATILE SPECIES DURING WARM-UP OF ICE MIXTURES	117
6.1	Introduction	118
6.2	A modified three-phase desorption model	120
6.3	TPD experiments	122
6.4	Results	123
6.4.1	Experimental TPD curves of binary ice mixtures	123
6.4.2	Simulations of binary ice mixtures	126
6.4.3	Tertiary ice mixtures	128
6.5	Discussion	128
6.5.1	Desorption from ice mixtures	128
6.5.2	The three-phase desorption model	130
6.5.3	Astrophysical implications	130
6.5.4	Future development – towards a four-phase model	132
6.6	Conclusions	132
7	PHOTODESORPTION OF CO ICE	135
7.1	Introduction	136
7.2	Experiments	137
7.3	Results	139
7.4	Discussion	140
7.4.1	Photodesorption mechanism	140
7.4.2	Astrophysical implications	141
8	PHOTODESORPTION OF CO, N₂ AND CO₂ ICES	143
8.1	Introduction	144
8.2	Experiments and their analysis	145
8.2.1	Experimental details	145
8.2.2	Data analysis	146
8.3	Results	150
8.3.1	CO and N ₂	150
8.3.2	CO ₂	153
8.4	Discussion	161
8.4.1	CO and N ₂ yields and mechanisms	161
8.4.2	The CO ₂ yield and mechanism	162
8.4.3	Astrophysical significance	164
8.5	Conclusions	168
9	PHOTODESORPTION OF H₂O AND D₂O ICES	169
9.1	Introduction	170
9.2	Experiments and data analysis	172
9.2.1	Experiments	172
9.2.2	Data Analysis	174
9.3	Results	175
9.3.1	The photodesorption process and products	175

9.3.2	Yield dependencies on temperature, fluence, ice thickness, flux and isotope	177
9.4	Discussion	181
9.4.1	The H ₂ O photodesorption mechanism	181
9.4.2	Comparison with previous experiments	183
9.4.3	Astrophysical consequences	183
9.5	Conclusions	186
10	FORMATION RATES OF COMPLEX ORGANICS IN UV IRRADIATED CH₃OH-RICH ICES	189
10.1	Introduction	190
10.2	Experiments and analysis	192
10.3	Experimental results	196
10.3.1	The CH ₃ OH UV photolysis cross-section	197
10.3.2	CH ₃ OH photodesorption yields	198
10.3.3	Dependence of photo-product spectra on experimental variables	199
10.3.4	Reference RAIR spectra and TPD experiments of pure complex ices	205
10.3.5	Identification of CH ₃ OH ice UV photoproducts	208
10.3.6	Abundance determinations of photoproducts	216
10.3.7	Ice formation and destruction during warm-up following irradiation	221
10.3.8	Dependence of ice products on physical conditions	223
10.4	Discussion	225
10.4.1	Comparison with previous experiments	225
10.4.2	Dependence of complex chemistry on experimental variables	226
10.4.3	A CH ₃ OH photochemistry reaction scheme	227
10.4.4	CH ₃ OH photo-dissociation branching ratios	229
10.4.5	Diffusion of radicals	231
10.5	Astrophysical implications	231
10.5.1	Potential importance of photochemistry around protostars	231
10.5.2	Abundance ratios as formation condition diagnostics	232
10.5.3	Comparison with astrophysical sources	234
10.6	Conclusions	236
10.7	Appendix	238
10.7.1	Photoproduct growth curves during UV-irradiation	238
10.7.2	Formation and destruction curves during warm-up	240
10.7.3	Formation rate parameters	241
11	PHOTOCHEMISTRY IN H₂O:CO₂:NH₃:CH₄ ICE MIXTURES	251
11.1	Introduction	252
11.2	Experimental	255
11.3	Photochemistry in pure ices and binary ice mixtures	256
11.3.1	CH ₄ , NH ₃ and CH ₄ :NH ₃ ice photolysis	257
11.3.2	CH ₄ :H ₂ O ice mixture photolysis	260

11.3.3	Pure CO ₂ and CH ₄ :CO ₂ ice photolysis	262
11.3.4	CO ₂ :NH ₃ ice mixture photolysis	264
11.3.5	The effect of H ₂ O at different concentrations	265
11.3.6	NH ₃ ice photodesorption	268
11.3.7	NH ₃ and CH ₄ photodestruction	269
11.4	Testing complex ice formation in astrophysical ice equivalents	272
11.4.1	Quantification of photolysis through RAIRS	273
11.4.2	TPD experiments	275
11.5	Discussion	280
11.5.1	Importance of acid-base chemistry in NH ₃ :X ice mixtures	280
11.5.2	Photodissociation branching ratios	281
11.5.3	Radical diffusion: dependence on H ₂ O content	281
11.5.4	Radical-radical versus radical-molecule reactions	281
11.5.5	Routes to complex organics in space	282
11.5.6	Future experiments	283
11.6	Conclusions	283
12	COLD GAS AS AN ICE DIAGNOSTIC TOWARDS LOW MASS PROTOSTARS	285
12.1	Introduction	286
12.2	Source selection	287
12.3	Observations	288
12.4	Results	288
12.5	Discussion	292
	BIBLIOGRAPHY	295
	NEDERLANDSE SAMENVATTING	305
	CURRICULUM VITAE	313
	AFTERWORD	317

1 INTRODUCTION

The chemistry and physics of the universe have been intertwined ever since molecules first appeared during the Dark Ages. Observations of molecules are therefore effective probes of physical processes in space, but astrochemistry is more than a means to a physics end. During star- and planet-formation the chemistry must evolve from atoms and ions to organic acids and sugars; astrochemistry sets the stage for the origin of life at the ever increasing number of exo-planets.

This chemical evolution depends on the presence of dust grains in the interstellar medium and on the icy layers that form around them. Ices form rapidly during the different stages of star formation through condensation of gas onto cold grains and through an active grain chemistry. In interstellar clouds, the birth places of stars, this results in an ice mixture with simple components: H_2O , CO_2 , CO , CH_3OH , NH_3 and CH_4 .

Ices around protostar do not remain simple for long. Heat and UV from the newborn star both evaporate ices back into the gas phase and open up reaction pathways towards a complex organic chemistry in the ice phase. The grain-gas interactions – freeze-out, quiescent ice reactions and the ice processing due to energy input from the new star – can be investigated in the laboratory in vacuum chambers that simulate the situation in space. This is a crucial compliment to astrophysical observations which under most circumstances only provide snapshots of the ongoing chemistry towards different objects.

The thesis aims to combine quantitative laboratory simulations with ice and gas observations to map out key gas-grain processes during star formation, and thus the chemical evolution from dark clouds to comets. The investigations rely on knowledge of the physics of low-mass star formation, which directs the chemistry, and on previous developments of observational and laboratory techniques to study ices. The following pages introduce these pre-requisites together with the current understanding of astrophysically important ice processes. The origin of chemistry goes further back than the first star formation event, however, and this dark age is the topic of the first section.

1.1 The first molecule

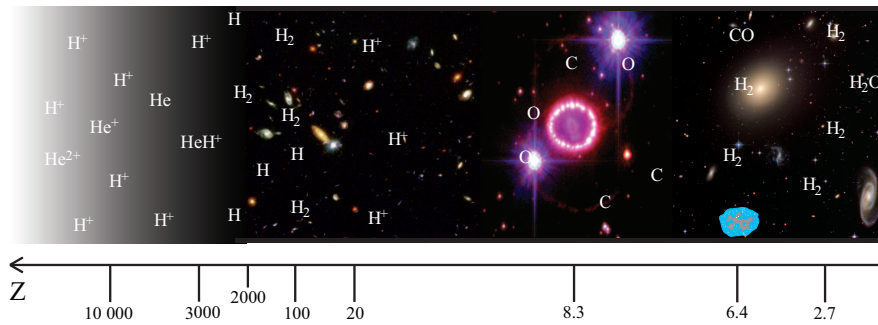


Figure 1.1 – The chemical evolution of the universe between $z=10,000$ and 0 showing the formation of the first molecules at $z \sim 3000$, the enhanced H_2 formation at $z \sim 100$, the formation of the first stars at $z \sim 20$ represented by a Hubble Deep Field image, the formation of heavier elements as the first stars explode in supernova-like events, the appearance of the first dust, and the potential ice formation and the definite CO , H_2 and H_2O formation in the more evolved universe. The astronomical images in the montage are Hubble observations credit Robert Williams and the Hubble Deep Field Team (STScI), P. Challis and R. Kirshner (Harvard-Smithsonian Center for Astrophysics), The Hubble Heritage Team (STScI/AURA) and ESA and NASA.

Fourteen billion years ago, the Big Bang created the universe hot, dense and filled with radiation – too hot for even the elements of atoms, such as protons, to exist at any length. As the universe expanded the energy spread out and the temperature decreased. After the first second of the Universe’s existence, it had already cooled enough for protons (hydrogen nuclei), neutrons and electrons to form and remain intact. 200 seconds later the temperature was ‘only’ a billion degrees, cool enough for protons and neutrons to combine to form helium, deuterium, beryllium and lithium nuclei. With further expansion and cool-down the nucleosynthesis stopped. Still the radiation field was too intense for atoms; a capture by a nucleus of an electron was immediately followed by photoionization, i.e. the stripping of electrons following the absorption of a high-energy photon. This continued for another 400 000 years, while the universe expanded, grew colder and grew darker (Dalgarno 2006).

Around this time, at a redshift¹ $z < 10000$, the photons had become scarce enough for atom-electron recombination to become significant, though it would take until $z < 2000$ for the Universe to become predominantly neutral (Galli & Palla 1998; Seager et al.

¹The redshift is produced by the Doppler effect from the expansion of the Universe. The higher the redshift of the observed light, the farther away and further back in time is its origin. For a matter dominated universe, $t = 14 \times 10^9 / (1 + z)^{3/2}$ years, where z is the redshift and t the age of the Universe when the light was emitted.

2000). This recombination of nuclei and electrons proceeded sequentially dependent on the ionization energies of the species; Helium was the first neutral species. The lack of photons during the next period in the Universe's history has provided the name of the epoch, the Dark Ages; its hospitality to neutral species meant the dawn of chemistry.

At a redshift $z \sim 3000$, He and H^+ (or He^+) radiatively associated to form the Universe's first molecular compound HeH^+ (He_2^+) (Galli & Palla 1998; Lepp et al. 2002). It took another $z = 1000$ before the first neutral molecule, H_2 , formed (Fig. 1.1). H_2 is still the most common molecule today though its dominant formation path has changed radically over the ages. At $z > 100$ H_2 formed from $H^+ + H$ radiative association, followed by H_2^+ charge transfer with H. Around $z = 100$ a new more efficient formation channel became available, associative detachment of H^- and H. Both these processes are very inefficient compared to the predominant formation mechanism today, which is H recombination on grain surfaces. Two H atoms cannot simply recombine in the gas phase. With no third body available, the energy released from the atoms binding together can only be irradiated away and this is extremely slow compared with the probability of the two atoms flying apart again because H_2 has no dipole moment.

Grain formation, and thus efficient H_2 formation, requires C, O and Si and this only became available after the birth and death of the first stars at $z \sim 15$. The collapse of gas into these first, giant stars ended the Dark Ages and the Universe was re-ionized by the starlight. Nucleosynthesis inside the stars turned hydrogen into carbon and oxygen and other heavier species. Many stars in this era ended in violent explosions – the most distant discovered is at $z = 8.3$ (Tanvir et al. 2009) – and thus ejected the new elements into the interstellar medium, dramatically changing the chemical conditions. Observations of probable dust continuum emission towards quasars at $z = 6.4$ indicate that these novae were efficient producers of small dust grains (Bertoldi et al. 2003). When protected from radiation, the grains are cold surfaces on which gas phase atoms and molecules condense to form icy layers and there is tentative evidence of ice formation already at this early epoch of the Universe (Dudley et al. 2008).

This enrichment of the interstellar medium with heavy atoms and dust grains continued for the next billions of years and is still continuing today. The organic chemistry observed here on Earth, on other bodies in our solar system, around new-born stars and in distant galaxies all has its origin in these blasts, which began when the Universe was only a little more than a billion years old.

1.2 Stellar birth, life and death

While the first stars are still somewhat of a mystery, the life cycle of stars such as our own is fairly well understood (Fig. 1.2). Except for dust particles and large molecules, most molecular compounds are easily destroyed when exposed to UV irradiation, which is universally present in the interstellar medium. Therefore the chemistry has to start over in each stellar cycle, which begins with the formation of an over-dense region, a cloud, consisting of gas and dust, both primordial H and He, and heavier elements produced in the previous stellar life cycles. These clouds contain enough matter to absorb some or all

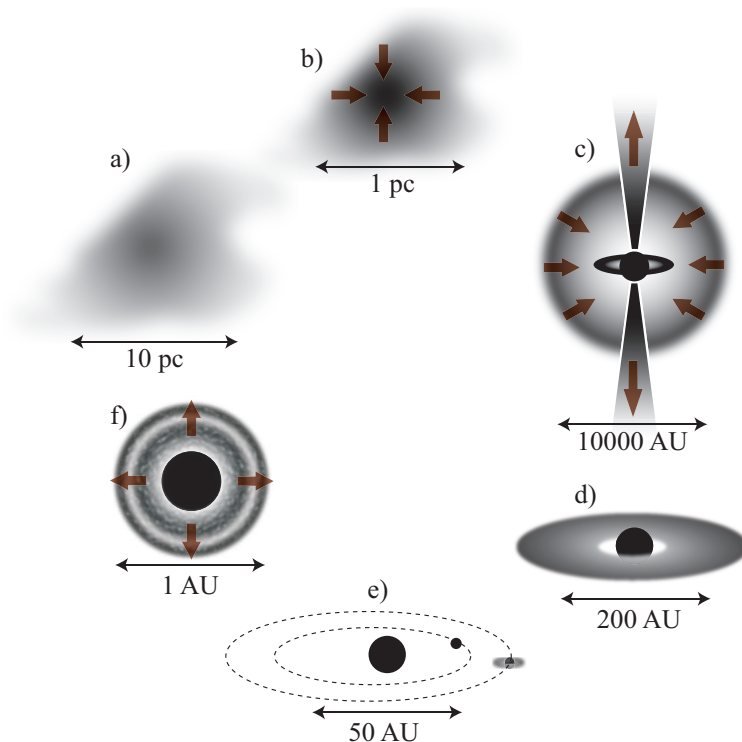


Figure 1.2 – The stellar life cycle from a) diffuse clouds to f) star death. The dense cloud (b) contains cores which collapse under their own gravity to form a protostar (c), which is still embedded in cloud material. As the cloud disperses, the pre-main sequence star and an accompanying disk are exposed (d). With time the disk material is incorporated into planets or dispersed resulting in a main sequence star with a planetary system (e). When the star dies, stellar winds and novae drive newly formed elements and dust grains back into the diffuse interstellar medium (f). The length scales for each stage are order of magnitude estimates.

of the interstellar UV light and thus protect molecules from destruction.

The most tenuous clouds, so called diffuse ones, are still harsh environments where molecules are continuously destroyed by UV light. The rich molecular inventory of such clouds discovered first in the 30s, through spectroscopic detections of CN, CH and CH⁺, came therefore as somewhat of a surprise (Snow & McCall 2006, for a review). Now it is well established that molecules of all sizes are present in these clouds including H₂, CO, carbon chains and H₂CO. Their presence despite the strong UV field implies efficient formation mechanisms. For most molecules ion-neutral reactions in the gas phase are fast enough to explain the observed abundances. Other molecules, especially H₂, require a grain reaction pathway.

The tenuous clouds can be compacted through a range of events, including colliding

diffuse cloud streams, and energy input from stellar winds and supernovae (Vázquez-Semadeni et al. 2003). The result is a dense, gravitationally bound cloud, whose interior is completely protected from external UV rays. The dense clouds are thus cold (~ 10 K) and molecules dominate the chemistry. The high densities and low temperatures result in rapid accretion of gas-phase molecules onto grain-surfaces, forming ices (van Dishoeck & Blake 1998, for a review). These grains are also active chemical sites, which is discussed further in §1.3.

Molecular clouds contain even denser core regions, which are the birth places of solar-type stars. The density of the cores is higher than 10^5 molecules cm^{-3} , which can be compared to molecular cloud densities of 10^3 – 10^4 molecules cm^{-3} and diffuse cloud densities of 1 – 10^2 molecules cm^{-3} , and to the atmosphere on earth with $> 10^{19}$ molecules cm^{-3} . If the core's density is high enough to induce a collapse under its own gravity it is termed pre-stellar, i.e., it will eventually form a star. This collapse releases a large amount of energy, which threatens to stop the collapse through the increased pressure building up from the heated gas. The presence of molecules prevents this from happening. Molecules are efficient coolants; they can be thermally excited through collisions at a range of temperatures, and then irradiate the energy at specific wavelengths. Some of the discrete radiation escapes from the core and thus carries away energy.

During the collapse, the protostar starts to release angular momentum through large outflows and through the formation of a dense disk, which continues to accrete material onto the protostar (Bachiller 1996; Jørgensen et al. 2005). Because of the high density of the disk ($< 10^6$ cm^{-3}), grains coagulate, forming larger and larger boulders, and eventually planets (Dullemond & Dominik 2005; Johansen et al. 2007). This process continues after the now pre-main sequence star has dispersed the last surrounding cloud material. The large number of discovered exo-planets (353 as this thesis goes into print) shows that the production of planets in such disks is quite efficient. The protoplanetary disk is less protected than the protostellar envelope and has a surface layer where the chemistry is dominated by UV radiation and heat from the protostar. Deeper in ices may still survive and continue to affect the chemistry actively (Chiang & Goldreich 1997). The composition of comets, which formed in the disk, suggests that at least some of the ice is pre-stellar in origin (Bockelée-Morvan et al. 2000).

Eventually the disk is cleared of gas by irradiation and winds from the star and by the gravitational pull of the young star and of planets. For the next billions of years most of the interesting chemistry in the solar system will take place in comets, and on planets and moons. As the star closes in on its end, its outer atmosphere becomes a production factory of dust particles and other complex molecules and aggregates of molecules, just as it did in the earlier generations. These particles and macromolecules are fed back into the diffuse interstellar medium and the process starts over, though more enriched in heavy elements than last time around.

This is the life cycle for solar-type stars and for low-mass stars in general. High-mass star formation probably shares some of the same processes, but their exact evolution from giant molecular clouds to stars is still contested. All types of star formation are however accompanied by a rich chemistry which evolves with the physical environment, dependent on changes in the density structure, temperature, availability of surfaces, UV

light flux and other energy fluxes. Molecular and atomic spectra are used routinely to probe the physical processes described in this section – it is often the most efficient means to investigate astrophysical processes, especially during the heavily obscured stages of star formation. Molecular and atomic abundances also affect their physical environment through for example cooling, as described above. This coupling between the chemistry and physics implies that understanding the chemical processes in space is important for most branches of astrophysics. The remainder of this introduction and this thesis both focus, however, on the understanding of astrochemistry for its own sake and how investigating gas-grain interactions provides crucial clues to how the chemistry evolved from dense molecular clouds to solar systems such as our own.

1.3 Ices in star forming regions

The presence of ices in general and water ice in particular in the interstellar medium was first proposed in the astrophysical literature by Eddington (1937), building on the argument that the obscuring clouds between stars had protected interiors, where water molecules could aggregate together to form small ice particles. This was 23 years after the discovery of the first interstellar absorption line (Hartmann 1904), and just prior to the first identification of an interstellar molecular species (Swings & Rosenfeld 1937). Eddington was right: ice is present in space. When progressing from diffuse regions to dense clouds, water (H_2O) ice is the first ice to form and it is the most common ice species throughout the molecular cloud in all but a few sources (Bergin et al. 2005; Sonnentrucker et al. 2008), closely followed by carbon dioxide (CO_2) and carbon monoxide (CO). Observations of ices and their implications for how the first ices form, how they are destroyed and how they react into more complex ones are the topics of this section and of Fig. 1.3.

1.3.1 Ice observations and infrared spectroscopy

Water ice was first detected in the 1970s. Shortly afterwards ices of different kinds were determined to be a common constituent of molecular clouds. (Gillett & Forrest 1973; Merrill et al. 1976). Over the years H_2O , CO_2 , CO , CH_3OH , NH_3 and CH_4 ice have all been observed, and some of their abundances have been established in a range of astrophysical environments, including the inner and outer regions of dense molecular clouds, protostellar envelopes and protoplanetary disks (Knez et al. 2005; Gibb et al. 2004; Boogert et al. 2008; Pontoppidan et al. 2005, and Chapter 2–3 of this thesis). These ices reside on the surfaces of (sub-)micron-sized dust particles, whose composition, origin and evolution are treated in detail by Whittet (1992).

Identification and abundance determinations of ices rely on infrared absorption spectroscopy, i.e., the different absorption patterns of different ice species superimposed on a background continuum light source, such as a protostar. The frequency of light that is absorbed by a certain molecule depends on the molecular motions that can be excited. When free-floating, molecules have degrees of freedom corresponding to translation, rotations and vibrations, and to electronic transitions. In an ice, the molecules are immobilized.

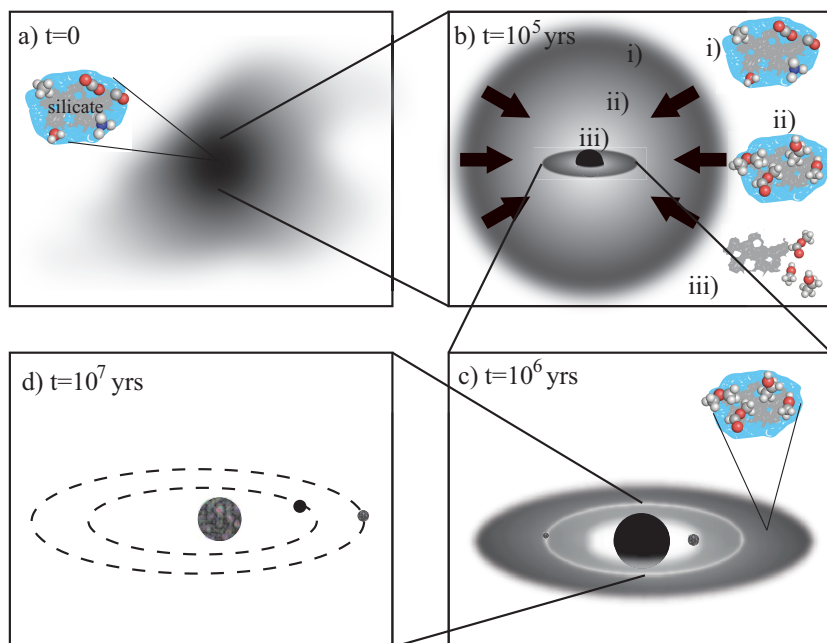


Figure 1.3 – The proposed ice evolution during star and planet formation starting with simple ice formation in dark clouds and cloud cores (a). Heat and UV from the protostar may result in a more complex ice mixture (b.ii), which evaporates close to the protostar (b.iii). Some of this ice becomes incorporated in the protoplanetary disk instead (c), and further into comets and planets (d).

Thus there is no translation nor any rotations. The molecule still vibrates, however, and these vibrations are excited by the absorption of infrared radiation.

In the gas phase these vibrationally excited states can be populated thermally as well, through collisions between molecules. This is not possible for ices, since the required temperatures exceed the evaporation temperatures of all common ices. Thus only infrared absorption spectroscopy of ices is possible – far-infrared transitions due to hindered rotational transitions can be populated thermally for the less volatile ices and H₂O ice has been observed in emission at these wavelengths (Molinari et al. 1999). In general, the investigation of ices in space is restricted to specific lines of sight, since background sources with strong infrared continua are rare, except for protostars. Therefore ices around protostars are among the most well studied, while less is known about ices in the densest cloud cores before the onset of star formation.

Figure 1.4 shows the infrared spectrum towards a protostar with several of the identified ice species marked out. Spectra of molecular clouds and towards circum-stellar disks share most of the spectral features found towards protostars, with clear detections of H₂O, CO₂ and CO ice and a deep silicate feature at 10 μ m from the grain cores them-

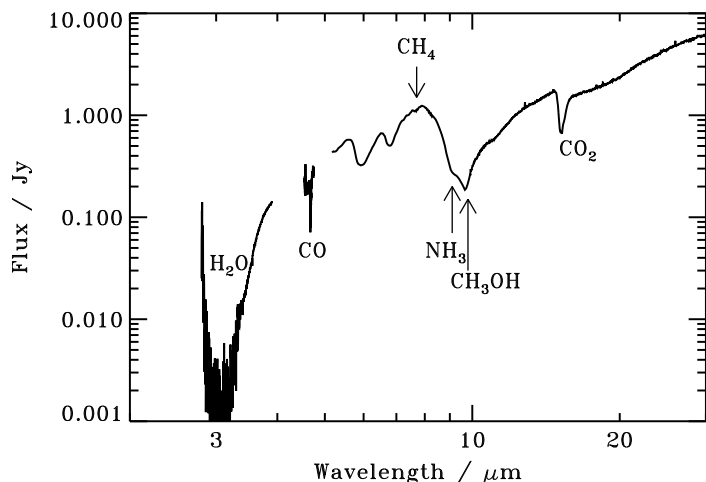


Figure 1.4 – Ice spectrum towards the low-mass protostar HH 46, which has been published by Boogert et al. (2004b), together with some peak assignments.

selves (Knez et al. 2005; Pontoppidan et al. 2005). The ice composition thus seems only marginally affected by the transition between these different evolutionary stages of low-mass star formation, suggesting that most of the ice forms already in the molecular cloud. This is supported by mapping of ice absorptions toward molecular clouds, which shows that once a certain distance threshold into the cloud is overcome, the water ice abundance is linearly correlated with the cloud material, i.e. it forms before the cloud core stage is reached. Some of the carbon dioxide ice is also observed towards the cloud edges. In contrast to water ice, it increases somewhat in abundance further into the cloud core. This second growth seems dependent on a catastrophic freeze-out of CO ice, which only happens in the cloud core itself (Pontoppidan 2006). These observations then imply a structured ice mantle with a layer of H₂O-rich ice directly on the grain core and a second layer of CO-rich ice on top.

This scenario is consistent with the observed ice spectra. The CO₂ ice absorption features have been compared with laboratory spectra (§1.4.2) and are best explained by CO₂ present in two separate ice environments: a H₂O-rich and CO-rich one. CO ice is observed to be mostly pure except for a small part mixed with CO₂. Once the protostar turns on these original ice mixtures are modified through distillation and segregation and pure CO₂ ice becomes common as well (Pontoppidan et al. 2008). These processes are the topic of Chapters 5–6, while the formation conditions of different ices during star formation is investigated through statistical analysis of a large sample of protostars with ice observations in Chapter 2.

The observations in Chapter 2 and 3 were mainly acquired with the *Spitzer Space Telescope*. Some infrared observations are possible through spectral windows in the atmosphere of the earth. Only space-born telescopes gives access to the entire infrared spectral region and *Spitzer* was the first space-born telescope with high enough sensitivity to carry out ice observations towards low-mass protostars. This has dramatically

increased the number of ice detections and thus our understanding of how the first ices form.

1.3.2 The first ices

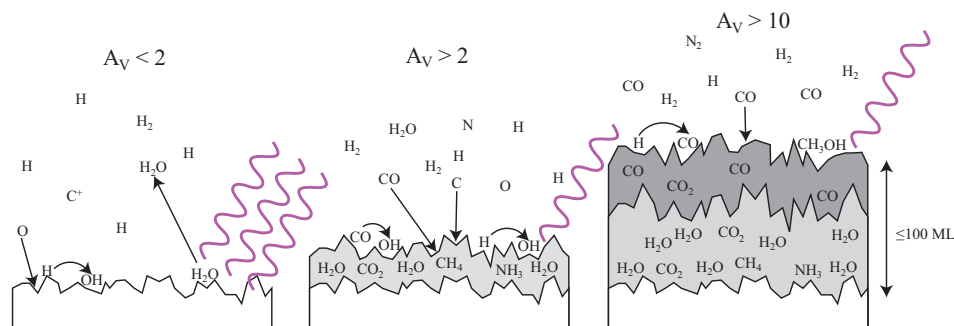


Figure 1.5 – The proposed ice evolution in molecular clouds before the onset of star formation resulting in a layered ice structure.

From observations, ices thus first appear in dense molecular clouds. The observations described above have shown that even there ice formation is not possible up to the edges of the clouds where the irradiation field is strong. This is not to say that molecules do not form on surfaces in these harsher environments. They do. They also evaporate due to different non-thermal processes, such as UV photodesorption, before an ice layer can be built up (Fig. 1.5).

The proposed formation paths of interstellar ices have changed through the decades as theory, observations and laboratory experiments have become more detailed. When Eddington first proposed the existence of ices in the interstellar medium, he assumed that they could form as in our atmosphere, where gas phase molecules freeze out on macromolecules or on soot particles. This may explain some of the observed ices in molecular clouds, especially CO ice, but for most ices, the gas phase production mechanisms are simply too inefficient to explain the observed abundances. This is especially true for H_2O , CH_3OH and CO_2 .

A decade after Eddington, van de Hulst (1946) first proposed an active ice chemistry where C, O and N atoms condense on particles consisting of dust and ice aggregates and subsequently react with hydrogen to form an ice consisting of H_2O , CH_4 and NH_3 . The hydrogenated atoms should dominate the ice composition since hydrogen is orders of magnitude more abundant than any of the heavier atoms and thus the probability for any specific atom to react with hydrogen far exceeds the probability of it reacting with another C or O atom. This framework of atom-radical reactions on ice or grain surfaces still holds, though the exact reaction schemes have evolved.

This ice formation framework reached a new level of sophistication when Tielens & Hagen (1982) proposed a combined gas and grain chemistry where atoms accrete onto grain surfaces, depending on their gas phase abundances and sticking probabilities. In their model the energy barrier for an atom, molecule or radical to hop around the surface is assumed to be lower than the desorption or evaporation barrier and thus a given atom will hop around the grain for a period of time, whose length depends on the grain temperature. If the atom encounters another atom or radical during its time on the grain, they react, since radical-radical reactions have no activation barriers. At typical molecular cloud temperatures of ~ 10 K, hydrogen atoms will scan the grain surface orders of magnitude faster than the second smallest common atoms, C, N and O. Therefore the formed ice is still predicted to be abundant in hydrogenated atoms, i.e. H_2O , CH_4 and NH_3 . Because of the different transition conditions between the atomic and molecular form for hydrogen and the heavier species, hydrogenation of molecules and oxygenation are important processes as well. CO forms efficiently in the gas phase, and thus CO ice is explained by direct freeze-out of the molecular gas. Hydrogenation of CO produces methanol, while its oxygenation results in CO_2 .

There are few laboratory studies of the proposed grain surface reactions. The hydrogenation of CO to form H_2CO and CH_3OH is an exception. A key experimental result is that in a molecular and atomic mixture of CO and C or N_2O and O, hydrogen atoms react preferentially with the atoms rather than the molecules (Hiraoka et al. 1998). Thus methanol is expected to form at a later stage than methane even if the carbon and carbon monoxide co-exist in the outer parts of molecular clouds. In pure CO ice, hydrogenation to form H_2CO and subsequently CH_3OH seems efficient though absolute rates are still lacking (Watanabe et al. 2003, Fuchs et al. A&A in press).

Combining the model, laboratory experiments and astrophysical observations, the ice chemistry is proposed to proceed as in Fig. 1.5. In the diffuse clouds and at the edges of denser clouds atoms accrete onto the surface for long enough to react with hydrogen. Efficient UV induced desorption (Chapter 7–9) prevents the formed molecule from remaining on the surface long enough to form more than a monolayer of ice (Hollenbach et al. 2009). As the cloud grows denser, or alternatively deeper into an existing cloud, atoms start to convert into molecules in the gas phase since they are now protected from most UV light. This also allows for the build-up of ices. O, C, N and CO accrete onto surfaces, and the atoms are preferentially hydrogenated as predicted by experiments. CO is thus not hydrogenated at this stage, but instead reacts with oxygen, probably in the form of OH, to form CO_2 . As the gas is depleted of C and O atoms and the density increases, CO accretes rapidly onto the surface with only a small portion being turned into CO_2 , while the remainder is either converted to CH_3OH or not reacting at all. Some non-thermal desorption is present deep into the cloud because of direct cosmic ray desorption, cosmic-ray induced UV desorption and desorption due to release of chemical energy (Shen et al. 2004; Garrod et al. 2007).

This figure is however a proposition, not a fact. Chapter 2–3 provides further observational evidence in its support, but the real lack is in laboratory data rather than in ice observations. Without laboratory tests, the relative and absolute efficiencies of these different reactions remain speculative.

A competing scenario is formation of complex molecules through energetic processing of simpler ices, such as CH_3OH , NH_3 and CH_4 . In this scenario cosmic rays and UV photons break apart the existing ices into smaller fragments which subsequently diffuse and recombine into more complex species (Fig. 1.6, taken from §10 shows this for CH_3OH). Energetic processing of ices through both direct cosmic ray bombardment and secondary UV photons are possible during the cold, protected stages of star formation – cosmic rays can penetrate deep into cloud cores and protostellar envelopes, and while externally produced UV rays are rapidly extinguished, cosmic rays produce an internal UV field through interactions with molecular hydrogen.

A few theoretical studies have investigated this route during star formation. Most recently Garrod & Herbst (2006) and Garrod et al. (2008) modeled the formation of complex molecules in ice through radical diffusion and recombination during the slow warm-up of ices in an in-falling protostellar envelope. The increasing temperature towards the protostar (20–100 K) allows for the diffusion of heavier and heavier radicals such as CH_3 and CH_2OH , which recombine to form larger and larger molecules. The model continues until all the ice is evaporated and the resulting gas phase abundances reproduce some of the abundance ratios and temperature structures seen in hot cores around protostars. Improvement of these model predictions is mainly limited by lack of quantitative experimental data on photodissociation branching ratios of simple ices, diffusion barriers of the formed radicals and binding energies of most complex molecules. The experimental quantification of this complex molecule formation route is the goal of Chapters 10 and 11.

1.3.4 Observations of evaporated ices in the gas phase

Ice evaporation is required to explain gas phase observations in cloud cores, at cloud edges and in protostellar envelopes. Thermal evaporation is possible once the protostar has turned on and started to heat up the cloud remnant. It explains the excess gas phase abundances of water and methanol in the inner regions of protostellar envelopes as well as the presence of more complex molecules; the high abundances of these complex species require either an efficient gas phase formation route from thermally desorbed CH_3OH ice or an efficient ice formation pathway followed by evaporation. In general, models predict that thermal evaporation of ices governs the gas phase chemistry during the warmer stages of star formation because of the large amounts of molecules bound up in ices during the preceding colder stages (e.g. Aikawa et al. 2008).

The evaporation temperatures for a number of ices have been investigated experimentally and the determined desorption energies range from the volatile N_2 and CO , desorbing ~ 30 K at laboratory time scales, to H_2O and larger organic molecules, which desorb above 150 K (e.g. Sandford & Allamandola 1988; Fraser et al. 2001; Collings et al. 2004; Öberg et al. 2005) – at astrophysical timescales the desorption temperatures are lower. Because of the large range in evaporation energies, thermal evaporation is expected to proceed sequentially during star formation starting with the most volatile species. Mixed ices may however not segregate completely prior to desorption, resulting in efficient trapping of volatile molecules in the water ice, which is further discussed in §1.4.3 and in Chapters

5–6.

Ices can also desorb non-thermally, through sputtering by particles in shocks, through cosmic ray spot-heating of the ice, through release of chemical energy during bond formation and through UV photodesorption (Shen et al. 2004). The relative importance of these different mechanisms in different astrophysical environments has so far been difficult to assess because of a lack of quantitative experimental data. Observations of excess gas phase water at cloud edges and carbon monoxide and methanol in cloud cores can only be explained by a high efficiency for at least one of the latter three mechanisms (Melnick & Bergin 2005; Garrod et al. 2007; Hollenbach et al. 2009), while dramatic enhancements of e.g. methanol in outflows are explained by grain sputtering, since methanol does not form efficiently through gas phase reactions (Blake et al. 1995; Garrod et al. 2006). Chapters 7–9 are dedicated to the quantification of one of these mechanisms, UV photodesorption of ices.

Thus ice chemistry and ice desorption are crucial to explain several kinds of gas phase observations. The inverse is also true; gas phase observations are crucial to understand the ice evolution inaccessible by infrared ice spectroscopy. While gas phase spectroscopy is possible at a range of frequencies, all of the above observations were carried out at millimeter and sub-millimeter wavelengths to probe pure rotational transitions. Such radio observations allow for investigations of orders of magnitude lower abundances of molecules compared to the infrared. Added to that, peak overlaps are significantly reduced in radio observations compared to infrared ice spectroscopy, facilitating molecular identifications. Thus while CH_3OH is the most complex ice molecule to be securely identified, the three times larger $\text{CH}_3\text{CH}_2\text{CHO}$ has been identified around protostars from its rotational spectra (Belloche et al. 2009). If the grain-gas interaction becomes well understood, rotational spectroscopy of gas phase molecules may provide powerful constraints on the ice evolution during the warm protostellar and disk stages and thus provide the stepping stone between the simple ice chemistry observed directly around protostars and the complex molecules found in comets and meteorites in our own solar system. The observations of non-thermally evaporated ice provides additional information, since it probes the chemical evolution before the onset of thermal evaporation. This is the topic of Chapter 12.

1.4 Ices in the laboratory

Laboratory solid-state astrophysics has two main objectives: identifications of ice spectral features and simulations of astrophysically relevant ice processes. Most chapters in this thesis fall in the second category, while it was with spectroscopy that this field of study began half a century ago.

1.4.1 The need for laboratory experiments

Astrophysical observations directly provide spectra of interactions between light and matter towards specific objects at specific times. Laboratory studies are thus first required

to identify what species produce the observed spectra. Laboratory spectroscopy is also needed to extract information about the physical conditions from the spectra, such as the density and temperature.

The second challenge of astrophysical observations, which laboratory studies address, is the fact that astrophysical time scales are typically orders of magnitude longer than human life spans – even the relatively fast collapse of cloud cores to form protostars takes a minimum of 1000 years. Thus it is seldom possible to observe either the chemical or the physical evolution of a specific object. Rather observations aim to provide ‘snapshots’ of the evolution towards a large set of objects at different evolutionary stages and then put them into an evolutionary sequence. This is not trivial and laboratory studies of different astrophysical processes are key to solve the puzzles. In the laboratory, the chemical evolution is sped up by increasing the UV flux or the heating rate or any other parameter of interest. It is therefore possible to investigate each step in the ice evolution on time scales of hours instead of thousands of years and then use the laboratory predictions of how the ice will change with time, temperature or flux to interpret the astrophysical observations.

1.4.2 Spectroscopy of astrophysical ice equivalents

The development of spectrographs and astrophysical spectroscopy are historically inseparable. When Joseph von Fraunhofer invented the spectrograph in 1817, he also discovered the Sun’s atomic absorption lines, though not identified as such until 1859 by Kirchhoff and Bunsen. It was also credit to visible spectroscopy that the presence of external galaxies was first established in the early 20th century; spectroscopy of the closest spiral galaxy, M31, (M for Charles Messier who cataloged it in 1734) revealed a stellar spectrum and a higher Doppler shift than had been observed anywhere in the Galaxy, both which separated it from local nebulae such as M42 and the Orion Nebula.

Infrared spectroscopy, the preferred tool for ice identification, was developed during the same period, though it did not reach the accuracy of visible spectroscopy until much later – one of William Herschel’s many discoveries was the presence of infrared light, which he first detected around 1800. Draper first managed to photograph infrared absorption bands in 1842 (Lewis 1895), while infrared *ice* spectroscopy dates back to the early 20th century.

Molecular vibrations are excited by infrared radiation dependent on the derivative of dipole moment function $d\mu/dR$. Most molecules have a permanent dipole moment, since all different atoms attract electrons differently, producing a charge imbalance in the molecule. Exceptions include both homo-nuclear diatomic molecules, such as molecular oxygen (O_2), and larger molecules that are symmetric, e.g. carbon dioxide or O-C-O. The latter kind still have dipole-allowed infrared absorption features, since $d\mu/dR \neq 0$ during some vibrations, while homo-nuclear di-atomics to a first order do not have any detectable infrared transitions – the quadrupole-allowed H_2 transitions are exceptions in astrophysical settings because hydrogen is so abundant.

In isolation, molecular vibrations have specific frequencies, dependent on the strength of the vibrating bond. In solids, interactions with the molecules around it modify these bond strengths, which often results in a range of overlapping frequencies for one type of

molecular vibration. For example the symmetric H_2O stretch vibrates at a frequency of 3657 cm^{-1} ($2.7\text{ }\mu\text{m}$) in a dilute gas, but at $3000\text{--}3600\text{ cm}^{-1}$ ($2.8\text{--}3.3\text{ }\mu\text{m}$) in an amorphous, i.e. disordered, ice. The feature changes again when the H_2O ice is in a mixture.

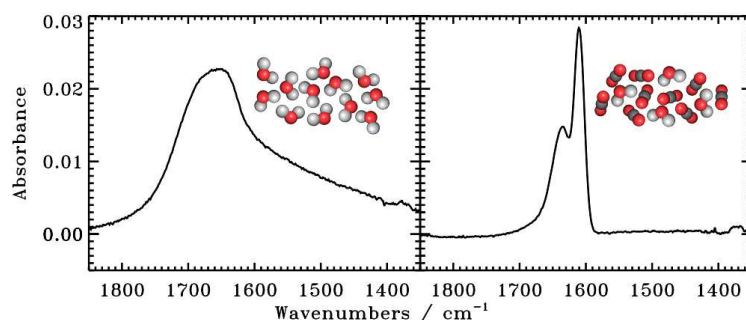


Figure 1.7 – The water infrared bending feature in a pure water ice (left panel) and in a carbon dioxide ice mixture (right panel).

The discoveries of ices in space prompted targeted spectroscopy of ices and ice mixtures to pursue the identifications of different infrared bands observed towards star forming regions, starting in the 1970s in Leiden. This spectroscopy began before the discovery of the $3.1\text{ }\mu\text{m}$ band, associated with H_2O ice, towards several astrophysical sources (Gillett & Forrest 1973; Merrill et al. 1976), and was further driven by the observation that the $3.1\text{ }\mu\text{m}$ profile does not match pure H_2O ice perfectly. Hagen et al. (1980) investigated the impact on the $3.1\text{ }\mu\text{m}$ feature when adding different molecules to the H_2O ice. They noted that in addition to profile changes due to overlap between features of different species, the ice mixture spectra also contained distorted isolated bands compared to the pure ice spectra. Figure 1.7 shows qualitatively the dramatic change of the water bending feature at $6\text{ }\mu\text{m}$ between pure H_2O ice and H_2O mixed with CO_2 ice (from Chapter 4). This both adds confusion and extra information when interpreting astrophysical observations; changes in shapes can easily be mistaken for spectral features of new species, but if correctly assigned the spectral shapes add information on the structure of the ice in addition to its composition. These distortions are almost impossible to calculate in amorphous ices though recent attempts exist (Mate et al. 2008). Therefore spectroscopy of different ice mixtures is an ongoing work of which Chapter 4 is part.

The set-up used for transmission infrared spectroscopy of ices in this thesis is shown in Fig. 1.8 and also discussed in detail by Gerakines et al. (1995). A gas mixture is prepared separately and then attached to the set-up, which consists of a high-vacuum chamber with infrared-transmitting windows, one or more inlet tubes for the gas mixture, an outlet for the pump and an infrared-transmitting window in the center of the chamber which is cooled by a helium cryostat down to 15 K. The ice mixture is built up diffusively by letting gas into the chamber, where it freezes out onto the cold window. The spectra of the ice can then be monitored with a Fourier transform infrared spectrometer ranging between $4000\text{--}400\text{ cm}^{-1}$ at 15–200 K.

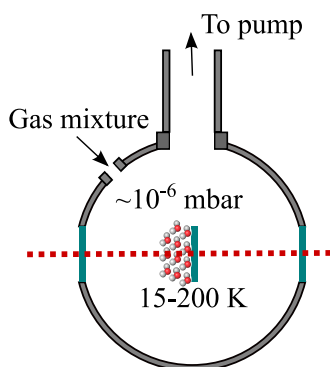


Figure 1.8 – A drawing of the key features of the HV set-up for transmission ice spectroscopy.

1.4.3 Ice dynamics – mixing, segregation and desorption

Amorphous ices may be best thought about as very viscous fluids, where the viscosity depends steeply on ice temperature. Below 20 K most ices are immobile on laboratory time scales. H_2 and H can still scan the surface and also penetrate somewhat into the ice (Ioppolo et al. 2008). CO and N_2 become mobile around 25 K (Öberg et al. 2005; Bisschop et al. 2006, Chapter 5). Other potentially important molecules and radicals sequentially start to diffuse in the ice, dependent on their binding energies. At higher temperature the ices start to evaporate, again dependent mainly on the binding energies, though the ice structure plays a role as well (Collings et al. 2004).

In the literature, ice dynamics are studied using a range of tools including infrared spectroscopy of the ice, quadrupole mass spectrometry of the desorbing molecules and quartz-balance measurements of the mass of the ice on the surface. Infrared spectroscopy can be used both to determine the amount of ice on a surface and to probe the ice structure. The latter is based on the dependence of infrared ice-band shapes on its bonding structure and the nature of its nearest neighbors as discussed above (Fig. 1.7). Thus ice spectroscopy can be employed to measure ice desorption, through continuous measurements of the ice amount as a function of temperature, as well as ice mixing and segregation through analysis of changes in the spectral band shapes.

Mass spectrometry is used to probe desorption at a higher time resolution and at a higher sensitivity than is possible with infrared spectroscopy of the ice. It is also the only molecule-specific tool available to probe species without dipole-allowed infrared transitions and complex ice species whose infrared bands are impossible to separate from the absorption bands of other species. Finally quartz balances provide the most accurate measurements of total ice desorption, both thermal and non-thermal, but cannot be used to determine which ice species desorb from an ice mixture.

Figure 1.9 illustrates the use of spectroscopy and mass spectrometry during segregation and desorption studies of $\text{H}_2\text{O}:\text{CO}_2$ ice mixtures when a particular ice mixture is heated with a linear heating ramp between 20 and 200 K (taken from Chapters 4–6). Before the onset of CO_2 desorption the spectral profile of CO_2 changes, indicating an ice re-

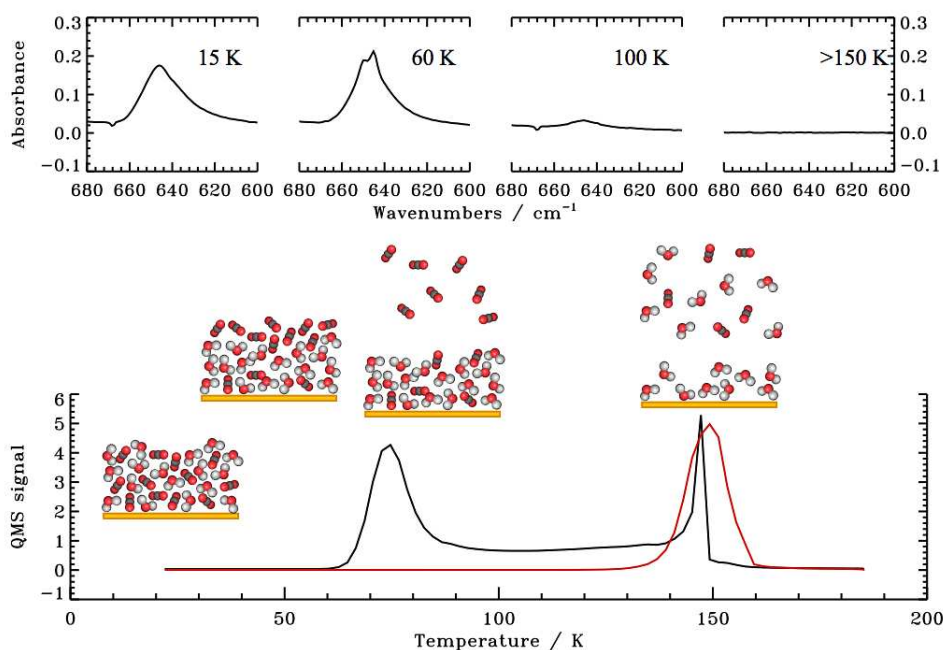


Figure 1.9 – The changes in a H₂O:CO₂ ice mixture with temperature and the recorded output by the mass spectrometer and the infrared spectrometer in response to the dynamical processes in the ice. The top panel shows the CO₂ bending mode at 15 μm at 15 K when mixed with H₂O, at 50 K when the ice is partly segregated ice, at 100 K when most CO₂ has desorbed and above 150 K following desorption of the H₂O ice and the CO₂ molecules trapped in the H₂O matrix. The bottom panel shows the CO₂ (black) and H₂O (red) ice desorption rates as a function of temperature. In this mixture most CO₂ desorbs around 70 K, but some is trapped in the H₂O ice and desorbs with H₂O at 150 K.

structuring. At higher temperatures the mass spectrometer starts to detect CO₂ molecules in the gas phase, indicative of ice desorption. Simultaneously the infrared spectroscopy reveals a loss in CO₂ absorbance. By combining the heating rate and the temperature at which the dynamical process occurs it is possible to derive an energy barrier for the dynamical process in question. This can subsequently be incorporated into an astrophysical model, predicting when and where ices segregate and desorb in space.

The simplest dynamical process in ices is thermal desorption of pure ices and this has been studied quantitatively by a number of groups. Desorption of binary mixtures is less understood, though a few composition specific models of e.g. H₂O:CO, CO:N₂ and CO:O₂ mixtures exist (Collings et al. 2003; Bisschop et al. 2006; Acharyya et al. 2007). Segregation and mixing of binary ices have not been treated quantitatively, except for

in the desorption studies, and the underlying mechanisms are still unknown. These two problems are treated by a combination of experiments and modeling in Chapters 5–6.

Desorption and ice structure changes can also be induced by cosmic ray/ion bombardment (Baratta et al. 1991) and UV photons (Westley et al. 1995a; Leto & Baratta 2003). UV photodesorption is potentially the life line between gas and ices in quiescent regions and thus three of the chapters here aim to quantify the rates and mechanisms of ice photodesorption. Previous photodesorption experiments showed a high desorption yield per incident UV photon for water ice (Westley et al. 1995a), while the yields for other astrophysically relevant ices have not been previously measured and often assumed to be negligibly small (e.g. Ruffle & Herbst 2001). Even in the water experiments an observed fluence dependence seems to limit the astrophysical applicability of the previous experimental results. To address this, photodesorption yields of pure and mixed ices containing CO, N₂, CO₂ and H₂O are presented in Chapters 7–9.

1.4.4 Ice chemistry

The formation of the first ices, such as CH₃OH and H₂O, is investigated in atomic bombardment experiments where the reactions of atoms or atoms and molecules are observed on ice surfaces (Hiraoka et al. 1998; Watanabe et al. 2003; Ioppolo et al. 2008). Qualitatively, hydrogenation of most molecules and all atoms seems highly efficient even at low temperatures, confirming the previous hypothesis that the observed simple ices, CH₃OH and smaller, form through this route.

Experiments on complex ice formation have investigated the effect of energetic bombardment of simpler ices with ions or UV photons (e.g. Stief et al. 1965; Hagen et al. 1979; Allamandola et al. 1988; Gerakines et al. 1995; Hudson & Moore 2000; Bennett et al. 2007). With a few exceptions, most studies have focused on the qualitative assignment of final products, following irradiation or bombardment of ice mixtures that are proposed to mimic ice compositions in star forming regions. The investigated ice mixtures are usually converted into a mixture of more complex species upon irradiation. Photolysis of ices is thus a potential pathway to complex molecule formation in space. The traditional approach with high-vacuum set-ups and irradiation during deposition followed by warm-up and analysis of the complex residue has provided valuable insights into the possible outcomes of UV- and ion-chemistry, but little quantitative data that can be tested against astrophysical observations.

The approach to UV induced ice chemistry in this thesis is different. The studies do not propose to perfectly imitate either the conditions or the ice compositions in space. Therefore the results are not meant to be directly translated into astrophysical predictions. Rather the aim is to run experiments from which physical properties can be extracted, such as photo-dissociation cross sections and branching ratios, and radical diffusion barriers in the ice. These physical properties, to a first approximation, do not depend on the time scale of the process and are thus equally valid in a laboratory setting and in space. Thus, astrochemical models including these barriers and cross sections can provide direct tests of the likelihood of snap-shot observations being due to a proposed chemical scenario.

This affects the design of the experiments. The experimental set-up used for the UV-experiments is described in detail below. The general philosophy has been to focus on pure ices or other well-constrained ice systems rather than ice mixtures with all components present in interstellar ices. The chemistry in these simpler ices are then investigated during the full range of laboratory conditions available including different radiation fluxes, ice temperatures, ice structures and so forth to provide the maximum amount of constraints on the underlying physical quantities, i.e. the diffusion and reaction barriers and dissociation cross-sections. The experimental results are presented in Chapter 10 and 11, while the quantitative modeling of these processes to extract the physical quantities will be presented in a series of papers by Garrod & Öberg (in preparation).

1.4.5 CRYOPAD

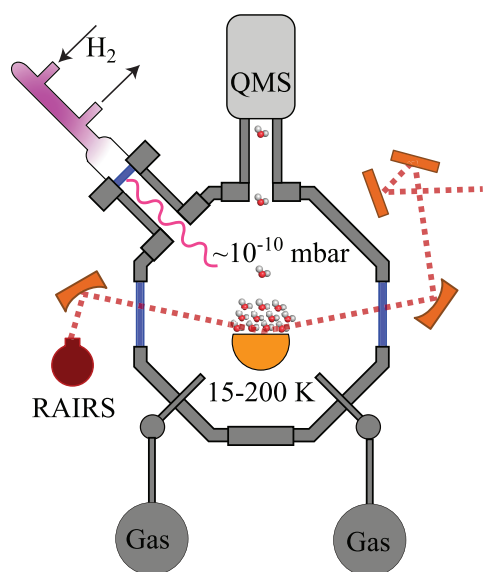


Figure 1.10 – A drawing of the key features of the experimental set-up CRYOPAD including the hydrogen discharge UV lamp. The temperature refers to the gold substrate on which the ices are deposited.

The ice dynamics, ice photodesorption and ice photochemistry experiments are all carried out under ultra-high vacuum conditions ($\sim 10^{-10}$ mbar) in the CRYOPAD set-up, which is described in detail in Öberg et al. (2005) and Fuchs et al. (2006). The set-up was built as part of the Ph.D. thesis project of van Broekhuizen (2005) and has been further modified during the present thesis to achieve its current form (Fig. 1.10). CRYOPAD was built with for the specific purpose of studying photochemistry, but as this thesis shows, it is a versatile instrument suitable for a range of dynamics and chemistry experiments.

In the beginning of each experiment, pure ices and ice mixtures are grown *in situ* with monolayer (ML) precision at thicknesses between 1 and 100 ML, by exposing a cold substrate at the center of the vacuum chamber to a steady flow of gas, directed along

the surface normal. The ultra-high vacuum allows for the study of thin ices, similar in thickness to those found in space, since the contamination level is low. The substrate is temperature controlled between 15 and 200 K.

The set-up is equipped with a Fourier transform infrared (FTIR) spectrometer in reflection-absorption mode (reflection-absorption infrared spectroscopy or RAIRS) and a quadrupole mass spectrometer (QMS) to investigate ice evolution and ice desorption. In the photo-experiments the ice films are irradiated at normal or 45° incidence with UV light from a broadband hydrogen microwave-discharge lamp, which peaks around Ly α at 121 nm and covers 115–170 nm or 7–10.5 eV (Muñoz Caro & Schutte 2003).

Compared to the interstellar environment CRYOPAD reproduces the ice temperature well. The vacuum consists mainly of H₂, as in space, and is comparable to the conditions of disk midplanes and pre-stellar cores. The UV irradiation is however several orders of magnitude higher compared to most astrophysical regions. This changes the relative time scales of photodissociation and radical diffusion – the two quantities governing complex ice chemistry – in the laboratory ice compared to astrophysical settings; hence the need of extracting underlying physical quantities from the experiments rather than applying laboratory ice product compositions and formation rates directly to the chemistry around protostars. Another major difference is the choice of substrate. Gold is inert and should thus not affect the chemistry observed in the lab, but additional effects of silicate grains on the chemistry in space can at this point not be excluded. In most regimes of interest the ice bulk or ice surface chemistry will dominate over the silicate grain surface chemistry, however, and then the difference between chemical pathways on the laboratory surface and astrophysical grains should be minimal.

1.5 This thesis

The first ices that form in dark clouds may be simple, but their evolution is complex. During star- and planet formation the original ices are exposed to atom-, UV- and ion-bombardment, and to heat, which interact to produce large organic molecules. The same bombardments and heat also evaporate ices into the gas-phase, further complicating the gas-grain interactions.

Though complex, these ice processes can be quantified through a combination of ice and gas observations, and laboratory spectroscopy and simulations. Chapters 2–3 set the stage for the thesis by presenting an inventory of simple ices in low-mass star forming regions and the constraints observations put on simple ice formation. This is used in Chapter 4–6 to experimentally investigate dynamics of astrophysically relevant ice mixtures. Chapter 7–11 continues with laboratory experiments on UV induced desorption and chemistry in pure and mixed ices. Chapter 12 concludes the thesis with a proposed approach to study these ice processes in space when it cannot be done directly through ice spectroscopy. The principal conclusions of this thesis, organized by chapter, are:

The Spitzer c2d ice survey towards low-mass protostars

Based on *Spitzer* data, with complimentary VLT and *ISO* observations, Chapters 2–3 investigate ice compositions and formation in the pre- and proto-stellar stages. The large sample size allows for a more statistical treatment than previously possible, which is fully exploited through variability plots, correlations studies, ice maps and principal component analysis.

Chapter 2 Ices towards low- and high-mass protostars form through a range of processes resulting in that ice abundances vary between a factor of two and orders of magnitude between different protostars. All identified variable ices either depend on protostellar heating, e.g. CO and pure CO₂, or the pre-stellar CO freeze-out fractions, which traces the lifetime and density of the cloud core before the onset of collapse to form a protostar. The results suggest that the ice chemistry generally proceed in four steps, starting with hydrogenation of atoms, followed by hydrogenation of molecules, UV and ion processing of pre-existing simple ices and finally ice and radical diffusion due to protostellar heating

Chapter 3 Statistics on the abundance and variance of the smallest organic molecules CH₄ towards a large sample of protostars shows that it is a more common ice constituent than previously assumed. Its strong correlation with H₂O and CO₂ confirms its proposed formation path from hydrogenation of carbon atoms during the early stages of cloud formation.

Spectroscopy and dynamics of ice mixtures

Amorphous ices are disordered and thus difficult to model. Yet, the macroscopic dynamics, revealed by spectroscopy and desorption patterns, can be quantified by combining understanding of bond strengths and diffusion barriers with empirical models on the effects of different environmental parameters. Once quantified, ice spectroscopy and ice dynamics can be used to trace the thermal history, such as the occurrence of transient heating events, in protostars and disks.

Chapter 4 Water ice in H₂O:CO₂ ice mixtures has significantly different spectral profiles and band strengths compared to pure ice, which can be understood from the caging of H₂O molecules by CO₂, preventing resonance vibrations between hydrogen-bonded H₂O molecules. This must be taken into account both to correctly identify minor ice species with overlapping absorption bands with H₂O and to derive accurate column densities of water ice in space.

Chapter 5 Segregation of ices proceeds through fast surface diffusion, followed by slower bulk segregation in both H₂O:CO₂ and H₂O:CO ices. This is reproduced in simulations where molecules diffuse through surface hopping and surface and bulk swapping. Ice segregation in thin ices can be characterized quantitatively, dependent only on the mixture composition and the relative binding energies of the involved

molecules. For $\text{H}_2\text{O}:\text{CO}_2$, surface segregation becomes important already at 30 K during protostellar collapse.

Chapter 6 Desorption from mixed ices depends on ice thickness, mixture ratios, heating rates and mixture constituents. Despite these numerous dependencies, the main attributes of desorption from mixed ices can be modeled with surprisingly few free parameters, when using a three-phase model where the ice bulk and ice surface are treated separately. The simplicity of the model allows for its use in large astrochemical networks and thus using observations of thermal desorption as an efficient probe during star formation.

UV induced desorption and chemistry in ices

UV photons are always present due to cosmic-ray induced radiation fields. Hence, photoprocesses are possible and potentially important at all stages of star formation and UV interactions with ice mantles have been proposed to explain excess gas in cold regions through photodesorption as well as the presence of complex molecules towards protostars through ice photochemistry.

Chapter 7 UV photodesorption of CO is orders of magnitude more efficient than previously assumed, but it is only possible from the surface layers of ices. CO has no dissociative transitions within the UV lamp spectral range and the photodesorption must thus occur through non-dissociative excitation followed by desorption. Pure N_2 ice, which does not have an allowed electronic transition in the UV lamp spectral range, has a much lower desorption efficiency. The high CO photodesorption yield per incident UV photon means that photodesorption may be the major link between the gas and the grain in quiescent regions.

Chapter 8 UV photodesorption of N_2 and CO_2 is also possible but through different mechanisms compared to CO: co-desorption following excitation of a neighboring molecule and desorption following photodissociation, respectively. The different mechanisms are apparent in the opposite ice thickness and temperature dependences of CO and CO_2 . Despite the different mechanisms both CO and CO_2 have photodesorption yields of $\sim 10^{-3}$, while N_2 co-desorption is an order of magnitude less efficient.

Chapter 9 UV photodesorption of H_2O ice is confirmed to be efficient ($1 - 4 \times 10^{-3}$ per incident UV photon), with an increasing efficiency with temperature for thick ices, similarly to CO_2 ; at higher temperatures the ice is more mobile and thus desorption is possible from deeper within the ice. The high yield especially affects the chemistry in regions with excess UV photons such as protoplanetary disks, where photodesorption will maintain molecules in the gas phase significantly further towards the mid-plane, compared to thermal desorption.

Chapter 10 UV photons drive a rich chemistry in ices, which has for the first time been quantified for CH_3OH dominated ices. The detected photoproducts reproduce

the gas phase compositions around low-mass protostars and in comets, strengthening the theory that both have a protostellar ice origin. The large amounts of HCOOCH_3 and other CHO-bearing molecules towards some protostellar regions are explained by the experiments as originating from photochemistry of CH_3OH in CO-rich ices, while pure CH_3OH photochemistry produces more $\text{CH}_3\text{CH}_2\text{OH}$ and related species. The quantified results are used to derive CH_3OH photodissociation branching ratios for the first time in either gas or ice, while absolute diffusion barriers requires more detailed modeling. The experiments predict certain molecules to co-vary and other ratios to depend on the local environment, which should provide observational tests on the importance of this formation pathway for observed complex molecules in astrophysical environments.

Chapter 11 The photochemistry of NH_3 -containing ices provides a pathway to forming amino acids and other prebiotically interesting molecules during star formation. The study confirms that amino acids and amino acid-like molecules form during photolysis of ices with CH_4 , NH_3 and CO_2 , including ice mixtures that are more representative of astrophysical situations than previous experiments. It is however the quantification of the simpler chemistry in binary mixtures with H_2O , CO_2 , NH_3 and CH_4 that provides data from which diffusion barriers and branching ratios can be derived. Their analysis reveals that diffusion is fast at 20 K in H_2O -poor mixtures and the relative production of radicals governs the chemistry, while in H_2O -rich mixtures the relative diffusion barriers of radicals instead decide the chemical evolution. This once again demonstrates the importance of constraining the underlying physics of ice processes rather than directly extrapolating results from the laboratory to the inter- and circum-stellar medium.

Observations of non-thermal ice desorption

Ices can only be observed in specific lines of sight because of the background light source requirement. In addition more complex ices cannot be observed directly by infrared spectroscopy because of overlapping features with simpler, more abundant ice species. Thus there is a need for complimentary methods to study the ice evolution.

Chapter 12 Photodesorption and other non-thermal desorption pathways provide means to observe ice compositions indirectly where direct ice spectroscopy is not feasible. This is tested in a pilot study of quiescent gas and ice towards a small sample of low-mass protostars. The observations are consistent with a representative fraction of the ice being constantly maintained in the gas phase due to non-thermal desorption. This opens up a door to studying the complex chemistry investigated in the previous chapters as it happens in the protostellar envelope and not just the evaporating end product.

1.6 Summary of main discoveries

Taken together, the results described in Section 1.5 can be summarized as follows.

1. Simple ices – from H_2O and CH_4 to CH_3OH – form sequentially during the dark cloud, cloud core and prestellar stages because of hydrogenation of atoms, direct freeze-out, hydrogenation of CO, O and N additions to CO and finally ice diffusion close to the protostar. The later an ice forms in this sequence, the more its abundance tends to vary between different sources. (Chapters 2, 3)
2. Thermal ice processes, such as segregation and desorption, depend on ice composition, mixture ratios, ice thicknesses and ice temperature. The dependences can be quantified and extrapolated to astrophysical conditions only by combining comprehensive sets of experiments with microscopic modeling, as illustrated by two test cases on desorption from, and segregation in, $\text{H}_2\text{O}:\text{CO}_2/\text{CO}$ ice mixtures. (Chapters 5, 6)
3. Photodesorption of pure ices is found to be much more efficient than previously assumed and photodesorption alone may be sufficient to explain puzzling observations of cold gas at the edges of clouds, in cloud cores and in protoplanetary disks. Furthermore, the photodesorption yield is constant, within a factor of three, for all common ice constituents, except for N_2 (Chapters 7–11). This suggests that photodesorption of ices results in an ice ‘fingerprint’ in the gas phase, which is found to be consistent with a proof-of-principle study on ice and gas phase abundances towards a few cold protostellar envelopes (Chapter 12).
4. Ice photochemistry efficiently converts simple ices into more complex species, which can explain the observed abundances of complex molecules around protostars and in comets and explain the chemical differences between different sources. The results were acquired through *in situ* quantification of photochemistry, which provides an unprecedented understanding of complex ice chemistry at the level of elementary processes, sufficiently detailed to model complex ice chemistry during star formation and to predict the formation of yet undetected, larger complex molecules. (Chapters 10, 11)

2 THE *c2d* SPITZER LEGACY: ICE FORMATION IN STAR-FORMING REGIONS

The *Spitzer Space Telescope* observed ices towards an unprecedented number of protostars during its five-year mission. Within the *c2d* legacy program more than 40 low-mass protostars have been analyzed for ice features in a series of papers including CH₄ ice in Chapter 3. The *c2d* data are here combined with ice observations from other *Spitzer* programs, and previous VLT and *ISO* data, to construct a general ice formation scenario. The analysis reveals that low- and high-mass protostars mainly differ in their content of CO, CH₄ and CO₂ ice. Within the low-mass sample, the variability with respect to H₂O ice, described by the standard deviation of the log-transformed abundances, of 19 unique ice components ranges from 0.1 to 1.1. Combining the analysis of abundance variations, ice maps and ice correlations, shows that ices form sequentially and that large abundance variations are mainly due to formation pathways depending on different prestellar CO freeze-out rates and protostellar heating. The first step in the ice formation sequence is hydrogenation of atoms, resulting in e.g. H₂O, CO₂:H₂O, CH₄, NH₃. From their almost constant abundances, this stage must be similar for all low-mass star formation. A second formation wave is due to reactions with accreted CO ice and possibly energetic processing of H₂O-rich ices in the cloud core, resulting in CO₂:CO, CO:H₂O, OCN⁻ and CH₃OH ice. These formation yields depend on the collapse time scale and prestellar densities, and as a result the ice abundances vary by an order of magnitude between different protostars. Third, some ice components, e.g. pure CO₂ and CH₃CH₂OH, form at higher temperatures following the turn-on of the protostar because of diffusion and desorption of ices. CH₃CH₂OH ice is an excellent fit for the 7.25 μm feature and may thus be possible to detect towards a range of objects.

Öberg et al., in preparation

2.1 Introduction

Grain surface chemistry is the proposed source of the simplest hydrogenated molecules, H_2 , H_2O and CH_4 , as well as the complex organics molecules detected in the gas phase around protostars (Tielens & Hagen 1982; Garrod et al. 2008). It is now more than three decades since the first ices were detected in the interstellar medium, but it was only with the advent of the *Spitzer Space Telescope* that ice abundances could be investigated towards a large number of lines of sight at reasonable integration times.

During the last five years *Spitzer* observed ices towards more than 40 low-mass protostars within the *c2d* program (Boogert et al. 2008; Pontoppidan et al. 2008; Öberg et al. 2008, Bottinelli et al. in prep, from now on Paper I-IV) and dozens of more within other programs (e.g. Zasowski et al. 2009), providing an unprecedented sample-size of protostellar ice sources. In addition, *Spitzer* has detected ices towards several background sources, looking through molecular clouds at a range of extinctions (e.g. Bergin et al. 2005; Knez et al. 2005), although the densest parts of prestellar cores are still inaccessible. Neither kind of observations were possible over the full 5–30 μm infrared spectral region towards low-mass protostellar sources before *Spitzer* and its sensitive detectors. The spectral cut-off of *Spitzer* at 5 μm entails, however, that the spectra must be complimented with ground-based observations to cover the strongest H_2O transition at 3 μm , the only CO transition at 4.65 μm , and the XCN feature at 4.5 μm , and thus to achieve a comprehensive picture of ice abundances during star formation (Pontoppidan et al. 2003; van Broekhuizen et al. 2005). Building on these previous studies and introducing new ice data, this study aims to provide a general scenario of ice evolution during low-mass formation by combining statistics on ice abundances with protostellar ice maps, spectral analysis and comparison with previous high-mass data.

Such a general scenario has been presented for ice formation during high-mass star formation from analysis of spectra from the *Infrared Space Observatory (ISO)* of both protostars and background sources (Gibb et al. 2000, 2004). From comparison between protostars and background stars, H_2O and CO_2 were found to have a quiescent cloud origin. Many other ices, e.g. CH_4 , NH_3 and CH_3OH , were only detected towards protostars, but because of high upper limits Gibb et al. (2004) did not use this to exclude a cloud formation route for CH_4 and NH_3 , especially since the CH_4 abundances are almost constant within the protostellar sample. CH_3OH abundances are in contrast highly variable between different high-mass protostars, which was explained by formation from intense UV or thermal processing. The XCN feature, as well, varied by an order of magnitude within the sample and a similar protostellar origin was thus inferred. In summary the ice formation, processing and destruction were proposed to proceed in four steps (Gibb et al. 2000, 2004).

1. H_2O , CO_2 and probably CH_4 and NH_3 ices form together in a H_2O -rich ice component during the prestellar stage by surface reactions.
2. CO and probably O_2 and N_2 ices form by direct freeze-out in a separate ice component, which is also present before the turn-on of the protostar.

3. Mild energetic processing, always present around high-mass protostars, results in CO₂ formation in the CO-rich ice and some evaporation of CO ice. It also cannot be excluded that CH₄ and NH₃ form at this stage since they are not observed in the pre-stellar stages. Simultaneously a third ice component consisting of CH₃OH and CO₂ forms.
4. Finally, after intense UV and thermal ice processing towards a few high-mass protostars, large amounts of CH₃OH and XCN form in the H₂O-rich ice and all pure CO ice evaporates.

Two of the above conclusions come from analysis of the CO₂ spectra. First, a CO₂ spectral wing observed towards the protostars is produced in the laboratory when CH₃OH mixed with CO₂ ice. Second, pure CO₂ ice can be produced by ice segregation and this was used to explain the presence of pure CO₂ ice spectra in the *ISO* sample (Ehrenfreund et al. 1998). More generally, laboratory spectroscopy has demonstrated that the spectral profiles of all astrophysically relevant ices depend on whether the ice is pure or in an ice mixture and also on the composition of the ice mixture (e.g. Hagen et al. 1980; Sandford & Allamandola 1990, Chapter 4). As seen with the CO₂ profile, this is used when interpreting astrophysical spectra to determine the structure of interstellar ices in addition to the abundances of the detected species. While the exact ice environment is difficult to ascertain, the profiles of pure ices, of ices in a hydrogen-bonded ice, e.g. H₂O-dominated, and in a CO-rich ice can usually be distinguished. In the analysis of ground-based, and *Spitzer* observations alike this is used to determine the amount of the most common molecules that reside in a H₂O-rich ice, in a CO-rich ice and in a pure phase. This is important since observations suggest that most astrophysical ices consist of H₂O-rich layer, covered by a CO-rich layer (Pontoppidan et al. 2008).

Parts of the *ISO* ice formation scheme has been challenged by ground-based observations of abundant CH₃OH ice towards low-mass protostars (Pontoppidan et al. 2003), demonstrating that no intense processing is required for its formation – most ice around low-mass protostars is protected from stellar UV-light. The XCN feature was also observed to be common in a large sample of low-mass protostars, though its band position appears shifted to higher frequencies compared to the high-mass sources (van Broekhuizen et al. 2005). Van Broekhuizen et al. (2005) decomposed the observed band into two different components, one of which compares well with laboratory studies of OCN⁻. The origin of the second component is contested and suggested carriers include chemisorbed CO on silicate grains (Fraser et al. 2005) in addition to different CN-containing molecules. In general the XCN carrier towards high-mass protostars is dominated by the OCN⁻ component, while low-mass protostars contain both components at a variable ratio. The band may thus have two different carriers, one which depends on stellar processing, and one which does not.

During the same period Pontoppidan et al. (2003) developed a new framework for analyzing the ice structure and evolution while investigating the CO-ice feature towards a sample of 39 low-mass protostars, many of them the same as studied with *Spitzer*. Rather than directly comparing each observation with laboratory spectra, Pontoppidan

et al. (2003) decomposed, phenomenologically, all observed CO ice spectral profiles into three unique components. These three components were then compared with laboratory spectra and could be assigned to pure CO ice, CO mixed with H₂O or CH₃OH ice, and a component identified with some CO in a CO₂-rich ice mixture (confirmed in Paper II). This approach requires a large data sample, but it also offers several advantages in comparison with the traditional source-by-source comparison with spectra of different laboratory ice mixtures (e.g. Merrill et al. 1976; Gibb et al. 2004; Zasowski et al. 2009). First it avoids the ‘mix-and-match’ problem; often a range of different ice mixtures are consistent with the shape of a spectral feature because several ice-mixture components affect the spectral profiles of e.g. CO and CO₂ similarly. A mix and match of laboratory spectra to produce the observed features thus says little about the range of possible ice compositions consistent with the spectral profiles. Second, the phenomenological decomposition ensures a consistent treatment of all kinds of sources, since the scaling of different components can be done automatically to the spectral profile without subjective preconceptions on what the ice mixture should contain towards certain objects. Third, the phenomenological division of a common spectral feature into a minimum number of components provides information on the sample as a whole, i.e. it directly shows which parts of the spectral profile are ubiquitous and which are environment dependent. This is crucial information when assigning a component carrier – without this, the degeneracy is almost always too large to say much at all about the structure of the ice from a spectral profile analysis. So far the component analysis approach has been applied to the CO ice band, the XCN-band, the CO₂ ice feature and the 5–7 μ m complex within the *c2d* program and an overlapping ground-based observational program (Pontoppidan et al. 2003; van Broekhuizen et al. 2005, Paper I,II).

A second advance in the studies of ice formation is the construction of ice maps from samples of low-mass protostars in the same cloud core. Pontoppidan et al. (2004) constructed such a map of CH₃OH and H₂O ice abundances towards the SMM4 protostellar envelope in Serpens, demonstrating that the CH₃OH formation is a local process. In a map of the Ophiuchus F core Pontoppidan (2006) showed that the abundances of CO₂, of CO mixed with H₂O and of CO ice generally all increase towards the cloud core, but the CO increase is most dramatic of the three, tracing the ‘catastrophic’ freeze-out of CO at high densities.

The key conclusions on ices during low-mass star formation coming out from the statistical studies and the ice maps so far are that a H₂O-rich ice forms first in the prestellar phase, containing trace amounts of CH₄ and NH₃, and large amounts of CO₂ mixed into it. Later in the cloud-core phase, pure CO ice freezes out on top of this ice mixtures and a second CO₂ formation phase takes place resulting in a CO dominated CO:CO₂ ice mixture. Once the protostar turns on, the CO ice is distilled from the ice mixture, resulting in a pure CO₂ ice. Close to the protostar, the water-rich ice will also start to segregate resulting in more pure ice layers. The origins of CH₃OH ice, the XCN band and the proposed NH₄⁺ ice – the species thought to be responsible for the bulk of the 6.85 μ m band – remain unclear. NH₄⁺ is one of several tentative band assignments, including HCOOH and HCOO⁻, in Paper I that requires further analysis. Most of the unassigned ice bands fall within 5–8 μ m because of the complex absorption pattern of most organic

and nitrogen-bearing species in this spectral region. One the goals of this chapter is to further constrain their carriers.

The overall aim of this chapter is to identify under which conditions the carriers of observed ice features form. This is pursued by combining the observational results from the four *c2d* ice survey papers with previous VLT surveys of CO and XCN⁻ ice data, nine additional low-mass ice sources observed with *Spitzer* outside of the *c2d* program and the *ISO* results on high-mass sources to analyze global trends and variations in ice abundances towards low-mass and high-mass protostars, with focus on the larger low-mass sample. Section 2.2 summarizes the observations and the analysis procedure applied to old as well as new observational data. Section 2.3 first identifies the most variable ice features using histograms and calculated standard deviations. The reasons for abundance variations is then explored through protostellar ice maps, abundance correlation plots and a principal component analysis of the low-mass sample. The results are discussed in §2.4 with respect to different ice formation scenarios, ice chemistry in low-mass versus high-mass star-forming regions and the identification of ice features in crowded spectral regions, including some new spectral comparisons. The results of this chapter will be incorporated in a future paper, which will contain additional ice data on background stars and low-mass protostars in isolated cores.

2.2 Observations and spectral analysis

Spitzer-IRS spectra were obtained as part of the *c2d* Legacy program (PIDs 172 and 179) as well as a dedicated open time program (PID 20604) and a few archival spectra observed as part of the GTO programs of Houck et al. Most sources in the sample were included in Papers II-III and thus have reported CO₂ and CH₄ ice abundances, while the *c2d* sources alone were investigated in Paper I and IV. The entire sample is listed in Table 2.1.

Of the sources not included in Papers I and IV, we have derived the NH₃ and CH₃OH ice abundances or upper limits and the 5–7 μm components strengths following the procedures previously described in Papers I and IV. In summary, five different components C1–5 are fitted to the 5–7 μm complex and their relative optical depths are reported in Table 2.2. The NH₃ and CH₃OH abundances towards the same sources are determined from their 9.0 and 9.7 μm features, using one of the methods in Paper IV, where the underlying silicate feature is removed by fitting a 4th order polynomial to the silicate band. Three possible sets of points are tested for defining the continuum and the variation in the resulting column densities are included when estimating the uncertainty in the derived abundances. After continuum subtraction, the NH₃ and CH₃OH integrated optical depths are derived by fitting two Gaussians to the observed spectra around the expected band positions, based on laboratory spectra, and integrating the Gaussian fits. The resulting abundances are reported in Table 2.3. Paper I also reported NH₄⁺ and HCOOH abundances, but because of their contested assignments no additional NH₄⁺ and HCOOH abundances are reported here. The NH₄⁺ abundances, as defined in Paper I, are however included indirectly since they were derived from the sum of the C3 and C4 abundances.

Table 2.1. The source sample of 56 low-mass YSOs and 2 background stars observed with *Spitzer*-IRS and 8 high-mass YSOs observed with *ISO*.

Source	Alias	RA J2000	Dec J2000	Cloud	Type
L1448 IRS1		03 25 09.4	+30 46 21.7	Perseus	low
L1448 NA		03 25 36.5	+30 45 21.4	Perseus	low
IRAS 03235+3004		03:26:37.5	+30:15:27.9	Perseus	low
IRAS 03245+3002		03:27:39.0	+30:12:59.3	Perseus	low
L1455 SMM1		03:27:43.3	+30:12:28.8	Perseus	low
RNO 15		03 27 47.7	+30 12 04.3	Perseus	low
IRAS 03254+3050		03:28:34.2	+31:00:51.2	Perseus	low
IRAS 03271+3013		03 30 15.2	+30 23 48.8	Perseus	low
B1-a		03 33 16.7	+31 07 55.1	Perseus	low
B1-c		03:33:17.9	+31:09:31.0	Perseus	low
B1-b		03:33:20.3	+31:07:21.4	Perseus	low
IRAS 03439+3233	B5 IRS3	03 47 05.4	+32 43 08.5	Perseus	low
IRAS 03445+3242	B5 IRS1	03 47 41.6	+32 51 43.8	Perseus	low
L1489 IRS	IRAS 04016+2610	04:04:43.1	+26:18:56.4	Taurus	low
IRAS 04108+2803		04:13:54.72	+28:11:32.9	Taurus	low
HH 300		04:26:56.30	+24:43:35.3	Taurus	low
DG Tau		04:27:02.66	+26:05:30.5	Taurus	low
IRAS 08242-5050	HH46 IRS	08:25:43.8	-51:00:35.6	HH46	low
IRAS 12553-7651		12:59:06.6	-77:07:40.0	Cha	low
IRAS 13546-3941		13:57:38.94	-39:56:00.2	BHR92	low
IRAS 15398-3359		15:43:02.3	-34:09:06.7	B228	low
GSS 30 IRS1		16:26:21.4	-24:23:04.1	Ophiuchus	low
WL 12		16:26:44.2	-24:34:48.4	Ophiuchus	low
Elias 29		16:27:09.42	-24:37:21.1	Ophiuchus	low
GY 224		16:27:11.2	-24:40:46.7	Ophiuchus	low
WL 20		16:27:15.7	-24:38:45.6	Ophiuchus	low
IRS 37		16:27:17.6	-24:28:56.5	Ophiuchus	low
WL 6		16 27:21.8	-24:29:53.3	Ophiuchus	low
IRS 42		16:27:21.5	-24:41:43.1	Ophiuchus	low
CRBR 2422.8-3423		16:27:24.61	-24:41:03.3	Ophiuchus	low
IRS 43		16:27:27.0	-24:40:52.0	Ophiuchus	low
IRS 44		16:27:28.1	-24:39:35.0	Ophiuchus	low
Elias 32	IRS 45	16:27:28.4	-24:27:21.4	Ophiuchus	low
IRS 46		16:27:29.4	-24:39:16.3	Ophiuchus	low
VSSG 17	IRS 47	16:27:30.2	-24:27:43.4	Ophiuchus	low
IRS 51		16:27:39.8	-24:43:15.1	Ophiuchus	low
IRS 63		16:31:35.7	-24:01:29.5	Ophiuchus	low
L1689 IRS5		16:31:52.1	-24:56:15.2	Ophiuchus	low
RNO 91	IRAS 16316-1540	16:34:29.3	-15:47:01.4	L43	low
IRAS 17081-2721		17:11:17.28	-27:25:08.2	B59	low
B59 YSO5		17:11:22.2	-27:26:02.3	B59	low
2MASSJ17112317-2724315		17:11:23.1	-27:24:32.6	B59	low
EC 74		18:29:55.72	+01:14:31.6	Serpens	low
EC 82		18:29:56.89	+01:14:46.5	Serpens	low
SVS 4-5	EC 88	18:29:57.6	+01:13:00.6	Serpens	low
EC 90		18:29:57.75	+01:14:05.9	Serpens	low
EC 92	SVS 4-10	18:29:57.9	+01:12:51.6	Serpens	low
CK4		18:29:58.21	+01:15:21.7	Serpens	low
CrA IRS 5		19:01:48.0	-36:57:21.6	Corona Australis	low
HH 100 IRS		19:01:50.56	-36:58:08.9	Corona Australis	low
CrA IRS7 A		19:01:55.32	-36:57:22.0	Corona Australis	low
CrA IRS 7 B		19:01:56.4	-36:57:28.0	Corona Australis	low
CrA IRAS32		19:02:58.7	-37:07:34.5	Corona Australis	low
L1014 IRS		21:24:07.5	+49:59:09.0	L1014	low
IRAS 23238+7401		23:25:46.65	+74:17:37.2	CB 244	low
W3 IRS5		02 25 40.8	+62 05 52.8		high

Table 2.1 (cont'd)

Source	Alias	RA J2000	Dec J2000	Cloud	Type
MonR2 IRS3		06:07:47.8	-06:22:55.0		high
GL989		06:41:10.1	+0:9:29:35.8		high
W33A		18:14:39.4	-17:52:01.3		high
GL 2136		18 22 27.0	-13 30 10.0		high
GL7009S		18:34:20.9	-05:59:42.2		high
S140 IRS1		22:19:18.17	+63:18:47.6		high
NGC7538 IRS9		23:14:01.6	+61:27:20.2		high
Elias 16		04:39:38.88	+26:11:26.6	Taurus	bg
EC 118	CK 2	18:30:00.62	+01:15:20.1	Serpens	bg

Table 2.2 – Optical depths of the 5–7 μm complex components for new sources.

Source	τ_{C1} (5.84 μm)	τ_{C2} (6.18 μm)	τ_{C3} (6.76 μm)	τ_{C4} (6.94 μm)	τ_{C5} (broad)
WL 12	0.012 \pm 0.003	0.000 \pm 0.002	0.049 \pm 0.004	0.136 \pm 0.003	0.014 \pm 0.071
WL 6	0.002 \pm 0.007	0.000 \pm 0.006	0.137 \pm 0.007	0.087 \pm 0.006	0.030 \pm 0.045
IRS 42	–	–	–	–	–
IRS 43	0.059 \pm 0.004	0.082 \pm 0.003	0.179 \pm 0.005	0.105 \pm 0.004	0.066 \pm 0.051
IRS 44	0.080 \pm 0.005	0.089 \pm 0.004	0.135 \pm 0.005	0.201 \pm 0.004	0.004 \pm 0.086
Elias 32	0.021 \pm 0.005	0.000 \pm 0.004	0.050 \pm 0.009	0.075 \pm 0.007	0.058 \pm 0.025
IRS 46	0.018 \pm 0.004	0.002 \pm 0.004	0.076 \pm 0.005	0.066 \pm 0.004	0.000 \pm 0.023
VSSG17	0.058 \pm 0.002	0.056 \pm 0.002	0.042 \pm 0.005	0.061 \pm 0.004	0.011 \pm 0.016
IRS 51	0.042 \pm 0.003	0.036 \pm 0.002	0.074 \pm 0.003	0.060 \pm 0.002	0.000 \pm 0.012
IRS 63	0.000 \pm 0.003	0.023 \pm 0.002	0.048 \pm 0.003	0.060 \pm 0.003	0.044 \pm 0.039

Table 2.3 – Ice column densities and abundances for new sources.

Source	N(H ₂ O) 10 ¹⁷ cm ⁻²	[NH ₃] %	[CH ₃ OH] %
WL 12	22.1 \pm 3.0	<3.8	<4.5
WL 6	41.7 \pm 6.0	2.9 \pm 0.4	<2.1
IRS 42	19.5 \pm 2.0	<2.1	11.9 \pm 1.1
IRS 43	31.5 \pm 4.0	–	–
IRS 44	34.0 \pm 4.0	3.7 \pm 0.4	<1.6
Elias 32	17.9 \pm 2.6	<5.2	12.4 \pm 1.9
IRS 46	12.8 \pm 2.0	5.1 \pm 0.9	<4.1
VSSG 17	17.0 \pm 2.5	<3.1	6.9 \pm 2.4
IRS 51	22.1 \pm 3.0	2.4 \pm 0.3	11.7 \pm 0.9
IRS 63	20.4 \pm 3.0	5.7 \pm 1.3	<1.8

2.3 Results

The complete ice data set contains seven identified molecules – H_2O , CO_2 , CO , CH_4 , NH_3 , CH_3OH and OCN^- – seven additional features attributed to CO and CO_2 (here and in the remainder of the chapter X:Y denotes species X found in an X:Y ice mixture) in different ice environments and seven ice components, yet to be firmly identified with a single carrier. The XCN feature decomposition in van Broekhuizen et al. (2005) is adopted consisting of features at 2165 (OCN^-) and 2175 cm^{-1} . The band assigned to HCOOH at 7.25 μm is included as the ‘7.25 μm band’. The range of ice abundances with respect to H_2O ice is presented in histogram form and parameterized with the standard deviation of the log-transformed abundances with respect to H_2O ice in §2.3.1. The sources of abundance variations for different species are then explored through correlation plots, ice mapping of the Oph-F core and a principal component analysis of the ice abundances.

2.3.1 Abundance variations of different ices

There are ice components with small deviations and others with a much broader observed range between different sources. This is illustrated in Fig. 2.1, which shows a direct comparison between a narrow (CO_2) and a broad (CH_3OH) ice abundance distribution. The CH_3OH ice abundance uncertainties are 5–30% (0.02–0.13 when log-transformed) and the CO_2 uncertainties are only a few percent. The difference in abundance variation is thus real. For most ice components presented in Fig. 2.2–2.4, the relative abundance uncertainty is less than 10%. Exceptions are CH_4 , NH_3 , OCN^- , XCN, the 2175 cm^{-1} feature, the 7.25 μm band and CH_3OH , which have uncertainties up to 30%. As reported below, all ices have log-transformed standard deviations above 0.1, equivalent to 30%, and thus ice abundance uncertainties do not alone explain the differences in ice abundance variations.

Figures 2.2–2.4 show the spread in ice abundances for all detected ice features, including significant upper limits, where the ice abundances with respect to the median have been log-transformed (power 10). The OCN^- abundances in Fig. 2.2 are derived from the 2165 cm^{-1} component in agreement with laboratory OCN^- spectra, while ‘2175 cm^{-1} ’ is the optical depth of the second XCN component and ‘XCN’ encompasses the entire feature.

Each histogram is centered on the median ice abundance with respect to H_2O ice, where the median is calculated from the detected ice abundances towards the low-mass protostars. The histogram bins are calculated from the variance among the detected ice abundances towards the same sample. Most histograms include only ice detections. The plots for OCN^- , XCN, the 2175 cm^{-1} feature, CH_3OH and NH_3 include upper limits as well, since most upper limits for these species lie below the median detected abundance and are thus significant. The high-mass protostellar abundance histograms are overplotted based on the median and bin size derived from the low-mass protostellar abundances. Table 2.4 lists the standard deviation from the median of the log-transformed abundances for all low-mass protostellar ices, in increasing order, which can be used as a numerical measure of the ice abundance variability during this star-formation stage. Table 2.4

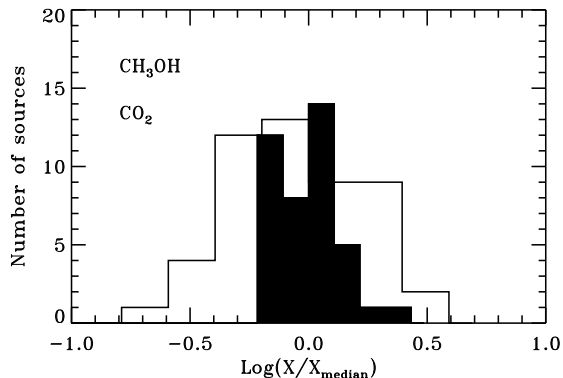


Figure 2.1 – Histograms of the CO_2 (solid) and CH_3OH ice abundances (black contours) towards low-mass protostars, illustrating the difference between an ice component with a narrow (CO_2) and a broad (CH_3OH) abundance distribution. The ice abundances are with respect to H_2O ice and are normalized to the median of each ice abundance.

also include commonly proposed formation mechanisms and identifications from previous studies; UV or ion processing can produce most molecules but is only listed specifically where there are observations that suggest this formation pathway.

CO_2 , CH_4 and NH_3 have all been suggested to form in the quiescent clouds. This is consistent with their narrow distributions and log-transformed standard deviations of <0.2 ; this early formation should be the least sensitive to cloud collapse time scales and thus to the evolutionary stage of the material in front of the protostar, which may either be dominated by the protostellar envelope or the surrounding cloud.

Among the total ice abundances, CO , OCN^- and CH_3OH have the broadest distributions for the low-mass protostars, i.e. there are order of magnitude abundance variations between different sources, and the log-transformed standard deviations are >0.2 . OCN^- and CH_3OH cover a similar abundance range towards the smaller high-mass sample, while the CO abundances towards the high-mass protostars are consistently low. The high-mass protostellar total ice abundances are also separated from their low-mass counterparts for CO_2 and CH_4 , where the high-mass abundances peak at a significantly lower level. Among the XCN components, the high-mass sample is slightly shifted to higher abundances for OCN^- and the total XCN components, and to lower abundances for the 2175 cm^{-1} component.

The CO and CO_2 component histograms are shown in Fig. 2.3. The $\text{CO}_2:\text{H}_2\text{O}$ component distribution towards low-mass protostars is narrow, while all other abundances have log-transformed standard deviations of >0.2 . The pure CO and CO_2 ice components are very broad in the low-mass sample, consistent with their predicted dependence on the envelope temperature. The component plots also reveal that the difference in CO_2 abundances between low-mass and high-mass stars is due to a difference in $\text{CO}_2:\text{H}_2\text{O}$; the other component abundances are not significantly different between the low-mass and

Table 2.4 – Standard deviations (SD) of log-transformed ice abundances, including upper limits (UL), and proposed carriers and surface formation pathways.

Ice feature	SD	SD UL	Proposed carriers	Formation pathways
C3	0.10		$\text{NH}_4^+ + \text{CH}_3\text{OH}^1$	NH_4^+ : acid-base chemistry ^{2,3,4}
CO_2	0.11			$\text{CO}+\text{O}(\text{H})^5$
$\text{CO}_2:\text{H}_2\text{O}$	0.12			$\text{CO}+\text{OH}^6$
7.25 μm	0.14		(HCOOH^1)	$\text{HCO}+\text{OH}^5$
NH_3	0.15	0.16		hydrogenation of N^5
CH_4	0.17			hydrogenation of C^5
C4	0.17		$\text{NH}_4^+^1$	heated NH_4^+ ice ¹
$\text{CO}_2:\text{CO}$	0.21			$\text{CO}+\text{O}(\text{H})$, UV/ion + $\text{CO}^{5,7,8}$
$\text{CO}:\text{H}_2\text{O}$	0.22			CO freeze-out and migration ⁷ , UV+ H_2O +carbon grain ⁹ , UV+ $\text{H}_2\text{O}:\text{CO}_2$ ice ¹⁰
CH_3OH	0.20	0.23		Hydrogenation of $\text{CO}^{11,12}$
C1	0.24		$\text{HCOOH} + \text{H}_2\text{CO}^1$	H_2CO : see CH_3OH
$\text{CO}:\text{CO}_2$	0.26			see $\text{CO}_2:\text{CO}$
XCN	0.21	0.27	$\text{OCN}^- + \text{CO-Si}^2$	see OCN^- and 3175 cm^{-1}
CO_2 shoulder 2175 cm^{-1}	0.28 0.17	0.29	$\text{CO}_2:\text{CH}_3\text{OH}^{13}$ $\text{XCN}+\text{CO-Si}^2$	co-formation CO-Si : chemisorption on on silicate grains ¹⁴
OCN^-	0.13	0.31		acid-base chemistry from $\text{NH}_3+\text{HNCO}^2$ UV/ions + $\text{NH}_3 + \text{COX}$ ice
C5	0.31		warm $\text{H}_2\text{O} + \text{anions}$ +refractory organics ¹	ice heating or acid-base chemistry or UV processing ¹
CO	0.31			freeze-out from gas-phase
C2	0.33		$\text{HCOO}^- + \text{NH}_3^1$	HCOO^- : acid-base chemistry from $\text{NH}_3+\text{HCOOH}^1$
pure CO	0.38			see CO
pure CO_2	0.53	1.09		thermal heating of $\text{CO}_2:\text{CO}$ or of $\text{H}_2\text{O}:\text{CO}_2^5$

¹Paper I, ²van Broekhuizen et al. (2004), ³Schutte & Khanna (2003), ⁴Raunier et al. (2004), ⁵Tielens & Hagen (1982), ⁶Chang et al. (2007), ⁷Ioppolo et al. (2009), ⁸Paper II, ⁹Mennella et al. (2004), ¹⁰Gerakines et al. (2000), ¹¹Watanabe et al. (2003), ¹²Fuchs et al. (in press), ¹³Dartois et al. (1999), ¹⁴Fraser et al. (2005), ¹⁵Chapter 5.

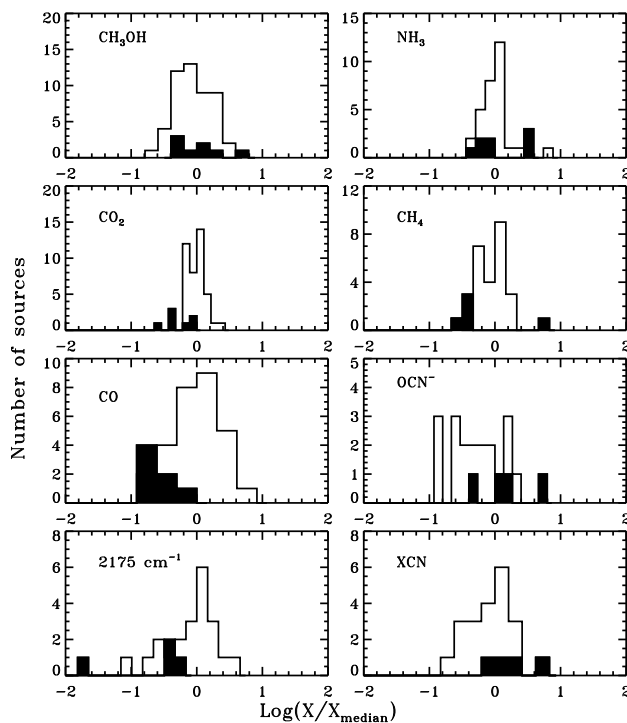


Figure 2.2 – Histograms of ice abundances towards low-mass protostars (black contours) and high-mass protostars (filled), where the ice abundances are with respect to H_2O ice and are normalized to the median of each ice abundance towards the low-mass protostars.

high-mass sample. All CO abundances are shifted to lower values for the high-mass sample, consistent with warmer envelopes around high-mass protostars compared to low-mass protostellar envelopes.

The $5\text{--}7\text{ }\mu\text{m}$ components, C1–5, and the $7.25\text{ }\mu\text{m}$ band span the full range of variations observed among the known ice abundances, from the extremely narrow distribution of C3 to the broad distributions of C2 and C5, while C1, C4 and the $7.25\text{ }\mu\text{m}$ bands are somewhere in between. This variation of the components with respect to H_2O ice was also noted in Paper I. The complexity and formation conditions of the carriers of these bands should thus cover the entire range of observed ice molecules. In Paper I, the $7.25\text{ }\mu\text{m}$ band is attributed to HCOOH , C1 to HCOOH and H_2CO , C2 to NH_3 and HCOO^- , C3 partly to CH_3OH and NH_4^+ , C4 to NH_4^+ and C5 has a number of potential carriers, including non-volatile organics and ions. The validity of especially the NH_4^+ , HCOOH and HCOO^- assignments is discussed further below.

To summarize, a large number of the investigated ices vary too much to form early on in the cloud together with H_2O and CO_2 . The following sections aim to constrain

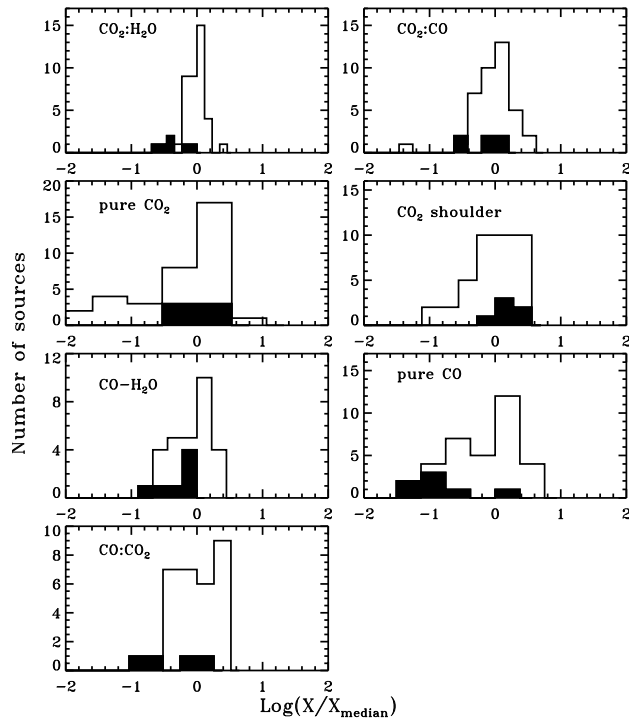


Figure 2.3 – Histograms of CO and CO₂ ice component abundances where X:Y should be read as amount of X in an X:Y mixture. Otherwise as in Fig. 2.3

the reasons behind these abundance variations which may a priori be caused by several different factors including:

1. different initial chemical conditions in different star-forming clouds,
2. different prestellar evolution timescales affecting both the CO freeze-out and the ice exposure to cosmic rays and cosmic-ray induced UV radiation,
3. whether the material in front of the protostar originates in the envelope or the surrounding cloud material and thus its evolutionary stage,
4. protostellar heating of the ice mantles causing ice diffusion and desorption, and
5. destruction or formation from stellar UV radiation.

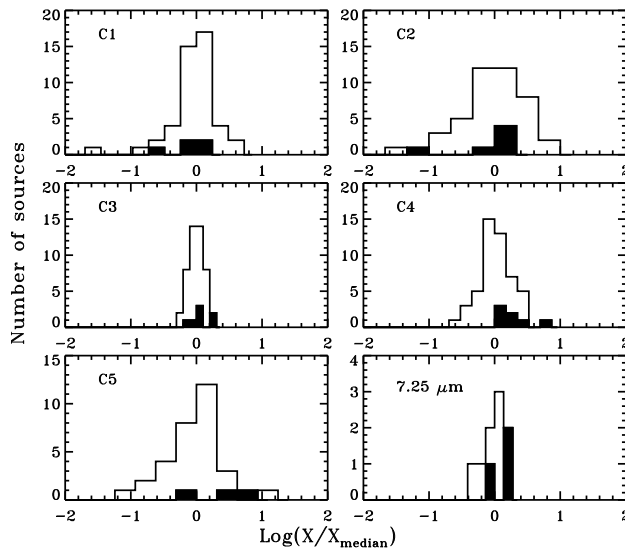


Figure 2.4 – Histograms of 5–7 μm component abundances and the 7.25 μm feature. Otherwise as in Fig. 2.2.

2.3.2 Protostars versus background stars

Only a handful of background stars have so far been investigated for ices within the *c2d* program, of which two were included in Paper I and one in Paper II. These two sources, Elias 16 and EC 118, are here used for comparison between quiescent clouds and protostars. H_2O , all CO_2 and CO components, except for pure CO_2 , and the C1-4 components are detected towards at least one of the background sources and thus do not require stellar processing to form. Of the undetected species, the upper limits for all features, except for pure CO_2 , are similar to the lowest abundances towards protostars. Hence, the current small sample of background sources do not provide any additional constraints on when and where these non-detected ices form.

2.3.3 Heating (in)dependencies

Protostellar ice heating was explored in Paper I and II as an underlying cause for observed abundance variations of the C1-5 components and CO_2 and CO ice. Ice heating is predicted to reduce the abundances of volatile ices, segregate previous ice mixtures and cause diffusion of ice radicals and thus the formation of more complex species. For example, pure CO ice evaporates already at low temperatures, while pure CO_2 is only expected to form after ice heating to at least 30 K from $\text{CO}_2:\text{CO}$ distillation or $\text{CO}_2:\text{H}_2\text{O}$ segregation (e.g. Chapter 5). The low abundances of CO and CH_4 ice towards high-mass stars confirm the sensitivity of volatile ices to the thermal envelope properties.

These well-understood dependencies of CO and CO₂ components on ice heating can be used to test the dependence of other ice components on ice heating. The two temperature tracers employed in Papers I and II are the fraction of CO in a H₂O-rich ice compared to pure CO ice and the fraction of CO₂ ice that is pure. The CO:H₂O component either form from chemistry inside the H₂O ice or through diffusion of CO into the H₂O ice upon heating. In either case CO:H₂O is less volatile than pure CO ice and the ratio should be temperature dependent.

Paper I found that the variation in C5 correlates with the fraction of CO in a H₂O-rich ice compared to pure CO ice, but only if high-mass sources are included. Excluding these high-mass sources removes the correlation. Furthermore, none of the other six most variable ice species (excluding CO and CO₂) are correlated with ice temperature tracers (either the CO or CO₂ ones) when only including the low-mass sample (not shown). Too many other factors may differ between low-mass and high-mass sources to deduce information about ice formation pathways including both types of objects in the same correlation plots, e.g. different formation pathways of similar features. Hence, except for the ice features already predicted to be temperature sensitive there is no additional evidence for the role of ice heating in simple ice formation. As discussed below it may still be needed to explain the presence of more complex ices indicated by the 7.25 μm feature, but there are too few detections of isolated complex ice features to check correlations.

2.3.4 Ice maps of the Oph-F core

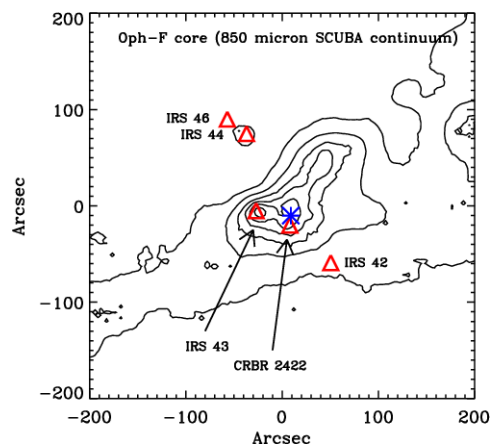


Figure 2.5 – A Scuba 850 μm map, tracing the dust emission of the Oph-F core taken from Pontoppidan (2006). The positions of the protostars in the ice map are marked with triangles.

A previous ice map of the Oph-F core revealed clear trends in the CO, CO₂ and CO:H₂O abundances; all three abundances decrease monotonically when the infrared sources are plotted versus distance away from the central core (Pontoppidan 2006). Note that the lines of sight to these sources probe primarily the dense quiescent core, rather

than ice formation during the protostellar phase. The same core is here mapped in all 19 ice features; Figure 2.5 shows the position of the protostars with respect to the Oph-F core. Figure 2.6 shows that most ice abundances have no clear trends with respect to the distance from the core. This is expected for species forming early during cloud formation (e.g. CH_4 and NH_3), which are independent of cloud core time scales and CO freeze-out, of species dependent on the protostar (e.g. pure CO_2 ice) and of components with multiple carriers as can be suspected for the C1-5 bands.

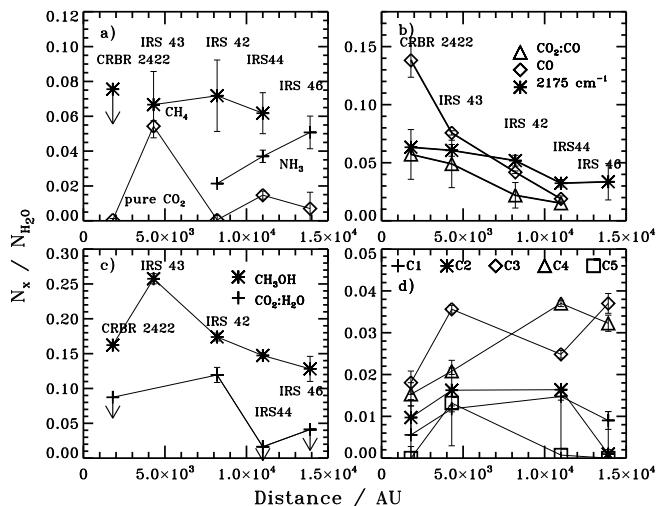


Figure 2.6 – Ice abundances at different distances towards the Oph-F core region. The 2175 cm^{-1} abundances are scaled by 20 and the CO abundances with 0.2 for clarity. The C1-C5 components are plotted optical depths scaled to the $3\text{ }\mu\text{m}$ H_2O ice feature since the band strengths of their carriers are unknown.

Of the three ices identified to increase towards the core by Pontoppidan (2006), the rapid and monotonic increase of the CO ice abundance towards the core region was interpreted as a catastrophic freeze-out of CO in the pre-stellar stage once a certain density and temperature is reached. The order of magnitude increase in CO ice with respect to H_2O is accompanied by a small increase the abundance of $\text{CO}:\text{H}_2\text{O}$ ice and a factor of three increase in the total CO_2 abundance, suggesting a CO_2 formation pathway from CO ice. This is confirmed in Fig. 2.6b, which shows that the $\text{CO}_2:\text{CO}$ increases towards the core. The only other species that increases monotonically towards Oph-F is the 2175 cm^{-1} band. OCN^- is not detected towards these sources and the 2175 cm^{-1} component is thus the entire XCN feature.

At least one other ice component, $\text{CO}_2:\text{H}_2\text{O}$, increases initially towards the core followed by a drop towards the centre-most source CRBR 2422.8-3423 (Fig. 2.6c). The pattern of CH_3OH and the C5 component is consistent with such a trend as well, but they are based on one detection and several upper limits each. This is consistent with that

$\text{CO}_2\text{:H}_2\text{O}$ and CH_3OH both have probable formation mechanisms that depend on the simultaneous presence of CO freeze-out and accreting H atoms and the gas phase H fraction should decrease towards the core. Thus the peak $\text{CO}_2\text{:H}_2\text{O}$ and CH_3OH abundances at a some distance from the core may be caused by prestellar conditions favouring CO and O hydrogenation outside of IRS 43, while all O or OH react with CO before a second H accretes onto the grain surface inside of IRS 43. $\text{CO}_2\text{:CO}$ may also form through cosmic rays and $\text{CO}+\text{O}$ reactions towards the center of the core.

No other ice abundances follow any trends towards the core, including the $7.25\ \mu\text{m}$ feature, the CO_2 shoulder and pure CO_2 ice, consistent with a map dominated by material in the quiescent cloud core.

2.3.5 XCN ice abundance correlations

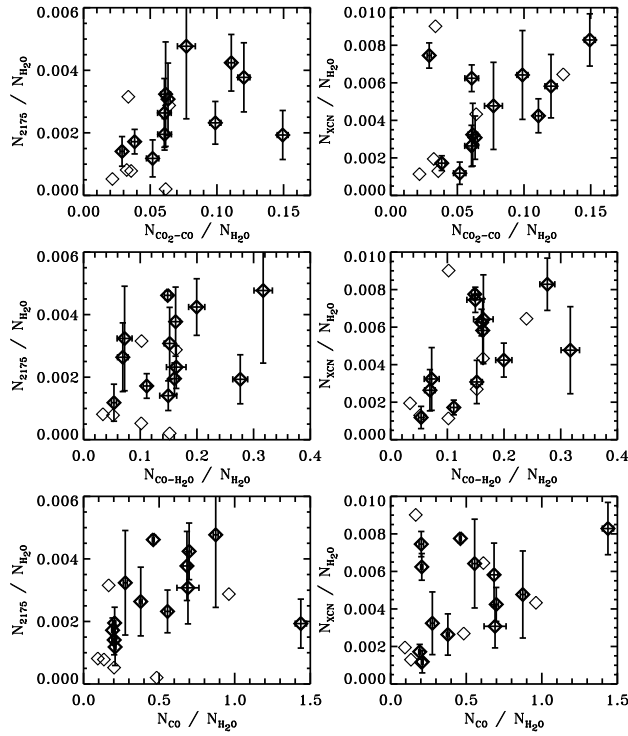


Figure 2.7 – Correlation plots of the total XCN band and the $2175\ \text{cm}^{-1}$ XCN component with $\text{CO}_2\text{:CO}$, $\text{CO:H}_2\text{O}$ and the total CO abundance, all with respect to H_2O ice. The grey diamonds are XCN and $2175\ \text{cm}^{-1}$ upper limits.

To test the XCN-related findings for the Oph-F core, correlations of CO-related species with the XCN components are investigated for the entire low-mass ice sample. Figure

2.7 shows that there is at best a tentative correlation between the 2175 cm^{-1} feature and $\text{CO}_2:\text{CO}$ and $\text{CO}:\text{H}_2\text{O}$ in the entire low-mass sample ($R=0.38$ and $R=0.41$). The correlations are stronger ($R=0.50$ and $R=0.56$, 12 mutual detections) and statistically significant at 95% level between the entire XCN feature and the same CO_2 and CO components. The correlations with the total CO abundance is weaker for both the 2175 cm^{-1} component and the entire XCN band, possibly because of the high volatility of CO compared to XCN. There are too few OCN^- detections towards low-mass protostars to carry out a similar correlation analysis. Thus, in a well constrained environment, i.e. the Oph-F core, the 2175 cm^{-1} component trace CO_2 present in a CO-rich ice and CO present in a H_2O -rich ice well, while in the sample as a whole the XCN band is better correlated with both. Both $\text{CO}:\text{H}_2\text{O}$ and $\text{CO}_2:\text{CO}$ are present towards quiescent lines of sight in clouds (Pontoppidan et al. 2003, Paper II). The correlations are thus indicative of a quiescently formed, CO-related, single carrier of the XCN band, with a varying profile dependent on the local environment.

2.3.6 Principal component analysis and ice abundance correlations

With 19 unique ice components, the number of possible correlations within the ice sample is large. Principal Component Analysis (PCA) offers a fast technique to reveal underlying structures in a multivariate sample by reducing the dimensions of the data set. This is done by projecting down both the sources and the source attributes, here the ice abundances with respect to H_2O ice, on principal components (PCs), which trace latent variables that govern the behavior of measurable quantities. In this data set, potential latent variables are the UV-field strength and the CO freeze-out fraction, which may govern the abundances of several of the observed spectral peaks.

The ice abundance data are projected onto principal components using the IDL routine *pca.pro*, which normalizes all data to zero mean and unity variance before calculating the eighteen eigenvectors of the data matrix, i.e. the principal components. The original ice abundance vectors are described perfectly by a combination of all principal components. The strength of PCA is that the principal components are chosen sequentially to explain the maximum variance in the data set. Therefore three principal components explain $\sim 50\%$ of the variation in this sample.

Figure 2.8 shows the sources and the ice abundances plotted with respect to the first three principal components. The sources have been color-coded based on their host cloud (see on-line version) and there are no apparent differences between the different cloud sources with respect to ice abundances. Initial cloud conditions are not then a source of ice abundance variations. IRS 51, EC 82 and EC 92 stand out in the source plots, demonstrating the potential use of PCA to detect special sources within large samples.

In the PCA ice abundances plots, species that appear close together are similarly described by the principal components in the plot and are thus likely correlated, especially if the same group re-occurs in different PC plots. Vice versa, species on opposite sides in the plot are anti-correlated. The first PC plot includes several expected groups such as CO and pure CO; $\text{CO}:\text{CO}_2$, $\text{CO}_2:\text{CO}$ and $\text{CO}:\text{H}_2\text{O}$; CO_2 , $\text{CO}_2:\text{H}_2\text{O}$ and the CO_2 shoulder. It also suggests that C1, C3 and NH_3 are related. When checked individually, the CO and

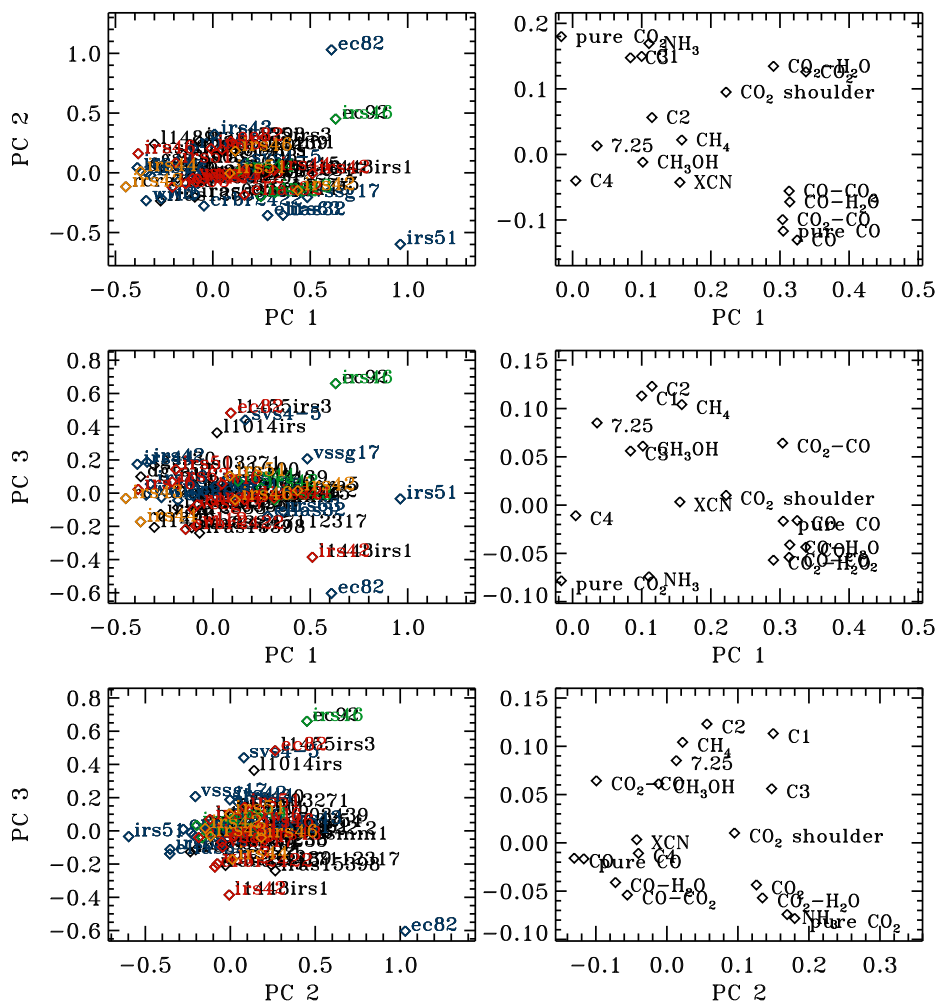


Figure 2.8 – Principal component analysis plots containing all low-mass sources and molecular detections. (In the online version the sources are color-coded with respect to star forming cloud: Ophiuchus = blue, Serpens = green, Perseus = red and CrA = orange.)

CO₂ species are all correlated significantly within each group at a 95-99.5% level. The proposed NH₃ correlations depend on a single source, EC 82, however and if this source is removed the NH₃ is no longer grouped with C1 and C3 in the PCA plot. C1 and C3 are correlated, though there is a large amount of scatter. In the PC1 versus PC3 plot, the C2 and C1 correlations with the 7.25 μm feature, and with CH₄ are significant, while there are too few overlaps between CH₄ and the 7.25 μm detections to evaluate their relationship. The other new groupings in the PC1 versus PC3 and PC2 versus PC3 are not significant, except for the XCN correlations already considered and C3 and the CO₂ shoulder.

PCA can thus not be used blindly to call species correlated, nor are all correlations visible when investigating only the first three PCs. The plots do, however, suggest several correlations that may otherwise not be investigated. The most significant discoveries in light of the further discussion are first that CO₂:CO is better correlated with the different CO abundances than with other CO₂ components, indicative of a universal conversion of pure CO ice into CO₂:CO during CO freeze-out. Second, the C3 correlations with C1 and the lack of correlation with NH₃ are important because of the suggested multiple carriers of C3, including H₂CO and NH₄⁺. Finally the relationship between C1, C2 and the 7.25 μm may provide evidence for complex ice formation as outlined further below.

The latent variables traced by PC1-3 are not obvious, but PC1 seems to generally trace the total CO and CO₂ ice abundances or CO freeze-out, PC2 depends on the CO versus CO₂ content or ice temperature and PC3 on the CH₄, C1, C2 and 7.25 μm feature abundances. This also explains some of the outlying sources – EC 82 is a warm source with silicate emission features, while IRS 51 contains an extremely large CO ice column, indicative of a low temperature environment. The latent variables thus suggest that CO freeze-out followed by new ice formation, ice heating, and potentially simple ice photolysis as traced by C1, C2 and 7.25 μm components, are the three most important factors for explaining ice abundance variations. This is consistent with the analysis in the previous sections, although the last PC assignment depends on what C1, C2 and the 7.25 μm features can be assigned to, which is the first topic of the next section.

2.4 Discussion

The previous section established that spectral ice features form during low-mass formation through a range of processes, some universally present, while others depend critically on the local pre- and proto-stellar conditions. Before discussing this further, the identifications of previously unassigned or tentatively assigned ice features are established following the constraints put on their carriers from the results and some new spectral comparisons §2.4.1. The sequential ice formation is then discussed followed by a preliminary comparison of low-mass versus high-mass ice sources and the proposed origin of their differences in ice abundances.

2.4.1 The XCN feature and other unidentified ice bands

The XCN feature can be at least partly assigned to OCN^- from comparison with laboratory spectra. The assignment of the 2175 cm^{-1} has been debated since laboratory OCN^- bands peak between 2155 and 2172 cm^{-1} (van Broekhuizen et al. 2004). The alternative assignment to CO-chemisorption onto silicate grains (Fraser et al. 2005) is however inconsistent with the increasing amount of the 2175 cm^{-1} carrier towards the Oph-F core region, where the grains should already be completely covered with the H_2O -rich ice. Proton bombardment of CO and N_2 containing ices does result in a new feature around 2180 cm^{-1} (Moore et al. 1983; Hudson et al. 2001), which may be the carrier of the 2175 cm^{-1} component towards protostars. The carrier is then most likely a radical, since it disappears at 35 K in the laboratory and this would explain its prevalence towards low-mass sources, and its low abundance towards high-mass ones. It is also consistent with the CO: CO_2 correlation, since it forms from CO in the laboratory.

As discussed above there is however evidence that the entire XCN feature is due to OCN^- ; 3 cm^{-1} is a relatively small frequency difference for an ice feature and OCN^- may not have been studied in an appropriate ice mixture yet. In a H_2O -rich ice mixture, the OCN^- band shifts to lower wave numbers at higher temperature, consistent with the trends of the XCN bands towards low-mass and high-mass sources. OCN^- formation should depend on CO freeze-out, since a plausible reaction pathway is radical chemistry of CO and NH to form HNC, followed by proton-loss in the presence of a strong base. This assignment is thus also consistent with the observed correlations. OCN^- can also form through ion or UV bombardment of the H_2O -rich ice layer (van Broekhuizen et al. 2004), but this is harder to reconcile with the close relationship between the XCN feature and different CO-related features for the low-mass stars.

To conclusively settle between these different scenarios requires a number of studies. First an assignment to the reported 2180 cm^{-1} feature in the laboratory to investigate its plausibility as a carrier in space, second a more quantitative understanding of how HNC and OCN^- form in interstellar ice analogues and third more cloud core observations to ensure that XCN generally forms towards cloud cores. Ice heating does however not seem necessary to form the XCN feature even though it may be responsible for its enhancement towards high-mass protostars. This is consistent with acid-base reactions, which are efficient already at 15 K (van Broekhuizen et al. 2005).

The $7.25\text{ }\mu\text{m}$ ice band has previously been assigned to HCOOH (Gibb et al. 2000, Paper I). At first glance the histogram plots suggest a low-temperature chemistry for the $7.25\text{ }\mu\text{m}$ band formation since the abundance varies by less than a factor five towards both low-mass and high-mass sources, including upper limits. Strict upper limits are however not possible to derive because of the inherent weakness of the feature and the low variation is probably due to the high detection threshold rather than to an inherent low variation in abundance of the carrier.

Another possible carrier of the $7.25\text{ }\mu\text{m}$ feature is $\text{CH}_3\text{CH}_2\text{OH}$. A spectral comparison between laboratory data and a *ISO* spectrum of W33A and a *Spitzer* spectrum of B1-b shows that the band widths and band positions of the $7.25\text{ }\mu\text{m}$ features towards the high-mass protostar W33A and the low-mass source B1-b agree better with pure $\text{CH}_3\text{CH}_2\text{OH}$

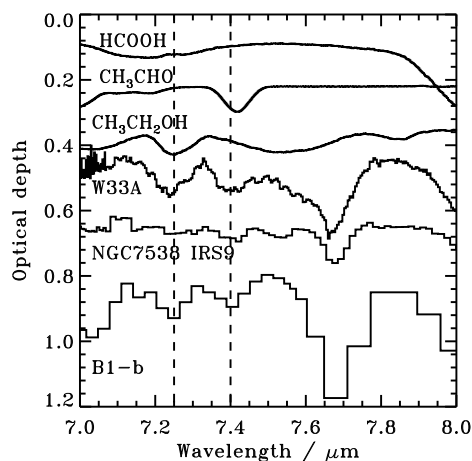


Figure 2.9 – *ISO* spectra at 7–8 μm for W33A, NGC7538 IRS9 and B1-b, following subtraction of a local spline continuum, plotted together with laboratory spectra of pure HCOOH, CH₃CHO and CH₃CH₂OH ices. The dashed lines mark the 7.25 and 7.40 μm features usually assigned to HCOOH and HCOO⁻. The feature at 7.67 μm is due to CH₄ ice.

ice than with pure HCOOH ice (Fig. 2.9). In all protostellar spectra a local spline continuum was fitted to 6.9, 7.16, 7.33, 7.77 and 7.85 μm . Though the HCOOH feature may become somewhat more narrow in ice mixtures (Bisschop et al. 2007a) it still does not fit the observed feature; the mismatch between the width of all plausible HCOOH spectral bands and the width of observed 7.25 μm feature was already noted in Paper I, though the HCOOH identification was still maintained. In a previous study the CH₃CH₂OH abundance was constrained for NGC7538 IRS9 from another CH₃CH₂OH feature at 3.4 μm to be <1.2% with respect to H₂O ice (Boudin et al. 1998). This agrees with the lack of a feature at 7.25 μm . No strong limits can be derived for W33A from the 3.4 μm band or any other bands within the *ISO* spectral range compared with the 7.25 μm feature.

Figure 2.9 also shows that the observed 7.40 μm is more likely due to CH₃CHO rather than HCOO⁻ – both have been proposed previously as carriers (e.g. Schutte et al. 1999; Gibb et al. 2004, Paper I). Hence, while HCOOH and HCOO⁻ cannot be excluded from the ice, their abundances cannot be determined from the 7.25 and the 7.42 μm ice features.

Both CH₃CH₂OH and CH₃CHO are readily formed by UV-induced chemistry in CH₃OH-rich ices (Chapter 10). From the PCA plots, the 7.25 μm band is related to C1 and C2, and possibly to CH₄. C1 and C2 both absorb at the typical position of HCO-bearing species and may thus trace either simple organic molecules such as H₂CO and HCOOH or a complex UV or cosmic-ray-induced chemistry in general, or both. The correlation with CH₄ is curious, but may be explained by an enhanced complex molecule production in the presence of CH₄ (Chapter 10). Though more sources need to be investigated in detail for limits on different complex organics, the combination of C1, C2 and the 7.25

and 7.40 μm features towards protostars may potentially be used as a tracer of a complex ice chemistry. An interesting first step would be to investigate the variability of the 7.25 μm to 7.40 μm ratio and how this relates to the complex ice chemistry investigated experimentally in Chapter 10.

In Paper I, two of the 5-7 μm spectral components, C3 and C4, were tentatively assigned to NH_4^+ , resulting in NH_4^+ abundances of 2–16% with respect to H_2O ice towards the low-mass protostars, 5–26% towards the high-mass protostars and 5–12% towards the background stars. The lack of correlation between NH_3 and C3 and C4 is not inconsistent with the identification of NH_4^+ , since a different fraction of NH_3 may be converted into NH_4^+ in different lines of sight. The NH_4^+ abundances are higher than those of its precursor NH_3 in most lines of sight, suggesting a very efficient conversion from NH_3 to NH_4^+ . This is consistent with acid-base chemistry with strong acids such as HNCO or HCOOH (Schutte & Khanna 2003; van Broekhuizen et al. 2004), which results in almost complete conversions from neutral to ionic form already at 15 K. There are two caveats, however, first the presence of C4 towards background stars is not consistent with its assignment to warm NH_4^+ , and second the production of strong acids must be efficient under quiescent conditions. OCN^- is certainly not the counter ion of NH_4^+ , since the OCN^- ice abundances are an order of magnitude lower than the reported NH_4^+ abundances. If a formation path from hydrogenation of atoms to other strong acids is identified, the NH_4^+ assignment may also be consistent with the lack of variability in C3 with respect to H_2O ice. This is however a big if, and experiments are surely required to test whether such formation paths exist, e.g. the viability of HCOOH formation from partial hydrogenation of CO followed by reaction with OH.

Despite these caveats NH_4^+ remains the most probable main carrier for the C3 band, mainly because of lack of options; the other plausible option is H_2CO , but it was excluded as a major carrier in Paper I because of constraints on other H_2CO features absorbing at 3.34–3.54 and at 5.8 μm , i.e. the position of C1. The C1 and C3 features correlate, albeit weakly ($R=0.42$, 48 detections), when normalized to the water abundances in each line of sight, as might be expected if both features partially share H_2CO as a carrier. A partial assignment of NH_4^+ to C3 therefore seems warranted and possibly to C4, but not the derivation of NH_4^+ abundances from integrating the entire C3 and C4 features.

2.4.2 Early versus late ice formation during low-mass star formation

Figure 2.10 summarizes the conclusions drawn in this section on when and where the identified ices form during the cloud core formation followed by star formation. Unidentified ice features are discussed in relation to the ice formation under ‘early’, ‘late’ and protostellar stages.

Previous ice survey studies noted that some ice abundances, e.g. that of CO_2 , are almost constant towards low-mass sources with respect to H_2O ice, while others, especially the ice abundances of CO, CH_3OH and XCN, vary by more than an order magnitude with respect to H_2O ice (Pontoppidan et al. 2003; van Broekhuizen et al. 2005, Paper II). The

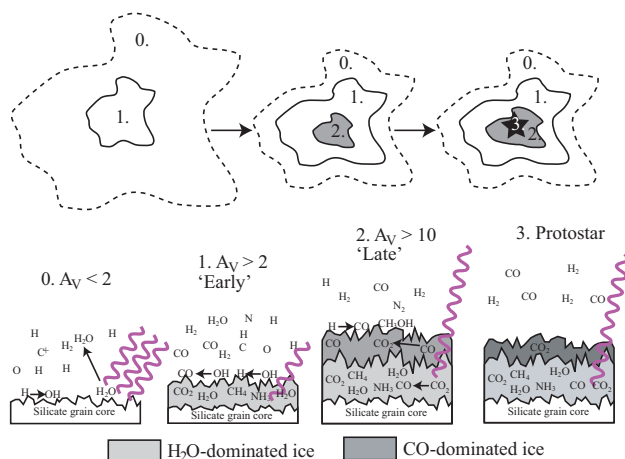


Figure 2.10 – The key ice reactions during the different stages of cloud and star formation. In the protostellar stage desorption of CO starts at 20 K and $\text{H}_2\text{O}:\text{CO}_2$ segregation at 30 K.

abundance histograms in §2.3.1 visualize these previous conclusions and also show that among the other identified ice features, NH_3 and CH_4 vary little if the large uncertainties in their abundances are taken into account, while all CO and CO_2 ice component abundances, except for $\text{CO}_2:\text{H}_2\text{O}$, vary by an order of magnitude or more. This difference in ice abundance patterns can be interpreted in terms of early, global cloud formation resulting in narrow distributions versus locally produced ices in the prestellar core or in the protostellar envelope resulting in broad distributions. This interpretation is supported by an early onset of CO_2 ice formation from ice mapping (Bergin et al. 2005) and the fact that ice spectra towards a few background stars contain H_2O and CO_2 ice features, whereas the upper limits of other ‘early’ species such as NH_3 and CH_4 are inconclusive (Knez et al. 2005). Species in Table 2.4 with log-transformed standard deviations <0.2 of the median are thus consistent with early formation in molecular clouds together with H_2O ice.

Figure 2.6 shows that large variations in ice abundances can be explained from different local prestellar conditions and thus large ice variations alone cannot be used as a signpost for ice processing during the protostellar stage. The CO, $\text{CO}:\text{H}_2\text{O}$, $\text{CO}_2:\text{CO}$, $\text{CO}_2:\text{H}_2\text{O}$ and XCN (2175 cm^{-1} feature) bands all grow with respect to H_2O ice towards the central Oph-F core region. The trends of these abundances towards the core suggests that fast CO accretion towards the core first produces hydrogenated CO (CH_3OH) and species forming from CO and hydrogenated atoms, e.g. CO_2 and HNCO . The latter then loses a proton to NH_3 to form OCN^- . As H atoms become scarce, reactions between CO and O(H) and energetic processing of both the H_2O and CO-rich ice layers begins to dominate the chemistry towards the cloud core and $\text{CO}_2:\text{CO}$, $\text{CO}:\text{H}_2\text{O}$ and OCN^- abundances continue to increase. Cosmic rays and secondary UV photons are present throughout the

cloud and thus energetic processing of ices is possible. Some of the ‘CO:H₂O’ increase may actually be ‘CO:H₂CO’ and ‘CO:CH₃OH’ increases instead, which may be the result of UV processing of CH₃OH ice (Chapter 10). The decrease in several ice abundances towards the core can also be understood from quiescent UV and ion processing, which continuously dissociate ices and therefore will result in a lowered ice abundances for species with higher dissociation cross-section than H₂O ice when their production channels are turned off.

The variable C1, C2 and C5 components are not significantly correlated with any of the CO and CO₂ features except for the previously reported tentative correlation between C5 and the CO-component ratios tracing protostellar heating (Paper I). As suggested above, C1, C2 and the 7.25 μm feature may be associated with complex organic carriers that form in the ice once it has been moderately heated and previously dissociated ices can recombine into larger molecules. The presence of C1 and C2 in clouds shows, however, that they probably have multiple carriers of which some are simple, e.g. H₂CO, and other more complex. The 7.25 μm feature together with pure CO₂ ice may in the end be the only features that form exclusively in heated ices.

2.4.3 Ice formation in low-mass versus high-mass protostars

The low- and high-mass protostars mainly differ in their CO, CH₄ and CO₂ ice abundances, which are all low towards the high-mass protostars. The low CO and CH₄ abundances can be explained by their high volatility and thus sensitivity to heating. The low CO₂ content can have several possible origins. The time scales for cloud formation and collapse may be different for low- and high-mass stars i.e. faster for the high-mass case, which allows less CO to freeze out and thus less CO₂ to form. Less CO freeze-out and thus less CO₂ formation would also be expected if the cloud spent less time at 20 K. Another possibility is a higher thermal or non-thermal destruction of the CO₂ ice towards the high-mass protostars; the higher irradiation field may photodissociate CO₂ into CO, which subsequently desorbs or CO₂ may simply thermally desorb. A larger high-mass protostellar sample would certainly aid in resolving which process is the dominating one for explaining the low CO₂ content. Such a sample is now just becoming available through new *Spitzer* data (Seale et al. 2009).

There is no evidence for a higher CH₃OH or XCN content towards high-mass stars, except for the single case of W33A. There is thus no evidence for a formation pathway of these species that involves stellar UV irradiation or excess heat. The 7.25 μm feature seems somewhat more common towards high-mass stars, indicative of a partial UV or thermal ice chemistry origin, consistent with an assignment to CH₃CH₂OH, which forms through diffusion of previously produced ice radicals in the warm envelope (Chapter 10). Of the 5–7 μm components, C1, C2 and C3 have similar relative optical depths with respect to H₂O ice towards both low-mass and high-mass sources, while the C4 and C5 are shifted to the high-abundance range towards the high-mass stars, again indicative of at least a partial formation pathway involving heat or UV irradiation or both, in agreement with the analysis in Paper I.

Most ice abundances are, however, remarkably similar towards low- and high-mass

protostars, further high-lighting the importance of the cold pre-stellar stage for ice formation up to the complexity of CH₃OH.

2.5 Conclusions

Large samples of ice sources are necessary both to identify general trends in the ice evolution and to identify which ice processes always precedes star formation and which depend on the local environment where the protostar forms. The variability of ice abundances, measured by the normalized standard deviation, ranges from 13% to an order of magnitude, stressing the different formation paths of different ices. The low-mass and high-mass protostellar ice abundances only differ significantly for the volatile species CO and CH₄ and for CO₂. There is thus no evidence for a richer UV-induced ice chemistry around high-mass protostars compared to low-mass protostars, as previously supposed.

From ice maps, CO freeze-out together with cosmic ray induced processing (through either direct ion bombardment or secondary UV photons) and atomic processing can produce local differences in ice abundances within the same cloud. In contrast, a principal component analysis (PCA) on the low-mass sample reveals that there is no overall, significant difference in ices between the investigated clouds. The PCA reveals a number of new correlations between the tentatively identified or unidentified features in the spectra with known ice species, e.g. between the 7.25 μm band and features at 5.8 and 6.2 μm , all which potentially trace more complex ices. The PCA also suggest that most of the variation in the data set is connected with the total CO₂ and CO ice content, the CO versus CO₂ content or ice temperature and the production of more complex species. This is consistent with the analysis of the single core Oph-F and of the abundance variations. PCA is thus a useful tool to get an overview of a large set of data – here more than 50 sources and 19 unique ice components.

A re-evaluation of previous assignments of the 5–7 μm components, and the 7.25 and 7.40 μm features has put the common assignments of the 7.25 and 7.40 μm features to HCOOH and HCOO⁻ into question – CH₃CH₂OH and CH₃CHO agree better with the observed band positions and band widths alike. The large amounts of NH₄⁺ tentatively reported previously should also be taken as upper limits, until more laboratory data becomes available. In general the field is in dire need of both sensitive, high-resolution spectral observations of ices in protostellar envelopes and towards background stars as well as quantitative laboratory work on the proposed formation paths of most ices.

The combined results from the ice abundance histograms, ice maps, correlation plots and PCA suggest an ice formation scenario through the following steps:

1. H₂O, CO₂, CH₄, NH₃ form through hydrogenation and oxygenation of atoms and small molecules at low cloud densities, when the gas phase is still rich in atoms. Some of the NH₃ is converted to NH₄⁺ through acid-base chemistry in the presence of quiescently produced acids.
2. Deeper into the cloud or at later times during the cloud collapse, CO freezes out catastrophically on top of the previous H₂O-rich ice. Some of the CO is converted

into H_2CO and CH_3OH , dependent on the H/H_2 ratio in the gas phase, and CO continues to react with OH to form CO_2 and probably with NH to form HNCO . HNCO reacts to form OCN^- in the presence of NH_3

3. All through the cloud evolution, the CO - and H_2O -rich ices are further processed by cosmic rays and cosmic-ray induced UV radiation (Shen et al. 2004). This together with CO reactions with heavier atoms become the dominant driver for ice evolution after the gas phase has been depleted of H and H processing is no longer possible. The result is $\text{CO}_2:\text{CO}$, $\text{CO}:\text{H}_2\text{O}$ ice mixtures and the continued production of OCN^- .
4. Once the protostar turns on, ices start to become mobile, resulting in radical diffusion, ice desorption and segregation. The proposed complex carriers of the C1 and C2 components and the $7.25 \mu\text{m}$ band may be associated with this ice formation phase. More background sources are however needed to check that complex ices cannot form prior to the onset of star formation and also a dedicated analysis towards which protostars the $7.25 \mu\text{m}$ band appears. Ice heating definitely results in pure CO_2 ice formation through ice distillation and segregation, and in CO and CH_4 evaporation. The C4 and C5 components and the XCN band assigned to OCN^- are all tentatively dependent on ice temperature.

3

THE *c2d* SPITZER SPECTROSCOPIC SURVEY OF CH₄ ICE AROUND LOW-MASS YOUNG STELLAR OBJECTS

CH₄ is proposed to be the starting point of a rich organic chemistry. Solid CH₄ abundances have previously been determined mostly towards high mass star forming regions. Spitzer/IRS now provides a unique opportunity to probe solid CH₄ towards low mass star forming regions as well. Infrared spectra from the *Spitzer Space Telescope* are presented to determine the solid CH₄ abundance toward a large sample of low mass young stellar objects. 25 out of 52 ice sources in the *c2d* (cores to disks) legacy have an absorption feature at 7.7 μm , attributed to the bending mode of solid CH₄. The solid CH₄ / H₂O abundances are 2-8%, except for three sources with abundances as high as 11-13%. These latter sources have relatively large uncertainties due to small total ice column densities. Toward sources with H₂O column densities above $2 \times 10^{18} \text{ cm}^{-2}$, the CH₄ abundances (20 out of 25) are nearly constant at $4.7 \pm 1.6\%$. Correlation plots with solid H₂O, CH₃OH, CO₂ and CO column densities and abundances relative to H₂O reveal a closer relationship of solid CH₄ with CO₂ and H₂O than with solid CO and CH₃OH. The inferred solid CH₄ abundances are consistent with models where CH₄ is formed through sequential hydrogenation of C on grain surfaces. Finally the equal or higher abundances toward low mass young stellar objects compared with high mass objects and the correlation studies support this formation pathway as well, but not the two competing theories: formation from CH₃OH and formation in the gas phase with subsequent freeze-out.

Öberg K. I., Boogert, A.C.A., Pontoppidan, K.M., Blake, G.A., Evans, N.J., Lahuis, F., van Dishoeck, E.F., 2008, ApJ, volume 678, pages 1032-1041

3.1 Introduction

The presence and origin of complex organic molecules in protostellar regions and their possible incorporation in protoplanetary disks is an active topic of research. CH₄ is proposed to be a starting point of a rich chemistry, especially when UV photons are present (Dartois et al. 2005). In particular CH₄ is believed to play a key role in the formation process of prebiotic molecules (Markwick et al. 2000).

CH₄ is less well studied in interstellar and circumstellar media compared to other small organic molecules because CH₄ has no permanent dipole moment and therefore cannot be observed by pure rotational transitions at radio wavelengths. Solid CH₄ was first detected through its bending mode at 7.67 μm from the ground by Lacy et al. (1991), and with the Infrared Space Observatory Short Wavelength Spectrometer (ISO-SWS) by Boogert et al. (1996) toward a few high-mass sources. Tentative claims have been made toward some other objects including low-mass protostars, but are inconclusive because of the low S/N ratio of these data (Cernicharo et al. 2000; Gürtler et al. 2002; Alexander et al. 2003). Solid CH₄ has also been detected from the ground through its stretching mode at 3.3 μm , but only toward the brightest high mass sources due to problems in removing the many atmospheric lines in this spectral region (Boogert et al. 2004a).

Models predict CH₄ to form rapidly on cool grains through successive hydrogenation of atomic C; similarly H₂O is formed through hydrogenation of atomic O (van de Hulst 1946; Allen & Robinson 1977; Tielens & Hagen 1982; Brown et al. 1988; Hasegawa et al. 1992; Aikawa et al. 2005). Observations of CH₄ hence provide insight into the basic principles of grain surface chemistry. Compared to H₂O the observed gas- and solid-state CH₄ abundances are low; reported CH₄ abundances are typically a few percent with respect to H₂O (Lacy et al. 1991; Boogert et al. 1998). This points to relatively low atomic C abundances at the time of CH₄ formation, with most C already locked up in CO as H readily reacts with C on surfaces (Hiraoka et al. 1998). This is in agreement with the high CH₃OH abundances in several lines of sight, formed by hydrogenation of CO (Dartois et al. 1999; Pontoppidan et al. 2003), and large CO₂ abundances, formed through oxidation of CO or hydrogenated CO. That these molecules are all formed through a similar process is corroborated by the profiles of solid CO₂ absorption bands, which usually show an intimate mixture of CO₂, CH₃OH and H₂O in interstellar ices (Gerakines et al. 1999; Boogert et al. 2000; Knez et al. 2005).

If CH₄ is formed efficiently through grain surface reactions as well, CH₄ should be similarly mixed with H₂O. Observations of solid CH₄ toward a few high mass young stellar objects (YSOs) show that the CH₄ absorption band profiles are broad and agree better with CH₄ in a hydrogen bonding ice, H₂O or CH₃OH, than with a pure CH₄ ice or CH₄ mixed with CO (Boogert et al. 1997). This profile analysis does not, however, exclude CH₄ formation from photoprocessing of CH₃OH (Allamandola et al. 1988; Gerakines et al. 1996). In addition, because of the small sample in previous studies, it is unclear if these broad profiles are a universal feature. Hence it cannot be excluded that CH₄ in some environments may form in the gas phase and subsequently freeze out.

Because formation pathway efficiency depends on environment, another method for testing formation routes is through exploring the distribution of CH₄ toward a large sample

of objects of different ages, luminosities and ice column densities. In addition, correlations, or lack thereof, with other ice constituents may provide important clues to how the molecule is formed. If CH_4 is formed through hydrogenation on grain surfaces in quiescent clouds, the CH_4 abundance with respect to H_2O should be fairly source independent since this mechanism mainly depends on the initial conditions of the cloud before the star forms, which seem to vary little between different star forming regions. Because of the generality of this mechanism, the CH_4 and H_2O , and possibly CO_2 , column densities should correlate over a large range of different environments. This is also the prediction of several models where the solid $\text{CH}_4/\text{H}_2\text{O}$ and CH_4/CO_2 ratios in dark clouds vary little both as a function of time (Hasegawa et al. 1992) and distance into a cloud that has collapsed (Aikawa et al. 2005). In contrast, CO , which is formed in the gas phase and subsequently frozen out, is predicted to only correlate with CH_4 during certain time intervals. If CH_4 instead forms in the gas phase, solid CH_4 should be better correlated with solid CO than with solid H_2O and CO_2 , since pure CH_4 freezes out and desorbs at similar temperatures to CO (Fraser et al. submitted to *A&A*, Collings et al. 2004). Finally, if CH_4 forms by UV photoprocessing of CH_3OH more CH_4 would also be expected to form toward sources with stronger UV-fields i.e. higher mass objects.

The objective of this study is to determine the CH_4 abundances and distribution pattern toward a sample of low mass young stellar objects, varying in evolutionary stage and total ice column density. The distribution pattern and correlations with other ice constituents within the sample as well as comparison with high mass young stellar objects will be used to constrain the CH_4 formation mechanism. This study is based on spectra acquired with the Spitzer Infrared Spectrometer (IRS) as part of our legacy program ‘From molecular cores to protoplanetary disks’ (*c2d*), which provides a large sample (41 sources) of infrared spectra of low mass star formation regions (Evans et al. 2003). In addition 11 sources are added from the GTO program 2 for which ground based 3-5 μm already exist (Pontoppidan et al. 2003). Overviews of the H_2O , CO_2 , CH_3OH and other ice species in these data are found in Boogert et al. (ApJ submitted, Paper I) and Pontoppidan et al. (ApJ submitted, Paper II). The detection of solid CH_4 toward one of the sources, HH46 IRS, was published by Boogert et al. (2004b). We have detected an absorption feature, which is attributed to solid CH_4 , toward 25 out of 52 low mass ice sources found in this *c2d* sample.

3.2 Source sample selection, observations and data reduction

The source sample consists of a combination of known low mass protostars and new protostars discovered by their Spitzer IRAC and MIPS broad-band SEDs. Spitzer/IRS spectra were obtained as part of the *c2d* Legacy program (PIDs 172 and 179) as well as a dedicated open time program (PID 20604) and a few archival spectra observed as a part of the GTO programs of Houck et al. Among the targets observed with the IRS short-long (SL) module, 41 ice sources were identified from their spectra in the *c2d* sample (Paper

I). The GTO sources are all associated with the Ophiuchus cloud and were selected based on previous ice observations at 3-5 μm (Pontoppidan et al. 2003). The source sample of 25 low mass protostars presented here was selected from the 41 *c2d* and 11 GTO ice sources based solely on the existence of an absorption feature at 7.7 μm , identified with solid CH₄ (Table 3.1). Due to the high sensitivity of the Spitzer/IRS, a large range of star formation stages are represented in the sample from very young YSOs at the interface of the Class 0/I stages (e.g. B1-c) to objects like RNO 91, identified as an inclined disk with a remnant envelope. It also includes VERY Low Luminosity Objects (VELLOs) such as L1014 IRS (Young et al. 2004). More information about the evolutionary stages of the objects are reported in Paper I.

The Spitzer/IRS spectra were reduced using the 2-dimensional Basic Calibrated Data (BCD) spectral images, produced by the Spitzer Science Center (SSC) pipeline version S13.2.0, as a starting point. The low resolution modules, which are the relevant ones for the solid CH₄ feature, were reduced in a similar way to ground-based spectra. First, the spectral and spatial dimensions were orthogonalized, and then the 2-dimensional images of the two nodding positions were subtracted in order to remove the extended emission. A fixed width extraction was performed and then the 1-dimensional spectra were averaged. Subsequently the spectra were divided by spectra of the standard star HR 2194, reduced in the same way, to correct for wavelength dependent slit losses. Finally the spectra were multiplied along the flux scale in order to match Spitzer/IRAC photometry. One source, EC 92, was carefully extracted manually due to multiple other sources present in the slit. More details about the reduction and the complete mid-infrared spectra of the *c2d* sources is presented in Paper I. The CH₄ 7.7 μm absorption feature falls within the range of the IRS modules SL1 and SL2. At these wavelengths the resolving power $R = \lambda/\Delta\lambda$ of IRS is 65 or 0.12 μm for SL1 and 125 or 0.06 μm for SL2 (IRS Data Handbook). The plotted spectra are made up using data from the main orders of SL1 and SL2, while the SL1 bonus order was only used to confirm detections. SL2 stops around 7.6 μm so the peak of the CH₄ absorption feature is always in SL1. The part of the spectra from the SL2 module is hence mainly used to determine the continuum and in some cases the shape of a low wavelength wing. When comparing observations to laboratory spectra, the laboratory spectra are always convolved to the resolution of SL1 (0.12 μm , sampled with two pixels per resolution element).

ISO-SWS spectra of four high mass YSOs are used for comparison between low mass and high mass protostars in this paper. The latest Standard Processed Data (SPD) pipeline version 10.1 products were taken from the ISO archive and the detector scans were cleaned from cosmic ray hits and averaged. The final spectra do not show significant differences with respect to the data published in Keane et al. (2001).

Table 3.1. The source sample of 25 low-mass YSOs observed with Spitzer-IRS and 4 high-mass YSOs with previously published ISO spectra.

Source	Alias	RA J2000	Dec J2000	Cloud	Type	Obs. ID
IRAS 03235+3004		03:26:37.5	+30:15:27.9	Perseus	low	9835520
IRAS 03245+3002		03:27:39.0	+30:12:59.3	Perseus	low	6368000
L1455 SMM1		03:27:43.3	+30:12:28.8	Perseus	low	15917056
IRAS 03254+3050		03:28:34.2	+31:00:51.2	Perseus	low	11827200
B1-c		03:33:17.9	+31:09:31.0	Perseus	low	13460480
B1-b		03:33:20.3	+31:07:21.4	Perseus	low	1596544
L1489 IRS	IRAS 04016+2610	04:04:43.1	+26:18:56.4	Taurus	low	3528960
IRAS 08242-5050	HH46 IRS	08:25:43.8	-51:00:35.6	HH46	low	5638912
IRAS 12553-7651		12:59:06.6	-77:07:40.0	Cha	low	9830912
IRAS 15398-3359		15:43:02.3	-34:09:06.7	B228	low	5828864
GSS 30 IRS1		16:26:21.4	-24:23:04.1	Ophiuchus	low	12699392
IRS 42		16:27:21.5	-24:41:43.1	Ophiuchus	low	12699648
IRS 43		16:27:27.0	-24:40:52.0	Ophiuchus	low	12699648
IRS 44		16:27:28.1	-24:39:35.0	Ophiuchus	low	12699648
IRS 63		16:31:35.7	-24:01:29.5	Ophiuchus	low	12676608
VSSG 17	IRS 47	16:27:30.2	-24:27:43.4	Ophiuchus	low	12698624
RNO 91		16:34:29.3	-15:47:01.4	L43	low	5650432
B59 YSO5	IRAS 16316-1540	17:11:22.2	-27:26:02.3	B59	low	14894336
2MASSJ1712317-2724315		17:11:23.1	-27:24:32.6	B59	low	14894592
SVS 4-5	EC 88	18:29:57.6	+01:13:00.6	Serpens	low	9407232
EC 92	SVS 4-10	18:29:57.9	+01:12:51.6	Serpens	low	9407232
CrA IRS 5		19:01:48.0	-36:57:21.6	Corona Australis	low	9835264
CrA IRS 7 B		19:01:56.4	-36:57:28.0	Corona Australis	low	9835008
CrA IRS32		19:02:58.7	-37:07:34.5	Corona Australis	low	9832192
L1014 IRS		21:24:07.5	+49:59:09.0	L1014	low	12116736
W33A		18:14:39.4	-17:52:01.3		high	32900920
NGC7538 IRS9		23:14:01.6	+61:27:20.2		high	09801532
GL989		06:41:10.1	+09:29:35.8		high	71602619
GL7009S		18:34:20.9	-05:59:42.2		high	15201140

3.3 Results

3.3.1 CH₄ column densities

Figure 3.1 shows the flux calibrated spectra of the 25 low mass YSOs containing the CH₄ 7.7 μm absorption feature. The spectra were converted to optical depth scale using a smooth spline continuum fitted to the 7-7.4 μm and 8.0-8.3 μm regions as shown in Fig. 3.1. A local continuum is necessary since the CH₄ feature lies on the edge of other broader features such as the 9.7 μm feature. Fitting the continuum is complicated by the presence of a weak HI recombination emission line at 7.5 μm (Pfund α) toward several of the sources e.g. the CrA sources, IRAS 03235+3004, L1489 IRS, RNO 91 and SVS 4-5. Of these ground based spectra around 4 μm exist for CrA IRS5, CrA IRS7b, IRAS 03235+3004, L1489 IRS and SVS 4-5. In all of these spectra the 4.05 μm HI Brackett α is clearly visible corroborating the identification of the emission feature with hydrogen.

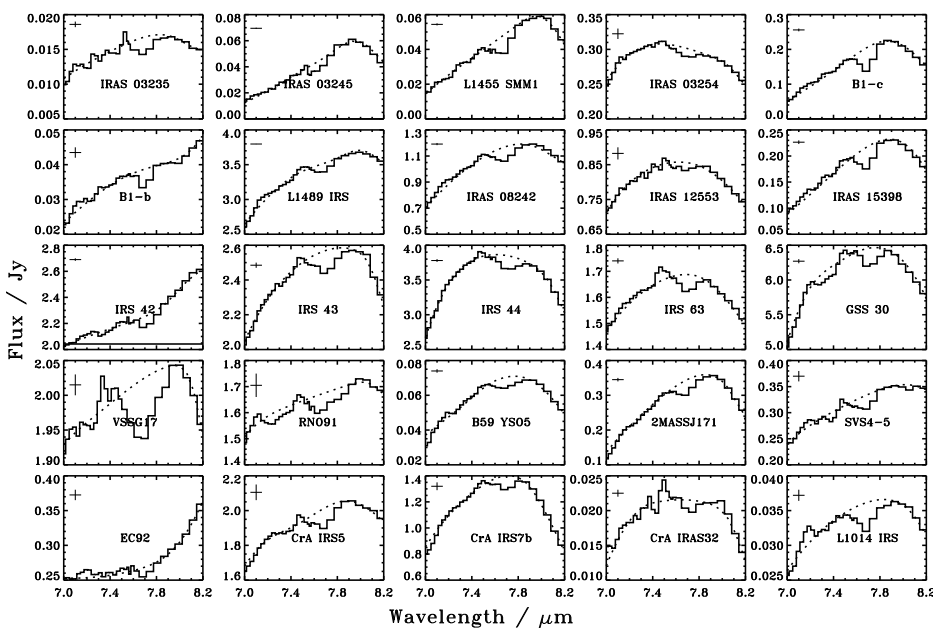


Figure 3.1 – The Spitzer-IRS spectra (solid line) of the CH₄ sources between 7.0 and 8.2 μm , plotted together with the chosen spline continua (dotted line). The tick bar in the upper left corner indicates the noise level derived within the *c2d* pipeline.

Table 3.2. Gaussian parameters of the observed absorption features and the CH₄ column densities and abundances relative to solid H₂O and upper limits of SO₂..

Source	λ μm	FWHM μm	τ_{peak} cm^{-1}	$\int \tau_{7.7}$ cm^{-1}	$\int \tau_{\text{CH}_4}$ cm^{-1}	$\text{N}(\text{CH}_4)$ 10^{17} cm^{-2}	$\text{N}(\text{CH}_4)$ $\text{N}(\text{H}_2\text{O}) \times 100$	$\text{N}(\text{SO}_2)_{\text{max}}$ $\text{N}(\text{H}_2\text{O}) \times 100$
IRAS 03235+3004	7.69±0.03	0.16±0.05	0.16±0.07	4.6±1.0	2.9±0.8	6.2±1.8	4.3±1.4	0.35±0.19
IRAS 03245+3002	7.59±0.03	0.20±0.08	0.17±0.04	3.2±0.1	3.2±0.4	6.8±0.8	1.7±0.3	0.08±0.01
L1455 SMM1	7.66±0.01	0.15±0.02	0.24±0.03	6.2±0.3	4.9±0.1	10±0.1	5.8±0.9	0.21±0.03
IRAS 03254+3050	7.68±0.01	0.20±0.03	0.040±0.008	1.4±0.2	0.7±0.1	1.6±0.3	4.0±0.9	0.45±0.14
B1-c	7.68±0.01	0.13±0.01	0.40±0.05	8.7±1.3	7.6±1.2	16±3	5.4±1.4	0.11±0.03
B1-b	7.70±0.01	0.10±0.01	0.16±0.01	2.7±0.1	2.8±0.1	5.9±0.2	3.3±0.6	0.00±0.01
L1489 IRS	7.68±0.01	0.13±0.01	0.037±0.006	0.93±0.04	0.64±0.04	1.4±0.1	3.1±0.2	0.14±0.01
IRAS 08242-5050	7.68±0.06	0.17±0.16	0.098±0.063	2.9±1.8	1.9±0.8	3.9±1.8	5.0±2.4	0.40±0.68
IRAS 12553-7651	7.66±0.02	0.18±0.04	0.026±0.005	0.6±0.1	0.5±0.1	1.1±0.1	3.8±0.9	0.13±0.03
IRAS 15398-3359	7.68±0.01	0.13±0.01	0.22±0.03	5.1±0.6	4.2±0.8	8.8±1.7	6.0±2.0	0.20±0.06
IRS 42	7.72±0.01	0.12±0.03	0.041±0.012	0.82±0.11	0.62±0.22	1.4±0.4	7.7±2.4	0.21±0.06
IRS 43	7.70±0.01	0.21±0.04	0.050±0.014	1.7±0.6	0.94±0.33	2.1±0.6	6.6±2.3	0.70±0.36
IRS 44	7.71±0.01	0.19±0.01	0.053±0.015	1.7±0.4	0.9±0.2	2.1±0.4	6.1±1.4	0.63±0.23
IRS 63	7.70±0.14	0.14±0.13	0.042±0.026	1.0±0.4	0.72±0.31	1.6±0.7	7.9±3.8	0.42±0.59
GSS 30	7.72±0.16	0.14±0.13	0.045±0.027	1.1±0.8	0.7±0.4	1.6±0.9	11±6.2	0.60±0.9
VSSG17	7.68±0.01	0.26±0.04	0.042±0.006	1.8±0.2	0.8±0.1	1.8±0.2	11±2.2	1.5±0.35
RNO91	7.69±0.03	0.27±0.13	0.038±0.009	1.6±0.7	0.68±0.17	1.6±0.5	4.8±1.6	0.76±0.44
B59 YSO5	7.70±0.01	0.19±0.06	0.096±0.050	3.2±3.4	1.8±0.9	3.8±2.0	2.7±1.6	0.31±0.37
2MASSJ17112317	7.69±0.01	0.17±0.06	0.13±0.052	3.9±2.0	2.5±1.0	5.4±2.2	2.8±1.2	0.20±0.23
SVS4-5	7.67±0.01	0.16±0.02	0.083±0.010	2.2±0.2	1.6±0.3	3.5±0.6	6.1±1.7	0.29±0.08
EC92	7.71±0.01	0.07±0.10	0.066±0.032	0.67±0.21	0.88±0.47	2.0±1.2	13±7.7	0.33±0.23
C+A IRS5	7.68±0.01	0.19±0.02	0.055±0.011	1.7±0.3	1.1±0.1	2.3±0.3	6.2±1.0	0.50±0.13
C+A IRS7b	7.69±0.02	0.16±0.05	0.080±0.019	2.2±0.5	1.5±0.5	3.1±1.1	3.0±1.2	0.19±0.08
C+A IRAS32	7.72±0.04	0.09±0.13	0.093±0.018	1.4±0.4	1.6±0.2	3.5±0.4	6.6±2.5	0.12±0.05
L1014 IRS	7.68±0.01	0.19±0.06	0.11±0.022	3.7±1.2	2.4±0.7	5.1±1.5	7.1±2.3	0.53±0.25
Average	7.69	0.16	0.10	2.7	1.5	4.1	5.8	0.34
Standard deviation	0.03	0.05	0.09	2.0	1.4	3.5	2.7	0.35

The spectra were also converted to optical depth scale by adopting a local, straight line continuum between 7.4 and 7.9 μm . The differences in optical depth using the two different continua are less than 20% for most sources, but between 30 and 60% for a few cases: CrA IRS 7B, IRAS 03235+3004, IRAS 12553-7651 and RNO 91. The resulting optical depth spectra using the smooth spline continuum subtraction are shown in Fig. 3.2.

The peak position, full width half maximum (FWHM) and peak optical depth of the 7.7 μm absorption feature along each line of sight were calculated from the best Gaussian fit between 7.5 and 7.9 μm (Table 3.2). The reported error estimates include uncertainties in the fit and choice of continuum. The typical peak position is 7.69 μm and the peak widths range from 0.07 to 0.27 μm . The features hence range from unresolved to barely resolved as the resolution at the center peak position is 0.12 μm . The large widths of the feature in the observed spectra, except for B1-b, suggest that CH₄ is generally in an H₂O or CH₃OH dominated mixture, where laboratory data show that the CH₄ feature has a width of up to 0.15 μm (Boogert et al. 1997).

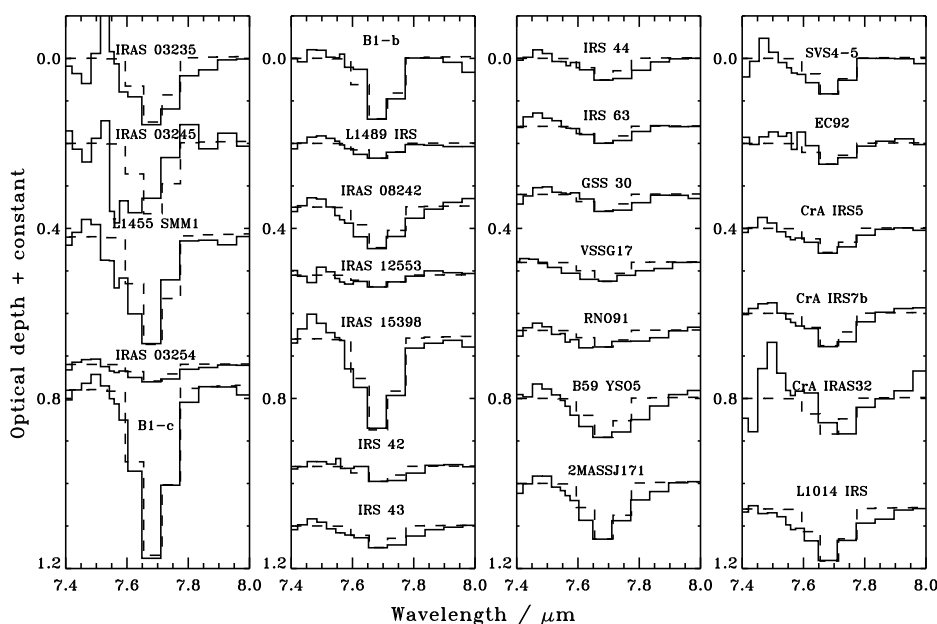


Figure 3.2 – Optical depth spectra of the CH₄ sources plotted together with laboratory spectra (dashed) of a CH₄:H₂O mixture 1:3 (Leiden databases at www.strw.leidenuniv.nl/~lab/databases) convolved to at the same resolution and sampled in the same way as the observational data.

Figure 3.3 compares the source with the deepest absorption feature, B1-c, with different CH₄ containing laboratory ice spectra, convolved to the resolution of IRS-SL1. In the three laboratory ice spectra used here – a H₂O dominated ice, an ice mixture that contains

equal parts of H₂O, CH₃OH and CO₂ and pure CH₄, all at 10 K – the CH₄ absorption profile has both different widths and peak positions. The derived column densities using the three different ice compositions are however the same within the uncertainties: 1.7, 1.6 and 1.7×10¹⁸ cm⁻² respectively. Toward most sources, as for B1-c, H₂O dominated ice spectra provide the best fit. Hence, comparisons with a H₂O:CH₄ 3:1 ice spectrum were used to determine the amount of CH₄ present in the observed spectra and also how much of the 7.7 μm feature can be accounted for by solid CH₄ (Fig. 3.2). Table 3.2 shows that CH₄ can account for 45–100% of the absorption.

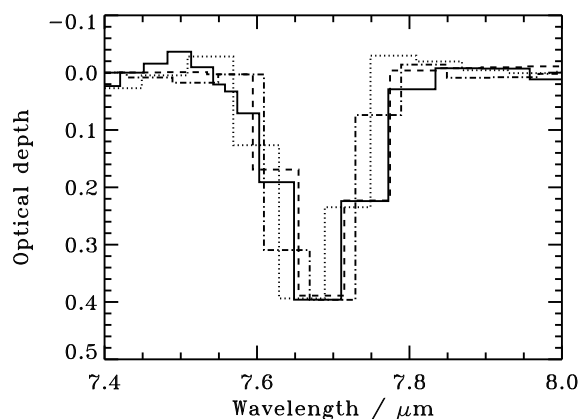


Figure 3.3 – Optical depth spectra of B1-c (solid line) plotted together with laboratory spectra of a CH₄:H₂O 1:3 mixture (dashed), a H₂O:CH₃OH:CO₂:CH₄ 0.6:0.7:1:0.1 mixture (dotted) and pure CH₄ ice (dashed-dotted).

The CH₄ column densities were calculated from the integrated optical depths of the laboratory spectra, scaled to the peak optical depths of the observations, and the band strength for the bending mode of solid CH₄ in a H₂O rich ice, 4.7 × 10⁻¹⁸ cm molecule⁻¹ (Boogert et al. 1997). The uncertainty in CH₄ column densities stems from both the baseline subtraction and the uncertainty in ice mixture composition even after a H₂O rich ice has been assumed. To obtain abundances with respect to solid H₂O, the CH₄ column densities were divided by the solid H₂O column densities from Paper I. Figure 3.4 shows the CH₄ abundances with respect to H₂O as a function of H₂O column density. The CH₄ abundances in the entire sample vary between 2 and 13% and it is seen in the plot that the sample can be split into two parts: sources with H₂O column densities around 2×10¹⁸ cm⁻² and sources with H₂O column densities of 3–40×10¹⁸ cm⁻². In the former group the CH₄ abundances with respect to H₂O vary between 6 and 13% and in the latter group all CH₄ abundances fall between 2 and 8%. Due to the low total column densities in the high abundance group, the uncertainties there tend to be larger. Below 3×10¹⁸ cm⁻² there also seem to be some negative correlation between column density and CH₄ abundance. Figure 3.4 also shows the CH₃OH abundances and upper limits towards the sources in this sample (Paper I). CH₃OH abundances span a larger interval than CH₄ and show none of the column density dependences visible for CH₄. The large variation for CH₃OH abundances is similar to what Pontoppidan et al. (2003) found for a different sample.

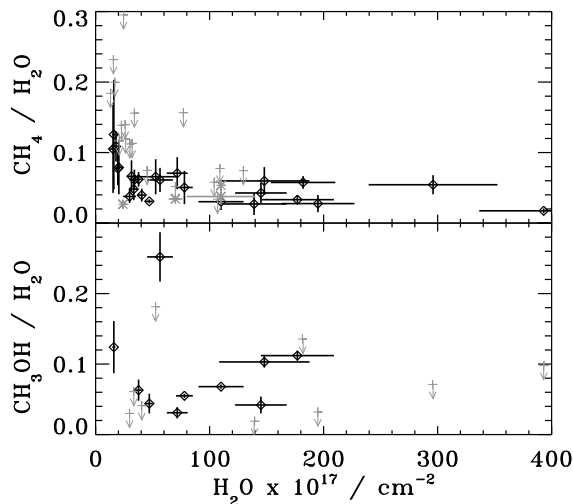


Figure 3.4 – CH₄ and CH₃OH ice abundances are plotted versus H₂O column densities for *Spitzer* (diamonds – black for detections and grey for upper limits) and *ISO* (stars) sources. In the upper panel sources with $2 \times 10^{18} \text{ cm}^{-2}$ H₂O ice have high CH₄ abundances, while the remaining sources have 4–5% CH₄. CH₃OH abundances show no similar groupings and span a larger interval.

The excess absorption (0–55%) of the observed $7.7 \mu\text{m}$ features in many of the astronomical objects is due to broader profiles than expected even for CH₄ in a H₂O rich ice. It is possible that an additional molecule is contributing to the optical depth of the $7.7 \mu\text{m}$ feature, e.g. solid SO₂. Solid SO₂ was suggested by Boogert et al. (1997) to explain the blue wing of the $7.7 \mu\text{m}$ feature in W33A. In contrast, another high mass source NGC7538 IRS9 displays no such wing. A comparison between these two sources and low mass sources from this sample shows that the same variation is present here (Fig. 3.5) – approximately 25% of the sources in this study have a clear blue wing, perhaps attributable to solid SO₂. The maximum amounts of SO₂ present in the observed ices is estimated by assuming that all excess absorption is due to SO₂ and using its measured band strength of $3.4 \times 10^{-17} \text{ cm molecule}^{-1}$ (Sandford & Allamandola 1993) (Table 3.2). The upper limits on the solid SO₂ abundances then vary between 0.1 and 1.5% with respect to H₂O.

In cases where the excess is similar on both sides of the CH₄ absorption, another source of the large widths of the features may be the choice of continuum; the spline continuum was difficult to fit because the CH₄ feature is generally shallow and overlapping with other, larger, features. It is possible that the wings toward several sources are not intrinsic, but a product of this fit. This is highlighted by a comparison between Fig. 3.1 and Fig 3.2, which shows that the sources with clear continua also have thinner absorption features than the average.

3.3.2 Upper limits of solid CH₄

Upper limits for solid CH₄ were determined for the 27 sources without CH₄ detections, in the sample of 52 low mass ice sources originally probed for CH₄, by estimating the

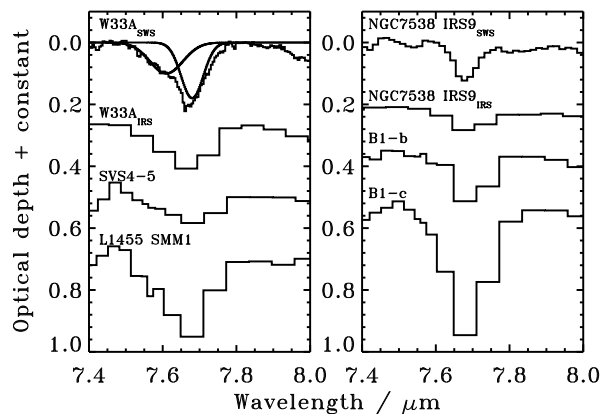


Figure 3.5 – 7.7 μm profile comparison between high mass sources (with their original SWS resolution and convolved to the resolution of IRS-SL1) and four low mass sources. Several of the low mass sources have similar profiles to W33A with a blue wing in addition to the 7.7 μm CH_4 feature. A few low mass sources also show thin profiles similar to that of NGC7538 IRS9.

maximum amount of a $\text{H}_2\text{O}:\text{CH}_4$ 3:1 ice that could hide under the noise. The average 3σ upper limit is 15% solid CH_4 with respect to solid H_2O , which is in the upper range of CH_4 abundances in the sources with solid CH_4 detections. All abundance upper limits below 30% are shown in Figure 3.4. Only one CH_4 upper limit, of $\sim 3\%$, falls below the average abundance of 4.8%. The lack of detection in these 27 sources is hence probably due to the spectral quality and low fluxes of the objects rather than a lower amount of solid CH_4 .

3.3.3 Molecular correlations

The objects in this sample may vary significantly in temperature structure as well as other environmental factors. Lack of correlations between molecular abundances may hence be due to either different formation pathways or differences in volatility. A lack of correlation between CH_4 and molecules of different volatility does hence not exclude that they formed in a similar manner. In pure form CH_4 has a similar volatility to CO (Collings et al. 2004). If CH_4 is mixed with H_2O significant amounts can be trapped inside of the H_2O ice, however, and then CH_4 has an effective volatility closer to that of H_2O and CO_2 .

The column densities of solid H_2O (26 detections) and CH_3OH (10 detections) have been derived in Paper I and solid CO (13 ground based observations) and CO_2 (25 detections) in Pontoppidan et al. (2003) and Paper II for many of the CH_4 sources. The column densities and abundances for these molecules are plotted versus CH_4 in Figs. 3.6 and 3.7. Where the plots reveal a linear relationship between molecules the best linear fit is also drawn. The Pearson product-moment correlation coefficient, R , was calculated to measure the strength of the correlation – R^2 directly gives the fraction of variance of the second molecule that is due to changes in CH_4 , assuming a linear relationship between the two molecules.

Figure 3.6 shows the correlations between the column densities of solid CH_4 and the four other ice components. Some correlation between column densities of ice species

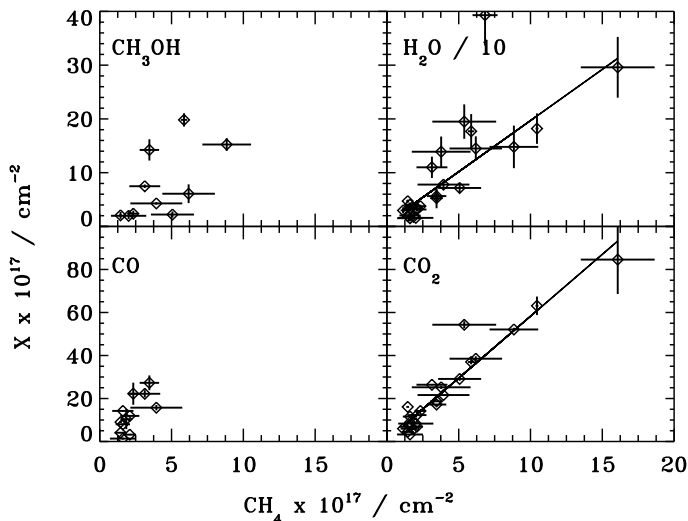


Figure 3.6 – The column densities of four ice species, CH₃OH, H₂O, CO and CO₂ are plotted versus the column densities of solid CH₄. Solid CH₄ is strongly correlated with solid CO₂ and H₂O. CH₄ is only weakly correlated with solid CO and CH₃OH, but this may be partly due to the fact that CO has only been observed and CH₃OH only detected towards much fewer targets. The outlier in the H₂O plot is IRAS 03245+3002.

and with total column density is always expected, but Fig. 3.6 shows that the strength of this correlation is variable between CH₄ and the different molecules. CH₄ correlates strongly ($R^2=0.91$) with CO₂, which is believed to form on grain surfaces. The correlation with H₂O, another species formed on surfaces, is weaker ($R^2=0.64$), but this correlation coefficient is significantly increased if one outlier, IRAS 03245+3002, is removed. R^2 is then 0.82 for the CH₄–H₂O correlation. IRAS 03245+3002 could have been identified previous to the correlation studies as an outlier since it is the only source with no CO₂ ice detection putting an upper limit on its CO₂/H₂O of 15%, compared to $30\pm 9\%$ for the entire sample. Even without removing the outlier the correlations are significant at the 99% level with 23 and 24 degrees of freedom (DF) respectively.

CH₄ and CH₃OH and CO are barely significantly correlated ($R^2=0.48$ with 8 DF and 0.49 with 11 DF respectively). The small number of CO abundances, which are only available for 11 of the targets in this study, complicates interpreting the low correlation plots between CO and CH₄. If only the sources for which CO measurements exist are used to calculate the CH₄–CO₂ and CH₄–H₂O correlations these are reduced to $R^2=0.46$ and 0.74 respectively.

The stronger correlation between CH₄ and CO₂ compared to CH₄ and H₂O is curious, but may be an artefact of the fact that the CO₂ column densities are better known for this sample than the H₂O column densities. For most sources in this sample the H₂O

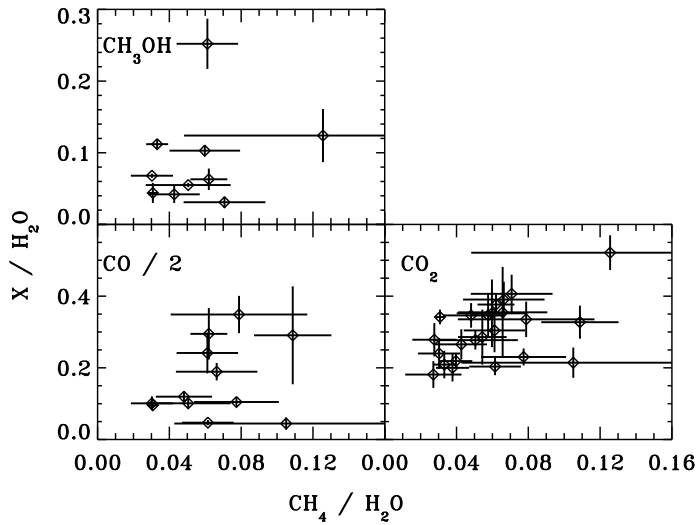


Figure 3.7 – The abundances of solid CH_3OH , CO and CO_2 relative to H_2O are plotted versus those of solid CH_4 . There is no correlation between the relative amounts of solid CH_4 and CH_3OH or CO . In contrast the CH_4 and solid CO_2 abundances are weakly correlated.

column densities are determined by estimating the depth of the H_2O libration feature, which is difficult due to the overlap with the silicate feature at $9.7 \mu\text{m}$. The uncertainties in these H_2O column densities were estimated to $\sim 30\%$ in Paper I after comparison between derived abundances from the $3 \mu\text{m}$ mode and the libration mode for the sources with $3 \mu\text{m}$ spectra. Furthermore the different amounts of CO_2 toward the different sources may introduce further error in the derived H_2O column densities as recently shown in Öberg et al. (2007a).

Figures 3.7 show the correlations between solid CH_4 and the other three ice species, with the abundances normalized to the solid H_2O column density - the main ice constituent (Fig. 3.7). When normalizing to H_2O there is no significant correlation at a 95% level between CH_4 and CH_3OH and CO (R^2 below 0.1) and at best a weak correlation between CH_4 and CO_2 ($R^2 = 0.27$). There is also no correlation between CH_4 abundances and any of the three CO components as defined by Pontoppidan et al. (2003), with the different components corresponding to pure CO and CO in a H_2O and CO_2 rich ice respectively.

3.3.4 Spatial trends

The average CH_4 abundance relative to H_2O and its standard deviation is shown for all clouds with more than one detection and for the entire sample in Table ???. The averages for the individual clouds range from 2.8% to 9%, with Serpens and Ophiuchus at 9 and

Table 3.3. The average CH₄ abundance relative to H₂O, and its standard deviation for five of the investigated clouds and for the entire sample.

Cloud	Number of sources	Average	St. dev.
Perseus	6	0.040	0.014
Ophiuchus	6	0.083	0.019
B59	2	0.027	–
CrA	3	0.052	0.019
Serpens	2	0.093	–
All	19	0.058	0.027

8% respectively. Whether the clouds are significantly different in their CH₄ abundances was evaluated using Analysis of Variance with the Statistics101 resampling software. Resampling is more robust than traditional statistical tests since there is no need to assume an underlying distribution, which is especially useful when the sample size is small. The test procedure starts with calculating the sum of the absolute deviations of the cloud averages from the sample average. The CH₄ abundances in the five clouds are then randomly resampled into five new groups with the same group size distribution as before and the absolute deviations of the group averages from the sample average is re-calculated. This is repeated 1000 times and the number of times the resampled sum of deviations exceeds the sum of deviations of the cloud averages is counted. The nul-hypothesis that the difference between the clouds is due to chance could then be rejected with 95% confidence. If Ophiuchus is removed from the sample there are no longer any significant differences between the clouds.

3.4 Discussion

3.4.1 Low vs. high mass YSOs

For comparison the solid CH₄ abundances with respect to H₂O for several high mass YSOs (Table 3.1) were re-derived and plotted relative to H₂O abundances from Gibb et al. (2004) in Fig. 3.4. These sources have been previously investigated for solid CH₄ by Boogert et al. (1996) and Gibb et al. (2004). The solid CH₄ abundances derived here are 30 to 60% higher than those published by Gibb et al. (2004) mainly due to a difference in band strength (7.3×10^{-18} molecules cm⁻¹ by Gibb et al. (2004) and 4.7×10^{-18} molecules cm⁻¹ here). The plot shows that the high mass ISO CH₄ sources fit in seamlessly with the low mass CH₄ sources with H₂O column densities above 2×10^{18} cm⁻². Figure 3.5 also shows that there is a similar variation in the 7.7 μm feature profile between low and high mass objects. There is hence no reason to expect large systematic differences in CH₄ abundances or formation pathways toward low and high mass YSOs.

3.4.2 Formation scenarios

The similar or higher abundance of CH₄ with respect to H₂O toward the low mass sources in this sample compared to what has been found previously toward high mass young stellar objects, suggests that the CH₄ formation rate is not dependent on stellar UV irradiation. Of the three formation scenarios for CH₄ suggested in the introduction, this study hence does not support a formation pathway connected to stellar UV processing of CH₃OH. Furthermore, in the sources with $2\text{--}40 \times 10^{18} \text{ cm}^{-2}$ H₂O the CH₄ abundance is nearly constant. In comparison the CH₃OH abundances vary by a factor of 10 and it seems unlikely that this would be the outcome if the main formation pathway of CH₄ is connected to CH₃OH through e.g. cosmic-ray induced UV processing of CH₃OH, which is also present under quiescent conditions.

Of the two remaining scenarios, formation in the gas phase with subsequent freeze-out and hydrogenation of C on grain surfaces, this study lends most support to the latter mechanism. First, under quiescent conditions, gas phase models predict steady state total CH₄/H₂ abundances of only around $10^{-7} - 5 \times 10^{-14}$ (Woodall et al. 2007; Bergin et al. 1995), compared with our inferred CH₄/H₂ abundances of $\sim 2 - 13 \times 10^{-6}$ (assuming a standard H₂O/H₂ ratio of 10^{-4}). In early times when C/CO > 1, the CH₄/H₂ can reach above 10^{-6} (Millar et al. 1991). Ices cannot form at extinctions lower than $\sim 2 A_V$, however (Cuppen & Herbst 2007). At extinctions higher than $2 A_V$, C/CO < 1 and hence freeze-out of the high CH₄ abundances at early times cannot be used to explain the high ice abundances. In addition, pure CH₄ has a similar volatility to CO, within a few degrees (Collings et al. 2004), and if both are formed in the gas phase and subsequently frozen out, the two molecules should correlate, both in absolute column densities and in abundances relative to the much less volatile H₂O. This study clearly shows that this is not the case.

This weak correlation between CO and CH₄ can be contrasted with the stronger correlations between CH₄ and CO₂ and H₂O column densities. Furthermore the lack of significant correlation with any species once the correlation with H₂O has been effectively divided out, by normalizing with the H₂O column densities, shows that CH₄ is not significantly better related to any other molecule than to H₂O. Together this suggests a formation scenario of CH₄ more related to H₂O and CO₂ formation, which both form on grains, rather than to CO. In theory the correlations could be single-handedly due to the fact that CH₄ has a higher desorption temperature than in its pure form due to mixing with H₂O. This, however, is only expected to occur if CH₄ is formed together with H₂O and hence CH₄ formation on grain surfaces is still the most plausible outcome of this study.

The hydrogenation scenario is also supported by the broad profiles of the features which have only been found in laboratory spectra when CH₄ is in a mixture with hydrogen bonding molecules, which are believed to form on grain surfaces. These conclusions are in agreement with studies of the solid CH₄ profiles toward high mass YSOs, which show that solid CH₄ is mixed with H₂O or possibly CH₃OH (Boogert et al. 1997) and also with the observed low gas/solid ratio of CH₄ compared to CO (Boogert et al. 2004a).

3.4.3 Differences between clouds

Figure 3.4 and Table 3.3 shows that the CH₄ abundances differ from cloud to cloud. In Fig 3.4, 4 of the 5 sources with high CH₄ abundances and H₂O column densities below $2 \times 10^{18} \text{ cm}^{-2}$ are Ophiuchus sources (the fifth is in Serpens). The two Ophiuchus sources that have higher H₂O ice abundances also have more 'normal' CH₄ abundances. This indicates that it is the low total column density towards four of the Ophiuchus sources rather than initial conditions in Ophiuchus as a whole that is responsible for the extreme CH₄ abundances found there. This may be due to that towards sources with low total column densities the C/CO ratio may be larger allowing for more CH₄ to form. The C/CO ratio is dependent on extinction for low extinctions, but not for high ones. This is consistent with our observation that CH₄ abundances are only dependent on total column densities for low column densities. Sakai et al. (ApJ in press) have instead suggested that different CH₄ abundances could be due to different collapse times. In clouds that collapse very fast, chemical equilibrium may not be reached favoring a C-based rather than CO-based chemistry. This question can only be settled if gas phase data for these sources become available.

3.4.4 Comparison with models

Solid CH₄ abundances have been modelled previously for a variety of conditions (Hasegawa et al. 1992; Aikawa et al. 2005). The predicted CH₄ ice abundances with respect to H₂O usually vary between $\approx 1-10\%$, with the main formation path being sequential hydrogenation of C atoms on grains at a time when a large fraction of the gas phase C has already been converted to CO, i.e. $C/CO < 1$. The observed abundances in our sample fall mostly within this range and are hence in general agreement with the models.

Aikawa et al. (2005) model molecular abundances on grain surfaces and in the gas phase during the collapse of a spherical cloud. Regardless of initial conditions and the central density when the collapse is stopped, the CH₄/H₂O and CH₄/CO₂ ice ratios are fairly constant as a function of radius in the cloud. The value of CH₄/H₂O ratio varies with initial conditions between a few and 10%. In contrast the CH₄/CO ratio is radius dependent. The model of Hasegawa et al. (1992) is more aimed at modelling interstellar clouds before collapse, but as they show the time evolution of the chemistry it may still be useful to compare with our observations. As in the collapse model, CH₄, CO₂ and H₂O trace each other fairly well, while CO and CH₄ are only correlated during some time intervals, regardless of initial conditions. Both these models are consistent with Fig. 3.6 where solid CH₄ is better correlated with H₂O and CO₂ than with CO.

3.5 Conclusions

We present Spitzer-IRS spectra of the solid CH₄ feature at $7.7 \mu\text{m}$ toward a large sample of low mass young stellar objects. Our conclusions are as follows:

1. 25 out of 52 low mass young stellar objects show a solid CH₄ feature at $7.7 \mu\text{m}$.

2. The solid CH₄ abundance with respect to H₂O is centered at 5.8% with a standard deviation of 2.7% in the sources with CH₄ detections. In the sources without detections the average upper limit is 15%, which is not significant compared with the detections.
3. The sources (two Ophiuchus and one Serpens) with more than 10% CH₄ all have H₂O column densities below $2 \times 10^{18} \text{ cm}^{-2}$. Due to the low total column densities, two of these three sources have uncertainties larger than 50%. Above $2 \times 10^{18} \text{ cm}^{-2}$ the sources (20 out of 25) have a fairly constant CH₄ abundance of $4.7 \pm 1.6\%$.
4. The $7.7\mu\text{m}$ feature profiles are significantly broader for all but one object than expected for pure solid CH₄ and toward most sources also broader than expected for CH₄ in H₂O dominated ices. Approximately 30% of the features have a blue wing, seen previously toward high mass YSOs and there attributed to solid SO₂.
5. The column densities of solid CH₄ and H₂O and CO₂ are clearly correlated, while CH₄ and CO and CH₃OH are only weakly correlated.
6. There is also no correlation between the CH₄ and CO abundances when both have been normalized to the H₂O abundance.
7. The Ophiuchus cloud has significantly higher CH₄ abundances compared to the rest of the sample, probably due to the low total column densities towards several of the sources. There are no significant differences between the remaining clouds.
8. The abundance variation is smaller for CH₄ compared to solid CH₃OH; CH₄ seems to belong to the class of molecules, also including H₂O and CO₂ that appear 'quiescent', i.e. their abundances are more or less constant, in contrast to highly variable ices like CH₃OH and OCN⁻. If the Ophiuchus sources are included CH₄ is somewhere between the two classes.
9. Sample statistics and comparison with model predictions support CH₄ formation through hydrogenation of C on grain surfaces.

4 EFFECTS OF CO₂ ON H₂O BAND PROFILES AND BAND STRENGTHS IN MIXED H₂O:CO₂ ICES

H₂O is the most abundant component of astrophysical ices. In most lines of sight it is not possible to fit both the H₂O 3 μm stretching, the 6 μm bending and the 13 μm libration band intensities with a single pure H₂O spectrum. Recent Spitzer observations have revealed CO₂ ice in high abundances and it has been suggested that CO₂ mixed into H₂O ice can affect the positions, shapes and relative strengths of the 3 μm and 6 μm bands. This is investigated experimentally through infrared transmission spectroscopy, which is used to record spectra of H₂O:CO₂ ice mixtures at astrophysically relevant temperatures and composition ratios. The resulting spectra shows that the H₂O peak profiles and band strengths are significantly different in H₂O:CO₂ ice mixtures compared to pure H₂O ice. The ratio between the strengths of the 3 μm and 6 μm bands drops linearly with CO₂ concentration such that it is 50% lower in a 1:1 mixture compared to pure H₂O ice. In all H₂O:CO₂ mixtures, a strong free-OH stretching band appears around 2.73 μm , which can be used to put an upper limit on the CO₂ concentration in the H₂O ice. The H₂O bending mode profile also changes drastically with CO₂ concentration; the broad pure H₂O band gives way to two narrow bands as the CO₂ concentration is increased. This makes it crucial to constrain the environment of H₂O ice to enable correct assignments of other species contributing to the interstellar 6 μm absorption band. The amount of CO₂ present in the H₂O ice of B5:IRS1 is estimated by simultaneously comparing the H₂O stretching and bending regions and the CO₂ bending mode to laboratory spectra of H₂O, CO₂, H₂O:CO₂ and HCOOH.

Öberg K. I., Fraser, H.J., Boogert, A.C.A., Bisschop, S.E., Fuchs, G.W., van Dishoeck, E. F., and Linnartz, H., 2007, A& A, volume 462, pages 1187-1198

4.1 Introduction

Infrared spectroscopy towards dense molecular clouds and young stellar objects (YSOs) often reveals prominent bands attributed to H₂O ice. The 3.08 μm (3250 cm^{-1}) band, attributed to the H₂O stretching mode, and the 6.0 μm (1700 cm^{-1}) band, attributed to the H₂O bending mode, are detected in many lines of sight (Willner et al. 1982; Tanaka et al. 1990; Murakawa et al. 2000; Boogert et al. 2000; Keane et al. 2001; Gibb et al. 2004; Knez et al. 2005). Also the observation of the H₂O libration mode at 13 μm (770 cm^{-1}) has been reported (Keane et al. 2001; Gibb et al. 2004). It is a long-standing problem in the interstellar community that the H₂O ice 6.0/3.08 band intensity ratio in astrophysical observations is up to 2 times higher than expected for pure H₂O ice (Keane et al. 2001).

This discrepancy has previously been explained by absorptions of other volatile molecules and organic refractory material absorbing around 6 μm (Schutte et al. 1996; Keane et al. 2001; Gibb & Whittet 2002). These theories were put forward to explain the strong absorption of the 6.0 μm feature as well as why its shape does not match that of pure H₂O ice very well in many lines of sight. Keane et al. (2001) identified two additional components in the H₂O 6.0 μm bending mode region, centered around 5.83 μm (1720 cm^{-1}) and 6.2 μm (1600 cm^{-1}), when subtracting a pure H₂O ice spectrum that was fitted to the 3.08 μm stretching band. Analyzing the residuals after subtracting the H₂O bending mode presupposes that the profile of the H₂O bending mode is well known. Hence knowledge of the H₂O bending mode profile in different environments is critical to correctly assign other species contributing to the 6 μm band.

Pontoppidan et al. (2005) showed that for observations of ices in circumstellar disks, part of the discrepancy in intensities between the H₂O bands may be due to disk geometry because of scattering at short wavelengths. However, since this anomaly is almost always present to some degree in disks and envelopes, as well as in clouds, it is unlikely to be the entire explanation. In the sources where the 13 μm H₂O libration band is visible, it is possible to fit the H₂O stretching and libration peaks with a single H₂O ice abundance, while fitting the 6 μm band independently results in a much higher column density (Gibb et al. 2004). The fact that the libration mode at 13 μm is in agreement with the 3 μm band refutes the idea that the excess at 6 μm is due to wavelength dependent scattering.

Recently Knez et al. (2005) suggested that the ratio in band intensity could be due to large amounts of CO₂ mixed in with the H₂O ice. Observations reveal that solid CO₂ is common in many lines of sight (Gerakines et al. 1999; Gibb et al. 2004). With the Infrared Space Observatory (ISO), the CO₂ stretching mode at 4.25 μm (2350 cm^{-1}) was observed toward Taurus background stars (Whittet et al. 1998; Nummelin et al. 2001). More recently the launch of the Spitzer Space Telescope made the CO₂ bending mode at 15 μm (670 cm^{-1}) available for observations and the band has been detected towards several background stars (Bergin et al. 2005; Knez et al. 2005). The average abundance with respect to H₂O ice towards the Taurus sources is 20%, but up to 37% has been observed (Knez et al., in prep.). Toward several protostars up to 35% of CO₂ compared to H₂O has been observed (Nummelin et al. 2001; Boogert & Ehrenfreund 2004), making CO₂ one of the most abundant ices after H₂O.

In a previous study, using the H₂O column density from the 3.08 μm band and labo-

ratory spectra of pure H₂O ice, Knez et al. (2005) determined that the H₂O bending mode contributes 77% and 69% to the observed 6.0 μm absorption features towards Elias 16 and CK 2, respectively. Using a combination of laboratory spectra of two H₂O:CO₂ mixtures, 1:1 and 10:1 respectively, they showed that 85% to 100% of the 6.0 μm band strength can be explained by H₂O. This is due to the smaller ratio between the stretching and bending mode strengths seen in an unpublished H₂O:CO₂ 1:1 spectrum by Ehrenfreund (private communication). This combination of spectra, together with a water-poor mixture spectrum, also fits the CO₂ profile well, with approximately 80% of the CO₂ in the water rich ice (Knez et al. 2005). Hence it is not unlikely that a significant part of the H₂O ice is in H₂O:CO₂ ice mixtures close to 1:1 in many lines of sight, even if the average abundances of H₂O and CO₂ is closer to 3:1.

The question that prompted this study is whether there is a change in H₂O band profiles and relative H₂O band strengths in ice mixtures compared to pure H₂O ice, for H₂O:CO₂ ice mixtures that are both astrophysically relevant and contain enough H₂O to observe with e.g. Spitzer. Such information in turn, is a prerequisite for determining whether additional species contribute to the 6 μm band. In this work we present a systematic study of the infrared properties of H₂O absorptions in H₂O:CO₂ ice mixtures around 1:1, for the temperature range of 15 to 135 K, in order to constrain the effect that CO₂ has on the shapes and relative band strengths of the H₂O bands.

4.1.1 Previous laboratory data

Two previous studies have reported changes in the H₂O bands in H₂O:CO₂ ice mixtures compared to pure H₂O ices (Hagen et al. 1983; Schmitt et al. 1989). In both cases, only one isolated H₂O:CO₂ mixture, 1:2 and 10:1 respectively, was investigated. In both the 1:2 and 10:1 H₂O:CO₂ mixture spectra a new H₂O band appears around 2.74 μm , the relative strength of the bending mode increases and all the band profiles change compared to a pure H₂O ice spectrum. No attempts were made to quantify these changes.

A number of later laboratory studies focused on H₂O:CO₂ ice mixtures as well, but to our knowledge none of them systematically studied the impact of CO₂ on water ice and none of them has reported on changes in the H₂O band profiles and band strengths due to CO₂. This is not surprising, since most of the studies focused on mixtures with H₂O as the dominant ice component (Hudgins et al. 1993; Bernstein et al. 2005). Only a few laboratory spectra of H₂O:CO₂ mixtures close to 1:1 exist in the literature (Gerakines et al. 1995; Palumbo & Baratta 2000; Gerakines et al. 2005). The effect of CO₂ on H₂O ice features is only considered by Gerakines et al. (2005), who concluded from the spectra of a H₂O:CO₂ 1.6:1 ice mixture that the relative H₂O band intensities were not affected by high concentrations of CO₂. Nevertheless, the 3.08/6.0 μm band strength ratio can be calculated from their reported integrated intensities and reveals a drop of $\sim 30\%$ compared to pure H₂O.

It is well known from matrix isolation experiments that the different H₂O bands have different relative band strengths dependent on H₂O cluster size (van Thiel et al. 1957). The band strength of the bending mode is much less affected by the H₂O cluster size than the stretching mode, when the H₂O cluster size is changed by varying the H₂O concentration

Table 4.1 – Ice mixtures studied in this work

Composition	H ₂ O (L) ^a	CO ₂ (L)	Total ice exposure (L)
pure H ₂ O	3000	0	3000
pure CO ₂	0	3000	3000
H ₂ O:CO ₂ 1:0.25	3000	750	3750
H ₂ O:CO ₂ 1:0.5	3000	1500	4500
H ₂ O:CO ₂ 1:1	3000	3000	6000
H ₂ O:CO ₂ 1:2	3000	6000	9000
H ₂ O:CO ₂ 1:4	3000	12000	15000
H ₂ O:CO ₂ 1:1	10000	10000	20000
H ₂ O:CO ₂ 1:1	1000	1000	2000

^a1 L (Langmuir) = 1×10^{-6} Torr s \approx 1 monolayer of molecules

in a N₂ matrix. The former band strength drops by 20% when the matrix to H₂O ratio is decreased by one order of magnitude while the stretching band strength increases by a factor of 10. The main intensity contribution in both bands comes from the monomer peak when the H₂O concentration is low and from a cluster mixture when the concentration is high (high concentration meaning N₂:H₂O 1:10, van Thiel et al. 1957). The position of the bending modes is approximately the same for all cluster sizes, while the major stretching mode peak shifts from 3400 cm⁻¹ at high H₂O concentrations to the position of the free-OH stretch at low concentrations (\sim 3690 cm⁻¹ or \sim 2.7 μ m). Finally, the relative band strengths are also affected by the type of matrix used, e.g. noble gas or nitrogen or oxygen. This has been reported also for H₂O in astronomically relevant matrices (Ehrenfreund et al. 1996). It is important to note that none of these matrices forms hydrogen bonds with H₂O, thus no conclusions about the band strengths and band profiles of H₂O can be drawn from these experiments concerning H₂O in a hydrogen bonding matrix. Another astrophysically relevant molecule, CO, does probably form hydrogen bonds with H₂O in amorphous ice mixtures (Schmitt et al. 1989). Matrix experiments have also shown that CO forms weak hydrogen bonds, while CO₂ does not (Tso & Lee 1985).

4.2 Experiment and data analysis

4.2.1 Experiment

All experiments were conducted in a high vacuum (HV) chamber described in detail elsewhere (Gerakines et al. 1995) at a base pressures below 1.3×10^{-6} Torr at room temperature. Ices of C¹⁸O₂ (Praxair 97% purity) and H₂O (deionized and further purified through sequential freeze-thawing in a vacuum manifold) were grown on a CsI window, precooled to 15 K (45 K for one specific experiment), via effusive dosing at a growth rate of $\sim 10^{16}$ molecules cm⁻² s⁻¹ roughly along the surface normal. C¹⁸O₂ was used instead of the main isotopologue of CO₂ to minimize overlap between H₂O and CO₂ spectral features. Trans-

Table 4.2 – The measured peak positions and the integration bounds in cm^{-1} (μm) used to compute the integrated intensities of the H_2O peaks

H_2O bands	Peak	Integration bounds	
		Lower	Upper
libration	780 (12.8)	500 (20.0)	1100 (9.09) ^a
bend	1655 (6.04)	1100 (9.09)	1900 (5.26)
bulk stretch	3279 (3.05)	3000 (3.33)	3600 (2.78)
free OH stretch	3661 (2.73)	3600 (2.78)	3730 (2.68)

^aThe CO_2 bending mode is excluded by explicitly taking into account only half of the libration mode profile (see text)

mission Fourier transform infrared spectra of the ice systems were recorded between $4000 - 400 \text{ cm}^{-1}$ ($2.5 - 25 \mu\text{m}$) at a spectral resolution of 2 cm^{-1} at fixed temperatures between 15 and 135 K, using a total of 256 scans. Background spectra were acquired prior to deposition for each experiment, at the same resolution and number of scans, and automatically subtracted from the recorded ice spectra.

The pure ices were grown *in situ* from C^{18}O_2 and H_2O gas bulbs that were filled to a total pressure of 10 mbar, prepared in a glass-vacuum manifold at a base-pressure of $\sim 10^{-4}$ mbar. Mixed ices were made by dosing gas from premixed $\text{H}_2\text{O}:\text{C}^{18}\text{O}_2$ bulbs, also prepared in the glass-vacuum manifold.

The ice mixtures studied here are summarized in Table 4.1. The relative concentrations for the $\text{H}_2\text{O}:\text{C}^{18}\text{O}_2$ mixtures range from 20 to 80% CO_2 , where the % are relative to the whole ice, i.e. 20% CO_2 is equivalent to a $\text{H}_2\text{O}:\text{CO}_2$ 4:1 mixture. The H_2O ice exposure was always kept at 3000 L (1 L (Langmuir) = 1×10^{-6} Torr s \approx 1 monolayer of molecules, assuming 10^{15} molecules cm^2 and a sticking probability of 1), except in two 1:1 control experiments with 1000 and 10000 L H_2O exposure, respectively. The nomenclature adopted is as follows, A:B denotes a mixture with A parts of H_2O and B parts of C^{18}O_2 .

4.2.2 Data analysis

The acquired spectra were first reduced to flatten the baseline by fitting a second order polynomial to the same 5 points, chosen by visual inspection well away from any features. This was done to facilitate comparison between laboratory and astronomical spectra. The curved baseline in the raw data is a real feature which is due to scattering within the ice. Flattening the spectra may hence distort profiles, but in our case no such distortion was noted. All reduced spectra can be found at <http://www.strw.leidenuniv.nl/~lab/databases>.

Figure 4.1 shows an overview spectrum of a $\text{H}_2\text{O}:\text{CO}_2$ 1:0.5 mixture. The use of the C^{18}O_2 isotope changes the position of the CO_2 bands compared to the main isotopologue, but does not affect the conclusions of this study. In addition to the C^{18}O_2 bending and stretching modes, there are two weak, narrow C^{18}O_2 overtone bands in the spectrum, at 3515 and 3625 cm^{-1} respectively, that overlap with the H_2O stretching bands. To calculate

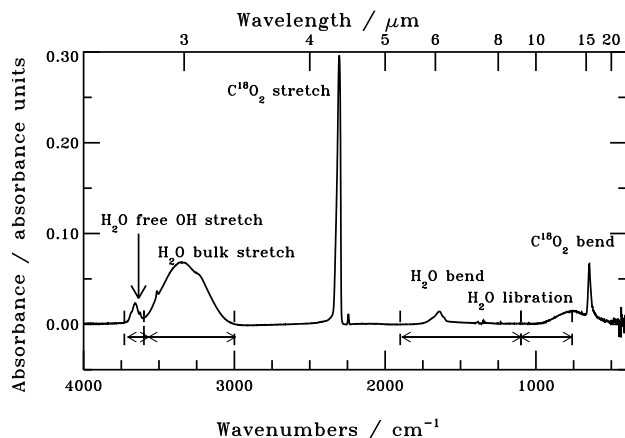


Figure 4.1 – Spectra over the 4000–400 cm^{-1} range of the $\text{H}_2\text{O}:\text{CO}_2$ 1:0.5 ice mixture at 15 K. The assignments of the major peaks are indicated. The double headed arrows indicate the integration ranges for determining the intensities of the various bands; for the libration mode, only half the range is indicated (see text). Note that all CO_2 frequencies are shifted compared to those observed in space, since in the present experiments C^{18}O_2 has been used.

the integrated intensities of the H_2O bands, the H_2O peak intensities were integrated over the same wavenumber range for all spectra (see Table 4.2 and Fig. 4.1). Where narrow CO_2 peaks overlapped with the H_2O bands, a Gaussian was fitted to the CO_2 peak and subtracted from the spectrum. A Gaussian could not be fitted to the CO_2 bending mode, which overlaps with the H_2O libration mode. The band strength of the H_2O libration band was instead calculated by doubling the band strength of the high frequency half of the band. The peak frequency of the H_2O libration mode varies in the different mixtures and since the lower frequency integration bound was set to the peak frequency, the lower bound is somewhat different for different mixtures. For pure H_2O ice, this procedure was found to be accurate to within 3% compared to integrating the whole profile. To further test the induced error of this approach the band strengths were also calculated by simply subtracting the integrated area of the CO_2 bending mode from the total integrated area. The difference was less than 5%. The large interval required for the H_2O bending mode is due to its substantial low frequency wing attributed to the librational overtone (Devlin et al. 2001), which in some spectra contains more than 50% of the integrated peak intensity. The 2.73 μm band is due to free-OH stretches and its assignment to H_2O monomers, dimers and small multimers is justified in the discussion part of this paper.

The substantial change in the H_2O band intensities between different mixtures reported here, prevents an independent check of the relative amount of H_2O deposited onto the surface. From three repeated experiments (of the 2:1 mixture) the standard deviations of the integrated H_2O peak intensities are estimated to be less than 10%. These experiments were carried out in the beginning and at the end of an experimental series and

for separately prepared mixtures. The standard deviation hence contains the error from mixing, absolute ice exposure, measuring errors and changes in the experiment over time. Additional errors may arise from the flattening of the spectra; the difference between integrated intensities for the raw and reduced spectra is the largest for the $6.0 \mu\text{m}$ H_2O band at low H_2O concentrations; up to 40% for the 1:4 mixture. For the astrophysically relevant mixtures this uncertainty is only 1 - 5%, however. Some systematic errors due to the mixing procedure cannot be excluded, but are difficult to quantify. Taking all error sources into account, we estimate that the relative band strengths are accurate within $\sim 10\%$ for the astrophysically relevant ice mixtures, i.e. ice mixtures with less or equal amounts of CO_2 compared to H_2O .

The band strengths, A , of the three H_2O bands present in pure H_2O ice were estimated for all mixtures using the measured band strengths for pure H_2O ice at 14 K by Gerakines et al. (1995). The band strengths for the pure H_2O bands were thus set to 2.0×10^{-16} for the H_2O stretching mode, 1.2×10^{-17} for the bending mode and 3.1×10^{-17} cm molecule^{-1} for the libration band. The band strengths of these bands in the $\text{H}_2\text{O}:\text{CO}_2$ mixtures were calculated by scaling each integrated intensity by the band strength of the pure H_2O ice band over the pure H_2O band integrated intensity:

$$A_{\text{H}_2\text{O}:\text{CO}_2=1:x}^{\text{band}} = \int_{\text{band}} I_{\text{H}_2\text{O}:\text{CO}_2=1:x} \times \frac{A_{\text{H}_2\text{O}}^{\text{band}}}{\int_{\text{band}} I_{\text{H}_2\text{O}}} \quad (4.1)$$

where $A_{\text{H}_2\text{O}:\text{CO}_2=1:x}^{\text{band}}$ is the calculated strength of each H_2O band in the 1: x $\text{H}_2\text{O}:\text{CO}_2$ mixture, $\int_{\text{band}} I_{\text{H}_2\text{O}:\text{CO}_2=1:x}$ the measured integrated intensity of the same band, $A_{\text{H}_2\text{O}}^{\text{band}}$ the known strength of the pure H_2O band and $\int_{\text{band}} I_{\text{H}_2\text{O}}$ the integrated intensity of the pure H_2O band. The band strengths of the free OH stretch in the different mixtures were scaled to the band strength of the bulk stretching mode in pure H_2O ice. The ratios of our measured integrated intensities for pure H_2O at 15 K coincided with those of Gerakines et al. within 10%.

The calculated strengths of all H_2O bands were plotted as a function of CO_2 concentration in the ice mixture and fitted by linear models as described in detail in section 4.2.2. These models are more accurate in predicting the band strengths for H_2O in a certain mixture than individual measurements, since they are derived from all experiments and hence the random errors are averaged out. Our model predictions agreed well with previously published isolated measurements. A spectrum by Schutte (Leiden Molecular Database) of $\text{H}_2\text{O}:\text{CO}_2$ 1:1.25 has a stretching to bending peak ratio which lies within 5% of the value predicted by our model fit. In addition, the ratio of stretching to bending modes in the $\text{H}_2\text{O}:\text{CO}_2$ 1.6:1 mixture from Gerakines et al. (2005) lies within 8% of our model value, further corroborating the results presented in this paper.

4.3 Results

4.3.1 Changes in H₂O band strengths and profiles with mixture composition

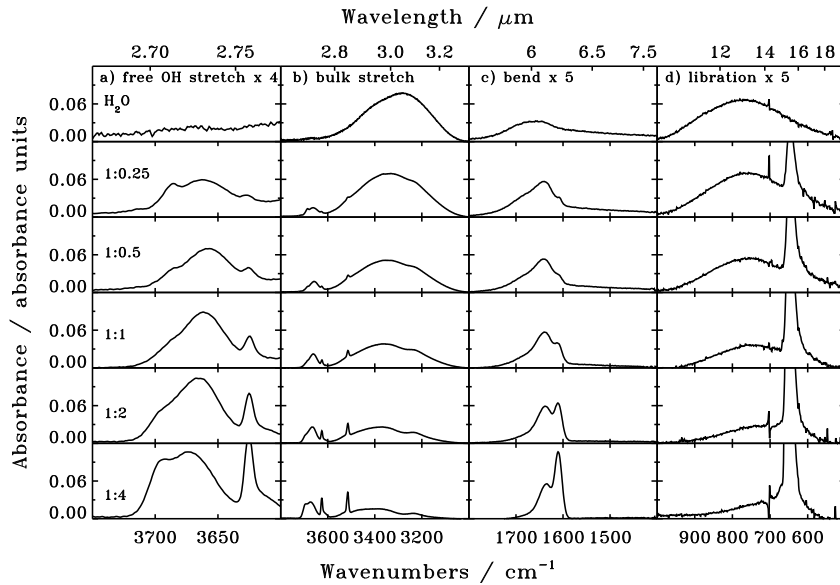


Figure 4.2 – Spectra over the 4000-400 cm^{-1} range at 15 K of the four H₂O peaks in H₂O:CO₂ 1: x ice mixtures for different CO₂ concentrations. Each column contains one of the H₂O modes and each row one of the H₂O:CO₂ mixtures: a) an expanded view of the H₂O free OH stretch, b) the H₂O bulk and free-OH stretch, c) the H₂O bend and d) H₂O libration. The intensities of the libration, bend and free-OH stretch bands have been scaled, with a scaling factor indicated in the first row. The H₂O exposure was kept constant in all experiments. The narrow peaks around 3500 and 3630 cm^{-1} have been previously assigned to CO₂ combination modes (Sandford & Allamandola 1990). The sharp feature around 700 cm^{-1} is an experimental artifact.

Figure 4.2 shows that the H₂O spectra at 15 K undergo two significant changes as the amount of CO₂ is increased from 0 to 80%; the profiles of the H₂O bending and stretching bands change dramatically and all H₂O integrated peak intensities change systematically with varying CO₂ concentration.

Of all modes, the profile the H₂O bending mode is most affected by the CO₂. In pure H₂O the bending mode consists of a broad peak centered at 1661 cm^{-1} (6.02 μm). The bending mode overlaps with the librational overtone, which shows up in the spectra as a low-frequency wing. To simplify comparison with astronomical observations, the wing is generally treated as a part of the bending mode when calculating band strengths. The band strength of the pure bending mode is smaller for the mixtures that have strong librational modes and hence strong librational overtones. In the spectrum of the 1:4 mixture, two

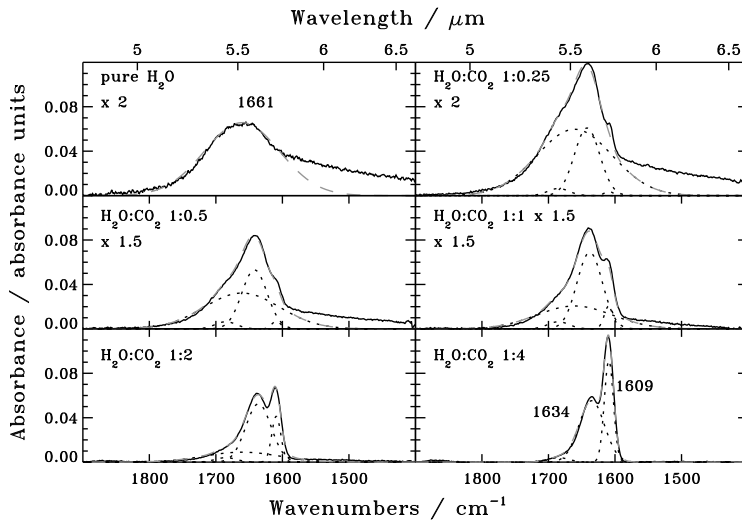


Figure 4.3 – The three Gaussian components present in the H_2O bending mode in mixtures with CO_2 disregarding the low frequency wing. In the upper row, first column the pure H_2O bending mode consists of a wing and a peak, where the peak was fitted with a Gaussian at 1661 cm^{-1} . In the lower row, second column, the H_2O bending mode in the 1:4 mixture can be separated into two narrow Gaussians at 1609 and 1634 cm^{-1} . The four other $\text{H}_2\text{O}:\text{CO}_2$ mixtures can be separated into these three components derived from the pure and 1:4 mixed ice. A small additional Gaussian centered at 1685 cm^{-1} accounts for some high frequency excess. The dotted lines indicate the individual Gaussian components and the dashed lines their sum.

narrow peaks are observed in the H_2O bending region at 1609 and 1634 cm^{-1} , instead of the broad peak and wing in the pure H_2O spectrum. The profiles of the bending mode in the other mixtures appear to be a composition of the peaks in the pure H_2O spectra and the $\text{H}_2\text{O}:\text{CO}_2$ 1:4 mixture. To test this, Gaussian profiles were fitted to the bending peak of the pure H_2O ice, disregarding the wing, and to the two peaks in the 1:4 mixture (Lorentzian profiles were also attempted but were impossible to match to the ice peaks). The IDL simplex optimization routine was used to fit two Gaussian peaks simultaneously to the band in the 1:4 spectrum. Figure 4.3 shows that the bending mode in all other mixtures can be separated into these three peaks; the slight misfit on the blue wing in all mixtures is corrected for by an additional, small Gaussian centered at 1685 cm^{-1} with FWHM (Full Width at Half Maximum) 35 cm^{-1} . The position of the 1634 cm^{-1} peak is shifted with CO_2 concentration (2 to 8 cm^{-1} for the different mixtures), but the FWHMs of the Gaussians were always kept constant. The other peak positions were also kept constant. The positions, widths and intensities of the Gaussians used to fit the bending mode for each mixture are listed in Table 4.3.

The same bulk stretching peak apparent in the pure H_2O spectra is visible in all mixture spectra (Fig. 4.2, column b). As more CO_2 is mixed in, it acquires more of a double

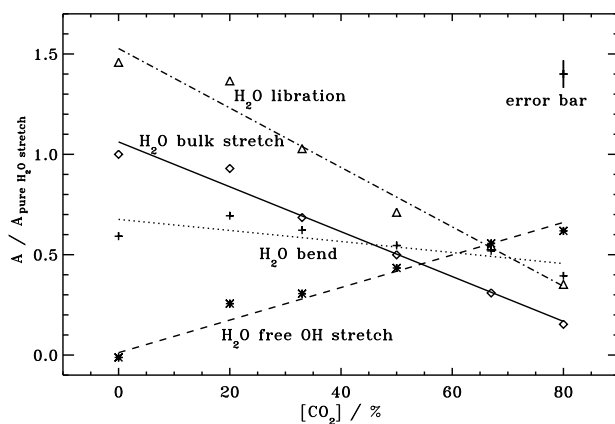


Figure 4.4 – The band strengths of the four main H₂O peaks in H₂O:CO₂ ice mixtures relative to that of the H₂O stretch in pure H₂O ice at 15 K. The band strengths of the libration, bend and free OH stretch modes have been multiplied by a factor of 10 to facilitate display. The estimated average error bar of the relative band strengths is shown in the upper right corner.

peak structure, but the total width of the band remains the same. In pure H₂O ice the peak at 3696 cm⁻¹ (2.71 μm) attributed to the free/dangling OH stretch was not detected (Rowland et al. 1991). In contrast, Fig. 4.2, column a, shows that a free OH H₂O stretching band, centered around 3660 cm⁻¹ (2.73 μm), attributed to the stretches of small H₂O clusters, is clearly present in all ice mixtures with CO₂ and is comparable in intensity to the bulk stretching band at high concentrations of CO₂. While the intensity of the H₂O libration mode clearly drops as more CO₂ is mixed in, it is difficult to tell whether the profile of the libration band is affected by the presence of CO₂, because of the overlap with the CO₂ bending mode.

Of all the H₂O bands, only the free OH stretching band grows in strength as the amount of CO₂ in the ice increases. The band strengths of all other H₂O ice bands drop with increased concentration of CO₂, as illustrated in Fig. 4.4, where all band strengths have been scaled to that of the H₂O stretch in pure H₂O ice. The band strength of the bulk stretching band and the libration band are strongly dependent on the CO₂ concentration, while the intensity of the bending mode is less affected, whether the librational overtone is included or not, in calculating its integrated intensity. The relationship between the integrated peak intensities and CO₂ concentration is well described by linear models within this experimental domain and the data can be fitted with a typical squared correlation coefficient $R^2 = 0.98$ (Table 4.5). The correlations for the band strengths of the bending mode are considerably less, $R^2 = 0.81$ and 0.89 at 15 K and 45 K, respectively. This is due to the relatively small change in band strength with CO₂ concentration.

In addition, the relative strengths of the various components of the bending modes were calculated from the previously fitted Gaussians. The integrated areas relative to the

pure H₂O bending mode are listed in Table 4.3 and plotted in Fig. 4.5 together with the area of the residual wing. The ratio between the 1661 and 1634 cm⁻¹ peaks is plotted and its significance in astrophysical applications is discussed in section 4.5.2. Table 4.3 also contains the total strength of the bending mode, excluding the wing. Due to the exclusion of the wing the drop in band strength with CO₂ concentration is smaller than in Fig. 4.4.

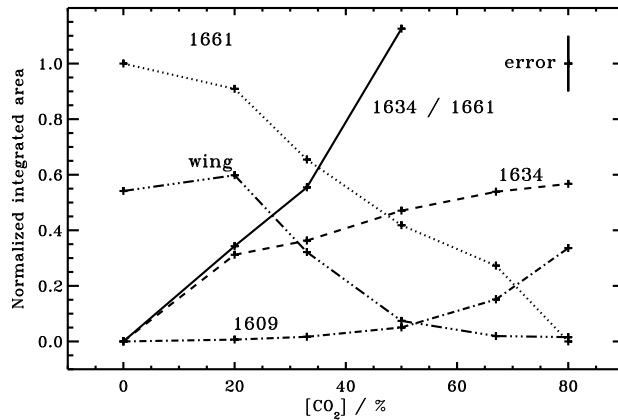


Figure 4.5 – The integrated area of the three Gaussian components present in the H₂O bending mode in mixtures with CO₂ and of the low frequency wing attributed to a librational overtone. The ratio between the 1634 and 1661 cm⁻¹ peaks is plotted as well. The estimated error, shown as an error bar in the top right corner, is mainly due to the error in the total band strength and not to the Gaussian fit.

4.3.2 Temperature dependence

The profiles of all H₂O bands in the H₂O:CO₂ mixtures change systematically with temperature to become more similar to the bands of pure H₂O ice as the temperature is increased (Fig. 4.6). This is especially apparent for the bending mode, where the narrow bands lose intensity and the broad band, associated with pure H₂O ice, gains intensity as the temperature rises. This is also seen in Fig. 4.7 where the bending mode of the 1:0.5 mixture at 15, 45 and 75 K has been decomposed into the same components derived from the pure H₂O and 1:4 mixture at 15 K. As the temperature increases the shapes of the components remain the same, but the ratio between the thin components and the pure H₂O component decreases. The ratios for all mixtures at 15, 45 and 75 K are listed in Table 4.4.

The strengths of all H₂O bands increase with temperature, except for the free OH stretching band which decreases and disappears completely above 90 K. Figure 4.8 shows that the bulk stretching band increases monotonically in band strength, while the bending and libration bands display jumps and local minima. These jumps are most pronounced

Table 4.3 – The peak positions, FWHM (full width at half maximum) and peak heights of the fitted Gaussian components of the H₂O bending mode, and the integrated area for each peak and their sum, excluding the libration overtone wing.

Ice mixture	Peak position [cm ⁻¹ (μm)]	FWHM [cm ⁻¹ (μm)]	Relative height	Relative area	Total area
Pure H ₂ O	1661 (6.02)	130 (0.49)	1	1	1
	wing			0.54	
H ₂ O:CO ₂ 1:0.25	1609 (6.22)	15 (0.059)	0.056	0.0067	1.29
	1642 (6.09)	49 (0.19)	0.93	0.31	
	1661(6.02)	130 (0.49)	0.91	0.91	
	1685 (5.93)	35 (0.12)	0.22	0.055	
	wing			0.60	
H ₂ O:CO ₂ 1:0.5	1609 (6.22)	15 (0.059)	0.14	0.017	1.09
	1642 (6.09)	49 (0.19)	1.1	0.36	
	1661(6.02)	130 (0.49)	0.65	0.65	
	1685 (5.93)	35 (0.12)	0.22	0.055	
	wing			0.32	
H ₂ O:CO ₂ 1:1	1609 (6.22)	15 (0.059)	0.42	0.050	0.96
	1638 (6.11)	49 (0.19)	1.4	0.47	
	1661(6.02)	130 (0.49)	0.40	0.42	
	1685 (5.93)	35 (0.12)	0.22	0.055	
	wing			0.07	
H ₂ O:CO ₂ 1:2	1609 (6.22)	15 (0.059)	1.3	0.15	0.99
	1636 (6.11)	49 (0.19)	1.6	0.54	
	1661(6.02)	130 (0.49)	0.27	0.27	
	1685 (5.93)	35 (0.12)	0.14	0.034	
	wing			0.02	
H ₂ O:CO ₂ 1:4	1609 (6.22)	15 (0.059)	2.8	0.34	0.94
	1634 (6.12)	49 (0.19)	1.7	0.57	
	1685 (5.93)	35 (0.12)	0.14	0.034	
	wing			0.01	

Table 4.4 – Ratios between 1634 and 1661 cm⁻¹ components for all mixtures at 15, 45 and 75 K

Composition	Ratio at given temperature		
	15 K	45 K	75 K
pure H ₂ O	0	0	0
H ₂ O:CO ₂ 1:0.25	0.34	0.12	0.034
H ₂ O:CO ₂ 1:0.5	0.55	0.28	0.11
H ₂ O:CO ₂ 1:1	1.1	0.49	0.11
H ₂ O:CO ₂ 1:2	2.0	0.73	0.17
H ₂ O:CO ₂ 1:4	>10	1.6	0.31

around the CO₂ desorption temperature (~90 K). As in the case of concentration dependency, the band strengths of the stretching and libration bands are more affected by

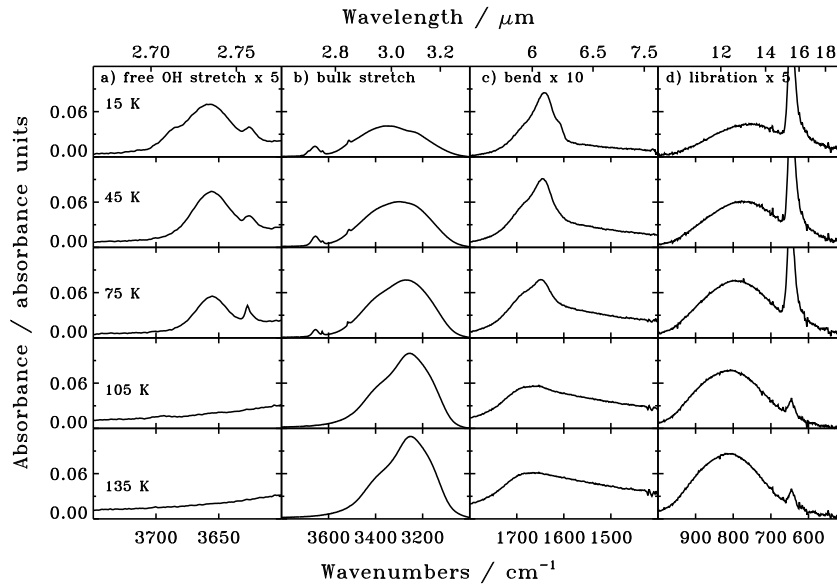


Figure 4.6 – Temperature dependence of the H_2O bands in a 1:0.5 $\text{H}_2\text{O}:\text{CO}_2$ mixture i.e. 67% H_2O and 33% CO_2 . Spectra at 4000–400 cm^{-1} of the four main H_2O peaks in a 1:0.5 ice mixture with CO_2 at temperatures between 15 and 135 K. Each column contains one of the H_2O vibrational modes and each row one of the temperatures. a) an expanded view of the H_2O free OH stretch, b) the H_2O bulk and free-OH stretch, c) the H_2O bend and d) H_2O libration. The spectra of libration, bending and free OH stretch have been scaled, with a scaling factor indicated in the top row.

temperature than the band strength of the bending mode (including or excluding the libration overtone wing). Note that the profile of the bending mode is the most affected by both changes in temperature and CO_2 concentration, however.

Different bands are thus differently affected by an increasing temperature. In addition, the spectra of ice mixtures with higher CO_2 concentration are more affected by changes in temperature than those of ices with less CO_2 ; the influence of CO_2 concentration on the intensity ratio between the bulk stretching and the bending modes (including the libration overtone wing) is plotted in Fig. 4.9 for different temperatures between 15 and 135 K. In this plot the CO_2 concentration on the horizontal axis is the initial one. Above 90 K most of the CO_2 has desorbed, which changes the mixture composition. In addition, the ratio between the stretching mode and the sum of the bending mode components (excluding the wing) at 15 K is plotted for comparison. The parameters of the linear fit to the 15 and 45 K measured points are included in Table 4.5.

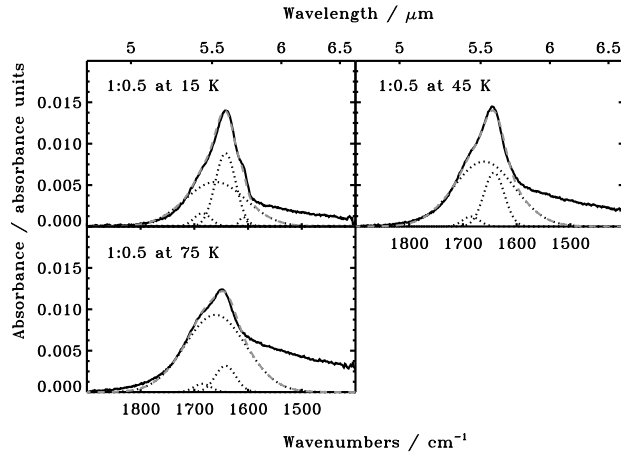


Figure 4.7 – The components present in the bending mode in the H₂O:CO₂ 1:0.5 mixture at different temperatures. The same components that were derived in Fig. 4.4 have been used to fit the bending mode at 15, 45 and 75 K. These components are always present regardless of temperature, but the ratios between the different components changes, especially the ratio between the thin 1634 cm⁻¹ and the pure H₂O 1661 cm⁻¹ components decreases with temperature.

Table 4.5 – The linear fit coefficients for the H₂O band strengths as functions of CO₂ concentrations in %, based on six experiments with 0 to 80% CO₂. The last two rows show the linear fit to the ratio between the bulk stretching and the bending mode.

Peak	Temperature [K]	Linear Coefficients		R^2
		constant [10 ⁻¹⁶ cm molecule ⁻¹]	slope	
H ₂ O libration	15	0.32±0.02	-3.2±0.4	0.99
	45	0.42±0.03	-2.7±0.6	0.92
H ₂ O bend	15	0.14±0.01	-0.5±0.2	0.81
	45	0.17±0.01	-0.6±0.1	0.89
H ₂ O bulk stretch	15	2.1±0.1	-22±2	0.99
	45	2.8±0.1	-21±2	0.98
H ₂ O free OH stretch	15	0	1.62±0.07	0.99
	45	0	1.40±0.05	0.99
H ₂ O bulk stretch / bend		constant	linear coefficient	R^2
	15	16.7±0.2	-0.160±0.005	0.99
	45	17.0±0.3	-0.101±0.008	0.99

4.3.3 Dependence on additional parameters: deposition temperature and ice thickness

When the ice mixture (H₂O:CO₂ 1:0.5) was deposited at 45 K instead of 15 K the profiles and band strengths of the ice bands did not change compared to those found when heating

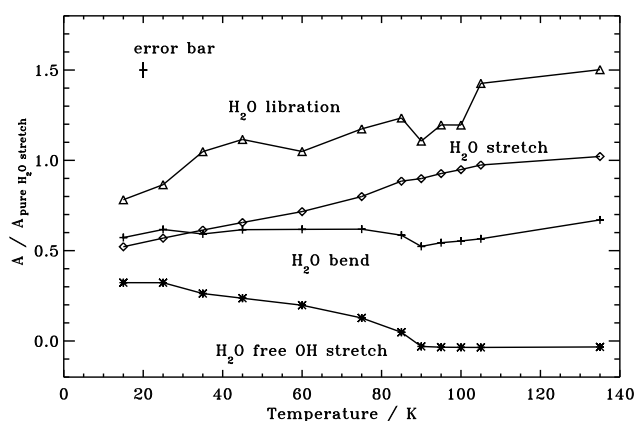


Figure 4.8 – The band strengths of the four main H₂O peaks in an initial 1:0.5 ice mixture with CO₂ at temperatures between 15 and 135 K relative to the band strength of the H₂O bulk stretch in pure H₂O ice at 15 K. The band strengths of the libration, bending and free-OH stretching mode have been scaled by 10 to facilitate viewing. The average error bar for the relative band strengths is shown in the upper left corner.

the 15 K mixture to 45 K. The profiles remain similar also at higher temperatures. As the ices are heated, the increase in H₂O bulk stretching band strength is significantly smaller for the ice deposited at 45 K compared to 15 K. In addition, 2-3 times as much CO₂ is retained in the H₂O ice at temperatures above the CO₂ desorption temperature of 85-90 K (Fig. 4.10).

Two control experiments with approximately three times more and three times less total ice thickness were run to test for changes in peak profiles and relative peak band strengths with thickness (not shown here). The relative peak band strengths did not change significantly for these experiments (i.e. less than the previously estimated experimental uncertainty of 10%). Nevertheless, the profile showed some thickness dependence, with the narrow peak in the bending mode being more pronounced for the experiments with less ice coverage.

4.4 Discussion

4.4.1 Ice structure

The changes in the H₂O spectral features in H₂O:CO₂ ice mixtures, compared to the pure H₂O ice, demonstrate that the mixed-in CO₂ does affect the H₂O ice structure. The nature of the interaction between H₂O and CO₂ is not obvious. One possible scenario is that the CO₂ is spread out in the ice more or less uniformly and that the change in the H₂O peak intensities and profiles is due H₂O bonding with CO₂. A second option is that instead

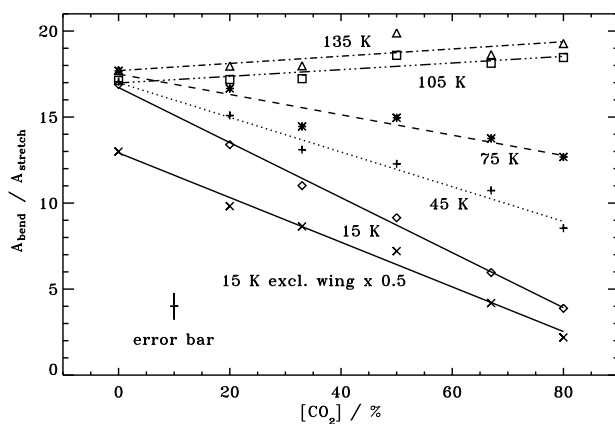


Figure 4.9 – The ratio between the H₂O bulk stretching and bending mode band strengths (including the libration overtone wing) for different temperatures in H₂O:CO₂ ice mixtures with increasing initial amounts of CO₂. The CO₂ concentration quoted is that of the initial ice mixture, while above 90 K most of the CO₂ has desorbed, changing the composition substantially. In addition the ratio between the stretching band and the bending mode components (excluding the libration overtone wing) is shown for 15 K (multiplied by 0.5 to facilitate viewing).

CO₂ forces the H₂O into small clusters, either in the gas-phase or upon arrival at the ice surface, since it is known from matrix isolated experiments and calculations that H₂O molecules form much stronger bonds with each other than with CO₂ (Tso & Lee 1985; Danten et al. 2005). The spectral changes would then originate from a different type of H₂O-H₂O interaction rather than H₂O bonding with CO₂.

The large decrease in band strength of the H₂O bulk stretching mode that is observed when CO₂ is mixed into the H₂O ice indicates that CO₂ destroys the bulk hydrogen-bond network, since the band strength of the stretching mode is weaker in small clusters compared to that in larger clusters and bulk ice (van Thiel et al. 1957). At the same time a new stretching peak appears at a higher frequency, i.e. more and more H₂O molecules are forced into a looser bound environment, which increases the intramolecular O-H bond strength, as the CO₂ concentration increases. The frequency of this band, $\sim 2.7 \mu\text{m}$, and its distinctness from the bulk stretching band make it possible to assign it to free OH stretches (Rowland et al. 1991), which in general occur both at surfaces of ice and in clusters. This agrees with more and more H₂O molecules isolated in clusters, and hence separated from the H₂O ice hydrogen-bond network as CO₂ is added, but not with a uniform arrangement with CO₂. Ehrenfreund et al. (1996) observed a similar band in different ice mixtures with 10% or less H₂O. They assigned it to overlapping peaks of H₂O monomers, dimers and small multimers consistent with our analysis. Similar conclusions were also drawn by van Thiel et al. (1957) based on their cluster experiments.

Simultaneously with the appearance of the free OH stretching band, the original broad

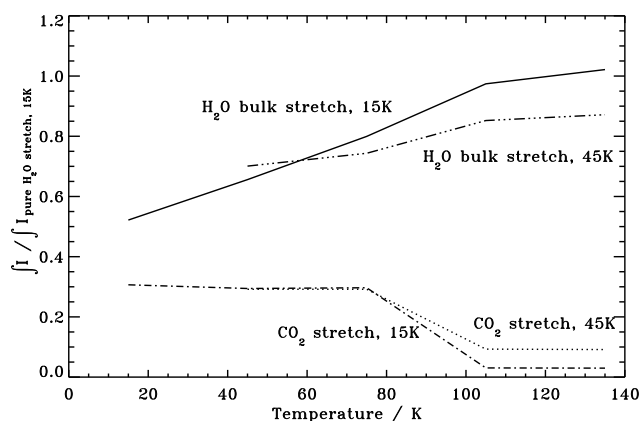


Figure 4.10 – The band strengths of the H_2O stretching mode deposited at 15 and 45 K in the 1:0.5 ices, respectively, relative to the band strength of the H_2O stretch in pure H_2O ice. The CO_2 stretching peak is plotted so the amount of CO_2 in the ice at different temperatures can be compared. The temperature labels given in the figure indicate the deposition temperature.

band in the bending region drops in intensity and two narrow peaks appear. The narrowest of the two dominates at high CO_2 concentration and is at the approximate position of the H_2O dimer in argon at 1611 cm^{-1} (Ayers & Pullin 1976). However, the bending mode peaks of H_2O monomers, dimers and small clusters are not far apart and shift in position between different matrices (Tso & Lee 1985; van Thiel et al. 1957), thus rather than being due to only H_2O dimers it is more likely that this peak is produced by a mixture of monomer, dimer and small multimer peaks that are overlapping. The H_2O - CO_2 dimer has its main peak around 1598 cm^{-1} (Tso & Lee 1985) and is not visible, further indicating that increasing the amount of CO_2 lead to a majority of the H_2O clustered with themselves rather than bonded with CO_2 .

Ehrenfreund et al. (1996) observed a similar bending mode to ours in a $\text{H}_2\text{O}:\text{N}_2:\text{O}_2$ 1:5:5 mixture with a narrow peak at 1606 cm^{-1} and a broader feature at 1630 cm^{-1} assigned to H_2O monomers, dimers and small clusters and bulk H_2O ice, respectively. The fact that the same bending mode is acquired when H_2O is mixed with other small molecules corroborates our interpretation that the H_2O spectrum is dominated by the interaction between the H_2O molecules regardless of mixture composition, as long as the mixed-in molecules cannot form hydrogen bonds, or more generally, cannot form bonds with H_2O of comparable strength to the H_2O - H_2O bond. Matrix-isolation experiments show that e.g. H_2O - CO , another astrophysically relevant combination, forms hydrogen bonds, while H_2O - CO_2 does not (Tso & Lee 1985).

As the ice is heated the multimer peaks disappear quickly and all other peaks become more like those of pure H_2O . As the temperature increases the H_2O molecules can reorientate on their lattice points to a greater degree and form larger and larger hydrogen-bonded

Table 4.6 – Column densities derived from the different fits to the B5:IRS1 spectra

Composition	N(H ₂ O _{total}) ^a (cm ⁻²)	N(H ₂ O _{mixed}) / N(H ₂ O _{total})	N(CO ₂ total) / N(H ₂ O _{total})	N(CO ₂ pure) / N(H ₂ O _{total})	N(CO ₂ mixed) / N(H ₂ O _{total})
pure H ₂ O at 15 K ^b	2.1×10 ¹⁸	0	0.32	0.32	0
H ₂ O:(H ₂ O:CO ₂ 1:0.5) = 3:1 at 15 K ^c	2.3×10 ¹⁸	0.25	0.23	0.10	0.13
H ₂ O:CO ₂ ~90:10 ^d assuming 15 K	2.2×10 ¹⁸	1	-	-	0.08-0.14
H ₂ O:(H ₂ O:CO ₂ 1:0.5) = 1:1 at 45 K ^e	1.7×10 ¹⁸	0.5	0.20	0	0.20

^afrom H₂O stretching mode^bfirst column in Fig. 4.11^csecond column in Fig. 4.11, preferred fit at 15 K^dthird column in Fig. 4.11^efourth column in Fig. 4.11, preferred fit at 45 K

clusters and finally entire networks. This leads to a very small fraction of free OH bonds compared to those taking part in hydrogen bonds and hence only bulk vibrations show up in the spectra at high temperatures. Above 90 K the desorption of CO₂ further allows the hydrogen-bonds to reform. The temperature affects the H₂O molecules directly as well as indirectly through its effect on the mobility and final desorption of CO₂.

This scenario generally holds independent of whether the ice is deposited at 15 or 45 K. At both temperatures the deposited ice should be amorphous and porous, resulting in some CO₂ molecules becoming trapped in the H₂O ice as the ice is heated and the pores collapse. The H₂O peak profiles are similar at all temperatures, but it is clear that more CO₂ is trapped inside the H₂O ice when the ice is deposited at 45 K compared to 15 K. Figure 4.10 shows that the higher fraction of CO₂ coincides with a lower intensity of the H₂O bulk stretching band, indicating that the trapped CO₂ makes it more difficult for the hydrogen bond network to reform. It is not clear at this stage why the ice deposited at 45 K is capable, when heated, of trapping more CO₂ within the matrix, but it is most likely a kinetic effect, related to the compactness of the ice. The different ice structure then affects the relative rates at which pores collapse versus CO₂ diffusion and desorption during the heating process (Collings et al. 2003).

All experimental results are hence consistent with a model in which the H₂O molecules are present in the ice either as bulk H₂O ice or as small H₂O clusters. A higher CO₂ concentration forces more H₂O molecules into the cluster state. Since H₂O bulk ice spectra are different from H₂O cluster spectra, adding CO₂ to H₂O ice will significantly change the shapes and band strengths of the different H₂O peaks compared to pure H₂O ice. It is expected that other small molecules that cannot form H-bonds (or only very weak ones), e.g. O₂ and N₂, will affect H₂O similarly to CO₂, as indicated by the matrix experiments of Ehrenfreund et al. (1996). Our group is currently conducting a systematic series of experiment investigating the effects of N₂, O₂ and CO on H₂O spectral features in ice mixtures.

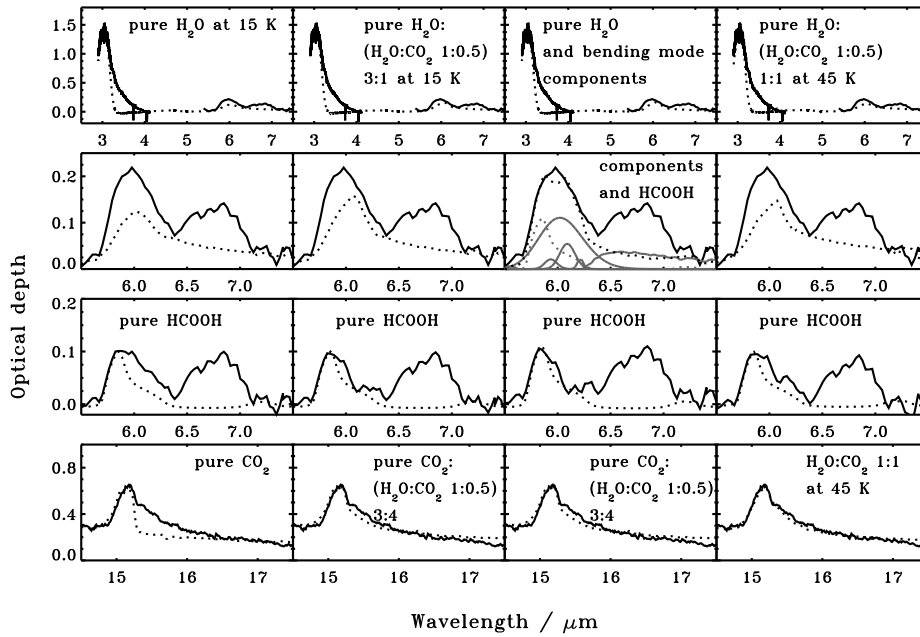


Figure 4.11 – Spectrum of the YSO B5 IRS1 (solid line) compared with laboratory spectra (dashed) of pure H_2O and CO_2 at 15 K (first column), a combination of pure H_2O and the $\text{H}_2\text{O}:\text{CO}_2$ 1:0.5 ice mixture at 15 K (second column) and 45 K (fourth column) and the derived bending mode components (third column). The silicate feature has been subtracted from the B5:IRS1 spectrum in all plots. In the upper row the spectrum has been fitted with respect to the $3\ \mu\text{m}$ H_2O stretching band. The effect on the H_2O bending mode region is shown in the second row. In the third row the H_2O (mixture) spectra have been subtracted from the star spectrum and the residual is compared with a pure HCOOH spectrum at 15 K. The last row shows the fit to the CO_2 bending mode using the ice mixture derived from the H_2O modes. The CO_2 peak has been shifted in the laboratory spectra to account for the shift in position between C^{16}O_2 and C^{18}O_2 used in this study. In the fourth column the spectrum of pure HCOOH was fitted together with the bending mode components to the $6.0\ \mu\text{m}$ band, to achieve an optimal fit while also being consistent with the band strength of the H_2O stretching mode. The individual components are plotted with a gray line.

4.4.2 Astrophysical implications

Recent Spitzer observations of the CO_2 bending mode at $15\ \mu\text{m}$ towards background stars indicate that 85% of the CO_2 column density is in a water-rich ice (Knez et al. 2005). To fit all H_2O and CO_2 features consistently, a combination of $\text{H}_2\text{O}:\text{CO}_2$ 10:1 and 1:1 at 10 K (with the ratios of the two mixtures varying between 1:0 and 1.3:1 for different sources) was used to fit the CO_2 profile (Knez et al. 2005). It is hence not unlikely that some of the observed H_2O ice is in mixtures with close to equal concentrations of CO_2 and H_2O .

This study shows that CO₂ in H₂O:CO₂ ice mixtures affects the H₂O spectrum in three observable ways:

1. a free OH stretch peak appears around 2.73 μm ,
2. the profile of the H₂O bending mode changes dramatically,
3. the H₂O stretching / bending mode strengths decrease linearly with CO₂ concentration.

When the free OH stretching region at 2.7 μm is observable the presence/absence of that band provides a stringent upper limit on the amount of CO₂ mixed into the H₂O ice. This region was covered by ISO for high mass YSOs and will be observed by Akari (ASTRO-F). It is not covered by Spitzer and cannot be observed from the ground. Hence it is not possible to use this region of the spectrum to constrain the CO₂ concentration in H₂O ice in most lines of sight.

Instead we will here use only spectral changes (2) and (3) to analyze the Spitzer and Keck spectra of the YSO B5:IRS1 after the silicate absorption has been removed (Boogert & Ehrenfreund 2004). We first compare the B5:IRS1 spectrum with laboratory spectra of pure H₂O, CO₂ ices at 15 K for reference. Then we deduce the maximum amount of H₂O that can be present in a H₂O:CO₂ 1:1 mixture without a change in peak position for the H₂O bending mode and then we present the best fit achieved by simultaneously comparing the H₂O stretching and bending regions and the CO₂ bending mode to laboratory spectra of pure H₂O, CO₂ and H₂O:CO₂ mixtures at 15 K. An equally good fit is achieved using laboratory spectra acquired at 45 K, which is also shown. In addition, we show that the average H₂O:CO₂ mixture in the line of sight can be deduced by fitting the 6.0 μm region with the bending mode components in Fig. 4.3, while keeping the total H₂O bending mode integrated intensity consistent with that of the H₂O stretching mode. For all cases we also attempt to fit the excess in the H₂O bending region with HCOOH. The presence of HCOOH is strongly indicated by absorption features at 7.25 and 8.2 μm (8.2 μm not shown). HCOOH has also been suggested before as the most likely candidate for the blue wing of the 6.0 μm band (Schutte et al. 1996).

In the analysis of B5:IRS1 we did not take into account the effect of grain shapes on the absorption profiles. The effect on the H₂O bending profile should be small, however, due to that the imaginary part of the optical constant (k) for the H₂O bending profile is small. When k is small it induces (through Kramers-Kronig relation) only small fluctuations of n around the central peak wave number so that particle scattering will not induce a significant change in band shape compared to transmission spectra.

In Fig. 4.11 the laboratory spectrum of pure H₂O is scaled to the 3.0 μm stretching band (upper row, first column). The fit in the bending mode region is shown in the second row and the spectrum after subtraction of the pure H₂O spectrum in the third row. A pure HCOOH spectrum was then scaled to the residual. The lower row shows the fit of the CO₂ bending mode when only a pure CO₂ spectrum is used. It is found that the fit between the pure laboratory ice spectrum and observed spectrum is poor. We subsequently tested the maximum amount of H₂O that can be mixed in the 1:1 mixture with CO₂ without visibly

changing the H₂O bending mode profile. If 6% of the total H₂O column density is in a 1:1 mixture there is a clear change in peak position of the bending mode so 5% was set as an upper limit.

In the second column a combination of pure H₂O and the H₂O:CO₂ 1:0.5 mixture at 15 K was used to fit the H₂O stretching and bending regions simultaneously. A good fit is also possible using the H₂O:CO₂ 1:1 and 1:0.25 mixture. The best fit is achieved using 3 parts pure H₂O ice and 1 part 1:0.5 mixture. The pure/mixture combination results in a smaller residual in the H₂O bending region when subtracted from the B5:IRS1 spectrum, compared to when only a pure H₂O spectrum is used. In addition, the fit with the spectrum of HCOOH to this residual is better. The same 1:0.5 ice mixture, together with pure CO₂, is also used to fit the CO₂ 15.2 μm bending mode. Approximately 50% of the CO₂ is found to be in a H₂O rich ice for the best fit. A combination of pure and 1:0.25 mixture also results in a good fit for the CO₂ bending mode, but a combination of pure ice and the 1:1 mixture. Hence fitting the H₂O and CO₂ ice modes simultaneously effectively constrains both the abundances and different environments of both H₂O and CO₂ ice.

The third column shows the best fit to the 6.0 μm region using the H₂O bending mode components derived previously and pure HCOOH. This method of estimating the composition of water rich ice has the advantage that no mix and matching with different laboratory spectra is needed and the uncertainty is easier to estimate. The three components were varied independently, but the wing residual was scaled to the pure H₂O component. The ratio between the broad pure H₂O peak at 6.02 μm (1661 cm^{-1}) and the 6.09 μm (1642 cm^{-1}) peak was used to constrain the amount of CO₂ present by comparing this ratio to Fig. 4.5. The total H₂O bending mode integrated intensity was constrained by the ratio between the stretching and bending mode band strengths including the wing (Table 4.5) and the ratio between the broad pure H₂O component and the narrow H₂O cluster bending component (Table 4.4). The latter comparison constrains the amount of H₂O mixed with CO₂, which must be fed back into the ratio between the stretching and the total bending mode strength to calculate a correct column density. A good fit was achieved for average H₂O:CO₂ mixtures 92:8 to 86:14, which is consistent with the derived composition from the best fit in the second column. When higher resolution spectra of this region will be available, it should be possible to analyze all the different components of the H₂O bending mode as demonstrated in the laboratory spectrum (Fig. 4.3). This will further constrain the mixture composition from the ratio between the two narrow bending peaks apparent in all mixture spectra. In the current spectrum the ratio between the two narrow peaks only puts an upper limit of 1:1 on the dominant H₂O:CO₂ mixture in the line of sight. The column densities derived from the fit of laboratory spectra and bending mode components are shown in Table 4.6.

All the fits above were done with spectra at 15 K. If the observed ice is at a higher temperature, the same amount of CO₂ mixed into the ice will result in a H₂O bending mode profile that is less different from pure H₂O ice (Fig. 4.6). The best fit at 45 K has an average mixture of H₂O:CO₂ \sim 1:0.23 (with 50% of the H₂O ice in a 1:0.5 mixture and 50% pure H₂O) and then no additional pure CO₂ is necessary to fit the CO₂ bending mode. A similar result is achieved when fitting the H₂O bending mode components and calculating the composition using the values of the component ratios for 45 K instead of

15 K in Table 4.4. More generally the ratio of the components constrains a region in the ice mixture-temperature space (initial mixture if the temperature is above 90 K) rather than determining an exact mixture composition. The fit to B5:IRS1 resulted in a ratio of the 1634 to 1661 cm⁻¹ components of 0.15. According to Table 4.4 this means that the temperature:composition is bound by 15 K:11±3%, 45 K:23±3% and 75 K:39±5% CO₂ relative to the H₂O ice abundance. Using the components to fit the bending region rather than spectra is advantageous if the temperature is unknown, since the ratio between the components sets bounds on the temperature and composition simultaneously and fully reveals the uncertainties involved. In most sources it is possible to independently constrain the temperature, however. For B5:IRS1 Boogert & Ehrenfreund (2004) have concluded that the bulk of the ice must be colder than 50K. For these temperatures the ratio of the bending mode components results in an average H₂O:CO₂ mixture of 11 to 23% CO₂ with respect to the H₂O ice. This can be further refined by more detailed radiative transfer modeling of the dust temperature in the source by fitting the spectral energy distribution. In contrast the total abundances of H₂O and CO₂ are only weakly dependent on temperature and can be determined within 15% uncertainty.

Note that the strengths of the stretching and libration bands are affected by CO₂, which needs to be taken into account when deducing the H₂O column density from the optical depths of the H₂O bands if a considerable amount of the H₂O is in mixtures with CO₂. In the example shown here the drop in band strength of the stretching band is only ~5% compared to the pure H₂O ice (Table 4.6). In the case where ~50% of the H₂O ice is in a 1:1 mixture with CO₂, as has been deduced for some background stars by Knez et al. (2005), the band strength of the H₂O stretching mode would drop by as much as ~25% compared to pure H₂O ice and the inferred H₂O column density would be ~33% higher.

Whether the results presented here can explain the ratio between the H₂O stretching and bending modes in all astrophysical sources has to be determined for each source individually because of the drastic change in the bending mode profile that accompanies the drop in ratio as the concentration of CO₂ is increased. In the case of B5:IRS1 the H₂O and CO₂ band shapes and intensities are well described by 50% of the CO₂ and 25% of the H₂O ice in a H₂O:CO₂ 1:0.5 ice mixture at 15 K and by 100% of the CO₂ and 50% of the H₂O ice in a H₂O:CO₂ 1:0.5 ice mixture at 45 K. These ratios in turn can provide interesting constraints on the H₂O and CO₂ formation routes.

4.5 Conclusions

1. The H₂O band profiles and strengths in astrophysically plausible mixtures with CO₂ are significantly different compared to pure H₂O ice. The changes in H₂O band profiles with CO₂ are greatest for the H₂O bending mode, while the stretching band displays more subtle changes.
2. The band strengths of all major H₂O bands depend linearly on CO₂ in the investigated domain of 20% to 80% of CO₂ in the ice mixture. The band strength ratio between the H₂O bulk stretching and bending modes is also linearly dependent

on CO₂ concentration in astrophysically relevant H₂O:CO₂ mixtures such that a H₂O:CO₂ 1:1 mixture has a ratio of half that of pure H₂O.

3. The H₂O bending mode in H₂O:CO₂ mixtures can be separated into three components due to pure H₂O ice, large H₂O and small H₂O clusters, respectively. In addition, a librational overtone overlaps with the bending mode.
4. The H₂O bending profile is visibly affected by as little as 6% H₂O in a H₂O:CO₂ 1:1 mixture. The composition of the H₂O rich ice is hence crucial to identify other species contributing to the 6 μm band.
5. A free OH stretching band appears with CO₂ concentration which can be used to put strict upper limits on CO₂ mixed with H₂O whenever the 2.7 μm region is observed.
6. If the ice temperature can be estimated independently, the total amount of CO₂ and H₂O as well as the amount of CO₂ mixed with the H₂O ice can be constrained by fitting the appropriate laboratory mixture spectra consistently to the H₂O and CO₂ bands.
7. The average H₂O:CO₂ ice mixture in any line of sight can be efficiently deduced by fitting the H₂O bending mode with components corresponding to pure and CO₂ rich ice. Especially if the ice temperature is uncertain, fitting the H₂O bending mode components to the bending mode region together with HCOOH, will effectively constrain the composition and temperature simultaneously.
8. The deduction of mixture composition is substantially dependent on the assumed dust temperature. The determination of total column densities of H₂O and CO₂ are only weakly dependent on the assumed dust temperature, however.

5

QUANTIFICATION OF SEGREGATION DYNAMICS IN ICE MIXTURES

The observed presence of pure CO₂ ice in protostellar envelopes, revealed by a double peaked 15 μm band, is often attributed to thermally induced ice segregation. The temperature required for segregation is however unknown because of lack of quantitative experimental data and this has prevented the use of ice segregation as a temperature probe. In addition, quantitative segregation studies are needed to characterize diffusion in ices, which underpins all ice dynamics and ice chemistry. This study aims to quantify the segregation mechanism and barriers in different H₂O:CO₂ and H₂O:CO ice mixtures. The investigated ice mixtures cover a range of astrophysically relevant ice thicknesses and mixture ratios. The ices are deposited at 16–50 K under (ultra-)high vacuum conditions. Segregation is then monitored as a function of time at 23–70 K through infrared spectroscopy; the CO₂ and CO band shapes are distinctly different in pure and mixed ices. The segregation barrier is determined using rate equations and the segregation mechanism is investigated through Monte Carlo simulations. Thin (8–37 ML) H₂O ice mixtures, containing either CO₂ or CO, segregate sequentially through surface processes, followed by an order of magnitude slower bulk diffusion. Thicker ices (>100 ML) segregate through a bulk process, which is faster than even surface segregation in thin ices. The thick ices must therefore be either more porous or segregate through a different mechanism, e.g. a phase transition, compared to the thin ices. The segregation dynamics of thin ices are reproduced qualitatively in Monte Carlo simulations of surface hopping and pair swapping. The experimentally determined surface-segregation rates follow the Arrhenius law with a barrier of 1080 ± 190 K for H₂O:CO₂ ice mixtures and 300 ± 100 K for H₂O:CO mixtures. Though the barrier is constant with ice mixing ratio, the segregation rate increases with CO₂ concentration. Dynamical ice processes can thus be quantified through a combination of experiments and different model techniques. Both surface and bulk segregation is proposed to be a general feature of ice mixtures when the average bond strengths of the mixture constituents in pure ice exceeds the average bond strength in the ice mixture. The derived segregation barrier for thin H₂O:CO₂ ice mixtures is used to estimate the surface segregation temperature during low-mass star formation to be 30 ± 5 K.

Öberg, K. I., Fayolle, E. C., Cuppen, H. M., van Dishoeck, E. F. and Linnartz, H., accepted for publication in A&A

5.1 Introduction

Ices form in dark clouds through accretion of atoms and molecules onto cold (sub)micron-sized dust particles. The atoms and molecules are subsequently hydrogenated and oxygenated on the grain surface to form ices such as H_2O (Merrill et al. 1976; Tielens & Hagen 1982; Watanabe et al. 2003; Ioppolo et al. 2008). This surface formation process is efficient enough that in the densest star-forming regions up to 90% of all molecules, except for H_2 exist in ice form (e.g. Bergin et al. 2002). Observations of dense clouds show that two of the most abundant ices, H_2O and CO_2 , form already at low extinctions, while the third major ice component, CO , freezes out in the cloud core (Bergin et al. 2005; Pontoppidan 2006; Sonnentrucker et al. 2008). These results predict a bi-layered ice composition, with a bottom layer dominated by a $\text{H}_2\text{O}:\text{CO}_2$ mixture of $\sim 5:1$ and top layer consisting of CO -rich ice. Infrared observations of the CO_2 ice bending mode around $15\ \mu\text{m}$ towards dark clouds confirm this scenario; the CO_2 spectral band consists of two or more distinct components consistent with laboratory ice spectra of $\text{H}_2\text{O}:\text{CO}_2$ and $\text{CO}:\text{CO}_2$ ice mixtures (Knez et al. 2005). In pure CO_2 ice spectra, the bending mode has a characteristic double peak (Sandford & Allamandola 1990, e.g.). This double-peak is not observed towards star-forming regions before the protostellar collapse and the turn-on of the protostar. This agrees with current astrochemical models, where pure CO_2 can only form through thermal processing of previously mixed $\text{H}_2\text{O}:\text{CO}_2$ and $\text{CO}:\text{CO}_2$ ices.

Heating of ice mixtures in the laboratory results in both sequential desorption, starting with the most volatile molecules, and in ice re-structuring, including ice segregation (e.g. Collings et al. 2004; Ehrenfreund et al. 1998). In $\text{H}_2\text{O}:\text{CO}_2$ and $\text{CH}_3\text{OH}:\text{CO}_2$ ice mixtures, ice segregation is identified from the growth of pure CO_2 ice features, especially the characteristic $15\ \mu\text{m}$ double peak. Thermal desorption of CO from CO_2 ice mixtures also results in the same pure CO_2 double-peak feature (van Broekhuizen et al. 2006). Ice heating is therefore inferred towards low and high-mass protostars wherever pure CO_2 ice is observed (Gerakines et al. 1999; Nummelin et al. 2001; Pontoppidan et al. 2008; Zasowski et al. 2009). Towards most of the protostars, low- and high-mass sources alike, the majority of the CO_2 ice is still present in the two phases typical for dark cloud cores, suggesting a range of ice temperatures in the protostellar envelope (Pontoppidan et al. 2008). The CO_2 spectra then contain information about the temperature structure of the protostellar surroundings. Maybe more importantly, the spectra contain information on the maximum temperature to which the icy grain mantles in the envelope have been exposed, since ice processing is irreversible. The fraction of pure CO_2 ice, with respect to the total CO_2 ice abundance towards a protostar, can therefore be used to constrain its thermal history, and its variability compared to current stellar luminosity measurements. Attempts to use this information quantitatively suffers from difficulties in determining the origin of the pure CO_2 ice, because of a lack of quantitative data on $\text{H}_2\text{O}:\text{CO}_2$ ice segregation, i.e. the segregation temperature of $\text{H}_2\text{O}:\text{CO}_2$ mixtures at these time scales is unknown.

Segregation is expected to occur whenever diffusion of molecules in the ice is possible and it is energetically favorable for molecules of the same kind to group together; for example H_2O molecules form stronger hydrogen-bonds with each other than with CO

and CO₂. Thus, ice segregation studies provide information on diffusion barriers. These barriers are currently the most important unknowns in models of complex organic ice formation, where large molecules form through recombination of smaller molecules and radicals that diffuse in the ice (Garrod et al. 2008). Ice diffusion barriers also govern selective desorption from ice mixtures, which is responsible for much of the chemical structure in protostellar envelopes. While experiments on ice chemistry and desorption provide some information on diffusion, the effects of diffusion are difficult to disentangle because of the additional dependencies of the experimental results on desorption and reaction barriers. Segregation studies offer a comparatively ‘clean’ environment to quantify diffusion within.

Segregation of thick ices (0.1–10 μm or 500–50,000 monolayers) has been studied qualitatively under high-vacuum conditions by multiple groups (Ehrenfreund et al. 1998, 1999; Dartois et al. 1999; Palumbo & Baratta 2000; Bernstein et al. 2005; Öberg et al. 2007a). The results differ somewhat between the different studies, but in general H₂O:CO₂ ice mixtures are observed to segregate between 60 and 75 K at laboratory time scales for mixtures between 9:1 and 1:1. Some of the observed differences are probably due to the different mixing ratios, since Ehrenfreund et al. (1999) demonstrated that segregation in CH₃OH:CO₂ ice mixtures depends on the original ice mixture composition; at 60 K only ice mixtures with ten times more CO₂ than CH₃OH segregate, at 100 K CH₃OH:CO₂ 1:3 ice mixtures segregate efficiently as well.

Recently Hodyss et al. (2008) investigated segregation in two 0.15 μm thick, H₂O:CO₂ ice mixtures (9:1 and 4:1, respectively) under high vacuum conditions. They observed an onset in segregation at 60 K, which they interpreted as resulting from the known, slow H₂O phase change from high density to low density amorphous ice between 38 and 68 K. The immediate segregation of an ice mixture deposited at 70 K shows, however, that segregation may also occur through diffusion. Consistent with previous investigations they found segregation to be more efficient in the 4:1 compared to the 9:1 ice mixture. Hodyss et al. (2008) also investigated the growth of segregated, pure CO₂ in the 4:1 ice mixture with time at three different temperatures and they observed a faster growth of the pure CO₂ feature, and also an increased final segregated fraction, at higher temperatures. The ice deposition temperature was important above 50 K in this study, while lack of quantified uncertainties prohibited an estimate of its significance at lower temperatures.

Building on these previous results, we aim to systematically investigate the segregation behavior of H₂O:CO₂ and H₂O:CO ice mixtures under astrophysically relevant conditions. The focus is on the CO₂ mixtures because of their previous use as temperature tracers around protostars. The CO mixtures are mainly included to test whether the deduced segregation mechanism for H₂O:CO₂ mixtures is molecule specific or if it can be applied more generally; The H₂O:CO segregation temperature and mechanism are however astrophysically relevant as well since H₂O:CO ice is present in star-forming regions (Chiar et al. 1994). For both ice mixtures, the segregation rates are measured under a range of experimental conditions, which are discussed in Section 5.2. The experiments are complemented by Monte Carlo simulations, introduced in Section 5.3, to test the theoretical outcome of different segregation mechanisms. The results of ultra-high- and high-vacuum experiments on segregation are presented together with the deduced segregation barriers

and the simulation results in Section 5.4. Based on the simulations and the experimentally determined segregation-rate dependencies, the possible segregation mechanisms are discussed in Section 5.5 followed by astrophysical implications.

5.2 Experiments

Quantitative experiments are carried out with thin ices, < 40 monolayers (ML), under ultra-high vacuum (UHV) conditions ($\sim 10^{-10}$ mbar) on the set-up CRYOPAD. Complimentary experiments on thick ices (> 100 ML) are performed under high vacuum (HV) conditions ($\sim 10^{-7}$ mbar) at a different set-up. CRYOPAD is described in detail by Fuchs et al. (2006). The set-up is equipped with a Fourier Transform InfraRed (FTIR) spectrometer in reflection-absorption mode (called Reflection-Absorption InfraRed Spectroscopy or RAIRS), which covers $4000\text{--}800\text{ cm}^{-1}$ with a typical spectral resolution of 1 cm^{-1} . The HV experiment is described in detail by Gerakines et al. (1995) and is equipped with a FTIR, set up in transmission mode, which spans $4000\text{--}600\text{ cm}^{-1}$ and is run at 1 cm^{-1} resolution.

In all experiments, the ices are built up diffusively on a gold surface (UHV) or a CsI window (HV) by introducing pre-mixed gases into the chamber at the chosen deposition temperature. The gas mixtures are prepared from $^{13}\text{CO}_2$ and ^{13}CO (Indugas, 98–99% isotopic purity) and deionized H_2O , which is further purified by several freeze-pump-thaw cycles. Because all experiments are with ^{13}CO and $^{13}\text{CO}_2$, the isotope mass is not written out explicitly in the remaining sections. The final mixture ratio is determined in each experiment using infrared spectroscopy and previously determined CO, CO_2 and H_2O transmission band strengths with $\sim 20\%$ uncertainty (Gerakines et al. 1995). The same band strengths are used to calculate absolute ice thicknesses, but in the thin ice experiments the band strengths are first scaled to account for the longer absorption pathway in RAIRS (Öberg et al. 2009b), which results in a $\sim 50\%$ uncertainty in the absolute ice thickness in these experiments. Based on the results of previous spectroscopic studies on mixed ices, the H_2O abundance is determined from the bending mode rather than the stretching feature (Öberg et al. 2007a; Bouwman et al. 2007).

In each segregation experiment the ice mixture is deposited at a temperature T_{dep} and then quickly heated ($\sim 5\text{ K min}^{-1}$) to a chosen segregation experiment temperature T_{exp} . The relative temperatures are controlled to a fraction of a degree, while the absolute temperatures have a $\sim 2\text{ K}$ uncertainty. The segregation is measured by acquisition of infrared spectra during 2–4 hours; the spectral profiles of pure and mixed CO_2 ice are distinctly different and can thus be used to measure the amount of segregated ice. In the thin ice experiment segregation is evaluated by using the CO and CO_2 stretching bands and in the thick ices by combining information from the CO_2 stretching and bending features.

Table 5.1 lists the experiments carried out under ultra-high vacuum conditions. The ice-mixture thickness is varied between 8 and 37 ML to explore the thickness dependence in the ice-thickness regime accessible by RAIRS; the CO_2 stretching feature is linear in absorbance for the first $\sim 5\text{--}10$ ML CO_2 ice (Teolis et al. 2007; Öberg et al. 2009b). At

higher coverage both the spectral shape and absorbance are affected by interference. This is only true for pure CO₂, thus a 30 ML thick 2:1 H₂O:CO₂ ice mixture is still accessible. Most H₂O:CO₂ experiments are carried out with a 2:1 mixture, but four other mixing ratios are included as well (Exps. 1, 2, 18 and 19). The 2:1 mixture was chosen as a standard experiment to facilitate the study of segregation dependencies over a range of conditions, which is not possible for more dilute mixtures at laboratory time scales. The deposition temperature is varied between 20 and 50 K and segregation is investigated between 50 and 60 K. Two additional experiments (Exps. 16 and 17) explore the impact of fast thermal annealing and of using an ice substrate instead of depositing the ice directly on the gold surface. The ice substrate is constructed by depositing a thick layer of H₂O ice onto the gold surface before depositing the ice mixture. The segregating ice mixture is thus isolated from the gold surface. Five experiments on H₂O:CO segregation (Exps. 20–24) at different temperatures and for different ice thicknesses and mixture ratios are included to test whether the H₂O:CO₂ segregation results can be generalized to other ice compositions. Table 5.2 lists the H₂O:CO₂ experiments carried out under high vacuum conditions, which are set up to explore temperature- and mixture-dependencies of ice segregation for thick ices between 100 and 300 ML and how this compares with the UHV thin ice experiments.

5.3 Monte Carlo simulations

Monte Carlo simulations are used to qualitatively investigate ice segregation through two different diffusion mechanisms. The stochastic method employed here builds on the lattice-gas Monte Carlo technique used by Los et al. (2006); Los et al. (2007) and Cuppen & Herbst (2007). In the simulations CO₂ and H₂O molecules are followed individually as a function of time, both position and environment, as they diffuse through the ice and desorb from it. The probability of a certain event in the simulation is governed by its energy barrier, which depends both on the kind of event and on the total energy difference before and after the event takes place. Exothermic events are therefore overall more likely to occur. Diffusion thus drives ice segregation when it is energetically favorable for molecules of the same kind to bind together rather than to bind with other types of molecules. The specific energy conditions for different types of diffusion is discussed further below.

In the simulation, the ice structure is modeled as a regular lattice with dimensions 25×25 (extended infinitely by periodic boundary conditions) $\times (h + 1)$, where h is the ice thickness in monolayers. The lattice is initially filled randomly with the two molecular species investigated for segregation, such that the first $(h - 1)$ layers are fully filled with molecules, the h layer is 75 % filled and the last $h + 1$ layer is 25 % filled. The partial fill of the top layers simulates the expected roughness of a surface. The ratio between the two molecular species occupying the sites is a given input parameter.

The molecular distribution changes with time through two diffusion mechanisms, hopping of molecules into empty sites and swapping of molecules between sites, and through desorption into the gas phase. The rates for these three processes R_h , R_s and R_d (where h is for hopping, s for swapping and d for desorption) are defined by

Table 5.1 – UHV ice-segregation experiments.

Exp.	CO ₂ /CO	H ₂ O : X	Thick. (ML)	T_{dep} (K)	T_{exp} (K)
1	CO ₂	10:1	37	19	60
2	CO ₂	3:1	36	19	60
3	CO ₂	2:1	8	19	53
4	CO ₂	2:1	8	19	58
5	CO ₂	2:1	11	19	50
6	CO ₂	2:1	11	19	55
7	CO ₂	2:1	11	19	60
8	CO ₂	2:1	13	19	50
9	CO ₂	2:1	18	19	55
10	CO ₂	2:1	18	19	60
11	CO ₂	2:1	20	19	53
12	CO ₂	2:1	27	19	56
13	CO ₂	2:1	30	19	50
14	CO ₂	2:1	17	40	55
15	CO ₂	2:1	21	50	55
16 ^a	CO ₂	2:1	10	19	55
17 ^b	CO ₂	2:1	9/75	19	53
18	CO ₂	1:1	13	19	50
19	CO ₂	1:1	13	19	55
20	CO	2:1	22	19	27
21	CO	1:1	10	16	27
22	CO	1:1	32	19	23
23	CO	1:1	31	19	25
24	CO	1:1	29	19	27

^aThe ice was annealed at 60 K for less than a minute before cooled back to the segregation temperature.

^b The H₂O:CO₂ ice mixture of 9 ML was deposited on top of 75 ML H₂O ice. The H₂O ice was deposited at 100 K to achieve a compact ice substrate and then cooled to 19 K before depositing the ice mixtures.

Table 5.2 – HV ice-segregation experiments.

Exp.	H ₂ O : CO ₂	Thick. (ML)	T_{dep} (K)	T_{exp} (K)
I	4:1	430	15	60
II	4:1	510	15	70
III	2:1	140	15	40
IV	2:1	160	15	45
V	2:1	240	15	50
VI	2:1	160	15	60
VII	2:1	180	15	70

$$R_i = \nu_i \times e^{-E_i/T_{\text{exp}}}, \quad (5.1)$$

where $i=h, s$ or d , ν_i is the vibrational frequency of the molecule in its binding site, which is $\sim 10^{12} \text{ s}^{-1}$ for physisorbed species (Cuppen & Herbst 2007), T_{exp} is the temperature at which the ice mixture is kept, and E_i is a barrier height in K for process i .

All barrier heights depend on the difference in binding energy before and after an event. In a binary mixture of molecules A and B, the total binding energy E_b depends on the number and nature of (next)-nearest neighbors (n_{nn}^A , n_{nn}^B , n_{nnn}^A , and n_{nnn}^B) surrounding the considered molecule and also on the specific molecule-to-molecule binding energies ε_b^{A-A} , ε_b^{A-B} and ε_b^{B-B} . The binding energy for next-nearest neighbors is defined to be $\frac{1}{8}$ weaker than for nearest neighbors because of the cubic geometry of the lattice. There is also an additional bulk energy term E_{bulk} , accounting for longer range effects. The total binding energy of a molecule A is thus described by

$$E_b^A = \varepsilon_b^{A-A}(n_{\text{nn}}^A + \frac{n_{\text{nnn}}^A}{8}) + \varepsilon_b^{B-A}(n_{\text{nn}}^B + \frac{n_{\text{nnn}}^B}{8}) + E_{\text{bulk}}. \quad (5.2)$$

The total hopping energy barrier for a molecule A into a neighboring site is defined by

$$E_h^A = \varepsilon_h^A + \frac{1}{2}\Delta E_b^A, \quad (5.3)$$

where ε_h^A is the barrier energy for a molecule to hop into a site where the total binding energy is the same before and after the event and ΔE_b^A is the difference in binding energy between the new and the old site. Hopping one site further has a barrier proportional to $2\varepsilon_h^A$. The total swapping energy barrier is defined by

$$E_s^{A-B} = \varepsilon_s^{A-B} + \frac{1}{2}\Delta E_b^A + \frac{1}{2}\Delta E_b^B, \quad (5.4)$$

where ε_s^{A-B} is the barrier energy for two molecules A and B to swap into sites where the total binding energy is the same before and after the event. The desorption energy E_d^A equals the binding energy E_b^A .

With the rates and barriers thus defined, the Monte Carlo method is used to simulate which of these processes occurs for a specific molecule through the random walk method.

The simulation starts with choosing time step Δt by picking a random number y between 0 and 1 and calculating the event time Δt_{event} from

$$\Delta t_{\text{event}} = \frac{-\ln(y)}{R_h + R_s + R_d} \quad (5.5)$$

for all molecules in the ice. The molecule with the smallest event time is selected and its event time defines the calculation time step. This molecule will then hop, swap or desorb at $t_{\text{current}} + \Delta t$ depending on the value of a second random number z between 0 and $R_h + R_s + R_d$. The molecular configuration in the lattice is subsequently updated to start a new calculation cycle.

In the simulation the energy barriers are chosen to represent a H₂O:CO₂ ice mixture (Table 5.3). Since this is a qualitative model, the values are approximate. The binding energies are based on TPD experiments, except for $\varepsilon_b^{\text{H}_2\text{O}-\text{CO}_2}$, which is assigned a lower value than $\varepsilon_b^{\text{CO}_2-\text{CO}_2}$ to make CO₂ segregation through hopping energetically favorable within the framework of the simulation. This may be counter intuitive since CO₂ and H₂O should form a hydrogen bond, which is stronger than the van-der-Waals interactions between two CO₂ molecules. From TPD experiments there is however no evidence for $\varepsilon_b^{\text{H}_2\text{O}-\text{CO}_2} > \varepsilon_b^{\text{CO}_2-\text{CO}_2}$ in ices (Collings et al. 2004). This may be due to steric effects, i.e. CO₂ molecules may be able to bind to more molecules in a pure CO₂ ice compared to in a H₂O-rich environment, resulting in an overall stronger bond for a CO₂ molecule that hops from a H₂O dominated site to a CO₂ dominated site despite the lower bond strength between individual CO₂ molecules. This requires both more experimental and theoretical investigations. Until such data exist, segregation through hopping cannot be excluded and it is thus included in the simulations, though segregation through swapping alone is simulated as well.

In contrast to CO₂ hopping, swapping only requires that the average pure ice band strengths are greater than the average band strengths in the mixture to drive segregation. In other words for the swap of a CO₂ molecule from an H₂O dominated environment with a H₂O molecule in a CO₂ dominated environment to be energetically favorable $\varepsilon_b^{\text{H}_2\text{O}-\text{H}_2\text{O}} + \varepsilon_b^{\text{CO}_2-\text{CO}_2} > 2 \times \varepsilon_b^{\text{H}_2\text{O}-\text{CO}_2}$. This is expected to hold, since H₂O can form considerably stronger hydrogen bonds to other H₂O molecules compared to with CO₂. In addition hopping of H₂O drives segregation under the condition $\varepsilon_b^{\text{H}_2\text{O}-\text{H}_2\text{O}} > \varepsilon_b^{\text{H}_2\text{O}-\text{CO}_2}$ though this process was less important in driving segregation at the temperatures and barriers chosen for the simulations. Thus diffusion in the ice will drive segregation under a range of different conditions with regards to relative energy barriers, and the dominating segregation mechanism may differ between different ice mixtures.

The hopping energies are multiples of the binding energies similarly to Cuppen & Herbst (2007) and Garrod et al. (2008), while the swapping barrier is unknown and we chose to set it to a factor three higher than the CO₂ hopping barrier. To investigate segregation through only hopping and only swapping, we also run simulations with only one of the mechanisms turned on. This is done computationally by increasing the barrier height by a factor of 10 for the excluded process compared to Table 5.3.

Table 5.3 – Defined binding, hopping and swapping energies of H₂O and CO₂.

Barrier type ^a	Energy / K
$\mathcal{E}_b^{\text{H}_2\text{O}-\text{H}_2\text{O}}$	1000
$\mathcal{E}_b^{\text{CO}_2-\text{CO}_2}$	500
$\mathcal{E}_b^{\text{H}_2\text{O}-\text{CO}_2}$	400
$\mathcal{E}_h^{\text{H}_2\text{O}}$	2400
$\mathcal{E}_h^{\text{CO}_2}$	1200
$\mathcal{E}_s^{\text{H}_2\text{O}-\text{CO}_2}$	3600
$\mathcal{E}_s^{\text{CO}_2-\text{H}_2\text{O}}$	3600

^a*b* = binding, *h* = hopping, *s* = swapping.

5.4 Results and analysis

The results and analysis of H₂O:CO₂ segregation under UHV and HV conditions, H₂O:CO₂ segregation under UHV conditions and Monte Carlo simulations are presented sequentially below. The CO₂ UHV experiments form the central part of this section, while the other studies present supporting information about the segregation mechanism.

5.4.1 UHV CO₂ ice mixture experiments

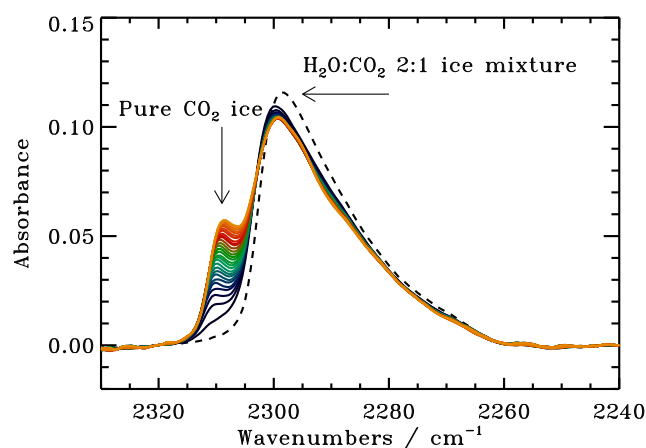


Figure 5.1 – Spectra illustrating the changes in the CO₂ stretching feature as the ice segregation proceeds in a 18 ML thick 2:1 H₂O:CO₂ ice at 55 K (Exp. 9) during 4 hours. The spectra are acquired every 5–15 minutes.

Figure 5.1 shows the evolution of the CO₂ stretching mode with time in a H₂O:CO₂ 2:1 ice mixture at 55 K during four hours. Following deposition at 20 K, the ice is first heated to 50 K, where the ice mixture spectra is acquired, and then further to 55 K. At

55 K a new feature appears within a few minutes at 2310 cm^{-1} , which is attributed to pure CO_2 ice (Fig. 5.2). The ice segregates quickly during the first hour before the rate levels off; after four hours the segregation still proceeds slowly however. Similarly to this experiment, all investigated $\text{H}_2\text{O}:\text{CO}_2$ 2:1 and 1:1 ice-mixture spectra change consistently with ice segregation when the ice mixtures are heated to 50–60 K and kept at the chosen segregation temperature for a minimum of two hours.

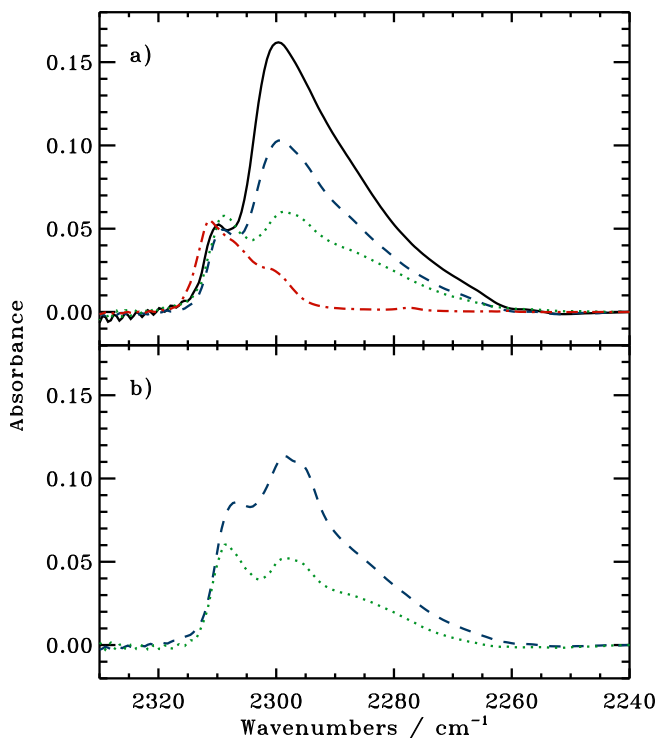


Figure 5.2 – The spectra illustrate the level of segregation the ice reached in 2:1 $\text{H}_2\text{O}:\text{CO}_2$ ice mixtures of different thicknesses in a) after ~ 3 hours at 55–56 K and in b) after ~ 2 hours at 60 K. The ice thicknesses are 27 ML (solid), 18 ML (dashed) and 11 ML (dotted). The partly segregated ices are plotted together with a spectra of pure CO_2 ice at 50 K (dashed dotted line) in panel a).

The early, fast segregation is inferred to be a surface process; the observed level of segregation does not depend on the initial ice thickness between 8 and 27 ML at early times for all ice temperatures, and also at late times for experiments at 55 K or colder. Figure 5.2a demonstrates this for 2:1 $\text{H}_2\text{O}:\text{CO}_2$ ice mixtures of three different thicknesses after three hours of segregation at 55 K, when the absolute amount of segregated ice is the same for all three ice mixtures within the experimental uncertainties. Segregation is somewhat thickness dependent at 60 K between 11 and 18 ML, which is indicative of a second bulk segregation process becoming efficient at this higher temperature (Fig. 5.2b).

Quantitatively, the amount of ice that is segregated at any time is calculated by simultaneously fitting a pure CO_2 ice spectrum and an appropriate $\text{H}_2\text{O}:\text{CO}_2$ ice mixture spectrum – both acquired at 50 K, where segregation is still slow – to the segregating ice using an IDL script. During the automatic fit, the template spectra are allowed to

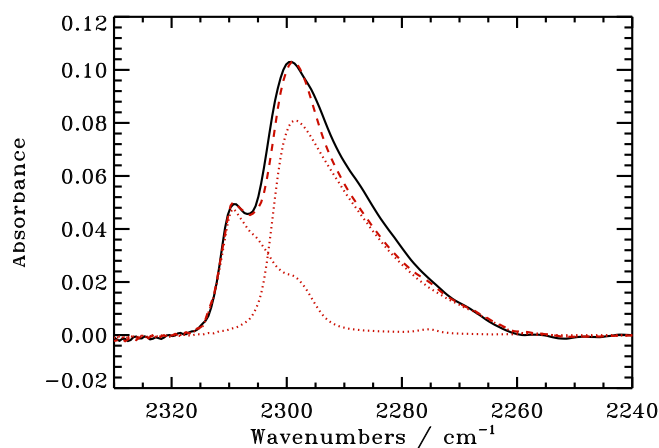


Figure 5.3 – The spectra of an 18 ML thick $\text{H}_2\text{O}:\text{CO}_2$ 2:1 ice mixture after ~ 3 hours at a segregation temperature of 55 K is fitted with a pure CO_2 spectra (2311 cm^{-1}) and a $\text{H}_2\text{O}:\text{CO}_2$ 2:1 mixture spectra at 50 K (dotted lines). The combined fit is plotted with a dashed line.

shift with at most a few wavenumbers to obtain an optimal fit as exemplified in Fig. 5.3. The fits are generally good except for a slight low-frequency mismatch, indicating that the structure of the mixed ice changes somewhat during heating. The resulting amount of segregated ice is plotted as a function of time in Fig. 5.4a for three 13–18 ML thick 2:1 $\text{H}_2\text{O}:\text{CO}_2$ ice mixtures at 50, 55 and 60 K, demonstrating that the segregation rate increases with temperature. The same trend is present for both thinner and thicker ices (not shown).

The segregation rate also depends on the ice mixing ratio as shown in Fig. 5.4b for 1:1 and 2:1 $\text{H}_2\text{O}:\text{CO}_2$ mixtures at 55 K. The initial rate is ~ 3 times higher in the $\text{H}_2\text{O}:\text{CO}_2$ 1:1 ice. This is also the case when comparing the 1:1 and 2:1 mixtures at 50 K. The upper limit on the segregation rate in the 10:1 mixture is a factor of 10 lower than the 2:1 rate. The segregation rate thus increases with a power 2–3 with the CO_2 concentration in the ice mixture (where the concentration is with respect to the total $\text{H}_2\text{O}+\text{CO}_2$ ice amount). Furthermore the steady-state segregation level is 70% higher in the 1:1 ices compared to the 2:1 mixtures, which is comparable to the CO_2 concentration increase. This suggests that the same total amount of ice is available for surface segregation in all ice mixtures and that the final level of ice segregation only depends on the amount of CO_2 in the top available ice layers.

In contrast to temperature and composition, the segregation rate is independent of the other experimental variables, including thermal annealing, deposition temperature below 50 K and the nature of the substrate (Figs. 5.4c and d). Figure 5.4c shows that an ice segregating at 55 K after a 1 min warm-up to 60 K behaves as a corresponding amorphous ice at 55 K, except for the first point, which can be attributed to segregation at 60 K. The same figure shows that increasing the deposition temperature from 18 to 40 K does not affect the segregation, while at 50 K the ice segregates during deposition (not shown). Any effect by the substrate on the segregation was investigated by comparing the segregation of two thin ices (8–9 ML) at 53 K after deposition directly on the gold substrate and

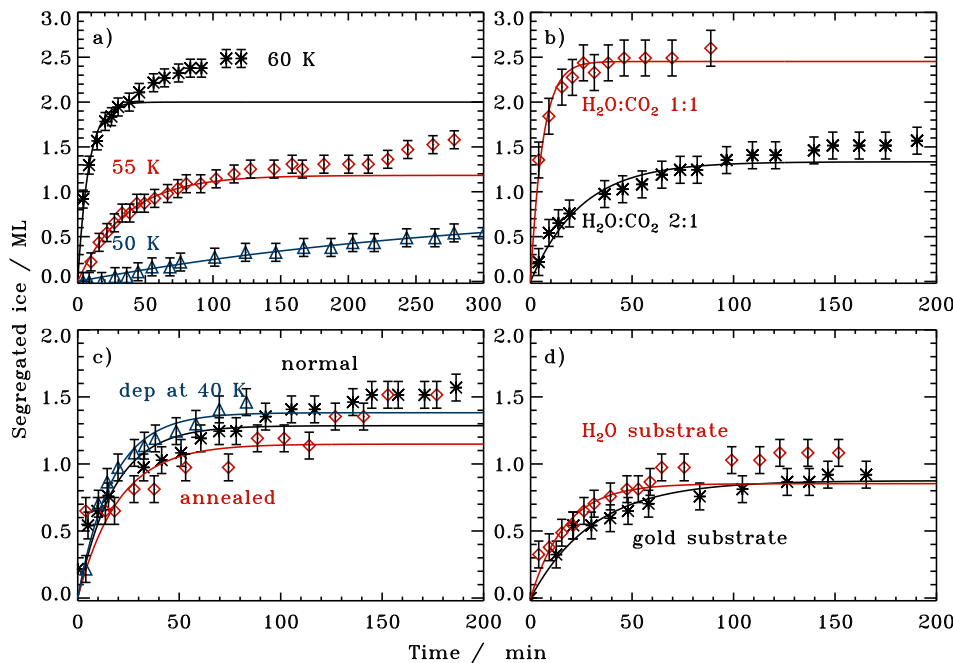


Figure 5.4 – The amount of segregated CO_2 ice (in ML) as a function of time in $\text{H}_2\text{O}:\text{CO}_2$ ices. Panel a) shows the increasing segregation rate with temperature when comparing experiments at 50 (triangles), 55 (diamonds) and 60 K (stars) (exp. 8–10). Panel b) shows the segregation at 55 K in a 1:1 (diamonds) and a 2:1 mixture (stars) in two 13 ML thick ices (exp. 9 and 20). Panel c) compares the segregation at 55 K for a quickly annealed ice (diamonds) with amorphous ice deposited at the ‘normal’ 19 K and at 40 K (exp. 8, 14 and 16). Finally the curves in d) show the segregation at 53 K for 8–9 ML thick ices deposited directly on the gold substrate and on top of 75 ML compact H_2O ice respectively (exp. 3 and 17). In each experiment, the segregation during the first 40–240 min is fitted with a function $A_\infty(1 - e^{-k_{\text{seg}}t})$ (solid lines).

on top of H_2O ice; there is no measurable difference between the outcome of the two experiments.

The initial segregation rate is measured quantitatively in each experiment by fitting an exponential function $A_\infty(1 - e^{-k_{\text{seg}}t})$ to the first 40–240 minutes of the segregation, where A_∞ is a steady-state amount of segregated ice, t is the segregation time in seconds and k_{seg} is a temperature dependent rate coefficient describing the segregation process. Such a functional form is expected for a process that eventually reaches a steady-state and as demonstrated in Section 5.4.4, this is consistent with the simulations of segregation through surface diffusion. Fig. 5.4 shows that the equation fits the early segregation well but at later times, the experiments and exponential fits deviate, especially for the warmest ices (Fig. 5.4a, 60 K). This suggests two types of segregation mechanisms with different

energy barriers, which are assigned to surface and bulk processes in Section 5.4.4. There are however too few points to fit both types of segregation in most experiments and thus we focus on the initial segregation rate alone. This is done by fitting the exponential growth function to early times, which is defined as 240 min at 50 K, 90 min at 52–56 K and 40 min above 56 K. At these times a single exponent fits the growth equally well as two exponents and the segregation is thus dominated by the fast process. To test the sensitivity of the fits to the fitting time intervals, these were varied by $\pm 50\%$. This does not affect the derivation of the segregation barrier, significantly, as shown further below. The results of these fits are shown for all experiments in Table 5.4. The rates are independent of ice thickness for 8–20 ML thick ices, while the thickest ice mixtures segregate somewhat slower compared to thinner ices kept at the same temperature. This decrease is barely significant, however, and it is probably due to RAIRS effects, which become important at these thicknesses as discussed in Section 5.2, rather than to real differences in the segregation behavior above 20 ML.

Table 5.4 – UHV ice-segregation coefficients for H₂O:CO₂ ices.

Exp.	A_∞ / ML	k / s ⁻¹
1	–	–
2	1.7 ± 0.1	(1.4 ± 0.3) × 10 ⁻³
3	0.8 ± 0.1	(5.4 ± 2.4) × 10 ⁻⁴
4	1.2 ± 0.1	(1.7 ± 0.5) × 10 ⁻³
5	<4	(3.1 ± 6.3) × 10 ⁻⁵
6	1.3 ± 0.1	(7.9 ± 1.9) × 10 ⁻⁴
7	1.7 ± 0.1	(3.3 ± 0.8) × 10 ⁻³
8	0.9 ± 1.2	(5.4 ± 9.6) × 10 ⁻⁵
9	1.2 ± 0.2	(4.7 ± 1.5) × 10 ⁻⁴
10	2.0 ± 0.1	(2.1 ± 0.4) × 10 ⁻³
11	1.4 ± 0.1	(4.9 ± 1.0) × 10 ⁻⁴
12	1.3 ± 0.4	(2.6 ± 1.4) × 10 ⁻⁴
13	<4	< 1.7 × 10 ⁻⁴
14	1.4 ± 0.1	(9.9 ± 2.1) × 10 ⁻⁴
15	–	–
16	1.1 ± 0.1	(1.1 ± 0.3) × 10 ⁻³
17	1.0 ± 0.1	(5.9 ± 1.7) × 10 ⁻⁴
18	1.6 ± 0.4	(4.2 ± 1.8) × 10 ⁻⁴
19	2.4 ± 0.1	(2.9 ± 0.4) × 10 ⁻³

Assuming that the segregation-rate coefficients can be described by the Arrhenius equation, $k = \Gamma \times e^{-E_{\text{seg}}/T}$, where Γ is the pre-exponential factor, E_{seg} the segregation barrier in K and T the ice temperature, the segregation energy can be extracted by plotting $\ln(k)$ versus $1/T$ and fitting a straight line to the points; the slope of the line is E_{seg} . This is shown in Fig. 5.5 for the rate coefficients belonging to the 8–13 ML experiments, resulting in a segregation barrier of 1080 ± 190 K for the 2:1 and 1050 ± 220 K for the 1:1 H₂O:CO₂ ice mixtures, where the uncertainties include both experimental and fit errors. If the time intervals chosen to fit the first exponential is allowed to vary by $\pm 50\%$ from

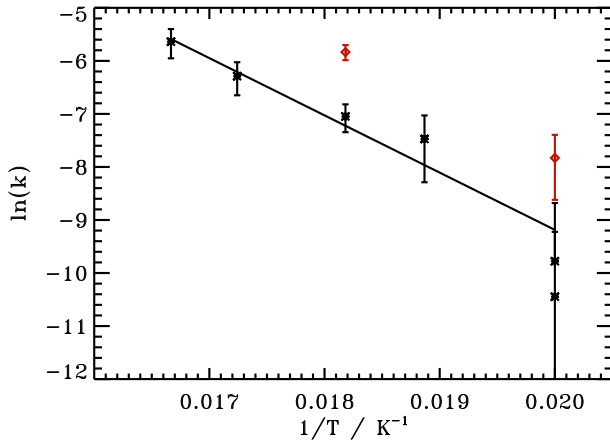


Figure 5.5 – The natural logarithm of the rate coefficients for segregation in 8–13 ML ices are plotted versus the inverse of the segregation temperature for H₂O:CO₂ 2:1 (crosses) and 1:1 mixtures (diamonds). The line is fitted to the 2:1 experiments.

the optimal value, the derived barrier is instead 1200 ± 250 K for the 2:1 mixtures. This probably overestimates the uncertainties. Still it is comforting that the derived value is well within the uncertainty of the segregation barrier derived from the optimal fitting time intervals, and the presented barrier for surface segregation is thus robust. The barriers are also not significantly different for the two mixtures, even though the rates are higher for the 1:1 ices; the pre-exponential factors amount to $2 \times 10^{(5 \pm 1)}$ for the 2:1 mixtures and $6 \times 10^{(5 \pm 1)}$ for the 1:1 mixtures. The pre-exponential factor can be understood as a diffusion frequency multiplied by the fraction of diffusion events that results in segregation. Its increase between the two mixing ratios is thus consistent with the increase in the number of CO₂ molecules available in the top layers.

Table 5.4 shows that the steady-state amount of segregated ice from the fast segregation mechanism is consistently between 1 and 2 ML in all experiments, except for the 1:1 mixtures as discussed above. The steady-state amount increases slightly between the 50–55 K and the 60 K experiments. This increase is however low enough that an average value over all ice temperatures and thicknesses can be used when quantifying the segregation process. Combining the information in this section, the amount of segregated ice $n_{\text{CO}_2}^{\text{seg}}$ in ML after a time t in seconds at an ice temperature T in K is well described by

$$n_{\text{CO}_2}^{\text{seg}} = 1.3 \pm 0.7 \left(1 - e^{-k_{\text{seg}} t} \right) \times \left(\frac{x}{0.33} \right) \quad \text{and} \quad (5.6)$$

$$k_{\text{seg}} = 2 \times 10^{(5 \pm 1)} \times e^{-(1080 \pm 190)/T} \times \left(\frac{x}{0.33} \right)^{2.5 \pm 1}, \quad (5.7)$$

where x is the CO₂ concentration in the ice with respect to the total CO₂:H₂O ice amount (in astrophysical settings this will be dominated by the H₂O ice fraction). At 60 K the second, bulk segregation rate is an order of magnitude lower than the initial surface segregation rate. There are too few measurements to quantify the bulk segregation further,

but this difference suggests that the barrier to segregate in the bulk is more than a factor of two larger than for the surface segregation evaluated here. In Section 5.4.4 this bulk segregation is simulated through molecular pair swapping with a three times higher energy barrier compared to CO₂ surface hopping.

5.4.2 HV CO₂ ice mixture experiments

Transmission spectroscopy in the HV set-up allows for the investigation of segregation in an order of magnitude thicker ice than is possible in CRYOPAD. Figure 5.6 shows the segregation of H₂O:CO₂ 2:1 mixtures through spectroscopy of both the CO₂ bending and stretching modes. Some ice rearrangement is also visible in the 4:1 mixture but there is no clear indication of segregation into two different ice phases. Thus, similarly to the thin ice experiments, the segregation rate depends on the ice mixture ratios.

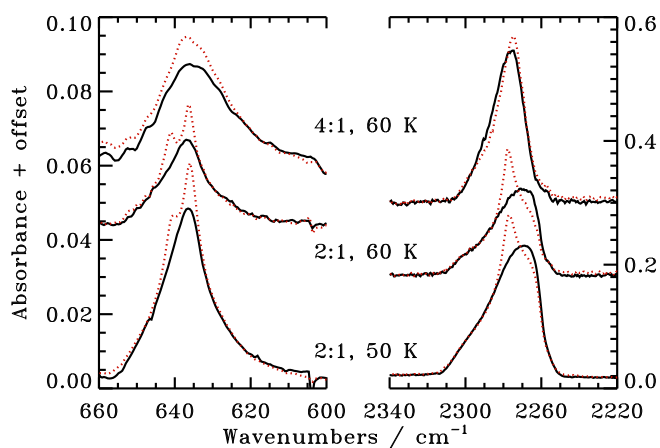


Figure 5.6 – CO₂ bending ($\sim 635\text{ cm}^{-1}$) and stretching ($\sim 2270\text{ cm}^{-1}$) spectral features at the onset (solid lines) and after 2 hours of heating at the segregation temperature (dashed lines) for three 160–510 ML thick H₂O:CO₂ ice mixture experiments.

The amount of segregated ice at each time step is derived using the same procedure for the thick ices as described above for the thin ices. Figure 5.7 shows the fraction (not the number of ML) of the ice mixture that is segregated as a function of time at segregation temperatures between 40 and 70 K. Above 50 K the segregation of the >140 ML ices reaches 50%, from which we infer, in agreement with previous studies, that segregation is a bulk process for thick ices deposited under high-vacuum conditions. It also shows however that a large fraction of the ice is protected from segregation at all ice temperatures, though this fraction is smaller than in the thin ice experiments that are dominated by surface diffusion. The segregated amount of ice as a function of time is fit to an exponential function in the low-temperature experiments – above 45 K, segregation is too fast for a reliable rate determination, i.e. the final segregated amount is reached within

a couple of measurements. In contrast to thin ices the segregation can be fitted with a single exponential function for all temperatures and the determined steady-state amount of segregated ice depends on the ice temperature; the segregated fraction varies between 20% and 55% at the investigated temperatures. The resulting bulk segregation rates at 40 and 45 K are $(2 \pm 6) \times 10^{-4}$ and $(5 \pm 3) \times 10^{-3} \text{ s}^{-1}$, respectively. Since the rates describe the segregation of a fraction of the ice rather than a number of monolayers they cannot be directly compared to the thin ice surface segregation rates – it is, however, clear that steady state is reached in a shorter time in the thick ice experiments than in the thin ices. The derived barrier from the 40 and 45 K experiments is $1270 \pm 560 \text{ K}$, which is consistent with the thin ice segregation barrier of $1080 \pm 190 \text{ K}$. The thick ice segregation, while more efficient, thus does not necessarily proceed through a separate mechanism.

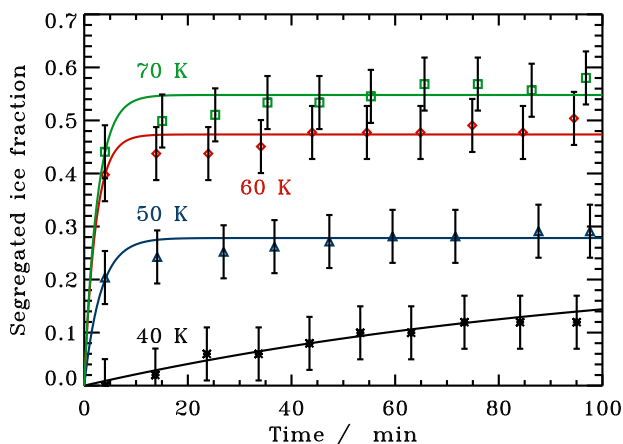


Figure 5.7 – The segregated ice fraction, with respect to the total CO_2 ice amount, as a function of time at 40 (stars), 50 (triangles), 60 (diamonds) and 70 K (circles) for 140–240 ML thick $\text{H}_2\text{O}:\text{CO}_2$ 2:1 ices. The solid lines are exponential fits.

5.4.3 UHV CO ice mixture experiments

Because of the high volatility of CO, $\text{H}_2\text{O}:\text{CO}$ segregation is investigated between 23 and 27 K. This is below the temperature range for the H_2O ice transition between high and low density amorphous phases, which occurs gradually between 38 and 68 K (Jenniskens & Blake 1994). The temperatures investigated for $\text{H}_2\text{O}:\text{CO}$ and $\text{H}_2\text{O}:\text{CO}_2$ segregation are similar in terms of % of the CO and CO_2 desorption temperature; CO desorbs at $\sim 30 \text{ K}$ and CO_2 at $\sim 70 \text{ K}$ from a H_2O ice substrate. Hence, if segregation occurs through a simple diffusion process with barriers proportional to the binding energy in CO and CO_2 ice mixtures, this is the predicted range of temperatures where the $\text{H}_2\text{O}:\text{CO}$ ice should segregate. Figure 5.8 shows the $\text{H}_2\text{O}:\text{CO}$ ice evolution when quickly heated from 16 to 25 K and then maintained at 25 K for four hours. The new band appearing around 2094 cm^{-1} at 25 K has the same width and a comparable position to a pure CO ice feature and this is interpreted as resulting from ice segregation. Segregation thus occurs and it occurs only in a part of the ice, similarly to the CO_2 mixtures.

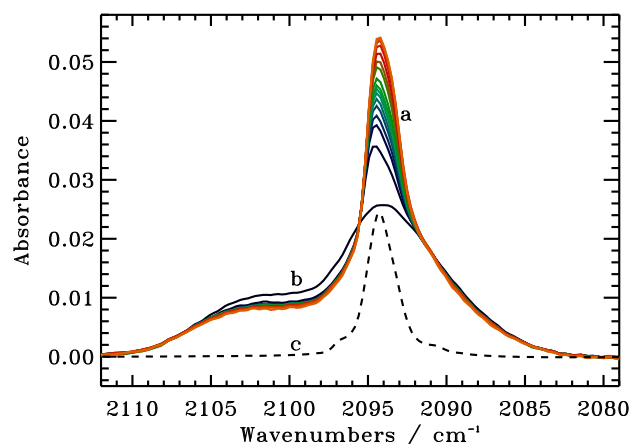


Figure 5.8 – Ice segregation in a 10 ML $H_2O:CO$ mixture observed through a) the changes in the CO stretching feature with time, plotted together with b) the original ice mixture spectra and c) a pure CO ice spectra (dashed line).

The segregation is quantified by fitting three Gaussians to the spectral feature, two belonging to CO ice in a H_2O mixture and one corresponding to the pure CO ice band (Fig. 5.9). The two mixed-ice Gaussians have been observed previously in several studies and are attributed to two different CO- H_2O interactions (Collings et al. 2003). The Gaussian parameters are free variables during the fit except for the FWHM of the pure CO Gaussian, which is constrained to be within 0.5 cm^{-1} of the pure CO ice value in Bouwman et al. (2007). The resulting Gaussian parameters for all $H_2O:CO$ experiments are reported in Table 5.5. The widths of Gaussians 1 and 3 are similar to those used to fit the same $H_2O:CO$ ice-mixture feature by Bouwman et al. (2007). Figure 5.9 shows that the spectral fit cannot exclude a few % of ice segregation at deposition. This does not affect the results since the reported level of segregation during the experiment is calculated from the increase of Gaussian 2 compared to deposition.

Table 5.5 – Parameters for the three Gaussians used to fit the CO feature.

Gaussian	Peak position (cm^{-1})	FWHM (cm^{-1})
1	2103.0–2102.4	6.1–6.4
2	2094.6–2093.8	2.1–2.5
3	2093.4–2092.7	8.4–8.7

Using the Gaussian fits, Fig. 5.10 shows the time evolution of the amount of segregated ice in the different CO ice mixtures, except for the 23 K ice where no segregation is observed. The segregation time series have the same shape as the CO_2 segregation curves, with a fast initial segregation resulting in <2 ML segregated ice, followed by a slower segregation process at the highest temperature. The ice composition dependence seems weaker, but is still present, compared to the CO_2 case. The segregation at 27 K is thickness dependent, which suggest that bulk diffusion has already become important at

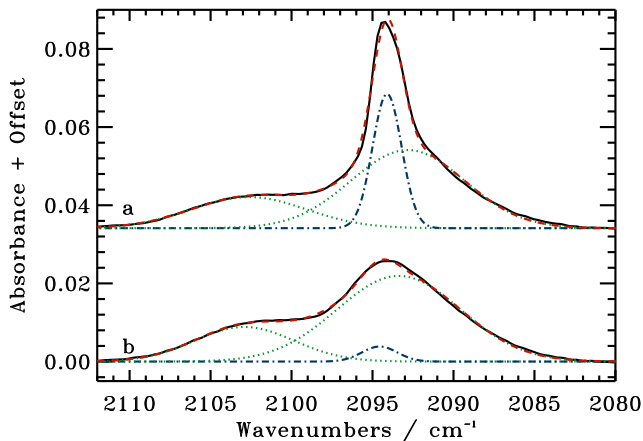


Figure 5.9 – The resulting fit of three Gaussians to a) a partially segregated 10 ML $H_2O:CO$ ice at 25 K and b) the original ice mixture at 16 K. The mixed-ice Gaussians are dotted, the pure CO Gaussian dashed-dotted and the combined dashed.

this temperature, though the initial rate should still be dominated by surface processes. Comparing the early-time rates of the 1:1 mixtures at 25 and 27 K results in an approximate barrier for the initial $H_2O:CO$ segregation of 300 ± 100 K, using the same fitting technique as for the CO_2 mixtures. This is significantly lower than the $H_2O:CO_2$ segregation barrier, as would be expected for the more volatile CO ice.

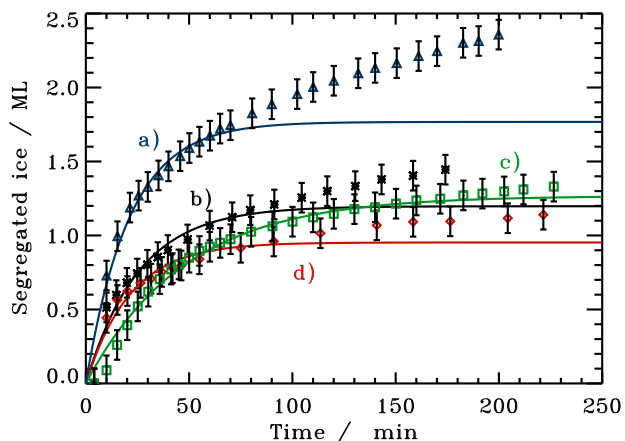


Figure 5.10 – The amount of segregated ice as a function of time in four $H_2O:CO$ mixtures: a) 1:1, 27 K, 29 ML, b) 2:1, 27 K, 22 ML, c) 1:1, 25 K, 31 ML and d) 1:1, 27 K, 10 ML.

5.4.4 Monte Carlo simulations

This section presents the results from six different ice segregation simulations, investigating the importance of swapping and hopping, and the effect of temperature on the

segregation behavior. Figure 5.11 shows the simulated H₂O:CO₂ ice segregation in a 5 ML thick 1:1 mixture using the Monte Carlo technique and inputs described in Section 5.3. The segregated ice fraction is quantified through an increase in the number of nearest neighbors of the same species, which is not directly comparable to the spectroscopic segregation observed in the experiments, though the two are linked. The simulated amount of segregated ice is thus presented in arbitrary units. With the specified energy barriers, segregation at 55 K occurs through a combination of hopping and swapping; removing one of the mechanisms decreases the total segregated fraction (Fig. 5.11).

The segregation through hopping is well defined by an exponential function, i.e. it is a single process approaching steady-state, while segregation through swapping, and segregation through swapping + hopping are both not. Instead segregation through swapping is initially fast and then continues to proceed slowly until the end of the simulation, long after the segregation through hopping has reached steady-state. The initial fast swapping is due to swapping with surface molecules, which explains that segregation through hopping and swapping is not additive. It also explains why segregation through only swapping cannot be fitted by a single exponential function, since it proceeds through two different processes, surface and bulk swapping. Of the three curves the swapping+hopping one is qualitatively most similar to the 55 and 60 K CO₂ UHV experiments and hopping alone cannot explain the non-exponential behavior of the experimental segregation curves during late times. It is however important that swapping alone may be able to reproduce the segregation behavior observed in the experiments and this implies that the CO₂-CO₂ binding energy is not required to be higher than the CO₂-H₂O one for segregation to occur through a combination of surface and bulk diffusion.

The segregation rate increases with segregation temperature in the simulation when both hopping and swapping are included, as is observed in the experiments. Figure 5.12 also shows that the curves at higher temperatures, i.e. 55 and 60 K, diverges more from an exponential growth compared to the 50 K simulation, suggesting an increasing importance of bulk-swapping with temperature. This is also consistent with the experimental results (Fig. 5.4a). The segregated fraction in the simulations increases more clearly with temperature than in the experiments, suggesting that the bulk process, swapping of bulk molecules, may be somewhat too efficient in the simulations.

5.5 Discussion

Following a brief comparison with previous experiments, this section combines the results from (U)HV H₂O:CO₂ and H₂O:CO segregation experiments and Monte Carlo simulations to constrain the segregation mechanics and the meaning of the empirically determined segregation rates and barriers. This information is then used to discuss the astrophysical implications of quantifying the segregation of binary ice mixtures.

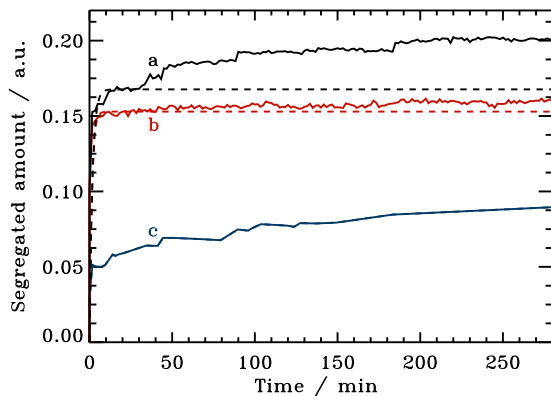


Figure 5.11 – Simulations of ice segregation in a $\text{H}_2\text{O}:\text{CO}_2$ 1:1 mixture at 55 K due to a) swapping and hopping, b) only hopping, and c) only swapping. The dashed lines show exponential fits to the first 30 min.

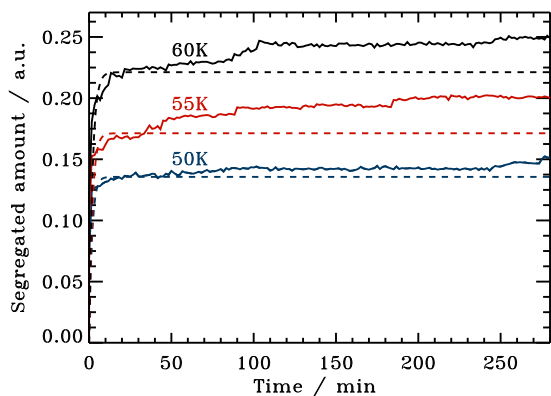


Figure 5.12 – Simulations of ice segregation in a $\text{H}_2\text{O}:\text{CO}_2$ 1:1 mixture at 50, 55 and 60 K due to a combination of swapping and hopping. The dashed lines show exponential fits to the first 30 min.

5.5.1 Comparison with previous experiments

Previous studies have focused on segregation in thick ices (>100 ML) under HV conditions. Of these studies, Hodyss et al. (2008) carried out the most similar experiments to our HV ones and thus we only compare these two sets of experiments. Hodyss et al. (2008) reported an increase in the segregated ice fraction and in the segregation rate between 55 and 70 K for a $\text{H}_2\text{O}:\text{CO}_2$ 4:1 mixture, which is comparable to what we observe between 40 and 60 K for a 2:1 mixture. The lower temperatures required in our experiment to achieve the same result are consistent with the observed dependence on composition for segregation in both studies. Similarly to Hodyss et al. (2008), we do not observe any dependence on the ice deposition temperature in our thin ice experiments, as long as the deposition temperature is lower than the lowest temperature for which segregation is observed. Qualitatively, the studies also agree on the segregation dependence on composition. A quantitative comparison is not possible since such data have not been reported

previously.

5.5.2 Segregation mechanisms

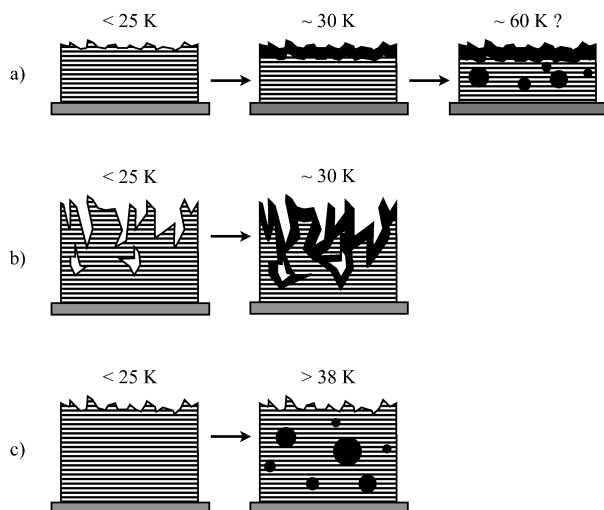


Figure 5.13 – The segregation mechanism in a) ices below 40 ML together with the two proposed segregation mechanisms for thick ices (>100 ML), through b) internal surface segregation and c) phase transitions. Black indicates segregated CO_2 ice and stripes the $H_2O:CO_2$ ice mixture. Each step is marked with the approximate temperature at which the mechanism becomes important at the time-scales of low-mass star formation, as discussed in Section 5.5.3.

The possible segregation mechanisms for thin and thick ice mixtures are summarized in Fig. 5.13. Thin binary $H_2O:CO_2$ ice mixtures, 8–37 ML, segregate differently compared to thick, >100 ML, ices. This implies either a thickness dependent segregation mechanism or a different ice structure above 100 ML compared to <40 ML. Segregation in thin ices is qualitatively reproduced by Monte Carlo simulations including surface hopping, surface swapping and the slower molecular swapping throughout the bulk of the ice. If thicker ices are more porous because of cracking, hopping and surface swapping may be possible throughout the ice resulting in the observed fast bulk segregation. Previous studies, including Hodyss et al. (2008), instead suggest that segregation is the product of a H_2O phase transition around the segregation temperature. Phase transitions may require a certain ice thickness to become effective and thus may only be important for thicker ices; the $H_2O:CO$ results show that phase transitions are not responsible for segregation in thin ices. The similar segregation barrier in thick ices and thin ices suggests that the mechanism is the same at all thicknesses and that the rate differences have a structural origin. The shorter times required to reach steady-state in thick compared to thin ices indicates, however, the opposite. More thick ice experiments containing molecules with different segregation temperatures are thus required to differentiate between these two segregation scenarios. In either case, these different segregation processes in thin and thick ices show that ice dynamics, including ice chemistry, is not necessarily thickness independent as has been previously assumed in the astrochemical literature.

The segregation growth curves of thin $\text{H}_2\text{O}:\text{CO}_2$ and $\text{H}_2\text{O}:\text{CO}$ ices have the same shape with an initial exponential growth up to 1–2 ML, followed by a slower growth at longer time scales. The segregation temperatures and inferred barriers differ by a factor 2–3. The desorption/binding energies of pure CO_2 and CO ices are similarly a factor of 2–3 different (Collings et al. 2004). The derived segregation barriers for the two types of mixtures are thus consistent with segregation through molecular hopping and swapping, with hopping and swapping barriers proportional to the desorption/binding energy of the most volatile mixture component. The similar ratio between the surface segregation barrier and desorption energies in the two types of ice mixtures, suggests that ice surface dynamics can be approximately parameterized based on desorption energies of pure ices alone.

Physically, it is not obvious from the simulations whether this initial surface segregation is dominated by surface hopping or surface swapping or whether it is even the same in both the $\text{H}_2\text{O}:\text{CO}_2$ and $\text{H}_2\text{O}:\text{CO}$ mixtures. Swapping is certainly required to explain the long-time growth of the segregated ice fraction. Depending on the relative barriers for hopping and swapping and the different binding energies in the ice, it may also be responsible for at least a part of the surface segregation as shown in Fig. 5.11. The similar behavior of the $\text{H}_2\text{O}:\text{CO}_2$ $\text{H}_2\text{O}:\text{CO}$ ices actually suggests that surface swapping rather than hopping drives surface segregation in both ices, since there is experimental evidence for a higher $\text{H}_2\text{O}:\text{CO}$ binding energy compared to the $\text{CO}:\text{CO}$ one in ices (Collings et al. 2003) and surface hopping can only drive segregation if the hopping molecules forms stronger bonds with its own kind. Quantitative $\text{H}_2\text{O}:\text{CO}_2$ desorption data is however required to exclude surface segregation through CO_2 hopping. A more quantitative simulation study of ice segregation is currently being pursued, which will address this question (Cuppen et al. in prep.). Until then, Eqs. 5.6 and 5.7 describe a non-specified surface segregation, while bulk segregation is approximately an order of magnitude slower in thin ices. From the experimental studies and the simulations, segregation is expected to occur in all ices, through swapping, where the binding energies of A-A + B-B are greater than $2\times\text{A-B}$. The segregation barrier is expected to be mixture dependent, but related to the pure ice binding energies.

5.5.3 Astrophysical implications

Nature is ‘non-cooperative’ in that the typical astrophysical ice thicknesses of <100 ML are not guaranteed to be in the thin ice regime where hopping and swapping alone are responsible for ice segregation. Yet, since 100 ML is the upper limit assuming spherical grains, most astrophysical $\text{H}_2\text{O}:\text{CO}_2$ ice mixtures are probably closer to the thin ice regime than the thick ice one. Therefore this section will discuss ice segregation during star formation under the assumption that this can be described by the same equations as thin ice surface segregation.

During star formation ices are heated in the collapsing envelope to a certain temperature, depending on their distance from the protostar. The amount of time they spend at these elevated temperatures before desorbing depends on the infall rate that transports ices from the outer to the inner parts of the protostellar envelope. This time scale τ_{crit}

for ice heating in the envelope during low-mass star formation thus depends on several different parameters of which the stellar luminosity is the most important one and will vary between different objects. Building on Eq. 7, the characteristic temperature T_{seg} at which segregation is important can be calculated as a function of this heating time scale $\tau_{\text{crit}} = k^{-1}$ for a known ice composition

$$T_{\text{seg}} = \frac{1080 \pm 190}{\log\left(2 \times 10^{5 \pm 1} \times \left(\frac{x}{0.33}\right)^{2.5 \pm 1} \times \tau_{\text{crit}}\right)}. \quad (5.8)$$

where x is the CO_2 concentration in the $\text{H}_2\text{O}:\text{CO}_2$ ice phase, which is set to 0.16 from the 5:1 ice mixture observed by Pontoppidan et al. (2008). Pontoppidan et al. (2008) also calculated that under the assumption of free-fall accretion, a dust grain is heated to 25–50 K by a solar-mass protostar for ~ 4000 years, while in a recent infall model it is at least a factor of 5 longer (Visser et al. 2009). Taking the lower limit 4000 yrs time scale for segregation, T_{seg} is 30 ± 5 K. This is low compared to previous estimates, of 50–100 K, and comparable to the temperature for CO distillation from $\text{CO}:\text{CO}_2$ ice mixtures, which is a competitive mechanism to form pure CO_2 ice. With this segregation temperature, segregation of $\text{H}_2\text{O}:\text{CO}_2$ ice is no longer excluded as a source for pure CO_2 ice around low-mass protostars. This temperature is only for surface segregation however. Therefore if more than 2 ML of pure CO_2 is present towards a low-mass protostar, distillation is still required. Observations show that in the sample of Pontoppidan et al. (2008), the average ice abundance of pure CO_2 with respect to H_2O ice is $2.4 \pm 2.4\%$. Similar values are also found towards the low-mass and high-mass sources in the sample when calculated separately for the two types of objects. With a total ice thickness of less than 100 ML, the amount of segregated CO_2 towards most sources is thus consistent with surface segregation as long as the observations are dominated by ice at > 30 K.

To understand the origin of pure CO_2 ice towards individual objects requires estimates of the infall rate, the stellar luminosity and the origin of the ice absorption features in the envelope, which is outside of the scope of this study. Such a model could however use pure CO_2 observations to constrain the thermal history of the protostellar envelope. While the characteristic temperatures of CO_2 segregation in a $\text{H}_2\text{O}:\text{CO}_2$ ice mixture and CO distillation from a $\text{CO}_2:\text{CO}$ ice are too close to differentiate their relative contributions towards most objects, their similarity is actually an asset when using pure CO_2 ice as a thermal probe. Both types of ice processing are irreversible; hence once segregated or distilled, the CO_2 ice will remain pure. Modeling of the amount of pure CO_2 ice in a protostellar envelope may then reveal the maximum size of the envelope that has been heated to 25–30 K. This inferred heating of the envelope in the past can be compared to the current luminosity of the protostar. A statistic on the discrepancy between the two would constrain the variability of protostars during an otherwise observationally inaccessible period of the stellar evolution.

This picture may be complicated by the presence of strong UV fields around some protostars. UV radiation can produce CO_2 from CO and H_2O ices through photochemistry, photodesorb pure CO_2 ice, and photodissociate CO_2 into CO and thus transform the pure CO_2 ice into a $\text{CO}_2:\text{CO}$ mixture (Watanabe & Kouchi 2002; Loeffler et al. 2005;

Öberg et al. 2009b; Gerakines et al. 1996). Of these processes, CO₂ formation through photochemistry should not affect the amount of pure CO₂ ice, since CO₂ then forms mixed with H₂O and CO ices. UV-induced destruction of some of the produced CO₂ ice may be important, however. Assessing its impact for a certain object requires an individual protostellar envelope model that includes UV-induced ice processes. Without such a model, pure CO₂ ice observations still provides a lower limit to the amount of heat experienced by the ices in a protostellar envelope.

5.6 Conclusions

Quantifying ice dynamics is possible through a combination of a relatively large set of laboratory experiments, spanning the available parameter space, rate-equation modeling and Monte Carlo simulations. This process is more time consuming than the qualitative studies we have been building on, but has the critical advantage of providing actual rates, which can be incorporated into astrochemical models. These rates can then be used to test hypotheses about ice dynamics in space. Quantified ice processes can also be used as quantitative probes, and thus provide powerful tools to investigate processes during star formation. The conclusion for the specific dynamical processes investigated in this study are:

1. Thin (8–37 ML) H₂O:CO₂ and H₂O:CO ice mixtures segregate through surface processes followed by an order of magnitude slower bulk diffusion.
2. The thin ice segregation process is qualitatively reproduced by Monte Carlo simulations where ices segregate through a combination of molecule hopping and swapping. Segregation is expected to be a general feature of ice mixtures where binding energies of all the mixture constituents are higher on average in the segregated ices compared to in the ice mixtures.
3. The surface segregation barrier is 1080 ± 190 K for the H₂O:CO₂ ice mixtures and 300 ± 100 K for H₂O:CO segregation.
4. H₂O:CO₂ surface segregation is ice-mixture ratio dependent, quantified as $k_{\text{seg}} = 2 \times 10^{(5 \pm 1)} \times e^{-1080 \pm 190/T} \times \left(\frac{x}{0.33}\right)^{2.5 \pm 1}$, where k_{seg} is the rate at which the top few monolayers segregate, T the ice temperature and x the CO₂ concentration in the ice with respect to the total ice amount.
5. Segregation in thick (> 100 ML) ices involves the bulk of the ice, which can be explained by ice cracking or H₂O phase transitions or both. Ice dynamics thus depends on the thickness of the investigated ice.
6. During low-mass star formation the surface segregation temperature of a typical thin H₂O:CO₂ 5:1 ice mixture is reduced to ~ 30 K, because of the longer time scales.

6 ENTRAPMENT AND DESORPTION OF VOLATILE SPECIES DURING WARM-UP OF ICE MIXTURES

Ice desorption determines the evolution of the gas-phase chemistry around protostars, and also the composition of comets forming in circumstellar disks. From observations, most CO₂ ice and some CO ice are present in H₂O-dominated ices. This is crucial, since volatile species are easily trapped in H₂O ice and thus desorb with H₂O. Yet, astrochemical models generally treat ice desorption as originating from pure ices. A few studies instead define different ‘flavors’ of CO with different desorption energies, but this approach is limited by lack of information on what fractions of volatile ice are trapped under different conditions. The aim of this study is two-fold: first to experimentally investigate how CO and CO₂ trapping in H₂O ice depends on ice thickness, mixture ratio and heating rate, and second to introduce a modified three-phase (gas, ice surface and mantle) model to treat ice mixture desorption with a minimum number of free parameters. In the experiments the fraction of trapped volatile species increases with ice thickness, H₂O:CO₂/CO mixing ratio and heating rate, resulting 5–17% trapped CO₂ and 2–5% trapped CO with respect to H₂O ice. This is reproduced quantitatively for binary ice mixtures by the modified three-phase model with a single diffusion parameter each for CO, CO₂ and H₂O; these parameters govern the relative diffusion rates between the mantle and the surface for the ice mixture molecules. The model furthermore reproduces the experimental results on dilute tertiary mixtures, but CO₂-rich tertiary ice mixture seems to require a more sophisticated parameterization of diffusion between the surface and mantle layers than currently incorporated. The three-phase model is also used to investigate trapping for astrophysically relevant ice mixtures and time-scales, resulting in ~14% trapped CO₂ ice and 1% trapped CO ice for a 100 ML thick H₂O:CO₂:CO 10:2:1 ice mixture, which is significantly less than previously assumed in CO ‘ice-flavor’ models.

Fayolle, E. C., Öberg, K. I., Cuppen, H., Visser, R. and Linnartz, H., in preparation.

6.1 Introduction

Ice-covered interstellar grains constitute a major reservoir of molecules during star formation; in the dense and cold phases of star and planet formation more than 90% of molecules, excluding H_2 , are found in icy grain-mantles (e.g. Bergin et al. 2002). These ices form through direct freeze-out of gas phase atoms and molecules and through their subsequent hydrogenation and oxygenation (Tielens & Hagen 1982, Chapter 2). The most abundant ice molecules are H_2O , CO and CO_2 with typical abundances of $2 \times 10^{-5} - 10^{-4}$ with respect to molecular hydrogen (Gibb et al. 2004; Boogert et al. 2008; Pontoppidan et al. 2008). From their presence in molecular clouds and models, these common ices mainly form in the cold pre-stellar phase (Knez et al. 2005, Chapter 2). Observationally most CO_2 ice is mixed with H_2O ice. Most CO ice is frozen out on top of this H_2O -rich mixture, but a fraction of the CO ice resides in the $\text{H}_2\text{O}:\text{CO}_2$ ice mixture (Tielens et al. 1991; Pontoppidan et al. 2003, 2008, Chapter 2).

Once the pre-stellar core starts to collapse, it heats up the icy grains and the ices start to evaporate. The nature of this desorption process, i.e. which molecules evaporate at which temperatures, dominates the evolution of the gas phase chemistry around the protostar and later in the circumstellar disks (Aikawa et al. 2008; Visser et al. 2009). Understanding ice mixture desorption and implementing the main features of this desorption process in astrochemical networks is therefore crucial when modeling the chemical evolution in protostellar envelopes and in protostellar disks.

Pure ice desorption energies have been determined experimentally for most simple ices, though some values are still contested (e.g. Sandford & Allamandola 1988; Fraser et al. 2001; Collings et al. 2004; Öberg et al. 2005; Brown & Bolina 2007). Laboratory studies on desorption of mixed ices consistently show that the desorption temperatures of mixed ices are different compared to such pure ice desorption (Bar-Nun et al. 1985; Sandford & Allamandola 1988; Collings et al. 2003, 2004). The differences are due to different binding energies between the mixture components compared to molecules of the same kind, e.g. for $\text{H}_2\text{O}:\text{CO}$ and $\text{CO}:\text{CO}$ the inferred binding energies are ~ 1200 and 830 K, respectively Collings et al. (2003), and to trapping of volatile species in the hydrogen-bonding ices H_2O and CH_3OH . In most H_2O -rich ice mixtures, volatile mixture components desorb at a minimum of two different temperatures corresponding to desorption from a H_2O surface and from molecules trapped inside the H_2O ice, which only desorb at the onset of H_2O desorption. Additional desorption is sometimes observed at the temperature for pure volatile ice desorption and during ice re-structuring, e.g. at the H_2O phase change from amorphous to crystalline. This H_2O -restructuring is important in ice mixtures dominated by H_2O and occurs at ~ 140 K in the laboratory (at astrophysical timescales the re-structuring temperature decreases), close to the onset of H_2O -desorption (Collings et al. 2004).

Of the three mixture desorption processes, entrapment of volatile species in H_2O ice is astrochemically most important to quantify. Trapping of CO results in a factor of five increase in the effective desorption temperature. In a recent cloud core collapse model, this would correspond to some CO desorbing 30 AU from the protostar compared to pure CO desorption at 3000 AU. The case is less dramatic, but still significant, for CO_2 , which

desorbs at ~ 300 AU when pure and again would desorb at 30 AU if trapped in H_2O ice (Aikawa et al. 2008).

Significant entrapment of volatile species in H_2O ice have been noted in all ice mixture desorption studies above. In addition, Sandford & Allamandola (1990) found that CO and CO_2 are trapped in different manners in H_2O ice and that the desorption behavior depends on whether a dilute mixture is used or a mixture rich in volatile species. Building on this Collings et al. (2004) showed that the fraction of a volatile ice that is trapped in H_2O is generally species specific. From experiments on $\text{H}_2\text{O}:\text{X}$ 20:1 ice mixtures, 16 astrophysically relevant ice species could be divided into three categories dependent on qualitative differences in the desorption behavior: H_2O -like species (NH_3 , CH_3OH and HCOOH) that are completely trapped in the H_2O matrix, CO-like species (N_2 , O_2 , CO and CH_4) that show some trapping, but all molecules are released during re-structuring, and intermediate species (H_2S , OCS, CO_2 , C_2H_2 , SO_2 , CS_2 and CH_3CN) that display intermediate behavior.

It is not obvious how this information should be incorporated into astrochemical gas-grain models. There are a few studies, which, using an array of rate equations, can account for all the observed evaporation characteristics of specific, binary ice mixtures (Collings et al. 2003; Bisschop et al. 2006). The molecular specificity of these models, together with a large number of fitting parameters has, however, prevented their incorporation into larger astrochemical models.

Instead, ice desorption is still mostly included into astrochemical models of protostars and disks using the pure ice desorption data, disregarding the possibility of trapping of the volatile molecules in the H_2O matrix (e.g. Aikawa et al. 2008). A few studies on gas-grain interactions during star formation have instead considered a few different flavors of each volatile ice, e.g. the CO ice abundance is split up into one part that evaporates at the pure CO temperature and one part that evaporates at the H_2O evaporation temperature (Viti et al. 2004; Visser et al. 2009). This has provided information on how important ice trapping may be for the chemical evolution during star formation. The approach also allows for the use of qualitative laboratory results, since different flavor fractions can be assigned to different species based on the classification in Collings et al. (2004). The uncertainties induced by this approach are, however, difficult to ascertain without knowledge of how the amounts of trapped ice depend on different ice variables. The first aim of this study is to provide such information.

Another problem with current gas-grain codes is that evaporation is often incorporated as a first order process, while it is a zeroth order process with respect to the total ice abundance for ices thicker than one monolayer. A three-phase gas-grain model, where the ice mantle and ice surface are treated as two different phases, solves this problem (Fig. 6.1). In a three-phase model desorption is only possible from the surface layer and it is a first order process with respect to surface abundances. The surface is replenished by molecules from the mantle and therefore the desorption kinetics are automatically treated correctly. Such a model also results in ice trapping, since the mantle is protected from desorption. The three-phase model was introduced by Hasegawa & Herbst (1993), but has not been used generally nor has it been further developed, despite its advantages in treating different ice processes. One urgent development is how to couple the surface and

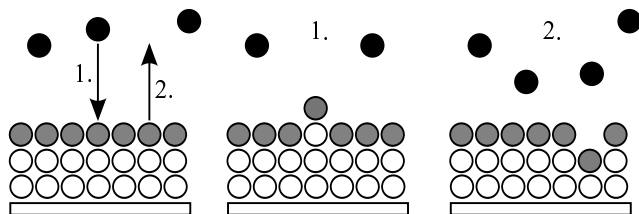


Figure 6.1 – A cartoon of desorption and accretion in a three-phase model consisting of mantle molecules (white), surface molecules (grey) and gas molecules (black). Accretion from the gas phase (1.) onto the surface results in the conversion of a surface molecule into a mantle molecule, and similarly desorption (2.) results in the conversion of a mantle molecule into a surface molecule.

the mantle correctly; the original model cannot, for example, account for the experimentally observed different trapping behavior of different molecules because diffusion rates are defined to be species independent.

In this chapter, we suggest that employing a modified form of the three-phase model by Hasegawa & Herbst (1993) allows for a quantitative treatment of evaporation of mixed ices. The model is tested against new data on evaporation from $\text{H}_2\text{O}:\text{CO}$, $\text{H}_2\text{O}:\text{CO}_2$ and $\text{H}_2\text{O}:\text{CO}_2:\text{CO}$ ices, which shows that the three-phase model can reproduce evaporation quantitatively from binary mixtures and some tertiary ice mixtures in a laboratory setting, while some further improvements are required to reproduce all tertiary results. The laboratory results are also discussed separately with respect to the effects of ice thickness, mixing ratio and heating rate on the amount of trapped ice. This is important information even if another model scheme is preferred to the three-phase model, such as working with different ice flavors. We finally discuss the differences between pure ice evaporation, flavored ice evaporation and the three-phase model of ice evaporation when the heating-rate is slowed down to 1 K per 100 years, appropriate for low-mass protostars.

6.2 A modified three-phase desorption model

Hasegawa & Herbst (1993) first introduced a three-phase (gas, ice surface and ice mantle) model to address grain-gas interactions and especially ice chemistry. In the context of desorption, the mantle acts as a reservoir of molecules, which replenishes the surface layer during desorption. In the Hasegawa & Herbst (1993) model, this replenishment is statistical, dependent only on the relative concentrations of the different species in the mantle; for a binary mixture A:B, the diffusion rate for a molecule A to reach the surface depends only on the ratio of the mixture in the mantle phase and the total desorption rate. This results in some desorption for volatile molecules around the pure ice desorption temperature, but also in their trapping, since the surface becomes more and more enriched in the least volatile species as more volatile molecules desorb.

When testing the original three-phase model, it results in too much trapped CO and

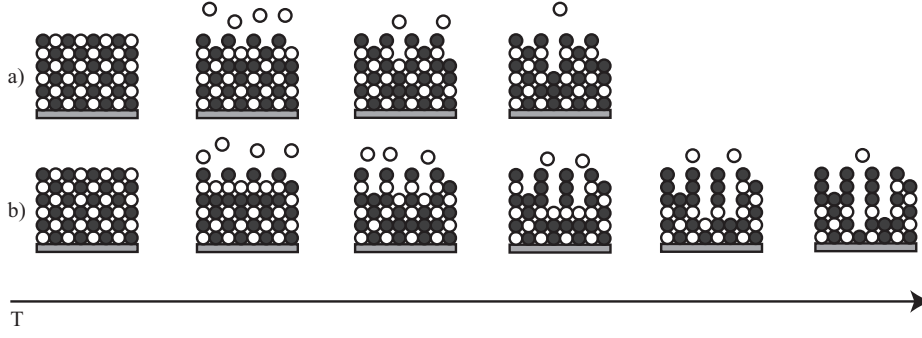


Figure 6.2 – A cartoon of desorption within the three-phase model framework from a binary mixture with a volatile component (white) and a non-volatile component (black), which does not desorb at the displayed temperature range. Only surface molecules can desorb. In the traditional model set-up (a) the surface is replenished based on the mantle composition alone, resulting in a large amount of trapped molecules. In our model the mantle-to-surface diffusion is modified such that more volatile species reach the surface faster, reducing the amount of trapped volatile species to fit experimental values.

CO₂ compared to the present experiments. To address this and to include the observed molecular-specific ice trapping into a three-phase model, the ice-mixture dependent rates for mantle molecules to migrate into the surface phase are modified by an experimentally fitted mantle-to-surface diffusion parameter, which is related to the relative diffusion barriers of the mixture constituents. Figure 6.2 shows the principal difference between desorption in the traditional three-phase model and a three-phase model, where the diffusion rate of the more volatile species is doubled compared to the less volatile species. This is incorporated into the models through a term P_i for each species i . The equations describing the changes in surface, mantle and gas abundances during desorption for each species i are then

$$\frac{dn_i^s}{dt} = -R_i^{\text{evap}} + \alpha \sum R_i^{\text{evap}} \times \frac{n_i^m}{n^m} P_i, \quad (6.1)$$

$$\frac{dn_i^m}{dt} = -\alpha \sum R_i^{\text{evap}} \times \frac{n_i^m}{n^m} P_i, \quad (6.2)$$

$$\frac{dn_i^g}{dt} = R_i^{\text{evap}}, \text{ and} \quad (6.3)$$

$$R_i^{\text{evap}} = n_i^s \times c_i \times e^{-E_i^{\text{evap}}/T} \quad (6.4)$$

where n_i^s , n_i^m , and n_i^g are the abundances of species i in the surface, mantle and gas phase respectively. R_i^{evap} is the evaporation rate for species i which depends on a pre-exponential factor c_i , the evaporation energy barrier E_i^{evap} and the temperature T in Kelvin.

α is the ice coverage, which is 1 as long as there is more than one monolayer of ice in the mantle layer, and n^m is the total amount of molecules in the mantle. The modified diffusion rate is modeled as

$$P_i = b_i \times e^{-E_i^{m-s}/T}, \quad (6.5)$$

where b_i is a normalization factor such that $\sum_i \frac{n_i^m}{n_m} \times P_i = 1$, E_i^{m-s} is a relative barrier for replacing a desorbed surface molecule with a mantle molecule of species i , which is derived from comparing the model with TPD experiments. The modified diffusion rate is described with an exponential function, since this kind of expression reproduced the segregation rate as a function of temperature in Chapter 5.

TPD experiments are simulated by solving the rate equations for each time-step (6 seconds) while increasing the temperature linearly with time, using the same heating rates as applied in the laboratory (0.1–10 K min⁻¹). The other model inputs are the pure ice desorption energies, the diffusion energies, total ice thickness and the ice mixture ratio. The same model can also be used to check the effect of applying an astrophysically relevant heating rate.

The evaporation energies are determined by comparing simulated and laboratory TPD experiments of pure ices and are then set as constants when modeling the mixture desorption. The E_i^{m-s} factors are determined empirically by comparing the simulated TPD and experimental TPD outcomes for different binary mixtures. With the model thus constrained, its predictive power is tested by simulating the desorption patterns of other binary and tertiary mixtures using the same values and comparing the simulated and experimental results.

The aim of the model is to predict entrapment of volatile species in the H₂O matrix. In other words, we do aim to perfectly reproduce the experimental desorption curves, e.g. the double-peak around the H₂O ice desorption temperature seen in some experiments. Simulating desorption at such a level of detail does require similar models to what has been used previously to model TPD experiments (Collings et al. 2003).

6.3 TPD experiments

All evaporation experiments are carried out under ultra-high vacuum conditions ($P \sim 10^{-9}$ mbar) in the set-up CRYOPAD, which is described in detail by Fuchs et al. (2006) and Öberg et al. (2005). Pure gas samples and gas mixtures are prepared separately. The ices are grown *in situ* by exposing a cold substrate at the center of the vacuum chamber to a steady flow of gas, directed along the surface normal. Evaporation is induced by linear heating of the substrate (and ice) in temperature programmed desorption (TPD) experiments. The evaporated gas phase molecules are detected by a quadrupole mass spectrometer (QMS). The desorption onset in the TPD curves can be directly related to the desorption energy in a pure ice (e.g. Fraser et al. 2001).

The set-up is also equipped with a Fourier transform infrared (FTIR) spectrometer in reflection-absorption mode (reflection-absorption infrared spectroscopy or RAIRS). The

FTIR covers $750 - 4000 \text{ cm}^{-1}$, which includes at least one vibrational band for each of the investigated molecules, and is run with a spectral resolution of 1 cm^{-1} . RAIR spectroscopy, together with previously determined band strengths for this RAIRS set-up (Öberg et al. 2009a,b), is used to determine the ice mixture composition in each experiment and to estimate the absolute ice thickness.

Table 6.1 lists the experiments in this study. The ice constituents, abundance ratios, thickness and heating rate are varied to investigate the dependencies of ice mixture desorption on different experimental variables. Isotopologues with ^{13}C were used in some of the experiments to ensure that small contaminations in the chamber do not influence the results. The CO and CO_2 gas both have a minimum 99% purity (indugas). The H_2O sample was prepared from deionized H_2O followed by several freeze-thaw cycles.

The trapped fractions of CO_2 and CO are listed both with respect to the initial CO_2 and CO abundances and the H_2O ice abundance, since both measures are used in the literature. The fractions of trapped ice were calculated by integrating the TPD curves; the fraction of trapped CO_2/CO with respect to the initial CO_2/CO ice content is defined as the ratio of the integrated desorption curve above 100 K and the integrated desorption curve between 20 and 160 K. The trapped fraction is calculated by multiplying this number with the initial CO_2/CO abundance with respect to the initial H_2O ice. RAIR spectra were also acquired during the desorption in some of the experiments, but a lack of accurate band strengths for trapped CO and CO_2 limits their quantitative use.

The ice thicknesses in Table 6.1 have absolute uncertainties of $\sim 50\%$ and relative uncertainties of $\sim 20\%$. The heating rate is accurate within a few percent and the amount of trapped ice within $\sim 20\%$ of the reported percentage values.

6.4 Results

The results are presented in three parts, starting with the experimental results on binary ice mixtures, followed by the model results on binary ice mixtures and experiments and models of tertiary ice mixtures.

6.4.1 Experimental TPD curves of binary ice mixtures

Figure 6.3 shows the desorption curves of CO_2 and CO from H_2O dominated ice mixtures together with pure CO and CO_2 TPD curves. As reported in previous studies on H_2O -rich mixtures, the volatile species desorb both around the desorption temperature of the pure ice and around the H_2O desorption temperature. CO and CO_2 mixture desorption differ, however, in the onset of the first mixture desorption peak compared to the onset of pure ice desorption; the CO_2 peak is slightly shifted towards lower temperatures compared to the pure ice, while the CO desorption from the H_2O mixture is shifted to a $\sim 5 \text{ K}$ higher temperature. This can be understood if CO_2 forms weaker bonds in a H_2O ice compared to a CO_2 ice, while CO forms stronger bonds with H_2O than to itself, confirming the assumptions made when simulating ice segregation in Chapter 5.

Table 6.1 – The TPD experiments.

Composition	Ratio	Thick. (ML)	Heating rate (K min ⁻¹)	Trapped CO/CO ₂ ice	
				% CO ₂ /CO ice	% H ₂ O ice
H ₂ O	-	24	1		
¹³ CO ₂	-	6	1		
¹³ CO	-	6	1		
H ₂ O:CO ₂	10:1	11	1	65	7
H ₂ O:CO ₂	10:1	18	1	77	8
H ₂ O:CO ₂	10:1	36	1	85	9
H ₂ O: ¹³ CO ₂	4:1	~11	10	46	12
H ₂ O: ¹³ CO ₂	4:1	~11	1	40	10
H ₂ O: ¹³ CO ₂	4:1	~11	0.1	37	9
H ₂ O: ¹³ CO ₂	4:1	~28	10	68	17
H ₂ O: ¹³ CO ₂	4:1	~28	1	64	16
H ₂ O: ¹³ CO ₂	4:1	~28	0.1	60	15
H ₂ O: ¹³ CO	5:1	19	1	24	5
H ₂ O: ¹³ CO	2:1	16	1	<13	<7
H ₂ O: ¹³ CO	2:1	6	1	<12	<6
H ₂ O:CO ₂ :CO	~11:4:1	16	1	32/17	12/2
H ₂ O:CO ₂ :CO	~20:1:1	30	1	92/96	5/5

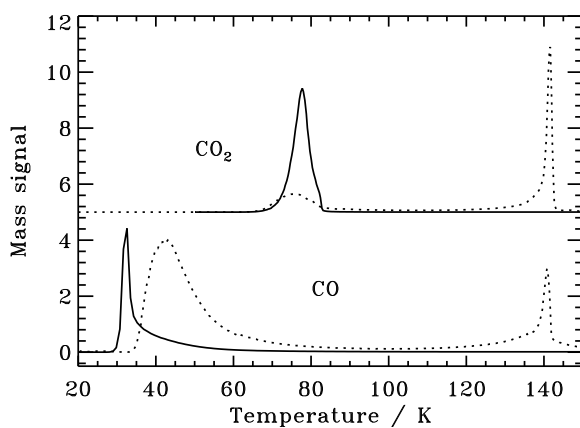


Figure 6.3 – Desorption of CO and CO₂ from pure ices (solid lines) and H₂O:CO 5:1 and H₂O:CO₂ 4:1 ice mixtures (dotted lines). The TPD curves have been normalized with arbitrary factors for visibility.

Similarly to Fig. 6.3, the TPD curves of all investigated ice mixtures contain two desorption peaks, though the fractions of trapped CO₂/CO in the H₂O ice vary significantly between the different experiments, dependent on ice composition, ice mixing ratio, ice

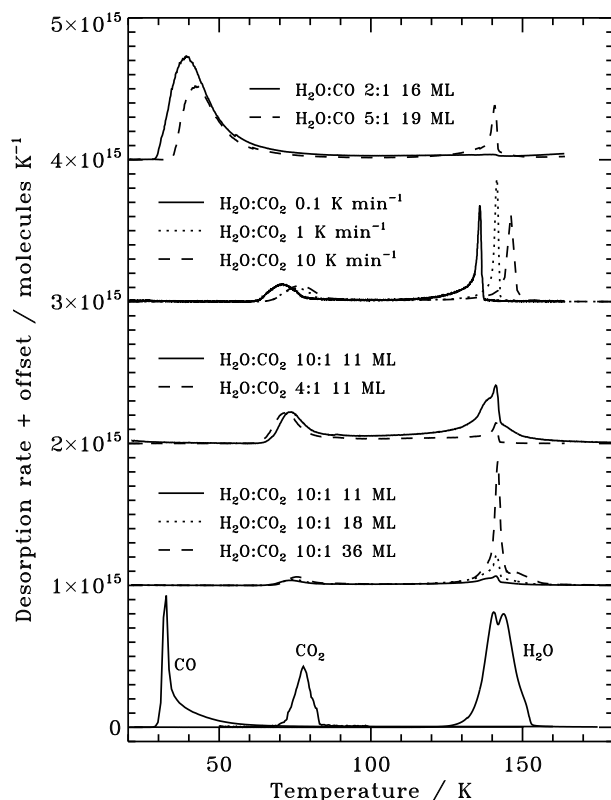


Figure 6.4 – Experimental CO and CO₂ TPD curves during warm-up of ice mixtures (offset for visibility), together with pure CO, CO₂ and H₂O ice TPD curves (bottom curves). The heating rate is 1 K min⁻¹, except for where noted otherwise. The TPD curves are scaled to correspond to the spectroscopically measured ice abundances when integrating the desorption curves.

thickness and heating rate during the TPD experiments.

These dependencies are displayed in Figure 6.4, which shows the experimental CO and CO₂ TPD curves from most of the binary ice mixture experiments listed in Table 6.1 together with the pure ice desorption curves (bottom curves). The heating rate is 1 K min⁻¹, except for where noted otherwise. Comparing the TPD curves of CO₂ desorption from the 11 ML thick H₂O:CO₂ 4:1 ice mixture and of CO desorption from the 19 ML thick H₂O:CO 5:1 ice mixture, shows that CO₂ is easier trapped of the two, in agreement with previous studies.

Starting at the top of the figure, a larger fraction of CO ice with respect to the initial CO abundance is retained in the H₂O ice in the more dilute ice mixtures. This is true for CO₂ as well. The next set of curves show that increasing the heating rate increases the amount of trapped CO₂ and shifts the desorption curves to higher temperatures – the

standard heating rate is 1 K min^{-1} . Quantitatively the fraction of trapped CO_2 increases from 60 to 68% of the total CO_2 abundances or 15–17% of the H_2O abundance when the heating rate is raised from 0.1 to 10 K min^{-1} . This is barely significant, but the trend seems to be real. The middle curves demonstrate the previously noted dependence on mixture ratio by plotting the TPD curves for CO_2 desorption from $\text{H}_2\text{O}:\text{CO}_2$ 10:1 and 4:1, 11 ML thick ice mixtures. The amount of trapped volatiles also depends on the ice thickness. The next to last set of curves shows how the amount of trapped CO_2 increases for the $\text{H}_2\text{O}:\text{CO}_2$ 10:1 ice mixtures between 11 and 36 ML (Fig. 6.4).

The trapped ice fractions for all experiments are reported in Table 6.1, where the amount of trapped volatile ice is defined both with respect to the initial volatile ice content and the initial H_2O abundance. The trapped fractions of CO_2 vary between 37 and 85% with respect to the initial CO_2 ice and between 5 and 17% with respect to H_2O . The trapped CO amounts between <12% and 24% with respect to CO, and 2% and 5% with respect to H_2O .

6.4.2 Simulations of binary ice mixtures

Figure 6.5 shows the simulated CO and CO_2 TPD curves for the ice mixtures investigated experimentally in Fig. 6.4. The desorption energies are derived from the experimental and simulated pure ice TPD curves (bottom curves) to be $E_{\text{H}_2\text{O}}^{\text{des}} = 4850 \text{ K}$, $E_{\text{CO}_2}^{\text{des}} = 2475 \text{ K}$ and $E_{\text{CO}}^{\text{des}} = 1050 \text{ K}$, assuming a pre-exponential factor of 10^{12} s^{-1} , which are in reasonable agreement with typical literature values within the $\sim 20\%$ uncertainties, though a higher binding energy has been reported for H_2O (Fraser et al. 2001). To keep the model simple, these binding energies are used to model ice mixture desorption as well, since the differences in binding energies for CO and CO_2 in H_2O ice mixtures do not affect the amount of trapped ice in the model.

Regardless of the choice of relative diffusion rates, the three-phase model reproduces the experimental trends with respect to mixture ratio, heating rate and ice thickness, shown here for a specific set of diffusion parameters (Fig. 6.5). This is intuitive when referring back to Fig. 6.2, which shows first that all ice is trapped below a certain ice depth and thus the trapped fraction will increase with ice thickness. Second, reducing the concentration of the volatile component will result in a faster cover of the surface by H_2O and third, when the heating rate is increased, the H_2O desorption temperature will be reached before all volatile species that could potentially reach the surface layer do so.

The shapes of the simulated curves deviate from the experimental curves for a couple of reasons. First, the model does not take into account that the pumping rate of desorbed species is limited in the experiment, which partly explains the tail during CO desorption. The model does also not account for multiple desorption sites with different binding energies or the desorption due to H_2O re-structuring around 140 K.

Similarly to the experiments, the simulated ice trapping during binary mixture desorption are quantified through the fractions of the volatile ice species that desorb below and above 100 K. The trapped CO and CO_2 fractions in the experiments and models agree quantitatively for a chosen set of binary ices when the relative ‘diffusion barriers’ are set to be $E_{\text{H}_2\text{O}}^{\text{m-s}} = 970 \text{ K}$, $E_{\text{CO}_2}^{\text{m-s}} = 665 \text{ K}$ and $E_{\text{CO}}^{\text{m-s}} = 617 \text{ K}$. These $E^{\text{m-s}}$ values are derived

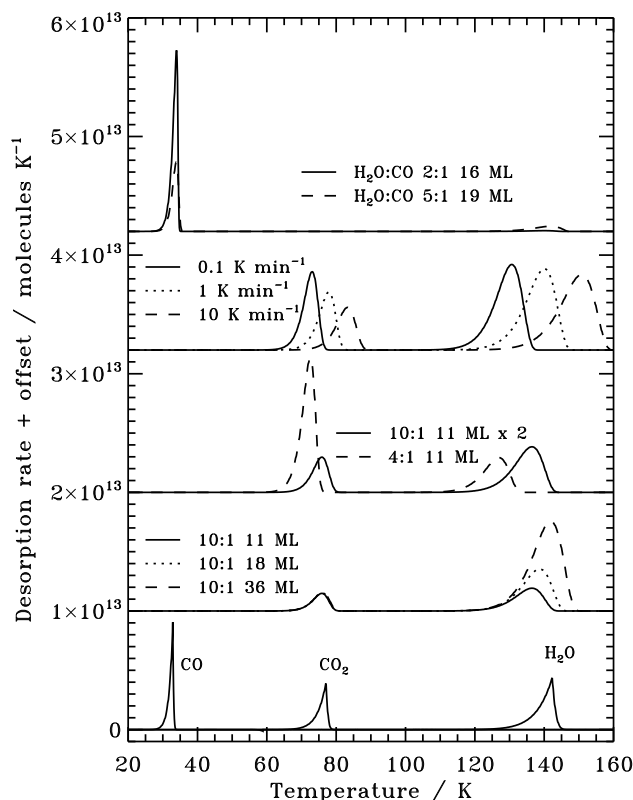


Figure 6.5 – Simulated CO and CO₂ TPD curves from pure ices, from H₂O:CO₂ 10:1 ice mixture of different thicknesses, from 11 ML H₂O:CO₂ 10:1 and 4:1 ice mixtures, from 28 ML H₂O:CO₂ 4:1 mixtures heated at different rates and from H₂O:CO ice mixtures.

from a subset of experiments and then used to model all TPD curves in Fig. 6.5. The CO₂ diffusion barrier is derived from comparing experiments and simulations of the three 10:1 ice experiments and the CO value is derived from the 5:1 experiment, while the H₂O value was arbitrarily chosen ahead of the fitting procedure; other sets of diffusion parameters may reproduce the experiments as well, since it is only the relative diffusion rates of H₂O and CO or CO₂ that determines the desorption behavior in the binary ices.

Figure 6.6 shows the fraction of the volatile ice trapped in the H₂O ice for experiments versus simulations using the derived relative diffusion barriers. The uncertainties include the measurement of the ice fractions and the choice of ice thickness and mixing ratio in the simulations when aiming to mimic the experiments. Within the uncertainties the simulations reproduce all binary ice mixture results quantitatively.

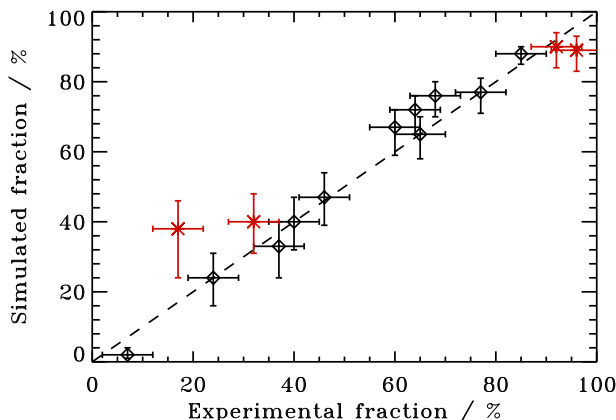


Figure 6.6 – The experimental and simulated CO and CO₂ ice fractions trapped in the H₂O ice during ice mixture desorption for all the investigated ice compositions, mixture ratios, thicknesses and heating rates. The dashed line indicates the position of a one-to-one correlation. The crosses indicate tertiary ice experiments.

6.4.3 Tertiary ice mixtures

Figure 6.7 shows the experimental and simulated TPD curves of two tertiary H₂O:CO₂:CO ice mixtures with different mixture compositions, one CO₂-rich mixture and one dilute mixture. The simulations are run with the parameters from the binary mixtures without any further attempt to optimize the fit.

Qualitatively the 20:1:1 mixture seems well reproduced by the simulation (top sets of TPD curves), while the simulation of the 11:4:1 mixture releases too little CO at the pure CO temperature and too much together with CO₂ (bottom sets of TPD curves). The fraction of CO trapped in H₂O is also predicted to be too large in the CO₂-rich experiment, 38% with respect to the initial CO content compared to the experimentally observed 17%.

The experimental and simulated amounts of CO and CO₂ trapped in the H₂O ice are overplotted in Fig. 6.6. Quantitatively the model predicts the correct amounts of trapped CO and CO₂ in the dilute mixture and of trapped CO₂ ice in the CO₂-rich tertiary mixture.

6.5 Discussion

6.5.1 Desorption from ice mixtures

Qualitatively the experimental results agree with those published by Collings et al. (2004) in the sense that CO₂ is more efficiently trapped than CO. Viti et al. (2004) quantified the trapped amounts of CO and CO₂ in the experiments by Collings et al. (2004) to model ice desorption around a protostar. They find that 30% CO and 90% CO₂ is trapped in H₂O ice with respect to the original CO and CO₂ abundance, which are both high compared to

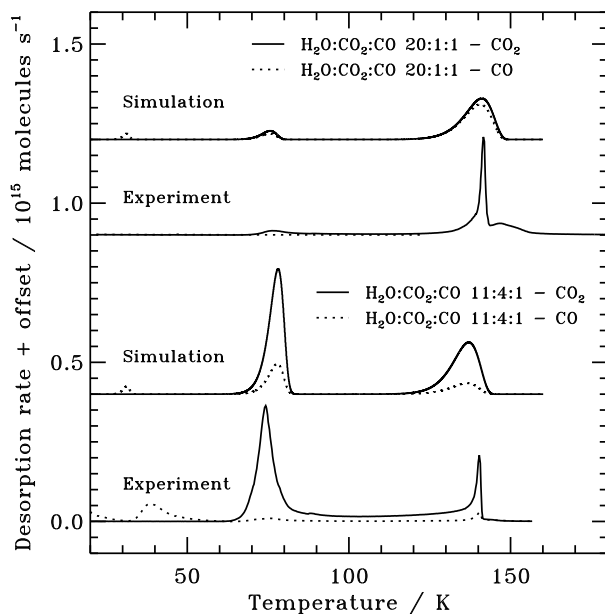


Figure 6.7 – Simulated and experimental CO and CO₂ TPD curves from tertiary H₂O:CO₂:CO ice mixtures. The heating rate is 1 K min⁻¹ and the ice thicknesses 16 ML for the 11:4:1 ice mixture and 30 ML for the 20:1:1 ice mixture.

most of the present experiments. The differences can be understood from the very dilute mixtures used by Collings et al. (2004), 20:1, when investigating ice desorption.

This difference between the previous and present experimental results together with the experimental TPD curves show that the fraction of trapped ice (whether measured with respect to volatile ice content or H₂O ice abundance) varies dependent on ice thickness, mixing ratio and heating-rate, which will vary in astrophysical environments as well. In other words, there is no constant fraction of CO or CO₂ ice that is trapped in a H₂O-dominated ice. In addition, the decreasing amount of CO₂ trapped in the H₂O ice as the heating rate is slowed down suggests that the trapping of volatile species is due to very slow diffusion of volatile species within a H₂O matrix rather than an actual entrapment that molecules cannot escape from. The opposite conclusion could be drawn by Sandford & Allamandola (1988) based on high-vacuum experiments with thick ices. This confirms the different dynamics of thin and thick ices found for ice segregation in Chapter 5.

In the tertiary mixtures, CO₂ desorption is not significantly affected by the presence of CO and the amount of trapped CO₂ is consistent with a H₂O:CO₂ mixture with the same mixture ratio and ice thickness. CO is affected by the presence of large amounts of CO₂. Less CO is trapped in the mixture with ~36% CO₂ with respect to H₂O ice than in an equivalent binary H₂O:CO mixture, indicative of a lower diffusion barrier for CO

in the CO₂-rich H₂O-mixtures compared to diffusion in H₂O:CO ices. This may be the result of CO₂ disrupting the hydrogen-bonding network (Sandford & Allamandola 1990, Chapter 4).

6.5.2 The three-phase desorption model

The modified three-phase model was set up to quantify the amounts of CO and CO₂ ices that desorb at the H₂O desorption temperature during ice mixture desorption with a minimum number of equations and fitting parameters.

The model reproduces the fraction of trapped ices observed in the binary TPD experiments for all different ice thicknesses, mixing ratios, heating rates and compositions with only one free parameter per species in addition to the pure desorption energies. To parameterize binary ice desorption from H₂:CO and H₂O:CO₂ ices thus only requires fitting one of the experiments to the model, though an averaged value from fits with three experiments was used for the H₂O:CO₂ ice mixtures. The other experimental results were then accurately predicted, within the experimental uncertainties, with the same parameters, except for CO desorbing from a CO₂-rich tertiary H₂O-ice mixture. Overall the simple parameterization of diffusion between the mantle and the surface used in this version of the three-phase model is thus sufficient.

The fact that the current model reproduces desorption from binary ice mixtures suggests that diffusion between the top ice layer and the layer right beneath it is efficient, while bulk diffusion is slow – consistent with the segregation experiments and simulations in Chapter 5. In other words, if a H₂O molecule reaches the surface because a CO₂/CO molecule desorbs from right on top of it, there is a high probability that it will swap places with an underlying CO₂/CO molecule. This process is what the modified three-phase model approximates by increasing the diffusion rate of volatile molecules to the surface and decreasing it for H₂O, compared to the original diffusion rates based on the mantle composition alone (Hasegawa & Herbst 1993). The decrease in water diffusion must equal the increase in diffusion of CO₂/CO, since the model in its current state does not allow for back-diffusion between the surface and the mantle.

Monte Carlo simulation including diffusion and desorption should however be used to demonstrate that this simple scheme of fast surface swapping and slow bulk swapping during warm-up of ices is sufficient to explain the experimental results and the successes of the modified three-phase model in reproducing them.

6.5.3 Astrophysical implications

Trapping of volatile ices in H₂O ice is a crucial parameter when predicting the chemical evolution during star and planet-formation. Understanding the uncertainties in model predictions of ice trapping is therefore important in e.g. ice-flavor models, but has so far not been evaluated. The modified three-phase desorption model is used here to test the effects of different initial ice compositions and ice thicknesses on ice mixture desorption. This can be used to design ice flavor models. Ultimately the three-phase model should, how-

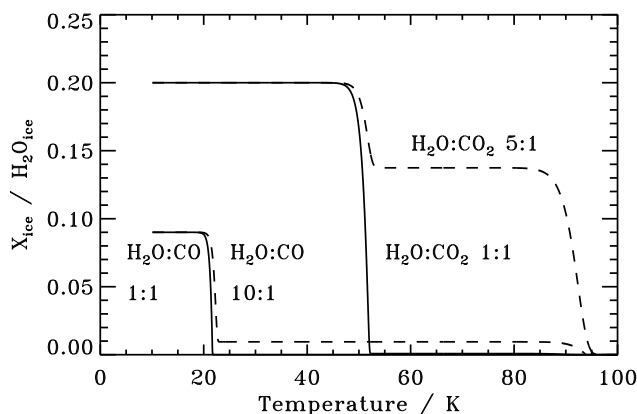


Figure 6.8 – The amount of CO and CO₂ ice during ice warm-up with 1 K per 100 years according to the three-phase model, assuming two different initial ice mixtures with H₂O.

ever, be integrated with a protostellar collapse model to model ice desorption efficiently and accurately during star formation.

Figure 6.8 shows the amount of CO and CO₂ ice with respect to the original H₂O ice abundance as a function of temperature, assuming two different initial binary ice compositions, a total H₂O ice thickness of 100 ML and a heating rate of 1 K per 100 years. The different initial conditions are based on ice observations towards protostars (Chapter 2). The CO₂ observations show that H₂O:CO₂ generally co-exist and have an abundance ratio of 5 to 1. In contrast most CO ice is in a pure layer on top of the H₂O-ice mixture, but some CO mixed in with the H₂O ice at a ~1 to 10 ratio.

The initial H₂O:CO₂ ice composition is first set to H₂O:CO₂ 5:1, which assumes that all H₂O and CO₂ form together. A H₂O:CO₂ 1:1 36 ML thick ice is also investigated, since from infrared spectroscopy of protostellar ices, we do not know whether all H₂O and CO₂ are mixed together or whether H₂O forms partly as a pure ice and then a H₂O:CO₂ mixture forms on top, corresponding to an ice composition of H₂O:CO₂/H₂O 1:1/4 (Chapter 4). Similarly, the initial H₂O:CO ice conditions are set to H₂O:CO 10:1 100 ML and H₂O:CO 1:1 18 ML. In all four cases the CO₂ and CO ice fractions are reported with respect to the total amount of H₂O ice, i.e. 100 ML. Thus the initial CO₂ and CO fractions are always 20 and 10% with respect to H₂O, respectively.

Starting with these compositions, Fig. 6.8 shows that almost no volatile ice is trapped in the 1:1 ice mixtures – the results of these compositions are not significantly different from assuming pure ice desorption. The H₂O:CO₂ 5:1 ice models result in that most of the CO₂ ice is trapped; at the onset of H₂O desorption the ice mixture contains ~14% of CO₂ ice with respect to the initial H₂O ice abundance. A smaller amount of CO is trapped in the 10:1 ice, ~1% with respect to the H₂O ice abundance. This is an order of magnitude lower than the values used in Visser et al. (2009) and Viti et al. (2004) and shows the importance

of modeling experimental results rather than assuming that a specific experiment can be used to generally predict processes under astrophysical conditions.

Based on these results, it will be difficult to explain more than a few percent of CO in comets, from CO trapped in H₂O ice during the pre- or proto-stellar stages.

6.5.4 Future development – towards a four-phase model

While this version of the three-phase model already provides some advantages in treating ice mixture desorption compared to previous attempts, it does have two areas that need further development. The first one is quite obviously a more accurate treatment of desorption of CO and other very volatile species from CO₂-rich H₂O-ice mixtures, whether tertiary ices or more complex. This may be solved by having relative diffusion probabilities that are constantly redefined in the model based on the ice composition according to some simple formula.

A second approach is to allow for continuous diffusion between the surface and mantle layer. This would require a revision of the current set of rate equations, since the three-phase model is set up such that the mantle to surface diffusion rate is identical to the ice desorption/accretion rate. It should however be possible to implement. In addition this more general approach is advantageous when using the three-phase model in the future to investigate ice chemistry.

A second challenge is how to deal with the astrophysical reality of two different ice mantle phases, a H₂O-rich ice phase and a CO-rich ice phase (Chapter 2). It is worth considering whether a four-phase model is necessary to produce realistic ice models both with respect to desorption and ice chemistry. At low temperatures the complex ice chemistry may for example be very different if CH₃OH fragments can only react with CO and other CH₃OH fragments and not with NH₃ and CH₄ fragments. Such a four-phase model would however be more complicated than most kinds of three-phase models and will only be attempted after diffusion between the mantle and the surface in the three-phase model has been successfully modeled.

6.6 Conclusions

Desorption from H₂O-rich ice mixtures is complex in that the amount of trapped ice depends not only on the species involved, but also on the mixture ratio, the ice thickness and the heating rate – there is no constant fraction of volatile species trapped in a H₂O ice. This ‘complex’ behavior can, however, be reproduced by a small improvement to the three-phase model by Hasegawa & Herbst (1993). Using pure ice desorption energies and one diffusion parameter for H₂O, CO₂ and CO each, the modified three-phase model can reproduce the amount of trapped ice quantitatively in all binary ice mixtures investigated, even though the diffusion parameter was fitted using only a few H₂O:CO₂ experiments and a single H₂O:CO experiment. The same three diffusion parameters also predict trapping accurately in H₂O-dominated tertiary H₂O:CO₂:CO ice mixtures, while desorption from

a CO₂-rich tertiary mixture requires a more sophisticated parameterization of diffusion in the ice than is currently implemented.

Extrapolating the model results to astrophysical heating rates and using a plausible H₂O:CO₂:CO 10:2:1 ice composition results in ~14% CO₂ and ~1% CO, with respect to H₂O ice, trapped inside of the H₂O ice. Trapping of CO in H₂O ice may thus be an order of magnitude less efficient than previously assumed. In previous models, experimental results on a H₂O:CO 20:1 mixture were assumed to translate directly to astrophysical conditions with a more CO-rich ice; the experiments and models here show that this is not a reasonable simplification. This further strengthens the underlying theme in this thesis that experimental studies must explore the entire parameter space available before extrapolating the results to astrophysical settings.

7

PHOTODESORPTION OF CO ICE

At the high densities and low temperatures found in star forming regions, all molecules other than H_2 should stick on dust grains on timescales shorter than the cloud lifetimes. Yet these clouds are detected in the millimeter lines of gaseous CO. At these temperatures, thermal desorption is negligible and hence a non-thermal desorption mechanism is necessary to maintain molecules in the gas phase. Here, the first laboratory study of the photodesorption of pure CO ice under ultra high vacuum is presented, which gives a desorption rate of 3×10^{-3} CO molecules per UV (7–10.5 eV) photon at 15 K. This rate is factors of 10^2 - 10^5 larger than previously estimated and is comparable to estimates of other non-thermal desorption rates. The experiments constrains the mechanism to a single photon desorption process of ice surface molecules. The measured efficiency of this process shows that the role of CO photodesorption in preventing total removal of molecules in the gas has been underestimated.

Öberg K. I., Fuchs, G.W., Awad, Z., Fraser, H.J., Schlemmer, S., van Dishoeck, E. F. and Linnartz, H., 2007, *ApJL*, volume 662, pages 23-26

7.1 Introduction

In the cold and dense interstellar regions in which stars are formed, CO and other molecules collide with and stick to cold (sub)micron-sized silicate particles, resulting in icy mantles (Léger et al. 1985; Boogert & Ehrenfreund 2004). Chemical models of these regions show that all molecules except for H₂ are removed from the gas phase within $\sim 10^9/n_{\text{H}}$ years, where n_{H} is the total hydrogen number density (Willacy & Millar 1998). For a typical density of 10^4 cm^{-3} , this time scale is much shorter than the estimated age of such regions and hence molecules like CO should be completely frozen out in these clouds. Yet, these clouds are detected in the millimeter lines of gaseous CO (Bergin et al. 2001, 2002). Similarly cold CO gas has been detected in the midplanes of protoplanetary disks (Dartois et al. 2003). A recent study of several disks (Piétu et al. 2007) even finds that the bulk of the gaseous CO is at temperatures lower than 17 K, below the condensation temperature onto grains. Thus some desorption mechanism is needed to keep part of the CO and other molecules in the gas phase. Clarifying this desorption mechanism is important in understanding the physical and chemical evolution of interstellar clouds. Because the sticking probability of even volatile species like CO has been shown to be unity (Bisschop et al. 2006), it is the desorption mechanism and rate that controls the allocation of molecules between gas and solid phase. This allocation of molecules affects the gas phase and surface reactions as well as the dust properties.

The case of CO is of particular importance, as it is the most common molecule after H₂ and the prime tracer of molecular gas. It is also a key constituent in the formation of more complex and pre-biotic species (Tielens & Charnley 1997), and its partitioning between the grain and gas phase therefore has a large impact on the possible chemical pathways (van Dishoeck 2006). In dense clouds without embedded energy sources, the grain temperature is low enough, around 10 K, that thermal desorption is negligible and hence desorption must occur through photon or cosmic ray induced processes. External UV photons from the interstellar radiation field can penetrate into the outer regions of dense clouds and cosmic rays are always present, even in the most shielded regions.

Photodesorption has been proposed as an important desorption pathway of ices in protoplanetary disks and other astrophysical regions with dense clumps of material and excess UV photons (Willacy & Langer 2000; Dominik et al. 2005). The lack of experimentally determined photodesorption rates for most astrophysically relevant molecules and conditions has prevented progress in this area, however, and theoretical estimates range by orders of magnitude, with desorption rates from 10^{-5} to 10^{-8} CO molecules UV-photon⁻¹ (Draine & Salpeter 1979; Hartquist & Williams 1990). Due to this low estimated rate, CO photodesorption has generally been regarded as an insignificant process in astrophysical environments.

As the present study shows, this assumption is not correct, and the actual desorption rate is at least two orders of magnitude larger than the previous high estimate. Here, we present the results of an experimental study under astrophysically relevant conditions of the photodesorption rate of CO ice and of the mechanism involved.

7.2 Experiments

The experimental set-up has been described in detail elsewhere (Fuchs et al. 2006). In these experiments, thin ices of 2 to 350 monolayers (ML) are grown at 15 K on a gold substrate under ultra-high vacuum conditions ($P < 10^{-10}$ mbar). The ice films are subsequently irradiated at normal incidence with UV light from a broadband hydrogen microwave discharge lamp, which peaks around 125 nm and covers 120–170 nm (7–10.5 eV) (Muñoz Caro & Schutte 2003). The lamp has a UV photon flux, measured with a NIST calibrated silicon diode, of $(6 \pm 2) \times 10^{13}$ photons $\text{s}^{-1} \text{cm}^{-2}$ at the substrate surface in its standard setting. The emission resembles the spectral distribution of the UV interstellar radiation field that impinges externally on all clouds as well as that of the UV radiation produced locally inside clouds by the decay of electronic states of H_2 , excited by energetic electrons resulting from cosmic-ray induced ionization of hydrogen (Sternberg et al. 1987). The setup allows simultaneous detection of molecules in the gas phase by quadrupole mass spectrometry (QMS) and in the ice by reflection absorption infrared spectroscopy (RAIRS) using a Fourier transform infrared spectrometer.

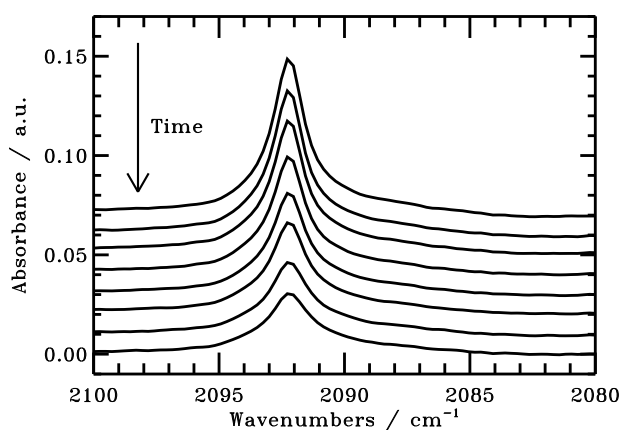


Figure 7.1 – RAIR spectra of the C^{18}O $\nu = 1 - 0$ vibrational band at 2040 cm^{-1} (2140 cm^{-1} for normal CO) acquired before irradiation of a 8 ML of C^{18}O ice and then after every hour of irradiation during 8 hours. The drop in integrated absorbance of the C^{18}O ice band is linear with UV irradiation time. In most of our experiments we used the C^{18}O isotopologue instead of C^{16}O to rule out any unwanted contributions from outgassing of the vacuum chamber. Control experiments with C^{16}O resulted in the same photodesorption rate within our experimental uncertainty.

Once an ice is grown, it remains stable until it is UV irradiated. The layer thickness of the ice is monitored by recording RAIR spectra (Fig. 7.1). The intensity of the CO RAIRS profile is linearly correlated with the layer thickness of the CO ice up to ~ 20 monolayers (ML). One monolayer is generally taken to consist of $\sim 10^{15}$ molecules cm^{-2} and the rate of the CO photodesorption is subsequently derived from the intensity loss

in the RAIR spectra as function of time (Fig. 7.2). From this loss of ice molecules and the known photon flux hitting the surface it is possible to calculate the desorption rate as the number of molecules desorbed per incident photon. Re-condensation will play a negligible role given the small surface area of the sample and the resulting underestimate of the actual photodesorption will be substantially lower than other sources of inaccuracy. Above 20 ML the photodesorption rate can no longer be calculated from the RAIRS profile as the integrated absorbance of the peak is no longer linearly dependent on the number of molecules. Instead a relative photodesorption rate can be determined by mass spectrometry of the desorbed gas phase molecules. This rate is converted to an absolute photodesorption rate by comparison with thin layer experiments where both QMS and RAIRS data are available. Simultaneous mass spectrometry of gas phase constituents shows that only CO molecules are desorbed. Furthermore the RAIRS results show that no other molecules are formed during the UV irradiation (i.e. less than 0.2% of the CO ice is converted to CO₂ after 8 hours of irradiation of 8 ML CO ice). This result is of importance as in traditional vacuum experiments with substantially thicker and less pure ices, reaction products have been identified upon UV photoprocessing (Loeffler et al. 2005) and this may affect the photodesorption efficiency.

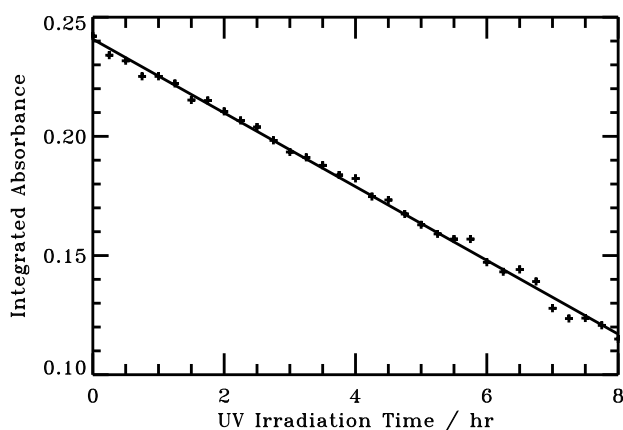


Figure 7.2 – The integrated absorbance of the CO RAIRS band acquired before irradiation of a 8 ML C¹⁸O ice and then after every 15 minutes of UV irradiation during 8 hours. The photodesorption rate is calculated from the slope of the fitted line. The fitted line gives a photodesorption rate in loss of integrated absorbance in integrated absorbance units (I.A.U.) per hour (here 0.015 I.A.U. hr⁻¹). The amount of integrated absorbance per monolayer can be derived from the integrated absorbance of 0.24 I.A.U. of 8 ML at time 0. Using the known UV flux and CO coverage, the loss of integrated absorbance per hour is converted to a photodesorption rate in CO molecules per UV (7-10.5 eV) photon: $R_{pd} = (0.015 \text{ I.A.U./hr}) \times (\text{hr}/3600 \text{ s}) \times (8 \text{ ML}/0.24 \text{ I.A.U.}) \times (10^{15} \text{ molecules cm}^{-2}/1 \text{ ML}) \times (1/6 \times 10^{13} \text{ photons s}^{-1} \text{ cm}^{-2}) = 0.003 \text{ molecules photon}^{-1}$

In these experiments the thickness of the ice, which is needed to determine the des-

orption rate, was calculated from the observed difference in desorption from multilayer coverages (constant rate) and monolayer coverages (decreasing rate). From the RAIR spectra at this turning point, the integrated absorbance of 1 ML is estimated to within 20%. The original thickness of the ice can then be calculated from the integrated absorbance of the RAIRS feature before onset of desorption. This technique is based on the assumption that the ice is quite flat, which is confirmed by the results of the experiments.

7.3 Results

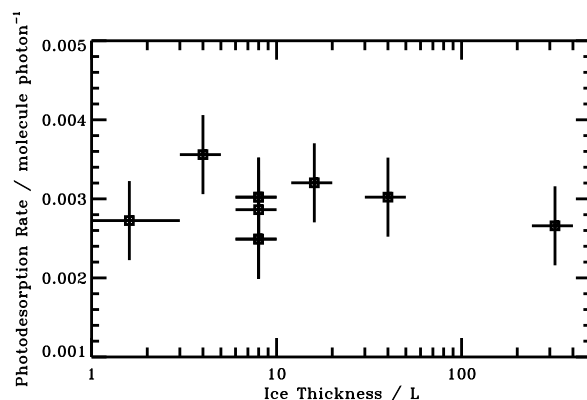


Figure 7.3 – The desorption rate of CO at different layer thicknesses. From repeated experiments around 8 ML the standard deviation in the photodesorption rate was determined, indicated by the size of the error bars. Within the experimental uncertainty derived from this spread, we conclude that the CO photodesorption rate is independent of the thickness of the CO ice.

The evaluation of the experiments results in a constant rate of $(3 \pm 1) \times 10^{-3}$ CO molecules photon⁻¹, averaged over the wavelength range of the lamp. This rate is fully reproducible from repeated experiments of 8 ML coverage and has a standard deviation of ~15% (Fig. 7.3). The uncertainty in the absolute value is somewhat larger, up to 30%, dominated by the uncertainty in the UV photon flux and coverage.

The thickness of the CO ice has been varied between 2 and 350 ML. We find that the photodesorption rate of CO is independent of the ice thickness (Fig. 7.3). This suggests that only the upper layers are involved in the photodesorption event. It is also consistent with a surface that is quite smooth, since at 2 ML the entire surface must still be covered to achieve the same photodesorption rate as for 350 ML. To confirm that the desorbed molecules only originate from the top layers we performed experiments with two layers of ices comprising different CO isotopologues. When 2 ML of C¹⁸O is deposited on top of 8 ML of C¹⁶O the desorption rate from the bottom layer drops with less than 20%. In

contrast depositing 4 ML of $C^{18}O$ on top of 8 ML of $C^{16}O$ ice reduces the $C^{16}O$ desorption rate with more than 80%. This confirms that mainly the top few layers of the CO ice are directly involved. Furthermore, the CO photodesorption rate is directly proportional to the photon flux within the flux range covered here ($(4 - 8) \times 10^{13}$ photons $s^{-1} cm^{-2}$).

In contrast to previous findings on H_2O photodesorption (Westley et al. 1995a), we find that the CO photodesorption rate is independent of the total photon dose as well as the irradiation time, as long as 1 ML is left on the surface. The mass signals show an onset of the photodesorption within the time constant of our QMS system (a few seconds) when the UV source is turned on.

In addition to the experiments on CO ices, a thin layer of N_2 ice (8 ML) was irradiated under the same conditions as the CO ices with the aim to compare the two photodesorption rates. It is found that N_2 has no detectable photodesorption in the present set-up, which puts an upper bound to the photodesorption rate of pure N_2 ice of 2×10^{-4} molecules $UV\text{-photon}^{-1}$.

7.4 Discussion

7.4.1 Photodesorption mechanism

The above experiments can be used to constrain the CO photodesorption mechanism. Its insensitivity to layer thickness (demonstrated in Fig. 7.3) indicates that only molecules from the top layers of the ice contribute to the photodesorption flux. In addition, it suggests that the CO photodesorption mechanism at these UV wavelengths does not involve the substrate. The linear dependence of the photodesorption rate on the UV intensity is not consistent with that the desorption is due to sublimation caused by heating of the ice as a whole. Together these results suggest that CO photodesorption occurs through a single photon-process, which is further supported by the immediate on-set of the desorption once the UV lamp is turned on. The opposite conclusion has previously been drawn for H_2O (Westley et al. 1995a).

The final support for a single-photon process is given by the different desorption rates for CO and N_2 ice. The two molecules have similar inter-molecular binding energies and ice structures (Fuchs et al. 2006), which suggests that any difference in photodesorption rate must involve the internal structure of the molecules. A relevant difference between the two species is that CO has an electric dipole allowed transition in the vacuum ultraviolet (7–10 eV) (Mason et al. 2006), exactly where the hydrogen lamp simulates the interstellar radiation field, while N_2 does not. This transition corresponds to the solid state equivalent of the $A^1\Pi-X^1\Sigma^+$ electronic excitation of gaseous CO and the most plausible photodesorption mechanism hence involves this transition. After UV absorption, the excited molecule relaxes via a radiationless transition into vibrationally excited states of the electronic ground state which subsequently transfer part of this intramolecular energy to the weak intermolecular bonds with neighboring CO molecules, resulting in a desorption event. This desorption event may consist of more than the originally excited molecule desorbing, but experiments with mixed CO/ N_2 ices are necessary to constrain this part of

the mechanism in more detail.

7.4.2 Astrophysical implications

The single photon mechanism of CO photodesorption means that the rate derived from these experiments can be easily applied to astrophysical environments without concerns about ice thicknesses and irradiation field strengths. It is illustrative to compare the photodesorption rate with other possible desorption routes in dark clouds. Since thermal desorption is negligible, species can only be kept in the gas phase through ice desorption induced by UV photons and cosmic rays. While cosmic rays have been proposed to directly desorb ices (Léger et al. 1985), the efficiency of heating an entire grain to the required desorption temperature rapidly drops with grain size so that usually only spot heating at an estimated rate of $70 \text{ molecules cm}^{-2} \text{ s}^{-1}$ is considered as a viable mechanism. The cosmic rays also produce UV photons so that the total photodesorption rate depends on both the external interstellar radiation field and the UV field produced inside the cloud by the cosmic rays. For a typical galactic cosmic ray flux, the resulting UV photon flux is of the order of $10^4 \text{ photons cm}^{-2} \text{ s}^{-1}$ with a factor of 3 uncertainty (Shen et al. 2004).

We calculated the desorption rate due to photodesorption in a dark cloud and compared this with the desorption due to spot-heating from Shen et al. (2004). Equations 8.2 and 8.3 describe the photodesorption rates of CO molecules from grain surfaces in $\text{molecules cm}^{-2} \text{ s}^{-1}$ due to external and cosmic ray induced UV photons, respectively, where $I_{\text{ISRF-FUV}} = 1 \times 10^8 \text{ photons cm}^{-2} \text{ s}^{-1}$ is the strength of the external irradiation field with energies 6-13.6 eV, $I_{\text{CR-FUV}}$ the strength of the UV field due to cosmic rays, γ is a measure of UV extinction relative to visual extinction, which is ~ 2 for small interstellar grains (Roberge et al. 1991), and Y_{pd} is the experimentally determined photodesorption rate.

$$R_{\text{UV-PD}} = I_{\text{ISRF-FUV}} e^{-\gamma A_V} Y_{\text{pd}} \quad (7.1)$$

$$R_{\text{CR-PD}} = I_{\text{CR-FUV}} Y_{\text{pd}} \quad (7.2)$$

Applying this model shows that photodesorption dominates at the edge of the cloud and becomes comparable (within the uncertainties of a few) to spot heating in the interior of a cloud, i.e. beyond a depth corresponding to an extinction of 3–4 A_V (Fig. 7.4). In the interior of the cloud the photodesorption rate due to cosmic rays is $\sim 30 \text{ molecules cm}^{-2} \text{ s}^{-1}$, which is equivalent to $\sim 10^{-8} \text{ molecules grain}^{-1} \text{ s}^{-1}$ for grains with a $0.1 \mu\text{m}$ radius. A rate of this magnitude may on its own explain the gas phase CO seen in dark clouds (Bergin et al. 2006). In comparison with the other plausible non-thermal desorption mechanisms, photodesorption has the advantage that the rate can now be determined experimentally and unambiguously included in astrophysical models.

One particularly interesting application of our derived photodesorption rate is to the case of CO in protoplanetary disks, where large abundances of cold CO-gas is observed. Aikawa & Nomura (2006) argue that the cold CO-gas can be explained by vertical mixing

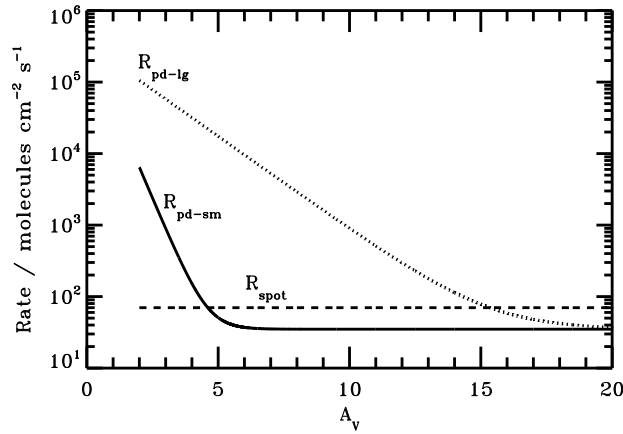


Figure 7.4 – The photodesorption rate of CO for small ($0.1 \mu\text{m}$, $R_{\text{pd-sm}}$, full line) and large (a few μm , $R_{\text{pd-lg}}$, dotted line) grains compared to desorption due to spot heating by cosmic rays (R_{spot} , dashed line). For small grains, applicable to dark clouds, the spot heating and photodesorption rates are comparable. When grains have grown to a few μm size the photodesorption dominates up to $A_V = 15$.

and Semenov et al. (2006) by a combination of radial and vertical mixing of disk material. With the high photodesorption rate of CO derived here, non-thermal desorption of CO may suffice to explain these observations. An important characteristic of disks compared to dense clouds is dust coagulation, which reduces the absorption of the external UV field since larger grains absorb less efficiently at short wavelengths. In Eq. 8.2 this corresponds to $\gamma \leq 0.6$ (van Dishoeck et al. 2006), assuming the grains have grown to at least μm size as indicated by infrared observations of the silicate feature from the surfaces layers of the inner disk (e.g. Bouwman et al. 2001) and by millimeter observations of the outer disk showing growth up to mm size (e.g. Rodmann et al. 2006). The photodesorption rate due to external photons then dominates over other non-thermal desorption rates up to $A_V = 15$, but detailed modeling is necessary to determine whether this rate is high enough to offer an alternative to the turbulence theory in explaining the observed CO gas. It is clear, however, that photodesorption can no longer be ignored in astrophysical models and may explain a large part of the gas observed in cold and dense regions.

8

PHOTODESORPTION OF CO, N₂ AND CO₂ ICES

A longstanding problem in astrochemistry is how molecules can be maintained in the gas phase in dense inter- and circumstellar regions at temperatures well below their thermal desorption values. Photodesorption is a non-thermal desorption mechanism, which may explain the small amounts of observed cold gas in cloud cores and disk mid-planes. This study aims to determine the UV photodesorption yields and to constrain the photodesorption mechanisms of three astrochemically relevant ices: CO, N₂ and CO₂. In addition, the possibility of co-desorption in mixed and layered CO:N₂ ices is explored. The experimental photodesorption studies are carried out under ultra high vacuum conditions and at astrochemically relevant temperatures (15 – 60 K) using a hydrogen discharge lamp (7–10.5 eV). The ice desorption is monitored by reflection absorption infrared spectroscopy of the ice and simultaneous mass spectrometry of the desorbed molecules. Both the UV photodesorption yield per incident photon and the photodesorption mechanism are highly molecule specific. The CO photodesorbs without dissociation from the surface layer of the ice, and N₂, which lacks a dipole allowed electronic transition in the wavelength range of the lamp, has a photodesorption yield that is more than an order of magnitude lower. This yield increases due to co-desorption when N₂ is mixed in with, or layered on top of, CO ice. CO₂ photodesorbs through dissociation and subsequent recombination from the top 10 layers of the ice. At 15 – 18 K the derived photodesorption yields are $2.7(\pm 1.3) \times 10^{-3}$ and $< 2 \times 10^{-4}$ molecules photon⁻¹ for pure CO and N₂, respectively. The CO₂ photodesorption yield is $1.2(\pm 0.7) \times 10^{-3} \times (1 - e^{-(x/2.9(\pm 1.1))}) + 1.1(\pm 0.7) \times 10^{-3} \times (1 - e^{-(x/4.6(\pm 2.2))})$ molecules photon⁻¹, where x is the ice thickness in monolayers and the two parts of the expression represent a CO₂ and a CO photodesorption pathway, respectively. At higher temperatures, the CO ice photodesorption yield decreases, while that of CO₂ increases.

Öberg K. I., van Dishoeck, E. F. and Linnartz, H., 2009, A&A, volume 496, pages 281-293

8.1 Introduction

In dark clouds molecules and atoms collide with and stick to cold submicron-sized dust particles, resulting in icy mantles (Léger et al. 1985; Boogert & Ehrenfreund 2004). The ices are subsequently processed by atom or light interactions to form more complex species (Tielens & Hagen 1982; Watanabe et al. 2003; Ioppolo et al. 2008). Observations show that H₂O, CO and CO₂ are the main ice constituents, with abundances up to 10⁻⁴ with respect to the total hydrogen density. These molecules are key constituents in the formation of more complex species (Tielens & Charnley 1997), and their partitioning between the grain and gas phase therefore strongly affects the chemical evolution in star- and planet-forming regions (van Dishoeck 2006).

Whether formed on the grains or frozen out from the gas phase, chemical models of cloud cores show that all molecules except for H₂ are removed from the gas phase within $\sim 10^9/n_{\text{H}}$ years, where n_{H} is the total hydrogen number density (Willacy & Millar 1998). For a typical cloud core density of 10⁴ cm⁻³, this time scale is much shorter than the estimated age of such regions and thus molecules like CO and CO₂ should be completely frozen out. Yet gas-phase molecules, like CO, are detected in these clouds (Bergin et al. 2001, 2002). Cold CO gas is also detected in the midplanes of protoplanetary disks (Dartois et al. 2003; Piétu et al. 2007) where the densities are higher and the freeze-out time scales are even shorter, suggesting the existence of either efficient non-thermal desorption or an efficient mixing process in the disks. Similarly Sakai et al. (2008) have detected cold HCO₂⁺, tracing gas phase CO₂, toward the embedded low-mass protostar IRAS 04368+2557 in L 1527 also referred to as L 1527 IRS. From the high column density and the thin line profile they conclude that the observed CO₂ cannot originate from thermal evaporation of ices in the hot inner regions of the envelope. They instead suggest gas phase formation of CO₂ to explain their observations, but do not consider non-thermal desorption in the cold envelope as an alternative. HCO₂⁺ is also detected by Turner et al. (1999) toward several small translucent molecular clouds. They conclude that the observed HCO₂⁺ can only form through gas phase chemistry for very specific C/O ratios and time spans and that the source of gas phase HCO₂⁺ may instead be desorbed CO₂ ice. Both the CO and CO₂ observations may thus be explained by non-thermal desorption of ices, but this has not been quantified to date.

In dense clouds and in outer disks and disk midplanes, desorption must occur non-thermally since the grain temperature is low enough, around 10 K, that thermal desorption is negligible. Suggested non-thermal desorption pathways include photon and cosmic ray induced processes and desorption following the release of chemical energy (Shen et al. 2004; Roberts et al. 2007). The importance of these processes depend both on the intrinsic desorption yields and on the local environment, especially the UV and cosmic ray fluxes. External UV photons from the interstellar radiation field can penetrate into the outer regions of dense clouds and disks and this UV field may be enhanced by orders of magnitude in disks through irradiation by the young star. In addition to direct interaction with ices, cosmic rays and X-rays also produce a UV field inside of the clouds through interaction with H₂.

UV photodesorption is therefore possible in most dense astrophysical environments,

but it has been proposed as an important desorption pathway of ices mainly in protoplanetary disks and other astrophysical regions with dense clumps of material and excess UV photons (Willacy & Langer 2000; Dominik et al. 2005). There is however a lack of experimentally determined photodesorption yields for most astrophysically relevant molecules. This has prevented progress in the field and in most models UV photodesorption is simply neglected. Recently we showed that CO photodesorption is an efficient process with a yield of $3(\pm 1) \times 10^{-3}$ photon⁻¹ (Öberg et al. 2007b). This is of the same order as H₂O photodesorption, investigated by Westley et al. (1995b,c), though the dependence of the H₂O yield on different parameters remains unclear. The photodesorption of H₂O and benzene in a H₂O dominated ice has also been investigated by Thrower et al. (2008) who only find substrate and matrix mediated desorption processes.

In this study we determine the photodesorption yield of CO₂ and its dependence on ice thickness, temperature, morphology, UV flux and integrated UV flux or fluence as well as UV irradiation time. In addition, we extend the previously reported investigation of CO and N₂ photodesorption to include different temperatures and ice morphologies. From the deduced yield dependencies we constrain the different desorption mechanisms and discuss the astrophysical implications.

8.2 Experiments and their analysis

8.2.1 Experimental details

The experimental set-up (CRYOPAD) is described in detail by Fuchs et al. (2006) and Öberg et al. (2007b). The set-up allows simultaneous detection of molecules in the gas phase by quadrupole mass spectrometry (QMS) and in the ice by reflection absorption infrared spectroscopy (RAIRS), with an angle of incidence of 84°, using a Fourier transform infrared (FTIR) spectrometer. The FTIR covers 1200 – 4000 cm⁻¹ with a spectral resolution of 0.5–1 cm⁻¹.

In the experiments presented here, thin ices of 2.1–16.5 monolayers (ML) are grown with monolayer precision under ultra-high vacuum conditions ($P \sim 10^{-10}$ mbar) at 15 – 60 K on a gold substrate that is mounted on a He cryostat. All experiments are conducted with the isotopologues ¹³C¹⁸O and ¹³C¹⁸O (Cambridge Isotope Laboratories 99% and 97% purity, respectively), ¹⁵N₂ (Campro Scientific 98% purity), and ¹³CO₂ (Indugas 99% purity) and ¹³C¹⁸O₂ (ICON Isotopes 96% purity) to avoid contributions from atmospheric contaminations as well as to be able to separate CO and N₂ mass spectrometrically with the QMS. Test experiments show that the isotopologue choices do not affect the experimental outcomes for any of the ices.

Within the uncertainties of the experiment, we also find that there is no difference in the photodesorption yield of 6.5 ML CO₂ ice deposited on top of another 7 ML CO₂ ice (of a different isotopologue), or 7 ML CO₂ on top of 10 ML of H₂O ice, compared with 6–7 ML CO₂ ice deposited directly onto the gold substrate. Since the character of the substrate seems to have no influence on the photodesorption process, all other experiments are carried out with CO₂ ices directly on top of the gold substrate.

The ice films are irradiated at normal or 45° incidence with UV light from a broadband hydrogen microwave discharge lamp, which peaks around Ly α at 121 nm and covers 115–170 nm or 7–10.5 eV (Muñoz Caro & Schutte 2003). All photodesorption experiments are performed in the same experimental chamber and the different UV angles of incidence are obtained by rotating the gold substrate. The lamp emission resembles the spectral distribution of the UV interstellar radiation field that impinges externally on all clouds. It is also consistent with the UV radiation produced locally inside clouds by the decay of electronic states of H₂, following excitation by energetic electrons resulting from cosmic-ray induced ionization of hydrogen, see e.g. Sternberg et al. (1987).

The 45° and the normal incidence irradiation settings produce the same experimental results, except for a reduced photon flux on the ice in the 45° setting due to geometry. The lamp UV flux is varied between 1.1 and 8.3×10^{13} photons cm⁻² s⁻¹ in the different experiments. The UV flux is monitored during all experiments using the photoelectric effect in a thin gold wire in front of the lamp. Before the start of the experimental run, this gold wire current was calibrated to an absolute flux in a separate set-up by simultaneously measuring the flux with a NIST calibrated silicon diode and the current induced in the gold wire. During the photodesorption experiments the flux onto the ice surface is also estimated by measuring the CO₂ photodissociation cross-section several times during the experimental run, at both normal and 45° incidence, and comparing our derived cross sections with the calibrated values in Cottin et al. (2003). This was deemed necessary since the calibration measurements were carried out with normal incidence in the separate set-up, while most experiments used a 45° incidence angle. To prevent photodesorption during these measurements, the CO₂ ice is covered with an inert ice layer. We find that in the normal incidence setting the resulting flux using this actimetry method deviates by a factor 0.9–1.4 from the photodiode-calibrated gold-wire results.

Tables 8.1 and 8.2 summarize the experiments in this study. In the CO experiments, the temperature is varied between 15 and 27 K, which is close to its thermal desorption temperature (Öberg et al. 2005). This complements the previous CO photodesorption experiments, which investigated the dependences of photodesorption on lamp flux and ice thickness at 15 K (Öberg et al. 2007b). In three additional experiments the photodesorption yield (or upper limits) of N₂ is determined, as well as the changes in CO and N₂ ice photodesorption in a CO:N₂ ice mixture and in a N₂/CO layered ice at 16 K. In the CO₂ experiments the temperature is set to 16 – 60 K, the irradiation flux to $1.1 - 8.3 \times 10^{13}$ photons cm⁻² s⁻¹ and the ice thickness to 2.1 – 16.5 ML.

8.2.2 Data analysis

The UV induced ice loss yield during each CO and CO₂ experiment is determined by RAIRS of the ice during irradiation. The intensity of the RAIRS profile is linearly correlated with the ice layer thickness of CO and CO₂ ice up to ~5 ML, but the RAIRS profile can be used up to 20 ML for analysis as long as the non-linear growth above 5 ML is taken into account (Fig. 8.1). The absolute loss yield in number of molecules lost per incident photon is calculated from the RAIRS intensity loss as a function of UV fluence.

For this calculation it is vital to have good estimates of the CO and CO₂ band strengths.

Table 8.1 – Summary of CO and N₂ experiments

No.	Composition	Temp. (K)	Thick. (ML)	UV flux (10 ¹³ cm ⁻² s ⁻¹)
1	¹³ CO	15	4	4.7
2	¹³ CO	22	3.5	4.7
3	¹³ CO	27	3.5	4.7
4	¹³ CO ^a	16	3	4.7
5	¹⁵ N ₂	16	4	4.7
6	¹³ CO: ¹⁵ N ₂ mixed	16	4:4	4.7
7	¹⁵ N ₂ / ¹³ CO layered	16	1/4	4.7

^aannealed ice (i.e. deposited at 27 K and then cooled down to 16 K)

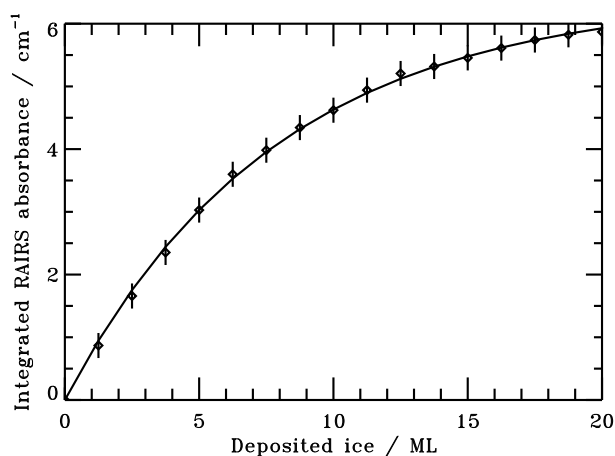


Figure 8.1 – The integrated absorbance of the ¹³C¹⁸O₂ stretching band as a function of deposited ice. The fitted exponential function is used to correct for non-linear growth of the integrated absorbance above 5 ML.

Due to the fact that all ice measurements are done using RAIRS, the ice thickness cannot be estimated from previously determined ice transmission band strengths. Instead the band strength of one ice monolayer is calculated from the observed difference in isothermal desorption from multilayer coverages (constant rate) and monolayer coverages (decreasing rate) as shown in Fig. 8.2. For CO this was done at 31 K and for CO₂ at 76 K. The integrated absorbance of 1 ML is estimated to within 40% from the RAIR spectra at this turning point, which in its turn is used to calculate a band strength relevant for RAIRS. The calculated band strengths are 0.07 and 0.55 cm⁻¹ ML⁻¹ for CO and CO₂ at their respective desorption temperatures. At 18 K the bands are somewhat weaker at 0.06 and 0.42 cm⁻¹ ML⁻¹, respectively. These values are highly set-up specific and they depend on such experimental parameters as mirror settings and should not be used for other purposes. This technique is based on the assumption that the ice is quite flat at the desorption temperature, which was confirmed by the previous CO experiments (Öberg et al. 2007b). For CO, the deduced ice thicknesses agree well (within 20%) with the theoretical

Table 8.2 – Summary of CO₂ experiments

No.	Composition	Temp. (K)	Thick. (ML)	UV flux (10 ¹³ cm ⁻² s ⁻¹)
1	¹³ C ¹⁸ O ₂	16	5.5	4.7
2	¹³ C ¹⁸ O ₂	18	2.1	2.3
3	¹³ C ¹⁸ O ₂	18	5.5	2.3
4	¹³ C ¹⁸ O ₂	18	5.6	2.3
5	¹³ C ¹⁸ O ₂	18	9.0	2.3
6	¹³ C ¹⁸ O ₂	18	16.5	2.3
7	¹³ C ¹⁸ O ₂	18	3.9	1.1
8	¹³ C ¹⁸ O ₂	18	4.7	3.5
9	¹³ C ¹⁸ O ₂	20	6.2	8.3
10	¹³ C ¹⁸ O ₂	18	6.5	8.3
11	¹³ C ¹⁸ O ₂ ^a	18	7.0	2.3
12	¹³ C ¹⁸ O ₂ ^a	16	4	4.7
13	¹³ C ¹⁸ O ₂	30	6.2	2.3
14	¹³ C ¹⁸ O ₂	40	5.8	2.3
15	¹³ C ¹⁸ O ₂	50	6.7	2.3
16	¹³ C ¹⁸ O ₂	60	3.3	2.3
17	¹³ C ¹⁸ O ₂	60	7.4	2.3
18	¹³ C ¹⁸ O ₂	60	5.8	1.1
19	¹³ C ¹⁸ O ₂	60	6.2	8.3
20	¹³ C ¹⁸ O ₂	60	11.0	2.3
21	¹³ CO ₂	16	3.8	4.7
22	¹³ CO/ ¹³ C ¹⁸ O ₂ ^b	18	10/5	2.3
23	N ₂ / ¹³ C ¹⁸ O ₂ ^b	18	20/5.4	2.3
24	¹³ C ¹⁸ O ₂ /CO ₂ ^b	18	6.5/7	2.3
25	¹³ C ¹⁸ O ₂ /H ₂ O ^b	18	7/10	2.3

^aAnnealed ice (i.e. deposited at 60 K and then cooled down to 16 or 18 K)

^bLayered ices

values for our chosen deposition pressure and deposition time (Attard & Barnes 2004). For CO₂, the measured ice thickness is ~30% lower than predicted, probably due to the fact that some of the CO₂ freezes out on the heating shield rather than depositing onto the substrate. Using this method we find that the relative band strengths of CO and CO₂ ice compare well (within 20%) with previously measured transmission band strengths (Hudgins et al. 1993; Gerakines et al. 1996). To convert the band strengths from cm⁻¹ ML⁻¹ to cm molecule⁻¹ a surface density of ~10¹⁵ molecules cm⁻² is assumed.

In the case of CO, there is no measurable photodissociation in this wavelength range and the measured photon-induced loss yield is the photodesorption yield (Gerakines et al. 1996; Cottin et al. 2003; Öberg et al. 2007b). Simultaneous QMS measurements of the desorbed CO gas phase molecules allow for the calibration of the QMS signal to an absolute photodesorption yield. The calibrated QMS signal for CO is used to determine the fraction of the CO₂ ice that photodesorbs as CO. It is also used, together with the

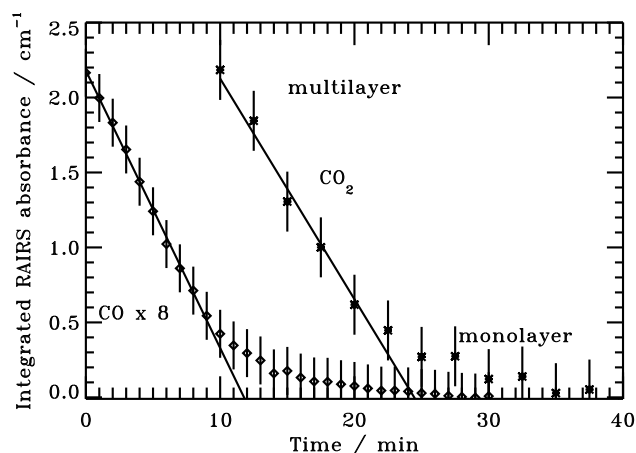


Figure 8.2 – The integrated absorbance of the $^{13}\text{C}^{18}\text{O}$ and $^{13}\text{C}^{18}\text{O}_2$ stretching bands as a function of time during isothermal desorption of ~ 5 ML ices at 31 and 76 K, respectively. The linear fits are used to distinguish between the multilayer and monolayer desorption regimes.

measured relative sensitivities of the QMS filament to CO and N_2 , to determine the N_2 photodesorption yield. The N_2 photodesorption yield cannot be determined by RAIRS since N_2 has no permanent dipole moment and thus no strong IR feature.

In contrast to CO, CO_2 has only dissociative transitions in the wavelength region of the lamp; a UV photon absorption dissociates CO_2 into $\text{CO} + \text{O}$ with a quantum yield of up to 98% in the gas phase (Slanger & Black 1978). Hence, UV irradiation induces chemistry as well as desorption (Gerakines et al. 1996). To determine the total photodesorption yield, the ice loss due to desorption must be separated from the conversion of CO_2 into other ice products. This is done by analysis of the RAIR spectra using two different methods: kinetic modeling and mass balance. The first method uses the different kinetics of surface processes, like desorption, and bulk processes, like ice photolysis, to distinguish between the two. Surface desorption from a multilayer ice is expected to be a zeroth order process and the photodesorption yield, which is determined from the derivative of the ice thickness with fluence, should therefore be constant with UV fluence. Photolysis into other species occurs throughout the ice at equal yield, since the ices here are thin enough that optical depth effects can be ignored, and is consequently expected to be a first order process. The contributions of desorption and photolysis to the observed ice loss is then determined by fitting the observed ice thickness versus fluence to the sum of a linear function and an exponential decay function, corresponding to a zeroth and a first order reaction. This method has the advantage that it is not dependent on identifying the photolysis products of CO_2 and it is used to derive photodesorption yields whenever the zeroth and first order curves are separable. This is mainly the case for the high temperature and high fluence experiments.

The mass balance analysis method compares the total ice loss with the simultaneous formation of other species in the ice; the final photodesorption yield is then defined as the loss yield of the original ice minus the formation yield of other carbon-bearing ice species. This is the only method that works for ices that are exposed to low fluences,

where the contributions from the zeroth and first order processes cannot be separated. In the CO₂ experiments CO, CO₃ and O₃ are the expected reaction products (Gerakines et al. 1996), with CO dominating. The photodesorption yield is then the CO₂ loss yield minus the formation yield of CO and CO₃, though as seen below the contribution from CO₃ is negligible. This method depends on the relative infrared band strengths of the formed molecules and is thus only accurate in the temperature range where the CO band strengths are measured, i.e. <30 K. As seen below, these two methods agree very well in the few cases where both methods are used to derive photodesorption yields.

The simultaneous mass spectrometry of gas phase molecules during irradiation reveals the nature of the desorbed species. This is limited by the fact that less volatile molecules (e.g. CO₂) adsorb onto the heating shield and other semi-cold surfaces inside the experiment before reaching the mass spectrometer. In the case of CO₂, only the fractions of the ice that desorb as CO and other volatile species are detected by the QMS. At temperatures above 30 K the conversion factor between QMS detected and desorbed CO changes due to a decrease in cryopumping of CO, which is accounted for when deriving the CO-from-CO₂ photodesorption yield. For both CO and CO₂, re-condensation onto the actual ice sample after desorption will play a negligible role given the small surface area of the sample and the resulting underestimate of the actual photodesorption will be substantially lower than other sources of inaccuracy.

To summarize, the main sources of uncertainty in these experiments are the photon flux and ice thickness calibrations of ~30% and 40%, respectively. In addition, from repeated experiments, the CO and CO₂ experimental results are found to vary with approximately 10% and 25%, respectively. The uncertainty is greater for CO₂ than for CO because of the extra steps in deriving the CO₂ photodesorption yield. The total uncertainty is ~60% for the CO₂ photodesorption yield and ~50% for the CO photodesorption yield. The N₂ photodesorption yield uncertainty is somewhat higher due to the larger uncertainty in the QMS measurements.

8.3 Results

8.3.1 CO and N₂

The results from photodesorption experiments of pure CO ice at 15 K are reported in Öberg et al. (2007b). The yield presented there is updated here using new ice thickness and lamp flux calibrations; at 15 K the CO photodesorption yield is $(2.7 \pm 1.3) \times 10^{-3}$ CO molecules per *incident* photon, averaged over the wavelength range of the lamp. The corresponding photodesorption quantum efficiency per *absorbed* UV photon in the surface layer is estimated using the lamp spectrum from Muñoz Caro & Schutte (2003) and the UV spectrum of CO ice from Mason et al. (2006). The UV ice absorption spectrum shows that the CO lines are resolved. The measured absorption spectrum $\int^{UV} A_{\lambda}^{ice} d\lambda$ is not calibrated to a UV cross section so in our calculation it is assumed that the total UV absorption cross section is the same in the ice as measured in the gas phase $\int^{UV} \sigma_{\lambda}^{gas} d\lambda$ (Eidelsberg et al. 1992, 1999). The fraction of incident photons that are absorbed in the

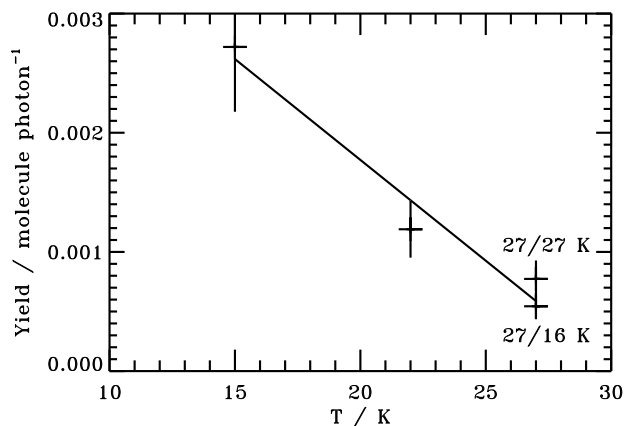


Figure 8.3 – The CO ice photodesorption yield as a function of ice deposition temperature between 15 and 27 K. The ices are photodesorbed at the deposition temperature except for ‘27/16 K’, where the ice is deposited at 27 K and then cooled down and irradiated at 16 K.

top monolayer, χ_{abs} , is calculated from

$$\chi_{\text{abs}} = \frac{\int^{\text{UV}} I_{\lambda}^{\text{UV-lamp}} A_{\lambda}^{\text{ice}} d\lambda}{\int^{\text{UV}} I_{\lambda}^{\text{UV-lamp}} d\lambda} \times \frac{\int^{\text{UV}} \sigma_{\lambda}^{\text{gas}} d\lambda}{\int^{\text{UV}} A_{\lambda}^{\text{ice}} d\lambda} \times N_s \quad (8.1)$$

by cross-correlating the UV-lamp spectrum with the absorption spectrum of CO ice, divided by the total UV flux, $\int^{\text{UV}} I_{\lambda}^{\text{UV-lamp}} d\lambda$, and then multiplying with the cross section conversion factor and the amount of molecules in one monolayer, N_s . The resulting absorption fraction is $5.5 \pm 0.2 \times 10^{-3}$, where the uncertainty reflects the error in the gas phase cross section. Comparison with our measured photodesorption yield results in an efficiency of 0.3–0.8 per absorbed photon at 15 K, including both the absorbance and the photodesorption uncertainties.

Figure 8.3 shows that the CO photodesorption yield decreases with ice temperature such that it is almost a factor of three lower at 27 K compared to 15 K. Within this temperature range the CO photodesorption yield is empirically described as linearly dependent on temperature: $2.7 \times 10^{-3} - (T - 15) \times 1.7 \times 10^{-4}$ molecules photon⁻¹, where T is temperature in K. An additional experiment, where the ice is deposited at 27 K and then cooled down to 16 K before irradiation, results in a similar desorption yield as when the ice is also desorbed at 27 K. In quantum efficiency terms this corresponds to 0.1–0.3 photodesorption events per absorbed photon in the top ice layer, at 27 K as well as for the annealed ice at 16 K. This indicates that the structure of the ice, rather than the temperature, affects the photodesorption yield. This is further supported by a change in RAIRS profile at 22 and 27 K compared to that at 15 K (Fig. 8.4). Changes in the CO spectra with temperature have been previously reported by e.g. Fuchs et al. (2006). These spectral profiles do not change visibly after a UV fluence of 7×10^{17} photons cm⁻² when the ices are irradiated at their deposition temperature (not shown). Figure 8.4 also shows the spectral profile of the annealed ice before and after irradiation, which has not changed significantly with cool

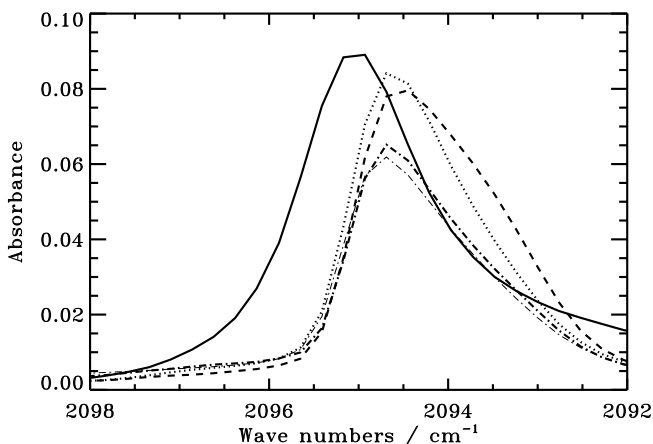


Figure 8.4 – CO spectra at 15 K (solid), 22 K (dotted), 27 K (dashed), and 16 K after deposition at 27 K (dash dotted), all acquired before irradiation. The figure also shows a spectrum of the annealed ice acquired after a UV fluence of $\sim 7 \times 10^{17}$ photons cm^{-2} (thin dash dotted).

down, and it has at most slightly shifted toward the 15 K ice spectral profile following irradiation. uncertainties.

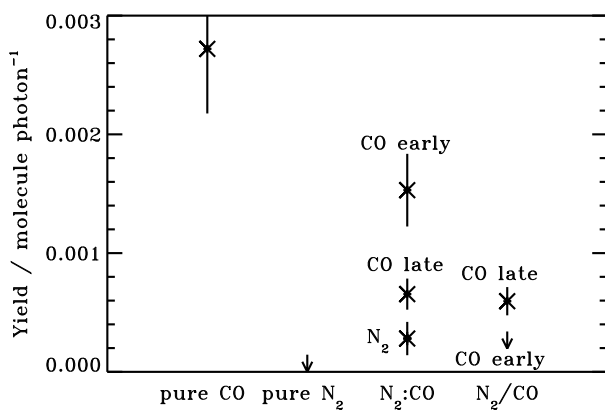


Figure 8.5 – The CO and N₂ desorption yields at 15/16 K in 4 ML pure CO and pure N₂ ices, a 4:4 ML mixed ice, and a N₂/CO 1/4 ML layered ice. 'Early' and 'late' marks the CO desorption yield in the beginning of the experiment and after a photon fluence of 8.5×10^{17} cm^{-2} .

In Öberg et al. (2007b) the N₂ photodesorption yield is constrained to a factor of 10 less than the CO yield at 15 K. With increased sensitivity of the mass spectrometer, N₂ photodesorption is now detected at a yield of 1.8×10^{-4} N₂ molecules photon⁻¹ or a factor of 15 lower than the CO photodesorption yield. This value has a factor of two uncertainty, mainly due to the uncertainty in the conversion of the mass spectrometer signal into an ice desorption yield. This measured yield is real, but because of continuous freeze-out of ~0.1 ML H₂O ice per hour the N₂ ice contains an H₂O impurity. A typical experiment lasts 5–6 hours resulting in a maximum 12% contamination level (a significant fraction of the

adsorbed H₂O molecules photodesorb themselves during the irradiation experiments). This probably affects the measured photodesorption yield due to co-desorption of ices and thus the measured yield should be used as a strict upper limit of pure N₂ photodesorption.

In two additional experiments a CO:N₂ mixture 4:4 ML and a N₂/CO layered 1/4 ML ice are irradiated at 16 K. Figure 8.5 shows that in the ice mixture experiment the N₂ desorption yield more than doubles compared to pure N₂ ice, while the CO desorption yield decreases by a factor of 2–4 compared to pure CO ice during the experiment. After a fluence of $\sim 2 \times 10^{17}$ photons cm⁻² the CO desorption yield is 50% of the photodesorption yield of pure CO. This is expected in a 1:1 mixture, since only 50% of the surface is covered with CO. With increasing fluence the CO desorption yield decreases such that it is only 25% of the yield of pure CO photodesorption after 8.5×10^{17} photons cm⁻². This can only be understood if the N₂ molecules desorb with a lower yield than the CO molecules, resulting in a decreasing CO surface concentration with UV fluence. In the layered experiment the CO photodesorption yield is initially below the detection limit. After a UV fluence of 8.5×10^{17} photons cm⁻² the yield increases to 25% of the pure CO photodesorption yield. The N₂ mass spectrometry signal does not reach equilibrium in the layered experiment, but the desorption yield seems to be at a similar level as in the mixed ice.

8.3.2 CO₂

8.3.2.1 Derivation of the total photodesorption yield

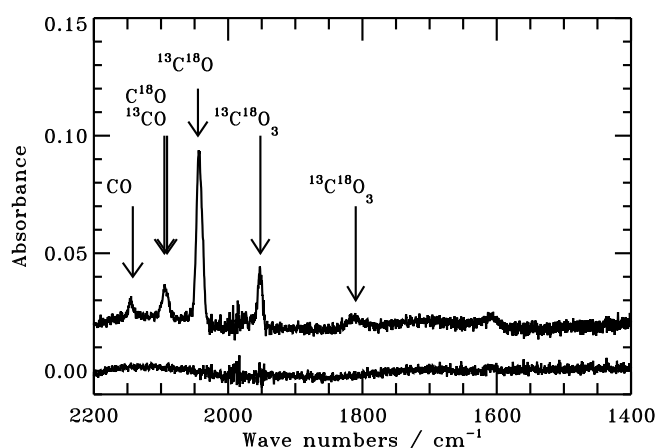


Figure 8.6 – $^{13}\text{C}^{18}\text{O}_2$ ice at 18 K before (bottom) and after (top) a UV fluence of 5×10^{17} photons cm⁻². Some of the original CO₂ ice is photolyzed into CO, CO₃ (ν_1 at 1953 cm⁻¹ and $2\nu_4$ in Fermi resonance with ν_1 at 1810 cm⁻¹).

To use the mass balance method to calculate the CO₂ photodesorption yield, it is necessary to constrain which molecules are formed during irradiation. Figure 8.6 shows the spectra of an 18 K, 9 ML thick CO₂ ice before and after a UV fluence of 5×10^{17} photons cm⁻². The only formed molecules are CO and CO₃, though O₃ formation cannot

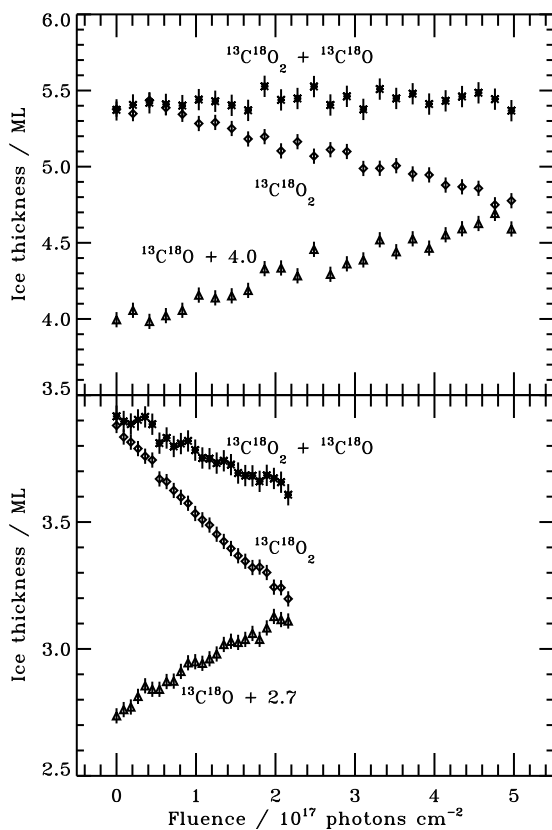


Figure 8.7 – Top: the ¹³C¹⁸O₂ ice thickness (diamonds) in a 18 K, 20/5.4 ML N₂/¹³C¹⁸O₂ layered ice as a function of fluence, plotted together with the formed ¹³C¹⁸O ice (triangles) and the constant calculated total ice thickness (stars). Bottom: the decreasing total ice thickness with UV fluence in an 18 K, 3.9 ML icet. The error bars indicate the relative uncertainty in the integrated absorbance (converted to a ML scale) of the RAIRS features within each experiment. This is also the case for similar plots throughout the paper

be excluded since the strong ν_3 ¹⁸O₃ band around 1040 cm⁻¹ is outside of the range of the detector. This is in agreement with Gerakines et al. (1996), who found CO, CO₃ and small amounts of O₃ after irradiating CO₂ with a similar fluence. The line positions are taken from Brewer & Wang (1972), Moll et al. (1966) and Gerakines & Moore (2001). The weak band around 1605 cm⁻¹ cannot be unambiguously assigned. The lack of other features in the spectra from e.g. carbon-suboxides put strict upper limits on the formation of such molecules to a fraction of a percentage of the original CO₂ ice. This is consistent with the experiments of Gerakines & Moore (2001) where no carbon-suboxides was detected after UV irradiation of pure CO₂ ice. In addition Temperature Programmed Desorption (TPD) experiments following irradiation show that ~10% of the original ice is photolyzed into CO, ~1% into O₂ or O₃ and ~0.1% into C₂. From this we infer that more than 99% of the carbon budget is bound up in CO₂, CO and CO₃ during the experiment.

The CO₂ and CO abundances during each experiment are calculated from their derived band strengths. The CO₃ band strengths have not been measured, however, and can only be crudely estimated. This will introduce a large uncertainty into the mass balance

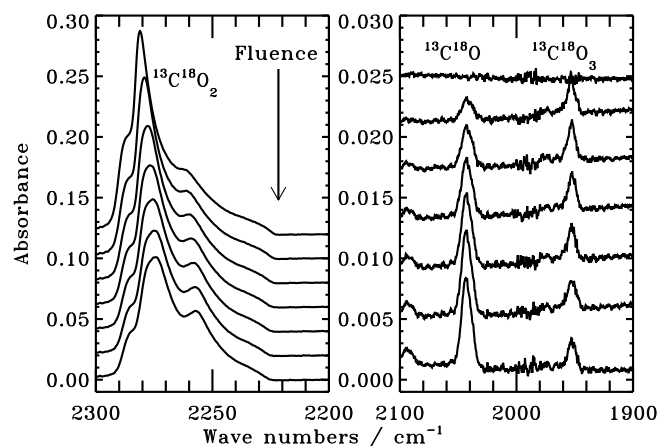


Figure 8.8 – RAIR spectra of the $^{13}\text{C}^{18}\text{O}_2$ stretching band at 2280 cm^{-1} , the $^{13}\text{C}^{18}\text{O}$ stretching band at 2045 cm^{-1} and the $^{13}\text{C}^{18}\text{O}_3$ ν_1 band at 1950 cm^{-1} acquired before irradiation of a 11 ML $^{13}\text{C}^{18}\text{O}_2$ ice at 18 K and then after every 8.3×10^{16} photons cm^{-2} .

calculations if CO_3 is formed at significant abundances. Figure 8.7 shows the calculated CO_2 and CO ice thicknesses as a function of fluence for a layered 20/5.4 ML N_2/CO_2 ice. The ice cover hinders desorption and the result is that 10% of the original CO_2 is photolyzed into CO . The fact that the lost CO_2 is perfectly compensated for by the formed CO ice shows that CO_3 is not a significant photolysis product. The lack of photodesorption in the layered experiment (top Fig. 8.7) is contrasted with the observed photodesorption of a 3.9 ML bare CO_2 ice (bottom Fig. 8.7).

The CO_3 abundance is also estimated independently by employing its only likely formation path and the fact that CO_3 reaches its final level within $\sim 5 \times 10^{16}$ photons cm^{-2} in all experiments (exemplified in Fig. 8.8 where the level does not change between 0.8 and 5×10^{17} photons cm^{-2}). CO_3 is expected to form from $\text{CO}_2 + \text{O}$, where the O originates from photolysis of another CO_2 molecule into $\text{CO} + \text{O}$. With photodesorption hindered, the amount of CO_3 then never exceeds the amount of CO in the ice. In the 20/5.4 N_2/CO_2 experiment, the CO_3 abundance reaches steady state when less than one percent of the CO_2 is converted into CO , which puts a 1% upper limit on the formed CO_3 . This is small compared to the ice loss during CO_2 photodesorption experiments, where typically 20% of the ice is lost.

From these results the mass balance photodesorption yield is defined as the CO_2 ice loss yield minus the CO formation yield. Figure 8.9 shows the CO_2 , CO and CO_2+CO ice thicknesses in an originally 6.5 ML thick CO_2 ice at 18 K as a function of UV fluence. Practically the photodesorption yield is derived from the slope of the total ice thickness as a function of fluence. This mass balance method of determining the photodesorption yield agrees very well with the yield determined through simultaneous kinetic modeling of bulk photolysis and photodesorption. In Figure 8.9 the CO_2 ice thickness is fitted to a function of the form $A(0) \times e^{-A(1)/\Phi} + A(2) + A(3) \times \Phi$ using the IDL script MPFIT, where Φ is the fluence. The photodesorption yield is determined from $A(3)$. The derived photodesorption yield is the same, within the uncertainties, to the yield derived from

fitting a linear function to the CO₂+CO ice thickness. This confirms the validity of both methods.

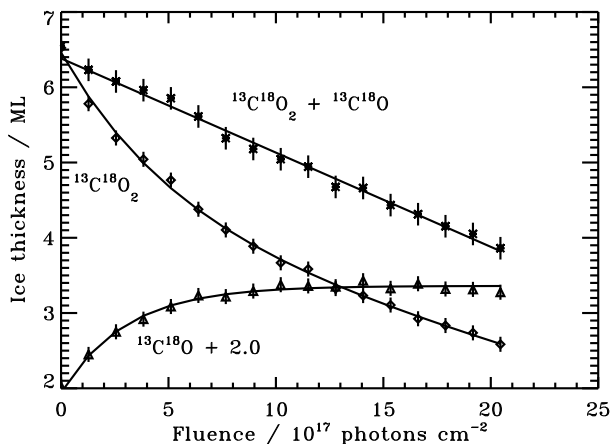


Figure 8.9 – The CO₂ ice thickness as a function of UV fluence (diamonds) plotted together with the formed CO layer thickness (triangles) and the calculated total ice thickness (stars). The CO₂ ice loss is fitted as a sum of photolysis (an exponential function) and desorption (a linear function).

Whichever method is used, the result is a linear coefficient, which gives a photodesorption yield in loss of ice monolayers per 10^{17} UV photons for a 6.5 ML ice at 18 K: $0.27 \text{ (ML)}/2.1 \text{ (} 10^{17} \text{ photons cm}^{-2}\text{)} = 0.13 \text{ ML} / \text{(} 10^{17} \text{ UV photons cm}^{-2}\text{)}$. This is further converted into a photodesorption yield in CO₂ molecules per UV photon (7-10.5 eV): $Y_{\text{pd}} = 0.13 \times 10^{-17} \text{ ML photon}^{-1} \text{ cm}^2 \times (10^{15} \text{ molecules cm}^{-2} / 1 \text{ ML}) = 1.3 \times 10^{-3} \text{ molecules photon}^{-1}$.

8.3.2.2 Desorption products

The total photodesorption yield is well constrained from the RAIR spectroscopy of the ice during irradiation. The question remains in which form CO₂ ice photodesorbs. Figure 8.10 shows mass spectra acquired during UV irradiation of a 6.2 ML ice at the two temperature extremes, 20 and 60 K. The only visible desorption products are CO and O₂, which puts strict upper limits on other potential volatile desorption products. Less volatile species like CO₂ ($m/z=49$ for $^{13}\text{C}^{18}\text{O}_2$) cannot be excluded, however, since their cryopumping efficiencies are up to two orders of magnitude higher than for CO. As described in Section 8.2.2 the measured CO QMS signal can be converted into a number of CO molecules desorbed per photon. This number is compared with the total CO₂ photodesorption yield to quantify the amount of the CO₂ ice that desorbs as CO. From QMS measurements during irradiation experiments, $\sim 20 - 50\%$ desorbs as the fragment CO (Fig. 8.11) and at most 5% as O₂. It is thus inferred that more than 50% of the desorbed ice comes off as less volatile species, most likely CO₂. This is supported by the fact that the amount of formed CO₃ ice is the same whether or not the ice is covered and therefore whether or not photodesorption is allowed. This makes it unlikely that CO₃ is photodesorbing in the uncovered experiments. In addition no other C-bearing molecules are formed at significant

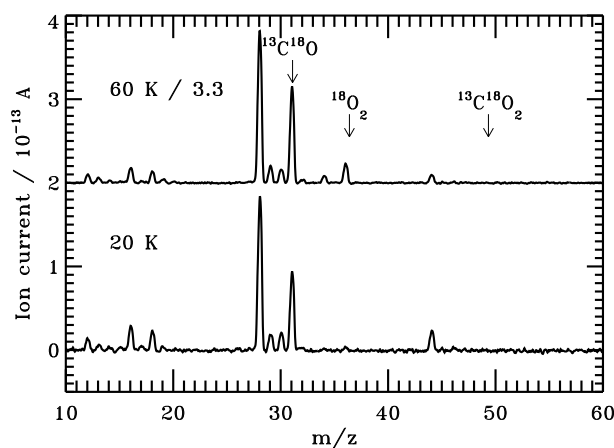


Figure 8.10 – Mass spectra acquired during irradiation of a 6.2 ML thick $^{13}\text{C}^{18}\text{O}_2$ ice at 20 and 60 K with a flux of 8.3×10^{13} photons $\text{cm}^{-2} \text{s}^{-1}$. The spectra at 60 K have been divided by 3.3 to account for the lower cryopumping of volatiles like CO and O_2 at 60 K compared to at 20 K. In each case the ice is irradiated for 3 hours before acquisition to ensure that the photodesorption rate is stable. Each acquisition lasts 3 hours and consists of ~ 100 averaged spectra. In addition to photodesorbed ices there are some background CO ($m/z=12, 16$ and 28), CO_2 ($m/z=44$) and possibly some background H_2O as well ($m/z=18$).

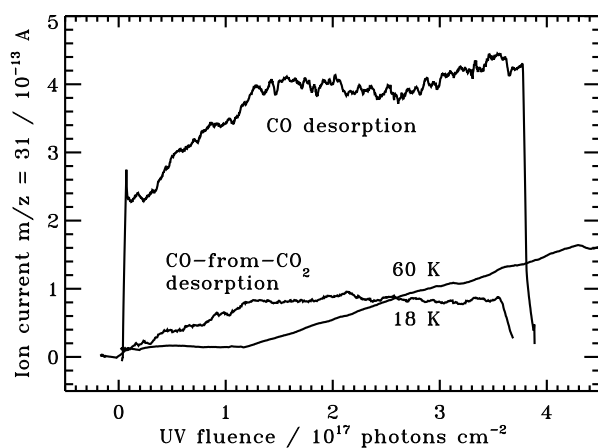


Figure 8.11 – The detected CO photodesorption during irradiation of a 4 ML $^{13}\text{C}^{18}\text{O}$ ice at 16 K and $^{13}\text{C}^{18}\text{O}_2$ ices at 18 K (5.5 ML) and at 60 K (7.4 ML), as a function of UV fluence. The 60 K signal has been divided by 3.3 to account for the lower cryopumping at 60 K compared to 18 K.

abundances, which only leaves CO_2 as a possible desorption product.

Below we separate the total CO_2 ice photodesorption yield (as measured with RAIRS) from the desorption of CO-from- CO_2 (measured with the QMS). The desorption of CO_2 molecules is taken to be the difference between the total CO_2 ice desorption and the CO-

from-CO₂ desorption. The total photodesorption quantum efficiency per absorbed UV photon in the surface layer is estimated to 0.4–1 using the lamp spectra from Muñoz Caro & Schutte (2003) and the calibrated UV spectra of CO₂ ice from Mason et al. (2006). As seen from the thickness dependence below, this efficiency decreases with depth into the ice.

8.3.2.3 Yield dependences on experimental parameters

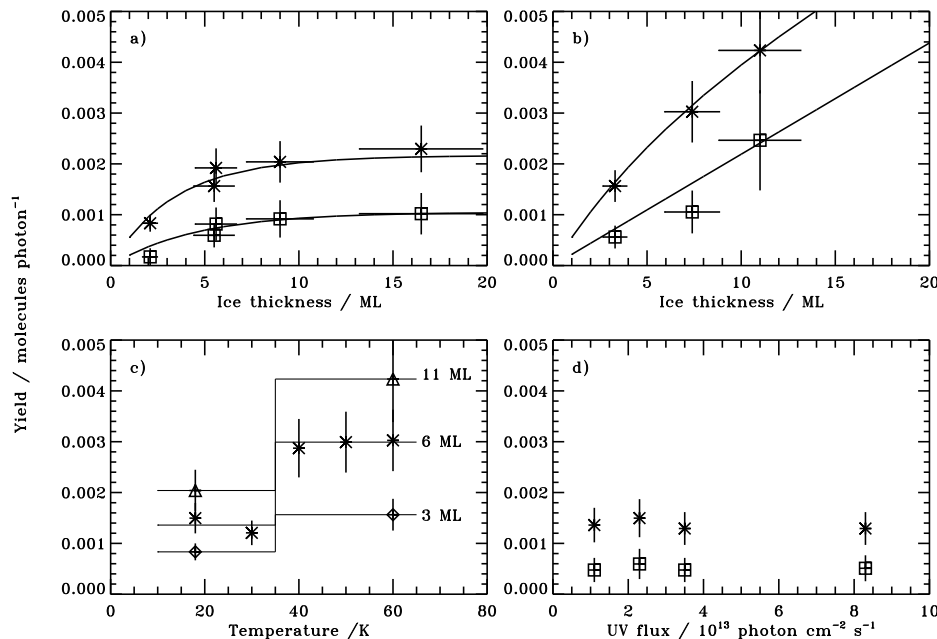


Figure 8.12 – Total CO₂ (crosses) and CO-from-CO₂ (squares) photodesorption yield dependences on different parameters. In a) CO₂ ices of different thicknesses are irradiated with the same UV fluence of $\sim 6 \times 10^{17}$ photons cm⁻² at 18 K and in b) at 60 K. Both the total CO₂ and the CO-from-CO₂ desorption yields are fitted with functions of the form $c \times (1 - e^{-(x/l)})$ at low temperatures (solid lines), where x is the ice thickness and l an ice diffusion parameter. The two measurements of 5.5 and 5.6 ML ices in a) are from the beginning and the end of a two-month long experimental series. Panel c) shows that the total photodesorption yield is constant with temperature within a low temperature region (<40 K) and within the warmer region 40–60 K for ~ 3 ML (diamonds), 6 ML (crosses) and 11 ML (triangles) thick ices, irradiated with fluences of $\sim 6 \times 10^{17}$ photons cm⁻². Finally panel d) demonstrates the independence of the total and CO-from-CO₂ photodesorption yields on the photon flux for 4–6.5 ML ices at 18 K.

Ice thickness. The total CO₂ photodesorption yield at 18 K is thickness dependent up to several monolayers (Fig. 8.12a), which is in contrast with the constant photodesorp-

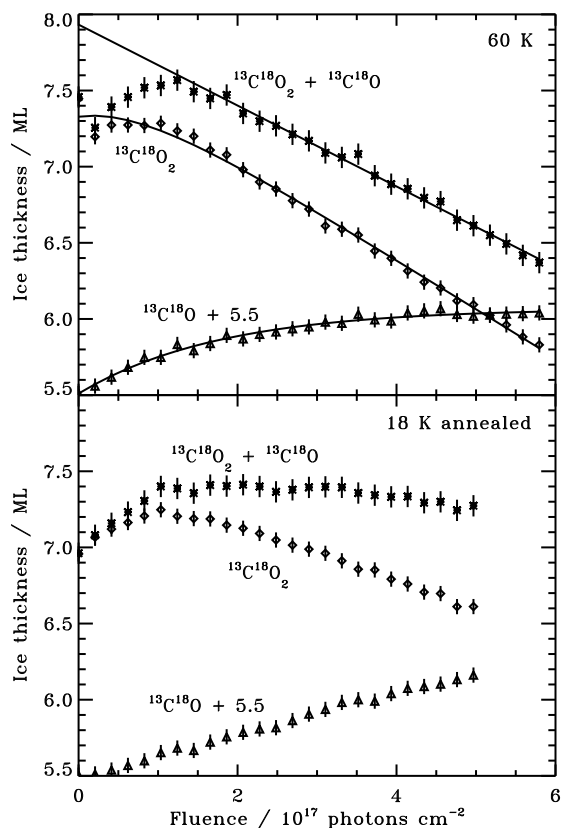


Figure 8.13 – The top panel shows the measured CO₂ layer thickness (diamonds) of an originally 7.4 ML CO₂ ice at 60 K as a function of UV fluence, plotted together with the formed CO layer thickness (triangles) and the calculated total ice thickness (stars). The CO₂ ice loss is fitted as a sum of photolysis (an exponential function) and desorption (a linear function). The bottom panel shows an 18 K experiment that has been thermally annealed at 60 K prior to irradiation at 18 K. Note the lack of evidence of photodesorption from this ice.

tion yield of CO reported in Öberg et al. (2007b). The total CO₂ photodesorption yield increases from 8×10^{-4} to 2.3×10^{-3} molecules photon⁻¹ when the ice is grown from 2 to 16 ML.

Figure 8.12a also shows simple models fitted to the measured yields of both the CO-from-CO₂ and the total CO₂ photodesorption. The desorption yield of the CO-from-CO₂ is well described by $1.1(\pm 0.2) \times 10^{-3} \times (1 - e^{-(x/4.6(\pm 2.2))})$, where x is the ice thickness in monolayers. The total CO₂ desorption dependence on thickness is a sum of the desorbed CO₂ and CO molecules and is thus modeled as $1.2(\pm 0.1) \times 10^{-3} \times (1 - e^{-(x/2.9(\pm 1.1))}) + 1.1(\pm 0.2) \times 10^{-3} \times (1 - e^{-(x/4.6(\pm 2.2))})$. Both models are fitted using the IDL routine MPFIT. Here the uncertainties only reflect the calculated model errors. As discussed in Section 8.2.2, the total uncertainty is 60%. From these expressions it is clear that more than 90% of the photodesorption events originate in the top 10 ML and 50% in the top 3 ML of the ice. They also expose the thickness dependence of the fraction of the CO₂ desorbing as CO; between 2 and 16 ML this fraction grows from 20 to 45%. The origin of the model and the full significance of the different exponential constants for CO and CO₂ desorption

is further discussed below.

The build-up of molecules in the 18 K CO₂ ice is linearly dependent on the ice thickness as expected for a photodesorption yield that is low in comparison to the total ice thickness. In all the ices, ~10% of the original ice is converted to CO and frozen into the CO₂ ice after a typical UV fluence of 5×10^{17} photons cm⁻². For comparison ~10% of the original ice is desorbed after the same fluence in a typical 5 ML experiment.

Figure 8.12b shows that the CO₂ photodesorption has a somewhat different thickness dependence at 60 K. The CO-from-CO₂ desorption dependence on thickness is indistinguishable from a linear function and is fitted linearly. The total CO₂ desorption is fitted well, but not uniquely, by $2.2(\pm 0.2) \times 10^{-3} \times (1 - e^{-(x/5.8(\pm 1.2))}) + 2.2(\pm 0.3) \times 10^{-4} \times x$ molecules photon⁻¹, where x is the ice thickness in monolayers. This formula indicates that photodesorption takes place deeper into the ice at higher temperatures and that the mean-free-path of CO becomes infinite.

Temperature. At temperatures higher than 30 K the CO₂ photodesorption is initially fluence dependent, which is not the case for colder ices. This is further discussed below; here the constant yield reached after a fluence of 2.0×10^{17} photons cm⁻² is used for comparison between the photodesorption yields at different temperatures. Figure 8.12c shows the total CO₂ photodesorption yield dependence on temperature for different ice thicknesses. At 18 and 30 K both the total and the CO-from-CO₂ photodesorption yields are indistinguishable within the experimental uncertainties. Between 30 and 40 K the photodesorption yield jumps and above 40 K the photodesorption yield is again independent of temperature.

The build-up of CO molecules in the CO₂ ice is also temperature dependent. Above 30 K, the CO build-up is less than 50% of the build-up at lower temperatures.

Photon flux. Figure 8.12d shows 4–6.5 ML CO₂ ices irradiated with different photon fluxes at 18 K. Between 1.1 and 8.3×10^{13} photons cm⁻² s⁻¹ the CO₂ photodesorption yield in molecules photon⁻¹ is constant within the experimental uncertainties. The CO desorbing from the CO₂ ice is independent of the lamp flux as well. At 60 K the ice is irradiated at two different fluxes and, similarly to the colder ice, the photodesorption yield is constant (not shown).

At 18 K, the produced CO ice increases throughout the experiment up to a fluence of $\sim 10 \times 10^{17}$ photons cm⁻². After 10×10^{17} photons cm⁻² the amount of CO ice reaches steady-state, which is only clearly visible in the experiment with the highest fluence. The observed independence of the CO-from-CO₂ photodesorption yield on CO ice content indicates that direct CO photodesorption from the formed CO ice plays a minor role during irradiation of the CO₂ ice.

Time and photon fluence. Figure 8.13 shows the photodesorption of a 60 K, 7.4 ML CO₂ ice irradiated with 2.3×10^{13} photons s⁻¹ cm⁻². At 60 K there is no measurable photodesorption during the first two hours or a fluence of 2×10^{17} cm⁻². This can be compared with the 4.0 ML CO₂ ice at 18 K in Fig. 8.7 (bottom), where photodesorption starts within a fluence of 10^{17} photons cm⁻². In the 60 K experiment, the total CO₂ photodesorption yield jumps to 3.0×10^{-3} molecules photon⁻¹ after a fluence of 2×10^{17} photons cm⁻² and remains constant for the remainder of the experiment. This photodesorption delay is observed in all 5–7 ML ices at 40–60 K and also at all thicknesses between 3–11 ML

at 60 K. The QMS measurements also show clear differences between the 18 K and the 60 K experiments (Fig. 8.11). At 60 K, the CO QMS signal is lower than at 18 K during the first 2×10^{17} photons cm^{-2} , corresponding to a yield $\sim 1 \times 10^{-4}$ molecules photon^{-1} . After the first 10^{17} photons cm^{-2} the CO signal increases rapidly with fluence.

To test whether this delay in photodesorption onset at 60 K is time or fluence dependent, a 5.8 ML ice is also irradiated at a 50% lower flux. In this experiment the photodesorption according to the RAIRS begins after the same photon fluence, which occurs after twice the amount of time compared with the experiment at a higher flux.

Thermal annealing. In one experiment, a 7.0 ML thick ice is deposited at 60 K and subsequently cooled down to 18 K before starting the irradiation. The CO-from-CO₂ photodesorption yield is $\sim 1 \times 10^{-4}$ photon^{-1} , while only an upper limit of 5×10^{-4} photon^{-1} is derived for the total CO₂ photodesorption from the RAIRS measurements. This is significantly lower compared to both unannealed experiments at 18 K and to 60 K experiments (Fig. 8.13). The CO-from-CO₂ QMS signal is similar to that from warm ices during the first 10^{17} photons cm^{-2} . The CO ice build-up, as measured from RAIRS, is similar to the un-annealed ice at 18 K.

8.4 Discussion

8.4.1 CO and N₂ yields and mechanisms

In Öberg et al. (2007b) we concluded that CO photodesorbs from the top one or two ice layers at 15 K. Recent theoretical work shows that CO only desorbs from the absolute surface layer (Takahashi & van Hemert, in prep.), which is supported by the new findings in this study.

The experiments show that the photodesorption of CO depends on thermal annealing, such that annealing at a higher temperature results in a lower desorption yield. The annealing most likely results in a more compact ice with a smaller effective surface area as well as stronger bound molecules. These two effects then add up to decrease the quantum efficiency of the photodesorption process. The reason for the linear dependence with temperature is unclear and may be coincidental. This behavior cannot be extrapolated to lower temperatures, since a 15 K ice should be amorphous.

The new photodesorption experiments with N₂ further constrain the CO photodesorption mechanism. Consistent with Öberg et al. (2007b) there is no evidence of direct N₂ photodesorption. The increase in photodesorption yield of N₂ when mixed with CO or grown in a monolayer on top indicates that $\sim 5\%$ of the UV photon absorptions of CO molecules result in the desorption of a neighboring molecule rather than the desorption of the originally excited molecule. The decreasing CO photodesorption in the mixed ice and the lack of initial CO desorption in the layered experiment also confirm that CO only desorbs from the top ice layer.

8.4.2 The CO₂ yield and mechanism

In contrast to CO and H₂O photodesorption (Andersson et al. 2006; Andersson & van Dishoeck 2008, Takahashi & van Hemert, in prep.), the photodesorption mechanism of CO₂ has not been theoretically addressed yet. From the dependencies reported here, the mechanism may be constrained, however, and it is similar to that of H₂O. CO₂ photodissociates to CO+O, where the products have excess energy. This is followed by both reactions in the ice to form the observed CO₃, and recombination to CO₂. Some of these reaction products subsequently desorb.

The flux independence of the CO₂ photodesorption has also previously been seen for H₂O and CO ices (Westley et al. 1995b; Öberg et al. 2007b, Öberg et al. accepted by ApJ). This independence is expected for single photon processes, but not for multi photon processes or desorption induced by excess heat from the lamp. This is consistent with the suggested mechanism of dissociation fragments and recombined molecules traveling through the ices before desorbing.

The CO₂ photodesorption yield is clearly thickness dependent, which is in contrast to the CO photodesorption from surfaces only. This difference can be understood from the fact that before a desorption event occurs, the CO₂ molecule is dissociated into energetic products (whether concerned with the fragments or recombined molecules), which may travel through several monolayers of ice before they are quenched by the surrounding matrix. Assuming a homogeneous ice, the probability of a molecule with excess energy, from dissociation or recombination, reaching the ice surface and desorbing is only dependent on the excess energy, the diffusion properties of the molecule and the ice depth at which it receives its excess energy. The diffusion properties of a molecule are simplest described by the average distance the molecule travels through the ice before being stopped. Defining l as the average distance traveled by a molecule before quenched by the surrounding ice, the fraction of particles with excess energy that will move through a slab of ice of thickness x is expected to be proportional to $e^{-x/l}$, assuming uniform photochemistry throughout the ice and that the direction the molecule travels is independent of ice depth. Integrating over the ice depth from 0 to x , the total desorption of particles between 0 and x is then proportional to $1 - e^{-x/l}$.

We find that this type of expression describes the photodesorption at low temperatures well, with an average travel distance or mean-free-path of 2.9 ML for the CO₂ photodesorption and 4.6 ML for the CO fragment desorption. The two different values for the mean-free-paths have large uncertainties and it is not clear that the difference is significant. The values are however consistent with the different sizes of CO and CO₂, since the larger molecule is expected to be less mobile in the ice. The different mean-free-paths may also be partly due to different mechanisms, i.e. dissociation versus recombination, through which the CO fragment and the recombined CO₂ molecule receive excess energy.

The different mean-free-paths for CO and CO₂ desorption from CO₂ ice can also be consistent with a different desorption mechanism of CO₂ molecules – momentum transfer to a surface CO₂ molecule from a smaller fragment originating in an underlying layer. This is observed in simulations by Andersson & van Dishoeck (2008) as an equally important photodesorption pathway for H₂O compared to desorption of the re-

combined molecule. The ice thickness dependence of this kind of process remains to be explored, since it requires more complex models than the simple mean-free-path model presented here.

Other desorption pathways of the CO fragment can however be ruled out from the experiments presented here. The desorbed CO molecules do not originate in photodesorption of CO ice, since the yield does not increase with an increasing fraction of CO in the ice – this fraction never reaches equilibrium during most low temperature experiments – while the CO QMS signal does. In addition, the underlying substrate seems to have no influence on the desorption yield; hence substrate mediated processes are excluded as well.

At temperatures above the pure CO desorption temperature of ~ 30 K, the increased photodesorption yield is most likely due to the increased mobility of CO₂ and CO in the ice. This is seen from the longer mean-free-path for desorbing CO₂ molecules and the infinite mean-free-path of CO. The latter points to a very high mobility of CO in the ice at these temperatures, which results in that most of the produced CO thermally desorbs once formed through CO₂ dissociation. It is also shown by the onset of O₂ photodesorption (Fig. 8.10). The desorption of O₂ is less than CO at any temperature (Section 8.3.2.1), but its mere presence shows that at 60 K oxygen atoms are very mobile and produced abundantly.

A curious and not yet fully understood feature is the delayed onset of both CO and CO₂ photodesorption from CO₂ ices at 40–60 K. Since it is a fluence rather than a time effect it is probably due to a re-structuring of the ice induced by UV irradiation. This restructuring is indicated by a change in the infrared spectral profile (not shown), which seems more pronounced for the warmer ices compared to the colder ones. This proposed re-structuring may also be responsible for the apparent initial increase in CO₂ in Fig. 8.13. Ice band strengths depend on ice structure (e.g. Öberg et al. 2007a) and this increase in CO₂ signal is most likely due to structural changes upon UV irradiation, modifying the strength of the CO₂ ice band, rather than more CO₂ molecules adsorbing. Similar changes in band strength have been previously observed in CO and in H₂O ices bombarded by ions (Loeffler et al. 2005; Gomis et al. 2004)

The importance of ice structure for the photodesorption yield is seen for CO as well, as discussed above. For CO₂ this importance is further shown by the experiment on a thermally annealed ice, where the photodesorption yield is $< 40\%$ of the yield of an amorphous ice. This is in contrast with the increased photodesorption yield for warm (40–60 K) ices, which are expected to have similar ice structures as the annealed ice. This new ice structure probably has a smaller effective ice surface compared to the 18 K amorphous ice, explaining the low photodesorption yield of the annealed ice. At temperatures above 40 K this decrease in surface does not affect the yield due to the high mobility of molecules in the ice. In summary, the CO₂ photodesorption yield is both temperature and structure dependent.

8.4.3 Astrophysical significance

8.4.3.1 CO and N₂

The relevance of CO photodesorption at 15 K is discussed in detail in Öberg et al. (2007b). The results here show that the previously reported yield is dependent on temperature and annealing between 15 and 27 K. The astrophysical significance of this dependence is probably limited, however. Because the desorption temperature and annealing temperature are similar, only a minor fraction of the pure CO ice will ever be annealed in astrophysical environments. Therefore the photodesorption yield derived at 15 K may be used for most purposes, also where a real temperature gradient exists.

While a temperature gradient may not significantly reduce the CO photodesorption yield, a layer of N₂ ice on top of the CO ice does. This layer may form either through later freeze-out or through selective photodesorption as shown in the experiments. Because of the peculiar photodesorption mechanism of CO ice, this study shows that a single monolayer of N₂ ice initially reduces the CO photodesorption yield with more than 80%. After a UV fluence of 8.5×10^{17} photons cm⁻² (corresponding to ~300 years of irradiation at cloud edges and ~3 million years in cloud cores), the yield has increased to 25% of the pure CO ice photodesorption yield, indicating that 25% of the N₂ layer is desorbed. This probably happens through CO co-desorption, since the photodesorption yield of pure N₂ is too low to account for the observed desorption. N₂ co-desorption is also observed in a mixed CO:N₂ ice where N₂ photodesorbs at a yield of 3×10^{-4} photon⁻¹. This is still a very low photodesorption yield compared to e.g. the CO photodesorption yield and its astrophysical significance is doubtful. Other non-thermal desorption mechanisms such as cosmic ray induced spot heating will likely be more important.

8.4.3.2 CO₂

At low temperatures and for thick ices the CO₂ photodesorption yield is $2.3(\pm 1.4) \times 10^{-3}$ photon⁻¹, which is almost identical to the CO photodesorption yield. Of the desorbed ice more than 50% desorbs in the form of CO₂, while the remaining 20–50% desorbs as CO. At higher temperatures some CO₂, up to 5%, also desorbs as O₂. This means that similar CO₂ and CO abundances are expected in regions where photodesorption dominates, assuming that the photodesorption yields of the two molecules are not much different for astrophysical ice morphologies compared to the pure ices studied here. This remains to be investigated, especially for the astrophysically relevant cases of CO ice on top of CO₂ ice, and CO:CO₂ and CO₂:H₂O mixtures (Pontoppidan et al. 2008). Based on our results we expect the recombined and thus energetic CO₂ molecule to penetrate at least as many CO ice layers during photodesorption as the 10 ML of CO₂ ice observed in this study, since CO forms a more loosely bound ice compared to CO₂. The behavior of CO₂ in a H₂O matrix is more difficult to predict. Hence, until such a laboratory study exists we recommend to use the equation presented here for CO₂ photodesorption, with the possible modification of taking into account that only a fraction of the ice is CO₂ ice.

In the regions in clouds and disks where ices begin to form, the ice thickness dependence of the CO₂ photodesorption needs to be taken into the account. As soon as the grain

is covered with less than 10 ML of CO₂ ice, the CO₂ photodesorption yield decreases considerably with ice thickness according to $1.2 \times 10^{-3} \times (1 - e^{-x/2.9}) + 1.1 \times 10^{-3} \times (1 - e^{-x/4.6})$ at 18 K, where x is the ice thickness and the two parts in the yield expression are due to CO₂ and CO desorption, respectively, during the irradiation of a CO₂ ice.

Heated or thermally annealed, i.e. heated and subsequently cooled down, CO₂ ice is observed toward many high- and low-mass protostars (Gerakines et al. 1999; Pontoppidan et al. 2008). Because of the irreversibility of the infrared spectroscopic signature of heated CO₂ ice, the two cannot be easily distinguished. At temperatures higher than the pure CO sublimation line at 25–30 K, the CO₂ photodesorption yield increases to $2.2 \times 10^{-3} \times (1 - e^{-x/5.8}) + 0.22 \times 10^{-3} \times x$ molecules photon⁻¹ for the CO₂ and the CO-fragment desorption, respectively. This results in a CO₂ yield increase of at most a factor of two. In addition, possible annealing may decrease the photodesorption yield to a value that is less than 40% of the cold amorphous CO₂ ice yield. The uncertainty in the photodesorption yield is thus an additional factor of 2–3 in thermally processed regions.

8.4.3.3 CO₂ astrophysical model

CO₂ is not detected directly in the radio regime due to its lack of a permanent dipole moment. It is instead traced by HCO₂⁺ toward e.g. the protostar L 1527 IRS. As a test case we use a simple model to investigate whether the recently observed HCO₂⁺ toward L 1527 IRS may be explained by photodesorption of CO₂ ice. Sakai et al. (2008) estimated the gas phase CO₂ abundance to be $> 2.9 \times 10^{-7}$ with respect to H₂, by using a simple reaction scheme for the CO₂ to HCO₂⁺ chemistry and assuming that the CO₂ is extended over the beam size of the IRAM 30 m telescope. Furlan et al. (2008) report a CO₂ ice abundance of 5×10^{-6} with respect to H₂ in L 1527 IRS, which is used in our model. This abundance is almost an order of magnitude lower than what is observed toward a large sample of low-mass protostars (Pontoppidan et al. 2008) and may be underestimated. The effect of increasing the CO₂ fractional abundance to $\sim 3 \times 10^{-5}$ is discussed below.

To simplify the calculation we assume that the average temperature is below 30 K and that the hydrogen density is constant throughout the envelope. At this low temperature thermal desorption of CO₂ is negligible and therefore the equilibrium gas phase abundance of CO₂ is dependent only on the UV photodesorption and the freeze-out rates. We also make the approximation that the total CO₂ abundance is constant throughout the envelope, since observations show that CO₂ forms in ices at the edges of clouds and does not increase deeper into the cloud (Pontoppidan 2006). The UV field is composed of the interstellar radiation field of 10^8 photons cm⁻² s⁻¹, which is attenuated with A_V , and the UV photons produced inside the cloud by cosmic rays. For a typical galactic cosmic ray flux, the resulting UV photon flux is of the order of 10^4 photons cm⁻² s⁻¹ with a factor of 3 uncertainty (Shen et al. 2004). Using our derived photodesorption yields and the estimated freeze-out rate of CO₂ we calculate the steady-state gas abundance of CO₂ as a function of A_V for small and large grains.

The photodesorption rates of CO₂ molecules from grain surfaces in molecules s⁻¹ due to external and cosmic ray induced UV photons, respectively, is described by

$$R_{\text{PD-ISRf}} = I_{\text{ISRf-FUV}} e^{-\gamma A_V} Y_{\text{pd}} (\pi a_{\text{gr}}^2), \quad (8.2)$$

$$R_{\text{PD-CR}} = I_{\text{CR-FUV}} Y_{\text{pd}} (\pi a_{\text{gr}}^2), \quad (8.3)$$

$$Y_{\text{pd}} = 0.0012(1 - e^{-x/2.9}), \quad (8.4)$$

$$x = n_{\text{CO}_2\text{-ice}} / (1 \times 10^{15} \times \pi a_{\text{gr}}^2 n_{\text{gr}}), \quad (8.5)$$

and

$$n_{\text{CO}_2\text{-ice}} = 5 \times 10^{-6} n_{\text{H}} - n_{\text{CO}_2\text{-gas}}, \quad (8.6)$$

where $I_{\text{PD-ISRf}}$ is the strength of the external irradiation field with energies 6-13.6 eV and $I_{\text{PD-FUV}}$ is the strength of the UV field due to cosmic rays. γ is a measure of UV extinction relative to visual extinction, which is ~ 2 for small interstellar grains and < 0.6 for grains of a few μm (Roberge et al. 1991; van Dishoeck et al. 2006), and a_{gr} is the grain radius. Y_{pd} is the experimentally determined CO₂ photodesorption yield for temperatures below 30 K (Eq. 8.4). x is the ice thickness in monolayers, which is defined in terms of the CO₂ ice abundance ($n_{\text{CO}_2\text{-ice}}$ in cm^{-3}), grain surface ($\pi a_{\text{gr}}^2 n_{\text{gr}}$ in $\text{cm}^2 \text{cm}^{-3}$) and amount of molecules per monolayer ($1 \times 10^{15} \text{cm}^{-2}$) in Eq. 8.5. Equation 8.6 states the relationship between the gas and ice phase CO₂ abundances ($n_{\text{CO}_2\text{-gas}}$ and $n_{\text{CO}_2\text{-ice}}$) when the total CO₂ abundance is $5 \times 10^{-6} n_{\text{H}}$ and n_{H} is set to $1 \times 10^4 \text{cm}^{-3}$.

The accretion rate of CO₂ molecules R_{acc} is a product of the molecular velocity, the grain surface, the sticking coefficients and the gas phase abundance of CO₂ according to

$$R_{\text{acc}} = -4.57 \times 10^4 \left(\frac{T}{m_{\text{CO}_2}} \right)^{\frac{1}{2}} (\pi a_{\text{gr}}^2) S n_{\text{CO}_2\text{-gas}}. \quad (8.7)$$

In Eq. 8.7 the gas temperature T is set to 10 K, m_{CO_2} is the CO₂ mass in atomic mass units, and S is the sticking coefficient, which is assumed to be 1 (Bisschop et al. 2006).

At steady-state the total photodesorption rate (i.e. the sum of Eqs. 8.2 and 8.3) is equal to the accretion rate. Figure 8.14 shows the resulting steady-state CO₂ gas phase abundance as a function of A_V for small classical 0.1 μm grains and after grain growth to a few μm . At $A_V < 3$ mag, CO₂ gas is photodissociated and the model is not valid there. Deep into the envelope, the gaseous CO₂ abundance due to cosmic ray induced photodesorption is $\sim 2 \times 10^{-8}$, which is about an order of magnitude lower than the observed CO₂ abundance. For small grains the external UV light also probably does not penetrate deep enough into the envelope to increase the average abundance significantly. On average about 1% of the total CO₂ abundance is kept in the gas phase through photodesorption. If the CO₂ ice abundance is increased to $\sim 3 \times 10^{-5}$, the CO₂ gas abundance increases by an order of magnitude at low extinctions. Deep into the cloud the abundance only increases by a factor of two, since the photodesorption rate only depends on the ice thickness up to ~ 10 ML. In cloud and envelope material dominated by small grains, photodesorption

probably does not explain gaseous CO_2 abundances of 5–10%, as observed toward L 1527 IRS, unless there is a strong internal UV source and the UV is scattered into the cavities created by the outflow (Spaans et al. 1995) where it can photodesorb material in the cavity walls. Indeed, L1527 IRS is well known for its prominent outflow and X shaped cavity wall on scales comparable to the IRAM 30m beam (MacLeod et al. 1994; Hogerheijde et al. 1998).

In disks, or in general where grain growth has occurred, the picture changes dramatically. Millimeter observations of outer disks show grain growth up to mm size (Rodmann et al. 2006; Lommen et al. 2007), and the UV irradiation may then penetrate deep into the disk releasing a high fraction of the CO_2 ice into the gas phase. At an A_V of 10 mag the CO_2 fractional abundance is now $\sim 1 \times 10^{-6}$ or 20% of the total CO_2 abundance. Similarly to the case with small grains, increasing the CO_2 ice abundance only increases the CO_2 gas abundance substantially at low extinctions.

This simple model thus shows that the experimentally determined CO_2 photodesorption yield is high enough to release large amounts of CO_2 ice into the gas phase if moderate grain growth has occurred. Even with small grains and no internal UV source except that produced by cosmic rays, photodesorption may keep up to $\sim 1\%$ of the total CO_2 abundance in the gas phase deep into cloud cores. This model stresses, once again, that photodesorption of ices needs to be taken into account when modeling gas-grain interactions.

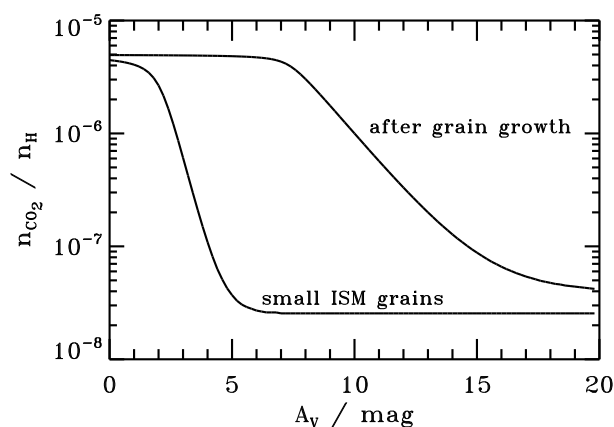


Figure 8.14 – The CO_2 gas phase abundance with respect to the total hydrogen ($\text{H}+\text{H}_2$) column density assuming a total (gas + ice) CO_2 abundance of 5×10^{-6} . The two tracks assume classical $0.1 \mu\text{m}$ grains and grain growth up to a few μm , respectively.

8.5 Conclusions

1. The CO photodesorption yield is temperature dependent between 15 and 27 K, which is described empirically by $2.7 \times 10^{-3} - (T - 15) \times 1.7 \times 10^{-4}$ molecules photon⁻¹. The anti-correlation between yield and temperature is probably due to ice re-structuring into a more compact configuration – the observed linearity may be coincidental, however. For most astrophysical applications the yield measured at 15 K is appropriate to use.
2. The CO photodesorption is initially reduced by more than 80% when the CO ice is covered by 1 ML of N₂ ice and decreases with UV fluence when mixed with N₂ due to surface build-up of N₂ ice, confirming that CO only desorbs from the ice surface.
3. N₂ co-desorbs with CO at 16 K in an ice mixture and in a layered ice with a yield of 3×10^{-4} molecules photon⁻¹.
4. A CO₂ photodesorption event starts with the photodissociation of a CO₂ molecule into CO and O. The fragments either desorb directly or react and recombine to form CO₂ and CO₃ before desorbing. The CO₃ yield is however less than 1% and the two main desorption products are CO and CO₂.
5. The CO₂ photodesorption yield is thickness dependent at all temperatures between 18 and 60 K. At 18–30 K the yield is well described by $1.2 \times 10^{-3} \times (1 - e^{-x/2.9}) + 1.1 \times 10^{-3} \times (1 - e^{-x/4.6})$, and at 40–60 K by $2.2 \times 10^{-3} \times (1 - e^{-x/5.8}) + 0.22 \times 10^{-3} \times x$ molecules photon⁻¹, where x is the ice thickness in monolayers. The first part in each yield equation is due to desorbing CO₂ molecules and the second part to desorbing CO molecules.
6. The thickness dependence of CO₂ photodesorption is understood from a mean-free-path perspective, where the different excited fragments travel a different average distance through the ice before being stopped. At higher temperatures, this mean free path increases due to increased mobility of molecules in the ice.
7. A simple model of an envelope using the observed CO₂ abundance in L 1527 IRS shows that CO₂ photodesorption can maintain CO₂ fractional abundances up to 1×10^{-6} in the gas phase at $A_V \sim 10$ mag after moderate grain growth and $2-3 \times 10^{-8}$ using small ISM grains. At lower extinctions the photodesorption is higher due to the external irradiation field and a high fraction of the total CO₂ ice abundance is maintained in the gas phase.

9 PHOTODESORPTION OF H₂O AND D₂O ICES

Gaseous H₂O has been detected in several cold astrophysical environments, where the observed abundances cannot be explained by thermal desorption of H₂O ice or by H₂O gas phase formation. These observations suggest an efficient non-thermal ice desorption mechanism. Here, we present experimentally determined UV photodesorption yields of H₂O and D₂O ice. The ice photodesorption is studied under ultra high vacuum conditions and at astrochemically relevant temperatures (18–100 K) using a hydrogen discharge lamp (7–10.5 eV), which simulates the interstellar UV field. The ice desorption is monitored using reflection absorption infrared spectroscopy of the ice and simultaneous mass spectrometry of the desorbed species. The photodesorption yield per incident photon, $Y_{\text{pd}}(T, x)$, is identical for H₂O and D₂O and its dependence on ice thickness and temperature is described empirically by $Y_{\text{pd}}(T, x) = Y_{\text{pd}}(T, x > 8)(1 - e^{-x/l(T)})$ where x is the ice thickness in monolayers (ML) and $l(T)$ a temperature dependent ice diffusion parameter that varies between ~ 1.3 ML at 30 K and 3.0 ML at 100 K. For thick ices the yield is linearly dependent on temperature due to increased diffusion of ice species such that $Y_{\text{pd}}(T, x > 8) = 10^{-3} (1.3 + 0.032 \times T)$ UV photon⁻¹, with a 60% uncertainty for the absolute yield. The increased diffusion also results in an increasing H₂O:OH desorption product ratio with temperature from 0.7:1.0 at 20 K to 2.0:1.2 at 100 K. The yield does not depend on the substrate, the UV photon flux or the UV fluence. The yield is also independent on the initial ice structure because UV photons efficiently amorphize H₂O ice. The results are consistent with theoretical predictions of H₂O photodesorption at low temperatures and partly in agreement with a previous experimental study. Applying the experimentally determined yield to a Herbig Ae/Be star+disk model shows that UV photodesorption of ices increases the H₂O content by orders of magnitude in the disk surface region compared to models where non-thermal desorption is ignored.

Öberg K. I., Visser, R., van Dishoeck, E. F. and Linnartz, H., 2009, ApJ, volume 93, pages 1209-1218

9.1 Introduction

H₂O, in solid or gaseous form, is one of the most common species in molecular clouds, typically only second to H₂ and sometimes to CO. This makes H₂O, together with CO, the dominant reservoir of oxygen during the critical stages of star formation (van Dishoeck et al. 1993). H₂O is thus a key molecule in astrochemical models and its partitioning between the grain and gas phase therefore has a large impact on the possible chemical pathways, including the formation of complex organics (Charnley et al. 1992; van Dishoeck 2006).

In cold, quiescent clouds H₂O forms through hydrogenation of O (O₂ or O₃) on cold (sub)micron-sized silicate grain surfaces forming icy layers (Tielens & Hagen 1982; Léger et al. 1985; Boogert & Ehrenfreund 2004; Miyauchi et al. 2008; Ioppolo et al. 2008). Other ices, like NH₃ and CH₄, probably form similarly, but observations show that H₂O is the main ice constituent in most lines of sight, with a typical abundance of 1×10^{-4} with respect to the number density of hydrogen nuclei. Gas phase H₂O formation is only efficient above 300 K (Elitzur & Watson 1978; Elitzur & de Jong 1978; Charnley 1997). At lower temperatures gas phase ion-molecule reactions maintain a low H₂O abundance around 10^{-7} (Bergin et al. 1995). Any higher abundances require either thermal desorption of the H₂O ice above ~ 100 K or non-thermal desorption at lower temperatures (Bergin et al. 1995; Fraser et al. 2001).

Gas phase H₂O is observed from the ground only with great difficulty. Still both isotopic and normal H₂O have been detected in astrophysical environments from ground based telescopes (Jacq et al. 1988; Knacke & Larson 1991; Cernicharo et al. 1990; Gensheimer et al. 1996; van der Tak et al. 2006). The *Infrared Space Observatory (ISO)* detected warm H₂O gas unambiguously toward several low- and high-mass young stellar objects (van Dishoeck & Helmich 1996; Ceccarelli et al. 1999; Nisini et al. 1999; Boonman & van Dishoeck 2003). *ISO* was followed by two other space based telescopes, the *Submillimeter Wave Astronomy Satellite (SWAS)* and *Odin*. In difference to *ISO*, *SWAS* and *Odin* are capable of detecting the fundamental ortho-H₂O 1₁₀ – 1₀₁ transition at 538.3 μm and hence probe cold H₂O gas (Melnick et al. 2000; Hjalmarson et al. 2003). Both telescopes have observed H₂O gas toward star forming regions and detected the expected enhancements near protostars and in outflows where thermal ice desorption or gas phase formation is possible (Hjalmarson et al. 2003; Franklin et al. 2008). Critical for the present study, H₂O gas has also been detected toward photon dominated regions (Snell et al. 2000; Wilson et al. 2003) and is also more abundant toward diffuse than toward dense clouds. These two results point to an efficient ice photodesorption mechanism (Melnick & Bergin 2005). The importance of photodesorption at the edges of clouds has more recently been modeled by Hollenbach et al. (2009). They find that the H₂O gas abundance is enhanced by orders of magnitude at $A_V=2-8$ mag into the cloud when including photodesorption of H₂O ice in their model at a rate derived from the results by Westley et al. (1995a). Circumstellar disks is a second region where the impact of photodesorption is expected to be large. Willacy & Langer (2000) showed that a photodesorption yield of 10^{-3} molecules per photon is enough to explain observed gas-phase CO abundances in the outer regions of flared disks. Employing a similar photodesorption yield for H₂O ice, the disk mod-

els of Dominik et al. (2005) and Willacy (2007) both predict the existence of significant amounts of gas phase H_2O in a layer above the midplane region.

With the advent of the *Herschel Space Observatory*, cold and warm H_2O gas observations on scales of protostellar envelopes and disks will for the first time become possible (van Kempen et al. 2008). In preparation for these and other observations, and to interpret data from *Odin* and *SWAS*, non-thermal processes need to be better understood. These non-thermal desorption processes include ion/electron sputtering, desorption due to the release of chemical energy and photodesorption. Of these, sputtering of ice by electrons and ions, has been investigated over a range of conditions during the past few decades (e.g. Brown et al. 1978; Famá et al. 2008) and the dependencies of the yield on e.g. ice temperature, projectile type and energy are rather well understood. In contrast, only a handful of laboratory studies exists on the efficiency of ice photodesorption (e.g. Westley et al. 1995a; Öberg et al. 2007b, 2009b).

Westley et al. (1995a,c) determined the photodesorption rate of H_2O ice experimentally to be $3 - 8 \times 10^{-3}$ molecules per UV photon for a 500 nm thick H_2O ice. In their experiment the photodesorption rate depends on UV fluence as well as temperature. The photon fluence dependence, together with the observed gas phase H_2 and O_2 during irradiation, was taken as evidence that H_2O photodesorption at low temperatures mainly occurs through desorption of photoproducts rather than of H_2O itself. Several questions remain regarding the applicability of their study to astrophysical regions due to the uncertainty of the proposed mechanism. In addition, their dependence on photon fluence is not reproduced in recent CO and CO_2 photodesorption experiments and cannot easily be explained theoretically (Andersson et al. 2006; Öberg et al. 2007b; Andersson & van Dishoeck 2008; Öberg et al. 2009b).

In a different experiment Yabushita et al. (2006) investigated H-atom photodesorption from H_2O ice during irradiation at 157 and 193 nm using time-of-flight mass spectrometry. They found that the temperature and hence the origin of the desorbed H atoms varies significantly between crystalline and amorphous ice at 100 K. This indicates that photodesorption depends on the ice morphology, which is in contrast to the findings of Westley et al. (1995a). Desorption of recombined D_2 during irradiation of D_2O ice at 12 K has also been found by (Watanabe et al. 2000). Both experiments provide valuable input for models, but cannot directly be used to determine the total H_2O photodesorption rate.

UV irradiation of H_2O ice results in photochemistry products as well as photodesorption. A variety of photochemistry products are readily produced during irradiation of H_2O dominated ice mixtures (D'Hendecourt et al. 1982; Allamandola et al. 1988). Pure H_2O ice photolysis results in the production of H_2O_2 , OH radicals and HO_2 at 10 K (Gerakines et al. 1996; Westley et al. 1995c). After a fluence of $\sim 5 \times 10^{18}$ UV photons cm^{-2} Gerakines et al. (1996) found that the final band area of the formed H_2O_2 was only $\sim 0.25\%$ compared to the H_2O band area and the OH band area was even smaller. No study exists for higher temperatures, but as photodissociation fragments become more mobile, e.g. O_2 formation would be expected (Westley et al. 1995a).

Only a handful models of ice photodesorption exists in the literature. Andersson et al. (2006); Andersson & van Dishoeck (2008) have investigated H_2O photochemistry and

photodesorption theoretically using classical dynamics calculations. In the simulations they followed H₂O dissociation fragments, after the absorption of a UV photon, in the top six monolayers of both crystalline and amorphous H₂O ice at 10 K. For each ice they found that desorption of H₂O has a low probability (less than 0.5% yield per absorbed UV photon) for both types of ice. The total H₂O photodesorption yield from the top six ice layers was calculated to be $\sim 4 \times 10^{-4}$ molecules per incident UV photon.

In the present study we aim at determining experimentally the photodesorption yields of H₂O and D₂O and their dependencies on ice thickness, temperature, morphology, UV flux and fluence as well as irradiation time. We use these results as input for an astrophysical model of a typical circumstellar disk to estimate the impact of photodesorption and to predict the observable column densities of H₂O as relevant to e.g. upcoming *Herschel* programs.

9.2 Experiments and data analysis

9.2.1 Experiments

The experimental set-up (CRYOPAD) is described in detail by Fuchs et al. (2006) and Öberg et al. (2007b). The set-up allows simultaneous detection of molecules in the gas phase by quadrupole mass spectrometry (QMS) and in the ice by reflection absorption infrared spectroscopy (RAIRS) using a Fourier transform infrared (FTIR) spectrometer. The FTIR covers 1200 – 4000 cm⁻¹ with a typical spectral resolution of 1 cm⁻¹. The experimental procedure to derive photodesorption yields is described extensively in Öberg et al. (2009b), where the photodesorption measurements of CO, N₂ and CO₂ ices are reported. Here the procedure is summarized and only modifications to the procedure are described in detail.

In the experiments, H₂O and D₂O ices of 1.5–28 monolayers (ML) are grown under ultra high vacuum conditions ($P \sim 10^{-9}$ mbar with the background pressure dominated by H₂) at 18 – 100 K on a gold substrate that is mounted on the coldfinger of a He cryostat. The H₂O sample is prepared from de-ionized H₂O that is purified through at least three freeze-thaw cycles. The D₂O sample is measured to have a 90% isotopic purity and is similarly freeze-thawed before use.

Within the experimental uncertainties, we find that there is no difference in the photodesorption rate of 9.5 ML D₂O ice deposited on top of 48 ML H₂O ice compared with 8.9 ML D₂O ice deposited directly onto the gold substrate. Since the nature of the substrate has no influence on the photodesorption, all other experiments are carried out with H₂O or D₂O ices deposited directly on the gold substrate.

The ice films are irradiated at normal or 45° incidence with UV light from a broadband hydrogen microwave discharge lamp, which peaks around Ly α at 121 nm and covers 115–170 nm or 7–10.5 eV (Muñoz Caro & Schutte 2003). The lamp UV photon flux is varied between 1.1 and 5.0×10^{13} photons cm⁻² s⁻¹ in the different experiments. The lamp flux is measured by a NIST calibrated silicon diode and actinometry as described in Öberg et al. (2009b).

Table 9.1. Summary of H₂O and D₂O experiments

No.	Species	Temp. (K)	Thick. (ML)	UV Flux (10^{13} cm ⁻² s ⁻¹)
1	H ₂ O	18	14	2.3
2	H ₂ O	18	15	3.5
3	H ₂ O	100	12	1.1
4	H ₂ O	100	13	5.0
5	H ₂ O	100	17	2.3
6	D ₂ O	18	10	2.3
7	D ₂ O	18	11	3.5
8	D ₂ O	18	17	2.3
9	D ₂ O	30	2.1	3.5
10	D ₂ O	30	3.2	3.5
11	D ₂ O	30	8.9	3.5
12	D ₂ O	30	11	3.5
13	D ₂ O	40	6	1.7
14	D ₂ O	40	14	1.1
15	D ₂ O	40	14	3.5
16	D ₂ O	60	9.6	1.1
17	D ₂ O	60	17	3.5
18	D ₂ O	100	1.5	1.9
19	D ₂ O	100	2.3	1.8
20	D ₂ O	100	5.1	2.3
21	D ₂ O	100	5.3	2.3
22	D ₂ O	100	6.8	1.8
23	D ₂ O	100	12	5.0
24	D ₂ O	100	13	1.1
25	D ₂ O	100	14	3.5
26	D ₂ O	100	16	2.3
27	D ₂ O	100	28	1.7
28	D ₂ O ^a	30	14	2.3
29	H ₂ ¹⁸ O	20	14	5.0
30	H ₂ ¹⁸ O	30	14	5.0
31	H ₂ ¹⁸ O	100	14	5.0
32	D ₂ O/H ₂ O ^b	30	9.5/48	2.3
33	N ₂ /D ₂ O ^b	18	20/14	2.3

^aAnnealed at 100 K for 1 hour^bIce layers

Table 9.1 summarizes the experiments. The majority of the photodesorption experiments is carried out with D₂O ice. These experiments are complimented with H₂O and H₂¹⁸O experiments to test isotope effects and to ensure the validity of mass spectrometric detections of OH (OD) and H₂O (D₂O) fragments. Layered experiments with H₂O and D₂O at 30 and 100 K and with N₂ on top of D₂O at 18 K are performed to check for substrate effects and to determine the ice loss behaviour when desorption is hindered.

9.2.2 Data Analysis

The UV induced ice loss rate during each H₂O and D₂O experiment is determined by RAIRS of the ice as a function of UV fluence. The intensity of the RAIRS profile is linearly correlated with the ice layer thickness up to ~20 ML, but the RAIRS profile can be used up to 50 ML for analysis as long as the non-linear growth above 20 ML is taken into account (Öberg et al. 2009b). One monolayer is generally taken to consist of $\sim 10^{15}$ molecules cm⁻² and the loss yield, in molecules photon⁻¹, of the original ice is subsequently derived from the intensity loss in the RAIR spectra as a function of fluence.

The determined ice loss yield is not necessarily the photodesorption yield. H₂O has only dissociative transitions in the wavelength region of the lamp. Hence, the UV irradiation induces photodesorption as well as photochemistry (Gerakines et al. 1996; Westley et al. 1995a). UV irradiation may also induce structural changes in the ice that modify the infrared spectral features. These bulk processes, photolysis and rearrangement, are separated from the photodesorption by exploiting the different kinetic order behavior of bulk processes and surface desorption, i.e. first versus zeroth order processes. This method is described in detail in Öberg et al. (2009b).

Using RAIRS to determine the desorption of molecules depends on a reliable conversion between the ice infrared absorbance and the amount of ice molecules. Due to the fact that all ice measurements are done using RAIRS, the ice thickness cannot be estimated from previously determined ice transmission band strengths. In Öberg et al. (2009b), the CO and CO₂ appropriate RAIRS band strengths are reported. The H₂O and D₂O band strengths are estimated by assuming that the relative band strengths of CO, CO₂ and H₂O ice are the same in transmission and reflection-absorption spectra. This is found to be accurate within a factor of two by Ioppolo et al. (2008). The thickness uncertainty is then ~50%. For the conversion between H₂O and CO and CO₂ band strengths, the measured band strengths of Hudgins et al. (1993) are used after modification as suggested by Boogert et al. (1997). The relative band strengths of H₂O and D₂O were measured by Venyaminov & Prendergast (1997). This results in H₂O and D₂O stretching band strengths of 0.95 and 0.68 cm⁻¹ ML⁻¹, respectively, for our set-up. These band strengths are converted to cm molecule⁻¹ assuming a monolayer density of 10¹⁵ molecules ML⁻¹ cm⁻².

Kinetic modeling of the integrated RAIRS profiles as a function of UV fluence and the determined band strengths together provide a total ice photodesorption yield. The simultaneous mass spectrometry of gas phase molecules during irradiation reveals the nature of the desorbed species, i.e. what proportion of H₂O ice desorbs as H₂O molecules versus photo-produced radicals and molecules. This is limited by the fact that less volatile molecules adsorb onto the heating shield and other semi-cold surfaces inside the experiment before reaching the mass spectrometer. Hence, the relative abundance of species with very different cryopumping rates, like H₂ and H₂O, cannot be derived. It is however possible to estimate the ratio of the predicted main desorption species: H₂O and OH.

The main sources of uncertainty in these experiments are the photon flux at the sample surface and ice thickness calibrations of ~30% and 50%, respectively. In addition, from repeated experiments, the H₂O experimental results vary with 20%. The total uncer-

tainty is hence $\sim 60\%$ for the total photodesorption rate. The relative desorption yields of different desorption products is more uncertain due to the additional assumptions that go into their derivation, i.e. that the products have similar pumping rates and QMS detection efficiencies. We estimate that the relative desorption yields thus have $\sim 30\%$ uncertainty in addition to the uncertainty of the total photodesorption yield.

9.3 Results

9.3.1 The photodesorption process and products

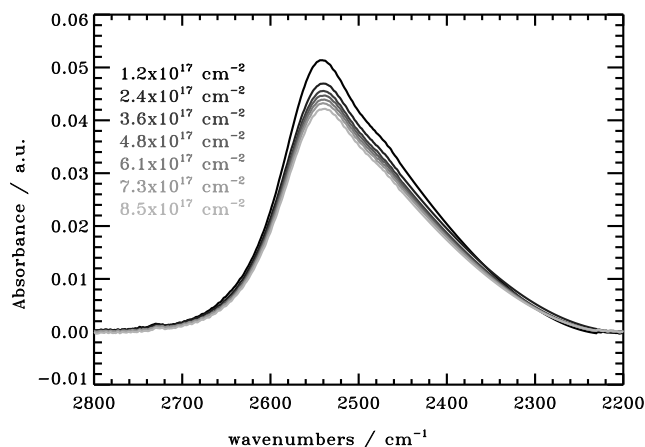


Figure 9.1 – Spectra of the D_2O stretching mode at 40 K as a function of UV fluence. The decreasing ice loss yield with fluence is due to the fact that ice is lost through a combination of bulk photolysis and photodesorption. The small bump at 2730 cm^{-1} is probably caused by the free OD stretch.

Figure 9.1 shows the RAIR spectrum of the D_2O stretching band at 40 K as a function of UV fluence. At 40 K the UV photons simultaneously induce dissociation of bulk D_2O ice and desorption of surface molecules. This is clearly seen in Fig. 9.2, where the ice thickness is plotted versus UV fluence. The ice loss is modelled by a combination of an exponential function and a linear function, where the exponential function describes the photolysis of bulk D_2O as a first order process similarly to Cottin et al. (2003). The linear part of the ice loss is interpreted as photodesorption of surface molecules, which should be a zeroth-order process (Öberg et al. 2007b). To test that this model holds, a D_2O ice is irradiated at 18 K when covered by a thick N_2 ice, which hinders desorption. The ice loss curve is then very well fitted ($\chi^2=1.8$ for 13 data points) by the exponential function derived from a bare 18 K ice. This shows that the observed exponential decay is indeed due to bulk photolysis with a possible contribution from ice rearrangement. As discussed below the ice structure is affected by the UV irradiation, but this rearrangement

seems complete within an UV fluence of 1×10^{17} photons cm^{-2} . It may hence contribute somewhat to the exponential decay of the RAIRS profile, but is completely filtered out from the photodesorption rate determination.

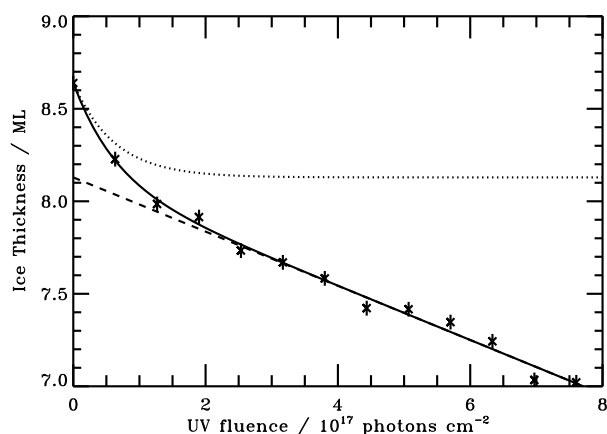


Figure 9.2 – The D₂O ice layer thickness as a function of UV fluence together with the fit (solid line), which is split up in ice loss due to bulk photolysis (dotted line) and photodesorption (dashed line). The fitted bulk photolysis contribution is offset for visibility.

There are no other species than H₂O (D₂O) visible in the RAIR spectra at any temperature. OH (OD) formation cannot be excluded, however, due to the spectral overlap of OH (OD) and H₂O (D₂O) transitions. Despite this overlap, photolysis of H₂O into OH will result in a measured decrease of the H₂O stretching band area. This is both because of the expected lower band strength of OH compared to H₂O and because the remaining H₂O stretching band strength decreases when the H₂O network is disturbed by other molecules or fragments (Öberg et al. 2007a; Bouwman et al. 2007). The lack of H₂O₂ formation is in contrast to e.g. Gerakines et al. (1996). This is not a contradictory result however, since less than 0.1% of the H₂O ice is expected to be converted after a similar fluence, which is close to the detection limit here for the strongest H₂O₂ band at 2850 cm^{-1} (Giguère & Harvey 1959).

During irradiation H₂ (D₂) is always detected by the mass spectrometer. At the highest fluxes OH (OD) and H₂O (D₂O) are detected as well. A 14 ML H₂¹⁸O ice is irradiated at 20, 30 and 100 K while acquiring mass spectra (Fig. 9.3) to quantify the relative desorption amounts of OH and H₂O without any overlap with background H₂O. The figure shows that the desorbing fraction of OH and H₂O changes somewhat with temperature from 1.0:0.7 at 20 K to 1.2:1.4 at 30 K to 1.2:2.0 at 100 K. No other species are observed at 20 and 30 K. In contrast, at 100 K, O₂ is photodesorbed as well. It is important to note that O₂ and H₂O have very different cryopumping rates and hence their relative mass spectromeric signals are not representative of their relative desorption rates. The upper limit of O₂ desorption is estimated from the fact that a factor of 1.9 more OH and H₂O is detected at 100 K compared to at 20 K, while the total photodesorption rate from RAIRS increases by a factor of 2.4. Hence at most one fifth of the H₂O photodesorbs as O₂ at high temperatures. Desorption of H₂O₂ cannot be excluded, even though it is

not detected, since it is notoriously difficult to detect with a QMS. No build-up of H_2O_2 is observed in the ice, which makes it unlikely that a large part of the ice is desorbed in the form of H_2O_2 . Disregarding the small amount of H_2O that does not desorb as either OH or H_2O , the H_2O yield relative to the total photodesorption yield is fitted linearly as a function of temperature for the 14 ML thick ice. This empirical fit yields an expression for the H_2O yield, $Y_{\text{pd,H}_2\text{O}}$, as a function of the total photodesorption yield, Y_{pd} :

$$Y_{\text{pd,H}_2\text{O}} = f_{\text{H}_2\text{O}} \times Y_{\text{pd}} \quad (9.1)$$

$$f_{\text{H}_2\text{O}} = (0.42 \pm 0.07) + (0.002 \pm 0.001) \times T \quad (9.2)$$

$$f_{\text{H}_2\text{O}} + f_{\text{OH}} \sim 1 \quad (9.3)$$

where f_x is the fraction of the total photodesorption that occurs through species x . The relative yields are probably somewhat thickness dependent (Andersson et al. 2006), but due to experimental constraints it is not possible to probe the relative yields for thinner ices.

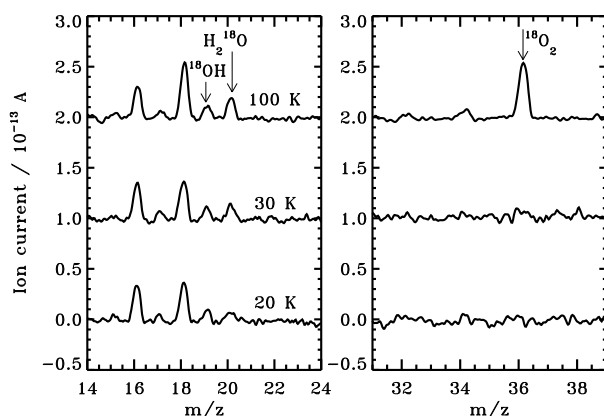


Figure 9.3 – The mass spectra recorded during irradiation of a 14 ML thick H_2^{18}O ice at 20, 30 and 100 K. In addition to photodesorbed ice product signals, background signals from H_2O , OH, O and O_2 are also seen.

9.3.2 Yield dependencies on temperature, fluence, ice thickness, flux and isotope

9.3.2.1 Temperature and photon fluence

Figure 9.4 shows the combined bulk photolysis and photodesorption for ~ 10 ML thick D_2O ices between 18 and 100 K. The ice loss is dominated by bulk photolysis at low temperatures and by photodesorption at higher temperatures. This conclusion follows from the observed facts that 1) the degree of steady state photolysis decreases with temperature and 2) that the photodesorption yield per incident photon, as measured by the slope of the

linear part of the fit, increases with temperature. This increase in photodesorption yield with temperature is shown explicitly in Fig. 9.5a. Between 18 and 100 K the dependence of the photodesorption yield on temperature for thick ices (>8 ML) is empirically fitted with a linear function:

$$Y_{\text{pd}}(T, x > 8) = 10^{-3} (1.3 (\pm 0.4) + 0.032 (\pm 0.008) \times T) \quad (9.4)$$

where T is the temperature in K and x the ice thickness in ML. The uncertainties are the model fit errors – the total uncertainty of the yield is 60% as stated above.

Figure 9.4 also shows that the onset of photodesorption is immediate, i.e. there is no fluence dependence, which is opposite to what was observed by Westley et al. (1995a). This difference may be explained by a non-linear H₂O freeze-out during the experiment, which is observed in this experiment (Fig. 9.6) and probably present in the Westley experiment as well. Even under UHV conditions there is always some H₂O present in the vacuum chamber. In our experiment this leads to an ice deposition rate of $\sim 0.1 \text{ ML hr}^{-1}$ at equilibrium, but up to 1 ML hr^{-1} is deposited during the first hour after cool down, which is of the same order as the photodesorption rate presented in Westley et al. (1995a). In their set-up it would not have been possible to separate this increased freeze-out rate from a lower desorption rate at the beginning of each experiment. This problem is circumvented here by using D₂O for most experiments and by letting the H₂O freeze-out reach equilibrium before starting the experiment.

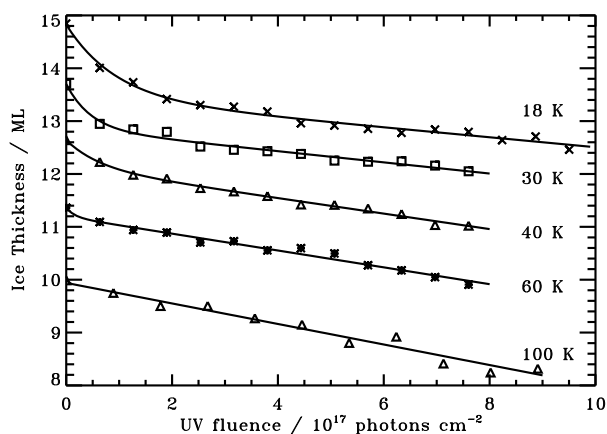


Figure 9.4 – Ice thickness (in ML) versus photon fluence (in $10^{17} \text{ photons cm}^{-2}$) for $\sim 10 \text{ ML D}_2\text{O}$ ices at different temperatures, displaying the temperature dependent degree of ice bulk photolysis versus ice photodesorption. The curves are offset for visibility. At lower temperatures the bulk photolysis dominates the ice loss, while it is not visible above 60 K. Simultaneously the photodesorption rate, the slope of the linear part of the ice loss, increases with temperature.

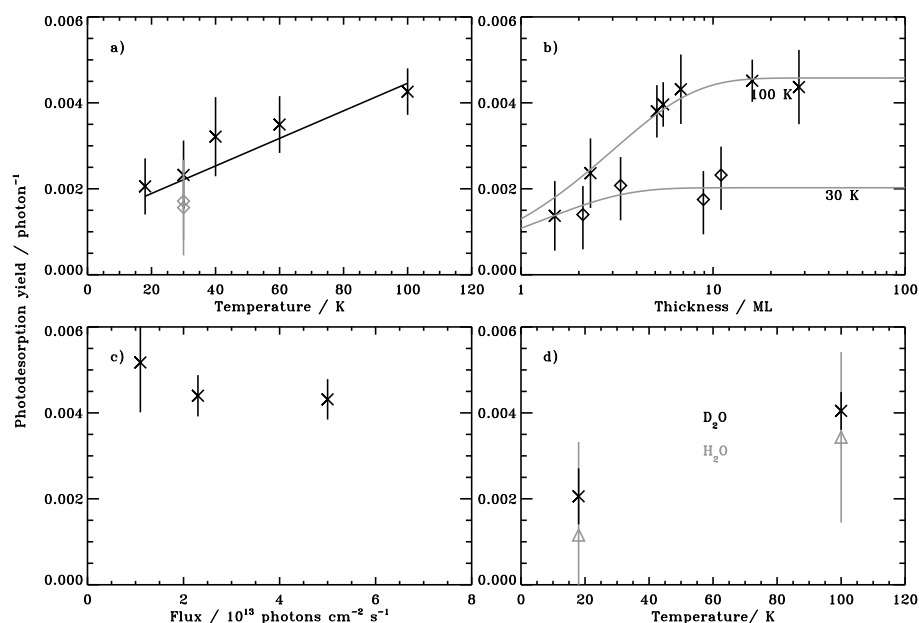


Figure 9.5 – The D_2O photodesorption yield as a function of temperature (a), ice thickness (b), lamp flux (c) and isotope (d). In the temperature plot (a) the ices are ~ 10 ML thick. The two grey diamonds mark the desorption rate from a $D_2O:H_2O$ layered ice and an annealed ice. In panel (b) the thickness dependence is plotted and fitted for ices at 30 and 100 K. In panel (c) the ices are 12–16 ML thick and irradiated at 100 K. The experiments marked with grey triangles in panel (d) are carried out with H_2O instead of D_2O .

9.3.2.2 Substrate and ice structure effects

In Fig. 9.5a one of the two additional points at 30 K represents the yield from a 9.5 ML D_2O ice deposited on top of a H_2O ice layer, showing that the substrate has no effect on the desorption yield. At 100 K this cannot be investigated due to mixing of the two layered ices, but D_2O experiments with different ice thicknesses indicate that the substrate has no effect at any temperature for ices thicker than 2 ML (Fig. 9.5b).

The structure independence seen by Westley et al. (1995a) is also confirmed here for a 30 K ice that is annealed at 100 K, until the spectra display a low frequency shoulder typical for crystalline ice (Hagen 1981), and is subsequently cooled down (the second additional point at 30 K in Fig. 9.5a). Figure 9.7 shows that this can be explained by the fact that the annealed ice returns to an amorphous state upon irradiation with less than 10^{16} UV photons. At 100 K the irradiation does not yield amorphous ice, probably because the temperature is high enough for displaced molecules to diffuse back into a crystalline structure.

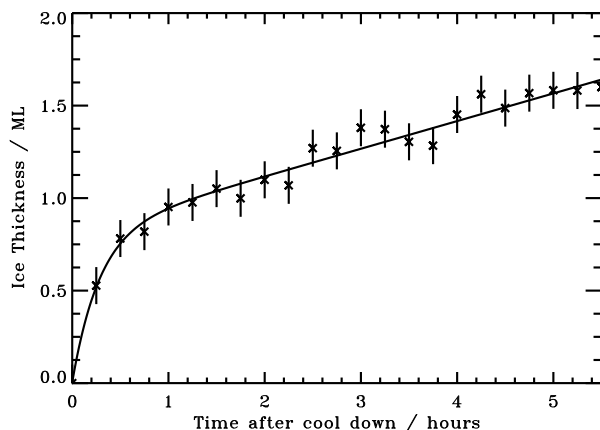


Figure 9.6 – The build-up of H₂O following cool down to 18 K (without UV irradiation), which is due to the small H₂O contamination always present, also under ultra high vacuum conditions. The non-linear behavior is a result of the time required to reach steady-state between H₂O freeze-out on the substrate, the desorption of adsorbed H₂O from the chamber walls and the H₂O pumping.

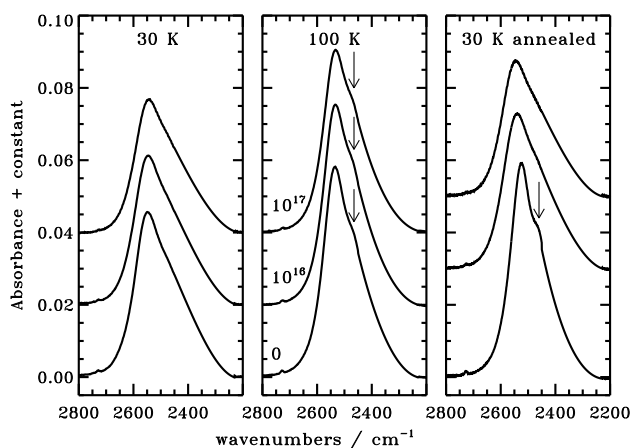


Figure 9.7 – Spectra of ices at 30 K (left) and 100 K (middle), and at 30 K, but deposited at 100 K (right), before onset of irradiation and after irradiation by $\sim 10^{16}$ and 10^{17} photons cm^{-2} as indicated in the middle figure. Note the disappearance of the crystalline feature around 2460 cm^{-1} (marked with arrows) with increasing UV fluence for the annealed ice.

9.3.2.3 Ice thickness

At 100 K, where photodesorption completely dominates over bulk photolysis, there is no photodesorption yield dependence on ice thickness for D₂O ices between 8 and 28 ML

(Fig. 9.5b) suggesting that the H₂O ice photodesorption is only important in the top few layers. At 30 K the photodesorption yield is constant down to at least 3 ML. At both temperatures the thickness dependence is fitted by a function of the type

$$Y(T, x) = Y_{\text{pd}}(T, x > 8)(1 - e^{-x/l(T)}) \quad (9.5)$$

where $Y(T, x)$ is the thickness and temperature dependent photodesorption yield, $Y_{\text{pd}}(T, x > 8)$ the yield for thick ices at a certain temperature, x the ice thickness and $l(T)$ is an ice diffusion parameter, whose origin is discussed further below. The IDL routine *mpfit* is used to fit the data with the results: $l(100 \text{ K}) = 3.0 \pm 1.0 \text{ ML}$ and $l(30 \text{ K}) < 2.7 \text{ ML}$, with the best fit of $l(30 \text{ K}) = 1.3 \text{ ML}$ shown in Fig. 9.5b. Thus photodesorption occurs deeper in the ice at 100 K compared to at 30 K by at least a factor of two. Extrapolating this to lower temperatures gives

$$l(T) \sim 0.6 + 0.024 \times T \quad (9.6)$$

9.3.2.4 Lamp flux

The independence of the photodesorption yield on lamp flux found by Westley et al. (1995a) for higher fluxes ($1 - 5 \times 10^{14} \text{ photons cm}^{-2} \text{ s}^{-1}$) is also seen in this study between $1.1 - 5.0 \times 10^{13} \text{ photons cm}^{-2} \text{ s}^{-1}$ for different temperatures and is shown for 100 K ices in Fig. 9.5c.

9.3.2.5 H₂O versus D₂O

Within the experimental uncertainties, there is no difference between the H₂O and D₂O photodesorption yields at 18 or 100 K (Fig. 9.5d). It should be noted that at 18 K the photodesorption yield of H₂O is highly uncertain, because the H₂O freeze-out rate dominates over the photodesorption rate during the experiment. Nevertheless, these experiments support the direct applicability of above results, on D₂O ices, to H₂O ices.

9.4 Discussion

9.4.1 The H₂O photodesorption mechanism

The UV photodesorption mechanism of H₂O ice does not depend on flux or substrate and is hence most likely due to direct absorption of UV light by H₂O molecules, resulting in dissociation of the molecule into fragments with excess energy. The experiments show that once dissociated one of four different outcomes ensues: the dissociated fragments (i) photodesorb directly, (ii) recombine and photodesorb or kick out a surface H₂O molecule, (iii) freeze out in the ice or (iv) recombine and freeze out in the ice. These are the same outcomes described in Andersson et al. (2006) when performing molecular dynamics simulations on H₂O photodesorption. At high temperatures (100 K) the dissociated OH or O fragments are also mobile enough to recombine to e.g. O₂.

The importance of the different pathways depends both on the temperature and where in the ice the molecule is dissociated. With increasing temperature the mobility of molecules, atoms and radicals is expected to increase. This, among other things, increases the reaction probability of OH and H. Assuming the same dissociation yield at all temperatures, the amount of radicals in the ice should then decrease with temperature since the increased mobility with temperature increases the recombination rate. This agrees well with the observed decrease in the steady state photolysis yield between 18 to 100 K (Fig. 9.4). The increased recombination rate also explains the increasing H₂O/OH gas phase ratio with temperature during photodesorption. Finally, the increased mobility of OH may also account for the observed photodesorbed O₂ at 100 K and its absence at temperatures below 30 K. Although it cannot be excluded that the O₂ forms also at lower temperatures and is thermally desorbed following formation above 30 K (Acharyya et al. 2007).

The increased mobility with temperature is also reflected in the ice thickness experiments, where the photodesorption occurs down to greater depths in the ice at 100 K compared to 30 K. The factor of two or larger penetration depth into the ice at 100 K compared to 30 K (Fig. 9.5b) agrees well with the increase of the photodesorption yield between 30 and 100 K (Fig. 9.5a). The increased photodesorption yield with temperature is then most likely due to an increased mobility rather than the overcoming of reaction barriers, as suggested by Westley et al. (1995c).

The simulations of Andersson et al. (2006) for an ice at 10 K indicate that photodesorption is only efficient in the top 2–3 layers for cold ices. At larger depths freeze-out of the dissociation products completely dominates. This is in excellent agreement with the results of the thickness dependent experiments at 30 K, where photodesorption is only important in the top 3 ML. The simulation is run at ps time scales, while the experiments cover several hours. The agreement for low temperatures between theory and experiment hence indicates that only short time scale processes matter for determining the photodesorption yield at temperatures below 30 K. At higher temperatures longer time scale processes, like thermal diffusion and desorption, increase in importance.

As mentioned above, the depth at which photodesorption occurs increases with temperature, but still there is a certain ice depth where freeze-out of the recombined H₂O is the only outcome. At 100 K the measurements are accurate enough to confirm that the mobility of the molecules following photodissociation and recombination is well described by a mean-free-path type model $c \times (1 - e^{-x/l(T)})$, where x is the ice thickness, l the diffusion mean-free-path and c the maximum desorption yield for infinitely thick ice. This is also the case for CO₂ photodesorption fragments (Öberg et al. 2009b) and may hence be a universal feature for molecules that photodesorb following dissociation. This mean-free-path behaviour is best explained with the desorption of the energetic photodissociation product or recombined molecule itself, but does not exclude the other outcome of the molecular simulations, i.e. that H₂O molecules also desorb indirectly from a kick of a H atom, which originates from photodissociation of another H₂O molecule.

9.4.2 Comparison with previous experiments

The results here agree on several important points with those of Westley et al. (1995a,c). The maximum total photodesorption yields ($\text{H}_2\text{O} + \text{OH}$) are the same within the reported uncertainties of both experiments. The determined photodesorption yield is likely a robust value, which is not significantly affected by different lamp spectral energy distributions, order of magnitude different UV fluxes and ice thicknesses. The present study also agrees with Westley et al. (1995a,c) on the photodesorption yield dependence on temperature and on the identification of the main desorption products – H_2 , O_2 and H_2O – with the one exception that we also detect OH.

The apparent fluence dependence in the Westley experiment can be explained with H_2O freeze-out during the early stages of the experiment, especially since they mention a large H_2O background pressure in their experiment. This is also in agreement with the mass spectrometer measurements of desorbed species shown in their paper (H_2 and O_2), which do not show any fluence dependent yields. The apparent fluence dependence led Westley et al. (1995a) to suggest that at low temperatures desorption occurs through reactions between O and OH. They subsequently claimed that while low temperature photodesorption occurs through photochemistry, high temperature photodesorption is a direct process. From the experiments here it is more likely that both low and high temperature photodesorption processes are dominated by direct photodesorption, but at high temperatures there is some additional desorption due to photochemistry of OH and O fragments.

Ion sputtering of ices has been more thoroughly investigated than ice photodesorption and recent experiments by Famá et al. (2008) on the temperature dependence of ion sputtering of H_2O ice suggest that the desorption mechanism is comparable for photodesorption and ion sputtering following the initial excitation by a photon or an ion. In particular, in both photodesorption and ion sputtering experiments, the desorption seems highly dependent on the formation and subsequent behavior of radicals and molecular products in the ice. More results are however required on e.g. the thickness dependence and the resulting desorption products during ion sputtering to make an actual comparison between the two processes. The absolute ion-sputtering yield of H_2O depends on both the ion energy and ionic species, but it is generally a factor of 10^3 to 10^4 higher than photodesorption yields i.e. close to unity. When evaluating the importance of the two processes in an astrophysical setting, it is important to note that the ion flux in most regions is orders of magnitude lower than the UV flux.

9.4.3 Astrophysical consequences

This study shows that pure H_2O ice photodesorbs directly or indirectly following fast intermediate photochemistry during which the photodissociated fragments recombine. The mechanism hence does not depend on the photon flux level or on build-up of radicals in the ice. This means that the yield derived in the laboratory can be directly applied to astrophysical environments. Deep into clouds and disks the rate may be considerably reduced due to e.g. CO ice covers. At the edges of clouds and disks, where other ices have not yet formed at large abundances, the rate for pure H_2O ice is directly applicable.

Here, as a test case, it is applied to the disk surrounding a Herbig Ae/Be star using models developed by Dullemond et al. (2001); Dullemond & Dominik (2004) to fit the observed spectral energy distributions of these objects. In the model the physical disk model is static and the chemistry is kept very simple, only including H₂O freeze-out, thermal and non-thermal desorption, and no gas phase chemical network except for the recombination of OH to form H₂O.

The model star has a mass of 2.5 M_⊙, a radius of 2.0 R_⊙ and an effective temperature of 10500 K, typical of a Herbig Ae/Be star, and it emits a pure blackbody spectrum. The accompanying disk has a mass of 0.01 M_⊙, with an R^{-1} surface density profile, and an outer radius of 300 AU. To avoid a sharp truncation, the surface density decreases as R^{-12} beyond the outer radius. The inner radius is set by a dust evaporation temperature of 1700 K. The radiation field and dust temperature throughout the disk are calculated using the radiative transfer package RADMC (Dullemond & Dominik 2004) and the resulting disk is in vertical hydrostatic equilibrium, with a flaring shape. The gas temperature is set equal to the dust temperature.

Gas phase H₂O is initially distributed uniformly throughout the disk at a constant abundance of $1.8 \times 10^{-4} \times n_{\text{H}}$, where n_{H} is the total number of hydrogen nuclei. This is somewhat artificial since H₂O forms on grain surfaces, but if the model is run long enough (here to $\sim 10^6$ years) the final distribution will not depend on the initial distribution between the gas and grain. The H₂O freezes out or adsorbs onto grain surfaces with the rate coefficient k_{ads} :

$$k_{\text{ads}} = \left(4.55 \times 10^{-18} \text{cm}^3 \text{K}^{-1/2} \text{s}^{-1}\right) n_{\text{H}} \sqrt{\frac{T_{\text{g}}}{M}} \quad (9.7)$$

where T_{g} is the gas temperature and M the molecular weight of water. The numerical factor assumes unit sticking efficiency, a mean grain radius of 0.1 μm and a grain abundance of 10^{-12} with respect to H₂ (Charnley et al. 2001). Once adsorbed onto the grains, the H₂O desorbs thermally with a rate coefficient k_{thd} :

$$k_{\text{thd}} = \left(1.26 \times 10^{-21} \text{cm}^2\right) A \frac{n_{\text{H}}}{n_{\text{s}}} e^{-\frac{E_{\text{b}}}{kT_{\text{gr}}}} \quad (9.8)$$

where n_{s} is the number density of solid water and T_{gr} is the grain temperature. The numerical factor assumes the same grain properties as in Eq. 9.7 and 10^6 binding sites per grain. The pre-exponential factor, A , and the binding energy, E_{b}/k , are set to $1 \times 10^{30} \text{cm}^{-2} \text{s}^{-1}$ and 5773 K, respectively (Fraser et al. 2001). Finally the H₂O photodesorption rate coefficient k_{pd} is defined as:

$$k_{\text{pd}} = \left(3.14 \times 10^{-14} \text{s}^{-1}\right) G_0 n_{\text{H}} Y_{\text{pd}} \quad (9.9)$$

where the numerical factor describes the UV photon flux onto a grain surface per unit time for the average interstellar field ($10^8 \text{photons cm}^{-2} \text{s}^{-1}$), G_0 is the scaling factor for the UV field that is output by RADMC for each grid point and Y_{pd} is the photodesorption yield. In addition to the external UV field a cosmic ray induced field is approximated by setting a lower limit on G_0 of 10^{-4} (Shen et al. 2004). The photodesorption results in the

release of both OH and H₂O. The released OH is quickly rehydrogenated in the model in the gas, however, and hence we let all H₂O ices desorb as H₂O molecules with the yield:

$$Y_{\text{pd,H}_2\text{O}}(T_{\text{gr}}, x) = 10^{-3} (1.3 + 0.032 \times T_{\text{gr}}) (1 - e^{-x/l(T)}) \quad (9.10)$$

where x is the ice thickness in ML and $l(T)$ the temperature-dependent diffusion length in ML (Eq. 9.6). The model is run for two scenarios - (i) without and (ii) with photodesorption. Each run is 3 Myrs, the typical age of a Herbig disk, which results in steady state gas and grain phase abundances. Figure 9.8a shows the gas phase H₂O fraction in the disk without photodesorption as a function of radial and vertical distance from the central protostar. As expected the H₂O is completely frozen out, except in the surface layer, when non-thermal desorption is excluded (Fig. 9.8a). When photodesorption is turned on, H₂O is kept in the gas phase further in toward the mid-plane (Fig. 9.8b). Without photodesorption 0.6% of the H₂O in the disk is in the gas phase at temperatures above the thermal desorption temperature of 100 K and 0.002% is in the gas phase below 100 K. With photodesorption included in the model, 0.6% of the H₂O is still present as warm gas, but now 2% of the total H₂O is in the gas phase at temperatures below 100 K. The total column density of warm $T > 100$ K H₂O gas, averaged over the entire disk, is hence the same in both cases ($1.4 \times 10^{17} \text{ cm}^{-2}$). In contrast the amount of cold H₂O gas averaged over the entire disk increases from 5.0×10^{14} to $4.5 \times 10^{17} \text{ cm}^{-2}$ when photodesorption is turned on. This means that a gas phase chemistry involving OH or H₂O is possible deep toward the disk midplane also in the outer disk. For comparison we also run our model using a constant surface photodesorption yield of 10^{-3} , which has often been used in the literature previously. For this particular model the total column density changes with less than a factor of two compared to using the derived yield equation from this study. The spatial distribution of gas phase H₂O is however different using the different yields due to the fact that using the constant yield overestimates the desorption rate in the surface region and underestimates it deeper into the disk.

This is a generic disk model commonly used to model disks around intermediate mass stars. To model an actually observed object would require a more detailed model that takes into account observed constraints on the disk structure. In addition, the calculated gas phase abundances may change somewhat when chemistry is taken into account. The general trend is however that photodesorption increases the amount of cold gas phase H₂O by orders of magnitude. This is also the result of a recent PDR model showing that the inclusion of chemistry, while important for more accurate predictions, will not reduce the predicted column density of gas phase H₂O dramatically (Hollenbach et al., ApJ, in press). Other effects such as grain growth may increase the photodesorption rate, but without a full chemical network it is unclear how much of this increase will be off-set by photodissociation of the desorbed H₂O. Probably only observations of cold H₂O on the scale of protoplanetary disks will yield an answer. The beam of the imminent *Herschel Space Observatory* is of the same order of magnitude as this modelled disk and hence these results show that large amounts of cold H₂O will be observable. For exactly this purpose – to observe cold H₂O gas – the WISH program was approved as a *Herschel*

key program. The amount of gas phase H₂O in disks due to non-thermal desorption may hence be answered very soon indeed.

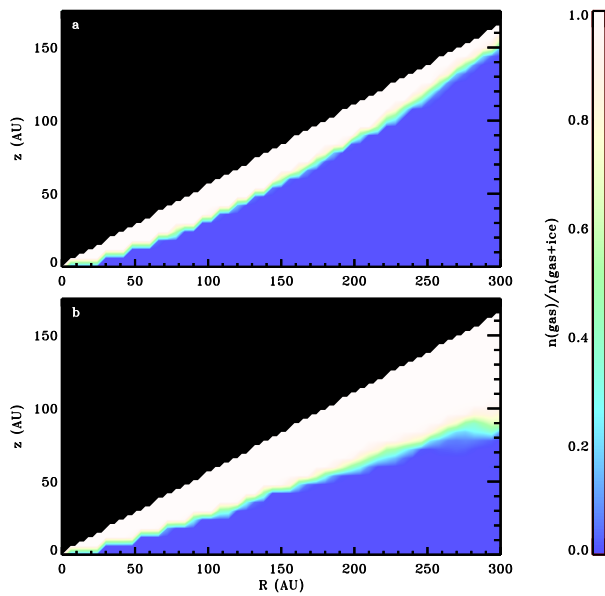


Figure 9.8 – Simulation of the distribution of gas phase over total H₂O ratio in a circumstellar disk without (a) and with (b) photodesorption. The white, H₂O-gas-dominated area extends more than 50 AU deeper into the disk when photodesorption is included, illustrating the large impact of photodesorption on the chemistry in the outer parts of disks.

9.5 Conclusions

1. The total D₂O and H₂O photodesorption yields are indistinguishable within the experimental uncertainties and are empirically described by $Y_{\text{pd}}(T, x) = Y_{\text{pd}}(T, x > 8)(1 - e^{-x/l(T)})$ where $Y_{\text{pd}}(T, x)$ is the thickness and temperature dependent photodesorption yield, x the ice thickness in monolayers and $l(T)$ an ice diffusion parameter that varies between 1.3 ML at 30 K and 3.0 ML at 100 K.
2. For thick ices (>8 ML), the yield depends linearly on temperature such that $Y_{\text{pd}}(T, x > 8) = 10^{-3} (1.3 + 0.032 \times T) \text{ photon}^{-1}$. The yields agrees, within the reported 60% uncertainty, with a previous experiment (Westley et al. 1995a).
3. The nature of the desorbed species is temperature dependent, with equal amounts of OH and H₂O detected at low temperatures. At higher temperatures the H₂O:OH

fraction is $\sim 2:1$ and in addition about a fifth of the ice photodesorbs as heavier fragments like O_2 . The fraction of the total photodesorption yield that results in H_2O molecules desorbing is described by $f_{H_2O} = (0.42 \pm 0.07) + (0.002 \pm 0.001) \times T$.

4. We find no yield dependence on photon flux or fluence. The fluence independence is in contrast with a previous experiment (Westley et al. 1995a).
5. We also find no dependence on the ice structure i.e. whether the D_2O ice is amorphous or crystalline. This is consistent with spectroscopic evidence of fast destruction of crystalline ice into an amorphous state following UV irradiation.
6. The photodesorption yield and dependencies found here are consistent with previous theoretical predictions of H_2O photodesorption, where the photodesorption is limited to the top few layers of the ice (Andersson et al. 2006). In addition we see that the photodesorption yield increases with ice temperature because of the increased mobility of the photolysis fragments, allowing desorption from deeper within the ice.
7. Applying the experimental yield to a Herbig Ae/Be star+disk model we calculate that the predicted amount of cold (< 100 K) gas phase H_2O , averaged over the entire disk, increases with orders of magnitude due to photodesorption.

10

FORMATION RATES OF COMPLEX ORGANICS IN UV IRRADIATED CH₃OH-RICH ICES

Gas-phase complex organic molecules are commonly detected in the warm inner regions of protostellar envelopes, so-called hot cores. Recent models show that photochemistry in ices followed by desorption may explain the observed abundances. This study aims to experimentally quantify the UV-induced production rates of complex organics in CH₃OH-rich ices under a variety of astrophysically relevant conditions. The ices are irradiated with a broad-band UV hydrogen microwave-discharge lamp under ultra-high vacuum conditions, at 20–70 K, and then heated to 200 K. The reaction products are identified by reflection-absorption infrared spectroscopy (RAIRS) and temperature programmed desorption (TPD), through comparison with RAIRS and TPD curves of pure complex species, and through the observed effects of isotopic substitution and enhancement of specific functional groups, such as CH₃, in the ice. Complex organics are readily formed in all experiments, both during irradiation and during the slow warm-up of the ices after the UV lamp is turned off. The relative abundances of photoproducts depend on the UV fluence, the ice temperature, and whether pure CH₃OH ice or CH₃OH:CH₄/CO ice mixtures are used. C₂H₆, CH₃CHO, CH₃CH₂OH, CH₃OCH₃, HCOOCH₃, HOCH₂CHO and (CH₂OH)₂ are all detected in at least one experiment. Varying the ice thickness and the UV flux does not affect the chemistry. The derived product-formation yields and their dependences on different experimental parameters, such as the initial ice composition, are used to estimate the CH₃OH photodissociation branching ratios in ice and the relative diffusion barriers of the formed radicals. At 20 K, the pure CH₃OH photodesorption yield is $2.1(\pm 1.0) \times 10^{-3}$ per incident UV photon, the photo-destruction cross section $2.6(\pm 0.9) \times 10^{-18}$ cm². Ice photochemistry in CH₃OH ices is efficient enough to explain the observed abundances of complex organics around protostars. Some complex molecules, such as CH₃CH₂OH and CH₃OCH₃, form with a constant ratio in our ices and this can be used to test whether complex gas-phase molecules in astrophysical settings have an ice-photochemistry origin. Other molecular ratios, e.g. HCO-bearing molecules versus (CH₂OH)₂, depend on the initial ice composition and temperature and can thus be used to investigate when and where complex ice molecules form.

Öberg, K.I., Garrod, R.T., van Dishoeck, E.F. and Linnartz, H., accepted for publication in A&A.

10.1 Introduction

Organic molecules of increasing complexity are being detected in star-forming regions (Blake et al. 1987; Nummelin et al. 2000; Bisschop et al. 2007c; van Dishoeck et al. 1995; Cazaux et al. 2003; Bottinelli et al. 2004, 2007; Belloche et al. 2009); however, the origins of these complex molecules are the subject of debate. Commonly-suggested formation routes include various gas-phase reactions involving evaporated CH₃OH ices, atom-addition reactions on dust grains, and UV- and cosmic ray-induced chemistry in the granular ices (Charnley et al. 1992; Nomura & Millar 2004, Herbst & Dishoeck 2009, AR&A in press). Recently, the focus has shifted to an ice formation pathway (e.g. Garrod et al. 2008), but due to the lack of quantitative experimental data, it is still not clear whether these molecules form in granular ices during the colder stages of star formation or in the warm gas close to the protostar. Nor has the relative importance of different grain formation routes been resolved. Establishing the main formation route is needed to predict the continued chemical evolution during star- and planet-formation and also to predict the amount of complex organics incorporated into comets and other planetesimals. In light of this, and the recent failures of gas phase chemistry to explain the observed complex molecules, we aim to quantify the formation of complex molecules through UV-induced chemistry in CH₃OH-rich ices.

Simple ices, such as solid H₂O, CO, CO₂, CH₄ and NH₃, are among the most common species found in dark cloud cores and towards protostars. The ices form sequentially in the cloud, resulting in a bi-layered structure dominated by H₂O and CO, respectively (Bergin et al. 2005; Knez et al. 2005; Pontoppidan 2006). Laboratory experiments suggest that CH₃OH also forms in the ice during the pre-stellar phase, through hydrogenation of CO (Watanabe et al. 2003), although, as yet, CH₃OH ice has only been detected toward protostars. Based on this formation route, CH₃OH is probably present in a CO-rich phase during most of its lifetime. More complex ices have been tentatively detected towards a few high-mass protostars (Schutte et al. 1999; Gibb et al. 2004), though specific band assignments are uncertain. Towards most other objects, derived upper limits on complex ices are too high to be conclusive.

Indirect evidence of complex molecule formation in ice mantles exists from millimeter observations of shocked regions and the innermost parts of low- and high-mass protostellar envelopes, so called hot cores and corinos. The observations by Arce et al. (2008) of HCOOCH₃, HCOOH and CH₃CH₂OH at abundances of $\sim 10^{-2}$ with respect to CH₃OH towards the low-mass molecular outflow L1157 are especially compelling; this outflow has been above 100 K for a period that is an order of magnitude shorter than is required for the gas-phase production of such complex molecules. Ice evaporation through sputtering is, in contrast, efficient in shocks (Jones et al. 1996). The observed abundances towards L1157 are remarkably similar to those observed in galactic-center clouds and high-mass protostars, suggesting a common formation route.

In hot cores and corinos, gas-phase production may still be a viable alternative for some of the detected molecules, because of the longer time scales compared to outflows. However, recent calculations and experiments suggest that some key gas-phase reactions are less efficient than previously thought; for example, the gas-phase forma-

tion of HCOOCH_3 was found to be prohibitively inefficient (Horn et al. 2004). Furthermore, Bisschop et al. (2007c) recently showed that complex oxygen-bearing molecules and H_2CO are equally well correlated with CH_3OH . Since CH_3OH and H_2CO are proposed to form together in the ice, this suggests that those complex oxygen-bearing molecules are also ‘first-generation’ ice products.

One possible ice formation route for complex species is atomic accretion and recombination on grain surfaces, which appears efficient for smaller species. Charnley (2004) suggested that the hot-core molecules may form either through hydrogenation of molecules and radicals, such as CO and HCCO, or through a combination of hydrogenation and oxidation starting with C_2H_2 . Similar reaction schemes are suggested to explain observations by e.g. Bisschop et al. (2008) and Requena-Torres et al. (2008). Such formation mechanisms have not been comprehensively tested under astrophysically relevant conditions, although the models of Belloche et al. (2009) found them to be ineffective in the formation of nitriles up to ethyl cyanide, under hot core conditions. Experimental studies show that dissociative reactions may be the favored outcome of hydrogenating larger molecules and fragments (e.g. Bisschop et al. 2007b), hampering the build-up of large quantities of complex molecules. Quantitative experiments are, however, still lacking for most reactions.

The alternative grain-surface formation route, which is investigated in this study, is the energetic destruction of the observed simple ices and subsequent diffusion and recombination of the radicals into more complex species. Within this framework, Garrod & Herbst (2006) and Garrod et al. (2008) modeled the formation of complex molecules during the slow warm-up of ices in an in-falling envelope, followed by ice evaporation in the hot core region. In the model, photodissociation of simple ices, especially CH_3OH , produces radicals in the ice. The luke-warm ices in the envelope (20–100 K) allow for the diffusion of ‘heavy’ radicals like CH_3 and CH_2OH , which recombine to form complex molecules. The model continues until all the ice is evaporated and the resulting gas phase abundances reproduce some of the abundance ratios and temperature structures seen in the galactic center and towards hot cores. Improvement of these model predictions is mainly limited by lack of quantitative experimental data on CH_3OH photodissociation branching ratios in ices, diffusion barriers of the formed radicals and binding energies of most complex molecules. The ultimate objective of the present study is to provide these numbers by experimental investigation of the photochemistry in CH_3OH -rich ices, followed by quantitative modeling (paper II, Garrod & Öberg, in preparation).

There have been multiple studies of photochemistry in ices containing organic molecules, stretching back to the 1960s (e.g. Stief et al. 1965). Most studies provide only a limited amount of the kind of quantitative data needed for astrochemical models and instead focus on the qualitative assignment of final photochemistry products, following irradiation of ice mixtures that are proposed to mimic ice compositions in star forming regions. To produce enough detectable products, deposition and irradiation were typically simultaneous in the early experiments, rather than a sequential deposition, irradiation and warm-up scheme. This was the approach of, for example, Hagen et al. (1979) and D’Hendecourt et al. (1982). Allamandola et al. (1988) included CH_3OH in ice mixtures in similar experiments and found that CH_3OH mainly photodissociates into smaller frag-

ments at 10 K, while several new unidentified features appear following the warm-up of the irradiated ice, indicating an efficient diffusion of radicals. Gerakines et al. (1996) investigated the photochemistry of pure CH₃OH ice more quantitatively at 10 K, and determined the CH₃OH photolysis cross section, and the H₂CO and CH₄ UV formation cross sections averaged over the lamp wavelength range at a specific flux setting. Gerakines et al. (1996) also detected HCOOCH₃, and several other complex species have also been identified in CH₃OH-rich ices following UV-irradiation, though some peaks have been assigned to different carriers in different studies. The difficulty in identifying most complex products is discussed by e.g. Hudson & Moore (2000) who investigated the production of complex molecules in CH₃OH:H₂O and CH₃OH:CO ice mixtures both following UV irradiation and ion bombardment in a number of studies, most recently in Moore & Hudson (2005) and Hudson et al. (2005).

A few studies exist on the formation of complex molecules from ion bombardment of pure CH₃OH ice, though similarly to the UV photolysis experiments, the formation of more complex molecules than CH₃OH is in general not quantified (Baratta et al. 2002; Bennett et al. 2007). Bennett et al. (2007) identified HCOOCH₃, HOCH₂CHO and (CH₂OH)₂, mainly based on comparison with calculated spectra and desorption patterns following irradiation, but provided only upper limits of their formation rates. The quantitative data from both studies include formation rates of small molecules and CH₃OH and H₂CO ion-bombardment dissociation rates. In a separate study Bennett & Kaiser (2007) determined the formation rate of HCOOCH₃ and HOCH₂CHO in a CO:CH₃OH ice mixture for the ion-bombardment flux used in their experiment.

The aim of this study and its follow-up paper is to combine experiments with kinetic modeling to completely quantify the photochemistry of CH₃OH rich ices. This includes determining the CH₃OH photodesorption yield, the CH₃OH dissociation branching ratios upon UV irradiation, the diffusion barriers of the formed radicals and reaction barriers to form more complex molecules, where present. Here, we present the experiments on CH₃OH ice chemistry under a large range of astrophysically relevant conditions and quantify the formation of all possible first generation complex molecules. To ensure that reaction products are correctly assigned, we also present RAIR spectra and temperature-programmed desorption experiments of all stable expected complex products, together with their derived binding energies.

The paper is organized as follows. Section 2 presents the experimental and data analysis methods. Section 3 reports on both qualitative and quantitative results of the experiments. Discussion follows in section 4, and includes estimates of photodissociation branching ratios and diffusion barriers. Preliminary astrophysical implications are discussed in section 5. A summary of results and concluding remarks are given in section 6.

10.2 Experiments and analysis

All experiments are carried out under ultra-high vacuum conditions ($\sim 10^{-10}$ mbar) in the CRYOPAD set-up, which is described in detail in Fuchs et al. (2006) and Öberg

Table 10.1 – Experimental parameters for UV-irradiation experiments.

Exp.	Species	Temp. ^a (K)	Thick. (ML)	UV flux ($10^{13} \text{ cm}^{-2} \text{ s}^{-1}$)
1	CH ₃ OH	20	21	1.1
2	CH ₃ OH	30	19	1.1
3	CH ₃ OH	50	20	1.1
4	CH ₃ OH	70	22	1.1
5	CH ₃ OH	20	19	4.3
6	CH ₃ OH	50	15	4.3
7	CH ₃ OH:CO	20	12:17	1.1
8	CH ₃ OH:CO	30	12:11	1.1
9	CH ₃ OH:CO	50	16:7	1.1
10	CH ₃ OH:CH ₄	30	11:27	1.1
11	CH ₃ OH:CH ₄	50	11:6	1.1
12	CH ₃ OH:CO	20	6:60	1.1
13	CH ₃ OH	20	6	1.1
14	CH ₃ OH	50	6	1.1
15	CH ₃ OH	20	4	4.3
16	CH ₃ OH	50	8	4.3
17 ^b	CH ₃ OH	20	18	1.1
18 ^c	CH ₃ OH	20	20	1.1
19	CH ₃ OD	20	~20	1.1
20	CH ₃ OD	50	~20	1.1
21	CD ₃ OH	20	~20	1.1
22	CD ₃ OH	50	~20	1.1

^a The ice-deposition and -irradiation temperature.

^b Following irradiation the ice is quickly heated to 50 K for 2 hours.

^c Following irradiation the ice is quickly heated to 70 K for 2 hours.

Table 10.2 – Pure ice spectroscopy and TPD experiments.

Species	Formula	Mass (amu)	Thick. ^a (ML)	$E_{\text{des}}^{\text{a}}$ (K)
Ethane	C ₂ H ₆	30	5 [3]	2300 [300]
Methanol	CH ₃ OH	32	25 [10]	4700 [500]
Acetaldehyde	CH ₃ CHO	44	4 [2]	3800 [400]
Dimethyl ether	CH ₃ OCH ₃	46	~4	3300 [400]
Ethanol	CH ₃ CH ₂ OH	46	5 [2]	5200 [500]
Formic acid	HCOOH	46	5 [2]	5000 [500]
Methyl formate	HCOOCH ₃	60	3 [1]	4000 [400]
Acetic acid	CH ₃ COOH	60	3 [1]	6300 [700]
Glycolaldehyde	HOCH ₂ CHO	60	3 [1]	5900 [600]
Ethylene glycol	(CH ₂ OH) ₂	62	7 [3]	7500 [800]

^aValues in brackets indicate uncertainties.

et al. (2009b). The ices are grown *in situ* with monolayer precision at thicknesses between 3 and 66 ML, by exposing a cold substrate at the center of the vacuum chamber to a steady flow of gas, directed along the surface normal. The substrate is temperature controlled between 20 and 200 K. The relative temperature uncertainty is less than a degree, while the absolute uncertainty is about two degrees. All UV-irradiation experiments are performed with CH₃OH from Sigma-Aldrich with a minimum purity of 99.8%. The mixed ice experiments contain CH₄ or CO gas of 99% purity (Indogas). Pure, complex ice experiments with C₂H₆, CH₃CHO, CH₃OCH₃, CH₃CH₂OH, HCOOH, HCOOCH₃, CH₃COOH, HOCH₂CHO and (CH₂OH)₂ are carried out with chemicals of 99–99.9% purity from Sigma-Aldrich. All liquid samples are further purified with several freeze-thaw cycles to remove any volatile gas from the sample. The dominant source of contaminants is from the vacuum inside of the chamber once the ice is deposited; during each experiment, up to 0.5 ML of H₂O adsorbs onto the substrate from the small H₂O contamination always present in the chamber. This has no measurable impact on the photochemistry from test experiments with CH₃OH isotopologues.

The set-up is equipped with a Fourier transform infrared (FTIR) spectrometer in reflection-absorption mode (Reflection-Absorption InfraRed Spectroscopy or RAIRS). The FTIR covers 750 – 4000 cm⁻¹, which includes vibrational bands of all investigated molecules, and is operated with a spectral resolution of 1 cm⁻¹. To increase the signal to noise the spectra are frequently binned when this can be done without reducing the absorbance of sharp features. RAIRS is employed both to acquire infrared spectra of complex molecules and to quantify the changing ice composition during UV irradiation of CH₃OH-rich ices. All spectra are corrected with a linear baseline alone, to avoid distorting any spectral profiles.

Temperature Programmed Desorption (TPD) is another analytical tool, which is employed in this study to identify ice photoproducts. In a TPD experiment, ice evaporation is induced by linear heating of the ice, here with a heating rate of 1 K min⁻¹. The evapo-

rated gas phase molecules are detected by a Quadrupole Mass Spectrometer (QMS). The resulting TPD curves depend on the evaporation energy of the ice, which can be uniquely identified for most of the investigated species. For mixed ices the TPD curve also depends on such quantities as ice trapping, mixing and segregation. The QMS software allows for the simultaneous detection of up to 60 different m/z values (the molecular mass divided by the charge). Hence in the TPD experiments of irradiated ices, all possible reaction-product masses, which contain at most two oxygen and two carbon atoms, are monitored.

In the CH₃OH photochemistry experiments, the ice films are irradiated at normal or 45° incidence with UV light from a broadband hydrogen microwave-discharge lamp, which peaks around Ly α at 121 nm and covers 115–170 nm or 7–10.5 eV (Muñoz Caro & Schutte 2003). The lamp flux was calibrated against a NIST calibrated silicate photodiode prior to the experimental series and is monitored during each experiment using the photoelectric effect in a gold wire in front of the lamp. The lamp emission resembles the spectral distribution of the UV interstellar radiation field that impinges externally on all clouds. It is also consistent with the UV radiation produced locally inside clouds by the decay of electronic states of H₂, following excitation by energetic electrons resulting from cosmic-ray induced ionization of hydrogen, see e.g. Sternberg et al. (1987). Each irradiation experiment is followed by a TPD experiment, where RAIR spectra are acquired every 10 K up to 200 K.

Supporting experiments consist of RAIR spectra and TPD curves of nine complex organic ices, which are potential photoproducts of CH₃OH ices. Spectra of these ices have been reported previously in the literature in transmission, but because of known band shifts in RAIRS compared to transmission spectroscopy, their RAIR spectra are also presented here.

The identification process is complicated by spectral overlaps of most of the potential photochemistry products. Thus great care is taken in securing each assignment, especially where they disagree with previous work or where disagreements between previous studies exist. To call an identification secure we test it to be consistent with up to seven criteria. These identification tools are described in detail in section 3.5.

Following the spectral band identification, RAIR spectroscopy is used to determine the initial CH₃OH ice abundance and the formed simple and complex ice abundances as a function of fluence during each photochemistry experiment. This requires known band strengths. The absolute RAIRS band strengths have been estimated previously in our set-up for CO and CO₂ ice (Öberg et al. 2009a,b). Using the same method, new measurements on CH₃OH are consistent with the CO and CO₂ results; i.e. the determined band strengths have the same relative values compared to the transmission band strength ratios reported in the literature, within 20%. The *relative* ice band strengths from transmission are thus still valid, with some exceptions, and most experimental objectives only require knowing the ice fraction that has been converted into products. The main caveat is that ices thicker than a few monolayers are not guaranteed to have a linear relationship between the absorbance of strong bands and ice thickness due to RAIRS effects (Teolis et al. 2007). This is circumvented by selecting weak enough bands, especially for CH₃OH, whose absorbance remains linear with respect to the amount of deposited ice at all the investigated ice thicknesses. The transmission band strength of CH₃OCH₃ is not present in the litera-

ture and its band strength is estimated by deposition of a dilute CH₃OCH₃:CH₃OH 1:10 mixture and assuming a constant sticking coefficient and that the CH₃OCH₃ is 'dragged' along with the CH₃OH to reach the substrate at a similar deposition rate.

Table 10.1 lists the CH₃OH, CH₃OH:CO and CH₃OH:CH₄ photochemistry experiments. The experiments are designed to study the impact of ice temperature, ice thickness, UV flux, UV fluence and mixed-in CO and CH₄ on the reaction-product abundances. Each ice is irradiated for ~6 hours at the reported flux. The high flux/fluence experiments are also used to determine the CH₃OH photodesorption rate using the same procedure as reported by Öberg et al. (2009b). In two experiments (17 and 18) the irradiation is followed by fast heating to a specified temperature to investigate the impact of the heating rate for radical diffusion. Table 10.2 lists the investigated complex organics for which RAIR spectra and TPD experiments have been acquired.

In addition to the experiments listed in Table 10.1 and 10.2, two experiments were performed to test the CO accretion rate due to UV-induced out-gassing from chamber walls and the life time of spectral features in the ice when diffusion is slow. In the first experiment a blank substrate was irradiated for the typical experiment time of six hours and a build-up of 0.2 CO ML was recorded. In the second experiment a photolyzed CH₃OH ice was monitored for five hours at 17 K after the UV lamp was turned off; the spectra of complex products did not change measurably during this period.

In all experiments, systematic uncertainties dominate and include the absolute calibration of the temperature (~2 K), the UV flux (~30%) and the conversion between transmission and RAIRS band strengths used to determine the absolute ice abundances (~50%), while the relative RAIRS band strengths are more accurate (~20% uncertainty from comparison between different transmission spectroscopy studies). The conversion between transmission and RAIRS band strengths will not affect the uncertainty of the photochemistry rates, since these depend only on the fraction of the ice that is converted into products. The determined diffusion barriers in Paper II are furthermore not affected by the uncertainty in UV flux because these only depend on which species the produced radicals react with, not on how many of them are produced per UV photon. Another source of error is the local baseline determination, which results in relative abundance uncertainties of up to 30% for a couple of the detected products, which is reported in detail in §10.3.6 for each species. Thus the formation yield of products relative to the original ice abundance has a total uncertainty of 35–50%.

10.3 Experimental results

This section begins with experimental results that quantify CH₃OH bulk photolysis (§10.3.1) and surface photodesorption (§10.3.2). §10.3.3 qualitatively describes how the CH₃OH photoproducts are affected by different experimental variables for the experiments listed in Table 10.1. This information, together with RAIR spectra and TPD data on pure complex organics in §10.3.4, is used in §10.3.5 to identify the CH₃OH photoproducts. Following identification, the formation of all identified products from pure CH₃OH ice photochemistry are shown quantitatively in §10.3.6. Section 10.3.7 describes quanti-

tatively the formation and desorption of molecules during warm-up of the irradiated ices. Finally, §10.3.8 summarizes the effects of different experimental parameters on the final ice composition after irradiation and during warm-up.

10.3.1 The CH₃OH UV photolysis cross-section

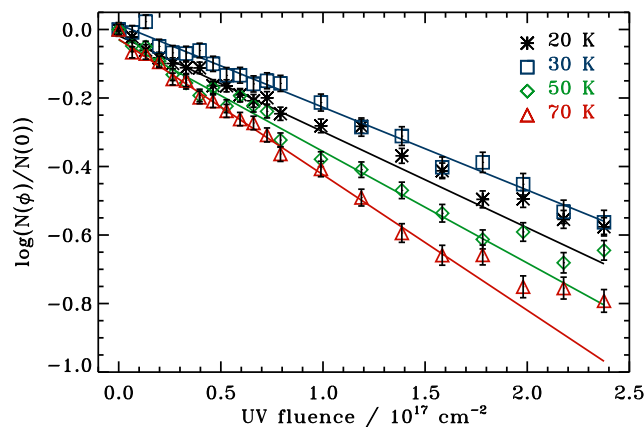


Figure 10.1 – The logarithm of the normalized CH₃OH abundance as a function of UV fluence at 20, 30, 50 and 70 K. The lines are exponential fits to the first 10¹⁷ photons in each experiment.

The UV-destruction cross-section of CH₃OH ice, averaged over the lamp spectrum, determines the total amount of radicals available for diffusion and subsequent reaction. The cross section is calculated from the measured loss of CH₃OH ice band intensity with fluence. The initial UV destruction of CH₃OH, i.e. before back-reactions to reform CH₃OH become important, in an optically thin ice is given by

$$N(\phi) = N(0)\exp(-\phi \times \sigma_{\text{ph}}), \quad (10.1)$$

where N is the CH₃OH column density in cm⁻², ϕ is the UV fluence in photons cm⁻² and σ_{ph} is the UV-photolysis cross section in cm². Figure 10.1 shows that photodestruction during the first 10¹⁷ photons is well described by this equation for ~20 ML thick ices at different temperatures. The loss of CH₃OH is calculated from the combination band around 2550 cm⁻¹ and the resulting photodissociation cross sections are 2.6[0.9], 2.4[0.8], 3.3[1.1] and 3.9[1.3] × 10⁻¹⁸ cm² at 20, 30, 50 and 70 K respectively. The uncertainties in brackets are the absolute errors; the relative uncertainties are 10–20%. The increasing cross section with temperature is indicative of significant immediate recombination of dissociated CH₃OH at low temperatures when diffusion is slow. The measured effective CH₃OH-ice cross sections thus underestimate the actual photodissociation rate. This is consistent with the higher gas-phase CH₃OH UV-absorption cross section; convolving the absorption spectra from Nee et al. (1985) with our lamp spectra results in a factor of three higher absorption rate than the observed photodissociation rate in the ice at 20 K.

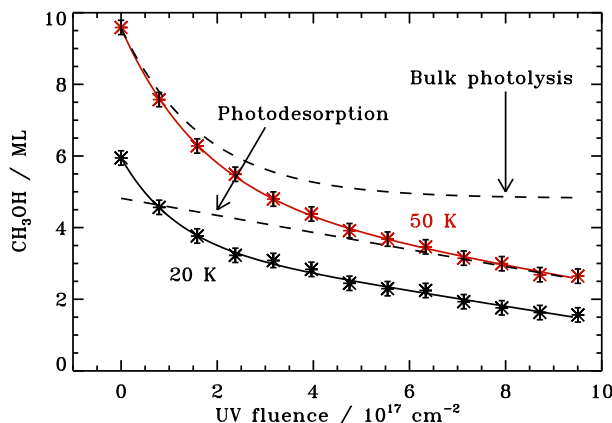


Figure 10.2 – The loss of CH₃OH ice through photolysis and photodesorption at 20 and 50 K as a function of UV fluence. The curves are fitted with $A_0 + A_1 \times \phi + A_2(1 - \exp(-\phi \times \sigma))$. The thin dashed lines show the offset decomposition of the function belonging to the 50 K experiment into its exponential photolysis part and its linear photodesorption part.

The measured photolysis cross sections also depend on whether a ‘clean’ CH₃OH band is used to calculate the CH₃OH loss. The ν_{11} CH₃OH band around 1050 cm⁻¹ is commonly used in the literature (Gerakines et al. 1996; Cottin et al. 2003). This band overlaps with strong absorptions of several complex photoproducts and using it results in a 30% underestimate of the CH₃OH destruction cross section at 20 K. This explains the higher cross-section value obtained in these experiments compared to Gerakines et al. (1996) and Cottin et al. (2003), who recorded 1.6×10^{-18} cm² and 6×10^{-19} cm², respectively. These destruction cross sections were also measured after greater fluences, $\sim 1.8 \times 10^{17}$ and $\sim 6 \times 10^{17}$ UV photons cm⁻², respectively, when back reactions to form CH₃OH confuse the measurements. The measurements in this paper thus demonstrate the importance of a high fluence resolution and of picking a ‘clean’ band when determining the photodestruction cross section of an ice.

10.3.2 CH₃OH photodesorption yields

Previous experiments show that several ices (pure CO, CO₂ and H₂O) are efficiently photodesorbed upon UV irradiation. To constrain the photodesorption of CH₃OH ice and thus determine the loss of CH₃OH molecules into the gas phase rather than into photoproducts in the ice, the same procedure is followed as reported by Öberg et al. (2009b). This method is based on the fact that photodesorption from a multilayer ice is a zeroth order process with respect to photon fluence, since it only depends on the amount of molecules in the surface layer. The photodesorption yield will thus not change with fluence as long as the original ice is sufficiently thick. In contrast ice photolysis is a first order process, since it depends on the total amount of ice. Through simultaneous modeling

of the ice loss with an exponential decay and a linear function, these two processes can be separated and the photodesorption yield determined (Fig. 10.2). The resulting yields are $2.1[1.0]\times 10^{-3}$ and $2.4[1.2]\times 10^{-3}$ desorbed molecules per incident UV photon at 20 and 50 K, respectively. There is thus no evidence for a temperature dependence of the photodesorption yield within the investigated temperature range.

These yields agree with previous photodesorption studies of other molecules (Westley et al. 1995a; Öberg et al. 2007b, 2009a,b) and confirms the assumption in several observational and model papers that most ice molecules have similar photodesorption yields, around 10^{-3} per incident UV photon. The CH_3OH photodesorption mechanism is suggested to be similar to H_2O and CO_2 , i.e. a photodesorption event is initiated by photodissociation of a surface CH_3OH molecule. The fragments contain excess energy and either desorb directly or recombine and desorb. The insensitivity to temperature suggest that longer range diffusion is comparatively unimportant and that most molecules desorb through the escape of the produced photodissociation fragments or through immediate recombination, in the same site, and desorption of the fragments following photodissociation. A more complete study including different ice thicknesses and temperatures is however required to confirm the proposed photodesorption pathway.

Another conceivable indirect photodesorption mechanism is desorption due to release of chemical heat following recombination of two thermalized radicals, first suggested by Williams (1968) and more recently investigated theoretically by Garrod et al. (2007). Its quantification requires more sensitive QMS measurements than is possible with this setup. The temperature independence suggests, however, that this is a minor desorption pathway in this setup, compared to direct photodesorption.

10.3.3 Dependence of photo-product spectra on experimental variables

The influence, if any, of different experimental variables on the resulting infrared spectra of irradiated CH_3OH ice is investigated in detail below. These dependences are then used in the following sections to identify absorption bands and to subsequently quantify reaction rates, diffusion barriers and photodissociation branching ratios. The results are also independently valuable, since many of these experimental variables also vary between different astrophysical environments.

10.3.3.1 UV fluence

In most experiments, the ices are exposed to a total UV fluence (i.e. total flux integrated over the time of the experiment) of $\sim 2.4 \times 10^{17} \text{ cm}^{-2}$, which is comparable to the UV fluence in a cloud core after a million years with a UV flux of $10^4 \text{ cm}^{-2} \text{ s}^{-1}$ (Shen et al. 2004). This agreement is important since the composition of photoproducts changes with UV fluence in all experiments. This is illustrated in Fig. 10.3, which shows spectra of an originally 20 ML thick CH_3OH ice at 50 K after different fluences. This effect is demonstrated numerically below for three of the bands representing complex OH bearing molecules (X- CH_2OH) at $866/890 \text{ cm}^{-1}$, simple photoproducts (CH_4) at 1301 cm^{-1} , and

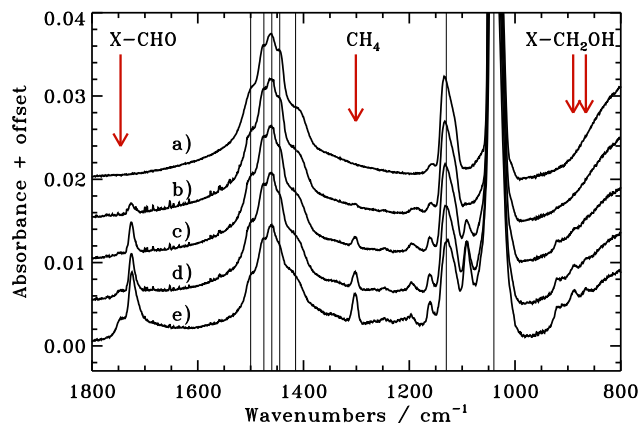


Figure 10.3 – The different growth rates of spectral features in a CH₃OH ice at 50 K a) before UV irradiation and after a UV fluence of b) 7×10^{15} , c) 4×10^{16} , d) 8×10^{16} and e) 2.4×10^{17} cm⁻². The CH₃OH features are marked with thin lines. New features are present at 1750–1700, 1400–1150, 1100–1050 and 950–850 cm⁻¹, including the bands belonging to CH₄, complex aldehydes and acids (X-CHO), and complex alcohols (X-CH₂OH), where X≠H.

HCO/COOH bearing complex molecules (shortened to X-CHO in most figures for convenience) at 1747 cm⁻¹. These molecular class assignments agree with previous studies and are discussed specifically in §10.3.5. After a fluence of $\sim 7 \times 10^{16}$ cm⁻² the relative importance of the integrated bands at 866/890, 1301 and 1747 cm⁻¹ is 0:90:10. After a fluence of $\sim 2.2 \times 10^{17}$ cm⁻² this has changed significantly to 35:34:31. The product composition after a particular fluence cannot therefore be linearly scaled to a lower or a higher fluence.

10.3.3.2 UV flux

The UV flux levels in the laboratory ($\sim 10^{13}$ cm⁻² s⁻¹) are orders of magnitude higher than those found in most astrophysical environments – the interstellar irradiation field is $\sim 10^8$ photons cm⁻² s⁻¹ (Mathis et al. 1983). Hence the product dependence on flux, if any, is required before translating laboratory results into an astrophysical setting. Figure 10.4 shows that two spectra acquired after the same fluence, but irradiated with a factor of four different flux, are identical within the experimental uncertainties. Numerically, the relative importance of the integrated bands at 866/890, 1301 and the 1747 cm⁻¹ are 15:56:29 in the low flux experiment and 24:51:25 for the high flux experiment after a total fluence of 2.2×10^{17} cm⁻². Including a 10–20% uncertainty in the band intensities, there is thus no significant dependence on flux within the explored flux range at 20 K. The same holds for similar experiments at 50 K (not shown). This does not exclude a flux dependence at astronomical time scales, but it does provide a benchmark for models aiming to translate laboratory results into astrophysical ones.

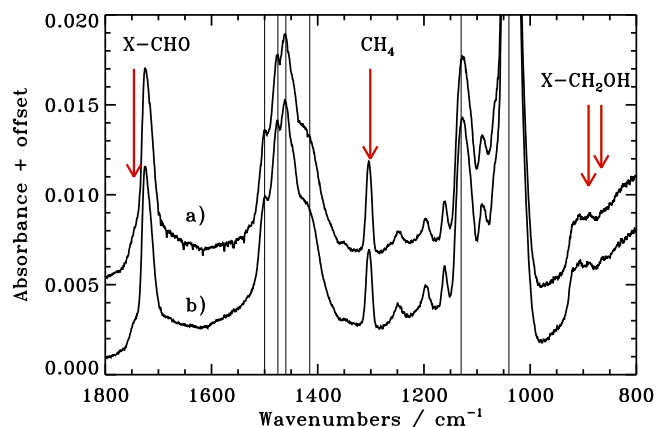


Figure 10.4 – The spectra of originally (a) 21 and (b) 19 ML thick CH_3OH ice irradiated with a UV flux of (a) $1.1 \times 10^{13} \text{ cm}^{-2} \text{ s}^{-1}$ and (b) $4.3 \times 10^{13} \text{ cm}^{-2} \text{ s}^{-1}$ at 20 K achieve the same fluence of $2.2 \times 10^{17} \text{ cm}^{-2}$. The CH_3OH features and some product bands are marked as in Fig. 10.3.

10.3.3.3 Ice thickness

Figure 10.5 shows that both the fractional CH_3OH destruction, as evidenced by e.g. the ν_7 band intensity, decrease around 1130 cm^{-1} , and the fractional formation of a few new spectral features are enhanced in thin ices ($\sim 6 \text{ ML}$) compared to the standard 20 ML experiment. However, this does not necessarily imply a different chemistry in thinner ices. Rather the difference in CH_3OH destruction may be explained by an increased escape probability of photoproducts in the thinner ice and by the greater importance of direct photodesorption. Similarly, the observed relative enhancements of the CO band at 2150 cm^{-1} and the 1700 cm^{-1} band in the 20 K experiment are probably due to the constant freeze-out of CO during the experiment, up to 0.2 ML out of 0.5 ML CO ice detected at the end of the 6 ML experiment, and its reactions to form more HCO-bearing carriers of the 1700 cm^{-1} band. Therefore, despite the apparent dependence of the spectral features on ice thickness, there is no significant evidence for different formation yields in 6 and 20 ML thick ices. This means that bulk reactions still dominate over the potentially more efficient surface reactions in ices as thin as 6 ML, at these fluences.

10.3.3.4 Ice temperature during irradiation

The photolyzed ice spectra depend on the ice temperature, illustrating the different temperature dependencies of different photochemistry products (Fig. 10.6). The $1727 (\text{H}_2\text{CO} + \text{X-CHO})$ and $1300 (\text{CH}_4)$ cm^{-1} features are most abundantly produced at the lowest investigated temperature of 20 K, while the $866/890 \text{ cm}^{-1}$ bands increase in strength with temperature and the $1747 (\text{X-CHO}) \text{ cm}^{-1}$ feature is barely affected by temperature changes. The different temperature dependencies can be used to infer the size of the main contributor to each band; photolysis fragments and molecules that form through hydrogenation of such fragments are expected to be most abundant at 20 K, while molecules that form from two larger fragments will be more efficiently produced at higher

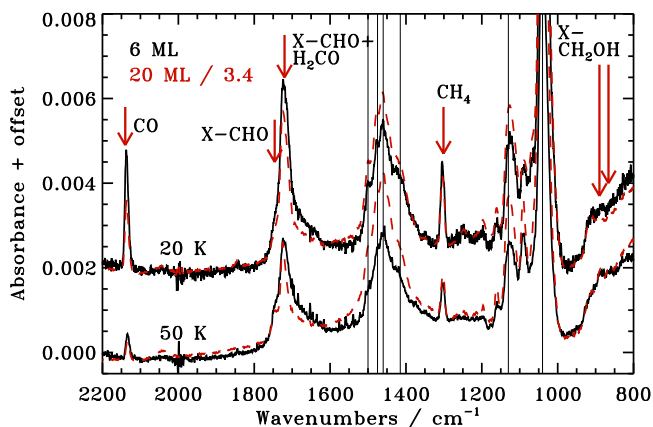


Figure 10.5 – The differences in the photolyzed CH₃OH spectra of two different original thicknesses after the same fluence of $\sim 2.4 \times 10^{17} \text{ cm}^{-2}$. The 20 ML (dashed lines) ice spectrum is normalized to have the same CH₃OH absorbance as the 6 ML (solid lines) ice experiment before irradiation to facilitate comparison of fractional photo-product rates. CO and H₂CO bands are marked in addition to the spectral features focused on in previous figures.

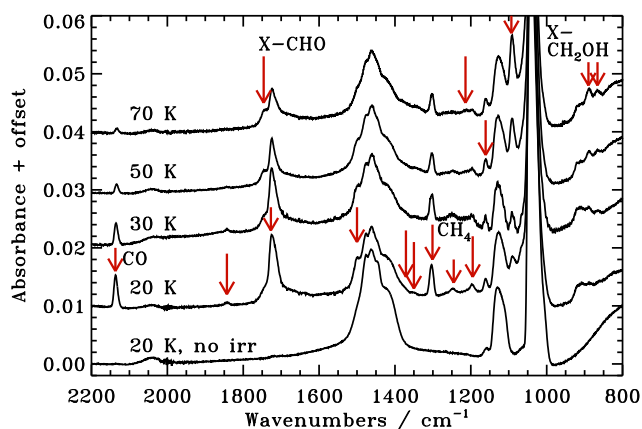


Figure 10.6 – The photolyzed CH₃OH spectra at different temperatures after the same fluence of $\sim 2.4 \times 10^{17} \text{ cm}^{-2}$ for 19–22 ML thick ices. The arrows mark new bands at the temperature at which they are most abundantly produced and some key features are also named.

temperatures where diffusion is facilitated. This is complicated by competition between different reaction pathways, which may inhibit the formation of some complex molecules at higher temperatures where new reaction channels become possible. Nevertheless, the dependence on temperature of different bands can aid in identifying their molecular contributors. All formed bands are thus classified according to the temperature at which they are most abundantly produced (Fig. 10.6), except for a few bands, where the dependence on temperature is too weak to assign them to a certain temperature bin. This information is summarized in Table 10.3.

10.3.3.5 Pure CH₃OH ice versus CH₃OH:CO 1:1 and CH₃OH:CH₄ 1:2 ice mixtures

In the set of experiments where CH₃OH is mixed with CH₄ or CO at ~1:1 ratio, the resulting photoproduct compositions are significantly different compared to those obtained from pure CH₃OH ice experiments. This is illustrated in Fig. 10.7 for ices irradiated at 30 K. In the CH₃OH:CH₄ mixture, bands corresponding to complex molecules at 822, 890, 956, 1161, 1350 and 1382 cm⁻¹ are enhanced, while in the CH₃OH:CO mixtures, the 1214, 1245, 1350, 1498, 1727, 1746 and 1843 cm⁻¹ bands grow faster compared to pure CH₃OH ice. A few bands are most prominent when no other species is added to the CH₃OH ice, for example the 866 and 1195 cm⁻¹ bands. The 1726-1747 cm⁻¹ band excess in the CO-containing ices shows that molecules that contain an HCO group can be overproduced by adding CO. Similarly, the band enhancements in the CH₄-containing ices are expected to arise from overproduction of CH₃-containing molecules. These observations are used below for band identifications and later to explain variations in abundances of different complex molecules in star-forming regions.

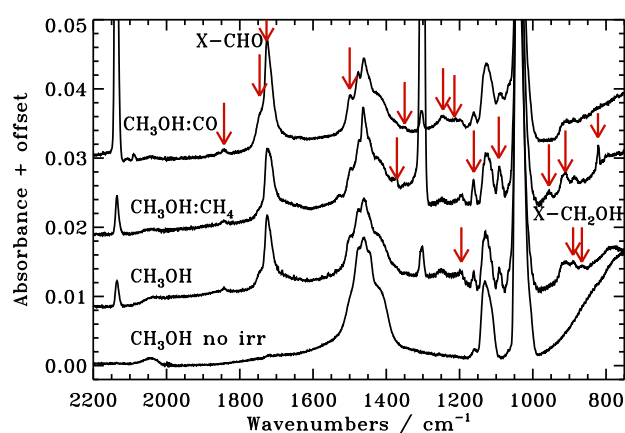


Figure 10.7 – Spectra of photolyzed pure CH₃OH (19 ML), and 1:1 CH₃OH:CO (23 ML) and 1:2 CH₃OH:CH₄ (38 ML) ice mixtures at 30 K after a fluence of $\sim 2.4 \times 10^{17}$ cm⁻². The spectra are scaled to correspond to the same initial CH₃OH abundance. The arrows mark product bands where they are most abundantly produced.

10.3.3.6 CH₃OH deuteration level

In the partially deuterated ices (CH₃OD and CD₃OH) some band positions do not change compared to regular CH₃OH, while others are either shifted or completely missing (Fig. 10.8). Bands that are present in the CH₃OH ice and missing in the CH₃OD experiments must originate from either OH(D)-containing molecules with the H involved in the vibrational mode in question or from simple hydrogenated species. These two groups of molecules are seldom confused and thus comparison between the photolyzed CH₃OH spectra and the photolyzed CH₃OD spectra can be used to assign some alcohol-bands. The band positions that are constant between the CH₃OH and CH₃OD do not however exclude the contributions of OH-containing molecules to these bands, since the OH group can be

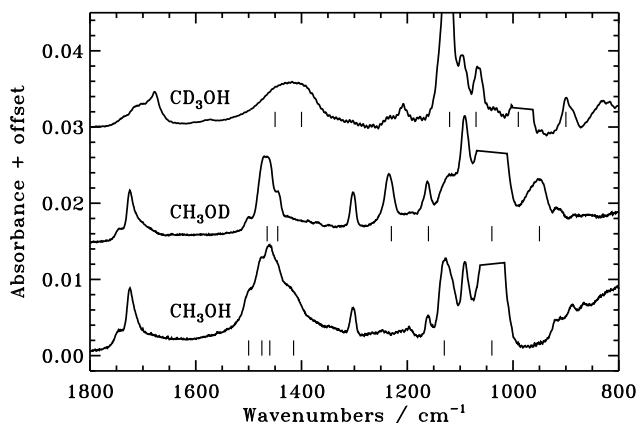


Figure 10.8 – The resulting spectra of photolyzed pure CH₃OH, CH₃OD and CD₃OH ices at 50 K after the same fluence of $\sim 2.4 \times 10^{17} \text{ cm}^{-2}$. The thin lines below each spectra mark the original CH₃OH, CH₃OD and CD₃OH features. The strongest band in each spectrum is blanked out for visibility.

present in the molecule without involvement in the vibration in question. Comparing the CH₃OH and CH₃OD experiments, the bands at 866 and 890 cm⁻¹ are obviously affected. The 1700 cm⁻¹ band is somewhat reduced in the CH₃OD experiment, suggesting that one of the carriers is HOCH₂CHO. An underlying broad feature around 1600 cm⁻¹ is also reduced in the CH₃OD experiment.

As expected, few of the bands in the CH₃OH experiments are still present in the UV-irradiated CD₃OH ice. The complex at 900-860 cm⁻¹ and some of the X-CHO features are exceptions, though the bands are shifted. The only bands expected to appear at their normal positions come from H₂O₂ and possible H₂O dependent on the main source of hydrogen in the ice; neither species is obviously present in the ice from the photolyzed CD₃OH-ice spectra.

10.3.3.7 Spectral changes during warm-up

Following irradiation at the specified temperatures, the ices are heated by 1 K min⁻¹ to 200 K and spectra acquired every 10 min. Figure 10.9 shows the irradiated CH₃OH ice between 20 and 190 K. The UV lamp is turned off during the warm-up and thus the ice composition only depends on thermal desorption and reactions of previously produced radicals. As the ice is heated (Fig. 10.9), several new spectral bands appear, while others increase or decrease in strength with temperature.

The 866, 890 and 1090 cm⁻¹ bands increase most dramatically in intensity during warm-up of the 20 K pure CH₃OH ice. Simultaneously the 1195 cm⁻¹ feature loses intensity. The 866 and 890 cm⁻¹ bands remain until 170 K and are the last sharp features to disappear. The 1747 and 1214 cm⁻¹ bands also increase in intensity with tempera-

ture. In contrast the bands at 1245, 1300, 1727 and 1850 cm^{-1} only lose intensity during warm-up. Most of these bands only disappear completely at the desorption temperature of CH_3OH , 120–130 K, indicating significant trapping of molecules inside the CH_3OH ice. Significant bulk chemistry is thus required to explain the results (see also §10.3.3.3). At 190 K there are still some shallow bands left, which only disappear after the substrate has been heated to room temperature.

Experiments 17 and 18 show that the warm-up rate matters somewhat for the final ice composition. The quantification and discussion of this effect is saved for Paper II.

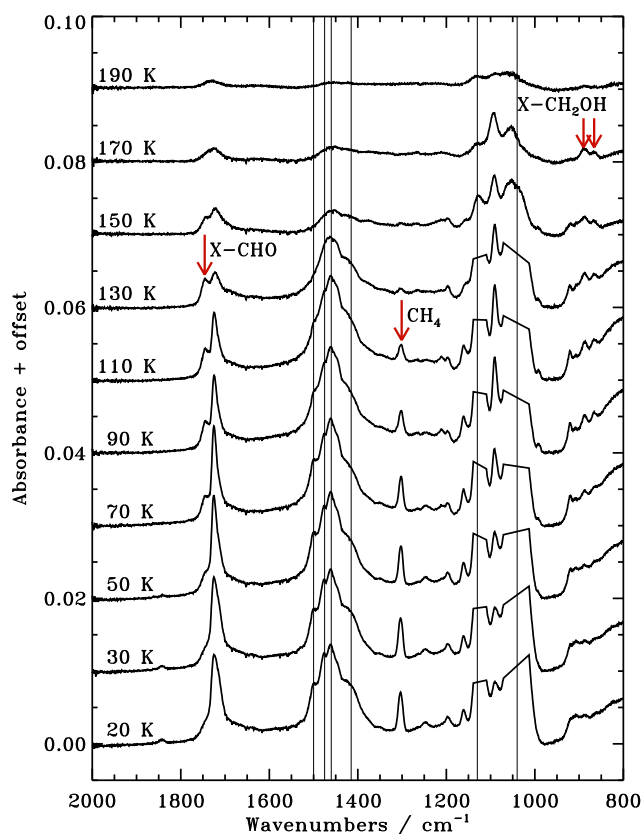


Figure 10.9 – The photolyzed ice spectra during warm-up following irradiation at 20 K with a fluence of $\sim 2.4 \times 10^{17} \text{ cm}^{-2}$ – the UV lamp is turned off during the warm-up. The thin lines mark CH_3OH features with the two strongest bands blanked out for visibility.

10.3.4 Reference RAIR spectra and TPD experiments of pure complex ices

Photolysis of CH_3OH ice and recombination of the fragments can theoretically result in a large number of new species. To facilitate the identification of these species, this section briefly presents new RAIR spectra and TPD time series of all stable, complex

photoproducts considered in this study. Radicals are expected to form in the photolyzed ice, but these cannot be produced in pure form in ices and thus comparison spectra are difficult to obtain.

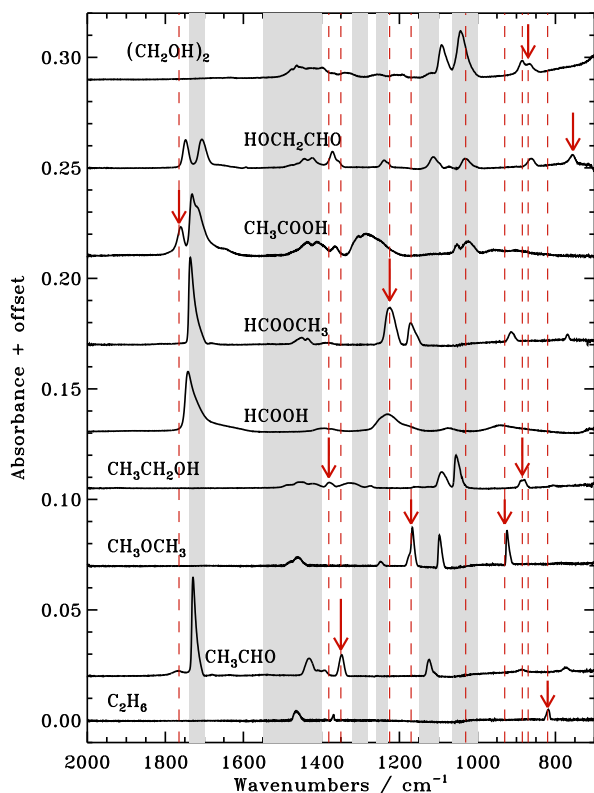


Figure 10.10 – RAIR spectra of 3–9 ML thick pure complex organic ices at 20 K (except for (CH₂OH)₂ at 150 K) used to identify stable photoproducts. The arrows indicate the bands mainly used for identification and abundance determinations – HCOOH has no sharp isolated feature. The dashed lines follow the arrows through all spectra to visualize overlaps with other spectral bands. The shaded regions show the wavelength regions where fundamental modes of CH₄, H₂CO and CH₃OH absorb.

Figure 10.10 shows the RAIR spectra of C₂H₆ (ethane), CH₃CHO (acetaldehyde), CH₃OCH₃ (dimethyl ether), CH₃CH₂OH (ethanol), HCOOH (formic acid), HCOOCH₃ (methyl formate), CH₃COOH (acetic acid) and HOCH₂CHO (glycolaldehyde) at 20 K and (CH₂OH)₂ (ethylene glycol) at 150 K. Below 150 K the (CH₂OH)₂ spectrum contains CH₃OH features despite the high stated purity (99%) of the sample. The spectral bands above 2000 cm⁻¹ are not shown since all complex molecule spectral features in that region overlap with strong CH₃OH features and thus cannot be used for identification. The figure illustrates that most bands overlap with at least one band from another complex molecule or with bands of H₂CO and/or CH₃OH, which is expected for complex molecules with the same or similar functional groups (e.g. absorption by HCO/COOH stretches at 1700–1750 cm⁻¹). The arrows indicate the bands mainly used for identification of each species. These bands are chosen to overlap as little as possible with strong absorption features of other species. For HCOOH, CH₃COOH, HCOOCH₃ and HOCH₂CHO there are no suit-

able bands for determining the produced abundances in most experiments, i.e. the isolated bands are too weak to provide detections or strict upper limits. For these molecules the arrows indicate the bands used to derive upper limits, while the 1700 cm^{-1} band is used to derive the sum of their abundances once the H_2CO contribution has been subtracted. Where bands are partly overlapping only the low- or high-frequency half of the band is used for identification.

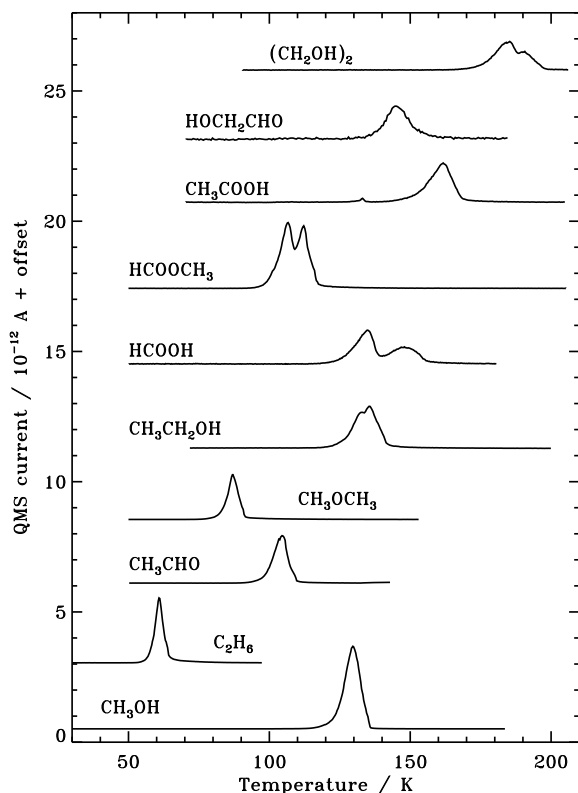


Figure 10.11 – TPD spectra of pure complex organic ices used to identify photoproducts together with a CH_3OH TPD curve.

Figure 10.11 displays the TPD curves for the same complex molecules as shown in Fig. 10.10. The QMS signal belonging to the molecular mass is plotted for each TPD experiment. The m/z values of all possible fragments have also been gathered, and are used to separate TPD curves of molecules of the same molecular mass that desorb in a similar temperature interval. For example, CH_3COOH and HCOOCH_3 both have a molecular mass of 60, but CH_3COOH frequently loses an OH group in the QMS, resulting in $m/z = 17$ and 43, while HCOOCH_3 does not. The TPD curves were modeled using the IDL routine MPFIT under the assumption of zeroth order desorption behavior, which is expected for multilayer ices. The desorption rate is then $\nu \times N_{\text{sites}} \times \exp(-E_{\text{des}}/T)$. The vibrational frequency ν is defined as a function of the desorption energy E_{des} : $\nu =$

$\sqrt{(2k_B N_{\text{sites}} E_{\text{des}} \pi^{-2} m^{-1})}$, where N_{sites} is the number of molecular sites per cm^{-2} and m is the molecular mass – N_{sites} is a constant and assumed to be 10^{15} cm^{-2} in line with previous studies. The resulting desorption energies are reported in Table 10.2. The uncertainties include both model uncertainty and experimental errors. The values agree with those published by Garrod & Herbst (2006), based on experiments on water rich ice mixtures by Collings et al. (2004), within 20%, except for HCOOCH₃ where the discrepancy is larger. This may however be due to experimental differences, i.e. pure ices here versus their ice mixtures, rather than experimental errors.

10.3.5 Identification of CH₃OH ice UV photoproducts

In addition to the complex molecules described in the previous section, smaller molecules and radicals that form via CH₃OH photodissociation are also considered when assigning spectral bands following CH₃OH ice photolysis. Identification of all photoproducts is a two-step process where the first step is the comparison between new band positions and experimentally or calculated band positions of molecules and fragments to establish a list of possible carriers to each observed band. In the second step the behavior of the band when changing experimental variables, as described in §10.3.3, is employed together with QMS data (Fig. 10.12) to determine which ones(s) of the possible candidates is the most important contributor to the formed band. Combining all information, a band identification is considered secure when consistent with the list of criteria below.

1. The spectral band position in the photolysis spectra must agree within 15 cm^{-1} of a measured pure ice band (e.g. Hudson et al. 2005) or within 50 cm^{-1} of a calculated band position for the species in question to be considered a candidate carrier of the observed band. In each case all spectral features within the spectrometer range are checked for consistency even if only one band is used for identification.
2. The temperature at which the band starts to disappear during warm-up is compared for consistency with the observed desorption temperatures of different complex molecules in pure-ice TPD experiments.
3. The mass signature in the TPD experiment following UV irradiation is checked at each temperature where a tentatively assigned band disappears during warm-up (Fig. 10.12).
4. The band positions of new carriers in UV-irradiated CH₃OH and partly-deuterated CH₃OH experiments are compared to check that the expected shifts occur as discussed in §10.3.3.6.
5. The irradiated spectra are examined for band enhancements and suppressions in CH₃OH mixtures with CO and CH₄. In CH₄ experiments, species containing CH₃ groups are expected to be over-produced compared to pure CH₃OH ice experiments. Similarly in CO containing experiments, HCO-group containing species should have enhanced abundances.

- Irradiation experiments at different temperatures are compared to ensure consistency with the expected relative diffusion barriers of differently sized radicals (see also §10.3.3.4).
- Finally, the temperatures at which radicals disappear during warm-up are compared with the spectroscopic appearance or increase of the molecular band in question; where radicals are detected, the loss of radical bands during warm-up should correspond to the enhancement of molecular bands formed from recombination of these same radicals.

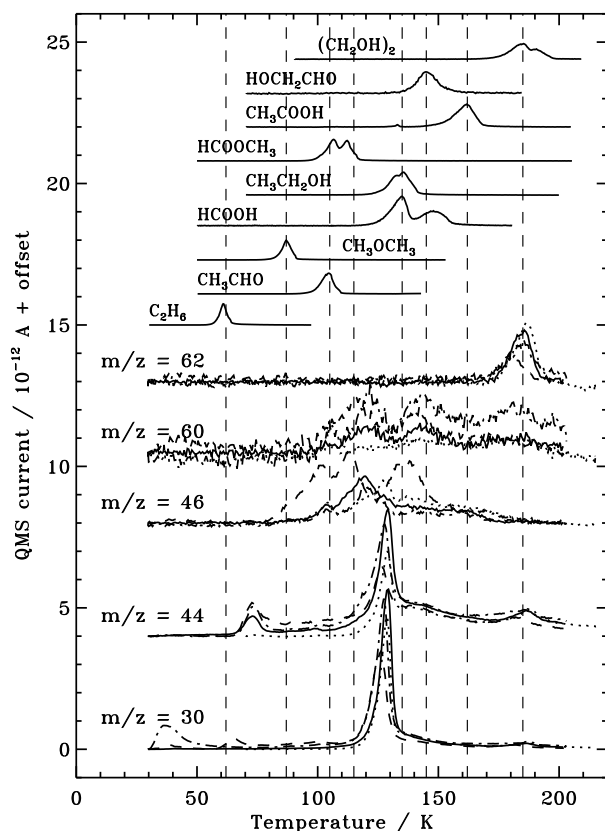


Figure 10.12 – TPD experiments following UV irradiation of a pure CH_3OH ice at 30 K (solid), 70 K (dotted), a $\text{CH}_3\text{OH}:\text{CH}_4$ 1:2 ice mixture at 30 K (dashed) and a $\text{CH}_3\text{OH}:\text{CO}$ 1:1 mixture at 30 K (dash-dotted). $m/z = 62$ can only contain contributions from $(\text{CH}_2\text{OH})_2$, $m/z = 60$ from $(\text{CH}_2\text{OH})_2$, HOCH_2CHO , CH_3COOH and HCOOCH_3 , $m/z = 46$ from HCOOH , $\text{CH}_3\text{CH}_2\text{OH}$ and CH_3OCH_3 , and $m/z = 44$ from CO_2 , CH_3CHO and all heavier complex organics. Finally $m/z = 30$ can contain contributions from C_2H_6 , CH_3OH , H_2CO and several heavier organics compounds. All TPD series are scaled to the same initial CH_3OH abundance to facilitate comparison.

All observed bands and their inferred carrier properties are listed in Table 10.3, i.e. if a band is enhanced in the $\text{CO}:\text{CH}_3\text{OH}$ mixture its main contributor contains a CO group, if it is enhanced in the $\text{CH}_4:\text{CH}_3\text{OH}$ mixture the main contributor contains a CH_3 group and if the band disappears in the CH_3OD experiment the main contributor contains an OH group.

Table 10.3 – Detected bands between 700 and 2200 cm⁻¹ and identifications.

Wavenumber (cm ⁻¹)	<i>T</i> _{form} (K) ^a	<i>T</i> _{des} (K) ^b	CO	CH ₃	OH	Candidates
2135	20	30	y			CO
1843	20	30	y			HCO
1746	70	140-190	y		y/-	HOCH ₂ CHO + HCOOH + CH ₃ CHO
1727	20	70/110/150	y			H ₂ CO + CH ₃ CHO + HCOOCH ₃
1498	20	70	y			H ₂ CO
1382	20	140		y		CH ₃ CH ₂ OH
1372	30	40		y		C ₂ H ₆
1350	20	100		y		CH ₃ CHO
1301	20	40		y		CH ₄
1245	20	70		y		H ₂ CO
1214	70	130		y		HCOOCH ₃
1195	20	50			y	CH ₂ OH
1161	50	90				CH ₃ OCH ₃
1093	70	110/130/180		y		CH ₃ OCH ₃ + CH ₃ CH ₂ OH + (CH ₂ OH) ₂
956	30	70		y		CH ₃ OCH ₃
921	?	110		y		HCOOCH ₃
911	?	150				(CH ₂ OH) ₂
890	70	180			y	CH ₃ CH ₂ OH
885	?	130		y	y	(CH ₂ OH) ₂ (+ HOCH ₂ CHO) ^c
866	70	150/180			y	C ₂ H ₆
822	30	50		y		

^aThe temperature at which the band carrier is most efficiently produced.

^bThe temperature at which the band starts to disappear during warm-up with 1 K min⁻¹.

^cMinor contributor in most experiments.

10.3.5.1 Small molecules: H₂, H₂O, CH₄, CO, O₂, H₂CO, H₂O₂ and CO₂

H₂ probably forms in the photolysis experiments, since CH₂OH is observed and thus H atoms must be produced in the ice (see below). Two H atoms can subsequently recombine to form H₂ as observed in D₂O photodesorption experiments (Watanabe et al. 2000) and following irradiation of H₂O:CH₃OH:NH₃:CO experiments (Sandford & Allamandola 1993). Detections or determinations of strict upper limits of H₂ are however not possible because of a lack of strong infrared transitions together with the expected fast desorption of any H₂ from ices above 20 K.

H₂O (D₂O) is visible during warm-up following the desorption of CH₃OH (CH₃OD). However, its origin is unclear, since H₂O is the main contaminant in the chamber. During irradiation, the H₂O stretching and libration modes are hidden under strong CH₃OH bands and thus cannot be used for identification. The 1670 cm⁻¹ bending mode coincides with the broad wing of the 1727 cm⁻¹ band found in most irradiated CH₃OH spectra. The wing is probably reduced in the CH₃OD ice, depending on the baseline determination, but it is also not visible in the CD₃OH ice (Fig. 10.8). Thus, there is no clear evidence for the amount that H₂O contributes to this feature. The best constraints on water formation come instead from the CH₃OD experiments where ~0.5 ML D₂O is detected at the end of the experiment, corresponding to a few percent with respect to the initial CH₃OD amount.

CH₄ is formed in all experiments, identified by its relatively isolated ν_4 band at 1301 cm⁻¹ (D'Hendecourt & Allamandola 1986). The CH₄ ν_3 feature at 3008 cm⁻¹ is also one of the few bands that are clearly visible on top of the CH₃OH bands in that region.

CO has a single strong feature at 2139 cm⁻¹ (Gerakines et al. 1995), which is shifted to 2135 cm⁻¹ in the experiments here. The feature cannot be confused with those of any other species and the identification is thus clear. Of the observed CO ice amount ~0.2 ML originates outside of the CH₃OH ice. This is however only significant for the thin (~6 ML) 20 K ice experiments. At 30 K and above the CO sticking coefficient is low (Bisschop et al. 2007c).

O₂ has no strong infrared bands. During warm-up of the 20 and 30 K experiment there is no $m/z = 32$ detected at the expected O₂ desorption temperature of ~30 K (Acharyya et al. 2007). In contrast there is a clear $m/z=28$ band from CO in this temperature region. If CO and O₂ can be assumed to behave similarly this puts an upper limit on the O₂ production to less than 5% of that of CO at 20 K.

H₂CO has three strong bands between 2000 and 800 cm⁻¹ at 1723, 1494 and 1244 cm⁻¹. The 1723 cm⁻¹ band overlaps with several complex spectral features, and the 1494 cm⁻¹ band sits on the shoulder of a strong CH₃OH band. The 1244 cm⁻¹ band is relatively isolated and has been used previously to constrain the H₂CO production (Bennett et al. 2007). All three bands are readily observed in the irradiated ices between 20 and 50 K. The 1244 and 1494 cm⁻¹ bands are strongly correlated and are most abundantly formed at low temperatures, while the 1723 cm⁻¹ band is less dependent on temperature, as expected from its multiple carriers. All three bands are enhanced in all CH₃OH:CO ice-mixture experiments and these identifications are therefore considered secure.

All fundamental H₂O₂ infrared bands completely overlap with strong CH₃OH bands in the investigated spectral region (e.g. Loeffler et al. 2006; Ioppolo et al. 2008). A small

$m/z=34$ peak was observed during CH₃OH desorption. Without comparison TPD this cannot be used quantitatively, however. Thus, while some H₂O₂ probably forms, its formation rate cannot be constrained experimentally.

CO₂ has a strong band at ~ 2340 cm⁻¹, which is seen in all experiments at high fluences. Because of purge problems this spectral region is somewhat polluted with CO₂ lines from gas outside of the vacuum chamber. This results in a larger uncertainty in the derived CO₂ abundance than would have been the case otherwise.

10.3.5.2 Radicals: OH, CH₃, HCO, CH₃O, CH₂OH

OH absorbs at 3423 and 3458 cm⁻¹ from a study on pure H₂O ice photolysis by Gerakines et al. (1996), using transmission spectroscopy. Bennett et al. (2007) calculated the band position to be at 3594 cm⁻¹ using the hybrid density functional theory with the 6-311G(d,p) basis set and refining the output with the coupled cluster CCSD(T) method – these calculations have typical gas-phase band-position uncertainties of 0.5–1% or <50 cm⁻¹ (Galabov et al. 2002). There are some shallow bands in the 3400–3600 cm⁻¹ wavelength region in our CH₃OH experiments, that disappear between 30 and 50 K, and that are also present in the CD₃OH ices but not in the CH₃OD ones. The bands are however an order of magnitude broader than observed for OH radicals in matrix studies (Acquista et al. 1968). This may be due to their interactions with other H-bonding molecules, but with such a disagreement present, these bands cannot be assigned to OH radicals with any certainty. The presence of the broad features also prevents the determination of strict upper limits.

HCO can be identified from its ν_2 band between 1840 and 1860 cm⁻¹ (Gerakines et al. 1996; Bennett et al. 2007). No stable species considered in this study absorbs in this region. Bennett et al. (2007) calculated the band positions of a large number of unstable species that can theoretically form in an irradiated CH₃OH ice and none of these have absorption features within 50 cm⁻¹ of 1840 or 1860 cm⁻¹. Furthermore the band enhancement in the CO ice mixture and the low temperature at which the bands disappear all point to HCO. The assignment of this band to HCO is thus considered secure.

Calculations predict that CH₃ absorb at 1361 and 3009 cm⁻¹ (Bennett et al. 2007). In the 30 K CH₄ ice mixture, two bands appear close to these wavelengths, at 1385 and 2965 cm⁻¹. Using the band width from the CH₄ ice mixture, this wavelength region could be used to constrain the CH₃ production in all ices. Unfortunately, the band strength is not known well enough to derive useful upper limits.

Bennett et al. (2007) calculated that the CO stretching band around 1170 cm⁻¹ is the strongest CH₂OH band within our spectral range. From matrix isolation experiments CH₂OH has been found to have one strong band at 1183 cm⁻¹ in agreement with the calculations (Jacox & Milligan 1973). Similarly to Gerakines et al. (1996) and Bennett et al. (2007), we detect a feature at 1195 cm⁻¹, which appears at the onset of irradiation in all pure CH₃OH experiments and is most abundant in the 20 K ice as would be expected for a radical (Fig. 10.6). The band is not enhanced in the CO- or CH₄-containing ice mixtures, which confirms that the band forms from CH₃OH alone. It is also not present in the CH₃OD ice after irradiation. The band starts to disappear around 50 K during warm-

up, at the same time other bands grow, which can be assigned to more complex CH_2OH bearing species. Thus we confirm the results of Gerakines et al. (1996) and Bennett et al. (2007) that the 1195 cm^{-1} band observed at low temperatures is due to CH_2OH . Above 50 K, it is only possible to derive CH_2OH upper limits, because of overlap with other absorption features.

CH_3O is predicted to have two fundamental transitions, isolated from strong CH_3OH bands, at 1319 and 1329 cm^{-1} (Bennett et al. 2007). The closest observed bands are the CH_4 band at 1300 cm^{-1} and a weak band at 1350 cm^{-1} . The 1350 cm^{-1} feature only starts to disappear at 70 K, which is a higher temperature than expected for a radical. It is also somewhat enhanced in CO- and CH_4 -containing mixtures. Hence there is no evidence for abundant build-up of CH_3O in any of the experiments. This is consistent with the comparatively small formation of CH_3O -containing molecules during warm-up of the irradiated ice as is reported in more detail below.

10.3.5.3 CH_3 -bearing complex molecules: C_2H_6 , CH_3CHO , $\text{CH}_3\text{CH}_2\text{OH}$, CH_3OCH_3

C_2H_6 is only detected in the UV-irradiated 30 K $\text{CH}_3\text{OH}:\text{CH}_4$ ice mixture experiment (Fig. 10.7). This ice spectrum contains a clear feature at 822 cm^{-1} with the expected band width of C_2H_6 . The band starts to disappear at 50 K during warm-up and it can thus be securely assigned to C_2H_6 . The same spectral region is used in the other experiments to derive strict upper limits on the C_2H_6 production.

Figure 10.13 shows that there is a shallow band at the frequency of the CH_3CHO 1350 cm^{-1} feature in most experiments and that CH_3CHO is the only molecule with a directly overlapping band, though the wing of the HOCH_2CHO band cannot be excluded as a carrier from spectral comparison alone. At 30 K, the feature is somewhat enhanced in both the CH_4 - and CO-containing mixtures, when comparing ices at the same temperature. The temperature at which the feature starts to disappear (100 K) is close to the expected desorption temperature for CH_3CHO from the pure TPD experiments. The feature is completely gone before the onset of CH_3OH desorption which excludes significant contributions from less volatile molecules, like HOCH_2CHO . Together these observations are only consistent with CH_3CHO as the main carrier.

Figure 10.13 also shows that a band at 1380 cm^{-1} in the photolysis spectra correlates with the pure $\text{CH}_3\text{CH}_2\text{OH}$ ice feature, but HOCH_2CHO is also a potential carrier. The band is, however, enhanced in the CH_4 -mixture experiments. Simultaneously a band at 885 cm^{-1} is enhanced (Fig. 10.13), which can be attributed to $\text{CH}_3\text{CH}_2\text{OH}$ as well. Furthermore, the 1380 cm^{-1} band starts to desorb at 120 K, with CH_3OH , while the complex HCO-bearing species only experience significant desorption at 150 K. This suggests that $\text{CH}_3\text{CH}_2\text{OH}$ is the main carrier of the 1380 cm^{-1} feature. The assignment is confirmed by a $m/z = 46$ detection at the desorption temperature of $\text{CH}_3\text{CH}_2\text{OH}$; the QMS signal is enhanced by about a factor of three in the CH_4 mixture experiment, which is of the same order as the RAIRS band enhancement. In the CO ice mixtures the contribution of HOCH_2CHO may however be significant and in these ices the 1380 cm^{-1} feature is only used to provide upper limits on the $\text{CH}_3\text{CH}_2\text{OH}$ production.

CH_3OCH_3 has not been generally considered as a photoproduct of CH_3OH ice in

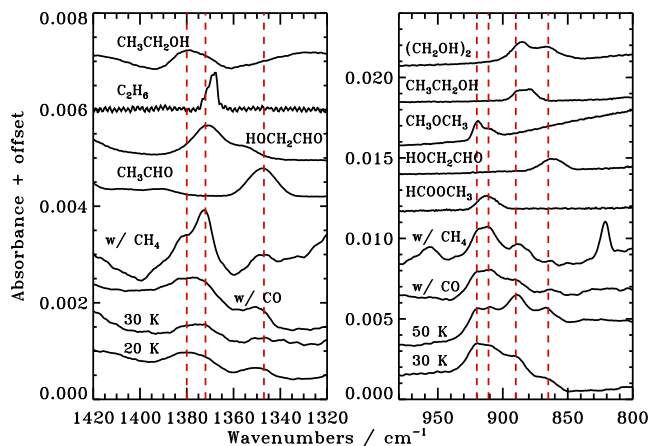


Figure 10.13 – The left panel shows spectra of UV-irradiated pure CH₃OH ice at 20 and 30 K, and CH₃OH:CO 1:1 and CH₃OH:CH₄ 1:2 ice mixtures at 30 K after the same fluence of 2.4×10^{17} cm⁻², together with pure ice spectra of the complex species that absorb in this region. The right panel shows the complex absorption pattern between 980 and 820 cm⁻¹ in pure ices at 30 and 50 K and mixed ices at 30 K, together with the possible carriers of these bands. In both panels the CH₃OH bands have been subtracted from the spectra for visibility and the features have been scaled to the initial CH₃OH abundance in each experiment to facilitate comparison. The dashed lines are present to guide the eye between band positions in the irradiated ices and in pure complex ice spectra.

previous experimental studies (Gerakines et al. 1996; Bennett et al. 2007). CH₃OCH₃ is however formed in the ice in our experiments; the feature at 1090 cm⁻¹, which can contain contributions from CH₃OCH₃, CH₃CH₂OH and (CH₂OH)₂ loses intensity at 90 K, before the onset of desorption of any of the other two species, which is only consistent with the presence of CH₃OCH₃ in the ice. Furthermore, Fig. 10.14 shows that the band seen around 1170 cm⁻¹ agrees better with CH₃OCH₃ than any other complex molecule and that it has no similarity with the nearby HCOOCH₃ band, with which it is usually identified (Gerakines et al. 1996; Bennett et al. 2007). The band is not significantly affected by the ice temperature during irradiation and during warm-up it starts to lose intensity around 90 K, close to the CH₃OCH₃ desorption temperature (Fig. 10.11). At the same time a *m/z* value of 46, characteristic of CH₃OCH₃, is detected by the QMS (Fig. 10.12). The 1170 cm⁻¹ band is enhanced in the CH₄ mixture and so is a feature at 920 cm⁻¹, which can also be attributed to CH₃OCH₃. Neither feature is enhanced in the CO ice mixture, which confirms the identification of the band carrier with CH₃OCH₃. The uncertainty of the integrated abundance of the CH₃OCH₃ feature is relatively large because of uncertainties in the baseline due to overlap with HCOOCH₃ and CH₃OH bands.

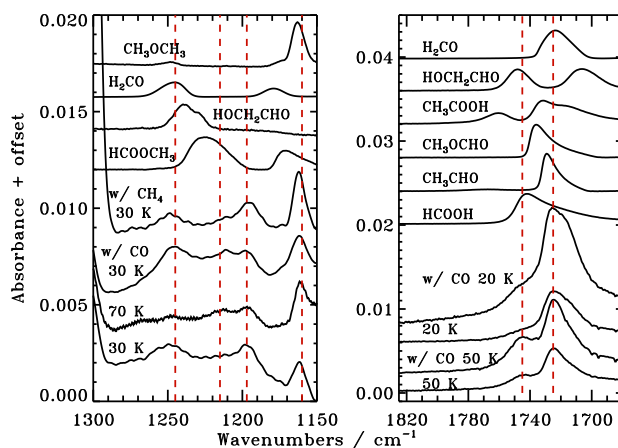


Figure 10.14 – The left panel shows the observed absorption bands between 1140 and 1290 cm^{-1} following UV irradiation of pure CH_3OH ice, $\text{CH}_3\text{OH}:\text{CO}$ 1:1 and $\text{CH}_3\text{OH}:\text{CH}_4$ 1:2 ice mixtures, and the possible carriers of these features. The right panel shows the 1700-1770 cm^{-1} HCO feature in irradiated pure CH_3OH ices at 20 and 50 K together with irradiated $\text{CH}_3\text{OH}:\text{CO}$ ~1:1 mixtures, and the possible carriers. In both panels the dashed lines indicate some of the complex band positions.

10.3.5.4 CHO-bearing complex molecules: HCOOH , HOCH_2CHO , HCOOCH_3 , CH_3COOH

In the pure CH_3OH ice experiments, none of the CHO-bearing species, except H_2CO and CH_3CHO , are uniquely identified. Similarly HCOOH and CH_3COOH have no unique bands. A mixture of these compounds can, however, be identified from the growth of the 1700 cm^{-1} complex (Fig. 10.14). The relative importance of the different contributors in different mixtures and at different temperatures can also be assessed by spectral comparison. Figure 10.14 shows that the shape of the 1700 cm^{-1} band depends on the ice temperature during irradiation. At lower temperatures, a broad feature, peaking at 1725 cm^{-1} dominates, which can be identified with H_2CO . At higher temperatures the band is more similar in width to CH_3CHO and HCOOCH_3 . This is true both when the ice is irradiated at higher temperatures and when an ice irradiated at 20 K is warmed up to >50 K. Simultaneously, the high frequency wing becomes more pronounced, suggesting an increasing importance of HOCH_2CHO , compared to HCOOH . This is the case in both pure and $\text{CH}_3\text{OH}:\text{CO}$ ice mixtures.

In the CO-dominated $\text{CH}_3\text{OH}:\text{CO}$ 1:10 mixtures, where the formation of many of the complex molecules is quenched, some of the weaker features of molecules like HOCH_2CHO and HCOOCH_3 are visible during warm-up of an ice irradiated at 20 K (Fig. 10.15). The final abundance ratio of $\text{HOCH}_2\text{CHO}/\text{HCOOCH}_3$ is approximately 1/2 at 100 K. However, HCOOCH_3 starts to form at a lower temperature; thus the ratio of the two species changes with temperature. The similar 1700 cm^{-1} feature in this experiment and in the

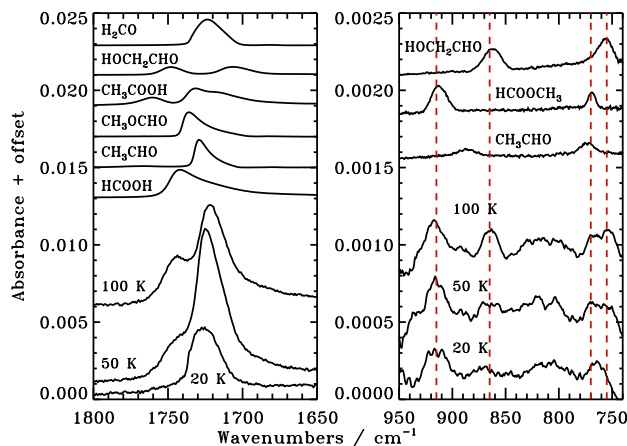


Figure 10.15 – The left panel shows the 1700 cm^{-1} feature during warm-up of a $\text{CH}_3\text{OH}:\text{CO}$ 1:10 ice from 20 to 100 K, after irradiation at 20 K, together with six possible carriers of these bands. The right panel shows the $950\text{--}750\text{ cm}^{-1}$ region in the same heated mixture together with possible carriers of the detected features. All spectra are scaled with the same fraction in both panels, so that the absorbance of each spectrum corresponds to $\sim 0.1\text{ ML}$ of each of the complex species.

pure CH_3OH ice experiments suggests that these two molecules contribute the same fractions to the 1700 cm^{-1} band in all mixtures, depending only on the temperatures at which they are irradiated, or the temperature to which they are subsequently heated.

10.3.5.5 $(\text{CH}_2\text{OH})_2$

$(\text{CH}_2\text{OH})_2$ is the main carrier of the 866 cm^{-1} feature in Fig. 10.13. This is inferred from the ice warm-up, where the band does not decrease by more than 10–20% around the desorption temperature of HOCH_2CHO – the only other possible carrier. The remainder of the band disappears around 180 K, the desorption temperature of $(\text{CH}_2\text{OH})_2$. The QMS simultaneously detects a strong $m/z=62$ signal. The assignment of this band to mainly $(\text{CH}_2\text{OH})_2$ is thus secure, but the uncertainty in the abundance is higher than for some other species because of a small contribution of a HOCH_2CHO feature to the band. In the CO ice mixtures the $(\text{CH}_2\text{OH})_2$ abundance is instead calculated from the 890 cm^{-1} band, which partially overlaps with a $\text{CH}_3\text{CH}_2\text{OH}$ ice feature.

10.3.6 Abundance determinations of photoproducts

Table 10.4 lists the possible photoproducts considered in the previous section that have strong infrared transitions, together with the bands used for quantification, the fitting regions, the band strengths and the estimated uncertainties of the integrated absorbance. The integrated absorbance of each molecular band is determined by first automatically scaling

Table 10.4 – Potential photoproducts with infrared transitions.

Species	Band	Position (cm^{-1})	Fit region (cm^{-1})	σ area (cm^{-1})	Band strength ^a (cm^{-1})
H ₂ O	ν_2	1670	1600–1670	ul ^b	1.2×10^{-17} (1)
CH ₃	ν_2	1385	1380–1390	ul	6.9×10^{-19} (2)
CH ₄	ν_4	1301	1290–1310	0.002	1.2×10^{-17} (3)
CO	ν_1	2135	2125–2145	0.001	1.1×10^{-17} (1)
HCO	ν_1	1850	1840–1860	0.0005	2.1×10^{-17} (2)
H ₂ CO	ν_2	1245	1228–1265	0.01	1.0×10^{-18} (4)
CH ₂ OH	ν_4	1195	1185–1195	0.01	1.6×10^{-17} (2)
C ₂ H ₆	ν_{12}	822	809–832	0.001	1.6×10^{-17} (5)
CO ₂	ν_1	2340	2330–2350	0.005	1.2×10^{-17} (1)
CH ₃ CHO	ν_7	1350	1337–1350	0.003	6.1×10^{-18} (5)
CH ₃ CH ₂ OH	ν_{12}	1380	1380–1395	0.002	1.9×10^{-18} (5)
HCOOH	ν_3	1740	1739–1773	ul	6.7×10^{-17} (6)
CH ₃ OCH ₃	ν_{10}	1161	1151–1171	0.003	1.2×10^{-17} (7)
HCOOCH ₃	ν_9	1214	1216–1233	ul	2.1×10^{-17} (2)
HOCH ₂ CHO	ν_6	861	851–871	ul	3.4×10^{-18} (8)
CH ₃ COOH	ν_{14}	1746/1770	1760–1772	ul	1.1×10^{-16} (9)
(CH ₂ OH) ₂	ν_{14}	866/890	851–876	0.006	3.4×10^{-18} (8)
X-CHO/ X-COOH ^c	CO- stretch	1680–1780	–	0.01	5.4×10^{-17} (2,6,8)

^aThe listed values are transmission band strengths, for our RAIRS experiments they are scaled by a factor of 5.5, determined empirically.

^bOnly an upper limit could be determined.

^cAn average of the HCOOH, HCOOCH₃ and HOCH₂CHO band strengths of 6.7, 4.8 and 4.6×10^{-17} cm^{-1} is used.

(1) Gerakines et al. (1995), (2) calculated band strengths from Bennett et al. (2007), (3) D’Hendecourt & Allamandola (1986), (4) Schutte et al. (1993), (5) Moore & Hudson (1998), (6) Hudson & Moore (1999), (7) from CH₃OH:CH₃OCH₃ ice mixture spectroscopy, (8) Hudson et al. (2005), (9) Maréchal (1987).

the previously acquired complex molecule spectra to the band over a defined fitting region, using a personal IDL routine. The scaled band in the complex molecule spectrum is then integrated to determine the molecular abundance rather than directly integrating the band in the irradiated CH₃OH spectra. The complex ice spectra used of comparison are pure ice spectra. Mixing these complex ices with CH₃OH may cause some changes in the band shape, position and strength of the complex features. The change in band shapes for some key species, such as CH₃OCH₃, between pure ice and ice mixtures with CH₃OH have therefore been investigated to ensure that they are not substantial enough to affect band assignments. The changes in band strengths remains unknown but are unlikely to exceed 20% from previous studies on organic species in pure ices and in hydrogen-bonding ices (Boogert et al. 1997). The fitting regions are chosen for each species to ensure that the template spectra are fitted to the part of the band that has no other possible contributors than the species in question. This is especially important in spectrally crowded regions, where the absorption features of different potential photoproducts partially overlap. For example, the CH₃CH₂OH spectrum is only fitted to the high frequency half of the 1360 cm⁻¹ band when determining the CH₃CH₂OH abundance to avoid contributions to the band intensity from HOCH₂CHO. The integrated absorbance uncertainty varies by an order of magnitude between the different species, mainly dependent on how crowded the region is, since a major source of error is the choice of the local baseline.

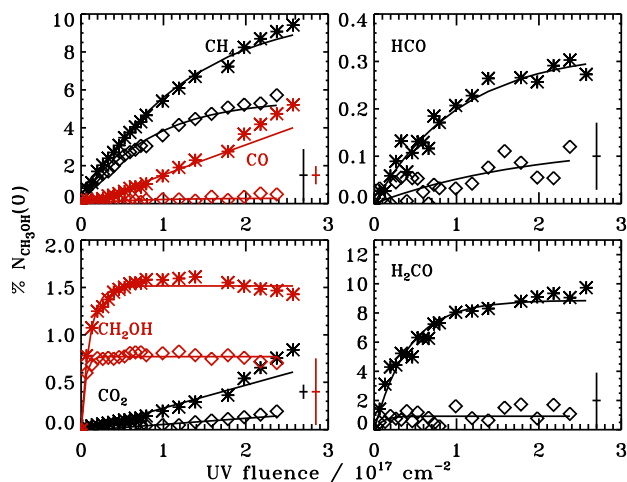


Figure 10.16 – The evolution of small CH₃OH photo-products with respect to UV fluence in % of the initial CH₃OH ice abundance (CH₃OH(0)) in each experiment during six hours of irradiation at 20 K (stars) and at 70 K (diamonds). The average abundance uncertainties are indicated in the bottom right corner of each panel. The lines are exponential fits to the abundance growths.

The integrated absorbance of each species is converted to an abundance using literature band strengths for pure ices, with a ~20% uncertainty. Calculated band strengths are less well defined for solid-state features, resulting in at least a factor of five uncertainty

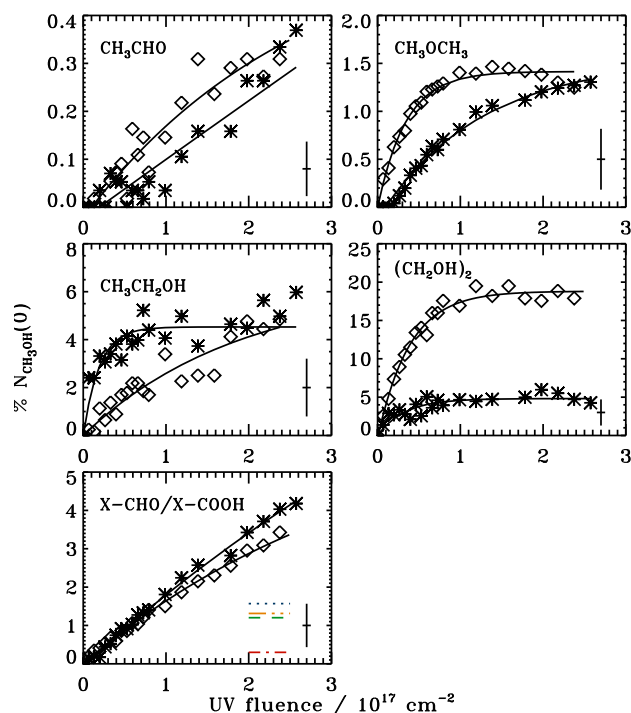


Figure 10.17 – The evolution of complex CH_3OH photo-products with respect to UV fluence in % of the initial CH_3OH ice abundance during six hours of irradiation at 20 K (stars) and 70 K (diamonds). In the bottom panel the final upper limit abundances in the 20 K ice of HCOOH (dotted), HCOOCH_3 (dashed), CH_3COOH (dashed-dotted) and HOCH_2CHO (yellow dashed-triple-dotted) are shown. The average uncertainty in each abundance is indicated in the bottom right corner. The lines are exponential fits to the abundance growths.

for the affected species (when comparing calculated values to experimental ones). All abundances are reported with respect to the initial CH_3OH abundance in each experiment to remove the uncertainty in the band strength conversion factor between transmission and reflection-absorption spectroscopy as well as to cancel the variations in the initial ice thickness between the different experiments. §10.3.3.3 showed that the ice chemistry does not depend significantly on ice thickness or irradiation flux and therefore only the results from the ~ 20 ML thick ices with the low irradiation flux are shown explicitly.

The sum of all CHO- and COOH-containing complex species, except for H_2CO and CH_3CHO , are also reported since these species have no uniquely detected features in most experiments. This sum is calculated by subtracting the H_2CO and CH_3CHO contributions from the 1700 cm^{-1} feature and calculating the remaining integrating absorbance. The integrated absorbance is converted into a molecular abundance by using an averaged band strength, which is within 20% of the reported band strengths of the three suspected main contributors, HCOOCH_3 , HOCH_2CHO and HCOOH . The fourth potential major contributor CH_3COOH has a factor of two larger band strength, but as shown below the CH_3COOH upper limits are strict in most experiments and thus it contributes at most 10% to the 1700 cm^{-1} feature.

Figures 10.16 and 10.17 show the photoproduct abundances with respect to the initial

Table 10.5 – Formation cross sections in 10⁻¹⁹ cm² during pure CH₃OH ice photolysis.

Species	20 K	30 K	50 K	70 K
CH ₄	7.0[1.2]	7.1[1.3]	5.8[1.3]	4.9[1.2]
CO	1.0[0.5]	1.0[0.6]	0.5[0.5]	0.6[0.5]
HCO ^a	0.4[0.2]	0.3[0.2]	0.3[0.2]	< 0.2
H ₂ CO	15.7[3.4]	15.4[3.8]	7.4[3.6]	< 3.3
CH ₂ OH ^a	3.7[1.0]	2.9[1.1]	2.8[1.1]	1.9[1.0]
CO ₂	0.2[0.2]	< 0.2	< 0.2]	< 0.2
CH ₃ CHO	< 0.1	< 0.1	< 0.1	0.2[0.1]
CH ₃ OCH ₃	0.6[0.7]	1.1[0.8]	2.2[0.7]	2.4[0.7]
CH ₃ CH ₂ OH	8.6[3.4]	8.8[3.8]	2.3[3.6]	3.9[3.3]
(CH ₂ OH) ₂	8.4[5.1]	10.4[5.7]	21.8[5.4]	32.2[5.0]
X-CHO/X-COOH	1.5[1.8]	1.7[1.9]	2.3[1.8]	2.0[1.7]

^aThe absolute uncertainty is a factor of 5 for HCO and CH₂OH.

CH₃OH abundance as a function of UV fluence in 20 and 70 K ices (growth curves for the other experiments are shown in the appendices (10.7.11–3). The abundances of all fragments and molecules that can form directly from CH₃OH photodissociation or from hydrogenation of a dissociation fragment have a clear inverse dependence on ice temperature, i.e., the abundances of CO, CH₄, HCO and H₂CO are significantly higher at low temperatures than at high temperatures, where recombination of large radicals dominates the chemistry. For the more complex products the temperature dependence varies. Abundances of molecules that contain an HCO- or a CH₃-group do not depend on temperature within the experimental uncertainties, while the (CH₂OH)₂ abundance is strongly temperature dependent.

Initial formation cross sections can be derived for the photochemistry products using

$$\frac{dn}{\phi t} = \sigma, \quad (10.2)$$

where n is the fractional abundance of the product with respect to CH₃OH, ϕ the fluence in cm⁻² and σ the formation cross section. A formation cross section only makes strict physical sense for fragments that form directly from CH₃OH photodissociation; however, it is also a relevant number whenever photodissociation is the formation-limiting step. Therefore, formation cross sections for all simple and complex products forming in the pure CH₃OH ice experiments between 20 K and 70 K are presented in Table 10.5. The cross sections are calculated from the first 5×10^{16} UV-photons cm⁻², which is within the linear growth regime for most molecules.

The complete shapes of the ice growth curves belonging to the small products, CH₄, CH₂OH, HCO and H₂CO, are proportional to $A_1(1 - e^{-A_2\phi})$, where ϕ is the fluence, A_1 the steady-state abundance, and A_2 combines information about the formation and destruction of the molecules in question in cm². At 50 and 70 K, this type of equation also fits the growth in abundances of complex species. Several complex production curves

are however better fitted with $A_1(1 - e^{-A_2(\phi - A_3)})$ at 20–30 K, where A_3 is a delay, in fluence units, before the production of the species in question starts. In other words, at low temperatures a certain build-up of radicals is required before the production of complex molecules becomes efficient (see also Fig. 10.3) and therefore a more general equation $A_1(1 - e^{-A_2(\phi - A_3)})$, is used to fit their abundances curves. The measured delay is typically $(1 - 2) \times 10^{16}$ photons cm^{-2} : significant for CH_3CHO and CH_3OCH_3 abundances and for the upper limits of HCOOCH_3 and HCOOH , but not for the CH_2OH containing molecules. CO and CO_2 cannot be fitted with either equation; the CO_2 growth rate even increases with fluence. This behavior is explained below when the complete reaction scheme for the ice is discussed in detail.

The exponential fits for all experiments are tabulated in the appendices (10.7.3). It should be noted however, that while this is a convenient way of describing the experimental outcomes, these equations cannot be directly translated to an astrophysical setting without intermediate modeling as will be discussed in §10.5.

10.3.7 Ice formation and destruction during warm-up following irradiation

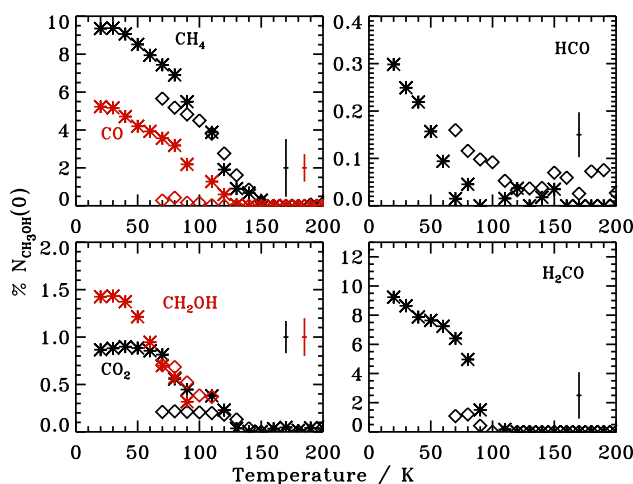


Figure 10.18 – The evolution of small CH_3OH photo-products, in % of the initial CH_3OH ice abundance in each experiment, during 1 K min^{-1} warm-up following UV irradiation at 20 K (stars) and 70 K (diamonds). The average uncertainty in each abundance is indicated to the right in each panel.

During warm-up after the completion of the UV-irradiation experiment, the ice composition changes due to recombination of diffusing radicals and sequential thermal desorption. This results in the depletion of volatile molecules and radicals from the ice as the temperature increases, while more complex molecules increase in abundance before they

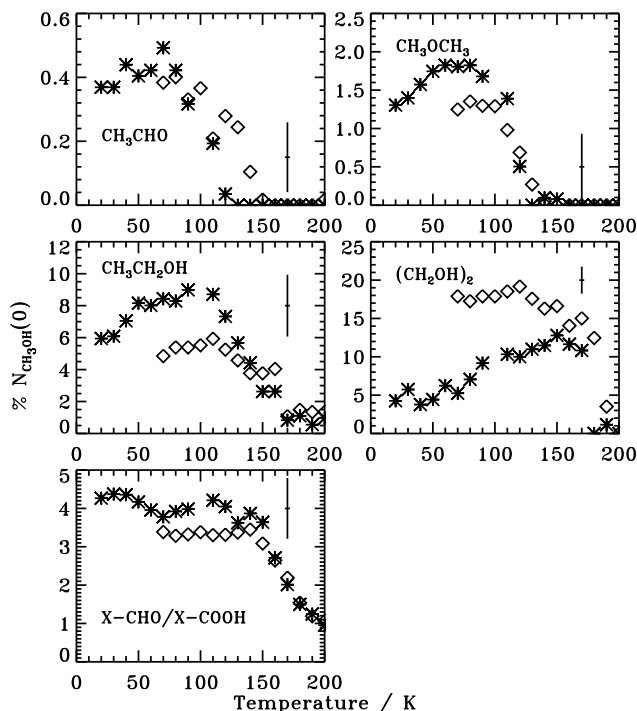


Figure 10.19 – The evolution of complex CH₃OH photo-products, in % of the initial CH₃OH ice abundance in each experiment, during 1 K min⁻¹ warm-up following UV irradiation at 20 K (stars) and 70 K (diamonds). The average uncertainty in each abundance is indicated to the right in each panel.

also start to desorb. The temperature at which a species displays a maximum abundance depends both on the diffusion barriers of the radicals it forms from and the desorption temperature of the complex molecule in question. Figure 10.18 shows that the small molecules and radicals follow the expected behavior. HCO disappears the fastest, though it is not below the noise level until 90 K. The other small molecules all desorb slowly, and only completely disappear at 120 K, the temperature at which CH₃OH starts to desorb. This is indicative of significant trapping of volatiles inside the CH₃OH ice.

The more complex molecules also behave as expected following the assumption that they form from recombining radicals; all complex ice abundances initially increase before desorption sets in (Fig. 10.19). The temperature at which a maximum abundance is reached during warm-up varies with molecular species and also somewhat with the ice temperature during irradiation; for example, it appears that CH₃CH₂OH formed in the warmer ices experiences somewhat less co-desorption with CH₃OH, and thus it desorbs mainly at its pure-ice desorption temperature. This can be understood from recent experiments that show that segregation is a general feature of mixed ices when kept at elevated temperatures; the ice irradiated at 50 and 70 K may thus be partially segregated before the onset of CH₃OH desorption, while the ices irradiated at 20–30 K do not have time to segregate before reaching the CH₃OH desorption temperature, at which they co-desorb.

Co-desorption with CH_3OH around 120 K is especially important for $\text{CH}_3\text{CH}_2\text{OH}$ and CH_3OCH_3 . CH_3CHO , CH_3OCH_3 and $\text{CH}_3\text{CH}_2\text{OH}$ reach maximum abundances at ~ 70 , 80 and ~ 110 K, respectively. $(\text{CH}_2\text{OH})_2$ only reaches a maximum at 120–150 K (Fig. 10.19). The formation and desorption pattern of X-CHO and X-COOH is, as expected, complicated with several peaks, corresponding to formation maxima of the different contributors to the band. The initial decrease suggests that the subtraction of H_2CO is imperfect and that up to 20% of the X-CHO/X-COOH abundance at low temperatures is due to H_2CO .

10.3.8 Dependence of ice products on physical conditions

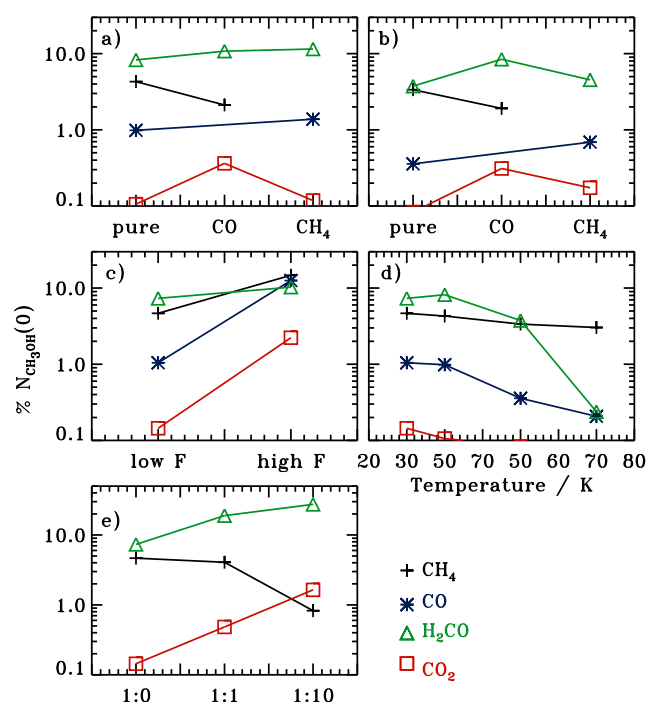


Figure 10.20 – The final simple ice abundances, with respect to initial CH_3OH abundance, after the completion of irradiation, plotted as functions of: a) and b) composition (pure CH_3OH vs $\text{CH}_3\text{OH}:\text{CH}_4$ 1:2 and $\text{CH}_3\text{OH}:\text{CO}$ 1:1 ice mixtures) at 30 and 50 K, respectively; c) fluence; d) ice temperature; e) amount of CO mixed into the ice. All ices were irradiated with 2.4×10^{17} photons cm^{-2} , except for the high flux/fluence case in c), in which a final UV fluence four-times greater was attained. In d) and e) the ice temperature is 20 K. The uncertainties are as in Fig. 10.16.

The previous two sections quantified the growth of complex ices in detail as a function of fluence and temperature under specific conditions. In this section, the focus is on the final complex ice abundances in each experiment after completion of irradiation at a low temperature and the maximum abundance reached during warm-up. This is used to determine trends in the final complex abundances as a function of the experimental conditions. Figures 10.20 and 10.21 show how the final irradiated ice composition changes with ice composition (pure vs. 1(2):1 mixtures with CO and CH_4), fluence, ice temperature during

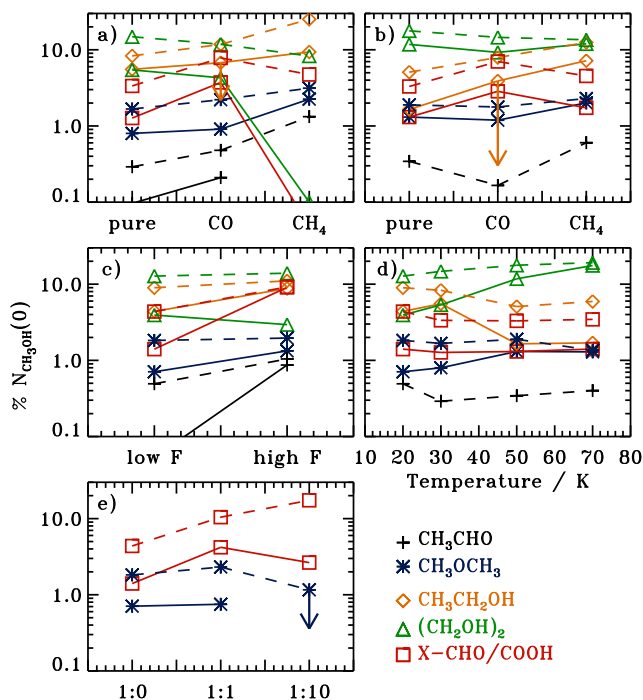


Figure 10.21 – The equivalent of Fig. 10.20 for the complex ice products, with the addition that the product abundances are shown both at the completion of irradiation (solid lines) and the maximum abundance reached during warm-up (dashed lines). The uncertainties are as in Fig. 10.17.

irradiation and the amount of CO mixed in at 20 K. The small photoproducts in Fig. 10.20 are all affected by temperature, though the CO-containing ones, much more severely than CH₄. Both CO₂ and H₂CO are enhanced in the CO-containing mixtures, while CO₂ and CO are the species most affected by increases in fluence.

Among the complex products in Fig. 10.21 CHO- and COOH-containing species are enhanced in the CO ice mixtures regardless of temperature, though CH₃CHO, is enhanced in the CH₄-containing ices as well. The CHO-containing molecules, except for CH₃CHO, thus trace CO-rich CH₃OH ices. In the CH₃OH:CO 1:10 mixture this enhancement of CHO- and COOH-bearing species is more extreme; only CHO- and COOH-bearing complex species are detected and these have a total abundance of maximum ~20% during warm-up. CH₃OCH₃, CH₃CH₂OH and CH₃CHO are enhanced in the CH₄ ice mixture at 30 K, but this enhancement almost disappears at 50 K, except for the case of CH₃CH₂OH. Thus, CH₃CH₂OH is the most sensitive tracer of the addition of CH₄ to the ice. Overall, the complex-product abundances do not change by more than a factor of 2–3 in 1(2):1 mixtures compared to pure CH₃OH ice, nor between ices at different temperatures. However, the X-CHO abundance increases by more than a factor of five in the CH₃OH:CO 1:10 mixture.

Of all detected complex molecules, (CH₂OH)₂ depends most steeply on ice tempera-

ture, especially in the ice mixtures; its abundance varies by almost an order of magnitude between experiments of different temperatures after UV irradiation of the ice is completed. The dependence is, however, significantly weakened by the time of desorption. Increasing the UV fluence increases the importance of CH_3CHO and the other CHO- and COOH-bearing species. In contrast, the CH_3 -containing species are not affected by fluence, while the $(\text{CH}_2\text{OH})_2$ abundance decreases somewhat, for a fluence increased from 2.4 to $9.6 \times 10^{17} \text{ cm}^{-2}$.

Different molecular production rates are thus affected differently by changes in ice composition, temperature and UV fluence. These varied responses of molecular production rates to changes in the experimental conditions can be used both to derive chemical properties and to make astrophysical predictions on complex molecule production. This is one of the topics in §10.4 and 10.5 below.

10.4 Discussion

10.4.1 Comparison with previous experiments

The simple ice products found in this study at 20 K are qualitatively comparable to those found previously in UV irradiated pure CH_3OH ices at 10–15 K. Quantitatively, the relative amount of formed CH_4 and H_2CO are the same compared to Baratta et al. (2002), while an order of magnitude more CO and CO_2 is reported by the end of their experiment. The CO and CO_2 abundances are enhanced by a similar factor in Gerakines et al. (1996) compared to the the experiments presented here. The enhancement may be due to the higher UV fluence used in the previous studies, since the relative CO content increases in our ices with fluence. The high CO abundance may also be partly a result of investigating thick ices (~ 0.1 – $1 \mu\text{m}$) in high vacuum chambers ($\sim 10^{-7}$ mbar); the ice thickness reduces the escape probability of CO through photodesorption and the high vacuum (as opposed to ultra-high vacuum) increases the chance of contaminations, which may change the final ice composition. The formation cross sections of CH_4 and H_2CO presented in §10.3.6 agree with those reported by Gerakines et al. (1996) within the experimental uncertainties of 50%. Thus, the overall agreement is good, between previous studies and the pure CH_3OH photochemistry experiment at 20 K presented here.

Complex products are difficult to identify in both UV irradiated and ion-bombarded CH_3OH -rich ices, which has resulted in different assignments in the literature to the same bands, or simply no presentation of absolute complex product abundances. As discussed in the band-assignment section, more stringent criteria for band identification allow for both more secure and more numerous band identifications. The most important disagreements between this and previous studies are the assignments of HCOOCH_3 and CH_3OCH_3 bands (Gerakines et al. 1996; Bennett et al. 2007). We agree with Bennett et al. (2007) on the assignments of bands to $(\text{CH}_2\text{OH})_2$, but are hesitant with HOCH_2CHO assignments in the CH_3OH -dominated ices, because of overlap with features from e.g. HCOOH . However, HOCH_2CHO may be produced more efficiently during ion bombardment than during UV irradiation, facilitating band identification; we do not find so sharp

a band at the position of one of the HOCH₂CHO bands as observed by Bennett et al. (2007) in their ion-bombardment study. No other complex molecules were identified in either study. Hudson & Moore (2000) also tentatively detected (CH₂OH)₂ following proton bombardment of a CH₃OH:H₂O mixture. Its formation appears prominent under a range of conditions.

Similarly to Bennett & Kaiser (2007), we do observe bands of HCOOCH₃ and HOCH₂CHO in a CO dominated CH₃OH ice mixture, indicating that overall the chemistry induced by UV radiation and ion bombardment is similar. HOCH₂CHO was also tentatively detected by (Hudson et al. 2005) following UV irradiation of a CO:CH₂OH 100:1 ice mixture, though more work is required to confirm its formation under those conditions.

10.4.2 Dependence of complex chemistry on experimental variables

Section 10.3 showed that the final results of CH₃OH photochemistry depend on the initial ice composition and the ice temperature during irradiation, but not on UV flux or ice thickness. The independence of ice thickness for the final abundances of complex species between 6 and 20 ML puts an upper limit on the efficiency of surface photochemistry versus bulk photochemistry. Employing a typical relative product abundance uncertainty of 10%, the upper limit on a relative enhancement in the 6 ML ice compared to the 20 ML one is $\sqrt{2 \times 10^2} \sim 14\%$. This puts an upper limit on excess production in the 6 top ML combined, while the upper limit on excess production in the very top layer is $6 \times 14 \sim 84\%$. Surface reactions are therefore at most twice as efficient as bulk reactions in producing complex molecules. This does not directly limit surface diffusion, since photodesorption is efficient enough that many of the radicals and recombined products in the surface layers may escape, thus lowering the efficient surface yield. In fact the initial rates in the 6 ML ices seem somewhat higher, though this difference is barely significant (Appendix 10.7.3).

The independence of the ice chemistry on UV flux, i.e. the ice composition depends only on the total UV fluence at any time, suggests that the experiments operate in a regime where photodissociation is the rate-limiting step for production of complex organics. If the opposite were true, more complex molecules should form at the lower flux level after the same fluence, when radicals have had more time to diffuse and recombine. This may be counter-intuitive since diffusion is expected to be slow at 20 K. It suggests that the chemistry, at least at low temperatures, is dominated by fast non-thermalized diffusion following photodissociation. This is consistent with the small differences in formation rates between 20 and 70 K – in cross-section terms, the formation rate increases by a factor of four or less for all complex organics. In contrast, formation rates dependent on thermal diffusion should change dramatically within this temperature regime since quantified segregation studies show that the thermal diffusion rate of molecules, such as CO₂, changes by an order of magnitude between only 50 and 60 K (Öberg et al., submitted). The low production rate of complex organics during irradiation at 20 K in the CH₃OH:CO 1:10 ice mixture is also consistent with the expected fast thermalization, and thus short diffusion range, of photo-fragments with excess energy (Andersson & van Dishoeck 2008). In this experiment it is instead thermal diffusion during warm-up that

dominate the complex organic production.

Whether thermalized or non-thermalized diffusion drives the chemistry thus depends on a number of factors, including the concentration of radicals in the ice and the temperature during irradiation. To quantify the relative importance of thermalized and non-thermalized diffusion for specific radicals at different temperatures requires quantitative modeling of the complex molecule production during both the irradiation and the warm-up phases. Qualitatively, an increase in thermal diffusion with temperature is required to understand the observed four times higher $(\text{CH}_2\text{OH})_2$ abundance and formation rate during irradiation at 70 K compared to 20 K. Faster diffusion is also required to explain the immediate onset in formation of most molecules at high temperatures, compared to the short delay at 20 K. Some molecular abundances, such as $\text{CH}_3\text{CH}_2\text{OH}$, seem hardly affected by a change in ice temperature. Still it must form at least partly through diffusion of radicals since there is an abundance increase during warm-up. The insensitivity to ice temperature during irradiation may instead be due to increased competition between other reaction pathways once the CH_2OH radical becomes mobile, especially to form $(\text{CH}_2\text{OH})_2$, as is discussed further below. The complexity of these interactions makes it impossible to better quantify the dependence on ice temperature for ice photochemistry until a complete grid of models has been run, which is the topic of Paper II.

CH_4 and CO are small molecules with a simple photodissociation chemistry: CH_4 mainly loses an H to form CH_3 , though direct dissociation to CH_2 is also possible (Romanzin et al. 2008), while CO does not photodissociate measurably with the UV lamp in this experiment (Öberg et al. 2007b). Previous experiments show that CO can react with hydrogen to form HCO, and with OH to form CO_2 (Watanabe et al. 2003; Hudson & Moore 1999). Thus adding CO or CH_4 to CH_3OH ice should as a first approximation not add any reaction pathways, but only provide excess functional group radicals. Figure 10.21 shows that enriching the ice with these molecules also increases the importance of ice temperature on the final ice composition. $(\text{CH}_2\text{OH})_2$ displays the most dramatic change; in the pure ice the final abundance changes by a factor of two between 30 and 50 K, in the CH_4 mixture the final abundance is an order of magnitude different at the two temperatures. This effect is mainly because less CH_4 is retained in the 2:1 ice mixture at 50 K compared to 30 K even though the same mixtures were deposited. The same is true for CO, where less than half of the originally deposited CO was trapped in the 50 K ice, resulting in less building material for HCO-containing species. This will be true in astrophysical ices as well and is therefore important to keep in mind, i.e. the building material of complex molecules will change with ice temperature also when the starting point is a typical interstellar ice mixture.

10.4.3 A CH_3OH photochemistry reaction scheme

When considering the possible chemistry induced in the CH_3OH ice through UV irradiation it is necessary to choose a level of complexity to investigate, since theoretically the products can continue to dissociate and recombine into ever more complex species. In this qualitative analysis we choose to only consider the dissociation and recombination of first generation radicals from CH_3OH dissociation, with one exception – the dissociation

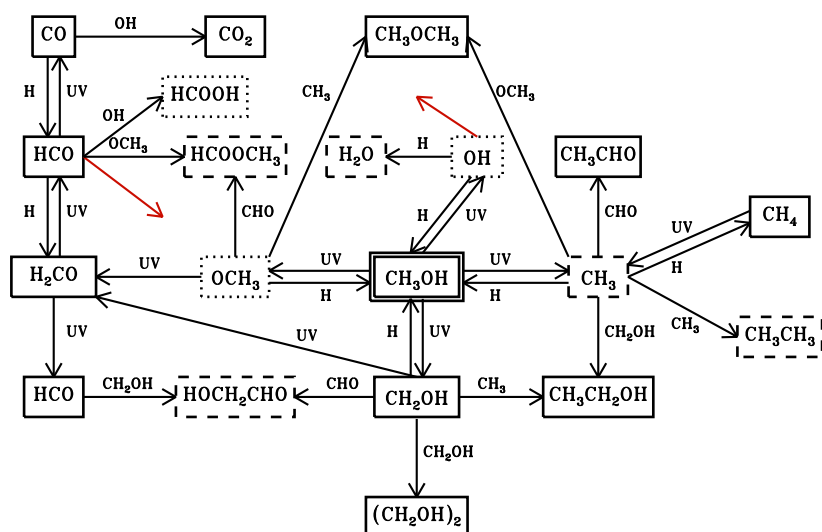


Figure 10.22 – The proposed reaction scheme to form the observed products following UV-irradiation of pure CH₃OH ice (solid boxes), of CO or CH₄:CH₃OH ice mixtures (dashed boxes) and products whose production could only be constrained with upper limits (dotted boxes). Though not shown for clarity, all reactions can be reversed. The two arrows of connecting to boxes indicate that the radicals in question take part in more reactions in other parts of the reaction scheme.

of H₂CO into HCO and CO and its reaction to CO₂. This path was included because it only results in smaller molecules that are easily detected and thus the kinetics can be modeled. In fact, the photodissociation track from CH₂OH/CH₃O to H₂CO and further to HCO and CO is an important strand of reactions to understand, since these are the only reactions that do not depend on diffusion and thus their production yields provide a clean measure of radical production due to photodissociation of small molecules and radicals. Qualitatively, the relative production rates of CH₂OH, H₂CO, HCO, CO and CO₂ agree well with the prediction of the reaction scheme that the observed normalized formation rates should decrease from one generation of species to the next (Fig. 10.16.)

Within this framework it is assumed that the vast majority of reactions consists of radical recombination without breaking of bonds i.e. no abstraction. This needs to be further tested through experiments and modeling, but so far there has been no reported evidence for abstraction in ice chemistry experiments.

Taking all this into account, Fig. 10.22 shows the proposed reaction scheme describing the formation of the observed species from photoproducted radicals. The scheme

shares many features with previous ones considered by e.g. Garrod & Herbst (2006). It starts with four possible photodissociation products of CH_3OH that form from breaking one bond i.e. CH_2OH , OCH_3 , CH_3 , OH and H (the evidence for no direct dissociation to H_2CO is discussed in §10.4.4). The formed radicals are then allowed to recombine into stable species or photo-dissociate further. This scheme should reproduce the chemistry in the ice at low fluences well. As the chemistry proceeds the destruction of complex molecules becomes important to obtain the observed equilibrium conditions and then a more elaborate reaction scheme is required to analyze the outcome.

Within the framework of Fig. 10.22, the final irradiated ice composition depends on both the production rate of each radical and the probability of two specific radicals finding each other and recombining in the ice. The radical production rate depends on the UV flux, the photodissociation branching ratio and photodissociation cross section of CH_3OH , and the relative photodissociation rates of CH_2OH , H_2CO and HCO into smaller species. Once produced, the radicals diffuse through the ice. The scheme shows that all complex molecules are formed in competition with several others that are formed from the same radicals. The recombination branching ratio of any one radical therefore depends both on the amount of other radicals and on their relative diffusion rates. As an example CH_2OH can react with H , CH_3 , HCO , OCH_3 and CH_2OH as well as further dissociate to H_2CO . Whether dissociation or recombination occurs depends on both the UV flux and the diffusion rates of CH_2OH and other radicals, and the amount of other radicals in the ice. At high UV fluxes and low temperatures further dissociation to H_2CO and recombination with the volatile H to reform CH_3OH should dominate. At slightly higher ice temperatures recombination with less volatile radicals will become competitive and finally, once CH_2OH can diffuse through the ice, the $\text{CH}_2\text{OH}+\text{CH}_2\text{OH}$ pathway will dominate, since CH_3OH ice photodissociation favors CH_2OH production as shown in §10.4.4.

To quantify which reaction pathway dominates at which temperature and flux, requires a large self-consistent model (see Paper II). Already this simplified analysis shows that all observed molecules can be formed straightforwardly with a simple reaction scheme involving recombination of small radicals. This is promising for quantification of complex ice chemistry, both in the laboratory and in space.

10.4.4 CH_3OH photo-dissociation branching ratios

UV photodissociation of CH_3OH ice can theoretically result in several different products. Experiments and calculations have shown that CH_3OH has multiple absorption bands in the range of our UV lamp, which are associated with fission of different bonds, producing the different radicals shown in Fig. 10.22 (e.g. Nee et al. 1985; Cheng et al. 2002). With a broadband UV lamp it is thus difficult to predict which dissociation fragments are formed and their relative importance.

While it is therefore not possible *a priori* to exclude any photodissociation pathways, the direct dissociation to form H_2CO is however eliminated as an important dissociation pathway by the experiments. H_2CO production depends dramatically on ice temperature, such that an order of magnitude less H_2CO forms at 70 K compared to 20 K. This

is consistent with a two-step process where CH₃OH is first photodissociated into CH₃O or CH₂OH followed by further photodissociation into H₂CO dependent on the relative time scales of diffusion and UV absorption at a certain temperature. The strong temperature dependence is inconsistent with H₂CO forming directly from CH₃OH since then a large amount of H₂CO should form at higher temperatures, similarly to CH₄, which only requires a single photodissociation event followed by diffusion of H to form. The considered photodissociation channels for this discussion are then CH₂OH + H, OCH₃ + H and CH₃ + OH.

Without a complete model, the branching ratios cannot be calculated accurately, but inspection of the experimental results allows for some conclusions. Under the assumption that both the photodissociation cross sections of the formed CH₃OH fragments and the rate at which they recombine with hydrogen are approximately the same, the amount of formed complex molecules can be used to assess the importance of different photodissociation pathways. First CH₃CH₂OH and CH₃OCH₃ both form through recombination of CH₃ with OCH₃ and CH₂OH, respectively. CH₃ is predicted to be most mobile of the three radicals and thus its diffusion should determine the recombination rates of both complex molecules. The relative production rates of CH₃CH₂OH and CH₃OCH₃ should then to a first approximation only depend on the OCH₃:CH₂OH branching ratio during CH₃OH photodissociation. The CH₃CH₂OH/CH₃OCH₃ abundance ratio is consistently 4 ± 2 at all fluences, temperatures and ice compositions. The value derived from the CH₄ ice mixture experiment at 30 K should describe the photodissociation branching ratio most accurate, since the enhancement of CH₃ radicals minimizes the effect of different diffusion properties of OCH₃ and CH₂OH. There the ratio is 5 ± 1 .

The importance of the CH₃+OH dissociation pathway is more difficult to assess. An upper limit can be estimated by comparing the detected (CH₂OH)₂ abundances and the upper limits on C₂H₆ at 30 K following irradiation of pure CH₃OH ice. Since CH₃ is more volatile than CH₂OH and thus diffuses faster, more C₂H₆ will form per produced CH₃ radical in the ice than (CH₂OH)₂ per produced CH₂OH and thus the estimated upper limit will not be very strict. The observed (CH₂OH)₂ abundance to C₂H₆ upper limit is ~ 40 in this experiment. The abundance of each complex molecule depends on the radical abundance squared, which results in a total branching ratio of CH₂OH:OCH₃:CH₃ of $5 \pm 1:1:<1$.

This effective photodissociation branching ratio of CH₃OH ice is not necessarily equal to the branching ratio of gas phase CH₃OH molecules. The effective branching ratio may favor the CH₃ radical since hydrogenation of CH₂OH and OCH₃ results in CH₃OH, while CH₃ hydrogenation produces CH₄ that mainly photodissociates back into CH₃. This may however be compensated for by a higher recombination rate of CH₃ and OH than between the larger fragments and H, since H will diffuse away from its dissociation partner faster. It is interesting to note that the calculated branching ratio is consistent with a purely statistical one, i.e. three different bond breaks result in CH₂OH and one each in CH₃ and OCH₃. The model in Part II will further demonstrate whether this simple treatment of the branching ratio is valid.

10.4.5 Diffusion of radicals

The diffusion barriers of all radicals involved in complex molecule formation can only be properly quantified by modeling the entire chemical network self-consistently under different irradiation and warm-up conditions. The relative heights of diffusion barriers can however be estimated from the decrease of radical abundances and the increase of molecular abundances during warm-up of irradiated ices. Inspection of the warm-up plots in Fig. 10.19 together with the reaction scheme in Fig. 10.22 qualitatively shows that the products of the radicals in question, H, OH, HCO, CH₃, OCH₃ and CH₃OH, depend differently on temperature.

The only radicals that are detected are HCO and CH₂OH. HCO clearly disappears faster of the two and thus has a lower diffusion barrier than CH₂OH. This is also evident when comparing (CH₂OH)₂ and X-CHO production during warm-up; the X-CHO abundance does not increase beyond 80 K, while (CH₂OH)₂ is produced up to at least 110 K. CH₃OCH₃ and CH₃CH₂OH behave similarly during warm-up, though CH₃CH₂OH grows to slightly higher temperatures, suggesting that CH₃ diffusion is the most important limiting step, but that OCH₃ and CH₂OH mobility matters as well. The OCH₃ and CH₂OH diffusion is even more important in reactions with HCO; during warm-up of the CH₃OH:CO 10:1 ice, HCOOCH₃ forms at lower temperatures, and thus consumes most of the HCO, compared to HOCH₂CHO. The increased importance of the diffusion capabilities of the heavier radicals in reactions with HCO compared to CH₃ suggest that the diffusion barrier for HCO is higher than for CH₃. This is confirmed by the slightly lower formation temperature of CH₃OCH₃ and CH₃CH₂OH compared to X-CHO. The OH barrier is the only one that cannot be assessed since it is only involved in CO₂ and HCOOH production. HCOOH is not uniquely identified and CO₂ production may instead be limited by CO diffusion. Combining the above results the relative diffusion barriers increases as H < CH₃ < HCO < OCH₃ < CH₂OH. This is in qualitative agreement with the assumptions by Garrod et al. (2008).

These relative diffusion barriers, together with the dissociation branching ratios and the observed dependences on ice composition are used below to test a possibility of an ice origin of observed complex molecules in different astrophysical environments.

10.5 Astrophysical implications

10.5.1 Potential importance of photochemistry around protostars

CH₃OH ice probably forms in dense cloud cores; it is absent from the cloud edges, but often abundant towards protostars. This is in contrast to for example CO₂ and H₂O ice, which are present already at a few A_V in dark clouds. Because of its formation deep into the cloud, the CH₃OH ice is shielded from external UV irradiation during most of its lifetime. A conservative test of whether enough radicals can be produced from irradiated CH₃OH ice to account for observations of complex molecules should then only include the locally produced UV field inside the cloud core from cosmic ray interactions with H₂. This cosmic-ray induced UV field results in an approximate flux of 10⁴ cm⁻² s⁻¹ (Shen

et al. 2004). During a million years in the cloud core CH₃OH ice is thus exposed to a fluence of $3 \times 10^{17} \text{ cm}^{-2}$, which is the same as the final fluence in most of the experiments here, where more than 50% of the CH₃OH is destroyed. Previous experiments at 10 K and the irradiated ice experiments at 20 K here show that of the radicals formed from photodissociation, a large fraction is either further dissociated or hydrogenated to form simpler species than CH₃OH. In this study ~25% of the destroyed CH₃OH is converted into simpler molecules at 20 K, but up to 50% in previous studies (Gerakines et al. 1996). The amount of ‘frozen in’ radicals may be further reduced in astrophysical environments, where hydrogen atoms accrete onto the ice surface and re-hydrogenate radicals. Hydrogenation studies of O₂ and CO have revealed that the hydrogen penetration depth at 10–15 K is limited to the top few monolayers (Ioppolo et al. 2008, Fuchs et al. A&A in press) and re-hydrogenation will therefore mainly affect predictions of the complex chemistry on the ice surface. The radical formation rates in CH₃OH ices thicker than a few monolayers and in CH₃OH ices covered by CO ice should not be significantly perturbed by this effect.

More than 50% of the photodissociated CH₃OH ice may thus result in ‘frozen in’ radicals or complex molecule formation at the dark cloud stage. Once the radicals become mobile following cloud core collapse and the turn-on of the protostar, the approximate complex molecule to CH₃OH ice abundance ratio is 25%, since each complex molecule forms from two CH₃OH fragments. This is assuming CH₃OH is the precursor of all complex O-bearing organics. The fraction of complex molecules in the ice will increase if CH₄, H₂O, CO and CO₂ ice take part in the photochemistry, which will depend on the structure of the ice. The ratio will also increase in protostellar envelopes if the effects of the enhanced UV-radiation field from the star are included for ices in the inner parts.

Laboratory data on ice photochemistry thus predict that a large fraction of CH₃OH will be converted into more complex molecules during the pre- and proto-stellar stages. This can be compared with observations. The sum of detected oxygen-rich complex molecule abundances is approximately 50% with respect to the CH₃OH abundances in hot cores (Bisschop et al. 2007c) and closer to 10-20% in other sources rich in complex molecules. Photochemistry in ices thus provide the right order of magnitude of complex ice species compared to what is observed in regions where ice desorption has occurred. This does not prove that the observed complex molecules have an ice origin, but quantified experimental results do provide a way to test this.

10.5.2 Abundance ratios as formation condition diagnostics

The analysis of the complex ice composition following irradiation in the laboratory can be used to test an ice formation scenario for complex species in star-forming regions. The first piece of information from the warm-up plots is that the ice temperature during irradiation only has a limited effect on most complex ice abundances at the time of desorption. Thus in protostellar envelopes with large CH₃OH ice fractions, where the complex ice chemistry is dominated by pure CH₃OH chemistry, similar relative fractions of complex ices would be expected in the gas phase over a large range of objects if only thermal desorption is assumed. If on the other hand the entire lifetime of the ice can be sampled

by non-thermal desorption, temperature effects on the ice composition may be observed. This temperature effect will be especially clear if the coldest parts are still dominated by a CO-rich CH₃OH ice, which is predicted to favor an HCO-rich complex chemistry. However, parts of the complex ice product composition seem robust to a range of physical conditions and can therefore be used to test formation scenarios without making assumptions about the original ice composition or the ice-desorption mechanism.

Regardless of mixture composition and ice temperature, the CH₃CH₂OH and CH₃OCH₃ ratio is constant in the experiments and it is thus expected to be constant in astrophysical environments as well, even though the ratio of 5 to 1 may not be reproduced in interstellar regions because of different time scales, desorption temperatures and gas phase destruction rates. The ratio may also be affected by hot gas-phase chemistry around high mass protostars. Indeed, the detected abundances of CH₃OCH₃ may be strongly affected by gas-phase processes; Garrod et al. (2008) found that gas-phase formation of this molecule, following the evaporation of methanol, is efficient, even with conservative rate estimates. Thus the CH₃CH₂OH and CH₃OCH₃ ratio can only be used directly as an ice chemistry test where the gas phase processing is negligible.

Similarly, the HCOOCH₃ and HOCH₂CHO ratio changes little with ice composition, though it does depend on ice temperature. Thus, while detailed modeling of absolute ratios of this pair of molecules is saved for Paper II, strong correlations between such pairs of molecules towards different astrophysical objects would support the idea that ice photochemistry followed by desorption is responsible for gas phase organics.

In contrast, the CH₃CH₂OH, HOCH₂CHO and (CH₂OH)₂ relative abundances at the time of ice desorption vary with ice temperature during irradiation and composition even on laboratory time scales. They range between 1:<1:1 (CH₃OH:CO 1:1, 30 K), 2:<1:10 (pure CH₃OH 70 K), 10:<1:4 (CH₃OH:CH₄ 1:2, 30 K) and <1:8:<1 (CH₃OH:CO 1:10 20 K) (Fig. 10.21). Of these product compositions, the pure CH₃OH and the different CO mixtures are perfectly plausible astrophysical compositions since CH₃OH is proposed to form from CO ice. The relative abundances of these three complex molecules can thus potentially be used to investigate when and under which conditions complex molecules form in different astrophysical objects, when an ice formation route has been established. This is pursued qualitatively below though there is a general lack of statistical samples that contain the diagnostically most valuable abundances.

The experiments did not consider the photochemistry of H₂O:CH₃OH ice mixtures because the expected formation path of CH₃OH from CO in astrophysical environments. Once the original ice heats up, mixing between the H₂O and CO-rich ice phase may however occur at a similar time scale as radical diffusion within the CO:CH₃OH ice, resulting in a different complex product composition than expected from radical reactions within the CO:CH₃OH phase. In a H₂O-rich environment, some of the CH₃OH photodissociation fragments should react with OH rather than other CH₃OH fragments, forming species such as HOCH₂OH. Observations of OH-rich complex species together with a quantification of the mixed H₂O:CH₃OH and the layered CH₃OH/H₂O chemistry may therefore provide constraints both on the initial ice composition and the efficiency of ice mixing in the protostellar stage.

10.5.3 Comparison with astrophysical sources

Complex molecules have been detected in the gas phase towards a variety of astrophysical environments. Table 10.6 lists the detected abundances towards a low-mass protostar IRAS 16293-2422, a sample of high-mass protostars, a low-mass outflow L1157, a galactic-center cloud MC G-0.02 and the comet Hale-Bopp. Typical uncertainties are factors of a few, but can be larger along some lines of sight.

Overall, complex-molecule abundances vary by less than an order of magnitude, with respect to CH₃OH, within these dramatically different astrophysical environments. For example the CH₃CH₂OH/CH₃OH ratio varies between 0.02 and 0.04 (Table 10.6). This suggests a formation scenario where reaction barriers are not rate determining, in agreement with an ice photochemistry scenario.

Focusing on specific ratios, the HOCH₂CHO to HCOOCH₃ ratio is only available in one of these environments and therefore not possible to use as a test. The CH₃CH₂OH to CH₃OCH₃ ratio is unity within the observational uncertainties towards the IRAS 16293-2422 core and the galactic center sources, but it is an order of magnitude lower in the high-mass hot core sample. This may be due to a more extended temperature gradient in the hot core objects, which would increase the importance of CH₃OCH₃ release into the gas phase at lower temperatures and thus over a larger volume. It may also be the result of gas phase chemistry modifying the released ice abundances. The physics of these objects thus needs to be addressed and more molecules observed, to confirm an ice origin of these complex molecules.

Another interesting ratio is the CH₃CHO to CH₃CH₂OH one, which varies by two orders of magnitude between the different objects (Table 10.6). In addition, an interferometric study has revealed spatial separations between these two species around the protostar IRAS 16293-2422 (Bisschop et al. 2008). Part of this may be due to different destruction efficiencies of CH₃CHO towards different objects. It is however difficult to explain such a lack of correlation with a more traditional ice formation scenario of complex molecules, through successive hydrogenation and oxygenation of small carbon chains. In such a reaction network CH₃CHO and CH₃CH₂OH are formed under the same conditions. In contrast, photochemistry of ices does not predict a correlation between CH₃CH₂OH and CH₃CHO since CH₃CHO formation may not even require CH₃OH as a starting point (Moore et al. 2003), while CH₃CH₂OH does.

The abundances of CHO-containing species are in general expected to vary between different astrophysical objects in the ice-photochemistry scenario because of their large enhancements in CO-rich and thus colder ices. Comparing the different types of sources in Table 10.6, only the single dish observations towards IRAS 16293 contain more HCOOCH₃ than CH₃OCH₃ or CH₃CH₂OH. This suggests that the complex molecules in the colder areas of IRAS 16293 are formed in a more CO-rich ice matrix than towards the warmer sources, which is consistent with the high volatility of CO. The uncertainties are yet too high for any conclusive comparison, however.

Quantitatively, the pure CH₃OH experimental results are in closest agreement with the ice desorption found in Hale-Bopp. This may not be too surprising, since these observations are less affected by gas-phase reactions that can both form and destroy com-

Table 10.6 – Abundances of complex molecules relative to CH₃OH.

	IRAS 16293-2422/A ^{a,b}	Hot cores ^c	L1157 ^d	MC G-0.02 ^e	Hale-Bopp ^f	CH ₃ OH ^g	CH ₃ OH:CO ^g
CH ₃ OH	1/1	1	1	1	1	1	1
CH ₃ CHO	0.038/<0.0016	2.9[3.1]×10 ⁻⁵	–	0.033	0.010	0.01	<0.04
CH ₃ CH ₂ OH	–/0.031	0.019[0.012]	0.007	0.040	<0.042	0.1	<0.01
CH ₃ OCH ₃	0.20/0.013	0.41[0.51]	–	0.050	–	0.04	<0.01
HCOOCH ₃	0.30/0.0084	0.089[0.084]	0.019	0.037	0.033	<0.03	>0.08
HOCH ₂ CHO	–/–	–	–	0.01	<0.017	<0.04	>0.04
(CH ₂ OH) ₂	–/–	–	–	0.01	0.10	0.4	<0.01

^aThe first value is from single dish data, the second from interferometric studies of the A core. ^bCazaux et al. (2003); Huang et al. (2005); Bisschop et al. (2008) and van Dishoeck & Herbst (2009). ^cAverage data and standard deviations towards a sample of seven high-mass hot cores (Bisschop et al. 2008). ^d(Arce et al. 2008). ^e(Requena-Torres et al. 2006, 2008). ^f(Crovister et al. 2004a). ^gThe relative abundance with respect to CH₃OH during warm-up of an irradiated 20 K pure CH₃OH ice and a CH₃OH:CO 1:10 ice mixture.

plex molecules. It may also be a sign of a warmer formation path compared to most larger-scale astrophysical objects, and thus an insignificant CO ice content. The almost one-to-one correlation is tentative evidence that cometary ices have reached their current composition through ice photochemistry, though both more cometary observations and actual modeling of their chemical evolution are necessary to evaluate whether this holds in general. The formation and destruction mechanisms around massive protostars are clearly too complicated to evaluate the origins of complex molecules there directly, without a more complete gas-grain model. In addition, time-scale effects may be significant for all astrophysical abundances compared to those found in the laboratory. It is, however, reassuring that the interferometric study towards the low mass protostar IRAS 16293, where high-temperature gas-phase reactions should be of less importance, agrees reasonably well with our experiments. Observations of HOCH₂CHO and (CH₂OH)₂ towards IRAS 16293 and other low-mass protostars would probably provide the strongest constraints available on the prevalence of UV-ice photochemistry in star-forming regions.

10.6 Conclusions

The major experimental and analytical results of this study are summarized below:

1. The CH₃OH ice photodissociation cross section increases from 2.6[0.9] to 3.9[1.3]×10⁻¹⁸ cm² between 20 and 70 K suggesting that a significant amount of the dissociated fragments recombines immediately to form CH₃OH at 20 K when radical diffusion in ices is slower.
2. CH₃OH ice photodesorbs with a yield of 2.1[1.0]×10⁻³ per incident UV photon at 20 K. The yield is independent of temperature and of the same order as the yields found previously for CO-, CO₂- and H₂O-ice photodesorption.
3. UV photolysis of 6–21 ML pure CH₃OH ice at 20–70 K results in a product mixture of simple and complex molecules, whose abundances have been quantified. The identified species are CO, CO₂, CH₄, HCO, H₂CO, CH₂OH, CH₃CHO, CH₃OCH₃, CH₃CH₂OH, (CH₂OH)₂ and a mixture of complex CHO- and COOH-containing molecules. The small temperature dependence may be explained by fast diffusion and recombination of non-thermalized radicals following CH₃OH photo-dissociation.
4. The final product composition following CH₃OH photolysis depends on UV fluence and temperature, but not on the UV flux level or the ice thickness when both are varied by a factor 3–4.
5. In CH₃OH:CO and CH₃OH:CH₄ 1:1(2) mixtures the complex molecules containing HCO- and CH₃ groups are moderately enhanced following UV irradiation compared to pure CH₃OH ice photolysis. In an irradiated CO:CH₃OH 10:1 ice mixture, the HCO-containing products dominate and both HCOOCH₃ and HOCH₂CHO are detected as the originally 20 K ice is warmed up. With the exception of this ice

the final complex product mixture is robust within a factor of few in all different experiments.

6. Additional formation of complex molecules occurs following irradiation at 20–70 K, when all ices are slowly heated with the UV lamp turned off; some abundances increase by up to a factor of ten between 20 and 100 K. Diffusion of thermalized radicals through the ice is thus important for complex molecule formation.
7. From abundance ratios of related products, formed during UV-irradiation of CH₃OH-rich ices, we infer an approximate CH₃OH photodissociation branching ratio into CH₂OH+H:OCH₃+H:CH₃+OH of 5:1:<1
8. From the peak formation temperature of related molecules during warm-up, we find that the relative radical diffusion barriers increase as H<CH₃ <HCO<OCH₃ <CH₂OH. While the mobility of the radical with the lowest barrier is most important in determining the formation temperature of the product, the diffusion barrier of the heavier radical matters as well. For example HCOOCH₃ forms at a lower temperature (from HCO and OCH₃) than HOCH₂CHO (from HCO and CH₂OH).
9. The predicted sum of oxygen-rich complex molecules compared to CH₃OH in ices is >25% after a UV fluence corresponding to 6 million years in a cloud core, followed by moderate ice heating to 30–50 K during the protostellar stage, though quantitative modeling is required to test the competition between radical diffusion, desorption, dissociation and recombination on astrophysical time scales.
10. Some complex molecular ratios, especially CH₃CH₂OH to CH₃OCH₃, do not depend significantly on experimental conditions and may thus to be constant in space as well, if gas-phase effects do not dominate. If quantitative modeling confirm this prediction, these ratios can be used to test the UV-induced ice formation scenario of complex molecules in astrophysical regions. Other ratios, such as (CH₂OH)₂/CH₃CH₂OH and HCOOCH₃/CH₃CH₂OH, depend both on the irradiated ice composition and the ice temperature and can therefore be used to investigate the formation conditions of observed complex molecules.
11. Comparison with astrophysical objects shows that the composition of complex ices in the Comet Hale-Bopp is readily explained by UV photolysis of pure CH₃OH ice, while CH₃OH in a CO-dominated ice can explain the variations in the HCOOCH₃ and CH₃CHO abundances between cold and warmer regions of proto-stars.

This study shows that complex ice chemistry can be quantified, though the process of doing so is more arduous than qualitative work. The discussed dependencies of molecule formation on different ice conditions show the impossibility of perfectly simulating the astrophysical ice evolution in the laboratory, especially since physical conditions vary in space as well. It is, however, possible to study ice processes under specific laboratory conditions, which through careful modeling (Paper II) can provide the energy barriers

that govern these reactions both in the laboratory and in star forming regions. These can then be used to model ice chemistry in all possible astrophysical environments.

10.7 Appendix

10.7.1 Photoproduct growth curves during UV-irradiation

10.7.1.1 Pure CH₃OH ice at different temperatures

Figures 10.23 and 10.24 show the increasing abundances of photoproducts during irradiation of pure CH₃OH ices at 30 and 50 K (experiments 2 and 3). The abundances are fitted as a function of UV fluence as described fully in §10.3.6 for 20 K and 70 K ices. The abundances follow the temperature trends suggested by the 20 K and 70 K ices (experiments 1 and 4), except possibly for CH₃CH₂OH, which seems to be enhanced at 30 K compared to the other ices. This enhancement is barely significant however. The fit coefficients and uncertainties for all irradiated ~20 L, pure CH₃OH ices are reported in Table 10.7

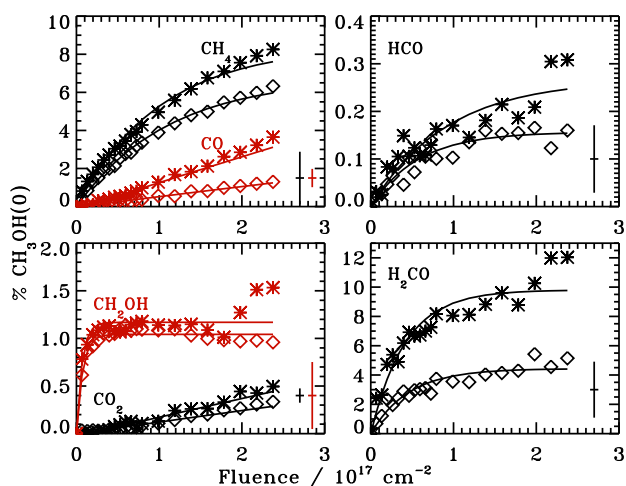


Figure 10.23 – The evolution of small CH₃OH photoproducts with respect to UV fluence in % of the initial CH₃OH ice abundance, CH₃OH(0), in each experiment at 30 K (stars) and 50 K (diamonds). The relative uncertainty for each abundance is indicated in the bottom right corner. The lines are exponential fits to the abundance growths.

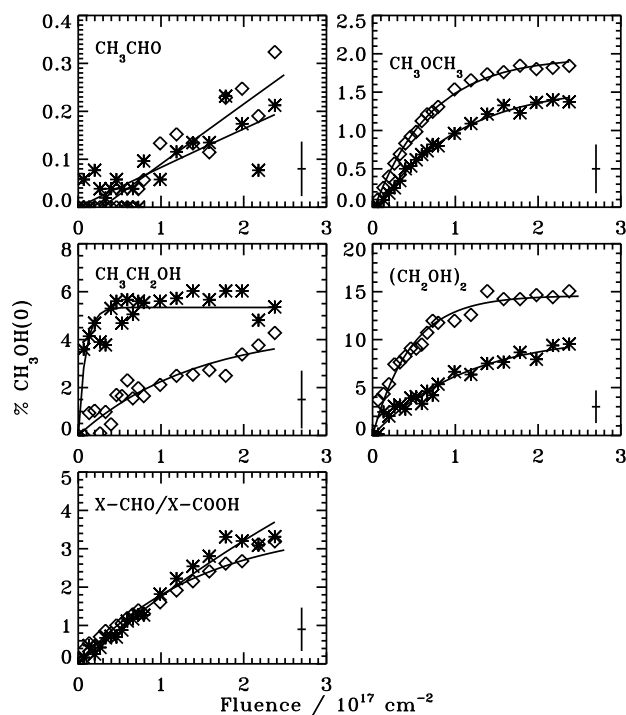


Figure 10.24 – The evolution of complex CH_3OH photoproducts with respect to UV fluence in % of the initial CH_3OH ice abundance. Otherwise as Fig. 10.23.

10.7.1.2 High fluence experiments

Figures 10.25 and 10.26 show the increasing abundances of photoproducts during irradiation at 20 K and 50 K with a high flux (experiments 5 and 6), together with the fitted growth curves. The first 2.5×10^{17} photons cm^{-2} are consistent with the low flux experiments within the experimental uncertainties. For molecules such as CH_3CHO that forms slowly, these experiments provide better constraints on the production rates than the low flux experiments. In contrast, molecules and fragments with high production rates are better constrained by the lower flux experiments, since they have a abundance determinations at a higher fluence resolution. The production rates of molecules that are destroyed/photodesorbed faster than they are produced at high fluences cannot be fit in these experiments. The fit coefficients of these experiments are reported in Table 10.7.

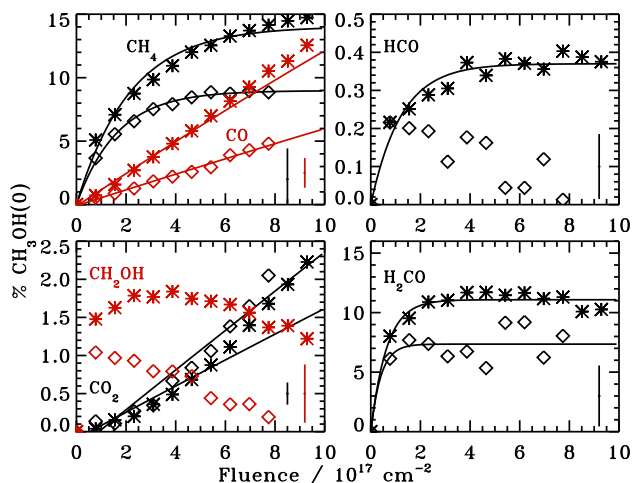


Figure 10.25 – The evolution of small CH₃OH photo-products with respect to UV fluence in % of the initial CH₃OH ice abundance (CH₃OH(0)) in the two high flux/fluence experiments at 20 K (stars) and 50 K (diamonds). The relative uncertainty for each abundance is indicated in the bottom right corner. The lines are exponential fits to the abundance growths.

10.7.1.3 CH₄ and CO mixtures

Figures 10.27–10.30 show the increasing abundances of photoproducts during irradiation of CH₃OH:CH₄ 1:2 and CH₃OH:CO 1:1 mixtures at 30 K and 50 K together with fitted growth curves. The temperature trends are similar to what is seen for pure CH₃OH ice. As suggested from the spectra in §10.3.3.5, all HCO containing species are increased in abundance in the CO mixtures, with the exception of CH₃CHO, which is mainly enhanced in the CH₄ ice mixture. The other two CH₃ containing species, CH₃CH₂OH and CH₃OCH₃, are also enhanced in the CH₄ mixture compared both to pure CH₃OH and the CO ice mixture – in the CO mixtures the abundance points represent upper limits. In contrast the (CH₂OH)₂ production is suppressed in both ice mixtures at 30 K. The fit coefficients of these experiments and CO:CH₃OH 1:1 mixture irradiated at 20 K are reported in Table 10.8.

10.7.2 Formation and destruction curves during warm-up

10.7.2.1 Pure CH₃OH at different irradiation temperatures

Figures 10.31 and 10.32 show the evolution of photoproduct abundances during warm-up following irradiation of pure CH₃OH ices at 30 and 50 K (experiments 2 and 3). The abundances follow the warm-up trends suggested by the 20 and 70 K ices (experiments 1 and 4). The CH₃CH₂OH desorption starts at a lower temperature than in pure CH₃CH₂OH, suggesting that similarly to the 20 K experiment, a substantial part of the CH₃CH₂OH desorbs together with CH₃OH.

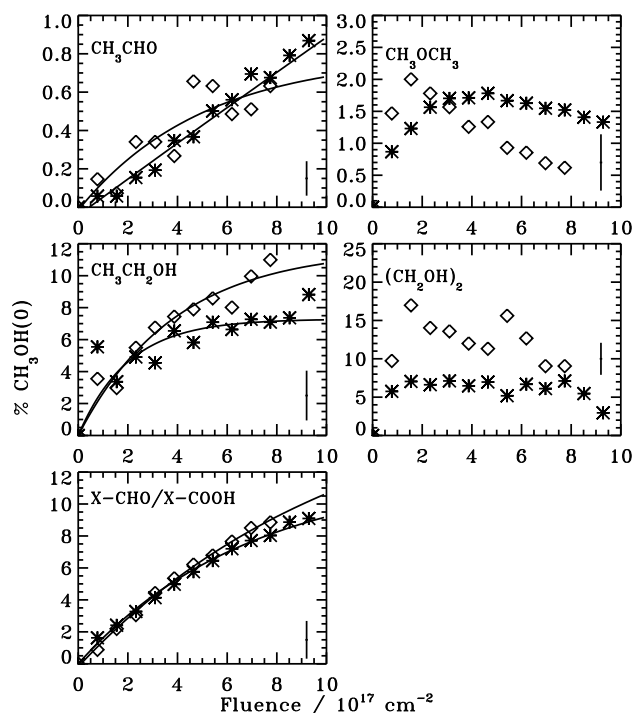


Figure 10.26 – The evolution of complex CH_3OH photo-products with respect to UV fluence in % of the initial CH_3OH ice abundance. Otherwise as Fig. 10.25.

10.7.2.2 CH_4 and CO mixtures

The warm-up trends are similar in the experiments where CH_4 and CO are mixed with the CH_3OH ice, at a 1(2):1 ratio, compared to the pure CH_3OH experiments (Figs. 10.33–10.36). The CH_3 -containing molecules CH_3CHO and $\text{CH}_3\text{CH}_2\text{OH}$ show a remarkable growth between 30 and 50 K, which is only hinted at in the pure CH_3OH experiments, suggesting a significant build-up of CH_3 radicals in these ice mixture experiments. In contrast the $(\text{CH}_2\text{OH})_2$ formation rate is low during warm-up of the 30 K experiments.

10.7.3 Formation rate parameters

The production of simple and complex molecules during UV irradiation is parameterized with $A_1(1 - e^{-A_2 \times (\phi - A_3)})$ for 13 of the experiments, where A_1 correspond to the equilibrium abundance in % of the initial CH_3OH abundance, A_2 is the fluence offset in 10^{17} cm^{-2} before production starts and A_3 describes the formation and destruction rates in fluence space in 10^{-17} cm^2 (Tables 10.7 and 10.8). The experiments include all pure 6–20 ML CH_3OH experiments irradiated with the normal flux setting, two 20 ML pure CH_3OH experiments irradiated with the higher flux setting, and all ice mixture experiments except for the $\text{CH}_3\text{OH}:\text{CO}$ 1:10 experiment. The 1:10 experiment is excluded since the formation

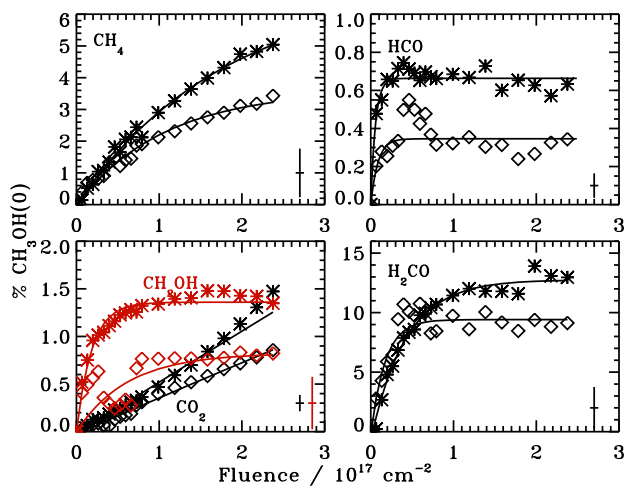


Figure 10.27 – The evolution of small photo-products with respect to UV fluence in % of the initial CH₃OH ice abundance in CH₃OH:CO 1:1 ice mixture experiments at 30 K (stars) and 50 K (diamonds).

of any molecules is too low to detect during irradiation itself. The fitted experiments are numbered as in Table 10.1.

It is important to note that the fitted formation ‘cross sections’ cannot be used directly in astrophysical models, but rather should be used to compare models of the experiments with the experimental results. The quoted uncertainties in the tables are the fit error and do not include systematic uncertainties, in particular the conversion error between integrated band strength and abundances of ~20% and the fluence uncertainty of ~30%.

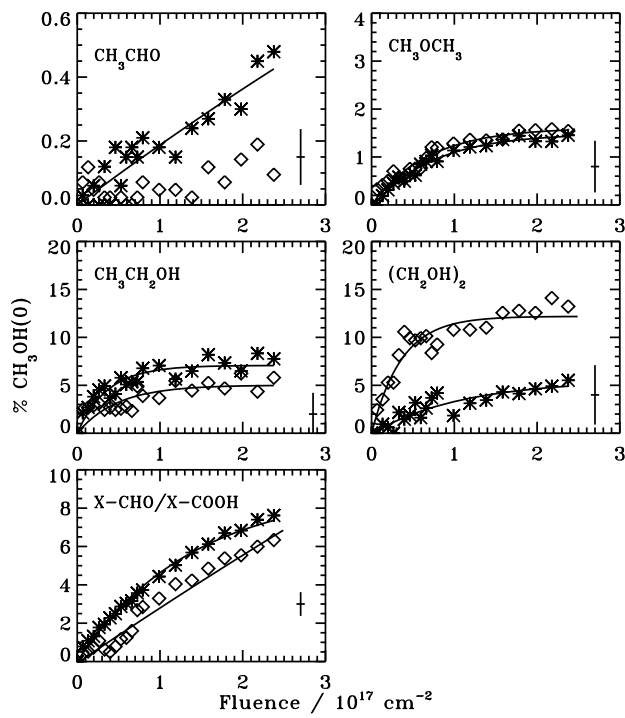


Figure 10.28 – The evolution of complex photo-products with respect to UV fluence in % of the initial CH_3OH ice abundance in $\text{CH}_3\text{OH}:\text{CO}$ 1:1 ice mixture experiments at 30 K (stars) and 50 K (diamonds).

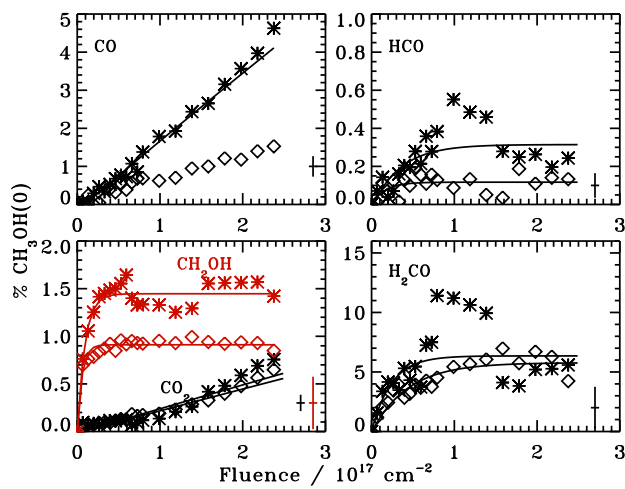


Figure 10.29 – The evolution of small photo-products with respect to UV fluence in % of the initial CH_3OH ice abundance in $\text{CH}_3\text{OH}:\text{CH}_4$ 1:2 ice mixture experiments at 30 K (stars) and 50 K (diamonds).

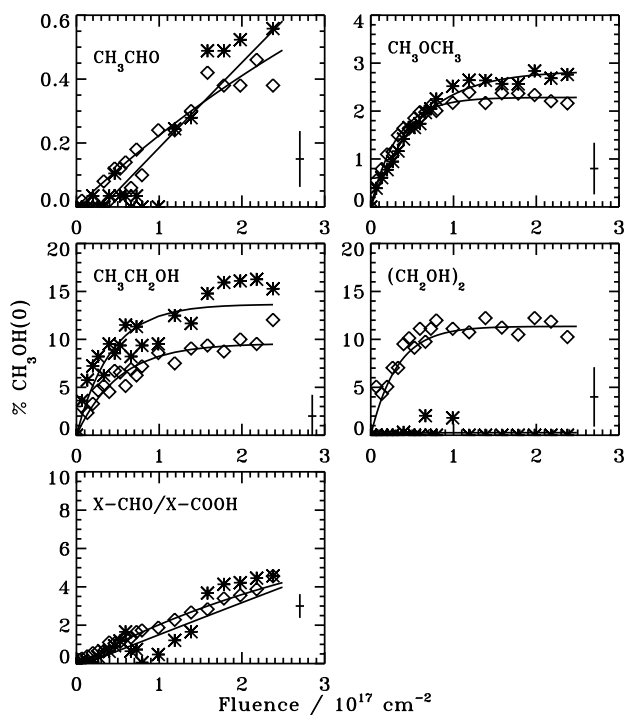


Figure 10.30 – The evolution of small photo-products with respect to UV fluence in % of the initial CH₃OH ice abundance in CH₃OH:CH₄ 1:2 ice mixture experiments at 30 K (stars) and 50 K (diamonds).

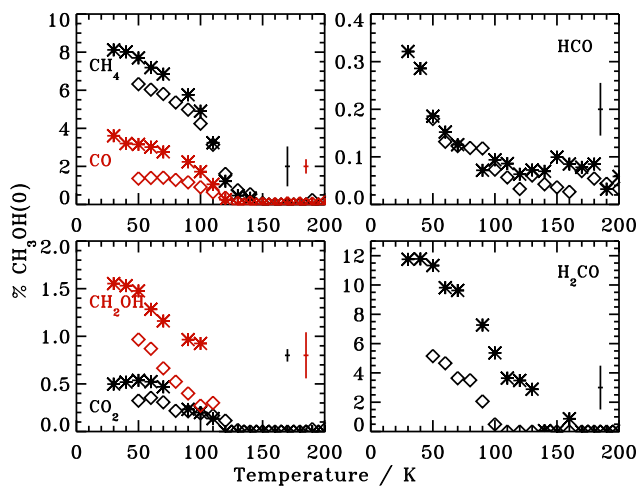


Figure 10.31 – The evolution of small CH₃OH photo-products with respect to UV fluence in % of the initial CH₃OH ice abundance in pure CH₃OH irradiation experiments at 30 K (stars) and 50 K (diamonds). The average uncertainties are indicated by the error bar to the right in each panel.

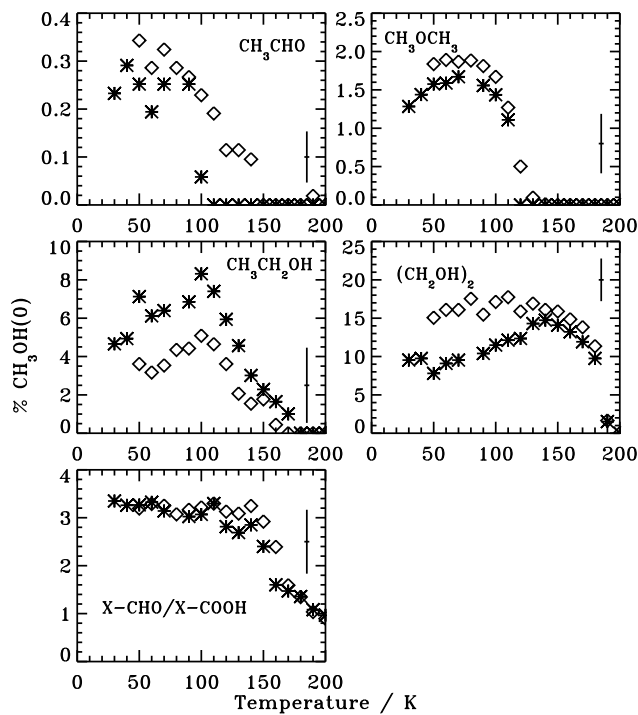


Figure 10.32 – The evolution of complex CH_3OH photo-products with respect to UV fluence in % of the initial CH_3OH ice abundance in pure CH_3OH irradiation experiments at 30 K (stars) and 50 K (diamonds). The average uncertainties are indicated by the error bar to the right in each panel.

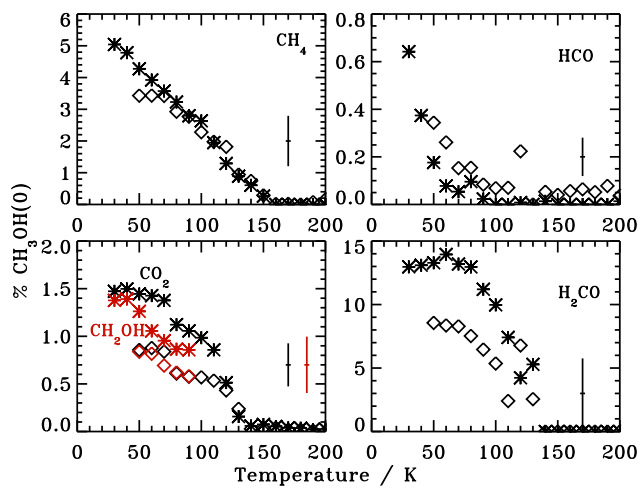


Figure 10.33 – The evolution of small photo-products, in % of the initial CH_3OH ice abundance, with respect to temperature following irradiation of $\text{CH}_3\text{OH}:\text{CO}$ 1:1 ice mixtures at 30 K (stars) and 50 K (diamonds). The average uncertainties are indicated by the error bar to the right in each panel.

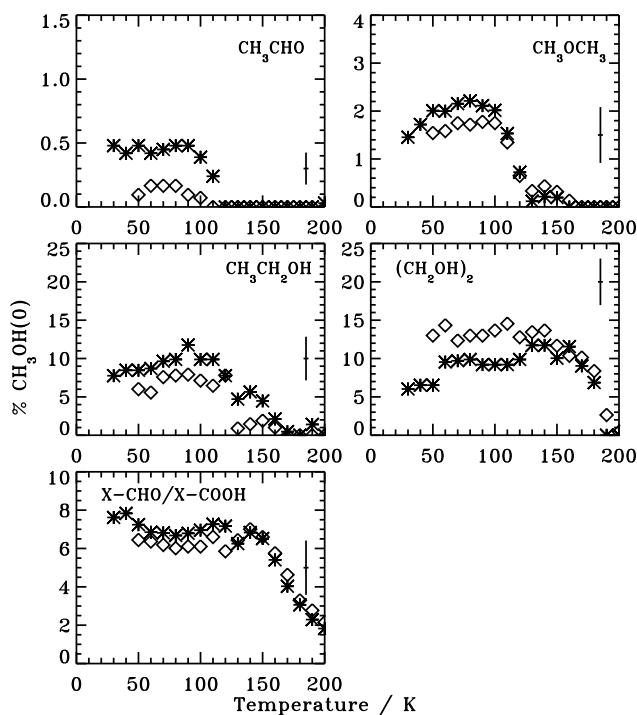


Figure 10.34 – The evolution of small photo-products, in % of the initial CH_3OH ice abundance, with respect to temperature following irradiation of $\text{CH}_3\text{OH}:\text{CH}_4$ 1:2 ice mixtures at 30 (stars) and 50 K (diamonds). The average uncertainties are indicated by the error bar to the right in each panel.

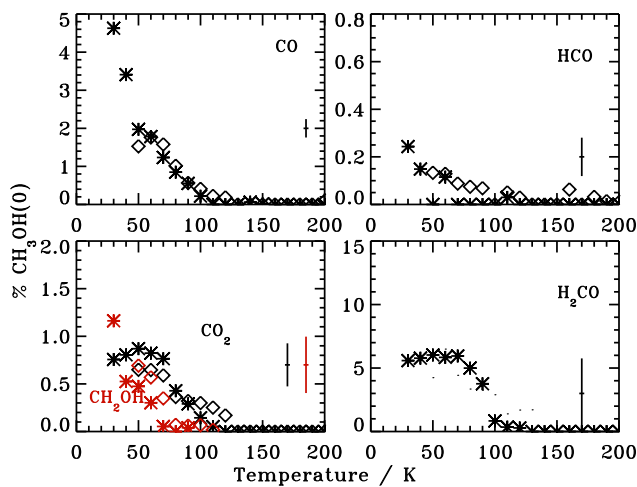


Figure 10.35 – The evolution of small photo-products, in % of the initial CH_3OH ice abundance, with respect to temperature following irradiation of $\text{CH}_3\text{OH}:\text{CO}$ 1:1 ice mixtures at 30 (stars) and 50 K (diamonds). The average uncertainties are indicated by the error bar to the right in each panel.

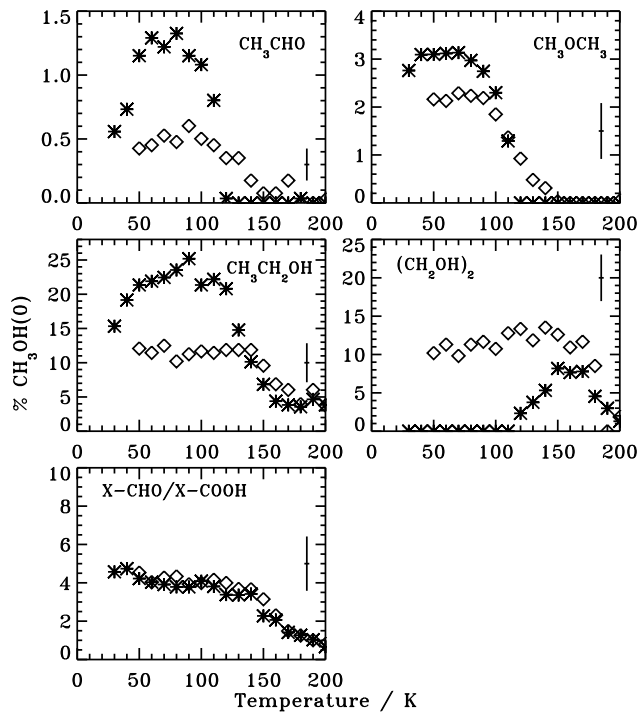


Figure 10.36 – The evolution of small photo-products, in % of the initial CH_3OH ice abundance, with respect to temperature following irradiation of $\text{CH}_3\text{OH}:\text{CH}_4$ 1:2 ice mixtures at 30 (stars) and 50 K (diamonds). The average uncertainties are indicated by the error bar to the right in each panel.

Table 10.7 – Photoproduct crosssection coefficients for pure CH₃OH experiments 1–6 as listed in Table 1.

		1	2	3	4	5	6
CH ₄	A ₁	11.1[0.5]	9.6[0.6]	7.2[0.5]	6.1[0.3]	14.7[0.3]	9.0[0.2]
	A ₂	0.69[0.06]	0.78[0.08]	0.80[0.10]	0.98[0.11]	0.39[0.02]	0.61[0.06]
	A ₃	0.0	0.0	0.0	0.0	0.0	0.0
CO	A ₁	<99	<99	<99	1.81[6.45]	<99	<99
	A ₂	0.021[0.001]	0.016[0.001]	0.02[0.16]	0.12[0.49]	0.015[0.001]	0.006[0.001]
	A ₃	0.16[0.02]	0.14[0.03]	0.07[0.09]	0.0	0.36[0.05]	0.17[0.17]
HCO	A ₁	0.32[0.04]	0.29[0.07]	0.16[0.03]	0.13[0.14]	0.37[0.02]	–
	A ₂	0.99[0.29]	0.88[0.37]	1.78[0.81]	0.53[0.87]	0.76[0.21]	–
	A ₃	0.0	0.0	0.0	0.0	0.0	–
H ₂ CO	A ₁	9.1[0.4]	10.3[0.5]	4.6[0.5]	1.1[0.3]	11.1[0.3]	7.5[0.4]
	A ₂	2.2[0.3]	2.0[0.3]	1.9[0.6]	3.5[3.9]	1.5[0.4]	2.3[1.4]
	A ₃	0.0	0.0	0.0	0.0	0.0	0.0
CH ₂ OH	A ₁	1.52[0.04]	1.17[0.04]	1.05[0.04]	0.77[0.03]	–	–
	A ₂	9.0[1.5]	13.6[3.8]	12.9[3.7]	20.8[9.9]	–	–
	A ₃	0.0	0.0	0.0	0.0	–	–
CO ₂	A ₁	<99	<99	<99	<99	<99	<99
	A ₂	0.008[0.025]	0.014[0.099]	0.015[0.117]	0.008[0.095]	0.002[0.001]	0.003[0.006]
	A ₃	0.17[0.05]	0.17[0.08]	0.08[0.11]	0.22[0.18]	1.13[0.09]	1.00[0.10]
CH ₃ CHO	A ₁	<99	0.9[3.5]	<99	0.47[0.18]	<99	0.82[0.18]
	A ₂	0.009[0.075]	0.10[0.46]	0.014[0.153]	0.51[0.32]	0.004[0.026]	0.19[0.08]
	A ₃	0.23[0.10]	0.0	0.30[0.11]	0.11[0.08]	0.54[0.25]	0.09[0.33]
CH ₃ OCH ₃	A ₁	1.5[0.3]	1.6[0.3]	1.9[0.2]	1.40[0.09]	–	–
	A ₂	0.86[0.38]	1.04[0.46]	1.50[0.38]	3.01[0.82]	–	–
	A ₃	0.10[0.08]	0.05[0.08]	0.03[0.05]	0.00[0.04]	–	–
CH ₃ CH ₂ OH	A ₁	4.7[0.3]	5.4[0.3]	4.8[2.1]	6.9[3.5]	7.4[0.6]	12.9[2.4]
	A ₂	4.4[1.3]	10.2[3.6]	0.63[0.47]	0.46[0.34]	0.50[0.14]	0.22[0.08]
	A ₃	0.0	0.0	0.0	0.0	0.0	0.0
(CH ₂ OH) ₂	A ₁	4.9[0.5]	10.5[2.0]	14.6[0.7]	18.8[0.6]	6.2[0.5]	12.0[0.6]
	A ₂	3.0[1.1]	0.88[0.31]	2.1[0.3]	2.6[0.3]	3.9[6.9]	3.0[2.3]
	A ₃	0.0	0.0	0.0	0.0	0.0	0.0
X-CHO/ X-COOH	A ₁	12.5[7.8]	6.1[2.0]	4.5[0.8]	8.4[3.7]	13.5[1.1]	16.8[3.2]
	A ₂	0.16[0.12]	0.37[0.17]	0.50[0.14]	0.21[0.11]	0.12[0.02]	0.10[0.03]
	A ₃	0.03[0.06]	0.04[0.06]	0.0	0.0	0.0	0.12[0.14]

Table 10.8 – Photoproduct crosssection coefficients for ice mixture experiments 7–11, 13, 14 as listed in Table 1.

		7	8	9	10	11	13	14
CH ₄	A ₁	8.7[0.9]	7.0[1.6]	3.7[0.6]	–	–	10.7[0.8]	5.6[0.8]
	A ₂	0.79[0.14]	0.54[0.19]	0.89[0.25]	–	–	1.27[0.22]	1.34[0.47]
	A ₃	0.0	0.0	0.0	–	–	0.0	0.0
CO	A ₁	–	–	–	<99	2.9[2.4]	<99	1.2[0.3]
	A ₂	–	–	–	0.02[0.01]	0.29[0.31]	0.03[0.01]	1.6[1.2]
	A ₃	–	–	–	0.11[0.05]	0.0	0.0	0.0
HCO	A ₁	0.98[0.02]	0.67[0.02]	–	0.34[0.04]	0.12[0.03]	–	–
	A ₂	18.2[3.7]	17.2[4.9]	–	2.9[1.2]	6.2[7.8]	–	–
	A ₃	0.0	0.0	–	0.03[0.06]	0.01[0.10]	–	–
H ₂ CO	A ₁	15.2[0.6]	12.8[0.7]	9.5[0.4]	7.1[0.7]	6.0[0.8]	5.4[0.9]	–
	A ₂	3.3[0.5]	2.4[0.5]	6.4[1.5]	3.7[1.6]	2.1[0.9]	7.3[7.8]	–
	A ₃	0.03[0.02]	0.02[0.03]	0.01[0.02]	0.0	0.0	0.0	–
CH ₂ OH	A ₁	2.08[0.08]	1.37[0.08]	0.81[0.10]	1.46[0.07]	0.91[0.06]	–	0.82[0.13]
	A ₂	4.4[0.7]	5.1[1.3]	1.8[0.6]	10.8[4.4]	17[12]	–	12[15]
	A ₃	0.0	0.0	0.0	0.0	0.0	–	0.0
C ₂ H ₆	A ₁	–	–	–	13.8[7.4]	–	–	–
	A ₂	–	–	–	1.2[1.5]	–	–	–
	A ₃	–	–	–	0.0	–	–	–
CO ₂	A ₁	<99	<99	8[23]	<99	<99	<99	<99
	A ₂	0.01[0.02]	0.01[0.05]	0.05[0.17]	0.01[0.06]	0.01[0.08]	0.01[0.11]	0.01[0.13]
	A ₃	0.10[0.03]	0.10[0.04]	0.07[0.07]	0.13[0.10]	0.0	0.26[0.07]	0.16[0.09]
CH ₃ CHO	A ₁	<99	<99	<99	<99	0.90[0.93]	<99	0.33[0.05]
	A ₂	0.01[0.16]	0.03[0.30]	0.01[0.37]	0.01[0.05]	0.31[0.43]	0.04[0.59]	6.4[5.0]
	A ₃	0.36[0.14]	0.0	0.0	0.32[0.09]	0.11[0.13]	0.0	0.0
CH ₃ OCH ₃	A ₁	1.2[0.3]	1.5[0.3]	1.6[0.2]	2.8[0.3]	2.3[0.2]	2.1[0.6]	0.8[0.3]
	A ₂	1.4[0.9]	1.4[0.8]	1.5[0.5]	1.8[0.6]	3.1[0.8]	1.4[1.0]	6[12]
	A ₃	0.09[0.12]	0.03[0.11]	0.0	0.0	0.0	0.06[0.14]	0.01[0.13]
CH ₃ CH ₂ OH	A ₁	10.0[0.4]	7.3[0.7]	5.2[0.6]	14.9[0.9]	10.0[0.9]	5.7[0.8]	8.1[6.2]
	A ₂	8.4[2.3]	2.6[0.8]	2.0[0.7]	1.9[0.3]	1.8[0.5]	12[14]	0.8[1.1]
	A ₃	0.0	0.0	0.0	0.0	0.0	0.01[0.04]	0.10[0.23]
(CH ₂ OH) ₂	A ₁	5.4[0.8]	5.5[3.3]	12.4[0.8]	–	11.4[0.9]	6.4[1.7]	14.6[2.8]
	A ₂	5.6[4.1]	0.9[1.3]	2.7[0.6]	–	3.8[1.2]	3.7[3.7]	1.9[1.1]
	A ₃	0.02[0.06]	0.01[0.28]	0.0	–	0.0	0.0	0.02[0.12]
X-CHO/ X-COOH	A ₁	12.1[0.7]	9.7[0.8]	17.2[7.3]	<99	11.3[8.3]	11.6[4.7]	8.3[3.1]
	A ₂	0.75[0.07]	0.64[0.09]	0.21[0.11]	0.02[0.01]	0.20[0.17]	0.41[0.25]	0.47[0.26]
	A ₃	0.0	0.0	0.05[0.04]	0.16[0.07]	0.0	0.0	0.0

11

PHOTOCHEMISTRY IN $\text{H}_2\text{O}:\text{CO}_2:\text{NH}_3:\text{CH}_4$ ICE MIXTURES

Photochemistry in NH_3 -containing ices provides a potential formation pathway to amino acids and other prebiotically interesting molecules during star formation. Quantifying this UV-induced ice chemistry *in situ* has so far failed for realistic astrophysical ice analogues because of a multitude of photoproducts with overlapping infrared spectral features. While such an analogue is included in this study, the focus is instead on the spectroscopic quantification of the photochemistry at 20 K in a number of binary ice mixtures containing H_2O , CO_2 , NH_3 and/or CH_4 . This allows us to acquire a general understanding of branching ratios and diffusion of radicals in ices, which can be subsequently applied to more complex ice mixtures. The production of C_2H_6 , C_2H_4 , N_2H_4 , CO , CO_3 , O_3 , CH_3NH_2 , HCN , CH_3OH , H_2CO , $\text{CH}_3\text{CH}_2\text{OH}$, CH_3CHO and OCN^- are quantified during UV irradiation, revealing a clear difference between species that form directly from reactions between first generation radicals and species forming from later generation products. From the different formation rates of C_2H_6 and C_2H_4 , the contested CH_4 photodissociation $\text{CH}_3:\text{CH}_2$ branching ratio is determined to be 3:1. The photochemistry in H_2O -poor and H_2O -rich ice mixtures differs because of the stronger binding environment in H_2O -rich ices, which increases the importance of relative diffusion barriers of radicals. Acid-base chemistry is found to be important in all $\text{NH}_3:\text{CO}_2$ containing ices; it increases the effective photodestruction cross section of NH_3 ice by up to an order of magnitude because of proton transfer from other photoproducts. Acid-base chemistry also increases the desorption temperatures of the products. To constrain the formation of glycine and other similarly complex products, TPD experiments following UV irradiation of NH_3 -containing ice mixtures are presented for the first time, which confirms that amino acids and amino acid-like molecules form during photolysis of $\text{CH}_4:\text{NH}_3:\text{CO}_2$ ice mixtures. A complete model and a set of experiments at different temperatures are needed to further constrain different diffusion barriers and thus to model the production of complex molecules, including amino acids, in space based on specific elementary reactions.

11.1 Introduction

The molecules of life, DNA, RNA and proteins, are built up from amino acids and sugars. Pre-biotic production pathways of sugars and different nitrogen-bearing organic molecules are thus of considerable interest and a necessary component of different origin-of-life scenarios. The recent discovery of CH₃CH₂OCHO and C₃H₇CN towards Sagittarius B2(N) is indicative of an efficient formation pathway to organic molecules of comparable complexity to the smallest amino acids during the early stages of star formation (Belloche et al. 2009). Laboratory and model efforts suggest that ice photochemistry on dust-grains during the protostellar stage produces complex molecules with high enough efficiency to explain the observed abundances (e.g. Muñoz Caro et al. 2002; Garrod & Herbst 2006; Garrod et al. 2008; Belloche et al. 2009, Chapter 10).

The ice-covered grains from the protostellar stage eventually become incorporated into the protoplanetary disk and there they collide and agglomerate to form larger and larger grains and eventually boulders and planetesimals. If the protostellar ices survive this stage, as suggested by models of Visser et al. (2009), the formed meteorites and comets may subsequently enrich planets with complex organic molecules. The importance of this last stage for the prebiotic chemistry on planets depends on the ice chemistry proceeding planet formation. This chapter aims to quantify the formation of nitrogen-containing complex molecules in a large set of ice-mixtures of astrophysical interest and thus to deduce the necessary conditions to produce amino acids and other pre-biotically interesting molecules during star- and planet-formation.

Simple ices form in molecular clouds through hydrogenation and oxygenation of atoms and unsaturated molecules. Observations of ices before the onset of star formation reveal H₂O ice to be the main constituent, followed by CO and CO₂ (e.g. Whittet et al. 1998; Bergin et al. 2002). CH₄ and NH₃ ice probably form before the protostellar stage as well, but have only been detected around protostars (Gibb et al. 2004; Knez et al. 2005, Chapter 2). NH₃ is the main ice-carrier of nitrogen that is directly observed; N₂ may be present, but has no strong infrared transitions and CN-bearing species have an order of magnitude lower abundance (van Broekhuizen et al. 2005). NH₃ ice was first discovered by Lacy et al. (1998) and is now established to exist at abundances of 5–10% with respect to H₂O ice towards both high-mass and low-mass protostars (Gibb et al. 2004, Bottinelli et al. in preparation). From the NH₃ ice spectral profile and its proposed formation pathway through hydrogenation of nitrogen, NH₃ should form in the H₂O-rich ice layer. This ice phase also contains 20–30% CO₂ and ~5% CH₄. In contrast CH₃OH ice probably forms in a CO-rich ice layer frozen out on top of the H₂O-rich ice.

Organic nitrogen-containing molecules have been detected in the gas phase in the hot regions close to protostars, in galactic center clouds, in a low-mass outflow and in cometary outflows (see Herbst & van Dishoeck 2009 for review). The most abundant species are HCN, CH₃CN and HNCO, but the recently discovered C₃H₇CN and NH₂CH₂CN have been detected with relatively high fractional abundances with respect to H₂, 1.0×10^{-9} and 2.2×10^{-9} , respectively (Belloche et al. 2008, 2009).

The four nitrogen containing organic molecules searched for towards a sample of high-mass protostellar hot cores, HNCO, CH₃CN, C₂H₅CN and NH₂CHO, were all found

to have high rotational temperatures, while CHO-containing molecules without nitrogen could be divided into two temperature bins, tracing the hot core and the luke-warm envelope, respectively (Bisschop et al. 2007c). The high temperature of the nitrogen-bearing species is consistent with their formation and trapping in the bottom ice layer, the H₂O-rich ice phase, while CHO-containing species forming in the CO-rich outer ice layer are more exposed and thus desorb easier because of heat and non-thermal desorption pathways. The abundances of nitrogen-bearing complex molecules and of the other detected complex species are not correlated between sources, again consistent with the formation of nitrogen-containing and CHO-containing complex molecules in different phases of the ice; the CHO-containing complex species depend on the original CH₃OH content (Chapter 10), while the N-containing species do not.

Some complex nitrogen-bearing molecules have been detected in comets as well, including HNCO and CH₃CN (Altwegg et al. 1999; Crovisier et al. 2004b). The simplest amino acid, glycine, is yet undetected towards both comets and star-forming regions despite deep searches. The current abundance upper limits are $\sim 10^{-11}$ with respect to hydrogen in the Orion star forming region, and 1×10^{-10} in the cold envelope and 7×10^{-9} in the hot core of the solar-type protostar IRAS 16293-2422 (Combes et al. 1996; Ceccarelli et al. 2000). Amino acids are however found in meteorites where more sensitive analysis methods are available (Engel & Macko 1997) – these acids probably formed during the proposed aqueous phase of the meteorite.

The photochemistry of NH₃ containing ices was first investigated for astrophysically relevant ice mixtures by Hagen et al. (1979), who irradiated a CO:H₂O:NH₃:CO₂ 50:1:1:0.09 ice at ~ 10 K with a UV lamp peaking at 160 nm. HNCO, H₂CO, NH₂CHO and HCOOH were identified among the products and unidentified larger molecules with molecular masses up to 514 amu were recorded mass-spectrometrically following warm-up of the photolyzed ice residue to room temperature. There is thus qualitative evidence for a nitrogen-based complex chemistry upon irradiation of NH₃-containing ice mixtures. Other early experimental studies investigated the qualitative effects of varying different species to the mixtures and changing the original abundance ratios (e.g. Allamandola et al. 1988; Grim et al. 1989; Schutte et al. 1993). Two of the main results were the relative ease at which XCN compounds, especially OCN⁻, and NH₂-containing molecules form in NH₃-containing ices. The largest infrared detected molecule is C₆H₁₂N₄ (Bernstein et al. 1995; Muñoz Caro & Schutte 2003).

Bernstein et al. (2002) and Muñoz Caro et al. (2002) first reported on efficient amino acid production following irradiation of ices in similar high-vacuum experiments; the amino acids were detected using gas chromatography and mass spectrometry of the irradiated ice residue after the sample was heated to room temperature. These studies were followed up with both models and isotopically labeled experiments to constrain the formation mechanisms (Woon 2002; Muñoz Caro et al. 2004; Elsila et al. 2007; Nuevo et al. 2007; Lee et al. 2009). The general conclusion was that amino acids form through a variety of radical-radical reactions; amino acid formation is more efficient in HCN-containing matrices, but pathways from NH₃ exist as well. It is however still unclear when these amino acids form, i.e. if there is a cold formation pathway during UV irradiation of the ice or if heating to room temperature is required.

Overall these experimental results are enticing since they suggest that amino acid production may be possible in interstellar ices. Final yields in a laboratory setting provide little information on the final fraction under different astrophysical conditions, however – the reported carbon-conversion efficiencies, up to 0.5%, may be a result of the experimental technique. These experiments were all carried out under high-vacuum conditions, where thick ices (tens of μm) were deposited at ~ 10 K while irradiating the ice to produce the maximum amount of radicals. The photolyzed ices were then heated to room temperature and the residue analyzed mass-spectrometrically. This procedure was necessary when carrying out experiments under high-vacuum and employing transmission spectroscopy. It is however difficult to deduce from these experiments which molecules form under interstellar conditions and at what abundances. Specifically, none of these studies provide any quantitative data on reaction rates of nitrogen-containing molecules. They thus do not present data that can be included in astrochemical models to test whether ice photochemistry produces the correct amounts and correct abundance ratios of complex molecules, under interstellar conditions and timescales, compared to astrophysical observations.

Despite a lack of this kind of data, a complex nitrogen chemistry was incorporated in a recent grain-gas model of the complex ice chemistry in protostellar envelopes and the subsequent desorption in the hot core close to the protostar (Garrod et al. 2008). The model assumes a perfectly mixed ice, which probably explains why it over-produces NH₂CHO, but under-produces CH₃CN and CH₃NH₂; if NH₃ is mainly formed in the H₂O-rich layer it will have more access to CH₄-dissociation products than to CO-reaction products. Model improvements are mainly limited by the lack of quantitative data on the NH₃ ice photochemistry.

Such quantitative data should be possible to derive from simpler binary ice mixtures, since e.g. the CH₃ diffusion barrier in all H₂O dominated ices should be approximately the same. Reaction barriers only depend on the two radicals reacting and while effective photodissociation cross sections may change with temperature or ice mixture because of changing diffusion barriers (Chapter 10), the branching ratio should solely depend on the UV lamp spectrum. Quantifying the complex ice chemistry of astrophysically relevant ice mixtures should thus be possible by first extracting physical quantities from simple, well-constrained ice mixtures and then performing experiments on more complicated mixtures to ensure that these results are consistent with predictions from the simpler ice experiments.

This chapter presents the production of moderately complex species, up to glycine, in a large set of ice mixtures during irradiation at 20 K and during warm-up between 20 and 230 K. In contrast to most previous experiments the irradiation is done after deposition and the complex molecule formation is followed *in situ* using infrared spectroscopy and temperature programmed desorption (TPD). The main part of the chapter focuses on the photodesorption, photodissociation and product formation during irradiation of pure and binary ices. Section 11.4 then presents the quantification of the same products in more complicated mixtures together with TPD experiments to identify the most complex photoproducts accessible for *in situ* study. The TPD experiments are performed following irradiation of an astrophysical ice analogue and five other mixtures, which are used to constrain the nature of the desorbing species. The results are used in the Discussion

section to constrain photodissociation branching ratios, relative diffusion barriers and the reaction pathways that the observed molecules form through. The implications for understanding ice chemistry in astrophysical environments are discussed, followed by proposed new experiments to further constrain the chemistry.

11.2 Experimental

All experiments are carried out on the set-up CRYOPAD under ultra-high vacuum conditions ($\sim 10^{-9}$ – 10^{-10} mbar). Pure and mixed ices are deposited diffusively at 18 K by introducing a gas (mixture) in the vacuum chamber along the surface normal of a gold substrate, which is temperature controlled down to 18 K with a 2 K uncertainty. The gas mixtures are prepared in a separate glass manifold with a base pressure of 10^{-4} mbar to have a total pressure of 10–20 mbar. The CO_2 , NH_3 and CH_4 gases have a minimum purity of 99.9% (Indugas). Samples containing H_2O are prepared from the vapor pressure of de-ionized H_2O , further purified through several freeze-thaw cycles.

The ices are probed through infrared spectroscopy in reflection-absorption mode (RAIRS) and the desorbed molecules during warm-up are investigated with a quadrupole mass spectrometer (QMS), facing the substrate. As described in Chapters 8–10 relative RAIRS band strengths are consistent with relative transmission band strengths and thus certain within 20–30%. Absolute band strengths have a 50% uncertainty, but this only affects the derived photodesorption rates – not the quantification of the chemistry.

The original ice mixture as well as changes in the ice composition induced by UV irradiation are quantified using RAIRS, while the QMS is employed to secure band identifications of photoproducts. The UV irradiation is provided by a hydrogen-discharge lamp with UV emission around Ly- α and through a broader continuum between 6 and 11.5 eV (Muñoz Caro & Schutte 2003). All ices are irradiated with a UV flux of $1.1(\pm 0.4) \times 10^{13}$ $\text{s}^{-1} \text{cm}^{-2}$ except for an experiment aimed to determine the photodesorption yield (Exp. 1), where a four times higher flux is used.

Table 11.1 lists the photochemistry experiments in terms of their mixture composition and total thickness. The set of experiments has been designed to test the influence of different combinations of H_2O , CO_2 , NH_3 and CH_4 on the complex product formation. Experiment 18 was chosen to mimic the H_2O -rich phase observed towards low-mass protostars (Chapter 2). All experiments are UV irradiated at 20 K followed by warm-up by 1 K min^{-1} to 150–230 K, while acquiring RAIRS every 10 min and monitoring the desorption products with the QMS at a range of mass signals between 2 and 62 amu. The ice thicknesses range between ~ 8 –78 monolayers (ML). This ice thickness regime is similar to what is expected in the dense and cold stages of star formation. Each ice in experiment 2–18 was irradiated for 6 hours, resulting in a UV fluence of $\sim 2.3 \times 10^{17} \text{ cm}^{-2}$. This is comparable to the fluence an ice in a cloud core is exposed to during 10^6 years because of cosmic-ray induced UV photons at a flux of 10^4 cm^{-2} (Shen et al. 2004).

Table 11.1. The composition and thickness of all photochemistry experiments.

Exp.	H ₂ O	CO ₂	CH ₄	NH ₃	Thickness (ML)	$\phi^a(10^{-18}\text{cm}^2)$
1				1	8	
2				1	51	1.5±0.5
3	1				43	
4		1			15	
5			1		47	
6	1			1	54	1.7±0.6
7	4			1	43	5.6±2.0
8		1		2.5	44	5.7±2.0
9			3	2	45	2.2±0.8
10	1	1.5			21	
11	6	1			35	
12	1		3		42	
13	2		1		37	
14		1	2		33	
15	1	1		1	69	
16	1		1	1	66	
17		1	1	1	78	
18	100	20	8	12	66	

^aThe initial NH₃ photodestruction cross section

11.3 Photochemistry in pure ices and binary ice mixtures

When quantifying the chemistry in pure ices and binary ice mixtures, the initial ice compositions, and the photodesorption and photodissociation yields are calculated from the listed ice bands in Table 11.2. Table 11.2 also lists the photoproducts considered in this section, together with the infrared bands used for quantification, transmission band strengths and literature references on the ice spectra. Most photoproduct bands are easily identified from their spectral positions alone, but a few bands require further analysis to assign them to specific complex species. The TPD experiments mentioned in this section are discussed in detail §11.4.2

Each abundance is quantified by fitting a local baseline around the spectral feature and then fitting one or multiple Gaussians to the band of interest using a personal IDL routine. The automatic fits are visually inspected to ensure that the fitted Gaussians are consistent with bands in pure and ice mixture reference spectra.

Table 11.2 – The original ice infrared bands and the photoproduct spectral features used for quantification.

Species	Band (cm ⁻¹)	Band strength ^a (cm ⁻¹)	Reference
CH ₄	1300	6.1×10 ⁻¹⁸	Moore & Hudson (1998)
NH ₃	1070	1.7×10 ⁻¹⁷	D'Hendecourt & Allamandola (1986)
CO ₂	2343	7.6×10 ⁻¹⁷	Gerakines et al. (1995)
H ₂ O	1670	1.2×10 ⁻¹⁷	Gerakines et al. (1995)
C ₂ H ₆	2976	1.1×10 ⁻¹⁷	Moore & Hudson (1998) ^b
	821	1.9×10 ⁻¹⁸	Pearl et al. (1991)
C ₂ H ₄	1436	2.9×10 ⁻¹⁸	Moore & Hudson (1998) ^b
N ₂ H ₄	2768	~1.5×10 ⁻¹⁷	assumed from NH ₃
CH ₃ NH ₂	2794	~5×10 ⁻¹⁸	assumed from C ₂ H ₆
HCN	2087	5.1×10 ⁻¹⁸	Gerakines et al. (2004)
H ₂ CO	1500	3.9×10 ⁻¹⁸	Schutte et al. (1993)
CH ₃ OH	1026	2.8×10 ⁻¹⁷	D'Hendecourt & Allamandola (1986)
CH ₃ CH ₂ OH	1044	7.3×10 ⁻¹⁸	Moore & Hudson (1998) ^b
CH ₃ CHO	1350	6.1×10 ⁻¹⁸	Moore & Hudson (1998) ^b
CO	2139	1.1×10 ⁻¹⁷	Gerakines et al. (1995)
CO ₃	2045	~7.6×10 ⁻¹⁷	assumed from CO ₂
O ₃	1045	1.4×10 ⁻¹⁷	Brewer & Wang (1972)
OCN ⁻	2165	1.3×10 ⁻¹⁶	van Broekhuizen et al. (2005)

^a The uncertainties in the tabulated transmission band strengths is ~20–30% when comparing results from different references, ice mixtures and ice temperatures.

^b In a H₂O ice matrix.

11.3.1 CH₄, NH₃ and CH₄:NH₃ ice photolysis

Figure 11.1 shows the spectra before and after photolysis of pure CH₄ ice, pure NH₃ ice and a CH₄:NH₃ ~3:2 ice mixture, all at 20 K. The bands used to quantify the considered photoproducts, C₂H₆, C₂H₄, N₂H₄, CH₃NH₂ and HCN, are marked. The strong C₂H₆ bands are assigned from spectral comparison alone, since these bands have no spectral overlap with other possible product bands (Moore & Hudson 1998). The C₂H₄ band at 1436 cm⁻¹ is weaker and partly overlapping with other bands, and its disappearance together with the C₂H₆ around 60 K was used to confirm the C₂H₄ assignment. The same assignments were made by Gerakines et al. (1996) and Moore & Hudson (1998).

The observed broad band at 2794 cm⁻¹ in the pure NH₃ ice agrees in band position and width with one of the N₂H₄ ice bands reported by Roux & Wood (1983). The N₂H₄ assignment is, however, tentative since no desorption data exist on N₂H₄ and most other N₂H₄ features overlap with strong NH₃ bands. The other likely pure NH₃ photoproduct, N₂H₂, is excluded as a carrier from comparison with spectra by Blau et al. (1961). Two other bands form in the pure NH₃ ice upon UV irradiation, at 2111 and 1507 cm⁻¹. The 2111 cm⁻¹ is probably due to N₂H₄ as well, while the 1507 cm⁻¹ band can be assigned to NH₂ (Gerakines et al. 1996) though NH₃⁺_{3/4} are candidates as well (Thompson & Jacox 2001). During warm-up most of the band disappears before NH₃ desorption, consistent with NH₂ as a main carrier, but with an unconfirmed assignment, its formation cannot be

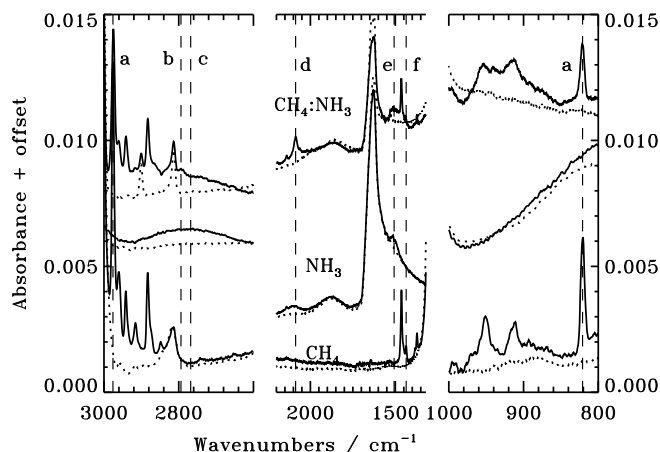


Figure 11.1 – The initial spectra (dotted lines) and spectra after photolysis (solid lines) of pure CH₄ ice, pure NH₃ ice and a CH₄:NH₃: ~3:2 mixture, all at 20 K. The bands used for quantifying the a) C₂H₆, b) CH₃NH₂, c) N₂H₄, d) HCN, e) NH₂ and f) C₂H₄ ice abundances are marked with dashed lines.

quantified.

The HCN and CH₃NH₂ ice features in the photolyzed CH₄:NH₃ ice mixture spectrum are assigned by comparing laboratory ice spectra from the NASA Goddard ice database by Moore et al. (<http://www-691.gsfc.nasa.gov/cosmic.ice.lab/spectra.html>) with spectra from the photolyzed CH₄:NH₃ ice mixture during warm-up. During the TPD experiments following photolysis, mass patterns consistent with HCN and CH₃NH₂ desorption are visible at 110 and at 120 K. Figure 11.2 shows the difference RAIR spectrum of the photolyzed CH₄:NH₃ ice mixture between 120 and 100 K, i.e. the spectrum acquired at 100 K subtracted from the spectrum acquired at 120 K. This reveals the spectral features of species that desorb in this temperature interval and is thus provides a method for band identifications. The agreement of this difference spectrum with the HCN + CH₃NH₂ bands is excellent. Figure 11.2 also shows that the bands selected to quantify HCN and CH₃NH₂ are distinguishable at 20 K.

Quantifying the formation of ice species with respect to the initial ice composition requires known transmission band strengths – all spectra here are acquired with RAIRS, but the relative band strengths are the same in transmission and reflection-absorption mode as long as the bands are not too strong. Transmission band strengths are available for C₂H₆, C₂H₄ and HCN ice, but not for N₂H₂ or CH₃NH₂ ice. The latter two band strengths are estimated by assuming a similar N-H/C-H band strength in the more complex molecules as in NH₃ and C₂H₆.

Figure 11.3 shows the formation of C₂H₆, C₂H₄, N₂H₂, HCN and CH₃NH₂ as a function of UV fluence in pure CH₄ ice, in pure NH₃ ice and in the CH₄:NH₃ ~ 3:2 ice mixture. The C₂H₆ and N₂H₄ production are only reduced by ~40% each in the mixture

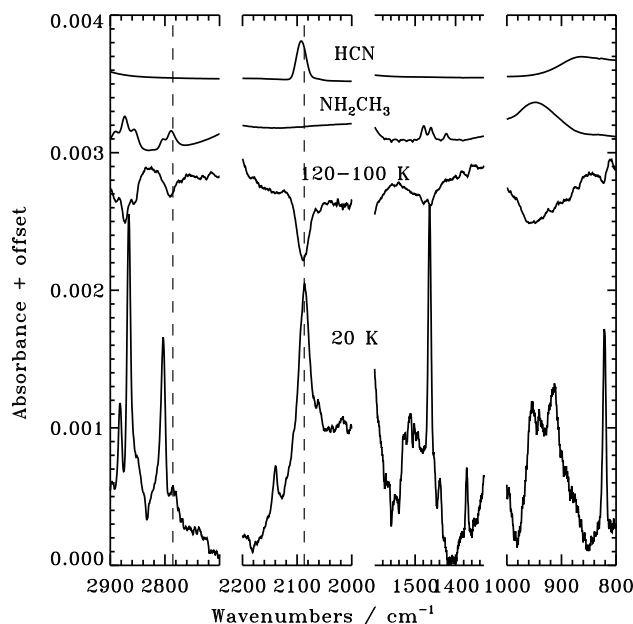


Figure 11.2 – Starting from the bottom the figure shows a photolyzed CH_4NH_3 ice spectrum at 20 K, a difference spectrum during warm-up of the same ice mixture, a CH_3NH_2 spectrum (mixed with H_2O) and a pure HCN ice spectrum. In the difference spectrum negative peaks signify desorption of the band carrier. The dashed lines show the agreement between the reference spectra and the photolysis experiment for the HCN and NH_2CH_3 bands used for quantification.

and this is with respect to the total ice thickness. Their production rates are thus the same, within the uncertainties, in the pure CH_4 ice and in the ice mixture with respect to the CH_4 and NH_3 abundances. The abundant C_2H_6 formation in the ice mixture indicates that it is mainly the formation of larger hydrocarbons that is suppressed in favor of HCN and CH_3NH_2 production in the ice mixture. This is consistent with the reduction in C_2H_4 production, which is evidence of that CH_2 , an ingredient in both C_2H_4 and C_3H_8 formation, is quickly consumed by reactions with NH_x in the ice mixture.

The two molecules forming from reactions of NH_3 and CH_4 fragments, CH_3NH_2 and HCN, depend differently on UV fluence (Fig. 11.3d.). The CH_3NH_2 ice abundance reaches steady-state faster than any other investigated molecule does, while the formation rate of HCN increases with fluence, indicative of a HCN formation pathway from first-generation photoproducts, such as CH_3NH_2 and CH_2NH .

By comparing the initial C_2H_6 formation in Fig. 11.3a and C_2H_4 formation in 11.3b, it is possible to constrain the CH_4 photodissociation branching ratio. This is done below using the initial formation cross sections of C_2H_6 and C_2H_4 in the pure CH_4 ice, which are $(3.2 \pm 1.3) \times 10^{-19}$ and $(3.6 \pm 1.5) \times 10^{-20}$ cm^2 after 4×10^{16} photons cm^{-2} . Gerakines

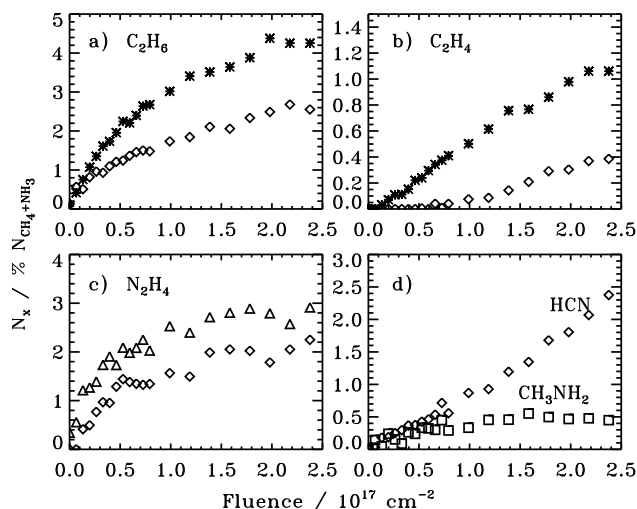


Figure 11.3 – The relative formation of five complex molecules, with respect to the initial total ice abundance, in pure CH₄ ice (stars), in pure NH₃ ice (triangles) and in a CH₄:NH₃ ~ 3:2 ice mixture (diamonds and squares) as a function of UV fluence at 20 K.

et al. (1996) finds a comparable C₂H₆/C₂H₄ product ratio (8/1) following pure CH₄ ice photolysis.

The chemistry in the pure and mixed ices are then proposed to proceed as shown in Fig. 11.4, where the reaction scheme for the mixed ice is constructed by combining the CH₄ and NH₃ reaction schemes with the bridging HCN and CH₃NH₂ reactions. The reaction schemes clearly show the additional number of steps required to form HCN compared to CH₃NH₂, which explains the initial delay in the HCN production. The early steady-state of CH₃NH₂ suggests that it easily photodissociates into HCN, even though the process probably requires several steps, and that this is an important formation path to HCN in the ice. This is also consistent with the almost constant formation rate of HCN once the initial delay is overcome.

11.3.2 CH₄:H₂O ice mixture photolysis

Figure 11.5 shows the initial and photolyzed spectra of pure CH₄ ice and a CH₄:H₂O~3:1 mixture, both at 20 K. There are no identified photoproducts following pure H₂O ice photolysis (not shown). This is in contrast with e.g. Gerakines et al. (1996), who detected OH and H₂O₂ formation. The observed rates were low, however, and neither would be expected to be observable at the ice thicknesses and UV fluences employed in this study. The photolyzed CH₄ and CH₄:H₂O ice spectra are plotted together with pure CH₃OH, H₂O, CH₃CH₂OH and CH₃CHO ice spectra to justify the complex photoproduct assignments. The most isolated bands of each complex ice species are used for quantification.

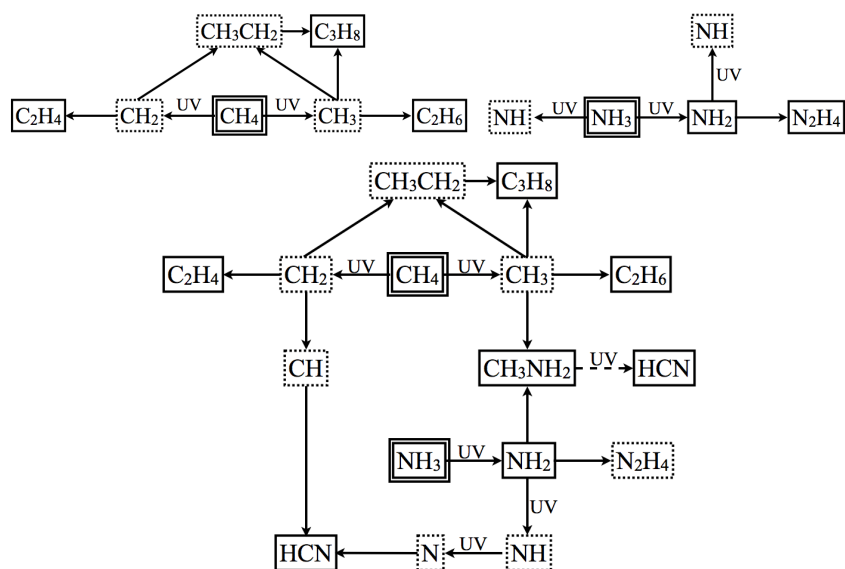


Figure 11.4 – The proposed reactions schemes following UV photolysis of pure CH₄ ice (upper left), pure NH₃ ice (upper right) and a CH₄:NH₃ ice mixture (bottom scheme). Solid boxes mark detected species and dotted boxes undetected ones. Dashed arrows mark photodissociation through several steps.

Similarly to the CH₄:NH₃ photochemistry, the formation rate of C₂H₆ does not change significantly between the pure CH₄ ice and the CH₄:H₂O 3:1 mixture, while the C₂H₄ production is significantly lowered in the latter case. Of the new complex molecules in the CH₄:H₂O mixture, CH₃OH forms the fastest, but reaches a similar steady-state level to CH₃CH₂OH. H₂CO, CH₃CHO and CH₃CH₂OH all start to form after a certain fluence level is reached, indicative of a second or later generation of photoproducts. CH₃CHO forms last. Qualitatively the product assignments agree with Moore & Hudson (1998) who also found a comparable CH₃OH/CH₃CH₂OH product ratio in their CH₄:H₂O 1:2 ice mixture.

CH₃CH₂OH and CH₃CHO are also photoproducts of pure CH₃OH ice (Chapter 10) and their product ratio is consistent between the CH₃OH and the CH₄:H₂O photolysis experiments. The formation path for CH₃CH₂OH must however be different in the two experiments since the CH₃CH₂OH to CH₃OH ratio is one order of magnitude higher in the CH₄:H₂O ice than in the CH₃OH ice following irradiation with the same fluence. Figure 11.7 shows that CH₃CH₂OH probably forms from C₂H₅ + OH in the CH₄:H₂O mixture versus CH₃ + CH₂OH in the CH₃OH ice (Chapter 10), while CH₃CHO is proposed to form through photodissociation of CH₃CH₂OH or radical-radical reactions between CH₃ and HCO in both cases; both formation paths are consistent with the late onset of CH₃CHO formation. The delay in H₂CO and CH₃CH₂OH formation is also explained

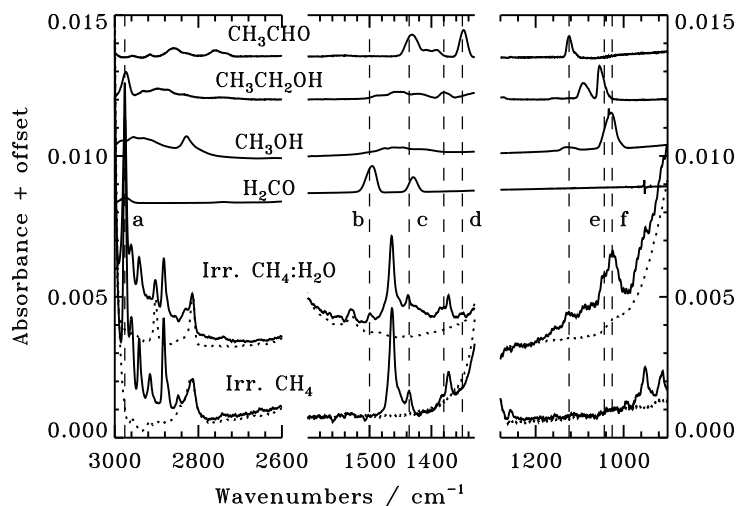


Figure 11.5 – The initial spectra (dotted lines) and spectra after photolysis (solid lines) of pure CH₄ ice and a CH₄:H₂O~3:1 mixture, both at 20 K. The bands used for quantifying the a) C₂H₆, b) H₂CO, c) C₂H₄, d) CH₃CHO, e) CH₃CH₂OH and f) CH₃OH ice abundances are marked with dashed lines.

by the reaction scheme, which shows that both species require one more reaction step compared to CH₃OH and C₂H₆ formation.

11.3.3 Pure CO₂ and CH₄:CO₂ ice photolysis

Pure CO₂ ice photolysis results in CO, CO₃ and O₃ formation, consistent with Gerakines et al. (1996). Figure 11.8 shows that in the CH₄:CO₂ ice mixture CO and CO₃ still form and so do C₂H₆ and C₂H₄. In addition, features belonging to CH₃OH, H₂CO and CH₃CHO are identified. HCOOH probably forms as well, but its most distinct band overlaps with features from H₂CO, CH₃CHO and CH₃COOH. The contribution of HCOOH to the 1700 cm⁻¹ complex can be investigated through difference spectra during warm-up, since the HCOOH desorption temperature is known from Chapter 10. This is shown in Fig. 11.9, where a HCO-X band disappears in the 130–160 K temperature range, where HCOOH desorbs. It is however not possible to determine the HCOOH formation during irradiation.

Therefore the quantitative analysis focuses on the other, securely identified ice photo-products. CO₃ and O₃ formation changes most dramatically between pure CO₂ photolysis and CH₄:CO₂ photolysis; the formation rates decrease with an order of magnitude in the mixture (Fig. 11.10). The CO formation rate does not change significantly indicating that CO is relatively unreactive. The extremely low CO₃ production in this ice mixture can be explained by fast hydrogenation of CO₃ to form H₂CO₃. Moore (1991) detected abundant H₂CO₃ during warm-up of an irradiated H₂O:CO₂ ice mixture and similar bands are also

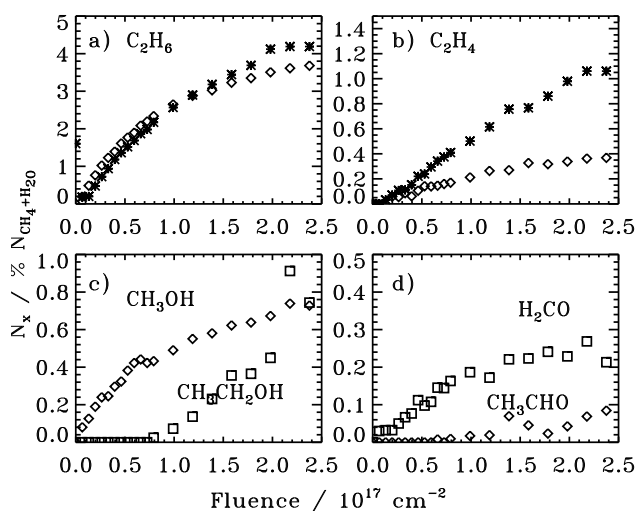


Figure 11.6 – The relative formation of six complex molecules, with respect to the initial total ice abundance, in pure CH_4 ice (stars) and in a $\text{CH}_4:\text{H}_2\text{O}\sim 3:1$ ice mixture (diamonds and squares) as a function of UV fluence at 20 K.

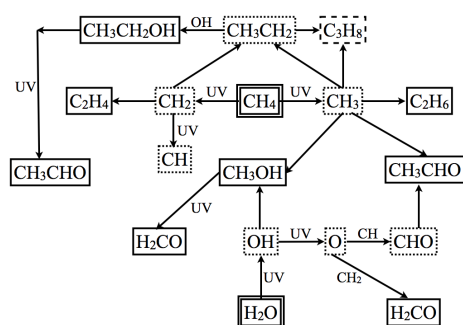


Figure 11.7 – The proposed reactions scheme following UV photolysis of a $\text{CH}_4:\text{H}_2\text{O}$ ice mixture. Solid boxes mark detected species, dashed boxes represent tentatively detected species from RAIRS or TPD curves and dotted boxes undetected species.

present during warm-up of the $\text{CH}_4:\text{CO}_2$ ices to 200 K.

Of the three new complex species, CH_3OH is formed at a similar rate compared to in the $\text{CH}_4:\text{H}_2\text{O}$ mixture, while CH_3CHO and H_2CO form at a higher rate. CH_3OH can form either through hydrogenation of CO or CH_3+OH reactions – its early steady-state suggests that CH_3+OH is the main formation path, since the CO continues to increase throughout the experiment and so should CH_3OH if it formed from CO.

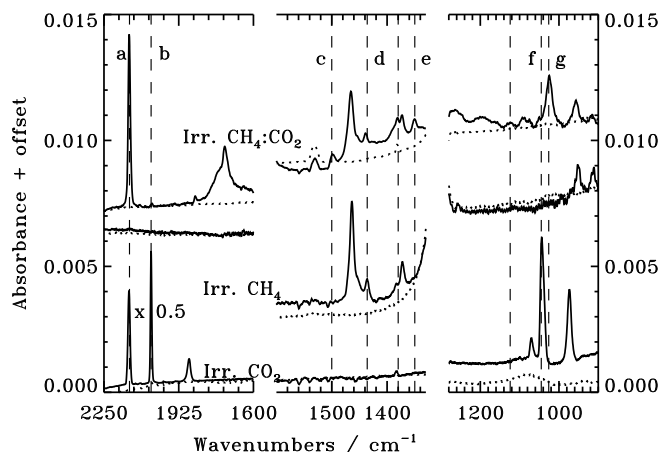


Figure 11.8 – The initial spectra (dotted lines) and spectra after UV photolysis (solid lines) of pure CO_2 ice, pure CH_4 ice and a $\text{CO}_2:\text{CH}_4 \sim 1:2$ mixture, all at 20 K. The bands used for quantifying the a) CO, b) CO_3 , c) H_2CO , d) C_2H_4 , e) CH_3CHO , f) O_3 and g) CH_3OH ice abundances are marked with dashed lines.

Figure 11.11 shows these reaction paths and proposed reaction paths for all infrared-detected products. The faster onset of CH_3CHO production in the $\text{CH}_4:\text{CO}_2$ ice mixture compared to the $\text{CH}_4:\text{H}_2\text{O}$ ice mixture suggests that $\text{CH}_3 + \text{HCO}$ is the dominating formation path in the $\text{CH}_4:\text{CO}_2$ ice rather than $\text{CH}_3\text{CH}_2\text{OH}$ photodissociation. HCOOH formation may occur through two different reaction pathways: hydrogenation of CO_2 and $\text{CO} + \text{HCO}$ reactions. The former is prohibitively slow for thermalized hydrogen atoms (Bisschop et al. 2007b), but it may still be fast for energetic species. In either case, the experiments here show that any kind of hydrogenation of CO and CO_2 is definitely less efficient than hydrogenation of the radical CO_3 . This is in agreement with previous comparison of molecule and atom hydrogenation efficiencies (Hiraoka et al. 1998).

11.3.4 $\text{CO}_2:\text{NH}_3$ ice mixture photolysis

Irradiation of a $\text{CO}_2:\text{NH}_3$ ice mixture produces a complex ice spectrum (Fig. 11.12). This has been previously observed for ice mixtures containing NH_3 , H_2O and CO and many of the new broad features can be ascribed to $\text{NH}_4^+:\text{XCOO}^-$ salts (Muñoz Caro & Schutte 2003). NH_2CHO has several spectral features in the 1400-1700 cm^{-1} region and probably contributes as well. Because of the overlap between different bands shown in Fig. 11.12, only the formation of CO and OCN^- (from its 2161 cm^{-1} band) can be quantified at this stage.

OCN^- is a common product from UV processing of C, O and NH_3 containing ices and its formation in the $\text{CO}_2:\text{NH}_3$ ice mixture is consistent with previous studies (e.g. van Broekhuizen et al. 2004). Figure 11.13 shows that similarly to what was observed

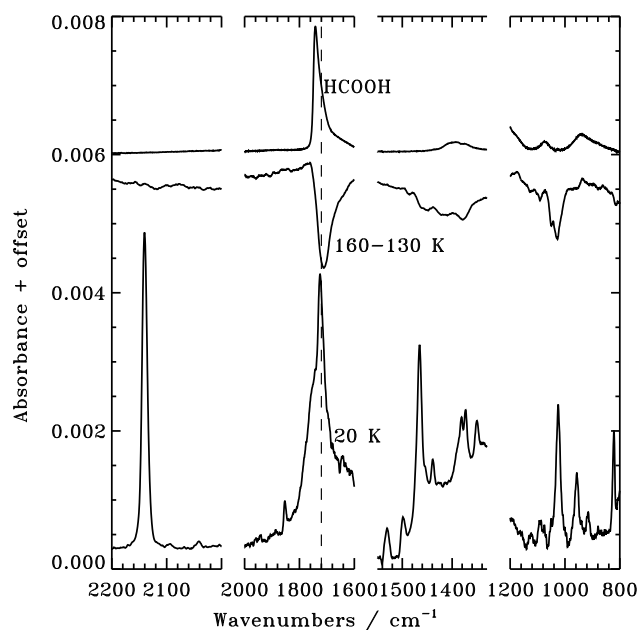


Figure 11.9 – Starting from the bottom the figure shows a photolyzed $\text{CO}_2:\text{CH}_4$ ice spectrum at 20 K, a difference spectrum during warm-up of the same ice mixture, and a pure HCOOH spectrum. In the difference spectrum negative peaks signify desorption of the band carrier.

for HCN in the $\text{CH}_4:\text{NH}_3$ mixture, OCN^- is not produced immediately at the onset of irradiation (i.e. within 10 minutes), indicative of a multi-step formation process. This explains the low yield of OCN^- with respect to NH_4^+ ; the lower limit on NH_4^+ formation is more than an order of magnitude greater than the OCN^- production. OCN^- is thus not the main counter ion of NH_4^+ . Figure 11.13 also shows that OCN^- does not desorb below 170 K.

With only two band assignments, the $\text{CO}_2:\text{NH}_3$ reaction scheme is speculative. The pathway to HNC and further to OCN^- may either be through $\text{CO}+\text{NH}$ or $\text{CO}+\text{NH}_2$ followed by photodissociation. From the $\text{H}_2\text{O}:\text{CO}_2$ and $\text{CH}_4:\text{CO}_2$ ice mixtures, both H_2CO_3 and HCOOH are expected products in the $\text{CO}_2:\text{NH}_3$ ice photolysis experiment. These two acids may very well be the main counter ions to NH_4^+ , since in the presence of NH_3 they should both be converted into their salt counterparts HCO_3^- and HCOO^- (Schutte & Khanna 2003).

11.3.5 The effect of H_2O at different concentrations

Figure 11.14 shows the spectra of pure NH_3 , $\text{H}_2\text{O}:\text{NH}_3$ 1:1 and $\text{H}_2\text{O}:\text{NH}_3$ 4:1 ice mixtures before and after the ices are irradiated with a UV fluence of $2.3 \times 10^{17} \text{ cm}^{-2}$. Adding different amounts of H_2O to NH_3 ice suppresses the production of the 2111 cm^{-1} and 2768 cm^{-1} features, observed in the pure ice photolysis experiment and there ascribed to N_2H_4 ; neither is observed in any of the $\text{H}_2\text{O}:\text{NH}_3$ ice mixture experiments, though

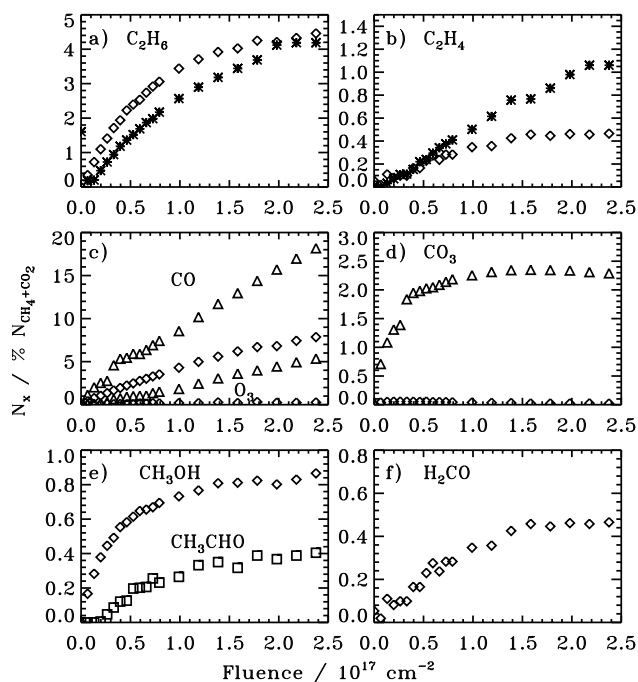


Figure 11.10 – The relative formation of eight photoproducts, with respect to the initial total ice abundance, in pure CH₄ ice (stars), pure CO₂ ice (triangles) and a CH₄:CO₂ ~ 2:1 ice mixture (diamonds and squares) as a function of UV fluence at 20 K.

overlap between the 2768 cm⁻¹ band and the H₂O feature wing prevents a strict upper limit. The 1507 cm⁻¹ band is still present in the H₂O mixtures. In addition, at least one new feature appears in the 4:1 ice mixture, and probably in the 1:1 ice as well, at 1470 cm⁻¹. In general the combined band around 1500 cm⁻¹ is more pronounced the more H₂O is added, indicative of either the onset of an acid-base chemistry or efficient trapping of NH₂; additional irradiation experiments are required to distinguish between the two carrier scenarios. Without a more strict assignment, the chemistry cannot be further quantified in the H₂O:NH₃ mixtures.

Photolysis of the H₂O:CO₂ mixtures results in several broad features, which are due to a combination of HCOOH and H₂CO₃. The bands cannot be easily separated during irradiation and therefore this chemistry is equally difficult to quantify as the H₂O:NH₃ chemistry.

In the CH₄:H₂O 3:1 and 1:2 ice mixtures C₂H₆, CH₃OH, CH₃CHO, CH₃CH₂OH and H₂CO all clearly form upon UV irradiation. The formation of the first four complex species is quantified in Fig. 11.15 with respect to the initial CH₄ ice abundance. Increasing the H₂O concentration reduces the relative C₂H₆ formation and increases the relative

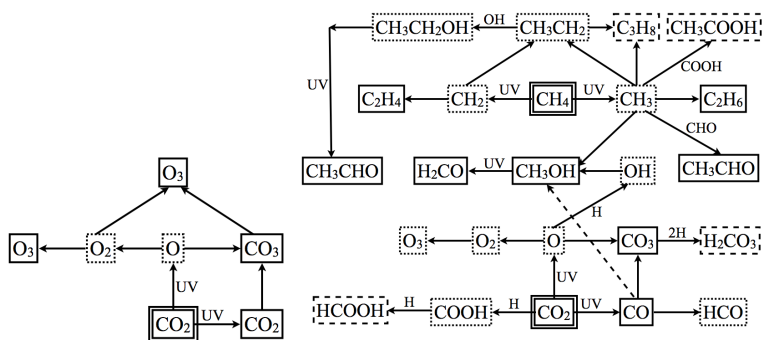


Figure 11.11 – The proposed reactions schemes following UV photolysis of pure CO₂ ice (left-hand scheme) and a CH₄:CO₂ ice mixture (right-hand scheme). Solid boxes mark detected species, dashed boxes tentatively detected species and dotted boxes represent undetected ones. Dashed arrows mark formation pathways that require several steps.

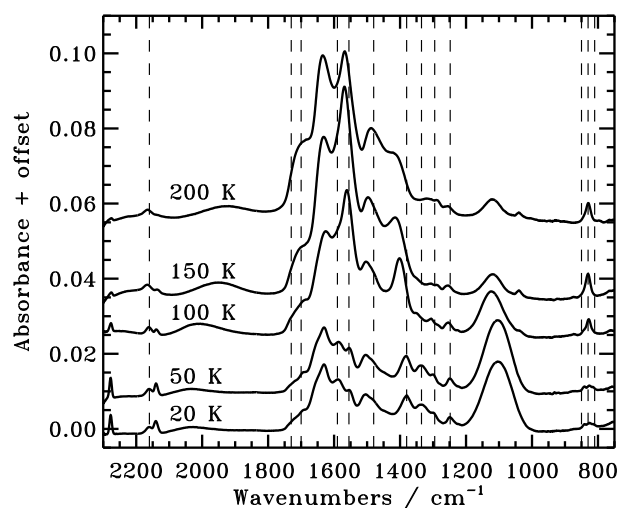


Figure 11.12 – Spectrum of irradiated NH₃:CO₂ ice during warm-up. All features exclusive to photolysis of CO₂:NH₃ ice mixtures compared to pure ices are marked with dashed lines. The OCN⁻ feature is at 2161 cm⁻¹.

formation rates of CH₃OH, CH₃CHO and H₂CO as expected when increasing the relative OH/CH₃ radical ratio in the ice.

During irradiation there is no obvious evidence for a slower radical diffusion because of higher binding energies in a H₂O-rich ice. During warm-up there are some differences between the two ice mixtures, however (Fig. 11.16). The CH₃OH and CH₃CHO abundances increase in both mixtures with temperature, but the CH₃CHO abundance increases more in H₂O-rich ice and the CH₃OH abundance in the H₂O-poor ice, indicative of different diffusion conditions in the H₂O-poor and the more strongly bound H₂O-rich

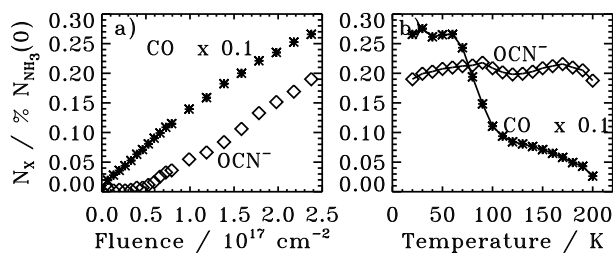


Figure 11.13 – The evolution of the OCN⁻ and CO abundances as a function of UV fluence at 20 K, and as a function of temperature during warm-up.

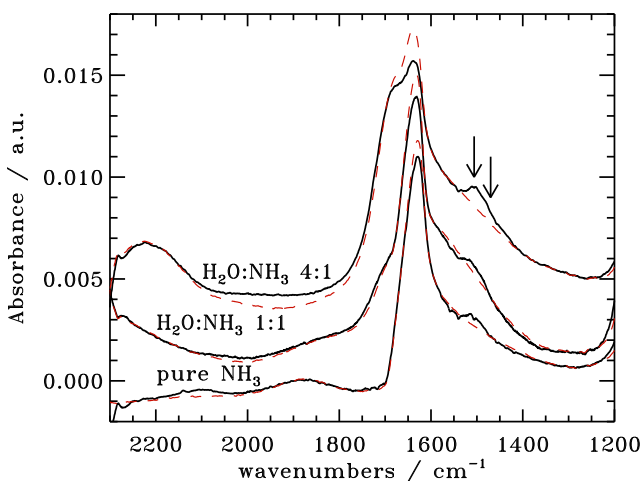


Figure 11.14 – Spectra of pure NH₃ ice, NH₃:H₂O 1:1 and 1:4 ice mixtures, before irradiation at 20 K (dashed lines) and after UV irradiation at 20 K (solid lines). The 1507 and 1470 cm⁻¹ features are marked with arrows.

mixture.

11.3.6 NH₃ ice photodesorption

The efficiency of photochemistry in both pure ices and mixtures is limited by the formation rates of radicals through photodissociation, which is discussed in the next subsection, and by the photodesorption rate, which continuously desorbs ice. Figure 11.17 shows the loss of NH₃ ice at 20 K as a function of UV fluence due to a combination of bulk dissociation and surface photodesorption, calculated from the 1070 cm⁻¹ band. The photodesorption yield is determined from the linear decrease in ice thickness, visible at later times, while the bulk dissociation follows an exponential decay (Öberg et al. 2009b,a). The combined linear and exponential fits result in a NH₃ photodesorption yield of $(1.2 \pm 0.7) \times 10^{-3}$ per incident UV photon. The main error comes from the ice thickness uncertainty; the fit error is ~15%.

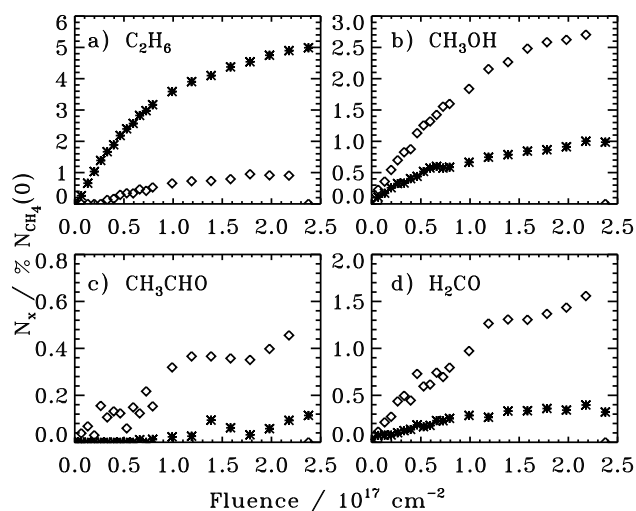


Figure 11.15 – The relative formation of four complex molecules in $\text{CH}_4:\text{H}_2\text{O}\sim 3:1$ and $1:2$ ice mixtures (stars and diamonds, respectively) with respect to the initial CH_4 ice abundance as a function of UV fluence at 20 K.

The derived photodesorption yield is similar, within a factor of three, to the yields determined previously for CO , CO_2 , H_2O and CH_3OH (Öberg et al. 2009b,a, Chapter 10), confirming the assumption of a comparable photodesorption yield for all ices with strong UV absorptions (Chapter 12).

11.3.7 NH_3 and CH_4 photodestruction

Figure 11.18 shows the normalized and log-transformed loss of NH_3 ice as a function of fluence for different ice mixtures. In contrast to Fig. 11.17 the ices are thick (~ 50 ML) and the fluence scale short to ensure that bulk processes dominate the ice loss, rather than photodesorption of surface molecules. The measured photodestruction rates for NH_3 during the first 4×10^{16} photons cm^{-2} are reported in Table 11.1 for pure NH_3 , $\text{NH}_3:\text{H}_2\text{O}$ 1:1 and 1:4, $\text{NH}_3:\text{CH}_4$ and $\text{NH}_3:\text{CO}_2$ ice mixtures.

The photodissociation rate for pure NH_3 ice is measured to be 1.0×10^{-18} cm^2 averaged over the wavelength range of the lamp. This is an order of magnitude lower than the measured gas phase photodesorption cross section (van Dishoeck 1988). A similar discrepancy was previously found for CH_3OH , indicating that fast recombination following photodissociation is a general feature of ice photolysis. The new NH_3 ice photodissociation rate is however a factor of 8 higher than previously measured for a thick $\text{NH}_3:\text{N}_2$ 1:10 ice mixture, which is probably the most comparable measurement to the present one, since all previous photodissociation measurements are for thick ices and thick pure ices (of 1000 ML or more) suffer from optical depth effects (Cottin et al. 2003). Furthermore,

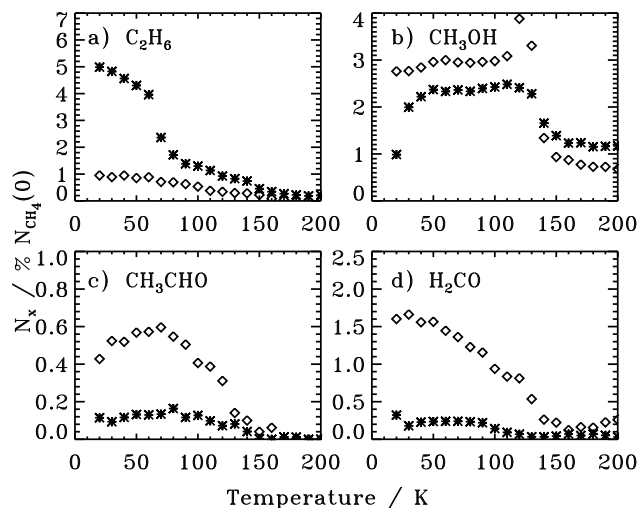


Figure 11.16 – The relative evolution of four complex molecules in CH₄:H₂O~3:1 and 1:2 ice mixtures (stars and diamonds, respectively) as a function of temperature during warm-up.

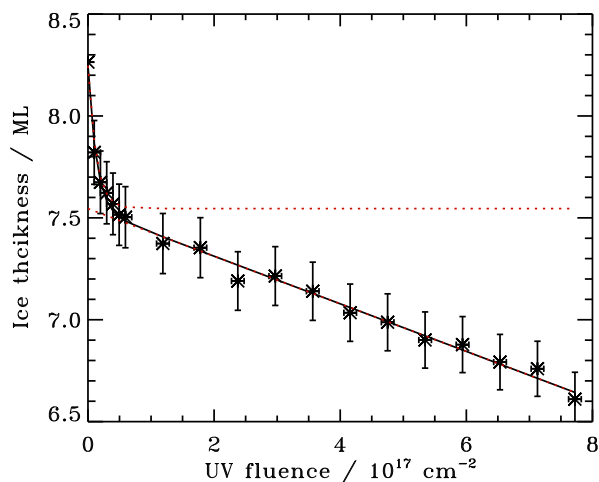


Figure 11.17 – The loss in NH₃ (stars) ice due to bulk dissociation (exponential part) and surface photodesorption (linear part). The combined fit is plotted with a solid line and the linear and exponential parts are overlaid with dotted lines.

Cottin et al. (2003) measured the photodissociation yield for an order of magnitude higher fluence, when back reactions become important; if the destruction cross section is measured over 2.3×10^{17} photons cm^{-2} , rather than just the initial few 10^{16} cm^{-2} , it would appear to be the same as measured by Cottin et al. (2003) within the experimental uncertainties. The higher photodissociation yield measured here should thus be more accurate, even though the precision of the measurements by Cottin et al. (2003) was higher.

The initial NH₃ photodestruction rate is indistinguishable in the NH₃:H₂O 1:1 mixture, the NH₃:CH₄ 2:3 mixture and the pure NH₃ ice. At higher fluences there is still

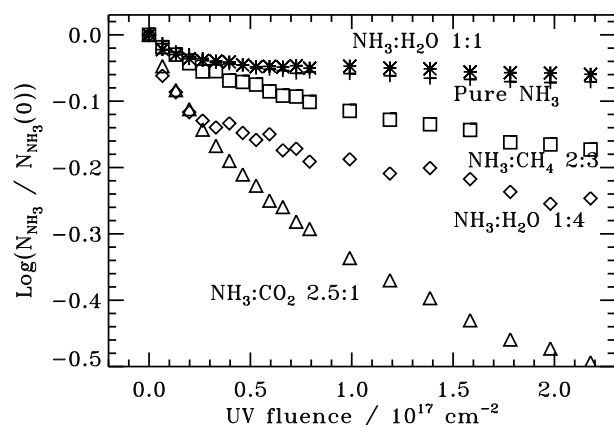


Figure 11.18 – The log-transformed normalized photodestruction rate of pure NH_3 (stars), $\text{NH}_3:\text{H}_2\text{O}$ 1:1 (crosses), $\text{NH}_3:\text{CH}_4$ 2:3 (squares), $\text{NH}_3:\text{CO}_2$ 2.5:1 (triangles) and $\text{NH}_3:\text{H}_2\text{O}$ 1:4 (diamonds) ice.

no measurable difference between the NH_3 photodissociation in pure NH_3 ice and in the $\text{NH}_3:\text{H}_2\text{O}$ mixture, while more NH_3 is being destroyed in the $\text{NH}_3:\text{CH}_4$ ice mixture. This difference suggests an efficient chemistry in the $\text{NH}_3:\text{CH}_4$ ice, which slows down the reformation of NH_3 from photodissociation fragments.

The initial photodestruction is significantly higher in the $\text{NH}_3:\text{CO}_2$ 2.5:1 and the $\text{NH}_3:\text{H}_2\text{O}$ 1:4 ice mixtures compared to pure NH_3 ice (the quoted uncertainties in Table 11.1 include the systematic uncertainties, the fit uncertainties are $\sim 0.2 \times 10^{-18} \text{ cm}^2$). In addition the destruction rate in the $\text{NH}_3:\text{CO}_2$ ice does not slow down with UV fluence. The higher initial photodestruction rate suggests an additional destruction mechanism to photodissociation, such as UV induced acid-base chemistry, i.e. NH_3 is both destroyed directly by the UV irradiation through photodissociation and indirectly through proton transfer from other photoproducts. This is the logical explanation for the high destruction rate in the $\text{NH}_3:\text{CO}_2$ ice mixture. The high rate in the 4:1 $\text{H}_2\text{O}:\text{NH}_3$ ice may also be due to a slower diffusion rate in a H_2O -rich ice, which limits back reactions. Both alternatives are discussed below together with new experiments that will constrain the relative importance of the two mechanisms.

None of this behavior is observed for CH_4 photodestruction in a similar set of ice mixtures (Fig. 11.19). Except for a 50% lower photodestruction cross section in the $\text{CH}_4:\text{NH}_3$ mixture, all CH_4 cross sections are $\sim 2.5 \times 10^{-18} \text{ cm}^2$, averaged over the wavelength range of the lamp, which is a factor of three higher than previously reported by Gerakines et al. (1996) and a factor of five lower than the gas phase value (van Dishoeck 1988). The factor of two smaller discrepancy between ice and gas phase CH_4 compared to the NH_3 case, is consistent with the expected higher volatility of CH_2/CH_3 relative to NH_2 ; the faster diffusion of CH_2/CH_3 should reduce the importance of immediate back reactions.

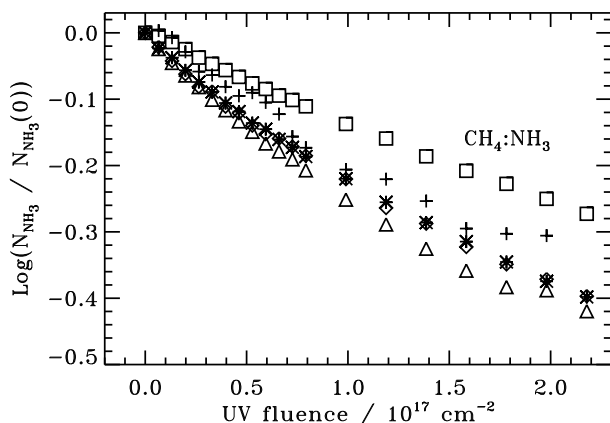


Figure 11.19 – The log-transformed normalized photodestruction rate of pure CH₄ (stars), CH₄:H₂O 3:1 (crosses), CH₄:NH₃ 3:2 (squares), CH₄:CO₂ 2:1 (triangles) and CH₄:H₂O 1:2 (diamonds) ice.

11.4 Testing complex ice formation in astrophysical ice equivalents

The comparison between photolysis of pure and binary mixtures shows that the binary reaction products are consistent with combining the pure reaction schemes with a few bridging reactions. In tertiary ice mixtures and in a four-component astrophysical ice analogue, the products are therefore expected to be consistent with the products from the binary mixtures, with some new bridging reactions combining e.g. the CH₃NH₂ and HCOOH products to form NH₂CH₂COOH in a NH₃:CH₄:CO₂ ice.

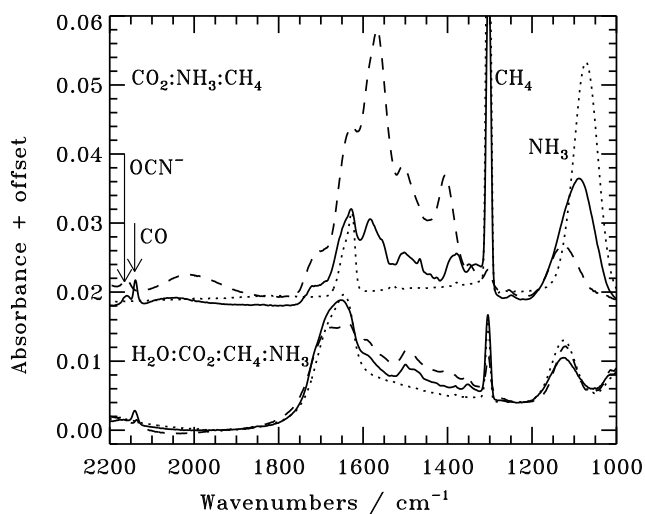


Figure 11.20 – Infrared spectra of an astrophysical ice equivalent and the NH₃:CO₂:CH₄ ice mixture before irradiation at 20 K (dotted line), following photolysis at 20 K (solid line) and after warm-up to 100 K (dashed line).

The RAIR spectra following photolysis of these ice mixtures are complicated and few of the products can be quantified spectroscopically (Fig. 11.20). Some attempts to assign peaks around $1500\text{--}1700\text{ cm}^{-1}$ have been made in previous studies following photolysis of comparable ice mixtures (Muñoz Caro & Schutte 2003), but this is not pursued here. Instead the carriers of bands outside of the $1500\text{--}1700\text{ cm}^{-1}$ spectral region, which can be securely assigned, are quantified using RAIRS. More complex products are then investigated through TPD experiments. No experiments resulted in any remaining residue after heating to room temperature as was observed in some previous experiments on thicker ices and after higher UV fluences (Greenberg 1983; Schutte & Khanna 2003).

11.4.1 Quantification of photolysis through RAIRS

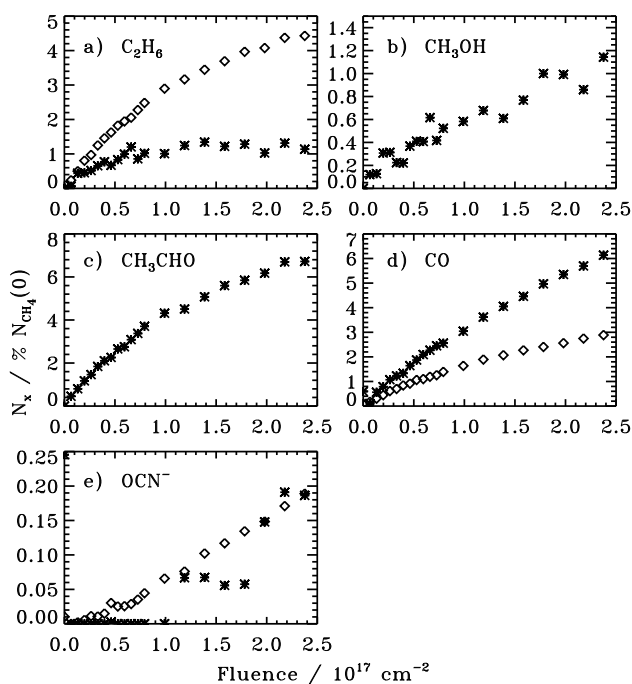


Figure 11.21 – The relative evolution of five photoproducts with respect to the initial CH_4 ice abundance in a $\text{H}_2\text{O}:\text{CO}_2:\text{NH}_3:\text{CH}_4$ 100:20:8:12 astrophysical ice equivalent (stars) and three molecules in a $\text{CO}_2:\text{NH}_3:\text{CH}_4$ ice mixture (diamonds) as a function of fluence at 20 K.

Despite the complexity of the spectra C_2H_6 , CH_3OH , CO and OCN^- formation can be identified in the astrophysical ice equivalent ($\text{H}_2\text{O}:\text{CO}_2:\text{NH}_3:\text{CH}_4$ 100:20:8:12) and in a tertiary $\text{CO}_2:\text{NH}_3:\text{CH}_4$ 1:1:1 ice mixture, through the same spectral features as in the binary ice mixtures. CH_3CHO probably forms as well though there are alternative

nitrogen-bearing carriers of the 1350 cm⁻¹ band. A comparable amount of OCN⁻ forms in both ice mixtures with respect to the CH₄ content in the ice, but the initial formation rate is lower in the H₂O-rich ice. The C₂H₆ formation is significantly reduced in the H₂O-rich ice compared to the tertiary ice mixture, suggesting that most of the CH₃ radicals react with other radicals than CH₃ in the H₂O-rich matrix forming some of the observed CH₃OH and possibly CH₃CHO.

Table 11.3 lists the formation cross sections for all detected photoproducts with known band strengths in the quantified experiments. These cross sections have a physical meaning for species that form directly through photodissociation, such as CO. For the other molecules it is simply a convenient measure of the initial photoproduction rate – the cross sections are calculated by fitting a line to the growth curves during the first 4 × 10¹⁶ photons cm⁻². This growth regime should only be marginally affected by back-reactions, except for the fast initial recombination reactions immediately following photodissociation. The cross-sections are listed with respect to initial CH₄, NH₃ and CO₂ abundances where relevant, i.e. where the product can form from photodissociation fragments of the molecule. The C₂H₆ formation is thus only listed with respect to the initial CH₄ abundance, while the CH₃NH₂ formation is listed with respect to both the CH₄ and the NH₃ abundances.

Table 11.3 – Cross sections with respect to the initial CH₄/NH₃/CO₂ abundances.

Experiment	Photoproduction cross sections / 10 ⁻¹⁹ cm ²						
	C ₂ H ₆	C ₂ H ₄	CH ₃ OH	CH ₃ CHO	CO	CO ₃	OCN ⁻
Pure CH ₄	3.2	0.36					
Pure CO ₂					13	5.5	
CH ₄ :NH ₃	4.2	0					
CH ₄ :CO ₂	7.7	0.6	2.4/-/4.3	0.34/-/0.62	14	-/-/0.5	
CH ₄ :H ₂ O 3:1	5.0	0.30	1.1/-/-	0.27/-/-			
CH ₄ :H ₂ O 1:2	2.8	<0.92	10/-/-	1.9/-/-			
NH ₃ :CO ₂					3.0		-/0.02/0.05
CH ₄ :NH ₃ :CO ₂	3.8				2.2		-/0.03/0.03
Astro mix	2.0		0.83/-/0.33	3.7/-/1.5	1.5		-/0/0

The initial formation rate of C₂H₆ is constant between the different experiments within a factor of three. In contrast the C₂H₄ rate is below the detection limit of ~ 10⁻²⁰ cm² in the CH₄:NH₃ mixture and the analogs and the rate thus changes by an order of magnitude.

The CH₃OH formation rate varies by an order of magnitude as well with respect to the initial CH₄ abundance in the different mixtures, indicating that the formation rate is dominated by the availability of OH radicals in the ice under most conditions, rather than the availability of CH₃. It is however also reduced in the analogue where H₂O ice is very abundant; H₂O may be too abundant in this case, caging any formed CH₃ and OH radicals from diffusing through the ice.

The CO production with respect to the CO₂ content is not affected by the presence of CH₄ and NH₃. It is however reduced by an order of magnitude in the NH₃-containing ices where acid base chemistry is feasible, i.e. the tertiary ice mixture and the analogue.

In contrast the CO₃ formation rate is reduced by an order of magnitude between the pure CO₂ ice and all other ice mixtures.

There are thus some significant quantitative differences between the binary ices and the astrophysical ice mixture analogue, which are difficult to predict without a quantitative model that takes into account the effects of acid-base chemistry and different diffusion barriers in different kinds of ices. Nevertheless, the fact that the expected photoproducts are formed in the tertiary ice and the analogue suggests that the initial hypothesis on the reaction schemes for these ices is correct; i.e. the chemistry consists of the binary ice reactions together with bridging reactions resulting in the formation of more complex molecules. Larger molecules should thus be present in the tertiary and analogue mixtures. This is the topic of the next section.

11.4.2 TPD experiments

This section investigates the TPD curves of the photolyzed astrophysical ice equivalent H₂O:CO₂:NH₃:CH₄ 100:20:12:8, together with TPD curves of five other photolyzed ice mixtures. The aim is to constrain which complex molecules form abundantly in the astrophysical ice equivalent by investigating the mass signals at each desorption peak and searching for similarities and differences between the different experiments.

The ices employed for comparison are the NH₃:CO₂ 1:1, NH₃:CH₄ 1:1, NH₃:CO₂:CH₄ 1:1:1, NH₃:CO₂:H₂O 1:1:1 and H₂O:CO₂:CH₄ 1:1:1 mixtures. All mixtures contain similar amounts of NH₃, CH₄ and CO₂ ice initially, within a factor of two, except for the analogue. All TPD curves are scaled by the same factor and the resulting TPD curves thus reflect the different formation efficiencies of different products in different ice mixtures.

Figures 11.22–11.24 present TPD curves for the nine m/z signals, which together contain all desorption peaks observed in the entire set of experiments. The nine m/z are 27, 29, 31, 41, 43, 45, 59, 60 and 61, which trace C₂H_{4/6} (27, 29), HCN (27), CH₃NH₂ (27, 29, 31), H₂CO (29), CH₃OH (29, 31), NH₂OH (31), CH₃CN (41), HNCO (43, 27), HCOOH (29, 45), CH₃COOH (45, 60), NH₂COOH (45, 61), NH₂CH₂COOH (29, 45, 59), CH₃NH₂COOH (29, 45, 60), H₂CO₃ (45, 61). m/z with contributions from the original ice components are purposefully avoided, i.e. $m/z=12-18$, 28 and 44, since desorption of the original ice components tend to dominate these mass signals.

The ices are heated at most to 230 K, because of experimental constraints, at which point ices are still desorbing. The desorption peaks are analyzed sequentially starting with this desorption feature around 230 K and then proceeding to lower temperatures. The resulting assignments to the desorption peaks are summarized in Table 11.4.

The 230 K desorption peak in Figs. 11.22–11.24 is present in the NH₃:CO₂:CH₄ mixture, but not in the H₂O:NH₃:CO₂ mixture, while the TPD was terminated at lower temperatures in the other experiments. The carrier of the peak must therefore contain a CH_x group. In the NH₃:CO₂:CH₄, it is present for all investigated m/z , including $m/z=60$ and 61. The high desorption temperature suggests a compound which exists as a salt in the ice. There is no infrared features left in the NH₃-free mixture above 200 K or in the CH₄:NH₃ mixture above 150 K and thus the molecule must contain nitrogen and a CO_x group. The

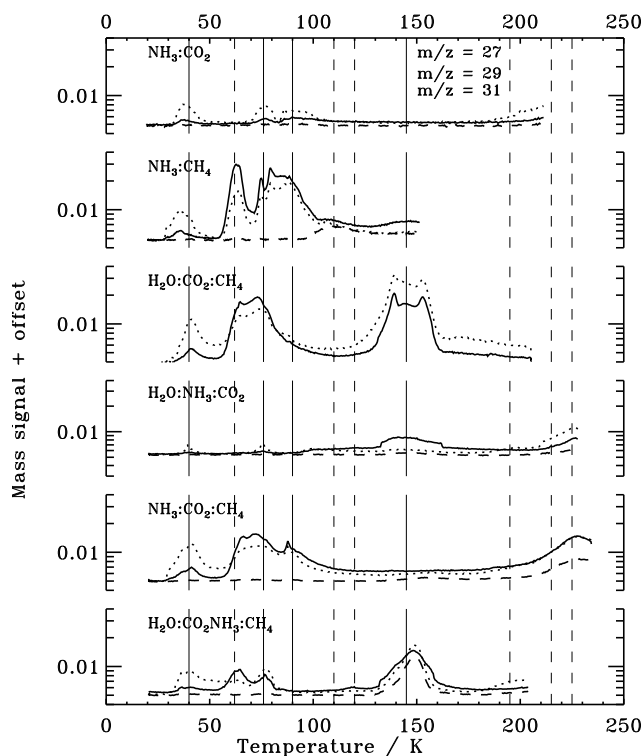


Figure 11.22 – TPD curves following photolysis of six ice mixtures for $m/z = 27$ (solid), 29 (dotted) and 31 (dashed). The thin solid lines mark the approximate desorption temperatures of CH₄, CO₂, NH₃ and H₂O. The thin dashed lines mark the desorption temperatures of different photolysis products, visible in at least one of the TPD experiments.

strong $m/z=43$, 45 and 46 peaks are indicative of CH₂COH and COOH functional groups. Glycine NH₂CH₂COOH and its structural isomer CH₃NHCOOH (CH₂COOH = 59 amu, NHCOOH = 60 amu, CH₂COH/NHCO = 43 amu, COOH=45 amu) are thus the most probable carriers though additional experiments, which include $m/z=75$ are needed to confirm the identification.

A second molecule, which does not contain a CH_x group, also desorbs around this temperature, since there is a desorption peak present at 225 K in the H₂O:NH₃:CO₂ mixture, consisting of $m/z=27$, 29, 31, 43, 45 and 46, but no 59, 60 or 61. NH₂CHO fits this mass pattern, but a new CO₂:NH₃ experiment is required to test whether the desorption is present there as well. HCOOH in its salt form is another option, which explains some of the observed mass signals.

The next desorption peak, working backwards, is at 215 K and contains $m/z=61$, but not 59 or 60 in both the H₂O:NH₃:CO₂ and NH₃:CO₂:CH₄ mixtures. $m/z=29$ and 45 are also prominent. This is indicative of NH₂COOH desorption (NH₂COOH = 61 amu,

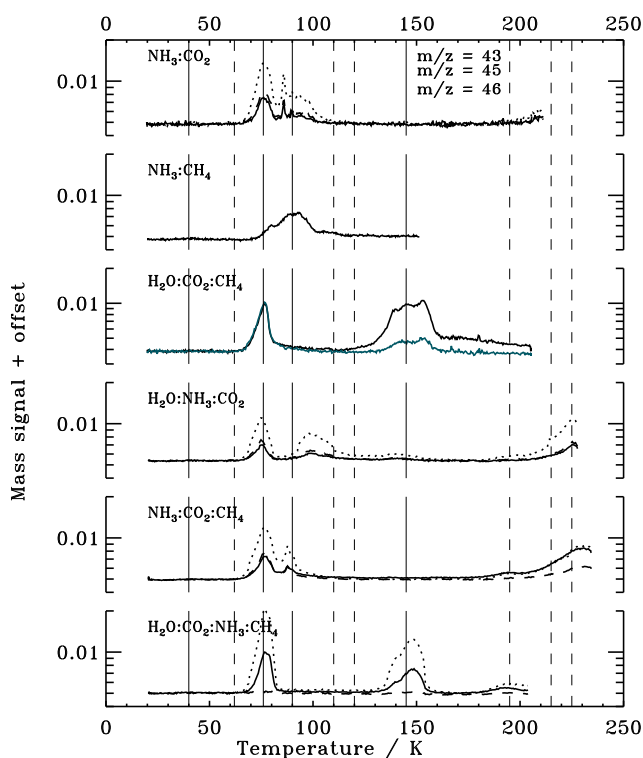


Figure 11.23 – TPD curves following photolysis of six ice mixtures for $m/z = 43$ (solid), 45 (dotted) and 46 (dashed). The thin solid lines mark the approximate desorption temperatures of CH_4 , CO_2 , NH_3 and H_2O . The thin dashed lines mark the desorption temperatures of different photolysis products, visible in at least one of the TPD experiments.

$\text{COOH} = 45 \text{ amu}$, $\text{COH} = 29 \text{ amu}$).

The desorption peak at 195 K is the first to be investigated that is certainly present in the astrophysical ice equivalent in the bottom panel in Figs. 11.22–11.24. It is also apparent in the $\text{NH}_3:\text{CO}_2:\text{CH}_4$ experiment with $m/z=60$, but in no other experiments. The absence in the $\text{H}_2\text{O}:\text{NH}_3:\text{CO}_2$ ice mixture is indicative of the molecule containing a CH_x group, while the absence in the N-free ice mixture advocates a molecule containing nitrogen or an acid, which requires the presence of NH_3 to exist in its ion form and thus desorbs at this high temperature. These facts and the mass pattern fits CH_3COOH and no other considered species.

H_2O desorbs at $\sim 145 \text{ K}$. This is accompanied with significant co-desorption of $m/z \leq 46$ in the astrophysical ice equivalent and in the $\text{H}_2\text{O}:\text{CO}_2:\text{CH}_4$ ice mixture, though the mass signals are different. In the astrophysical ice the $m/z=45$ signal is stronger than the $m/z=43$ signal, while the relation is the opposite in the nitrogen free mixture. Both peaks have multiple possible carriers, but the $\text{H}_2\text{O}:\text{CO}_2:\text{CH}_4$ peak must be dominated by

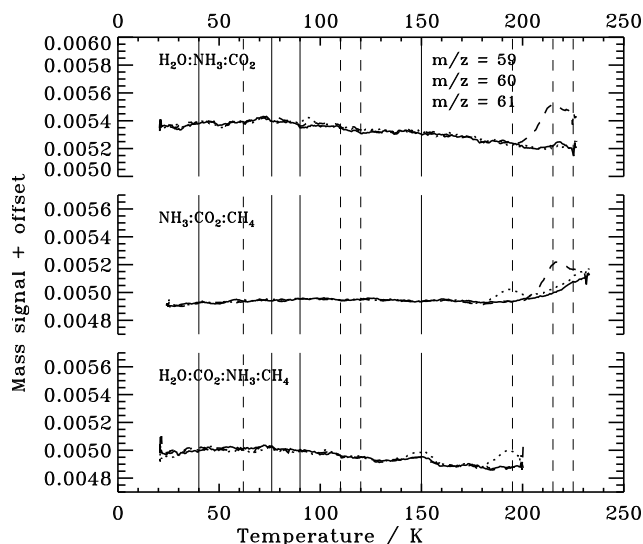


Figure 11.24 – TPD curves following photolysis of six ice mixtures for $m/z = 59$ (solid), 60 (dotted) and 61 (dashed). The thin solid lines mark the approximate desorption temperatures of CH_4 , CO_2 , NH_3 and H_2O . The dashed lines mark the desorption temperatures of different photolysis products, visible in at least one of the TPD experiments.

a $\text{C}_2\text{H}_x\text{O}$ type species, while the peak in the astrophysical ice equivalent has a main carrier with a CO_2 -group such as HCOOH .

The astrophysical ice equivalent and the $\text{CH}_4:\text{NH}_3$ ice mixture contain a peak at ~ 120 K. The lack of any m/z above 27 suggests that HCN is the carrier – HCN desorbs with NH_3 in the $\text{NH}_3:\text{CH}_4$ mixture from the RAIRS. Next, a desorption peak at 110 K is most obvious in the $\text{CH}_4:\text{NH}_3$ ice mixture and its mass pattern with $m/z=27-31$ makes its assignment to CH_3NH_2 secure.

There is no co-desorption with NH_3 in the astrophysical ice equivalent. The next peak at ~ 76 K is due to co-desorption with CO_2 , which contains no obvious evidence for desorption of complex species. Finally the main $\text{C}_2\text{H}_4/6$ desorption peak at ~ 62 is present in all CH_4 containing ice mixtures.

There is no separate desorption peak for HNCO in any of the experiments, which is at first glance surprising since OCN^- is formed according to the RAIR spectra. Also according to the RAIR spectra, OCN^- starts to desorb around 200 K, and this temperature region does contain m/z signals of 28, 26 and 43. OCN^-/HNCO must thus desorb together with other species at this temperature. It probably explains the strong $m/z=43$ signal at this time; while $\text{NH}_2\text{CH}_2\text{COOH}$ may contribute to $m/z=43$, a rather awkward dissociation is required to form it and OCN is a more likely main contributor.

The (tentative) assignments of all desorption peaks are summarized in Table 11.4. TPD experiments following ice photolysis thus provide ample evidence for a complex NH_3 based chemistry in NH_3 -containing ice mixtures up to the formation of simple amino

Table 11.4. The TPD detected species in key ice mixtures with H₂O:CO₂:CH₄:NH₃.

Temp. (K)	<i>m/z</i>	Assignment
62	27, 30, 29	C ₂ H ₄ , C ₂ H ₆
76	varied	CO ₂ co-desorption
90	varied	NH ₃ co-desorption
110	31, 29, 27	CH ₃ NH ₂
120	27	HCN
145	varied	H ₂ O co-desorption
195	45, 43, 47, 60	CH ₃ COOH ion
215	61, 45, 46, 31	NH ₂ COOH ion
225	45, 43, 46	NH ₂ CHO (+HCOOH) ion
230	60, 59, 45, 43, 46	NH ₂ CH ₂ COOH+CH ₃ NHCOOH ions (+HNCO)

acids, such as glycine. TPD curves provide little quantitative information, however and no information on when these species form during photolysis.

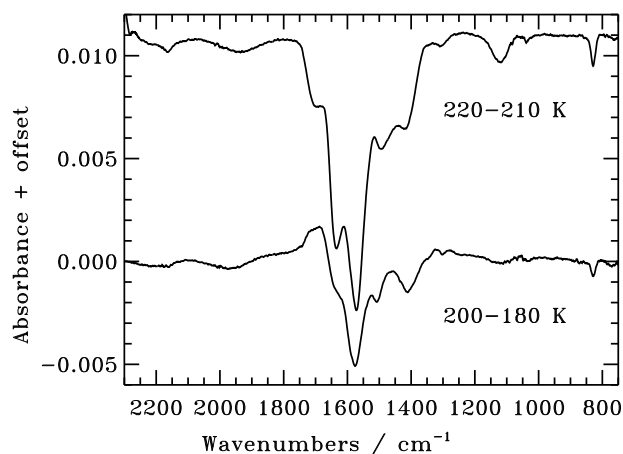


Figure 11.25 – Infrared difference spectra of the NH₃:CO₂:CH₄ ice mixture during warm-up, where negative peaks indicate destruction of the carrier in the temperature interval.

The TPD curves suggest that inspecting difference spectra from before and after specific desorption peaks may result in the assignment of some infrared peaks and the derivation of the final abundance of the complex molecule in question. Figure 11.25 shows the difference spectra of the NH₃:CO₂:H₂O mixture between 220 and 210 K and between 200 and 180 K. According to the TPD curves two different carriers are desorbing at these temperatures. Yet the difference spectra share several bands, indicating that some of the changes in the RAIRS are due to ice re-structuring, such as dissolution of the salt networks, rather than desorption. Difference spectra during desorption are thus not very useful for NH₃:CO₂-containing ice mixtures when trying to assign RAIRS features to complex molecules.

Modeling the ice chemistry in the simpler ice mixtures and then using these models to predict the chemistry in astrophysical ice analogues thus remains the best option for quantifying the complete chemistry of the H₂O-rich ice phase during star formation.

11.5 Discussion

11.5.1 Importance of acid-base chemistry in NH₃:X ice mixtures

The photodestruction rate of pure NH₃ and of NH₃ in different ice mixtures differs by a factor of four after a low fluence and by an order of magnitude after an equivalent photon exposure to a million years in a cloud core, i.e. $\sim 3 \times 10^{17}$ photons cm⁻² (Shen et al. 2004). In contrast the CH₄ photodissociation rate increases by at most 50% between the pure ice and a similar set of ice mixtures as investigated for NH₃.

There are a number of processes that can affect the effective photodissociation cross sections in ices of which the diffusion and escape rates of radicals have been shown to be important previously (Chapter 10). The diffusion rate can be increased by increasing the ice temperature and decreased by the presence of a strongly binding ice such as H₂O. An increased diffusion rate should increase the recombination rate. An increasing temperature may also result in desorption of radicals, which has the opposite effect of decreasing the recombination rate, which is probably why the effective CH₃OH photodissociation rate increases with temperature (Chapter 10). The lowered diffusion rate in a H₂O-rich ice may explain why the NH₃ photodissociation cross section is higher in the H₂O:NH₃ 4:1 mixture compared to pure NH₃ ice. A similar effect would be expected for CH₄. This is not observed, but may be due to the fact that the highest H₂O concentration investigated is H₂O:CH₄ 2:1 and a 5:1 experiment is required to investigate this further.

The increased photodestruction rate of NH₃ in the H₂O ice may also be due to a photo-induced acid-base chemistry where H₂O or a H₂O:NH₃ photoproduct acts as a weak acid. Acid-base chemistry is the only explanation for the extremely efficient indirect photodestruction of NH₃ in a CO₂ ice mixture. There NH₃ must be lost both by photodissociation and by proton transfer from photoproducts, such as HCOOH and H₂CO₃, to form NH₄⁺. Acid base chemistry in NH₃ and CO₂ containing ices also explains the high desorption temperatures of several of the complex molecules, e.g. NH₂COOH, CH₃COOH and possibly NH₂CH₂COOH/CH₃NHCOOH, since salts form stronger bonds than the covalent bonds between the neutral molecules in the ice.

The impact on the chemical pathways of this proton transfer is not clear. The tentatively detected complex molecules in the NH₃:CO₂:X mixtures can all be qualitatively explained by radical-radical reactions, e.g. NH₂+CH₂+COOH to form NH₂CH₂COOH, followed by proton loss to NH₃ to form NH₄⁺. This indicates that the acid-base chemistry does not effect the formation pathways of species, but only the final form of the products and therefore their desorption temperatures. The predicted high desorption temperatures of most nitrogen-containing organics may explain why no glycine has been detected in space yet – it is probably present in the gas phase in a very small region around protostars.

11.5.2 Photodissociation branching ratios

H₂O, CH₄ and NH₃ all photodissociate through the loss of one or multiple hydrogen atoms or a hydrogen molecule, while CO₂ exclusively photodissociates into CO+O in the gas phase (van Dishoeck 1988). The H₂O and NH₃ photodissociation branching ratios cannot be quantified in the pure ices because of the lack of secure product detections and band strengths. Their gas phase values are however well known and should be valid in the solid state as well. The gas phase CH₄ photodissociation branching ratio into CH₃ and CH₂ is more controversial and experiments have suggested values between 5:1 and 1:1 (Romanzin et al. 2008).

Following CH₄ photolysis in the pure ice, both C₂H₆ and C₂H₄ are detected. The growth curve of C₂H₄ contains a small fluence delay, but it is not large enough to infer that C₂H₄ is a second generation product as e.g. CH₃CH₂OH seems to be in the CH₄:H₂O ice. Thus the initial growth of both C₂H₄ and C₂H₆ is assumed to be caused by CH₃+CH₃ and CH₂+CH₂ radical reactions. Further assuming that the diffusion barriers of CH₃ and CH₂ are comparable, the CH₄ branching ratio can be constrained from the initial C₂H₆ and C₂H₄ production rate, which is ~9:1. Since each reaction requires two radicals, the dissociation branching ratio is inferred to be ~3:1.

The product ratios during UV irradiation will also depend on the relative radical diffusion barriers. Quantifying these barriers requires, however, a model that simultaneously considers all possible reactions pathways.

11.5.3 Radical diffusion: dependence on H₂O content

Diffusion data can also be extracted by monitoring the further formation of complex molecules during warm-up after the UV lamp has been turned off. This is most obvious when comparing the CH₃OH and CH₃CHO formation in a H₂O-poor and a H₂O-rich H₂O:CH₄ ice mixture during warm-up, following irradiation at 20 K. In the H₂O-poor ice mixture CH₃OH forms during warm-up, but almost no CH₃CHO. In the H₂O-rich ice the situation is the opposite. In both ices more OH than CHO radicals are expected to form, since OH is a direct photodissociation product of H₂O. The growth of CH₃OH in the H₂O-poor ice mixture, where diffusion is fast, is thus expected. The enhanced growth of CH₃CHO in the H₂O-rich ice is best explained by a slower diffusion rate of OH in this ice mixture, because of the hydrogen-bonding environment, which allows the more volatile CHO radical to react with the available CH₃ radicals before OH diffusion becomes possible. While branching ratios can be directly extrapolated from simpler to more complex ice mixtures, it is clear that adding H₂O may change the relative diffusion pattern of the involved radicals significantly and this must be further investigated as outlined below.

11.5.4 Radical-radical versus radical-molecule reactions

The CHO radical belongs to the set of species in the considered reaction schemes which form from hydrogenation and oxygenation of molecules rather than radicals, i.e. CO+H,

though photodissociation pathways from other molecules are possible as well. The formation of CO₃ and O₃ in the CO₂ ices are other examples as is the tentative evidence for HCOOH formation. Hydrogenation of CO is possible for thermalized hydrogen atoms, while hydrogenation of CO₂ is not (Watanabe et al. 2000; Bisschop et al. 2007b). The definite formation of CO₃ from CO₂+O shows that atom addition to CO₂ is possible for at least energetic atoms – whether the O needs to be energetic to react with CO₂ should be tested through irradiation of matrix-isolated CO₂ followed by warm-up. CO₂ hydrogenation may thus be important for energetic hydrogen atoms and HCOOH may form from CO₂ + H* + H.

The order of magnitude decrease in CO₃ and O₃ formation in the ice mixtures compared to the pure CO₂ ice and the far smaller effect on CO production demonstrates that radicals are preferentially hydrogenated in ice mixtures of molecules and radicals, in agreement with Hasegawa et al. (1992). A quantitative measurement of this effect would be possible if the relative production rate of HCOOH and H₂CO₃ could be determined under some specific conditions and this is being pursued.

11.5.5 Routes to complex organics in space

Chapter 10 showed that photolysis of CH₃OH and CO:CH₃OH ices results in the formation of all common C, O and H bearing complex organic species observed in star forming regions. Several of the same species form abundantly, i.e. a few percent with respect to CH₄, during photolysis of H₂O:CO₂:CH₄ ice mixtures as well. The dominating formation pathway of e.g. CH₃CHO will therefore depend on 1) the initial ice abundances and 2) the efficiency of ice mixing during warm-up. Other complex molecules, such as (CH₂OH)₂, are still expected to form solely in the CH₃OH:CO ice phase.

The N-containing organic species require NH₃ or XCN to form (a very minor route through N₂ photolysis cannot be excluded). The NH₃ is expected to reside solely in the H₂O-rich phase, while the XCN species may form in either the CO-rich or the H₂O-rich ice phases (Chapter 2). The order of magnitude higher abundances of NH₃ compared to e.g. OCN⁻ and HCN suggest, however, that formation paths of the majority of nitrogen-containing complex species should be possible to predict from the experiments on H₂O-rich ices, without simultaneous consideration of the chemistry in the CO:CH₃OH ice phase.

The pure and binary ice experiments, where the product formation is quite well understood, produce complex photoproducts in accordance with simple radical-radical and radical-molecule reaction schemes. The same complex molecules seem to form in the astrophysical ice analogue and in the binary ice mixtures it can be thought of as being composed of. Quantitative difference between the two types of mixtures highlight the importance of H₂O and its impact on the relative diffusion barriers of different radicals as discussed further below. To quantitatively test whether the analogue chemistry is consistent with predictions from the binary ice mixtures requires a complete model of the chemistry of both the binary and the analogue mixtures. Such a model should preferentially be calibrated against the better understood chemistry in the simple ice mixtures and then model the analogue based on this calibration. The predicted chemistry can then be

compared quantitatively with the growth curves in the analogue and qualitatively with the results from the TPD experiments.

Even without such a model, it is clear that substantial amounts of amino acids and amino acid-like compounds can form in NH_3 and CO_2 containing ices. The experiments also show that these large molecules can form during irradiation of astrophysically plausible ice mixtures at 20 K or due to diffusion of formed radicals during warm-up of the same ices to at most 200 K. Room temperature induced reactions are therefore not required to form such complex molecules, which is promising for the formation of large molecules in ices in space.

11.5.6 Future experiments

An accurate prediction of the complex chemistry in astrophysically realistic ice mixtures requires a number of additional experiments focusing on the impact of H_2O on the diffusion of radicals and molecules, especially CH_3 , CH_2 , NH_2 , NH , CO and HCO . This can be achieved by quantifying the changes in the chemistry of the binary mixtures investigated here when they are mixed with five times as much H_2O and then irradiated at 2–3 temperatures, e.g. 20, 40 and 60 K. Analysis of these new experiments and especially the determination of product branching ratios under different conditions will result in relative diffusion barriers and their relative dependence on the ice mixture composition. These experiments would also constrain the mechanism behind the increasing photodestruction cross section of NH_3 in a H_2O -dominated matrix.

11.6 Conclusions

There is no doubt that complex nitrogen-bearing molecules can form through photochemistry in the H_2O -rich ice observed towards protostars. The experimental quantification of this formation process is non-trivial because of overlapping infrared spectral features in astrophysical ice mixtures analogues. This difficulty was addressed by combining the quantification of a small set of photolysis products in a range of pure ices, binary ice mixtures and more complex astrophysical ice analogues, and TPD experiments constraining the formation of more complex species. The main findings from this approach are summarized below.

1. The product ratio of C_2H_6 and C_2H_4 in pure CH_4 ice implies a CH_4 photodissociation branching ratio of $\text{CH}_3:\text{CH}_2$ of 3:1, averaged over the wavelength range of the lamp.
2. In binary $\text{CH}_4:\text{NH}_3/\text{H}_2\text{O}/\text{CO}_2$ and $\text{NH}_3:\text{CO}_2$ ice mixtures the formation curves of C_2H_6 , CH_3NH_2 and CH_3OH are consistent with formation from two first generation radicals, while HCN , $\text{CH}_3\text{CH}_2\text{OH}$, CH_3CHO and OCN^- formation requires several reaction steps. This is consistent with reaction schemes, where products

form from radical-radical and radical-molecules reactions, and radicals are produced both from photodissociation of the original ice constituents and through photodissociation of first-generation photoproducts.

3. Increasing the H₂O concentration in the ice increases the diffusion barriers of hydrogen-bonding radicals relative to non-hydrogen-bonding radicals, which changes the chemical evolution of the ice.
4. NH₃ ice is both destroyed directly by UV photons through photodissociation and indirectly through proton transfer with other photoproducts. In CO₂ containing ices, the indirect acid-base NH₃ destruction path is up to an order of magnitude more important.
5. The most abundant photoproducts in the binary ices are also detected upon irradiation of a H₂O:CO₂:NH₃:CH₄ 100:20:12:8 astrophysical ice analogue. The formation rates are however different compared to most binary ices because of acid-base chemistry and the different diffusion pattern in H₂O-rich and H₂O-poor ices.
6. TPD experiments of tertiary ice mixtures show that glycine can form already at low temperatures in ices containing CO₂:NH₃:CH₄. Other detected photoproducts are NH₂CHO, CH₃COOH and NH₂COOH. All exist in salt form because of proton transfer with NH₃, which results in higher desorption temperatures than e.g. H₂O ice.

The results suggest that the information from the pure and binary ice mixture experiments can be used to predict the chemistry in astrophysical ice analogues both in the laboratory and under astrophysical conditions. Quantifying the complex N-bearing ice chemistry during star and planet formation is thus within reach.

12

COLD GAS AS AN ICE DIAGNOSTIC TOWARDS LOW MASS PROTOSTARS

Up to 90% of the chemical reactions during star formation occurs on ice surfaces, probably including the formation of complex organics. Only the most abundant ice species are however observed directly by infrared spectroscopy. This study aims to develop an indirect observational method of ices based on non-thermal ice desorption in the colder part of protostellar envelopes. The IRAM 30m telescope was employed to observe two molecules that can be detected both in the gas and the ice, CH₃OH and HNCO, toward 4 low mass embedded protostars. Their respective gas-phase column densities are determined using rotational diagrams. The relationship between ice and gas phase abundances is subsequently determined. The observed gas and ice abundances span several orders of magnitude. Most of the CH₃OH and HNCO gas along the lines of sight is inferred to be quiescent from the measured line widths and the derived excitation temperatures, and hence not affected by thermal desorption close to the protostar or in outflow shocks. The measured gas to ice ratio of $\sim 10^{-4}$ agrees well with model predictions for non-thermal desorption under cold envelope conditions and there is a tentative correlation between ice and gas phase abundances. This indicates that non-thermal desorption products can serve as a signature of the ice composition. A larger sample is however necessary to provide a conclusive proof of concept.

Published by Öberg K. I., Bottinelli, S. and van Dishoeck, E. F., 2009, A&A, volume 494, pages L13-L16

12.1 Introduction

In cold pre-stellar cores, more than 90% of all molecules, except for H_2 , are found in ices (Caselli et al. 1999; Bergin et al. 2002). These ices build up through accretion of atoms and molecules onto cold (sub)micron-sized silicate particles and subsequent hydrogenation to form e.g. H_2O from O (Léger et al. 1985; Boogert & Ehrenfreund 2004). Observations show that H_2O is the main ice constituent in most lines of sight, with a typical abundance of 1×10^{-4} with respect to H_2 , followed by CO, CO_2 and CH_3OH (Gibb et al. 2004; Pontoppidan et al. 2004).

During star formation, these ices may be modified by interactions with cosmic rays, UV irradiation, and heating to form complex organic species (Garrod et al. 2008). Gas phase complex species have been observed toward several high and low mass protostars, so-called hot cores and corinos (Bisschop et al. 2007c; Bottinelli et al. 2007). Whether these molecules are formed in the ice and subsequently evaporated, or formed in the hot gas phase from desorbed simpler ices such as CH_3OH is still debated. This is not easily resolved because the abundances of the solid complex molecules are too low to be detected with infrared observations of ices even if they are present in the ice. Therefore, observing gas-phase abundances in the cold envelope may be the most robust constraint on complex ice processes available.

Experimental investigations have concluded that non-thermal desorption is efficient for several common ice molecules, such as CO, CO_2 , and H_2O , with photodesorption yields of $\sim 10^{-3}$ per incident photon (Westley et al. 1995a; Öberg et al. 2009b,a). Photodesorption is possible inside cold dark cloud cores and protostellar envelopes because of constant UV fields generated from cosmic ray interactions with H_2 (Shen et al. 2004). Thus a small, but significant, part of the molecules formed in the ice should always be present in the gas phase. This explains observed abundances of gas phase CH_3OH in translucent clouds, dark cloud cores and protostellar envelopes (Turner 1998; Maret et al. 2005; Requena-Torres et al. 2007). The amount of CH_3OH gas observed in these environments suggests that complex molecules (e.g. methyl formate) that form in the ice should be observable in the gas phase due to ice photodesorption, if their abundance ratios with respect to CH_3OH in the ice are the same as observed in hot cores and corinos.

For the first time, we combine infrared ice observations and millimeter gas observations for the same lines of sight to investigate the connection between ice and quiescent gas abundances. We focus on the only commonly observed ice components that have rotational transitions in the millimeter spectral range – CH_3OH and HNCO . The CH_3OH ice abundances in low mass protostellar envelopes vary between 1–30% with respect to H_2O ice (Boogert et al. 2008). It is also one of the most common hot corino gas phase molecules with typical abundances of $10^{-7} - 10^{-6}$ with respect to H_2 . HNCO gas is also commonly detected in hot cores. Solid HNCO (in the form of OCN^-) is only detected toward a few low mass protostars, but strict upper limits exist for more, resulting in an abundance span of an order of magnitude (van Broekhuizen et al. 2005). These large variations in ice abundances imply that CH_3OH and HNCO are appealing test cases for our theory that quiescent complex gas abundances reflect the composition of the co-existing ice mantles, under the assumption that OCN^- is protonated during desorption.

We have observed gas phase CH₃OH and HNCO with the IRAM 30m toward four low mass protostars for which CH₃OH and HNCO ice detections or upper limits already exist. Two of these sources also have OCN⁻ ice upper limits. These sources are complemented with literature values to constrain further the relationship between ice and gas phase abundances.

12.2 Source selection

Table 12.1 – Targets with pointing positions and ice data.

Source	RA	Dec	V_{LSR} km s ⁻¹	α 2–24 μm	cloud
IRAS 03254+3050	03:26:37.45	+30:51:27.9	5.1	0.90	Perseus
B1-b	03:33:20.34	+31:07:21.4	6.5	0.68	Perseus
L1489 IRS	04:04:43.37	+26:18:56.4	7.1	1.10	Taurus
SVS 4-5	18:29:57.59	01:13:00.6	7.8	1.26	Serpens

The four sources IRAS 03254+3050, B1-b, L1489 IRS and SVS 4-5 were chosen from the ‘cores to disks’ (*c2d*) sample of low mass protostars with ice detections (Boogert et al. 2008) to span CH₃OH abundances of 4 – 25% with respect to H₂O. The *c2d* sample partly overlaps with an earlier ground based survey using the VLT, for which the OCN⁻ abundances and upper limits were determined (van Broekhuizen et al. 2005) and two of the sources have OCN⁻ ice upper limits (Table 12.1–12.2).

Table 12.2 – Targets with ice data.

Source	H ₂ O col. dens. 10 ¹⁸ cm ⁻²	CH ₃ OH % H ₂ O	HNCO % H ₂ O
IRAS 03254+3050	3.66	<4.6	–
B1-b	17.67	11.2	–
L1489 IRS	4.26	4.9	<0.06
SVS 4-5	5.65	25.2	<0.27

According to the classification scheme of Lada & Wilking (1984), all sources are embedded class 0/I sources with spectral energy distribution (SED) slopes in the mid-infrared 2–24 μm between 0.68 and 1.26. Their envelopes are of similar mass, as traced by the H₂O ice abundance, with the possible exception of B1-b, which has a factor of 3 higher column density. Except for SVS 4-5 the sources are isolated on the scale of the IRAM 30m beam. Both B1-b and L1489 IRS have however moderate outflows associated with them that may contribute to the detected lines (Jørgensen et al. 2006; Girart et al. 2002).

SVS 4 region is one of the densest nearby star-forming regions and SVS 4-5 is located $\sim 20''$ away from the class 0 low-mass protostar SMM 4, which has a large envelope and an associated outflow. In addition, the young stellar objects SVS 4-2–12 are all located within $30''$ of SVS 4-5 and the emission from SVS 4-5 is probably contaminated by emission from its surroundings when observed with a beam of width as large as $24''$ (as is the case here). Despite these complications in interpreting the data, SVS 4-5 is included in the sample because of its unusually high CH_3OH ice abundance, which was determined from ice mapping of the SVS 4 region by Pontoppidan et al. (2004).

12.3 Observations

The observations were carried out in March 2008 with the 30-m telescope of the Institut de RadioAstronomie Millimétrique (IRAM). The positions used for pointing are listed in Table 12.1. The line frequencies are taken from the JPL molecular database. Although the observations were centered on the protostars themselves, the choice of low excitation lines and relatively large beams ensures that the cold outer envelope is almost completely sampled. Specifically, we targeted CH_3OH transitions with E_{up} , the energy of the upper level of the transition, between 7 and 100 K. The HNC lines were observed after the preliminary reduction of the CH_3OH data, and because of its low excitation temperature we chose to observe two of the lowest lying HNC transitions with E_{up} of 15 and 19 K. The observations were carried out using four different receiver settings with the frequency ranges shown in Table 12.3. Each receiver was connected to a unit of the autocorrelator, with spectral resolutions of 80 or 320 kHz and bandwidths between 80 and 480 MHz, equivalent to a velocity resolution of 0.3, 0.4 and 0.2 km s^{-1} in settings 1, 2, and 3/4, respectively. Typical system temperatures were 100-200 K, 200-500 K, and 700-1000 K, at 3, 2, and 1 mm, respectively.

All observations were carried out using wobbler switching with a $110''$ throw in azimuth. Pointing and focus were regularly checked using planets or strong quasars, providing a pointing accuracy of $3''$. All intensities reported in this paper are expressed in units of main-beam brightness temperature, which were converted from antenna temperatures using main beam efficiencies of 76, 69, and 50%, at 3, 2, and 1 mm. At these wavelengths, the beam sizes were 24, 16, and $10''$, respectively.

12.4 Results

Figure 12.1 shows the spectra derived for setting 1, which is the only setting in which CH_3OH is detected. Figure 12.2 shows the obtained spectra in settings 3 and 4, with all targets observed in both settings except for B1-b. The observed lines were fitted with a single Gaussian to calculate the line widths and integrated intensities in Table 12.3. The Gaussian fits were restricted to exclude the wings observable for B1-b and SVS 4-5. The resulting line widths range from 0.4 to 4.0 km s^{-1} , but three of the sources (B1-b, IRAS 03254, and L1489 IRS) consistently have line widths of below 1 km s^{-1} (Table 12.4).

Table 12.3 – Observed frequencies and targeted molecules at the four different settings.

Frequency (GHz)	Transition ^a	E_u (K)	rms (mK)	Integrated intensity [uncertainty] (K km s ⁻¹)			
				IRAS 03254	B1-b	L1489 IRS	SVS 4-5
CH₃OH							
96.739 (E ⁻)	2 ₁₂ – 1 ₁₁	20.0	11–15	0.11 [0.03]	1.65 [0.22]	0.10 [0.03]	1.47 [0.33]
96.741 (A ⁺)	2 ₀₂ – 1 ₀₁	14.4		0.16 [0.04]	2.18 [0.21]	0.17 [0.05]	2.72 [0.58]
96.745 (E ⁺)	2 ₀₂ – 1 ₀₁	27.5		0.017 [0.017]	0.37 [0.20]	0.024 [0.024]	0.64 [0.39]
96.756 (E ⁺)	2 ₁₁ – 1 ₁₀	35.4		<0.01	0.09 [0.26]	<0.024	0.074 [0.030]
251.738 (A [±])	6 ₃₃ – 6 ₂₄	98.6	28–40	<0.033	–	<0.079	<0.26
HNCO							
109.906	5 ₀₅ – 4 ₀₄	15.4	15–23	0.038 [0.030]	–	<0.027	0.22 [0.07]
131.886	6 ₀₆ – 5 ₀₅	18.6	19–29	<0.021	0.43 [0.06]	<0.037	0.22 [0.07]

^a The quantum numbers for the pure rotational transitions of CH₃OH and HNCO are J_{K_a, K_c} and $J_{K_a, K_c, 1}$, respectively.

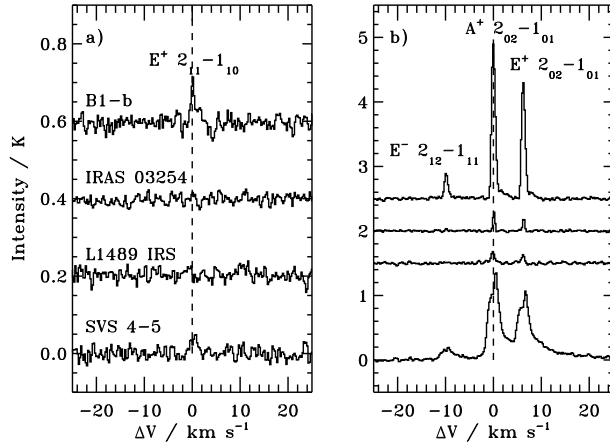


Figure 12.1 – The observed CH_3OH lines in setting 1 toward the four low mass protostars plotted versus ΔV , the deviation from the source V_{lsr} . The data in the left panel are centered on a rest frequency of 96.756 GHz and in the right panel on a rest frequency of 96.741 GHz.

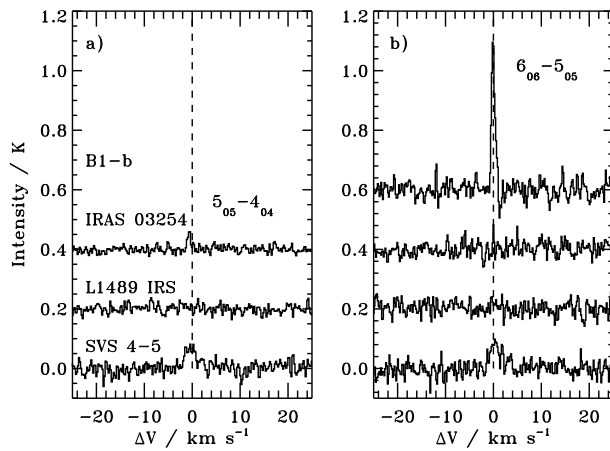


Figure 12.2 – The observed HNC lines in setting 3 and 4 plotted versus ΔV , the deviation from the source V_{lsr} . The data in the left panel are centered on a rest frequency of 109.906 GHz and in the right panel on 131.886 GHz.

Coupled with the low excitation temperatures (below), we most likely probe the quiescent envelope rather than outflows or hot corinos. The fourth source SVS 4–5 has several emission components, reflecting the complexity of the SVS 4 region and containing contributions from non-quiescent gas in for example the nearby outflow from SMM 4. The typical envelope angular size for the source distance is $\sim 1'$, which is larger than the largest beam size. Hence, we assume in the analysis that there is no beam dilution.

In Figs. 12.3 and 12.4, we use the rotational diagram method (Goldsmith & Langer 1999) to derive rotational temperatures and column densities. The relations evident in the CH_3OH diagrams are approximately linear, with a possible slight deviation for the one CH_3OH A detection. A line is fitted to all CH_3OH detections, with the assumption that the populations of E and A species are approximately equal. The 2σ upper limits

(derived from the rms in Table 12.3) are overplotted to enable us to ensure that they do not provide further constraints on the fitted line. Except for SVS 4-5, HNC0 column densities were derived using the CH₃OH rotational temperatures. The lower limit to the CH₃OH temperature of 4 K was used for IRAS 03254 to accommodate the strict upper limit from setting 3 (Table 12.4). The resulting CH₃OH and HNC0 temperatures vary between 4 and 9 K and the CH₃OH and HNC0 column densities vary between $1.8 - 27 \times 10^{13}$ and $0.095 - 2.4 \times 10^{13} \text{ cm}^{-2}$, respectively. CH₃OH is easily sub-thermally excited at the expected densities in outer protostellar envelopes of approximately 10^4 cm^{-3} and hence the rotational temperature cannot be directly translated into a kinetic temperature (Bachiller et al. 1995).

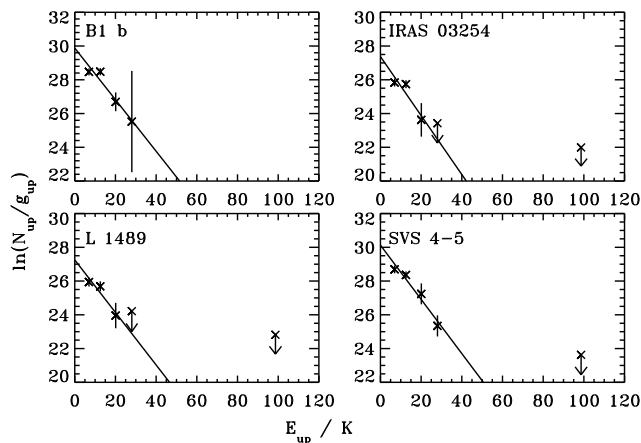


Figure 12.3 – CH₃OH rotation diagrams including detections and upper limits.

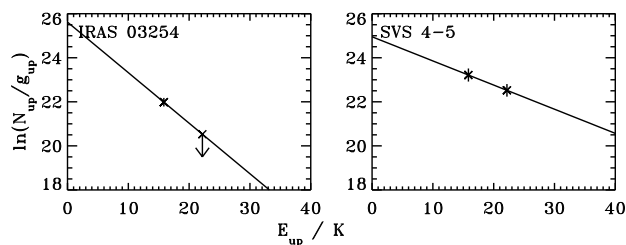


Figure 12.4 – HNC0 rotation diagrams where both lines are detected or the upper limit is strict.

In previous studies, gas phase CH₃OH was observed toward three other low mass protostars that were also observed by Spitzer to study ices (Boogert et al. 2008): Elias 29, R CrA 7A, and B (Table 12.4). The line widths imply that the observed CH₃OH lines toward Elias 29 trace quiescent material, while those observed toward R CrA 7A and B

Table 12.4 – The calculated temperatures and column densities.

Source	Molecule	Line width (km s ⁻¹)	T_{rot} (K)	N_{X} ($\times 10^{13}$ cm ⁻²)
IRAS 03254	CH ₃ OH	0.42–0.49	6±2	1.8±1.8
	HNCO	0.77	~4	~0.48
B1-b	CH ₃ OH	0.77–0.88	7±1	25±13
	HNCO	0.86	~7	~2.4
L1489 IRS	CH ₃ OH	0.75–0.97	6±2	1.8±1.3
	HNCO	–	~6	<0.095
SVS 4-5	CH ₃ OH	2.4–4.0	7±1	27±10
	HNCO	2.6–2.9	9±6	0.38±0.38
Elias 29 ^a	CH ₃ OH	1.3	~9	~0.73
R CrA 7A ^b	CH ₃ OH	2.4–3.0	18±2	59±28
R CrA 7B ^b	CH ₃ OH	2.1–2.6	19±1	94±28

^aBuckle & Fuller (2002) ^bderived from Schöier et al. (2006) using rotational diagrams.

do not.

Figure 12.5 shows the correlation between gas and ice abundances of CH₃OH and HNCO, including the literature sources. The abundances are with respect to the H₂O ice column density, which was found to correlate well with the cold dust column density (Whittet et al. 2001). Hence this is a reasonable normalization factor for the lines of sight with quiescent gas, here defined to be line widths $\lesssim 1$ km s⁻¹, that originates in the cold envelope. It is not a priori a good normalizer for sources with non-quiescent emission, but for consistency the same normalization method is used for all sources. Figure 12.5 illustrates a possible correlation between the gas and ice abundances and upper limits for the quiescent sources – the correlation is not statistically significant due to the many upper limits. The two open triangles in the figure are the RCrA sources, whose higher ratio of gas to ice phase abundance can be attributed to an enhanced radiation field in the region (van Kempen et al. 2008). The measured average gas to solid abundance ratio is 1.2×10^{-4} for the quiescent gas. This probably underestimates the true gas to ice ratio because the absorption and emission observations differ, i.e., the gas phase observations probe on average less dense regions than the ice observations.

12.5 Discussion

Ice photodesorption predicts gas to ice ratios of $10^{-4} - 10^{-3}$ (see Appendix) for typical photodesorption yields and envelope conditions. The measured gas to ice ratio in this study of 1.2×10^{-4} agrees well with this prediction, when accounting for the fact that the measured ratio probably underestimates the true gas to ice ratio. The dashed lines in Fig. 12.5 further show that all quiescent detections and upper limits are consistent with gas to ice ratios of $(1 - 5) \times 10^{-4}$. This agreement and the narrowness of the line widths, supports the interpretation that the emission in these lines of sight originates in the cold,

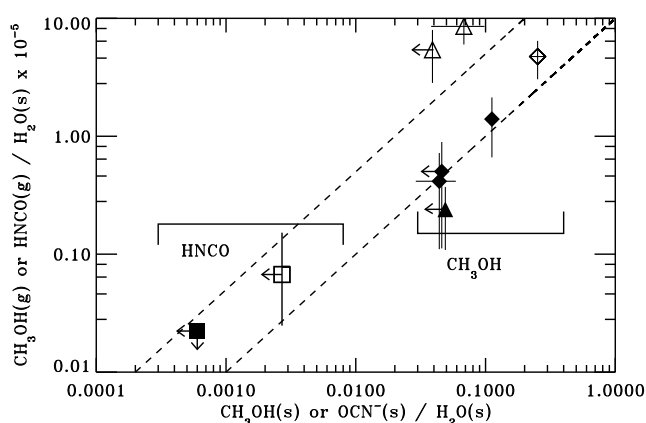


Figure 12.5 – The correlation between ice and gas phase abundances of CH_3OH (diamonds and triangles) and HNCO (squares). The filled symbols represent quiescent gas ($<1.3 \text{ km s}^{-1}$) and the open symbols non-quiescent gas ($>2.4 \text{ km s}^{-1}$). In the case of CH_3OH , the diamonds represent measurements from this study and triangles from the literature. The dashed lines show constant $\text{CH}_3\text{OH}(\text{gas})/\text{CH}_3\text{OH}(\text{solid})$ or $\text{HNCO}(\text{gas})/\text{OCN}^-(\text{solid})$ ratios of 1×10^{-4} and 5×10^{-4} .

quiescent envelope. It also demonstrates that photodesorption alone is sufficient to release the observed ice into the gas, even though other non-thermal processes are not excluded since lack of experimental studies on most non-thermal desorption pathways prevents us from quantifying their relative importance. Gas phase reactions can however be excluded since there is no efficient gas phase reaction pathway to form either CH_3OH or HNCO at the observed abundances (Garrod et al. 2007, Hassel private comm.).

The tentative correlation between gas and ice phase abundances in this pilot study supports the idea that it is possible to determine ice composition by observing the small fraction of the ice that is non-thermally released into the gas phase. To show conclusively that this method works, the size of the sample studied here must be increased and the uncertainty in the derived column densities must be reduced by observing more emission lines. It is also important to remember that until photodesorption data are available for all potential ice species there will be at least a factor of two uncertainty in ice composition estimates using this method due to the different break-up probabilities of different molecules during photodesorption (Öberg et al. 2009b,a). Nonetheless, the method presented here represents a significant improvement on the current lack of observational tools to study complex ices in quiescent regions.

Appendix: Derivation of gas to ice ratios

The gas to ice ratio for a particular species in a protostellar envelope can be estimated by assuming a steady-state between photodesorption and freeze-out:

$$Y_{\text{pd}} \times I_{\text{UV}} \times \sigma_{\text{gr}} \times f_x = 4.57 \times 10^4 \times \left(\frac{T}{m_x} \right)^{\frac{1}{2}} \times \sigma_{\text{gr}} \times n_x^{\text{g}} \quad (12.1)$$

$$f_x = \frac{n_x^{\text{i}}}{n^{\text{i}}} \quad (12.2)$$

where Y_{pd} is the photodesorption yield set to be $(1 - 3) \times 10^{-3} \text{ photon}^{-1}$ from our experiments, I_{UV} is the cosmic-ray-induced UV field of $10^4 \text{ photons cm}^{-2} \text{ s}^{-1}$ and σ_{gr} is the grain cross section. The cosmic-ray-induced UV flux assumes a cosmic ray ionization rate of $1.3 \times 10^{-17} \text{ s}^{-1}$. Because photodesorption is a surface process, the photodesorption rate of species x depends on the fractional ice abundance f_x , which is defined to be the ratio of the number density of species x in the ice, n_x^{i} , to the total ice number density, n^{i} . The freeze-out rate of species x depends on the gas temperature T , which is set to 15 K, the molecular weight m_x , and the gas number density n_x^{g} . For an average molecular weight of 32, this results in a gas phase abundance $n_x^{\text{g}}/n_{\text{H}}$ of $(3 - 9) \times 10^{-4} f_x/n_{\text{H}}$. From this and an average total ice abundance $n^{\text{i}}/n_{\text{H}}$ of 10^{-4} , the predicted gas to ice phase abundance ratio is:

$$\frac{n_x^{\text{g}}}{n_x^{\text{i}}} \sim \frac{(3 - 9) \times 10^{-4} / n_{\text{H}} \times f_x}{n^{\text{i}} / n_{\text{H}} \times f_x} \sim (3 - 9) / n_{\text{H}} \quad (12.3)$$

For a typical envelope density of 10^4 cm^{-3} , ice photodesorption hence predicts a gas to ice ratio of $10^{-4} - 10^{-3}$. The derivation of a gas to ice ratio from observed cold gas emission lines and ice absorption features in the same line of sight is complicated by the fact that different regions can contribute by varying amounts. The emission features trace gas in the envelope and cloud both in front and behind the protostar, while the ice absorption features only trace envelope material directly in front of the protostar. The column is hence twice as long for the gas observations. This is probably more than compensated for by using beam averaged gas column densities, as is done in this study, because the large beam traces on average less dense material compared to the pencil beam of the ice absorption observations. Note also that the CH_3OH ice abundance may vary between lower and higher density regions. To quantify a conversion factor between the observed and true gas to ice ratio requires detailed modeling of each source which is outside the scope of this study. Instead we here assume that the observed ratio is a lower limit to the true ratio.

BIBLIOGRAPHY

- Acharyya, K., Fuchs, G. W., Fraser, H. J., van Dishoeck, E. F., & Linnartz, H. 2007, *A&A*, 466, 1005
- Acquista, N., Schoen, L. J., & David R. Lide, J. 1968, *J. Chem. Phys.*, 48, 1534
- Aikawa, Y., Herbst, E., Roberts, H., & Caselli, P. 2005, *ApJ*, 620, 330
- Aikawa, Y. & Nomura, H. 2006, *ApJ*, 642, 1152
- Aikawa, Y., Wakelam, V., Garrod, R. T., & Herbst, E. 2008, *ApJ*, 674, 984
- Alexander, R. D., Casali, M. M., André, P., Persi, P., & Eiroa, C. 2003, *A&A*, 401, 613
- Allamandola, L. J., Sandford, S. A., & Valero, G. J. 1988, *Icarus*, 76, 225
- Allen, M. & Robinson, G. W. 1977, *ApJ*, 212, 396
- Altwegg, K., Balsiger, H., & Geiss, J. 1999, *Space Sci. Rev.*, 90, 3
- Andersson, S., Al-Halabi, A., Kroes, G.-J., & van Dishoeck, E. F. 2006, *J. Chem. Phys.*, 124, 64715
- Andersson, S. & van Dishoeck, E. F. 2008, *A&A*, 491, 907
- Arce, H. G., Santiago-García, J., Jørgensen, J. K., Tafalla, M., & Bachiller, R. 2008, *ApJ*, 681, L21
- Attard, G. & Barnes, C. 2004, *Surfaces* (Oxford Science Publications), 1–5
- Ayers, G. P. & Pullin, A. D. E. 1976, *Spectrochimica Acta*, 32A, 1629
- Bachiller, R. 1996, *ARA&A*, 34, 111
- Bachiller, R., Liechti, S., Walmsley, C. M., & Colomer, F. 1995, *A&A*, 295, L51
- Bar-Nun, A., Herman, G., Laufer, D., & Rappaport, M. L. 1985, *Icarus*, 63, 317
- Baratta, G. A., Leto, G., & Palumbo, M. E. 2002, *A&A*, 384, 343
- Baratta, G. A., Spinella, F., Leto, G., Strazzulla, G., & Foti, G. 1991, *A&A*, 252, 421
- Belloche, A., Garrod, R. T., Müller, H. S. P., et al. 2009, *A&A*, 499, 215
- Belloche, A., Menten, K. M., Comito, C., et al. 2008, *A&A*, 482, 179
- Bennett, C. J., Chen, S.-H., Sun, B.-J., Chang, A. H. H., & Kaiser, R. I. 2007, *ApJ*, 660, 1588
- Bennett, C. J. & Kaiser, R. I. 2007, *ApJ*, 661, 899
- Bergin, E. A., Alves, J., Huard, T., & Lada, C. J. 2002, *ApJ*, 570, L101
- Bergin, E. A., Ciardi, D. R., Lada, C. J., Alves, J., & Lada, E. A. 2001, *ApJ*, 557, 209
- Bergin, E. A., Langer, W. D., & Goldsmith, P. F. 1995, *ApJ*, 441, 222
- Bergin, E. A., Maret, S., van der Tak, F. F. S., et al. 2006, *ApJ*, 645, 369
- Bergin, E. A., Melnick, G. J., Gerakines, P. A., Neufeld, D. A., & Whittet, D. C. B. 2005, *ApJ*, 627, L33
- Bernstein, M. P., Cruikshank, D. P., & Sandford, S. A. 2005, *Icarus*, 179, 527
- Bernstein, M. P., Dworkin, J. P., Sandford, S. A., Cooper, G. W., & Allamandola, L. J. 2002, *Nature*, 416, 401
- Bernstein, M. P., Sandford, S. A., Allamandola, L. J., Chang, S., & Scharberg, M. A. 1995, *ApJ*, 454, 327
- Bertoldi, F., Carilli, C. L., Cox, P., et al. 2003, *A&A*, 406, L55

- Bisschop, S. E., Fraser, H. J., Öberg, K. I., van Dishoeck, E. F., & Schlemmer, S. 2006, *A&A*, 449, 1297
- Bisschop, S. E., Fuchs, G. W., Boogert, A. C. A., van Dishoeck, E. F., & Linnartz, H. 2007a, *A&A*, 470, 749
- Bisschop, S. E., Fuchs, G. W., van Dishoeck, E. F., & Linnartz, H. 2007b, *A&A*, 474, 1061
- Bisschop, S. E., Jørgensen, J. K., Bourke, T. L., Bottinelli, S., & van Dishoeck, E. F. 2008, *A&A*, 488, 959
- Bisschop, S. E., Jørgensen, J. K., van Dishoeck, E. F., & de Wachter, E. B. M. 2007c, *A&A*, 465, 913
- Blake, G. A., Sandell, G., van Dishoeck, E. F., et al. 1995, *ApJ*, 441, 689
- Blake, G. A., Sutton, E. C., Masson, C. R., & Phillips, T. G. 1987, *ApJ*, 315, 621
- Blau, E. J., Hochheimer, B. F., & Unger, H. J. 1961, *J. Chem. Phys.*, 34, 1060
- Bockelée-Morvan, D., Lis, D. C., Wink, J. E., et al. 2000, *A&A*, 353, 1101
- Boogert, A. C. A., Blake, G. A., & Öberg, K. 2004a, *ApJ*, 615, 344
- Boogert, A. C. A. & Ehrenfreund, P. 2004, in *ASP Conf. Ser. 309: Astrophysics of Dust*, ed. A. N. Witt, G. C. Clayton, & B. T. Draine, 547–572
- Boogert, A. C. A., Helmich, F. P., van Dishoeck, E. F., et al. 1998, *A&A*, 336, 352
- Boogert, A. C. A., Pontoppidan, K. M., Knez, C., et al. 2008, *ApJ*, 678, 985
- Boogert, A. C. A., Pontoppidan, K. M., Lahuis, F., et al. 2004b, *ApJS*, 154, 359
- Boogert, A. C. A., Schutte, W. A., Helmich, F. P., Tielens, A. G. G. M., & Wooden, D. H. 1997, *A&A*, 317, 929
- Boogert, A. C. A., Schutte, W. A., Tielens, A. G. G. M., et al. 1996, *A&A*, 315, L377
- Boogert, A. C. A., Tielens, A. G. G. M., Ceccarelli, C., et al. 2000, *A&A*, 360, 683
- Boonman, A. M. S. & van Dishoeck, E. F. 2003, *A&A*, 403, 1003
- Bottinelli, S., Ceccarelli, C., Lefloch, B., et al. 2004, *ApJ*, 615, 354
- Bottinelli, S., Ceccarelli, C., Williams, J. P., & Lefloch, B. 2007, *A&A*, 463, 601
- Boudin, N., Schutte, W. A., & Greenberg, J. M. 1998, *A&A*, 331, 749
- Bouwman, J., Ludwig, W., Awad, Z., et al. 2007, *A&A*, 476, 995
- Bouwman, J., Meeus, G., de Koter, A., et al. 2001, *A&A*, 375, 950
- Brewer, L. & Wang, J. L.-F. 1972, *J. Chem. Phys.*, 56, 759
- Brown, P. D., Charnley, S. B., & Millar, T. J. 1988, *MNRAS*, 231, 409
- Brown, W. A. & Bolina, A. S. 2007, *MNRAS*, 374, 1006
- Brown, W. L., Lanzerotti, L. J., Poate, J. M., & Augustyniak, W. M. 1978, *Phys. Rev. Lett.*, 40, 1027
- Buckle, J. V. & Fuller, G. A. 2002, *A&A*, 381, 77
- Caselli, P., Walmsley, C. M., Tafalla, M., Dore, L., & Myers, P. C. 1999, *ApJ*, 523, L165
- Cazaux, S., Tielens, A. G. G. M., Ceccarelli, C., et al. 2003, *ApJ*, 593, L51
- Ceccarelli, C., Caux, E., Loinard, L., et al. 1999, *A&A*, 342, L21
- Ceccarelli, C., Loinard, L., Castets, A., Faure, A., & Lefloch, B. 2000, *A&A*, 362, 1122
- Cernicharo, J., Noriega-Crespo, A., Cesarsky, D., et al. 2000, *Science*, 288, 649

- Cernicharo, J., Thum, C., Hein, H., et al. 1990, *A&A*, 231, L15
- Chang, Q., Cuppen, H. M., & Herbst, E. 2007, *A&A*, 469, 973
- Charnley, S. B. 1997, *ApJ*, 481, 396
- Charnley, S. B. 2004, *Advances in Space Res.*, 33, 23
- Charnley, S. B., Rodgers, S. D., & Ehrenfreund, P. 2001, *A&A*, 378, 1024
- Charnley, S. B., Tielens, A. G. G. M., & Millar, T. J. 1992, *ApJ*, 399, L71
- Cheng, B.-M., Bahou, M., Chen, W.-C., et al. 2002, *J. Chem. Phys.*, 117, 1633
- Chiang, E. I. & Goldreich, P. 1997, *ApJ*, 490, 368
- Chiar, J. E., Adamson, A. J., Kerr, T. H., & Whittet, D. C. B. 1994, *ApJ*, 426, 240
- Collings, M. P., Anderson, M. A., Chen, R., et al. 2004, *MNRAS*, 354, 1133
- Collings, M. P., Dever, J. W., Fraser, H. J., & McCoustra, M. R. S. 2003, *Ap&SS*, 285, 633
- Combes, F., Q-Rieu, N., & Wlodarczak, G. 1996, *A&A*, 308, 618
- Cottin, H., Moore, M. H., & Bénilan, Y. 2003, *ApJ*, 590, 874
- Crovisier, J., Bockelée-Morvan, D., Biver, N., et al. 2004a, *A&A*, 418, L35
- Crovisier, J., Bockelée-Morvan, D., Colom, P., et al. 2004b, *A&A*, 418, 1141
- Cuppen, H. M. & Herbst, E. 2007, *ApJ*, 668, 294
- Dalgarno, A. 2006, *Faraday Discussions*, 133, 9
- Danten, Y., Tassaing, T., & Besnard, M. 2005, *J. Phys. Chem. A*, 109, 3250
- Dartois, E., Demyk, K., d'Hendecourt, L., & Ehrenfreund, P. 1999, *A&A*, 351, 1066
- Dartois, E., Dutrey, A., & Guilloteau, S. 2003, *A&A*, 399, 773
- Dartois, E., Muñoz Caro, G. M., Deboffe, D., Montagnac, G., & D'Hendecourt, L. 2005, *A&A*, 432, 895
- Devlin, J. P., Sadlej, J., & Buch, V. 2001, *J. Phys. Chem. A*, 105, 974
- D'Hendecourt, L. B. & Allamandola, L. J. 1986, *A&AS*, 64, 453
- D'Hendecourt, L. B., Allamandola, L. J., Baas, F., & Greenberg, J. M. 1982, *A&A*, 109, L12
- Dominik, C., Ceccarelli, C., Hollenbach, D., & Kaufman, M. 2005, *ApJ*, 635, L85
- Draine, B. T. & Salpeter, E. E. 1979, *ApJ*, 231, 438
- Dudley, C. C., Imanishi, M., & Maloney, P. R. 2008, *ApJ*, 686, 251
- Dullemond, C. P. & Dominik, C. 2004, *A&A*, 417, 159
- Dullemond, C. P. & Dominik, C. 2005, *A&A*, 434, 971
- Dullemond, C. P., Dominik, C., & Natta, A. 2001, *ApJ*, 560, 957
- Eddington, A. S. 1937, *The Observatory*, 60, 99
- Ehrenfreund, P., Dartois, E., Demyk, K., & D'Hendecourt, L. 1998, *A&A*, 339, L17
- Ehrenfreund, P., Gerakines, P. A., Schutte, W. A., van Hemert, M. C., & van Dishoeck, E. F. 1996, *A&A*, 312, 263
- Ehrenfreund, P., Kerkhof, O., Schutte, W. A., et al. 1999, *A&A*, 350, 240
- Eidelsberg, M., Jolly, A., Lemaire, J. L., et al. 1999, *A&A*, 346, 705
- Eidelsberg, M., Rostas, F., Breton, J., & Thieblemont, B. 1992, *J. Chem. Phys.*, 96, 5585
- Elitzur, M. & de Jong, T. 1978, *A&A*, 67, 323

- Elitzur, M. & Watson, W. D. 1978, *ApJ*, 222, L141
- Elsila, J. E., Dworkin, J. P., Bernstein, M. P., Martin, M. P., & Sandford, S. A. 2007, *ApJ*, 660, 911
- Engel, M. H. & Macko, S. A. 1997, *Nature*, 389, 265
- Evans, II, N. J., Allen, L. E., Blake, G. A., et al. 2003, *PASP*, 115, 965
- Famá, M., Shi, J., & Baragiola, R. A. 2008, *Surf. Sci.*, 602, 156
- Franklin, J., Snell, R. L., Kaufman, M. J., et al. 2008, *ApJ*, 674, 1015
- Fraser, H. J., Bisschop, S. E., Pontoppidan, K. M., Tielens, A. G. G. M., & van Dishoeck, E. F. 2005, *MNRAS*, 356, 1283
- Fraser, H. J., Collings, M. P., McCoustra, M. R. S., & Williams, D. A. 2001, *MNRAS*, 327, 1165
- Fuchs, G. W., Acharyya, K., Bisschop, S. E., et al. 2006, *Faraday Discussions*, 133, 331
- Furlan, E., McClure, M., Calvet, N., et al. 2008, *ApJS*, 176, 184
- Galabov, B., Yamaguchi, Y., Remington, R. B., & Schaefer, H. F. 2002, *J. Phys. Chem. A*, 106, 819
- Galli, D. & Palla, F. 1998, *A&A*, 335, 403
- Garrod, R. T. & Herbst, E. 2006, *A&A*, 457, 927
- Garrod, R. T., Park, I. H., P., C., & Herbst, E. 2006, *Faraday Discussions*, 133, 51
- Garrod, R. T., Wakelam, V., & Herbst, E. 2007, *A&A*, 467, 1103
- Garrod, R. T., Weaver, S. L. W., & Herbst, E. 2008, *ApJ*, 682, 283
- Gensheimer, P. D., Mauersberger, R., & Wilson, T. L. 1996, *A&A*, 314, 281
- Gerakines, P. A., Bray, J. J., Davis, A., & Richey, C. R. 2005, *ApJ*, 620, 1140
- Gerakines, P. A. & Moore, M. H. 2001, *Icarus*, 154, 372
- Gerakines, P. A., Moore, M. H., & Hudson, R. L. 2000, *A&A*, 357, 793
- Gerakines, P. A., Moore, M. H., & Hudson, R. L. 2004, *Icarus*, 170, 202
- Gerakines, P. A., Schutte, W. A., & Ehrenfreund, P. 1996, *A&A*, 312, 289
- Gerakines, P. A., Schutte, W. A., Greenberg, J. M., & van Dishoeck, E. F. 1995, *A&A*, 296, 810
- Gerakines, P. A., Whittet, D. C. B., Ehrenfreund, P., et al. 1999, *ApJ*, 522, 357
- Gibb, E. L. & Whittet, D. C. B. 2002, *ApJ*, 566, L113
- Gibb, E. L., Whittet, D. C. B., Boogert, A. C. A., & Tielens, A. G. G. M. 2004, *ApJS*, 151, 35
- Gibb, E. L., Whittet, D. C. B., Schutte, W. A., et al. 2000, *ApJ*, 536, 347
- Giguère, P. A. & Harvey, K. B. 1959, *J. Molec. Spectrosc.*, 3, 36
- Gillett, F. C. & Forrest, W. J. 1973, *ApJ*, 179, 483
- Girart, J. M., Curiel, S., Rodríguez, L. F., & Cantó, J. 2002, *Rev. Mexicana Astron. Astrofis.*, 38, 169
- Goldsmith, P. F. & Langer, W. D. 1999, *ApJ*, 517, 209
- Gomis, O., Leto, G., & Strazzulla, G. 2004, *A&A*, 420, 405
- Greenberg, J. M. 1983, *Advances in Space Research*, 3, 19
- Grim, R. J. A., Greenberg, J. M., de Groot, M. S., et al. 1989, *A&AS*, 78, 161

- Gürtler, J., Klaas, U., Henning, T., et al. 2002, *A&A*, 390, 1075
- Hagen, W. 1981, *Chem. Phys.*, 56, 367
- Hagen, W., Allamandola, L. J., & Greenberg, J. M. 1979, *Ap&SS*, 65, 215
- Hagen, W., Allamandola, L. J., & Greenberg, J. M. 1980, *A&A*, 86, L3
- Hagen, W., Tielens, A. G. G. M., & Greenberg, J. M. 1983, *A&AS*, 51, 389
- Hartmann, J. 1904, *ApJ*, 19, 268
- Hartquist, T. W. & Williams, D. A. 1990, *MNRAS*, 247, 343
- Hasegawa, T. I. & Herbst, E. 1993, *MNRAS*, 263, 589
- Hasegawa, T. I., Herbst, E., & Leung, C. M. 1992, *ApJS*, 82, 167
- Hiraoka, K., Miyagoshi, T., Takayama, T., Yamamoto, K., & Kihara, Y. 1998, *ApJ*, 498, 710
- Hjalmarson, Å., Frisk, U., Olberg, M., et al. 2003, *A&A*, 402, L39
- Hodyss, R., Johnson, P. V., Orzechowska, G. E., Goguen, J. D., & Kanik, I. 2008, *Icarus*, 194, 836
- Hogerheijde, M. R., van Dishoeck, E. F., Blake, G. A., & van Langevelde, H. J. 1998, *ApJ*, 502, 315
- Hollenbach, D., Kaufman, M. J., Bergin, E. A., & Melnick, G. J. 2009, *ApJ*, 690, 1497
- Horn, A., Møllendal, H., Sekiguchi, O., et al. 2004, *ApJ*, 611, 605
- Huang, H.-C., Kuan, Y.-J., Charnley, S. B., et al. 2005, *Advances in Space Research*, 36, 146
- Hudgins, D. M., Sandford, S. A., Allamandola, L. J., & Tielens, A. G. G. M. 1993, *ApJS*, 86, 713
- Hudson, R. L. & Moore, M. H. 1999, *Icarus*, 140, 451
- Hudson, R. L. & Moore, M. H. 2000, *Icarus*, 145, 661
- Hudson, R. L., Moore, M. H., & Cook, A. M. 2005, *Advances in Space Research*, 36, 184
- Hudson, R. L., Moore, M. H., & Gerakines, P. A. 2001, *ApJ*, 550, 1140
- Ioppolo, S., Cuppen, H. M., Romanzin, C., van Dishoeck, E. F., & Linnartz, H. 2008, *ApJ*, 686, 1474
- Ioppolo, S., Palumbo, M. E., Baratta, G. A., & Mennella, V. 2009, *A&A*, 493, 1017
- Jacox, M. E. & Milligan, D. E. 1973, *J. Mol. Spec.*, 47, 148
- Jacq, T., Henkel, C., Walmsley, C. M., Jewell, P. R., & Baudry, A. 1988, *A&A*, 199, L5
- Jenniskens, P. & Blake, D. F. 1994, *Science*, 265, 753
- Johansen, A., Oishi, J. S., Low, M.-M. M., et al. 2007, *Nature*, 448, 1022
- Jones, A. P., Tielens, A. G. G. M., & Hollenbach, D. J. 1996, *ApJ*, 469, 740
- Jørgensen, J. K., Bourke, T. L., Myers, P. C., et al. 2005, *ApJ*, 632, 973
- Jørgensen, J. K., Harvey, P. M., Evans, II, N. J., et al. 2006, *ApJ*, 645, 1246
- Keane, J. V., Boonman, A. M. S., Tielens, A. G. G. M., & van Dishoeck, E. F. 2001, *A&A*, 376, L5
- Knacke, R. F. & Larson, H. P. 1991, *ApJ*, 367, 162
- Knez, C., Boogert, A. C. A., Pontoppidan, K. M., et al. 2005, *ApJ*, 635, L145
- Lacy, J. H., Carr, J. S., Evans, II, N. J., et al. 1991, *ApJ*, 376, 556

- Lacy, J. H., Faraji, H., Sandford, S. A., & Allamandola, L. J. 1998, *ApJ*, 501, L105+
- Lee, C.-W., Kim, J.-K., Moon, E.-S., Minh, Y. C., & Kang, H. 2009, *ApJ*, 697, 428
- Léger, A., Jura, M., & Omont, A. 1985, *A&A*, 144, 147
- Lepp, S., Stancil, P. C., & Dalgarno, A. 2002, *J. of Phys. B Atom. Mol. Phys.*, 35, 57
- Leto, G. & Baratta, G. A. 2003, *A&A*, 397, 7
- Lewis, E. P. 1895, *ApJ*, 2, 1
- Loeffler, M. J., Baratta, G. A., Palumbo, M. E., Strazzulla, G., & Baragiola, R. A. 2005, *A&A*, 435, 587
- Loeffler, M. J., Teolis, B. D., & Baragiola, R. A. 2006, *J. Chem. Phys.*, 124, 104702
- Lommen, D., Wright, C. M., Maddison, S. T., et al. 2007, *A&A*, 462, 211
- Los, J. H., van den Heuvel, M., Enckevort, W. J. P., et al. 2006, *Calphad*, 30, 216
- Los, J. H., van Enckevort, W. J. P., Meekes, H., & Vlieg, E. 2007, *J. Phys. Chem. B*, 111, 782
- MacLeod, J. M., Avery, L. W., & Harris, A. 1994, *JRASC*, 88, 265
- Maréchal, Y. 1987, *J. Chem. Phys.*, 87, 6344
- Maret, S., Ceccarelli, C., Tielens, A. G. G. M., et al. 2005, *A&A*, 442, 527
- Markwick, A. J., Millar, T. J., & Charnley, S. B. 2000, *ApJ*, 535, 256
- Mason, N. J., Dawes, A., Holtom, P. D., et al. 2006, *Faraday Discussions*, 133, 1
- Mate, B., Galvez, O., Martin-Llorente, B., et al. 2008, *J. Phys. Chem. A*, 112, 457
- Mathis, J. S., Mezger, P. G., & Panagia, N. 1983, *A&A*, 128, 212
- Melnick, G. J., Ashby, M. L. N., Plume, R., et al. 2000, *ApJ*, 539, L87
- Melnick, G. J. & Bergin, E. A. 2005, *Advances in Space Research*, 36, 1027
- Mennella, V., Palumbo, M. E., & Baratta, G. A. 2004, *ApJ*, 615, 1073
- Merrill, K. M., Russell, R. W., & Soifer, B. T. 1976, *ApJ*, 207, 763
- Millar, T. J., Bennett, A., Rawlings, J. M. C., Brown, P. D., & Charnley, S. B. 1991, *A&AS*, 87, 585
- Miyauchi, N., Hidaka, H., Chigai, T., et al. 2008, *Chem. Phys. Lett.*, 456, 27
- Molinari, S., Ceccarelli, C., White, G. J., et al. 1999, *ApJ*, 521, L71
- Moll, N. G., Clutter, D. R., & Thompson, W. E. 1966, *J. Chem. Phys.*, 45, 4469
- Moore, M. 1991, *Spec. Acta A: Mol. Spec.*, 47, 255
- Moore, M. H., Donn, B., Khanna, R., & A'Hearn, M. F. 1983, *Icarus*, 54, 388
- Moore, M. H. & Hudson, R. L. 1998, *Icarus*, 135, 518
- Moore, M. H. & Hudson, R. L. 2005, in *IAU Symposium, Vol. 231, Astrochemistry: Recent Successes and Current Challenges*, ed. D. C. Lis, G. A. Blake, & E. Herbst, 247–260
- Moore, M. H., Hudson, R. L., & Ferrante, R. F. 2003, *Earth Moon and Planets*, 92, 291
- Muñoz Caro, G. M., Meierhenrich, U., Schutte, W. A., Thiemann, W. H.-P., & Greenberg, J. M. 2004, *A&A*, 413, 209
- Muñoz Caro, G. M., Meierhenrich, U. J., Schutte, W. A., et al. 2002, *Nature*, 416, 403
- Muñoz Caro, G. M. & Schutte, W. A. 2003, *A&A*, 412, 121
- Murakawa, K., Tamura, M., & Nagata, T. 2000, *ApJS*, 128, 603

- Nee, J. B., Suto, M., & Lee, L. C. 1985, *Chem. Phys.*, 98, 147
- Nisini, B., Benedettini, M., Giannini, T., et al. 1999, *A&A*, 350, 529
- Nomura, H. & Millar, T. J. 2004, *A&A*, 414, 409
- Nuevo, M., Chen, Y.-J., Yih, T.-S., et al. 2007, *Advances in Space Research*, 40, 1628
- Nummelin, A., Bergman, P., Hjalmarsen, Å., et al. 2000, *ApJS*, 128, 213
- Nummelin, A., Whittet, D. C. B., Gibb, E. L., Gerakines, P. A., & Chiar, J. E. 2001, *ApJ*, 558, 185
- Öberg, K. I., Boogert, A. C. A., Pontoppidan, K. M., et al. 2008, *ApJ*, 678, 1032
- Öberg, K. I., Fraser, H. J., Boogert, A. C. A., et al. 2007a, *A&A*, 462, 1187
- Öberg, K. I., Fuchs, G. W., Awad, Z., et al. 2007b, *ApJ*, 662, L23
- Öberg, K. I., Linnartz, H., Visser, R., & van Dishoeck, E. F. 2009a, *ApJ*, 693, 1209
- Öberg, K. I., van Broekhuizen, F., Fraser, H. J., et al. 2005, *ApJ*, 621, L33
- Öberg, K. I., van Dishoeck, E. F., & Linnartz, H. 2009b, *A&A*, 496, 281
- Palumbo, M. E. & Baratta, G. A. 2000, *A&A*, 361, 298
- Pearl, J., Ngoh, M., Ospina, M., & Khanna, R. 1991, *J. Geophys. Res.*, 96, 17477
- Piétu, V., Dutrey, A., & Guilloteau, S. 2007, *A&A*, 467, 163
- Pontoppidan, K. M. 2006, *A&A*, 453, L47
- Pontoppidan, K. M., Boogert, A. C. A., Fraser, H. J., et al. 2008, *ApJ*, 678, 1005
- Pontoppidan, K. M., Dullemond, C. P., van Dishoeck, E. F., et al. 2005, *ApJ*, 622, 463
- Pontoppidan, K. M., Fraser, H. J., Dartois, E., et al. 2003, *A&A*, 408, 981
- Pontoppidan, K. M., van Dishoeck, E. F., & Dartois, E. 2004, *A&A*, 426, 925
- Raunier, S., Chiavassa, T., Duvernay, F., et al. 2004, *A&A*, 416, 165
- Requena-Torres, M. A., Marcelino, N., Jiménez-Serra, I., et al. 2007, *ApJ*, 655, L37
- Requena-Torres, M. A., Martín-Pintado, J., Martín, S., & Morris, M. R. 2008, *ApJ*, 672, 352
- Requena-Torres, M. A., Martín-Pintado, J., Rodríguez-Franco, A., et al. 2006, *A&A*, 455, 971
- Roberge, W. G., Jones, D., Lepp, S., & Dalgarno, A. 1991, *ApJS*, 77, 287
- Roberts, J. F., Rawlings, J. M. C., Viti, S., & Williams, D. A. 2007, *MNRAS*, 382, 733
- Rodmann, J., Henning, T., Chandler, C. J., Mundy, L. G., & Wilner, D. J. 2006, *A&A*, 446, 211
- Romanzin, C., Bénilan, Y., Jolly, A., & Gazeau, M.-C. 2008, *Advances in Space Research*, 42, 2036
- Roux, J. A. & Wood, B. E. 1983, *J. Opt. Soc. Am.*, 73, 1181
- Rowland, B., Fisher, M., & Devlin, J. P. 1991, *J. Phys. Chem.*, 95, 1378
- Ruffle, D. P. & Herbst, E. 2001, *MNRAS*, 322, 770
- Sakai, N., Sakai, T., Aikawa, Y., & Yamamoto, S. 2008, *ApJ*, 675, L89
- Sandford, S. A. & Allamandola, L. J. 1988, *Icarus*, 76, 201
- Sandford, S. A. & Allamandola, L. J. 1990, *ApJ*, 355, 357
- Sandford, S. A. & Allamandola, L. J. 1993, *Icarus*, 106, 478
- Schmitt, B., Greenberg, J. M., & Grim, R. J. A. 1989, *ApJ*, 340, L33

- Schöier, F. L., Jørgensen, J. K., Pontoppidan, K. M., & Lundgren, A. A. 2006, *A&A*, 454, L67
- Schutte, W. A., Allamandola, L. J., & Sandford, S. A. 1993, *Icarus*, 104, 118
- Schutte, W. A., Boogert, A. C. A., Tielens, A. G. G. M., et al. 1999, *A&A*, 343, 966
- Schutte, W. A. & Khanna, R. K. 2003, *A&A*, 398, 1049
- Schutte, W. A., Tielens, A. G. G. M., Whittet, D. C. B., et al. 1996, *A&A*, 315, L333
- Seager, S., Sasselov, D. D., & Scott, D. 2000, *ApJS*, 128, 407
- Seale, J. P., Looney, L. W., Chu, Y.-H., et al. 2009, *ApJ*, 699, 150
- Semenov, D., Wiebe, D., & Henning, T. 2006, *ApJ*, 647, L57
- Shen, C. J., Greenberg, J. M., Schutte, W. A., & van Dishoeck, E. F. 2004, *A&A*, 415, 203
- Slinger, T. L. & Black, T. 1978, *J. Chem. Phys.*, 68, 1844
- Snell, R. L., Howe, J. E., Ashby, M. L. N., et al. 2000, *ApJ*, 539, L101
- Snow, T. P. & McCall, B. J. 2006, *ARA&A*, 44, 367
- Sonnentrucker, P., Neufeld, D. A., Gerakines, P. A., et al. 2008, *ApJ*, 672, 361
- Spaans, M., Hogerheijde, M. R., Mundy, L. G., & van Dishoeck, E. F. 1995, *ApJ*, 455, L167+
- Sternberg, A., Dalgarno, A., & Lepp, S. 1987, *ApJ*, 320, 676
- Stief, L. J., Decarlo, V. J., & Hillman, J. J. 1965, *Can. J. Chem.*, 43, 2490
- Swings, P. & Rosenfeld, L. 1937, *ApJ*, 86, 483
- Tanaka, M., Sato, S., Nagata, T., & Yamamoto, T. 1990, *ApJ*, 352, 724
- Tanvir, N. R., Fox, D. B., Levan, A. J., et al. 2009, *ArXiv e-prints*
- Teolis, B. D., Loeffler, M. J., Raut, U., Famá, M., & Baragiola, R. A. 2007, *Icarus*, 190, 274
- Thompson, W. & Jacox, M. 2001, *J. Chem. Phys.*, 114, 4846
- Thrower, J. D., Burke, D. J., Collings, M. P., et al. 2008, *ApJ*, 673, 1233
- Tielens, A. G. G. M. & Charnley, S. B. 1997, *Ori. of Life and Evol. of the Bio.*, 27, 23
- Tielens, A. G. G. M. & Hagen, W. 1982, *A&A*, 114, 245
- Tielens, A. G. G. M., Tokunaga, A. T., Geballe, T. R., & Baas, F. 1991, *ApJ*, 381, 181
- Tso, T. & Lee, E. K. C. 1985, *J. Phys. Chem.*, 89, 1612
- Turner, B. E. 1998, *ApJ*, 501, 731
- Turner, B. E., Terzieva, R., & Herbst, E. 1999, *ApJ*, 518, 699
- van Broekhuizen, F. A. 2005, PhD thesis, Leiden Observatory, Leiden University
- van Broekhuizen, F. A., Groot, I. M. N., Fraser, H. J., van Dishoeck, E. F., & Schlemmer, S. 2006, *A&A*, 451, 723
- van Broekhuizen, F. A., Keane, J. V., & Schutte, W. A. 2004, *A&A*, 415, 425
- van Broekhuizen, F. A., Pontoppidan, K. M., Fraser, H. J., & van Dishoeck, E. F. 2005, *A&A*, 441, 249
- van de Hulst, H. C. 1946, *Recherches Astronomiques de l'Observatoire d'Utrecht*, 11, 2
- van der Tak, F. F. S., Walmsley, C. M., Herpin, F., & Ceccarelli, C. 2006, *A&A*, 447, 1011

- van Dishoeck, E. F. 1988, in *Rate Coefficients in Astrochemistry*, ed. T. J. Millar & D. A. Williams, 49
- van Dishoeck, E. F. 2006, *Proceedings of the National Academy of Science*, 103, 12249
- van Dishoeck, E. F. & Blake, G. A. 1998, *ARA&A*, 36, 317
- van Dishoeck, E. F., Blake, G. A., Jansen, D. J., & Groesbeck, T. D. 1995, *ApJ*, 447, 760
- van Dishoeck, E. F. & Helmich, F. P. 1996, *A&A*, 315, L177
- van Dishoeck, E. F., Jonkheid, B., & van Hemert, M. C. 2006, *Faraday Discussions*, 133, 231
- van Dishoeck, E. F., Blake, G. A., Draine, B. T., & Lunine, J. I. 1993, in *Protostars and Planets III*, ed. E. H. Levy & J. I. Lunine, 163–241
- van Kempen, T. A., Doty, S. D., van Dishoeck, E. F., Hogerheijde, M. R., & Jørgensen, J. K. 2008, *A&A*, 487, 975
- van Thiel, M., Becker, E. D., & Pimentel, G. C. 1957, *J. Chem. Phys.*, 27, 486
- Vázquez-Semadeni, E., Ballesteros-Paredes, J., & Klessen, R. S. 2003, *ApJ*, 585, L131
- Venjaminov, S. & Prendergast, F. 1997, *Ana. Biochem.*, 248, 234
- Visser, R., van Dishoeck, E. F., Doty, S. D., & Dullemond, C. P. 2009, *A&A*, 495, 881
- Viti, S., Collings, M. P., Dever, J. W., McCoustra, M. R. S., & Williams, D. A. 2004, *MNRAS*, 354, 1141
- Watanabe, N., Horii, T., & Kouchi, A. 2000, *ApJ*, 541, 772
- Watanabe, N. & Kouchi, A. 2002, *ApJ*, 567, 651
- Watanabe, N., Shiraki, T., & Kouchi, A. 2003, *ApJ*, 588, L121
- Westley, M. S., Baragiola, R. A., Johnson, R. E., & Baratta, G. A. 1995a, *Nature*, 373, 405
- Westley, M. S., Baragiola, R. A., Johnson, R. E., & Baratta, G. A. 1995b, *Nature*, 373, 405
- Westley, M. S., Baragiola, R. A., Johnson, R. E., & Baratta, G. A. 1995c, *Planet. Space Sci.*, 43, 1311
- Whittet, D. C. B. 1992, *Dust in the galactic environment*
- Whittet, D. C. B., Gerakines, P. A., Hough, J. H., & Shenoy, S. S. 2001, *ApJ*, 547, 872
- Whittet, D. C. B., Gerakines, P. A., Tielens, A. G. G. M., et al. 1998, *ApJ*, 498, L159
- Willacy, K. 2007, *ApJ*, 660, 441
- Willacy, K. & Langer, W. D. 2000, *ApJ*, 544, 903
- Willacy, K. & Millar, T. J. 1998, *MNRAS*, 298, 562
- Williams, D. A. 1968, *ApJ*, 151, 935
- Willner, S. P., Gillett, F. C., Herter, T. L., et al. 1982, *ApJ*, 253, 174
- Wilson, C. D., Mason, A., Gregersen, E., et al. 2003, *A&A*, 402, L59
- Woodall, J., Agúndez, M., Markwick-Kemper, A. J., & Millar, T. J. 2007, *A&A*, 466, 1197
- Woon, D. E. 2002, *ApJ*, 571, L177
- Yabushita, A., Kanda, D., Kawanaka, N., Kawasaki, M., & Ashfold, M. N. R. 2006, *J. Chem. Phys.*, 125, 3406

- Young, C. H., Jørgensen, J. K., Shirley, Y. L., et al. 2004, *ApJS*, 154, 396
Zasowski, G., Kemper, F., Watson, D. M., et al. 2009, *ApJ*, 694, 459

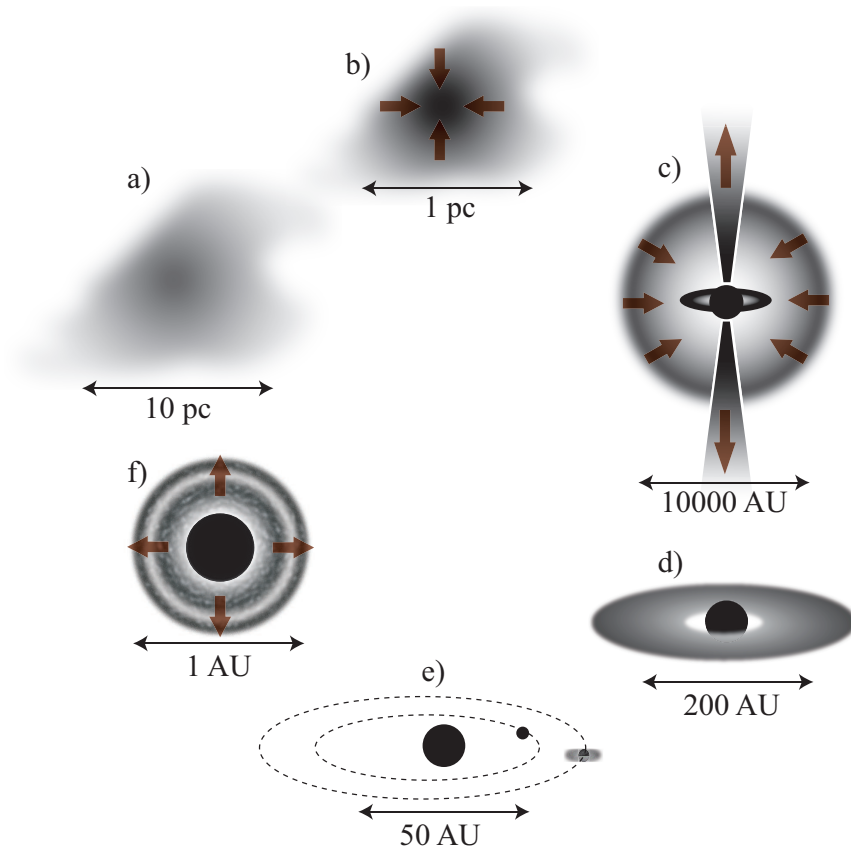
NEDERLANDSE SAMENVATTING

De eerste chemie

Veertien miljard jaar geleden ontstaat uit de Big Bang een heet en stralingsgedomineerd universum waarin zelfs atomen niet kunnen overleven. Het heelal expandeert, wordt kouder en de eerste atomen ontstaan. Het heelal wordt ook donker. De 'Dark Ages' beginnen en de eerste chemische reactie vindt plaats. Een ion en een atoom gaan een binding aan en het eerste molecuul in het heelal is een feit. Andere moleculen volgen, en dat terwijl koolstof, zuurstof en alle andere zwaardere elementen nog moeten worden gevormd in sterren. Sterren die miljoenen jaren later ontstaan en het heelal verlichten. De 'Dark Ages' komen tot een eind. In de sterren wordt waterstof omgezet in koolstof en zuurstof en zwaardere atomen. Deze elementen worden later door de sterren de ruimte ingeslingerd tijdens hun explosieve einde. In de miljarden jaren die volgen wordt op deze manier de ruimte tussen de sterren gevuld met materie - het ijle interstellair medium - dat meer en meer zware elementen evenals kleine stofdeeltjes gaat bevatten. De organische chemie die we op Aarde kennen, op andere hemellichamen in ons zonnestelsel, rond jonge sterren en in afgelegen melkwegstelsels vindt haar oorsprong in deze kosmische explosies in een periode dat het heelal net een miljard jaar oud was.

Kosmische kraamkamers

Het bestuderen van sterren is bijna net zo oud als de mensheid zelf. Het onderzoek aan het interstellair medium is net 100 jaar oud. Daar waar deze materie geconcentreerd voorkomt wordt bij zichtbare golf lengtes de blik op de achterliggende sterren verhinderd, zoals de zon schuil gaat achter wolken in onze dampkring. De donkere interstellair wolken bestaan uit gas en stof en vormen de materie waaruit nieuwe sterren ontstaan. Ze zijn koud (-263 °C) en roteren langzaam. Sommige kosmische wolken bevatten genoeg materie om onder hun eigen zwaartekracht te bezwijken (Figuur 1). De wolk stort ineen, wordt warmer en gaat sneller roteren om energie en impuls te behouden. Temperatuur en dichtheid lopen dusdanig op dat een protoster ontstaat. De jonge ster omringt zich met stof en gas uit de oorspronkelijke wolk. Deze materie wordt verder door de ster opgezogen of door straling van de ster weggeblazen. Daarbij ontstaat rond de ster een schijf bestaand uit materiaal waaruit later planeten vormen: stofdeeltjes botsen, plakken aan elkaar en gruis, kiezel, rotsen en uiteindelijk kometen en planeten kunnen ontstaan. De chemische evolutie van deze proto-planetaire schijf is bepalend voor het ontstaan van (pre)biotische moleculen op planeten, en daarmee van het leven zelf. Een goed begrip van dit proces vereist kennis van de processen die de chemie in een proto-planetaire schijf sturen.



Figuur 1 – De geboorte van een ster start in een interstellaire wolk (a) die onder zijn eigen gewicht ineen stort (b) en een protoster vormt (c). Hieruit ontstaat een reguliere hoofdreeks ster die wordt omhuld door een schijf van gas en stof (d). Dit materiaal vormt de basis voor de planeten (e). Wanneer de ster sterft, wordt nieuw materiaal in de ruimte gestuwd (f) en de cyclus kan opnieuw beginnen.

Ijs en gas rond jonge sterren

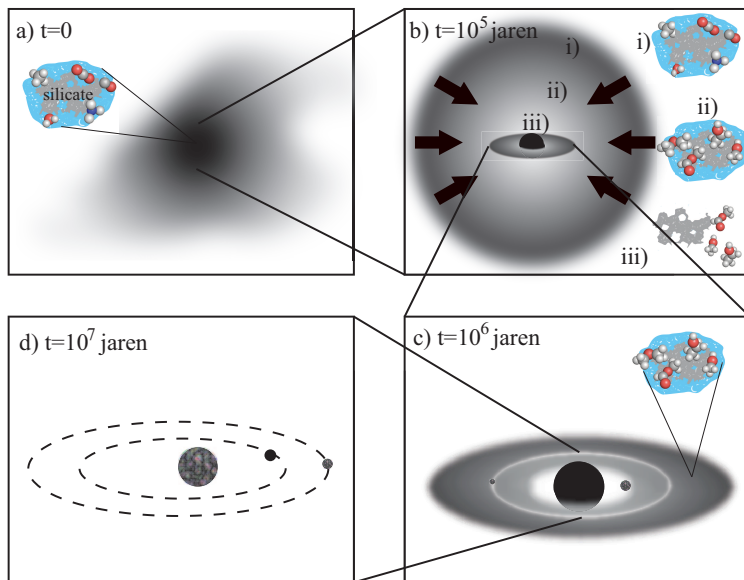
Interstellaire wolken en proto-planetaire schijven bestaan uit een mengsel van gas en microscopisch kleine stofdeeltjes. De chemische samenstelling van deze materie verandert gedurende het stervormingsproces. In de eerste fase, voordat de wolk gravitationeel instabiel wordt, bevinden zich de meeste atomen (waterstof, stikstof, zuurstof en koolstof) en moleculen (zoals moleculair waterstof en koolstofmonoxide, CO) in de gasfase. De dichtheden in de wolk zijn te gering om via drie-deeltjes botsingen chemische reacties te realiseren. Bij zo'n botsing vormen twee deeltjes een nieuw molecuul en het derde deeltje voert gelijktijdig overvloedige energie af, zodat het reactieproduct chemisch stabiliseert. Zelfs botsingen van twee deeltjes in de ruimte zijn zelden, tenzij één van de deeltjes

geladen is en de botsingspartner over een grotere afstand kan aantrekken. Vergeleken met de Aarde, waar reacties vooral via drie-deeltjes botsingen plaatsvinden, worden chemische gasfase processen in de ruimte vrijwel volledig gedomineerd door wisselwerkingen tussen ionen en en neutrale deeltjes. De resulterende reactie producten vormen exotische moleculen, zoals onverzadigde koolstofketens, die in onze eigen atmosfeer niet voorkomen.

Wanneer de dichtheid in de wolk toeneemt, verandert de chemie. Meer en meer gasfase deeltjes vriezen vast op de koude stofdeeltjes en vormen aan het oppervlak een laagje ijs. Zelfs koolstofmonoxide kan bij de lage temperaturen in de wolk (-263 °C) vastvriezen op de stofdeeltjes. Atomair en moleculair waterstof vriest bij nog lagere temperaturen vast, maar kan bij ook wat hogere temperaturen kortstondig op een oppervlak vertoeven en is daarbij zeer mobiel. Dit vormt de basis voor een andere chemie – in de vaste stof – waarbij moleculen ontstaan door reacties van waterstof met andere moleculen (of zichzelf) die zitten vastgevroren op het oppervlak. In reacties van waterstof atomen met zuurstof wordt water gevormd en waterstof atoom interacties met koolmonoxide ijs leidt tot de vorming van formaldehyde en methanol. Op het moment dat de protoster begint te stralen bevat het circumstellaire ijs vooral water, koolstofmonoxide, koolstofdioxide, en in mindere mate methaan, methanol en ammoniak. De bouwstenen voor een complexe organische chemie bevinden zich dus in het ijs aan het oppervlak van circumstellaire stofdeeltjes die zelf het materiaal vormen waaruit planeten ontstaan.

Meer complexe moleculen, zoals ethanol, ontstaan vervolgens in het ijs door de bestraling met ultraviolet licht dat afkomstig is van de protoster en kosmische achtergrondstraling (Figuur 2). Ook thermische effecten, waarbij het ijs opwarmt, spelen een rol. Ijs dat zich in de buurt van de protoster bevindt, sublimeert, waarmee een volgende chemische fase wordt ingeleid: vaste stof reactieproducten kunnen nu met elkaar en reeds voorhanden moleculen in de gasfase reageren. Ijs dat niet verdampt wordt uiteindelijk een bestanddeel van kometen en planeten. Vaste stof astrochemische processen tijdens stervorming bepalen derhalve ook de chemische ontwikkeling van planeten.

Met behulp van spectroscopie is het mogelijk deze chemische evolutie waar te nemen; moleculen absorberen of emitteren licht bij zeer specifieke golflengtes. Het resulterende spectrum is uniek. Door bv. absorptiesignalen te meten in sterlicht dat door een interstellaire wolk of circumstellaire schijf heengaat, kan de dichtheid van een bepaald molecuul worden gemeten. Hiervoor is het wel noodzakelijk dat de spectrale eigenschappen van een molecuul bekend zijn en dit is te realiseren met laboratorium metingen. In het laboratorium worden ook de chemische processen onderzocht die onder astronomische omstandigheden een belangrijke rol spelen. Dit is noodzakelijk omdat chemische processen in de ruimte zeer langzaam plaatsvinden. Astronomische waarnemingen laten ‘snap-shots’ zien van verschillende fases in de chemische evolutie in het heelal. Met laboratorium werk is het mogelijk deze ‘snap-shots’ in een compleet beeld in te passen.



Figuur 2 – Een schematische weergave van de ijs evolutie tijdens ster- en planeetvorming. In donkere wolken wordt ijs gevormd bestaand uit eenvoudige componenten (a, b.i). Warmte en UV straling van de protoster veroorzaken een complexer ijs mengsel (b.ii), dat in de buurt van de protoster verdampt (b.iii). Ijs dat niet verdampt eindigt in de proto-planetaire schijf (c) en vormt het materiaal waaruit planeten en kometen ontstaan (d).

Vaste stof laboratorium astrofysica

Vaste stof astrofysisch laboratorium onderzoek heeft twee doelstellingen: spectra van ijs zijn nodig om astronomische waarnemingen te interpreteren en fysisch-chemische informatie is nodig om de processen te karakteriseren die een rol spelen tijdens de vorming van sterren en planeten. Ijs spectroscopie wordt vooral in het infrarood toegepast. De infrarode spectra hangen af van het soort ijs, bv. water of koolstofmonoxide, en of het ijs puur is of gemengd met andere moleculen. Een vergelijk tussen een laboratorium en astronomisch spectrum laat zien welk soort ijs een rol speelt tijdens stervorming en of het gelaagd of gemengd ijs betreft.

De tweede doelstelling – het simuleren van astrofysische en astrochemische processen onder laboratorium gecontroleerde en astronomisch relevante omstandigheden – vereist dat experimenten onder zeer goede vacuüm condities en bij zeer lage temperaturen plaatsvinden. De druk in de dichtste interstellaire wolken is nog steeds bijzonder laag en vergelijkbaar met het beste vacuüm dat op Aarde kan worden gerealiseerd. In het laboratorium worden daarom ultra-hoge vacuüm systemen gebruikt waarin ijs op een helium gekoeld oppervlak tot -260 °C kan worden afgekoeld. Door de invloed van straling en warmte

te bestuderen is het mogelijk te voorspellen hoe een vergelijkbaar inter- of circumstellair ijs op straling en warmte in de ruimte reageert. Laboratorium werk maakt het mogelijk astronomische waarnemingen te interpreteren. De waarnemingen leveren wederom informatie waaruit nieuwe experimenten voortvloeien. De conclusies die daaruit volgen worden met nieuwe waarnemingen getest. De kring is rond. Dit proefschrift is op een identieke wijze opgebouwd.

Dit proefschrift: complexe processen in eenvoudige ijzen

Ijzen spelen dus een belangrijke rol gedurende de verschillende fases van ster- en planeetvorming, van interstellaire wolken tot kometen zoals we die kennen uit eigen zonnestelsel. Hun evolutie is bepalend voor de chemie zoals die op Aarde plaatsvindt. Hun evolutie bepaalt op dit moment ook de toekomstige chemie in planetenstelsels rond andere sterren. Ook de vraag hoe het leven op Aarde is ontstaan en hoe waarschijnlijk het is, dat leven elders is of zal ontstaan, kan alleen worden beantwoord wanneer duidelijk is welke rol inter- en circumstellair ijs daarbij speelt. Het overkoepelend doel van dit proefschrift is om astronomische waarnemingen en laboratorium experimenten te combineren en te begrijpen hoe ijs vormt, hoe het verandert en hoe het verdampt. De belangrijkste conclusie die uit dit onderzoek volgt is, dat het mogelijk is om in eenvoudige ijzen de complexe processen die optreden tijdens verhitting, bestraling met UV licht of samenwerking met andere ijs deeltjes, kwantitatief te beschrijven. Dit is de voorwaarde om deze processen in astrochemische modellen mee te nemen en middels waarnemingen te testen. Zeker nu in de komende jaren nieuwe waarneemfaciliteiten operationeel worden, waarmee de evolutie van ijs in de verschillende fases gedetailleerd in beeld kan worden gebracht.

Met de lancering van de Spitzer ruimte telescoop, enkele jaren geleden, werd het voor de eerste keer mogelijk om ijs te onderzoeken rond jonge sterren met een massa vergelijkbaar met die van onze eigen zon. Tot dan toe waren alleen veel zwaardere sterren observationeel toegankelijk. Uit dit onderzoek van ijs rond een groot aantal protosterren volgt dat eenvoudig ijs – met water, methaan en methanol – wordt gevormd in een reeks opeenvolgende processen: hydrogenatie van atomen, accretie op het oppervlak, hydrogenatie van koolstofmonoxide, zuurstof en stikstof addities en diffusie in de buurt van de protoster. Hoe later een molecuul vormt in deze reeks, des te meer variatie wordt er gevonden in de moleculabundanties voor verschillende bronnen. Dit is bv. het geval voor methanol en de organische chemie op exo-planeten kan dus behoorlijk verschillen van die op onze eigen planeet (Hoofdstukken 2 en 3).

De invloed van warmte en ijs compositie op de dynamica van waterrijk ijs wordt behandeld in Hoofdstukken 4–6. Laboratorium werk aan ijs levert spectroscopische data en gegevens waarmee segregatie en desorptie worden gekarakteriseerd. Door koolstofdioxide (CO₂) toe te voegen aan waterijs wordt de ijs matrix van waterstofbruggen danig verstoord, hetgeen resulteert in significante spectrale veranderingen van de water ijs absorpties.

Voordat gemengd H₂O-CO₂ ijs sublimeert tijdens verhitting, verandert eerst de struc-

tuur waarbij water en koolstofdioxide worden gescheiden. Deze segregatie maakt het mogelijk om de verwarming van ijs gedurende stervorming zichtbaar te maken. Daarmee kan segregatie worden gebruikt als een thermische methode om de evolutie van een protoster te beschrijven. De segregatie van ijsmengsels van water met koolstofmonoxide of koolstofdioxide vindt plaats door middel van een snel diffusieproces aan de oppervlakte van het ijs, gevolgd door een langzamer diffusieproces in de rest van het ijs. De water en koolstofdioxide segregatie is veel sneller dan tot nu toe werd aangenomen en wordt in een proto-stellare omgeving reeds relevant bij temperaturen van rond de 30 K (- 243 °C), waarmee kan worden verklaard dat er puur koolstofdioxide ijs wordt waargenomen rond protosterren.

Een ander effect dat optreedt bij verwarming is de verdamping van ijs, waardoor moleculen in de gasfase terecht komen. Uit laboratorium studies volgt dat een gemengd en puur ijs op sterk verschillende wijze verdampen. Vooral de aanwezigheid van vluchtige stoffen in water ijs wordt als een belangrijk uitgangspunt gezien, dat bepalend is voor de gas samenstelling in de schijf of de ijs samenstelling in kometen. Kwantitatieve data ontbreken grotendeels. Door systematisch H₂O ijs van CO₂ en CO te voorzien, hebben we een model ontwikkeld waarmee het mogelijk is om het proces voor verschillende laboratorium omstandigheden weer te geven en toe te passen op astronomische omstandigheden. Hiermee is het voor de eerste keer mogelijk gebleken de verdamping van ijsmengsels zoals gemeten in het laboratorium te koppelen aan astrofysisch modellen.

Ijs kan ook verdampen als gevolg van UV bestraling (Figuur 2). Hierdoor kunnen – ongeacht de heersende temperaturen – moleculen vanuit het ijs in de gasfase worden gebracht, d.w.z. ook voor temperaturen onder de sublimatie temperatuur. Theoretische studies voorspellen echter dat UV fotodesorptie alleen efficiënt is na voorafgaande UV fotodissociatie, en verwaarloosbaar langzaam in alle andere gevallen. Hoofdstukken 7 en 8 laten echter zien, dat de UV fotodesorptie snelheden van koolstofmonoxide – dat niet dissocieert – en koolstofdioxide – dat wel uiteenvalt – vergelijkbaar zijn. Water en methanol ijs blijken ook efficiënt te fotodesorberen (Hoofdstukken 9 en 10). Dit verklaart astronomische waarnemingen van water, koolstofmonoxide en methanol in de gasfase bij temperaturen waarbij deze zouden moeten zijn vastgevroren op stofdeeltjes.

UV bestraling van ijs kan ook een complexe fotochemie initiëren waarbij het uiteenvallen van ijs moleculen aan de basis staat van nieuwe chemische reacties. Dit is voor de eerste keer kwantitatief onderzocht voor methanol ijs en verschillende ammoniak houdende ijs mengsels (Hoofdstukken 10 en 11). De fotochemie van methanol ijs wordt gezien als de bron waaruit complexe moleculen rond protosterren vormen. Astronomische gasfase waarnemingen laten inderdaad een veelvoud aan chemische producten zien – organische zuren, esters, ethers en suikers – in de nabijheid van jonge sterren waar ijs wordt bestraald met UV licht en thermisch verdampt (Figuur 2). Het is tot nu toe niet mogelijk geweest om deze hypothese te testen, omdat kwantitatieve informatie niet voorhanden was. In Hoofdstuk 10 wordt aangetoond dat alle astronomische geïdentificeerde complexe moleculen door fotochemische reacties in methanol ijs kunnen ontstaan. De waargenomen verhoudingen voor verschillende astronomische omgevingen blijken te kunnen worden verklaard door de opeenvolgende vorming van moleculen voor toenemende temperaturen. De laboratorium resultaten zijn ook consistent met de relatieve hoeveelheden aan com-

plexe moleculen die in kometen zijn aangetroffen. Dit is mogelijkwijze gerelateerd aan de oorsprong van een pre-biotische chemie in ons zonnestelsel.

Hoofdstuk 11 bouwt hierop voort met vergelijkbaar onderzoek aan ammoniak houdend ijs met het doel ook de pre-biotisch relevante stikstof chemie te bestuderen. De belangrijkste conclusie is dat complexe ijs chemie, resulterend in de vorming van bv. eenvoudige aminozuren, kan worden beschreven, uitgaande van eenvoudige ijsmengsels die twee i.p.v. zes van de belangrijkste bestanddelen van inter- en circumstellair ijs bevatten. Dit maakt het mogelijk om de pre-biotische evolutie van aminozuren en organische suikers uiteindelijk te voorspellen.

Astronomische ijs waarnemingen laten alleen spectra zien van de meest voorkomende (en veelal dus minder complexe) moleculen. Complexere moleculen kunnen niet rechtstreeks in de vaste stof worden geïdentificeerd. Het is wel mogelijk om deze moleculen in de gasfase waar te nemen onder de aanname dat het verdampte ijs producten betreft. In het geval van thermische verdamping is dit problematisch. De benodigde hogere temperaturen zijn niet typisch voor de koude fases in het stervormingsproces. Bovendien is het moeilijk om dan gasfase reactieproducten te koppelen aan oorspronkelijk ijs bestanddelen. De situatie is anders bij verdamping door middel van UV bestraling of een ander niet-thermisch proces. In dit geval kunnen gasfase moleculen bij lagere temperaturen worden gebruikt als een analytische probe voor de oorspronkelijke ijs samenstelling. Dit is het onderwerp van Hoofdstuk 12, waar in een proefstudie de gas en ijs abundanties van twee moleculen worden vergeleken voor een reeks van protosterren. De resultaten zijn in overeenstemming met een model waarin de ijs moleculen constant door UV straling in de gasfase worden gebracht, maar een groter aantal protosterren is nodig om dit éénduidig te kunnen concluderen.

CURRICULUM VITAE

I was born the 27th of August 1982 to Christina and Tomas Öberg in Nyköping, Sweden; a town most noted for Nyköping Gästabud (Banquet) in 1317 when King Birger entertained his two brothers regally before throwing them into the castle dungeon, the dungeon key into the moot and left the brothers to starve to death. At the age of six, the family relocated to the beautiful naval town Karlskrona, in the south of Sweden, where I attended primary, secondary and high school (Chapmanskolan) – my high school senior project was supervised by my father and resulted in my first publication. Equally enticed by history, literature, art and science during most of these years I decided to focus on a science career and after a challenge from my father I applied and was admitted to the California Institute of Technology (Caltech).

At Caltech I pursued research projects in physical chemistry and astrochemistry under the supervision of Prof. Jack Beauchamp and Prof. Geoffrey Blake, resulting in two publications. The summer between junior and senior year I first visited Leiden, with a Caltech summer research fellowship, and at the end of the summer, Leiden University and Prof. Dr. Ewine van Dishoeck had become my top choice for graduate school. I received my B.Sc. in chemistry, cum laude, 2005 and took up a Ph.D. position under the supervision of Prof. Dr. Ewine van Dishoeck and Prof. Dr. Harold Linnartz in Leiden the same fall.

During the following four years I researched the chemistry of interstellar ices through laboratory simulations in the Raymond and Beverly Sackler Laboratory for Astrophysics, ice observations with the *Spitzer Space Telescope* and gas observations with the IRAM 30m telescope (Pico Veleta, Spain) and the JCMT (Hawaii, U.S.A.). The result is this thesis. The different chapters have been presented at conferences in Paris (France), Belfast (UK), London (UK), Hong Kong (China), Arcachon (France) and Green Bank (U.S.) and at visits to Estec (Netherlands) and a number of U.S. institutes including University of Arizona, UC Santa Cruz, Berkeley, the Harvard-Smithsonian Center for Astrophysics and University of Michigan. In addition, I have had longer working visits to Université de Cergy-Pontoise in Paris, France. In Leiden I also supervised two M.Sc. projects and was a teaching assistant for courses on Pulsars and on research for B.Sc. students.

In October I will start a three-year postdoctoral position as a Hubble fellow at the Harvard-Smithsonian Center for Astrophysics (Cambridge, U.S.).

Refereed papers

1. *Formation rates of complex organics in UV irradiated CH₃OH-rich ices I: Experiments (Chapter 10)*
Öberg K. I. ; Garrod, R. T.; van Dishoeck, E. F.; Linnartz, H., 2009, accepted for publication in *Astronomy & Astrophysics*
2. *Quantification of segregation dynamics in ice mixtures (Chapter 5)*
Öberg K. I. ; Fayolle, E. C.; Cuppen, H. M.; van Dishoeck, E. F.; Linnartz, H., 2009, accepted for publication in *Astronomy & Astrophysics*
3. *Photodesorption of ices II: H₂O and D₂O (Chapter 9)*
Öberg K. I. ; Visser, R.; van Dishoeck, E. F.; Linnartz, H., 2009, *Astrophysical Journal*, volume 93, pages 1209-1218
4. *Photodesorption of ices I: CO, N₂ and CO₂ (Chapter 8)*
Öberg K. I. ; van Dishoeck, E. F.; Linnartz, H., 2009, *Astronomy & Astrophysics*, volume 496, pages 281-293
5. *Cold gas as an ice diagnostic toward low mass protostars (Chapter 12)*
Öberg K. I. ; Bottinelli, S.; van Dishoeck, E. F., 2009, *Astronomy & Astrophysics*, volume 494, pages L13-L16
6. *The c2d Spitzer spectroscopic survey of ices around low-mass young stellar objects, III. CH₄ (Chapter 3)*
Öberg K. I. ; Boogert, A.C.A.; Pontoppidan, K.M.; Blake, G.A.; Evans, N.J.; Lahuis, F.; van Dishoeck, E.F., 2008, *Astrophysical Journal*, volume 678, pages 1032-1041
7. *The c2d Spitzer spectroscopic survey of ices around low-mass young stellar objects. II. CO₂*
Pontoppidan, K. M.; Boogert, A. C. A.; Fraser, H. J.; van Dishoeck, E. F.; Blake, G. A.; Lahuis, F.; **Öberg, K. I.**; Evans, N. J., II; Salyk, C., 2008, *Astrophysical Journal*, volume 678, pages 1005-1031
8. *The c2d Spitzer spectroscopic survey of ices around low-mass young stellar objects. I. H₂O and the 5-8 μm bands*
Boogert, A. C. A.; Pontoppidan, K. M.; Knez, C.; Lahuis, F.; Kessler-Silacci, J.; van Dishoeck, E. F.; Blake, G. A.; Augereau, J.-C.; Bisschop, S. E.; Bottinelli, S.; Brooke, T. Y.; Brown, J.; Crapsi, A.; Evans, N. J., II; Fraser, H. J.; Geers, V.; Huard, T. L.; Jørgensen, J. K.; **Öberg, K. I.**; Allen, L. E.; Harvey, P. M.; Koerner, D. W.; Mundy, L. G.; Padgett, D. L.; Sargent, A. I.; Stapelfeldt, K. R., 2008, *Astrophysical Journal*, volume 678, pages 985-1004
9. *Photodesorption of CO ice (Chapter 7)*
Öberg K. I. ; Fuchs, G.W.; Awad, Z.; Fraser, H.J.; Schlemmer, S.; van Dishoeck, E. F.; Linnartz, H., 2007, *Astrophysical Journal Letters*, volume 662, pages L23-L26

10. *Band profiles and band strengths in mixed H₂O:CO ices*
Bouwman, J.; Ludwig, W.; Awad, Z.; **Öberg K. I.**; Fuchs, G.W.; van Dishoeck, E. F.; Linnartz, H., 2007, *Astronomy & Astrophysics*, volume 476, pages 995-1003
11. *Effects of CO₂ on band profiles and band strengths of H₂O in mixed H₂O:CO₂ ices (Chapter 4)*
Öberg K. I.; Fraser, H.J.; Boogert, A.C.A.; Bisschop, S.E.; Fuchs, G.W.; van Dishoeck, E. F.; Linnartz, H., 2007, *Astronomy & Astrophysics*, volume 462, pages 1187-1198
12. *Desorption rates and sticking coefficients of CO and N₂ interstellar ices*
Bisschop, S. E.; Fraser, H. J.; **Öberg, K. I.**; van Dishoeck, E. F.; Schlemmer, S., 2006, *Astronomy & Astrophysics*, volume 449, pages 1297-1309
13. *Simple optical sensors for amine vapors based on dyed silica microspheres*
Öberg, K. I.; Hodyss, R.; Beauchamp J. L., 2006, *Sensors and Actuators*, volume 115, pages 79-85
14. *Competition between CO and N₂ desorption from interstellar ices*
Öberg K. I.; van Broekhuizen, F.; Fraser, H. J.; Bisschop, S. E.; van Dishoeck, E. F.; Schlemmer, S., 2005, *Astrophysical Journal*, volume 621, pages L33-L36
15. *Methane abundance variations toward the massive protostar NGC 7538 IRS 9*
Boogert, A. C. A.; Blake, G. A.; **Öberg, K. I.**, 2004, *Astrophysical Journal*, volume 615, pages 344-353
16. *Distribution and levels of brominated flame retardants in sewage sludge*
Öberg K.; Öberg, T.; Warman, C., 2002, *Chemosphere*, volume 48, pages 805-809

AFTERWORD

I feel, and have always felt, with Kant that the starry heavens above me and the moral law within me are most worthy of our investigation and our wonder. The Sterrewacht taught me how to study the stars. Its expectation of excellence and dedication challenged me to make this thesis as good as it possibly could be, its continuous support made the hard work possible – it made it fun. Credit also to the dedicated support staff at the Sterrewacht, who have always been quick to help when I have encountered computer problems or needed assistance with paper work.

The roots of this thesis go deeper than my arrival to Leiden. They go first and foremost to my extraordinary family, whose passion for exploring and preserving this world trained me to be a researcher long before I knew what it was, and who continue to inspire everything I do. Pappa, Mamma, Lars and Erik, I know I have lived far away for a long time, but knowing that you are there whenever it matters is my foundation. Lars and Erik you have been the guardians of my mind, ensuring that it never lost touch with exploring topics outside of science – my lasting passion for the humanities is credit to you.

Nine years ago, a dedicated group of high school teachers gave me the confidence to apply to Caltech. Caltech was a birth through fire experience into science, which taught me to think, to ask questions and to solve problems as I scarce had thought my mind capable of. I cannot imagine a better training ground for a scientist than I was given there, both in the class room and in the research groups of Jack Beauchamp and Geoffrey Blake - the ground work for this thesis was laid there. Geoff first introduced me to the wonders of astrochemistry and gave me my first telescope experience. The telescope was the Keck at Hawaii, and no surprise I have been in the field ever since. Caltech may be a scientist's playground but without my adopted family, Bernadette, Courtney, Hesper, Jackie and Vicki, I would probably have gone insane under the workload – I really cannot wait to be back in the U.S. with you.

The actual thesis work began four years ago when I started by Ph.D. project in the astrochemistry and laboratory astrophysics groups at the Sterrewacht. It has been a privilege to be your colleague and I have enjoyed our, sometimes rather lively, discussions about science and life outside of it. I am a better experimentalist, a better observer and even learned some modeling because of you. My Ph.D. had a flying start because of the previous work of Willem Schutte, Fleur van Broekhuizen, Helen Fraser, Stephan Schlemmer and Guido Fuchs in the Sackler lab, especially on CRYOPAD, and their impact on seven of the thesis chapters is thus considerable. I also learned to teach during the past two years, thanks to Saskia and Edith, who showed great patience in training me to be a supervisor. My learning experiences during my Ph.D. have not been limited to Leiden; this thesis has benefitted from discussions and collaborations within the Spitzer *c2d* team, especially Adwin Boogert and Klaus Pontoppidan, and with Sandrine Bottinelli and Rob Garrod and many others.

Several of my colleagues and collaborators have become dear friends, and while there is too little space to mention you all – I have been too fortunate in the number of good people surrounding me – if I could dedicate the thesis a second time, it would be to you. My past and current office mates, Bastiaan, Claire, Kalle, Saskia and Suzanne, have often been first to share both my frustrations and my triumphs and being able to vent to you pulled me through the less triumphant times. Suzanne you were my first friend here and having you in Leiden for two years made the hard times less hard and the good times better. Tonie and Christian, and Jeanette, I am sorry to abandon you – your care and distracting capabilities have ensured that I never really lost myself in work. To you and my other fellow Scandinavians: it has been amazing to have a bit of home here in Leiden.

At the end, I am overwhelmed with how my life has worked out during the past eight years. I had rather outrageous dreams of the kind of career I wanted in high school. Or so I thought. Because of your support and your belief in me, reality has been better.

Two things fill the mind with ever-increasing wonder and awe,
the more often and the more intensely the mind of thought is drawn to them:
the starry heavens above me and the moral law within me.

Translation from Critique of Practical Reason by Immanuel Kant